Introduction to High Energy Physics

DONALD H. PERKINS

4th edition

Introduction to High Energy Physics, 4th Edition

This highly regarded text provides an up-to-date and comprehensive introduction to modern particle physics.

Extensively rewritten and updated, this fourth edition includes all the recent developments in elementary particle physics, as well as its connections with cosmology and astrophysics. As in previous editions, the balance between experiment and theory is continually emphasised. The stress is on the phenomenological approach and basic theoretical concepts rather than rigorous mathematical detail. Short descriptions are given of some of the key experiments in the field, and how they have influenced our thinking. Although most of the material is presented in the context of the Standard Model of quarks and leptons, the shortcomings of this model and new physics beyond its compass (such as supersymmetry, neutrino mass and oscillations, GUTs and superstrings) are also discussed. The text includes many problems and a detailed and annotated further reading list.

This is a text suitable for final-year physics undergraduates and graduate students studying experimental or theoretical particle physics.

DONALD H. PERKINS is Emeritus Professor of Physics in Oxford University. After receiving his first degree and Ph.D. at Imperial College, University of London, he joined Bristol University as G.A. Wills Research Associate, later becoming Lecturer and then Reader in physics. He spent the year 1955–6 and part of 1961 at the Lawrence Radiation Laboratory, University of California, and in 1966 became Professor of Elementary Particle Physics at Oxford. He is a Fellow of the Royal Society of London and his awards include the Guthrie Medal of the Institute of Physics, the Holweck Medal of the Société Francaise de Physique and the Royal Medal of the Royal Society. His early experimental research was in studies of high energy cosmic rays. Later he moved to the field of neutrino physics, where he was involved in the discovery and early studies of neutral weak currents, the quark substructure of nucleons and interquark interactions (quantum chromodynamics), using accelerator neutrino beams. Professor Perkins has served on the UK Science and Engineering Research Council, as a member and chairman of the CERN Scientific Policy Committee and as UK delegate to the CERN Council. He is an author of *Study of Elementary Particles by the Photographic Method* (with C.F. Powell and P.H. Fowler).

Introduction to High Energy Physics

4th Edition

Donald H. Perkins
University of Oxford

CAMBRIDGE
UNIVERSITY PRESS



PUBLISHED BY THE PRESS SYNDICATE OF THE UNIVERSITY OF CAMBRIDGE
The Pitt Building, Trumpington Street, Cambridge, United Kingdom

CAMBRIDGE UNIVERSITY PRESS
The Edinburgh Building, Cambridge CB2 2RU, UK
40 West 20th Street, New York, NY 10011-4211, USA
10 Stamford Road, Oakleigh, VIC 3166, Australia
Ruiz de Alarcón 13, 28014, Madrid, Spain
Dock House, The Waterfront, Cape Town 8001, South Africa

http://www.cambridge.org

Fourth edition © Donald H. Perkins 2000

This book is in copyright. Subject to statutory exception
and to the provisions of relevant collective licensing agreements,
no reproduction of any part may take place without
the written permission of Cambridge University Press.

First published by Addison-Wesley Publishing Company Inc. 1972
Fourth edition first published by Cambridge University Press 2000
Reprinted 2001

Printed in the United Kingdom at the University Press, Cambridge

Typeface Times 11/14pt. *System* LaTeX 2_ε [DBD]

A catalogue record of this book is available from the British Library

Library of Congress Cataloguing in Publication data

Perkins, Donald H.
Introduction to high energy physics / Donald H. Perkins. – 4th ed.
p. cm. ISBN 0 521 62196 8 (hc.)
1. Particles (Nuclear physics) I. Title.
QC93.2.P47 1999
529.7'2–dc21 98-51723 CIP

ISBN 0 521 62196 8 hardback

Contents

Preface *page* xi

1 Quarks and leptons **1**
1.1 Preamble 1
1.2 The Standard Model of particle physics 7
1.3 Particle classification: fermions and bosons 12
1.4 Particles and antiparticles 13
1.5 Free particle wave equations 16
1.6 Helicity states: helicity conservation 19
1.7 Lepton flavours 20
1.8 Quark flavours 22
1.9 The cosmic connection 26
Problems 33

2 Interactions and fields **35**
2.1 Classical and quantum pictures of interactions 35
2.2 The Yukawa theory of quantum exchange 36
2.3 The boson propagator 37
2.4 Feynman diagrams 38
2.5 Electromagnetic interactions 40
2.6 Renormalisation and gauge invariance 42
2.7 Strong interactions 43
2.8 Weak and electroweak interactions 46
2.9 Gravitational interactions 51
2.10 The interaction cross-section 51
2.11 Decays and resonances 55
Problems 61

3	**Invariance principles and conservation laws**	**63**
3.1	Translation and rotation operators	63
3.2	The parity operation	65
3.3	Pion spin and parity	66
3.4	Parity of particles and antiparticles	69
3.5	Tests of parity conservation	72
3.6	Charge conjugation invariance	73
3.7	Charge conservation and gauge invariance	75
3.8	Baryon and lepton conservation	79
3.9	CPT invariance	81
3.10	CP violation and T violation	81
3.11	Neutron electric dipole moment	83
3.12	Isospin symmetry	87
3.13	Isospin in the two-nucleon and pion–nucleon systems	88
3.14	Isospin, strangeness and hypercharge	91
	Problems	93
4	**Quarks in hadrons**	**95**
4.1	Charm and beauty; the heavy quarkonium states	95
4.2	Comparison of quarkonium and positronium levels	102
4.3	The baryon decuplet	109
4.4	Quark spin and colour	114
4.5	The baryon octet	115
4.6	Quark–antiquark combinations: the light pseudoscalar mesons	118
4.7	The light vector mesons	121
4.8	Other tests of the quark model	123
4.9	Mass relations and hyperfine interactions	126
4.10	Electromagnetic mass differences and isospin symmetry	129
4.11	Magnetic moments of baryons	130
4.12	Mesons built of light and heavy quarks	132
4.13	The top quark	134
	Problems	139
5	**Lepton and quark scattering**	**140**
5.1	The process $e^+e^- \to \mu^+\mu^-$	140
5.2	e^+e^- annihilation to hadrons	144
5.3	Electron–muon scattering, $e^-\mu^+ \to e^-\mu^+$	147
5.4	Neutrino–electron scattering, $\nu_e e \to \nu_e e$	150
5.5	Elastic lepton–nucleon scattering	154
5.6	Deep inelastic scattering and partons	155
5.7	Deep inelastic scattering and quarks	159

5.8	Experimental results on quark distributions in the nucleon	162
5.9	Sum rules	166
5.10	Summary	168
	Problems	168
6	**Quark interactions and QCD**	**171**
6.1	The colour quantum number	171
6.2	The QCD potential at short distances	172
6.3	The QCD potential at large distances: the string model	178
6.4	Gluon jets in e^+e^- annihilation	180
6.5	Running couplings in QED and QCD	181
6.6	Evolution of structure functions in deep inelastic scattering	186
6.7	Gluonium and the quark–gluon plasma	190
	Problems	192
7	**Weak interactions**	**194**
7.1	Classification	194
7.2	Lepton universality	195
7.3	Nuclear β-decay: Fermi theory	197
7.4	Inverse β-decay: neutrino interactions	201
7.5	Parity nonconservation in β-decay	202
7.6	Helicity of the neutrino	205
7.7	The $V - A$ interaction	206
7.8	Conservation of weak currents	209
7.9	The weak boson and Fermi couplings	210
7.10	Pion and muon decay	210
7.11	Neutral weak currents	213
7.12	Observation of $W^{\pm}$ and Z^0 bosons in $p\bar{p}$ collisions	215
7.13	Z^0 production at e^+e^- colliders	220
7.14	Weak decays of quarks. The GIM model and the CKM matrix	221
7.15	Neutral K mesons	226
7.16	CP violation in the neutral kaon system	232
7.17	Cosmological CP violation	237
7.18	D^0–$\bar{D}^0$ and B^0–$\bar{B}^0$ mixing	238
	Problems	239
8	**Electroweak interactions and the Standard Model**	**242**
8.1	Introduction	242
8.2	Divergences in the weak interactions	243
8.3	Introduction of neutral currents	245
8.4	The Weinberg–Salam model	246

8.5 Intermediate boson masses 248
8.6 Electroweak couplings of leptons and quarks 249
8.7 Neutrino scattering via Z exchange 250
8.8 Asymmetries in the scattering of polarised electrons by deuterons 253
8.9 Observations on the Z resonance 255
8.10 Fits to the Standard Model and radiative corrections 260
8.11 W pair production 262
8.12 Spontaneous symmetry breaking and the Higgs mechanism 263
8.13 Higgs production and detection 271
Problems 274

9 Physics beyond the Standard Model 276
9.1 Supersymmetry 277
9.2 Grand unified theories: the SU(5) GUT 278
9.3 Unification energy and weak mixing angle 280
9.4 Supersymmetric SU(5) 282
9.5 Proton decay 282
9.6 Neutrino mass: Dirac and Majorana neutrinos 284
9.7 Neutrino oscillations 287
9.8 Magnetic monopoles 299
9.9 Superstrings 300
Problems 301

10 Particle physics and cosmology 303
10.1 Hubble's law and the expanding universe 303
10.2 Friedmann equation 304
10.3 Cosmic microwave radiation: the hot Big Bang 307
10.4 Radiation and matter eras 311
10.5 Nucleosynthesis in the Big Bang 313
10.6 Baryon–antibaryon asymmetry 317
10.7 Dark matter 319
10.8 Inflation 326
10.9 Neutrino astronomy: SN 1987A 330
Problems 336

11 Experimental methods 338
11.1 Accelerators 338
11.2 Colliding-beam accelerators 343
11.3 Accelerator complexes 346
11.4 Secondary particle separators 346
11.5 Interaction of charged particles and radiation with matter 349

11.6 Detectors of single charged particles 355
11.7 Shower detectors and calorimeters 368
Problems 375

Appendix A *Table of elementary particles* 377
Appendix B *Milestones in particle physics* 379
Appendix C *Clebsch–Gordan coefficients and d-functions* 386
Appendix D *Spherical harmonics, d-functions and Clebsch–Gordan coefficients* 393
Appendix E *Relativistic normalisation of cross-sections and decay rates* 396

Glossary 398
Answers to problems 408
Bibliography 412
References 418
Index 421

Preface

The main object in writing this book has been to present the subject of elementary particle physics at a level suitable for advanced physics undergraduates or to serve as an introductory text for graduate students.

Since the first edition of this book was produced over 25 years ago, and the third edition over 10 years ago, there have been many revolutionary developments in the subject, and this has necessitated a complete rewriting of the text in order to reflect these changes in direction and emphasis. In comparison with the third edition, the main changes have been in the removal of much of the material on hadron–hadron interactions as well as most of the mathematical appendices, and the inclusion of much more detail on the experimental verification of the Standard Model of particle physics, with emphasis on the basic quark and lepton interactions. Although much of the material is presented from the viewpoint of the Standard Model, one extra chapter has been devoted to physics outside of the Standard Model and another to the role of particle physics in cosmology and astrophysics.

Many – indeed most – texts on this subject place particular emphasis on the power and beauty of the theoretical description of high energy processes. However, progress in this field has in fact depended crucially on the close interplay of theory and experiment. Theoretical predictions have challenged the ingenuity of experimentalists to confirm or refute them, and equally there have been long periods when unexpected experimental discoveries have challenged our theoretical description of high energy phenomena. In this text, I have tried to emphasise some of the experimental aspects of the subject and have given brief descriptions of some of the key experiments. Some knowledge of elementary quantum mechanics has been assumed, but generally I have tried to present the material from a phenomenological and empirical viewpoint, with a minimum of theoretical formalism. A short chapter on experimental methods and techniques has been included, placed at the end of the book so as not to interrupt the flow of the main material.

Although the intention is that the different chapters should be read in sequence, I have tried to make each one reasonably self-contained, at the price of occasional repetition. For a shorter course, sections or even whole chapters could be left out without too much loss to the remaining material. For example, Chapters 9, 10 and 11 and possibly much of Chapter 3 could be omitted on a first pass through the text.

References to original papers are not comprehensive but have been cited where I thought this was necessary. At the end of the book I have included short bibliographies for further reading, relating to the chapter material in general as well as to specific topics. Sets of problems, mostly numerical, are included at the ends of chapters.

No textbook can cover this entire subject, even at a superficial level. I have tried to compensate for this shortcoming, and to put the subject matter on a historical footing, by including as Appendix B a chronological list of the most important advances in the subject over the last 100 years. This is accompanied by a short summary of the significance and importance of these developments.

For those readers who wish to delve into the theoretical aspects of the subject at a deeper level, I suggest the following texts, in ascending order of difficulty:

Gottfried, K., and V. F. Weisskopf, *Concepts of Particle Physics* (Oxford: Oxford University Press 1984)

Halzen, F., and A. D. Martin, *Quarks and Leptons: An Introductory Course in Modern Particle Physics* (New York: Wiley 1984)

Close, F. E., *Introduction to Quarks and Partons* (London: Academic 1979)

Griffiths, D., *Introduction to Elementary Particles* (New York: Wiley 1987)

Aitchison, I. J., and A. J. Hey, *Gauge Theories in Particle Physics* (Bristol: Adam Hilger 1982)

For a comprehensive text on the key experimental developments in particle physics, including many original papers, I recommend

Cahn, R., and G. Goldhaber, *The Experimental Foundations of Particle Physics* (Cambridge: Cambridge University Press 1991)

Acknowledgements

It is a pleasure to thank Beverly Roger for her invaluable assistance with typing of the text, and Irmgaard Smith for producing many of the line drawings. For permission to reproduce various photographs, figures and diagrams I am indebted to the authors cited in the text and to the following laboratories and publishers:

American Institute of Physics, publishers of *Physical Review*, for Figures 1.2, 6.14 and 6.15
Brookhaven National Laboratory for Figure 4.11
Cambridge University Press for Figure 9.9
CERN Information Services for Figures 1.6, 1.10, 2.7, 2.8, 4.18, 5.10, 7.12, 11.4 and 11.16
DESY Laboratory, Hamburg, for Figures 5.15 and 11.17
European Southern Observatory for Figure 10.9
Fermilab Media Services for Figures 4.20 and 4.21
Pergamon Press, Oxford, for Figure 1.9
Rutherford Appleton Laboratory for Figure 11.9
Stanford Linear Accelerator Center for Figure 4.4
Professor Y. Totsuka of the Superkamiokande Collaboration for Figure 9.4

Donald H. Perkins

1

Quarks and leptons

1.1 Preamble

The subject of elementary particle physics may be said to have begun with the discovery of the electron 100 years ago. In the following 50 years, one new particle after another was discovered, mostly as a result of experiments with cosmic rays, the only source of very high energy particles then available. However, the subject really blossomed after 1950, following the discovery of new elementary particles in cosmic rays; this stimulated the development of high energy accelerators, providing intense and controlled beams of known energy that were finally to reveal the quark substructure of matter and put the subject on a sound quantitative basis.

1.1.1 Why high energies?

Particle physics deals with the study of the elementary constituents of matter. The word 'elementary' is used in the sense that such particles have no known structure, i.e. they are pointlike. How pointlike is pointlike? This depends on the spatial resolution of the 'probe' used to investigate possible structure. The resolution is Δr if two points in an object can just be resolved as separate when they are a distance Δr apart. Assuming the probing beam itself consists of pointlike particles, the resolution is limited by the de Broglie wavelength of these particles, which is $\lambda = h/p$ where p is the beam momentum and h is Planck's constant. Thus beams of high momentum have short wavelengths and can have high resolution. In an optical microscope, the resolution is given by

$$\Delta r \simeq \lambda / \sin\theta$$

where θ is the angular aperture of the light beam used to view the structure of an object. The object scatters light into the eyepiece, and the larger the angle of scatter θ and the smaller the wavelength λ of the incident beam the better is the resolution. For example an ultraviolet microscope has better resolution and reveals

more detail than one using visible light. Substituting the de Broglie relation, the resolution becomes

$$\Delta r \simeq \frac{\lambda}{\sin\theta} = \frac{h}{p\sin\theta} \simeq \frac{h}{q}$$

so that Δr is inversely proportional to the momentum q transferred to the photons, or other particles in an incident beam, when these are scattered by the target.† Thus a value of momentum transfer such that $qc = 10\,\text{GeV} = 10^{10}\,\text{eV}$ – easily attainable with present accelerator beams – gives a spatial resolution $hc/(qc) \sim 10^{-16}$ m, about 10 times smaller than the known radius of the charge and mass distribution of a proton (see Table 1.1 for the values of the units employed).

In the early decades of the twentieth century, particle-beam energies from accelerators reached only a few MeV (10^6 eV), and their resolution was so poor that protons and neutrons could themselves be regarded as elementary and pointlike. At the present day, with a resolution thousands of times better, the fundamental pointlike constituents of matter appear to be quarks and leptons, which are the main subject of this text. Of course, it is possible that they in turn may have an inner structure, but there is no present evidence for this, and whether they do will be for future experiments to decide.

The second reason for high energies in experimental particle physics is simply that many of the elementary particles are extremely massive and the energy mc^2 required to create them is correspondingly large. The heaviest elementary particle detected so far, the 'top' quark (which has to be created as a pair with its antiparticle) has $mc^2 \simeq 175$ GeV, nearly 200 times the mass–energy of a proton.

At this point it should be mentioned that the total energy in accelerator beams required to create such massive particles in sufficient intensities is quite substantial. For example, an energy per particle of 1 TeV (10^{12} eV) in beams consisting of bunches of 10^{13} accelerated particles every second will correspond to a total kinetic energy in each bunch of 1.6 megajoules, equal to the energy of 30 000 light bulbs, or of a 15 tonne truck travelling at 30 mph.

1.1.2 Units in high energy physics

The basic units in physics are length, mass and time and the SI system expresses these in metres, kilograms and seconds. Such units are not very appropriate in high energy physics, where typical lengths are 10^{-15} m and typical masses are 10^{-27} kg.

Table 1.1 summarises the units commonly used in high energy physics. The unit of length is the *femtometre* or *fermi*, where 1 fm = 10^{-15} m; for example, the root mean square radius of the charge distribution of a proton is 0.8 fm. The

† To be exact, in an elastic collision with a massive target, the momentum transfer will be $q = 2p\sin(\theta/2)$, if θ is the angle of deflection.

Table 1.1. *Units in high energy physics*

(a)

Quantity	High energy unit	Value in SI units
length	1 fm	10^{-15} m
energy	1 GeV $= 10^9$ eV	1.602×10^{-10} J
mass, E/c^2	1 GeV/c^2	1.78×10^{-27} kg
$\hbar = h/(2\pi)$	6.588×10^{-25} GeV s	1.055×10^{-34} J s
c	2.998×10^{23} fm s^{-1}	2.998×10^{8} m s^{-1}
$\hbar c$	0.1975 GeV fm	3.162×10^{-26} J m

(b)

natural units, $\hbar = c = 1$		
mass, Mc^2/c^2	1 GeV	
length, $\hbar c/(Mc^2)$	1 GeV^{-1} = 0.1975 fm	
time, $\hbar c/(Mc^3)$	1 GeV^{-1} $= 6.59 \times 10^{-25}$ s	
Heaviside–Lorentz units, $\epsilon_0 = \mu_0 = \hbar = c = 1$		
fine structure constant	$\alpha = e^2/(4\pi) = 1/137.06$	
Relations between energy units		
1 MeV $= 10^6$ eV	1 GeV $= 10^3$ MeV	1 TeV $= 10^3$ GeV

commonly used unit of energy is the GeV, convenient because it is typical of the mass–energy mc^2 of strongly interacting particles. For example, a proton has $M_p c^2 = 0.938$ GeV.

In calculations, the quantities $\hbar = h/(2\pi)$ and c occur frequently, sometimes to high powers, and it is advantageous to use units in which we set $\hbar = c = 1$. Having chosen these two units, we are still at liberty to specify one more unit, e.g. the unit of energy, and the common choice, as indicated above, is the GeV. With $c = 1$ this is also the mass unit. As shown in the table, the unit of length will then be 1 GeV^{-1} = 0.197 fermi, while the corresponding unit of time is 1 GeV^{-1} $= 6.59 \times 10^{-25}$ s.

Throughout this text we shall be dealing with interactions between charges – which can be the familiar electric charge of electromagnetic interactions, the strong charge of the strong interaction or the weak charge of the weak interaction. In the SI system the unit electric charge, e, is measured in coulombs and the fine structure constant is given by

$$\alpha = \frac{e^2}{4\pi\epsilon_0\hbar c} \simeq \frac{1}{137}$$

Here ϵ_0 is the permittivity of free space, while its permeability is defined as μ_0,

such that $\epsilon_0\mu_0 = 1/c^2$. For interactions in general, such units are not useful and we can define e in Heaviside–Lorentz units, which require $\epsilon_0 = \mu_0 = \hbar = c = 1$, so that

$$\alpha = \frac{e^2}{4\pi} \simeq \frac{1}{137}$$

with similar definitions that relate charges and coupling constants analogous to α in the other interactions.

1.1.3 Relativistic transformations

In most of the processes to be considered in high energy physics, the individual particles have relativistic or near relativistic velocities, $v \sim c$. This means that the result of a measurement, e.g. the lifetime of an unstable particle, will depend on the reference frame in which it is made. It follows that one requirement of any theory of elementary particles is that it should obey a fundamental symmetry, namely invariance under a relativistic transformation, so that the equations will have the same form in all reference frames. This can be achieved by formulating the equations in terms of 4-vectors, which we now discuss briefly, together with the notation employed in this text.

The relativistic relation between total energy E, the vector 3-momentum $\mathbf{p}$ (with Cartesian components p_x, p_y, p_z) and the rest mass m for a free particle is

$$E^2 = \mathbf{p}^2c^2 + m^2c^4$$

or, in units with $c = 1$

$$E^2 = \mathbf{p}^2 + m^2$$

The components p_x, p_y, p_z, E can be written as components of an energy–momentum 4-vector p_μ, where $\mu = 1, 2, 3, 4$. In the Minkowski convention used in this text, the three momentum (or space) components are taken to be real and the energy (or time) component to be imaginary, as follows:

$$p_1 = p_x, \quad p_2 = p_y, \quad p_3 = p_z, \quad p_4 = iE$$

so that

$$p^2 = \sum_\mu p_\mu^2 = p_1^2 + p_2^2 + p_3^2 + p_4^2 = \mathbf{p}^2 - E^2 = -m^2 \tag{1.1}$$

Thus p^2 is a relativistic invariant. Its value is $-m^2$, where m is the rest mass, and clearly has the same value in all reference frames. If E, $\mathbf{p}$ refer to the values measured in the lab frame $\sum$ then those in another frame, say $\sum'$, moving along

the x-axis with velocity βc are found from the Lorentz transformation, given in matrix form by

$$p'_\mu = \sum_{\nu=1}^{4} \alpha_{\mu\nu} p_\nu$$

where

$$\alpha_{\mu\nu} = \begin{vmatrix} \gamma & 0 & 0 & i\beta\gamma \\ 0 & 1 & 0 & 0 \\ 0 & 0 & 1 & 0 \\ -i\beta\gamma & 0 & 0 & \gamma \end{vmatrix}$$

and $\gamma = 1/\sqrt{1-\beta^2}$. Thus

$$\begin{aligned} p'_1 &= \gamma p_1 + i\beta\gamma p_4 \\ p'_2 &= p_2 \\ p'_3 &= p_3 \\ p'_4 &= -i\beta\gamma p_1 + \gamma p_4 \end{aligned}$$

In terms of energy and momentum

$$\begin{aligned} p'_x &= \gamma(p_x - \beta E) \\ p'_y &= p_y \\ p'_z &= p_z \\ E' &= \gamma(E - \beta p_x) \end{aligned}$$

with, of course, $\mathbf{p}'^2 - E'^2 = -m^2$. The above transformations apply equally to the space–time coordinates, making the replacements $p_1 \to x_1(= x)$, $p_2 \to x_2(= y)$, $p_3 \to x_3(= z)$ and $p_4 \to x_4(= it)$.

The 4-momentum squared in (1.1) is an example of a Lorentz scalar, i.e. the invariant scalar product of two 4-vectors, $\sum p_\mu p_\mu$. Another example is the phase of a plane wave, which determines whether it is at a crest or a trough and which must be the same for all observers. With $\mathbf{k}$ and ω as the propagation vector and the angular frequency, and in units $\hbar = c = 1$,

$$\text{phase} = \mathbf{k}\cdot\mathbf{x} - \omega t = \mathbf{p}\cdot\mathbf{x} - Et = \sum p_\mu x_\mu$$

The Minkowski notation used here for 4-vectors defines the *metric*, namely the square of the 4-vector momentum $p = (\mathbf{p}, iE)$ so that

$$\text{metric} = (\text{4-momentum})^2 = (\text{3-momentum})^2 - (\text{energy})^2$$

In analogy with the space–time components, the components $p_{x,y,z}$ of 3-momentum are said to be *spacelike* and the energy component E, *timelike*. Thus,

if q denotes the 4-momentum transfer in a reaction, i.e. is $q = p - p'$ where p, p' are the initial and final 4-momenta, then

$$\begin{aligned} q^2 > 0 \quad &\text{is spacelike,} \quad \text{e.g. in a scattering process} \\ q^2 < 0 \quad &\text{is timelike,} \quad \text{e.g. the squared mass of a free particle} \end{aligned} \tag{1.2}$$

A different notation is used in texts on field theory. These avoid the use of the imaginary fourth component ($p_4 = iE$) and introduce the negative sign via the metric tensor $g_{\mu\nu}$. The scalar product of 4-vectors A and B is then defined as

$$AB = g_{\mu\nu}A_\mu B_\nu = A_0 B_0 - \mathbf{A} \cdot \mathbf{B} \tag{1.3}$$

where all the components are real. Here $\mu, \nu = 0$ stand for the energy (or time) component and $\mu, \nu = 1, 2, 3$ for the momentum (or space) components, and

$$g_{00} = +1, \quad g_{11} = g_{22} = g_{33} = -1, \quad g_{\mu\nu} = 0 \quad \text{for } \mu \neq \nu \tag{1.4}$$

This metric results in Lorentz scalars with sign opposite to those using the Minkowski convention in (1.2), so that a spacelike (or timelike) 4-momentum has $q^2 < 0$ (or $q^2 > 0$) respectively. Sometimes, to avoid writing negative quantities, re-definitions have to be made. In deep inelastic electron scattering, q^2 is spacelike and negative, as defined in (1.3), and in discussing such processes it has become common to define the positive quantity $Q^2 = -q^2$. This simply illustrates the fact that the sign of the metric is just a matter of convention and does not in any way affect the physical results.

1.1.4 Fixed-target and colliding beam accelerators

As an example of the application of 4-vector notation, we consider the energy available for particle creation in fixed-target and in colliding-beam accelerators (see also Chapter 11).

Suppose an incident particle of mass m_A, total energy E_A and momentum $\mathbf{p}_A$ hits a target particle of mass m_B, energy E_B, momentum $\mathbf{p}_B$. The total 4-momentum, squared, of the system is

$$p^2 = (\mathbf{p}_A + \mathbf{p}_B)^2 - (E_A + E_B)^2 = -m_A^2 - m_B^2 + 2\mathbf{p}_A \cdot \mathbf{p}_B - 2E_A E_B \tag{1.5}$$

The centre-of-momentum system (cms) is defined as the reference frame in which the total 3-momentum is zero. If the total energy in the cms is denoted E^*, then we also have $p^2 = -E^{*2}$.

Suppose first of all that the target particle (m_B) is at rest in the laboratory (lab) system, so that $\mathbf{p}_B = 0$ and $E_B = m_B$, while E_A is the energy of the incident particle in the lab system. Then

$$E^{*2} = -p^2 = m_A^2 + m_B^2 + 2m_B E_A \tag{1.6}$$

Secondly, suppose that the incident and target particles travel in opposite directions, as would be the case in an e^+e^- or a $p\bar{p}$ collider. Then, with p_A and p_B denoting the absolute values of the 3-momenta, the above equation gives

$$\begin{aligned} E^{*2} = -p^2 &= 2(E_A E_B + p_A p_B) + (m_A^2 + m_B^2) \\ &\simeq 4E_A E_B \end{aligned} \tag{1.7}$$

if $m_A, m_B \ll E_A, E_B$. This result is for a head-on collision. For two beams crossing at an angle θ, the result would be $E^{*2} = 2E_A E_B(1 + \cos\theta)$. We note that the cms energy available for new particle creation in a collider with equal energies E in the two beams rises linearly with E, i.e. $E^* \simeq 2E$, while for a fixed-target machine the cms energy rises as the square root of the incident energy, $E^* \simeq \sqrt{2m_B E_A}$. Obviously, therefore, the highest possible energies for creating new particles are to be found at colliding-beam accelerators. As an example, the cms energy of the Tevatron $p\bar{p}$ collider at Fermilab is $E^* = 2$ TeV $= 2000$ GeV. To obtain the same cms energy with a fixed-target accelerator, the energy of the proton beam, in collision with a target nucleon, would have to be $E_A = E^{*2}/(2m_B) \simeq 2 \times 10^6$ GeV $= 2000$ TeV.

1.2 The Standard Model of particle physics

1.2.1 The fundamental fermions

Practically all experimental data from high energy experiments can be accounted for by the so-called *Standard Model* of particles and their interactions, formulated in the 1970s. According to this model, all matter is built from a small number of fundamental spin $\frac{1}{2}$ particles, or *fermions*: six *quarks* and six *leptons*. For each of the various fundamental constituents, its symbol and the ratio of its electric charge Q to the elementary charge e of the electron are given in Table 1.2.

The *leptons* carry integral electric charge. The electron e with unit negative charge is familiar to everyone, and the other charged leptons are the muon μ and the tauon τ. These are heavy versions of the electron. The neutral leptons are called *neutrinos*, denoted by the generic symbol ν. A different 'flavour' of neutrino is paired with each 'flavour' of charged lepton, as indicated by the subscript. For example, in nuclear β-decay, an electron e is emitted together with an electron-type neutrino, ν_e. The charged muon and tauon are both unstable, and decay spontaneously to electrons, neutrinos and other particles. The mean lifetime of the muon is 2.2×10^{-6} s, that of the tauon only 2.9×10^{-13} s.

Neutrinos were postulated by Pauli in 1930 in order to account for the energy and momentum missing in the process of nuclear β-decay (see Figure 1.1). The actual existence of neutrinos as independent particles, detected by their interactions, was

Table 1.2. *The fundamental fermions*

Particle	Flavour			$Q/\|e\|$
leptons	e	μ	τ	-1
	ν_e	ν_μ	(ν_τ)	0
quarks	u	c	t	$+\frac{2}{3}$
	d	s	b	$-\frac{1}{3}$

first demonstrated in 1956. The tau neutrino is shown in parentheses because its interactions have not so far (1999) been observed.

The *quarks* carry fractional charges, of $+\frac{2}{3}|e|$ or $-\frac{1}{3}|e|$. In the table, the quark masses increase from left to right, just as they do for the leptons (see Tables 1.4 and 1.5). And, just as for the leptons, the quarks are grouped into pairs differing by one unit of electric charge. The quark type or 'flavour' is denoted by a symbol: u for 'up', d for 'down', s for 'strange', c for 'charmed', b for 'bottom' and t for 'top'. How did such odd names get chosen? The 's for strange' quark terminology came about because these quarks turned out to be constituents of the so-called 'strange particles' discovered in cosmic rays (long before quarks were postulated). Their behaviour was strange in the sense that they were produced prolifically in strong interactions, and therefore would be expected to decay on a strong interaction timescale (10^{-23} s); instead they decayed extremely slowly, by weak interactions. The solution to this puzzle was that these particles carried a new quantum number, S for strangeness, conserved in strong interactions – so that they were always produced in pairs with $S = +1$ and $S = -1$ but they decayed singly and weakly, with a change in strangeness, $\Delta S = \pm 1$, into non-strange particles (see Figure 1.10). The choice of the name 'c for charm' was perhaps a reaction to strangeness, while 'top' and 'bottom' are logical names for the partners of up and down quarks. In turn, the up and down quarks were so named because of isospin symmetry (see Section 3.12), according to which each possesses one of the two components $\pm\frac{1}{2}$ of an isospin vector of value $I = \frac{1}{2}$, which, like a spin vector, can point 'up' or 'down'.

While leptons exist as free particles, quarks seem not to do so. It is a peculiarity of the strong forces between the quarks that they can be found only in combinations such as uud, not singly. This phenomenon of quark confinement is, even today, not properly understood.

Protons and neutrons consist of the lightest u and d quarks, three at a time: a proton consists of uud, a neutron consists of ddu. The common material of the present universe is the stable particles, i.e. the electrons e and the u and

d quarks. The heavier quarks s, c, b, t also combine to form particles akin to, but much heavier than, the proton and neutron, but these are unstable and decay rapidly (in typically 10^{-13} s) to u, d combinations, just as the heavy leptons decay to electrons. Only in very high energy collisions at man-made accelerators, or naturally in cosmic rays, are the heavy, unstable varieties observed.

Table 1.2 shows that the three lepton pairs are exactly matched by the three quark pairs. As we shall see later, it is necessary to introduce a further degree of freedom for the quarks: each flavour of quark comes in three different *colours* (the word 'colour' is simply a name to distinguish the three types). If we allow for three colours, the total charge of the u, c, t quarks is $3 \times 3 \times \frac{2}{3} = 6|e|$, that of the d, s, b quarks is $-3 \times 3 \times \frac{1}{3} = -3|e|$ and that of the leptons is $-3 \times 1|e| = -3|e|$. The total charge of all the fermions is then zero. This is the actual condition that the Standard Model should be free of so-called 'anomalies' and is a renormalisable field theory. It is also, it turns out, a property of the grand unified theories that unify the strong, electromagnetic and weak interactions at very high energies, as described in Chapter 9.

1.2.2 The interactions

We have looked at the particles; the Standard Model also comprises their interactions. As we discuss in the next chapter, the different interactions are described in quantum language in terms of the exchange of characteristic *bosons* (particles of integral spin) between the fermion constituents. These boson mediators are listed in Table 1.3.

There are four types of fundamental interaction or field, as follows.

Strong interactions are responsible for binding the quarks in the neutron and proton, and the neutrons and protons within nuclei. The interquark force is mediated by a massless particle, the *gluon*.

Electromagnetic interactions are responsible for virtually all the phenomena in extra-nuclear physics, in particular for the bound states of electrons with nuclei, i.e. atoms and molecules, and for the intermolecular forces in liquids and solids. These interactions are mediated by *photon* exchange.

Weak interactions are typified by the slow process of nuclear β-decay, involving the emission by a radioactive nucleus of an electron and neutrino. The mediators of the weak interactions are the $W^{\pm}$ and Z^0 bosons, with masses of order 100 times the proton mass.

Gravitational interactions act between all types of particle. On the scale of experiments in particle physics, gravity is by far the weakest of all the fundamental interactions, although of course it is dominant on the scale of the universe. It is supposedly mediated by exchange of a spin 2 boson, the *graviton*. Very refined

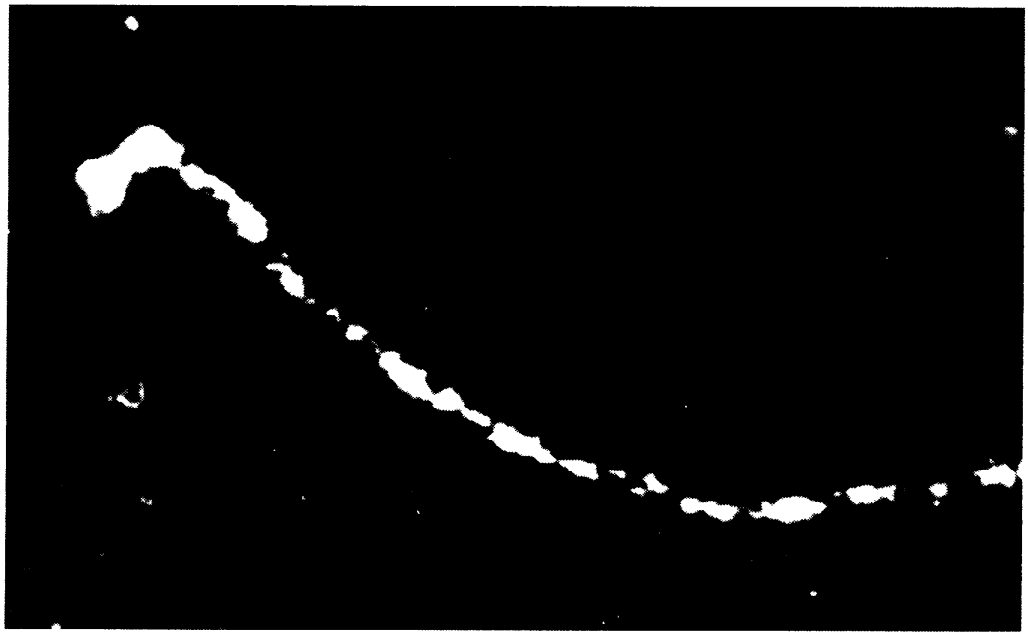

Fig. 1.1. Cloud chamber photograph of the birth of an antineutrino. It depicts the β-decay of the radioactive nucleus ^{6}He $\rightarrow$ ^{6}Li $+ e^- + \bar{\nu}_e + 3.5$ MeV. The long track is that of the electron, the short thick track that of the recoiling ^{6}Li nucleus. Some momentum is missing, and has to be ascribed to an uncharged particle (an antineutrino) travelling upwards in the picture (after Csikay and Szalay 1957). The cloud chamber consists essentially of a glass-fronted cylindrical tank of gas saturated with water vapour. Upon applying a sudden expansion by means of a piston at the rear of the chamber, the gas cools adiabatically and becomes supersaturated. Water vapour therefore condenses as droplets, preferentially upon charged ions created, for example, by the passage of a charged particle through the gas. The cloud chamber was invented by C.T.R. Wilson for a quite different purpose: to try to reproduce, in the laboratory, the 'glory' phenomenon he had observed on a Scottish mountain top. Wilson failed in this endeavour but by 1912 had given the world a valuable new technique for nuclear research.

Table 1.3. *The boson mediators*

Interaction	Mediator	Spin/parity
strong	gluon, G	1^-
electromagnetic	photon, γ	1^-
weak	$W^{\pm}$, Z^0	1^-, 1^+
gravity	graviton, g	2^+

experiments to detect gravitons (en masse, as gravitational waves) are currently under way.

To have four independent and apparently unrelated interaction fields is rather unsatisfactory, and physicists from Einstein onwards have speculated that the

different interactions are different aspects of a single, unified field. In the 1970s, experiments showed that the weak and electromagnetic interactions can indeed be unified, and would have the same strength at very high energies; only at lower energies is the symmetry broken so that their apparent strengths are very different. Thus some progress has been made and more is expected.

We shall be discussing these interactions in more detail in Chapter 2, but simply remark here that, in the everyday world, all four are of importance. The physical processes in the Sun – our chief source of energy on Earth – provide a good illustration. The Sun originally condensed under gravity from a cloud of hydrogen, until the core reached by compression a high enough temperature (10^7 degrees) for thermonuclear fusion reactions to begin. In these reactions hydrogen is converted to helium. The first-stage reaction is actually a weak interaction, $p + p \rightarrow d + e^+ + \nu_e$: two protons fuse to form a deuteron d, a positron e^+ and a neutrino ν_e. As described in subsection 9.7.1, these neutrinos have been detected, and incidentally present a problem. Subsequent stages involve strong nuclear interactions. The energy liberated is transmitted principally in the form of X-rays from the core to the photosphere; electromagnetic interactions are involved here and in the transmission of heat and light to the outside universe. Although the strong nuclear reactions proceed rapidly, the overall timescale is set by the very slow first-stage weak interaction, which alone guarantees the long life of the solar system. The main point to be made is that all four fundamental interactions play a vital and balanced role in stellar evolution.

To indicate the relative magnitudes of the four types of interaction, the comparative strengths of the force between two protons when just in contact are very roughly as follow

strong	electromagnetic	weak	gravity	(1.8)
1	10^{-2}	10^{-7}	10^{-39}	

The timescales for the decay of unstable particles via one or other of the fundamental interactions are also very different. As detailed in Table 2.2, a typical mean lifetime τ for decay through a weak interaction is 10^{-10} s, which is easily measurable, while that for a strong interaction will be about 10^{-23} s, which cannot be measured directly. However, the Uncertainty Principle relates the lifetime and the uncertainty in energy of a state. An unstable particle does not have a unique mass, but a distribution with 'width' $\Gamma = \hbar/\tau$. So, when τ is very short, its value can be inferred from the measured width Γ.

1.2.3 Limitations of the Standard Model

Most of the material in this text will be presented in the context of the Standard Model of particle physics. This provides an extremely compact and successful description of the properties of the fundamental constituents discussed above, as well as of the electromagnetic, weak and strong interactions between them. It accounts for an enormous body of experimental data, from laboratory experiments ranging up to the highest available collision energies, of order 1 TeV (10^{12} electronvolts). However, the Standard Model does have limitations. Gravitational interactions are not included, and persistent attempts over many years to find a way of incorporating gravity have made little progress. In the Standard Model, neutrinos are assumed to be massless, but there is growing evidence, from the solar and atmospheric anomalies discussed in Chapter 9, that neutrinos do have finite masses; and this is regarded as one possible manifestation of physics beyond that encompassed by the Standard Model. The model is also somewhat inelegant, as it contains some 17 arbitrary parameters (masses, mixing angles, coupling constants etc.), and one has to ask where all those numbers come from. The origin of the parameters and the underlying reasons for the 'xerox copies' – six quark and six lepton flavours – is not at all understood. As we shall see, it appears that in trying to understand some of the major features of our universe, such as the preponderance of 'dark matter' and the large matter–antimatter asymmetry, we will also require new and presently unknown physics beyond that of the Standard Model, as discussed in Chapters 9 and 10. But equally, it seems fairly certain that the model will form an integral and important part of a more complete theory of particles in the far future.

1.3 Particle classification: fermions and bosons

Fundamental particles are of two types; particles with half-integral spin ($\frac{1}{2}\hbar, \frac{3}{2}\hbar, \ldots$) are called fermions because they obey Fermi–Dirac statistics, while those with integral spin ($0, \hbar, 2\hbar, \ldots$) obey Bose–Einstein statistics and are called bosons.

The statistics obeyed by a particle determines how the wavefunction ψ describing an ensemble of identical particles behaves under interchange of any pair of particles, say 1 and 2. Clearly the probability $|\psi|^2$ cannot be altered by the interchange $1 \leftrightarrow 2$, since the particles are indistinguishable. Thus, under interchange $\psi \rightarrow \pm\psi$. There is a fundamental theorem, called the spin-statistics theorem, which is a sacrosanct principle of quantum field theory and according to which the following rule holds:

under exchange of identical bosons $\psi \rightarrow +\psi$; ψ is symmetric

under exchange of identical fermions $\psi \rightarrow -\psi$; ψ is antisymmetric

As an application of this rule, suppose one tries to put two identical fermions in the *same* quantum state. Then the wavefunction under interchange of these two identical particles would not change. It is necessarily symmetric under this operation. But this is forbidden by the above rule, according to which the wavefunction *must* change sign. This gives rise to the famous Pauli principle: two or more identical fermions cannot exist in the same quantum state. However, there are no restrictions on the number of bosons in the same quantum state; an example of this is the laser.

One exciting possible extension beyond the Standard Model is the concept of *supersymmetry*, which predicts that, at a high energy scale, of order 1 TeV = 10^{12} eV, there should be fermion–boson symmetry. Each fermion will have a boson partner and vice versa. The reasons behind this postulate and the experimental limits on possible supersymmetric particle masses are given in Chapter 9.

1.4 Particles and antiparticles

Perhaps the two greatest conceptual advances in physics over the last century have been the theory of relativity and the quantum-mechanical description of phenomena on the atomic or subatomic scale. These led Dirac in 1931 to the prediction of *antiparticles*, i.e. objects with the same mass and lifetime as the corresponding particles but with opposite sign of charge and magnetic moment.

Without discussing the full theory of antiparticles here, we can outline the underlying ideas very briefly. The relativistic relation between the total energy E, momentum p and rest mass m of a particle is

$$E^2 = p^2c^2 + m^2c^4 \tag{1.9}$$

which for $pc \ll mc^2$ can be expanded to give the usual expression for the kinetic energy,

$$T = E - mc^2 = mc^2(1 + p^2/m^2c^2)^{1/2} - mc^2 \simeq p^2/2m$$

However, from (1.9) we see that the total energy E can in principle assume negative as well as positive values,

$$E = \pm\sqrt{p^2c^2 + m^2c^4} \tag{1.10}$$

Classically, negative energies for free particles appear to be completely meaningless. In quantum mechanics, however, we represent the amplitude of an infinite stream of particles, say electrons, travelling along the positive x-axis with

3-momentum p by the plane wavefunction

$$\psi = Ae^{-i(Et-px)/\hbar} \tag{1.11}$$

where the angular frequency is $\omega = E/\hbar$, the wavenumber is $k = p/\hbar$ and A is a normalisation constant. As t increases, the phase advances in the direction of increasing x. Formally, however, (1.11) can also represent particles of energy $-E$ and momentum $-p$ travelling in the negative x-direction and *backwards in time* (i.e. replacing Et by $(-E)(-t)$ and px by $(-p)(-x)$):

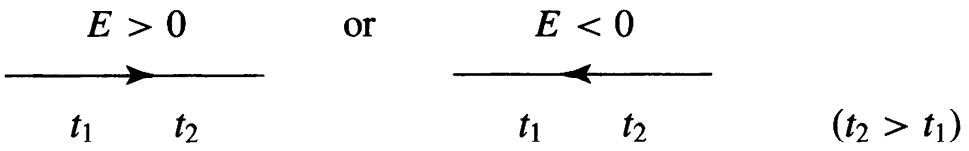

Such a stream of negative electrons flowing backwards in time is equivalent to positive charges flowing forward, and thus having $E > 0$. Hence, the negative energy particle states are connected with the existence of positive energy antiparticles of exactly equal but opposite electrical charge and magnetic moment, and otherwise identical. The *positron* – the antiparticle of the electron – was discovered experimentally in 1932 in cloud chamber experiments with cosmic rays (see Figure 1.2).

Dirac's original picture of antimatter, developed in the context of electrons, was that the vacuum actually consisted of an infinitely deep sea of completely filled negative energy levels. A positive energy electron was prevented from falling into a negative energy state, with release of energy, by the Pauli principle. If one supplies energy $E > 2mc^2$, however, a negative energy electron at A in Figure 1.3 could be lifted into a positive energy state B, leaving a 'hole' in the sea corresponding to creation of a positron together with an electron. However, such a picture is not valid for the pair creation of bosons.

In non-relativistic quantum mechanics, the quantity ψ in (1.11) is interpreted as a single-particle wavefunction, equal to the probability amplitude of finding the particle at some coordinate. In the relativistic case however, multi-particle states are involved (with the creation of particle–antiparticle pairs) and, strictly speaking, the single-particle function loses its meaning. Instead, ψ has to be treated as an *operator* that *creates or destroys particles*. Negative energies are simply associated with destruction operators acting on positive energy particles to reduce the energy within the system. The absorption or destruction of a negative energy particle is again interpreted as the creation of a positive energy antiparticle, with opposite charge, and vice versa. This interpretation will be formalised in the discussion of Feynman diagrams in Chapter 2.

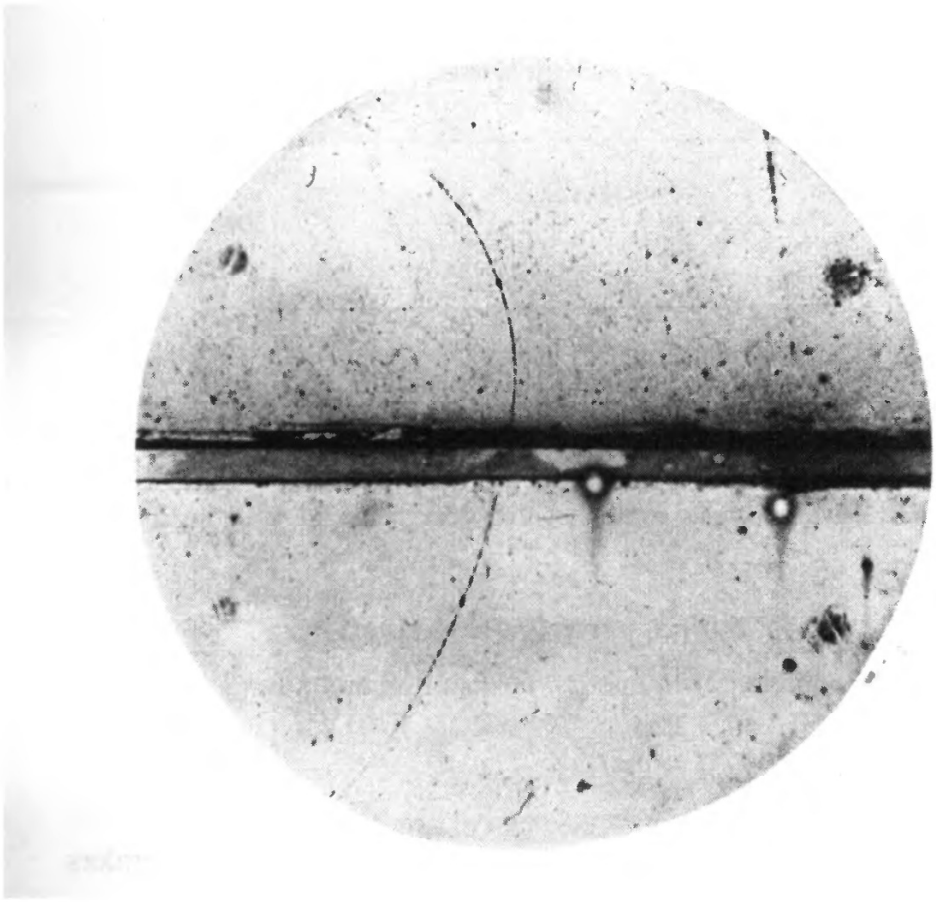

Fig. 1.2. The discovery of antimatter. The picture shows the track of a positron observed by Anderson in 1932 in a cloud chamber placed in a magnetic field and exposed to cosmic rays. Note that the magnetic curvature of the track in the upper half of the chamber is greater than that in the lower half, because of the loss of momentum in traversing the metal plate; hence the particle was proved to be positively charged and travelling upwards. This discovery was confirmed a few months later by Blackett and Occhialini (1933). With a cloud chamber whose expansion was triggered by electronic counters surrounding it (rather than the random expansion method of Anderson) they observed the first examples of the production of e^+e^- pairs in cosmic ray showers. The antiparticle of the proton – the antiproton – was first observed in accelerator experiments in 1956, but the bound state of positron and antiproton, i.e. the anti-hydrogen-atom, not until 1995.

The existence of antiparticles is a general property of both fermions and bosons, but for fermions only there is a conservation law: the difference in the number of fermions and antifermions is a constant. Formally one can define a fermion number, $+1$ for a fermion and -1 for an antifermion, and postulate that the total fermion number is conserved. Thus fermions and antifermions can only be created or destroyed in pairs. For example, a γ-ray, in the presence of a nucleus to conserve momentum, can 'materialise' into an electron–positron pair and an e^+e^- bound state, called positronium, can annihilate to two or three γ-rays. An example of an e^+e^- pair is shown in Figure 1.4.

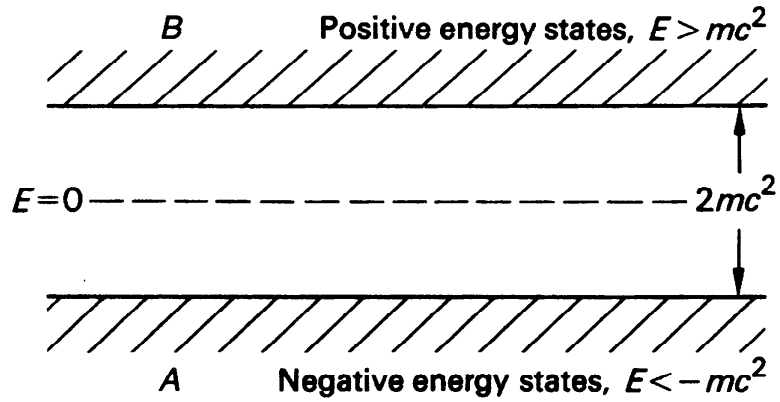

Fig. 1.3. Dirac picture of e^+e^- pair creation, when an electron at A is lifted into a positive energy state at B, leaving a 'hole' in the negative energy sea, i.e. creating a positron.

1.5 Free particle wave equations

The relativistic relation between energy, momentum and mass is given in (1.9):

$$E^2 = p^2c^2 + m^2c^4$$

If we replace the quantities E and p by the quantum mechanical operators

$$E_{\text{op}} = i\hbar\frac{\partial}{\partial t}, \quad p_{\text{op}} = -i\hbar\nabla = -i\hbar\frac{\partial}{\partial \mathbf{r}} \tag{1.12}$$

where $\mathbf{r}$ is the position vector, we get the *Klein–Gordon wave equation*

$$\frac{1}{c^2}\frac{\partial^2\psi}{\partial t^2} = \nabla^2\psi - \frac{m^2c^2}{\hbar^2}\psi \tag{1.13}$$

As described above, it is often more convenient to work in units such that $\hbar = c = 1$, in order to avoid writing these symbols repeatedly, so that the above equation becomes

$$\frac{\partial^2\psi}{\partial t^2} = (\nabla^2 - m^2)\psi \tag{1.14}$$

This wave equation is suitable for describing spinless (or scalar) bosons (since no spin variable has been introduced). In the non-relativistic case, if we define $E = p^2/(2m)$ as the kinetic energy rather than the total energy then substituting the above operators gives the *Schrödinger wave equation* for non-relativistic spinless particles:

$$\frac{\partial\psi}{\partial t} - \frac{i}{2m}\nabla^2\psi = 0 \tag{1.15}$$

Note that the Klein–Gordon equation is second order in the derivatives, while

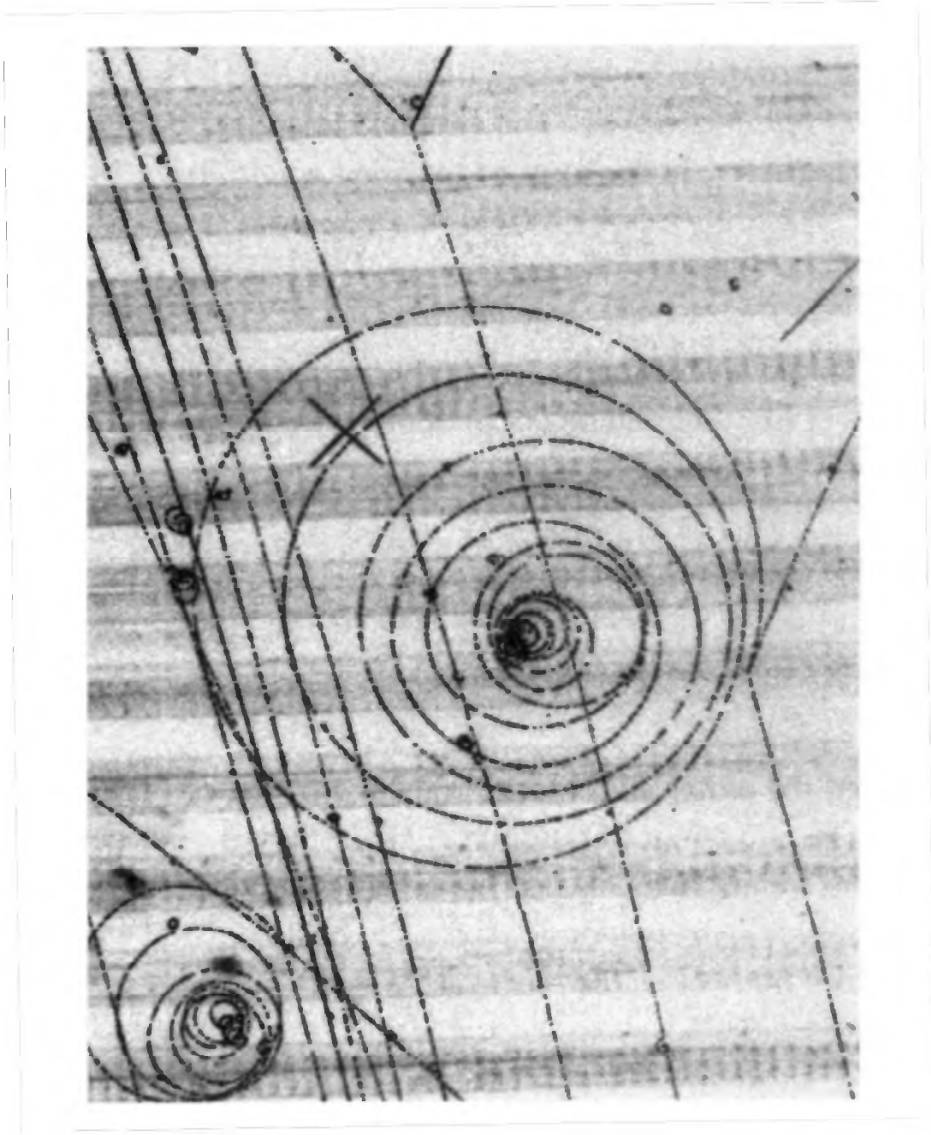

Fig. 1.4. Observation of an electron–positron pair in a bubble chamber filled with liquid hydrogen. An incoming negative pion – itself a quark–antiquark combination – undergoes charge exchange in the reaction $\pi^- + p \rightarrow n + \pi^0$. This strong interaction is followed by electromagnetic decay of the neutral pion. The usual decay mode is $\pi^0 \rightarrow 2\gamma$, the γ-rays then converting to e^+e^- pairs in traversing the liquid. In about 1% of events, however, the decay mode is $\pi^0 \rightarrow \gamma e^+e^-$: the second γ-ray is 'internally converted' to a pair. Since the neutral pion lifetime is only 10^{-16} s, the pair appears to point straight at the interaction vertex. The bubble chamber detector was invented by Glaser in 1952. It consists basically of a tank of superheated liquid (hydrogen in the above example), prevented from boiling by application of an overpressure. When the overpressure is released, boiling initially occurs along the trails of charged ions left behind by passage of fast charged particles through the liquid and leaves tracks of bubbles that can be photographed through a front window. As in the cloud chamber, a magnetic field normal to the plane of the picture serves to measure particle momentum from curvature.

the Schrödinger equation is first order in time and second order in space. This is unsatisfactory when we are dealing with high energy particles, where the description of physical processes must be relativistically invariant, with space and time coordinates occurring to the same power.

Dirac set out to formulate a wave equation symmetric in space and time, which was *first order in both derivatives*. The simplest form that can be written down is that for massless particles, in the form of the *Weyl equations*

$$\frac{\partial \psi}{\partial t} = \pm \left(\sigma_1 \frac{\partial \psi}{\partial x} + \sigma_2 \frac{\partial \psi}{\partial y} + \sigma_3 \frac{\partial \psi}{\partial z} \right) = \pm \boldsymbol{\sigma} \cdot \frac{\partial}{\partial \mathbf{r}} \psi \tag{1.16}$$

Here the σ's are unknown constants. In order to satisfy the Klein–Gordon equation (1.14), we square (1.16) and equate coefficients, whence we find

$$\sigma_1^2 = \sigma_2^2 = \sigma_3^2 = 1$$

$$\sigma_1 \sigma_2 + \sigma_2 \sigma_1 = 0, \quad \text{etc.} \tag{1.17}$$

$$m = 0$$

These results hold for either sign on the right-hand side of (1.16), and both must be considered. The σ's cannot be numbers since they do not commute, but they can be represented by matrices, in fact the equations (1.17) define the 2×2 Pauli matrices, which we know from atomic physics to be associated with the description of the spin quantum number of the electron:

$$\sigma_1 = \begin{pmatrix} 0 & 1 \\ 1 & 0 \end{pmatrix}, \quad \sigma_2 = \begin{pmatrix} 0 & -i \\ i & 0 \end{pmatrix}, \quad \sigma_3 = \begin{pmatrix} 1 & 0 \\ 0 & -1 \end{pmatrix} \tag{1.18}$$

Using (1.12) we can also express (1.16) in the forms

$$E\chi = -\boldsymbol{\sigma} \cdot \mathbf{p}\chi \tag{1.19a}$$

$$E\phi = +\boldsymbol{\sigma} \cdot \mathbf{p}\phi \tag{1.19b}$$

where E and $\mathbf{p}$ are the energy and momentum operators. χ and ϕ are two-component wavefunctions, called spinors, and are separate solutions of the two Weyl equations, and $\boldsymbol{\sigma}$ denotes the Pauli spin vector, with Cartesian components $\sigma_1, \sigma_2, \sigma_3$ as above. As indicated below, the two Weyl equations have in total four solutions, corresponding to particle and antiparticle states with two spin substates of each.

If the fermion mass is now included, we need to enlarge (1.16) or (1.19) by including a mass term, giving the *Dirac equation*,

$$E\psi = (\boldsymbol{\alpha} \cdot \mathbf{p} + \beta m)\psi \tag{1.20a}$$

Here, the matrices $\boldsymbol{\alpha}$ and β are 4×4 matrices, operating on four-component

(spinor) wavefunctions (particle, antiparticle and two spin substates for each). The matrices α and β are

$$\alpha = \begin{pmatrix} 0 & \sigma \\ \sigma & 0 \end{pmatrix}, \quad \beta = \begin{pmatrix} 1 & 0 \\ 0 & -1 \end{pmatrix}$$

where each element denotes a 2×2 matrix and '1' denotes the unit 2×2 matrix. The matrix α has three components, just as does σ in (1.18). Here, we have quoted the so-called Dirac–Pauli representation of these matrices, but other representations are possible.

Usually, the Dirac equation is quoted in a covariant form, using (1.12) in (1.20a), as

$$\left(i\gamma_\mu \frac{\partial}{\partial x_\mu} - m\right)\psi = 0 \tag{1.20b}$$

where the γ_μ (with $\mu = 1, 2, 3, 4$) are 4×4 matrices related to those above. In fact

$$\gamma_k = \beta\alpha_k = \begin{pmatrix} 0 & \sigma_k \\ -\sigma_k & 0 \end{pmatrix}, \quad k = 1, 2, 3 \quad \text{and} \quad \gamma_4 = \beta \tag{1.20c}$$

The Dirac equation is fully discussed in books on relativistic quantum mechanics, and we have mentioned it here merely for completeness; we shall not discuss it in detail in this text. Occasionally we shall need to quote results from the Dirac equation without derivation. However, it turns out that, in most of the applications with which we shall be dealing in high energy physics, the fermions have extreme relativistic velocities so that the masses can be neglected and the Dirac equation breaks down into the two much simpler, decoupled, Weyl equations as described above.

1.6 Helicity states: helicity conservation

For a massless fermion of positive energy, $E = |\mathbf{p}|$ so that (1.19a) satisfies

$$\frac{\boldsymbol{\sigma}\cdot\mathbf{p}}{|\mathbf{p}|}\chi = -\chi \tag{1.21}$$

The quantity

$$H = \frac{\boldsymbol{\sigma}\cdot\mathbf{p}}{|\mathbf{p}|} = -1 \tag{1.22}$$

is called the *helicity* (or handedness). It measures the sign of the component of spin of the particle, $j_z = \pm\frac{1}{2}\hbar$, in the direction of motion (z-direction). The z-component of spin and the momentum vector $\mathbf{p}$ together define a screw sense, as in Figure 1.5. $H = +1$ corresponds to a right-handed (RH) screw, while particles with $H = -1$ are left-handed (LH).

The solution χ of (1.19a) represents a LH, positive energy, particle but it can also represent a particle with negative energy $-E$ and momentum $-\mathbf{p}$. Thus $-E\chi = -\boldsymbol{\sigma} \cdot (-\mathbf{p})\chi$, or $H = \boldsymbol{\sigma} \cdot (-\mathbf{p})/|\mathbf{p}| = +1$. This state is interpreted, as before, as that of the antiparticle. Thus, (1.19a) represents *either* a LH particle *or* a RH antiparticle, while the independent solution (1.19b) corresponds to a RH particle or a LH antiparticle state.

Helicity is a well-defined, Lorentz-invariant quantity for a massless particle, for the simple reason that such a particle travels at velocity c. In making a Lorentz transformation to another reference frame of relative velocity $v < c$, it is therefore impossible to reverse the helicity. As discussed below, neutrinos have very small, possibly even zero, masses, and are well described by one of the two Weyl equations. By contrast, it turns out that solutions of the Dirac equation (1.20), with its finite mass term, are *not* pure helicity eigenstates but some admixture of LH and RH functions. However, provided they are extreme relativistic, massive fermions (electrons for example) can also be described well enough by the Weyl equations.

For interactions involving *vector* or *axial vector fields*, i.e. those mediated by vector or axial vector bosons, *helicity is conserved in the relativistic limit.* The reason is that such interactions do not mix the separate LH and RH solutions of the Weyl equations. This means for example that a LH lepton, undergoing scattering in such an interaction, will emerge as a LH particle, irrespective of the angle of scatter, provided it is extreme relativistic. On the other hand, a *scalar* interaction does not preserve the helicity and does mix LH and RH states. In the Dirac equation, the mass term represents such a scalar-type interaction and because of its presence, massive leptons with v less than c are superpositions of LH and RH helicity states. In the successful theory of electroweak interactions discussed in Chapter 8, the elementary leptons and bosons start out as massless particles. Scalar field particles, called Higgs bosons, are associated with an all-pervading scalar field which is postulated to interact with, and give mass to, these hitherto massless objects.

Helicity conservation holds good in the relativistic limit for any interaction that has the Lorentz transformation properties of a vector or axial vector, and it therefore applies to strong, weak and electromagnetic interactions, which are all mediated by vector or axial vector bosons. Consequently, in a scattering process at high energy, e.g. of a quark by a quark or a lepton by a quark or lepton, a LH particle remains LH, and a RH particle remains RH. This fact, together with the conservation of angular momentum, determines angular distributions in many interactions, as described later in the text.

1.7 Lepton flavours

The masses, or mass limits, of the known leptons are given in Table 1.4. The masses are quoted in energy units, i.e. the value of the rest energy mc^2, in eV

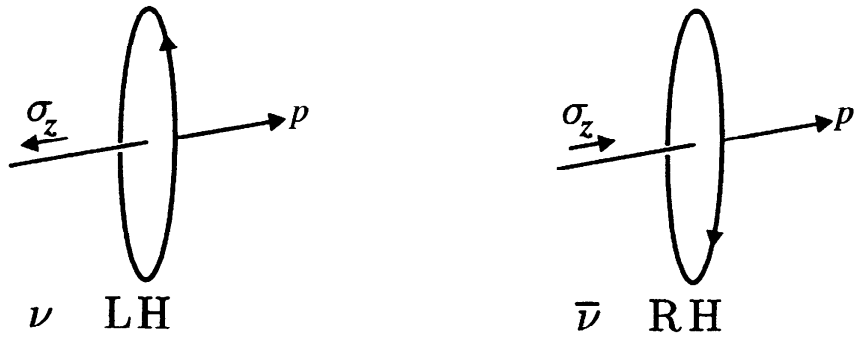

Fig. 1.5. A neutrino has LH polarisation, while an antineutrino is RH.

or MeV. As noted previously, the μ and τ are heavier unstable versions of the electron. The muon μ was discovered as a component of the cosmic radiation in 1937. The muons are decay products of short-lived mesons, which are integral-spin particles produced in the upper atmosphere by primary cosmic ray protons from space. The τ lepton was first observed in accelerator experiments in 1975. These three 'flavours' of charged lepton are paralleled by three flavours of neutral lepton (neutrino). The upper limits to the neutrino masses are all small in comparison with those of the corresponding charged leptons, with which they are produced in partnership in weak interactions. In the Standard Model, neutrinos are assumed to be massless.

Charged leptons undergo both electromagnetic and weak interactions, while neutrinos interact only weakly. Of all the fundamental fermions, neutrinos are unique in that they are completely longitudinally polarised. Only the projection $j_z = -\frac{1}{2}\hbar$ is observed, corresponding to the pure helicity state $H = -1$ in (1.22). As explained above, the momentum and spin vectors between them define a 'screw sense' or handedness as in Figure 1.5; the neutrino ν is said to be left-handed, while its antiparticle, the antineutrino $\bar{\nu}$ is right-handed. Thus both are described by the first of the Weyl solutions (1.19a).

As previously explained, such pure helicity states are only possible for strictly massless particles, by Lorentz invariance. For the same reason, a massless neutrino cannot possess a magnetic dipole moment, since if it did the spin direction could be flipped by an applied magnetic field.

The fact that neutrinos occur in different flavours, as do the charged leptons, was established in experiments with high energy neutrinos from accelerators in 1962. The neutrino beams were produced – just as they are in cosmic rays – by the decay in flight of pions created in high energy proton collisions, the decay products being muons and neutrinos. The latter, in their subsequent weak interactions, were found to produce charged muons, but never electrons. This behaviour is formalised

Table 1.4. *Lepton masses in energy units* mc^2

Flavour	Charged lepton mass	Neutral lepton mass
e	$m_e = 0.511$ MeV	$m_{\nu_e} \leq 10$ eV
μ	$m_\mu = 105.66$ MeV	$m_{\nu_\mu} \leq 0.16$ MeV
τ	$m_\tau = 1777$ MeV	$m_{\nu_\tau} \leq 18$ MeV

by ascribing conserved *lepton flavour numbers* L_e, L_μ, L_τ, equal to $+1$ for each lepton and -1 for each antilepton of the appropriate flavour. For example, the decay of the positive pion is written

$$\begin{array}{cccc} & \pi^+ & \rightarrow & \mu^+ + \nu_\mu \\ L_\mu & 0 & & -1 \quad +1 \end{array}$$

and the interaction of an electron-type neutrino with a nucleon as

$$\begin{array}{cccc} & \nu_e + n & \rightarrow & p + e^- \\ L_e & +1 \quad 0 & & 0 \quad +1 \end{array}$$

The decay

$$\mu^+ \rightarrow e^+ + \nu_e + \bar{\nu}_\mu$$

is allowed by conservation of lepton number, while the decay

$$\mu^+ \rightarrow e^+ + \gamma$$

is forbidden (the limit on the branching ratio is $\leq 10^{-9}$). Examples of the interactions of muon- and electron-type neutrinos are given in Figure 1.6.

The masslessness of neutrinos and the strict conservation of lepton flavour are actively questioned at the present time, largely as a result of the 'solar neutrino problem'. There is mounting evidence that lepton-flavour-number conservation may start to break down on long enough timescales, i.e. for distances L and neutrino energies E such that $L/E \geq 1000$ m MeV^{-1}, leading to 'oscillation' of one type of neutrino flavour into another (see Section 9.7).

1.8 Quark flavours

Table 1.5 and Figure 1.7 show the masses of the various flavours of quark. As remarked before, quarks do not exist as free particles and thus the definition of mass is somewhat arbitrary, as it must depend on the magnitude of the potential binding the quarks together in, for example, a proton. The numbers in Table 1.5 are meant

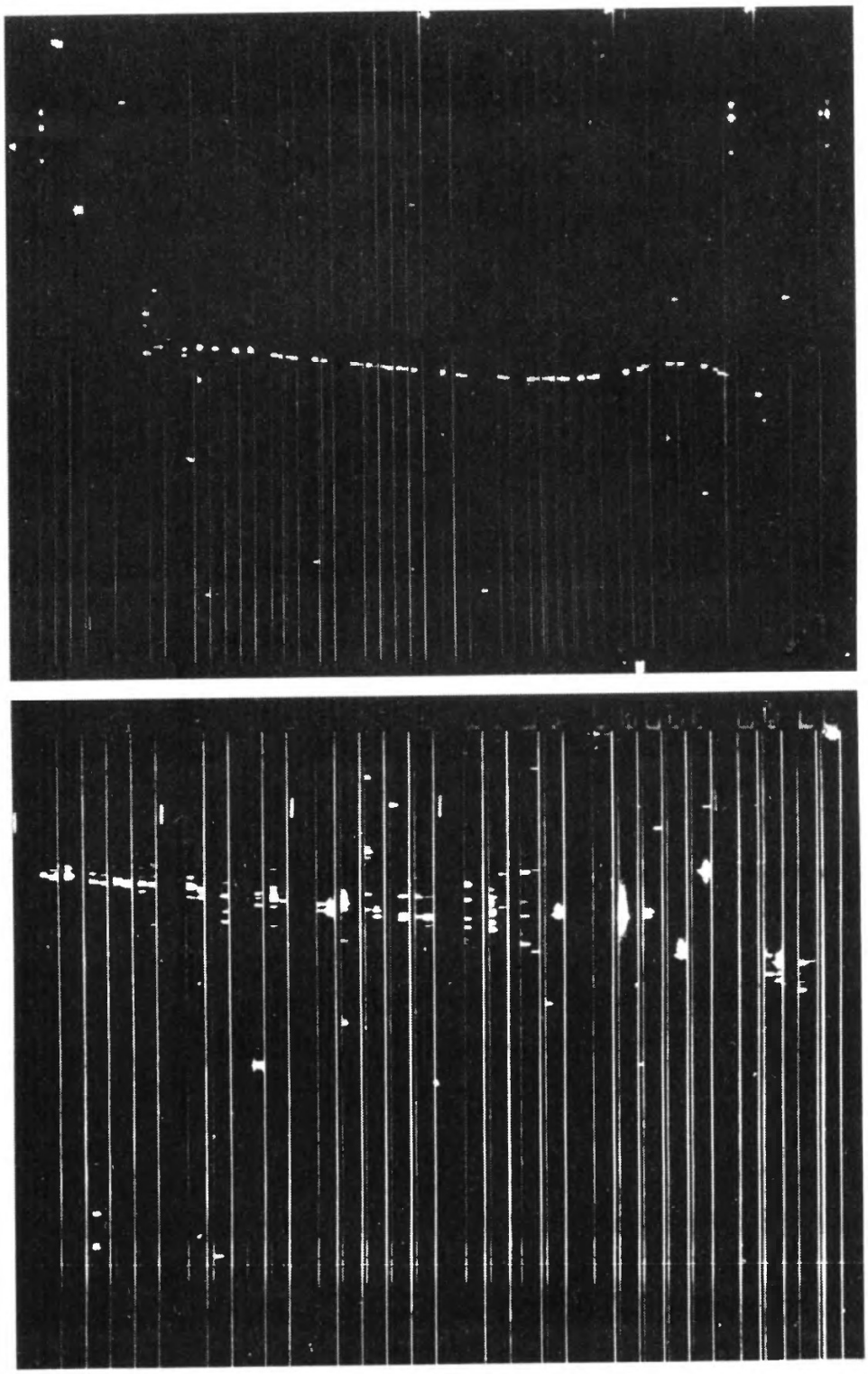

Fig. 1.6. Interactions of a neutrino beam, from the left, of about 1 GeV energy in a CERN experiment employing a large spark chamber array, where charged particle trajectories are revealed as rows of sparks between metal plates. Such discharges are known as Geiger discharges and follow from complete breakdown of the gas at sufficiently high applied voltage. At the top is the interaction of a muon-type neutrino, ν_μ, giving rise to a secondary muon, which traverses many plates before coming to rest. The event at the bottom is attributed to an electron-type neutrino, ν_e, which upon interaction transforms to an electron; the latter produces scattered sparks characteristic of an electron–photon shower, quite distinct from the rectilinear muon track. (Courtesy of CERN Information Services.)

Table 1.5. *Constituent quark masses*

Flavour	Quantum number	Rest mass, GeV/c^2
up or down	—	$m_u \simeq m_d \simeq 0.31$
strange	$S = -1$	$m_s \simeq 0.50$
charm	$C = +1$	$m_c \simeq 1.6$
bottom	$B = -1$	$m_b \simeq 4.6$
top	$T = +1$	$m_t \simeq 180$

to be indicative only. First we remark that just two types of quark combinations are established as existing in nature:

$$\begin{aligned} \text{baryon} &= QQQ \qquad \text{(three quark state)} \\ \text{meson} &= Q\bar{Q} \qquad \text{(quark–antiquark pair)} \end{aligned} \tag{1.23}$$

These strongly interacting quark composites are collectively referred to as *hadrons*. As we shall see, the fact that two, and only two, types of quark combination occur is successfully accounted for in the theory of interquark forces, called quantum chromodynamics (QCD).

The conservation rule for fermions (Section 1.4) applies of course to both leptons and baryons. It means that leptons and baryons can only be created or destroyed in pairs, of lepton and antilepton or baryon and antibaryon.

The fact that a proton ($=uud$), with $m_pc^2 = 938.27$ MeV, has almost the same mass as a neutron ($=udd$), with $m_nc^2 = 939.57$ MeV, indicates that we may define an effective 'constituent' light quark mass $m_u \simeq m_d \simeq m_N/3$. This as yet unexplained equality in the u and d masses was in fact formalised (long before the discovery of quarks) by the hypothesis of *isospin symmetry*, to be discussed in Chapter 3. The strange quark s is a component of the so-called *strange particles* discovered in cosmic rays in the 1950s, whose strange behaviour was resolved with the realisation that these particles were produced *in pairs* of opposite 'strangeness' in strong interactions. The discovery of the c quark resulted from the observation of massive meson states of the type $\psi = c\bar{c}$ in 1974, and that of the b quark followed from the detection of even heavier mesons $\Upsilon = b\bar{b}$ in 1977. The list was completed with the observation of the most massive quark, the top quark t, in 1995; it had to await the development of a proton–antiproton colliding-beam accelerator with sufficient energy.

As will be described in Chapter 2, quarks are held together by exchange of neutral gluons, the carriers of the strong force, and the 'constituent' quark masses quoted in Table 1.5 will of course include all such quark binding effects. However,

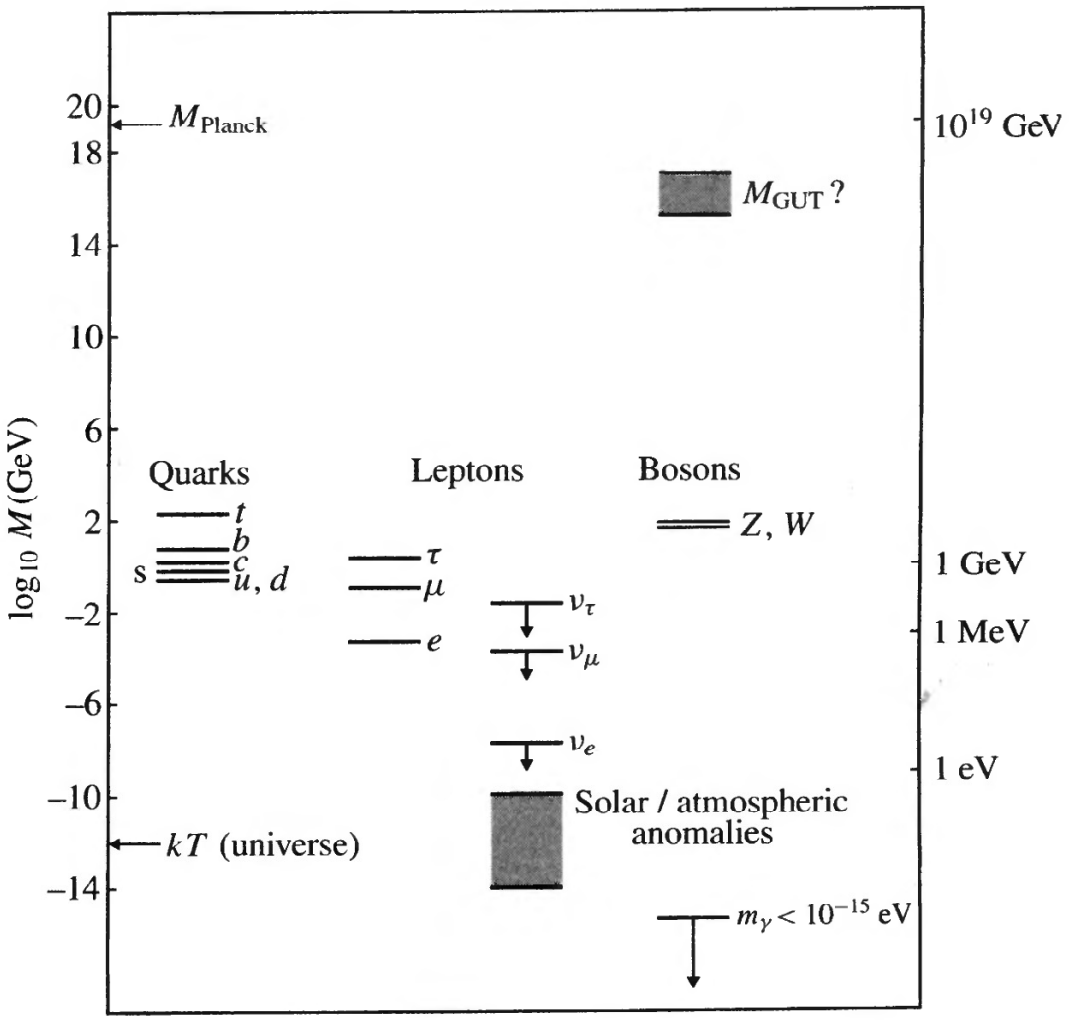

Fig. 1.7. The mass spectrum of leptons and quarks. The values shown for neutrinos are upper limits from direct measurements, and the solar and atmospheric neutrino anomalies (see Chapter 9) suggest even smaller masses. Other important mass scales are also shown: the Fermi or electroweak scale at 100 GeV, typified by the $W^{\pm}$ and Z^0 boson masses; the Planck mass scale, of order 10^{19} GeV, at which gravitational interactions are expected to become strong (see Chapter 2): and the value, $kT \simeq 1$ meV, of the cosmic microwave radiation ($T = 2.7$ K) in the universe today.

in very high energy 'close' collisions, quarks can be temporarily separated from their retinue of gluons, and the relevant masses, the so-called 'current' or 'bare' quark masses, are smaller than the constituent masses by about 0.30 GeV/c^2.

In strong interactions between the quarks, the flavour quantum number, denoted by the initial of the quark name in capitals S, C, B, T is conserved. So, for example, in a collision between hadrons containing u and d quarks only, it is possible to produce hadrons containing strange quarks, but only as a quark–antiquark ($s\bar{s}$) pair. Quarks may in fact change flavour, in such a way that $\Delta S = \pm 1$, $\Delta C = \pm 1$ etc., but this is only possible for a weak interaction. An example is the weak decay $\Lambda \rightarrow p\pi^-$, which in quark language is $sud \rightarrow uud + d\bar{u}$. An example of a

Table 1.6. *Quark composition of some meson and baryon states (masses in MeV/c^2 in parentheses), together with values of strangeness, S*

Meson	Composition	S	Baryon	Composition	S
$\pi^+(140)$	$u\bar{d}$	0	$p(931)$	uud	0
$K^0(498)$	$d\bar{s}$	+1	$\Lambda(1116)$	uds	−1
$K^-(494)$	$\bar{u}s$	−1	$\Xi^0(1315)$	uss	−2
$\rho^-(770)$	$\bar{u}d$	0	$\Sigma^+(1189)$	uus	−1
$\omega^0(783)$	$u\bar{u}$	0	$\Omega^-(1672)$	sss	−3

strangeness-conserving strong interaction followed by a weak $\Delta S = 1$ decay is given in Figure 1.10.

Since quarks have half-integral spin, it follows that baryons must have half-integral spin, and mesons integral spin.

Examples of mesons and baryons are given in Table 1.6, which spells out their quark composition and gives their strangeness value.

1.9 The cosmic connection

1.9.1 Early work in cosmic rays

Particle physics was born during the first half of the twentieth century, with the discovery of new types of particle in cosmic rays. The discovery of the positron in 1932 has already been mentioned. The next major discoveries were of the pions and muons. Figure 1.8 shows examples of the positive pions first observed in cosmic rays. Pions are generated in the atmosphere by nuclear collisions of incoming cosmic ray protons. The mean lifetime of the charged pion (25 ns) is short enough that virtually all pions decay in flight, in the stratosphere, to muons and neutrinos: $\pi \rightarrow \mu + \nu_\mu$. The neutral pion undergoes decay $\pi^0 \rightarrow 2\gamma$ with a very short lifetime (10^{-16} s), and is the source of the electron–photon cascades that develop in the high atmosphere and form the so-called 'soft' component of the cosmic rays. The muon has a much longer mean lifetime (2200 ns) and, if they are energetic enough to penetrate through the atmosphere – requiring some 2–3 GeV of energy – some muons will survive to form the 'hard' component of cosmic radiation at sea level, while others decay in flight ($\mu^+ \rightarrow \bar{\nu}_\mu + e^+ + \nu_e$). Together with the charged pions, the muons are thus responsible for the atmospheric neutrinos ν_μ and ν_e and their antiparticles. The flux at sea level of such neutrinos – with mean energy about 1 GeV – is roughly 1 cm^{-2} s^{-1}, while that of the charged muons at sea level is about 10^{-2} cm^{-2} s^{-1}. Atmospheric neutrinos are discussed in subsection 9.7.2.

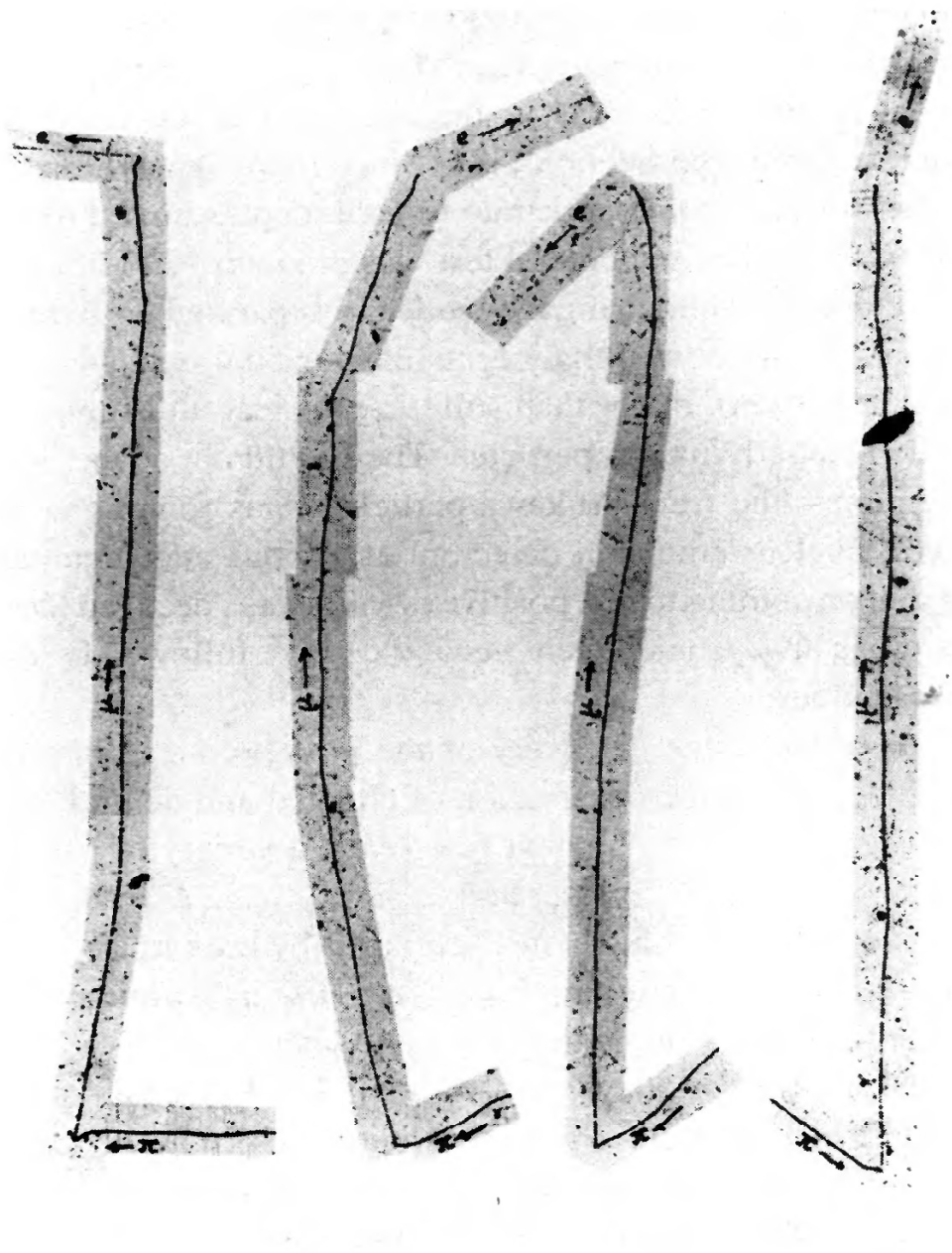

Fig. 1.8. Photomicrograph showing four examples of the decay of a positive pion upon coming to rest in nuclear emulsion exposed to cosmic rays, $\pi^+ \rightarrow \mu^+ + \nu_\mu$. The muon has a fixed kinetic energy (4.1 MeV) so that in each case the muon track has almost the same range (600 μm), thus proving that the decay is two-body. The muon in turn decays to an electron, $\mu^+ \rightarrow e^+ + \nu_e + \bar{\nu}_\mu$. This is a three-body decay, as is proved from the continuous energy spectrum of the decay electron. The original discovery of the pion was made in 1947 by Lattes *et al.* with less sensitive emulsions, which could not record the track of the decay electron. Nuclear emulsion consists of small (0.2 μm diameter) microcrystals of silver bromide suspended in gelatin and specially sensitised. An ionising particle leaves latent images in the crystals it traverses, which, upon development and fixation, are revealed under a microscope as a track of black silver grains. The use of photographic emulsions to record ionising radiations goes back to the discovery of radioactivity at the end of the nineteenth century. However, the main contribution to high energy physics came with the specially concentrated emulsions produced from 1946 onwards, which led to the discovery of the pions (positive, negative and neutral), K mesons and hyperons, all in cosmic rays. Even today (1999) nuclear emulsions, because of their excellent spatial resolution (0.5 μm), still have applications, e.g. in studies of neutrino oscillations.

Initially the muon, discovered in cloud chambers in 1937, and at that time called the mesotron, was mistakenly identified with a heavy quantum that had been postulated by Yukawa in 1935 as the exchange boson responsible for the short-range nuclear force (see Section 2.2). Since it was known that cosmic rays – presumably the muons – could penetrate to great depths underground, this soon appeared unlikely. However, the crucial test was made in 1946 in experiments by Conversi, Pancini and Piccioni, using magnetically separated positive and negative muons at sea level. These showed that negative muons decayed when they came to rest in light nuclei (carbon), rather than suffering nuclear absorption, as predicted for the negatively charged Yukawa particles. They could not be the 'strong quanta' predicted. The pion – the 'real' Yukawa particle – was found one year later, in experiments with nuclear emulsion detectors at aircraft and mountain altitudes, demonstrating that on coming to rest positive pions always decayed (see Figure 1.8) while negative pions always underwent nuclear capture followed by disintegration of the capturing nucleus.

The same year that saw the discovery of the pion produced the first evidence for 'strange particles', with the observation of charged and neutral 'V particles' – see Figures 1.9 and 1.10. Over the next few years, a variety of particles – called collectively K mesons, e.g. $K^+ = u\bar{s}$, and hyperons, e.g. $\Lambda = uds$ – in which a u or d quark or antiquark in a nucleon is replaced by an s quark, were found in cosmic rays. It was this proliferation of new particles that stimulated the building of giant high energy accelerators in the 1950s and later.

It is of interest that, even 50 years after their heyday, cosmic rays continue to have an influence in particle physics. Neutrinos produced naturally in the atmosphere have suggested new phenomena, with the observation of the 'flavour anomaly' in the ratio of numbers of ν_e and ν_μ particles, discussed in Chapter 9.

1.9.2 Particle physics in cosmology

In recent decades the study of particle physics has become intimately connected with cosmology and the evolution of the universe. It is generally assumed that the universe originated some 10–15 billion years ago in a 'Big Bang' expansion, the temperature T for the particles and radiation being given, at least in the early stages, by

$$kT = \text{constant} \times \frac{1\ \text{MeV}}{t^{1/2}} \tag{1.24}$$

where k is Boltzmann's constant and t is the time of expansion in seconds. Evidence for the Big Bang hypothesis is shown in Figure 1.11, which is a modern version of the plot originated by Hubble in 1929. It indicates a general velocity of

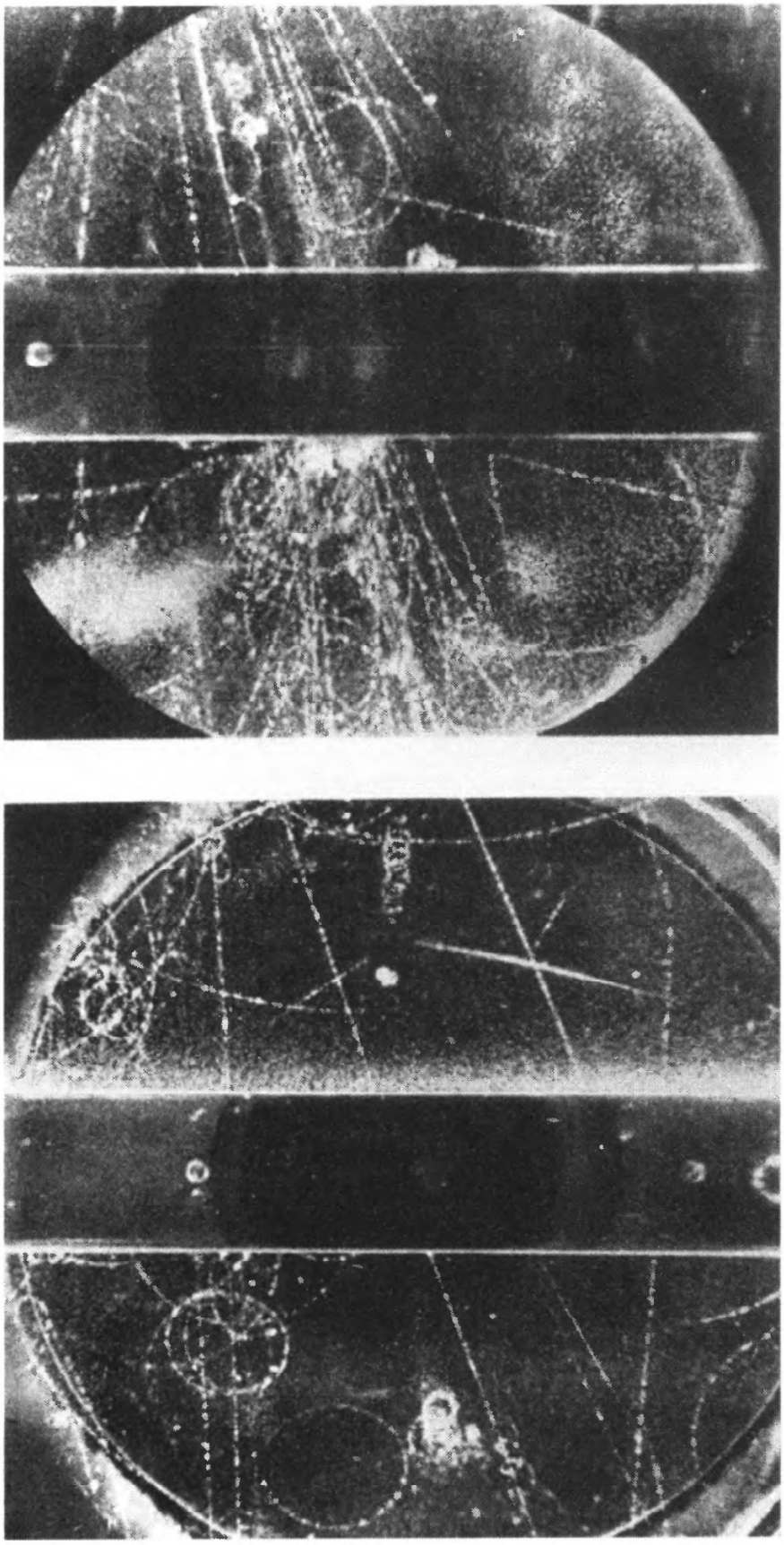

Fig. 1.9. First observation of 'V events' in a cloud chamber by Rochester and Butler (1947). The upper picture is of a neutral V event (the fork is a few millimetres below the metal plate) and was probably due to $K^0 \rightarrow \pi^+ + \pi^-$. The lower picture reveals a charged V event near the right-hand top corner, probably due to what is now known as the decay $K^+ \rightarrow \mu^+ + \nu_\mu$.

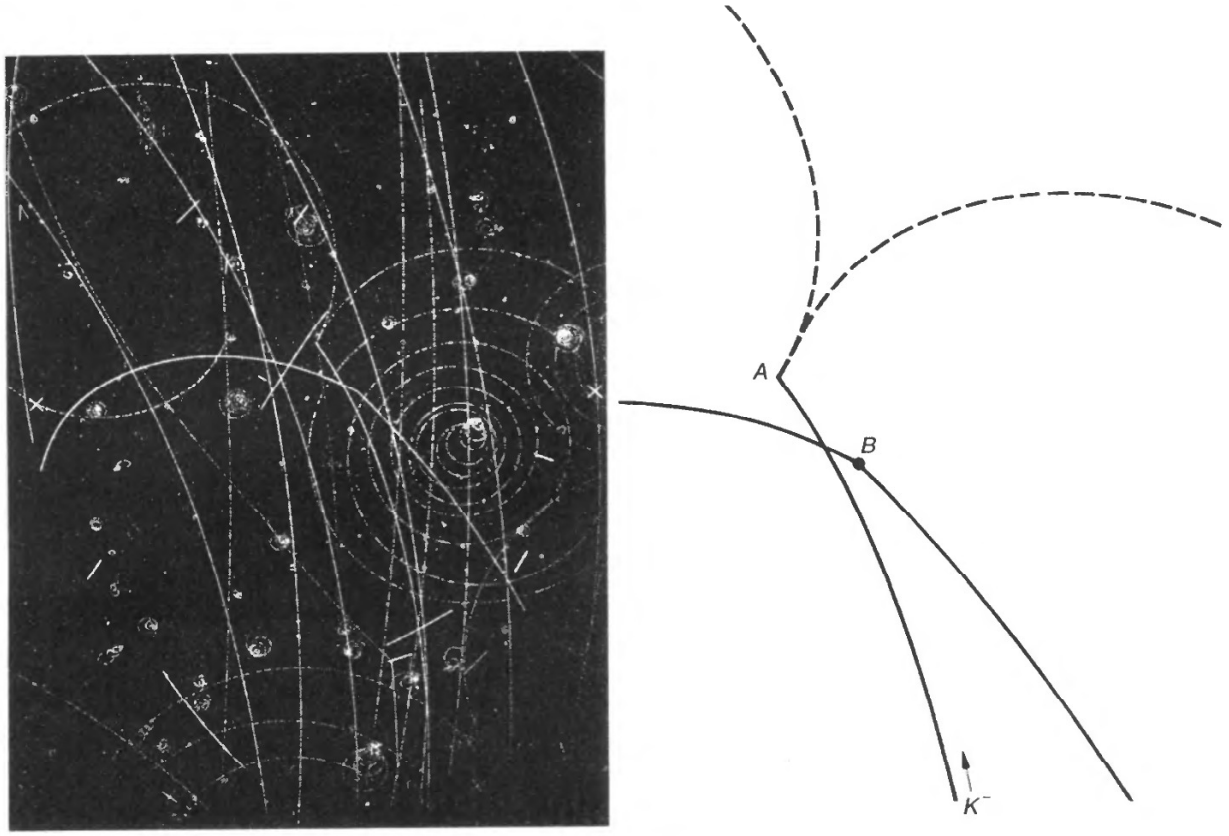

Fig. 1.10. Example of conservation and violation of the strangeness quantum number in the strong and weak interactions respectively. In this photograph, an incident K^- meson comes to rest at the point A and interacts with a proton in the liquid hydrogen of the bubble chamber, according to the strangeness-conserving strong interaction

$$K^- + p \rightarrow \Lambda + \pi^0$$

or in quark language

$$s\bar{u} + uud \rightarrow sud + u\bar{u}$$

The neutral pion in this example undergoes electromagnetic decay according to the rare mode $\pi^0 \rightarrow \gamma e^+ e^-$, the e^+e^- pair appearing to point directly to the interaction point A because the neutral pion lifetime is only 10^{-16} s. The Λ particle, after travelling a few centimetres (corresponding to a lifetime of 10^{-10} s), decays weakly at the point B according to the strangeness-changing reaction

$$\Lambda \rightarrow p + \pi^-$$

or in quark terms

$$sud \rightarrow uud + d\bar{u}$$

recession between any two objects proportional to the distance between them, i.e. a uniform expansion in all directions.

The constant on the right-hand side of (1.24) is a number close to unity which, as shown in Chapter 10, has an exact value that depends on the number of different

types of quark and lepton constituents involved. Accordingly, the number of fundamental fermions determines the rate of expansion and cooling of the early universe. So, it is believed that the heavier quarks and leptons, so extremely rare in the cold, present-day universe, must have played a key role in the early evolution of the cosmos. It is indeed clear that the nature of the fundamental particles and their interactions, as studied in high energy physics experiments, has a crucial bearing on our understanding of the development of the universe. For example, important quantities such as the primordial helium–hydrogen ratio turn out to depend critically on the number of lepton species, and this primordial ratio in turn affects the whole of the later stages of evolution of the stars.

While the heavier charged leptons μ and τ appear irrelevant today, this may not be the case for the more stable neutrinos, ν_e, ν_μ, ν_τ. The amount of very heavy elements in the universe is, we believe, controlled by their current production rate in rapid neutron capture processes in supernova explosions. The mechanism of supernovae seems to depend in turn on the number of neutrino species and their fundamental interactions (see Section 10.9).

From (1.24) we see that at very short times the thermal energy kT would be large enough for the creation from radiation of all the types of particles that can be made in the laboratory, including the heaviest and most transient. They and the radiation (i.e. the photons) would be in thermal equilibrium. For example, for $t = 10^{-12}$ s, $kT \simeq 10^6$ MeV, which is approximately the energy limit attainable with present-day accelerators. Today, when $t \simeq 10^{18}$ s, we are left with the cooled remnant of that explosion, with a radiation temperature of a few degrees absolute and kT of order one milli-electronvolt. This remnant is the cosmic microwave radiation, discovered in 1965 by Penzias and Wilson, which is almost isotropic in space and has the Planck distribution typical of a 'black body' in thermal equilibrium at 2.7 K. The observation of the microwave radiation forms the second plank of support for the Big Bang hypothesis, while the third plank is provided by the value of the helium–hydrogen ratio already mentioned.

These introductory remarks on the cosmological aspects of particle physics show that our search towards higher energies in accelerator experiments is also in a sense a look backward in time to the early moments of creation, and indeed the symbiosis of particle physics and cosmology has become an important theme of the last decades. In particular, (1.24) indicates that at early enough times in the expansion, the temperatures and energies per particle must have been far higher than anything that we can ever produce artificially in the laboratory. At that time, processes could well have occurred involving extremely massive particles and new types of interaction, and some of the major features of the present universe, such as the ratio of matter to light and the asymmetry between matter and antimatter, could have been determined at this epoch.

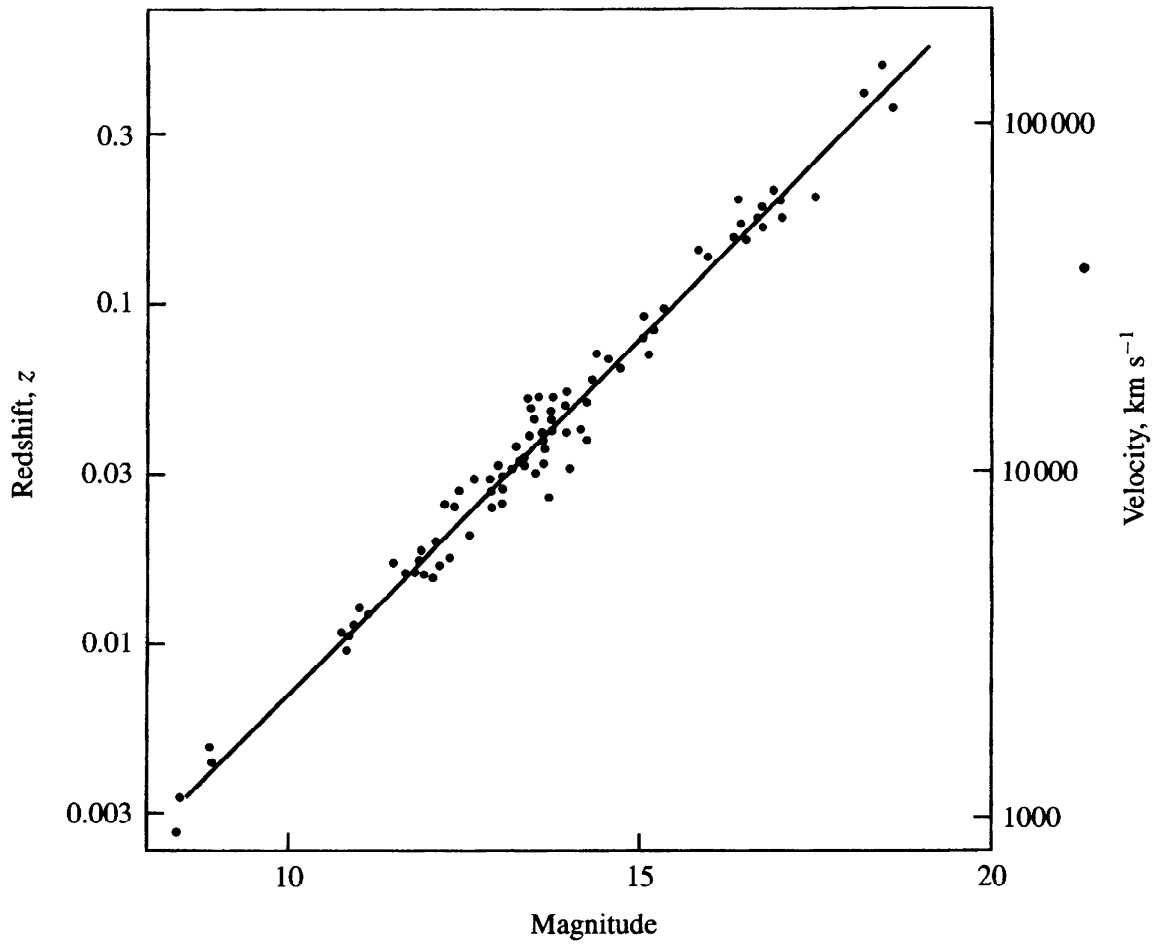

Fig. 1.11. Hubble plot, showing the redshift of light within a certain waveband from distant galaxies, plotted against their magnitude (the brightness varying inversely as the magnitude). The redshift can be interpreted as the Doppler effect due to recessional velocity, whilst the brightness of a 'standard galaxy' will vary inversely as the square of the distance to it. The straight line shows the variation predicted if the velocity of recession is proportional to distance, as expected in the Big Bang model.

It is a remarkable fact that a comparison between the potential energy and kinetic energy on large scales in the cosmos indicates that at least 90% (and possibly as much as 99%) of the matter of the universe consists of unknown particles. This so-called 'dark matter' in the form of (so far) undetected particles, shows that astronomical observations probing to ever greater distances may in turn lead us to new concepts in particle physics. A brief discussion of these possibilities and speculations is also given in Chapter 10.

Finally, it should be remarked that, implicit in our discussion of phenomena over a huge range of scale – from microscopic structure at 10^{-17} m, as probed by the highest energy particle colliders, out to 10^{25} m as probed by the largest telescopes – is of course the assumption that the 'laws' of physics are truly universal, over more than 40 orders of magnitude in distance or time. We should not be frightened to assert this; after all, Newton, over 300 years ago, was bold enough to propose

that the same universal law of gravitation should apply to a falling apple and to the planets in orbit about the sun, at 10^{12} times the distance.

Problems

1.1 An electron of energy 20 GeV is deflected through an angle of 5° in an elastic collision with a stationary proton. What is the value of the square of the 4-momentum transfer, q^2, and down to what approximate distance does such a collision probe the internal structure of the proton? (The mass of the electron can be neglected compared with the energies involved. The proton mass Mc^2 is 0.938 GeV.)

1.2 The flux of primary cosmic rays averaged over the Earth's surface is approximately 1 $\text{cm}^{-2}\ \text{s}^{-1}$, and their average kinetic energy is 3 GeV. Show that the power transferred to the Earth from cosmic rays is about 2.5 gigawatt. (Earth radius = 6400 km.)

1.3 The values of mc^2 for the pion π^+ and muon μ^+ are 139.57 MeV and 105.66 MeV respectively. Find the kinetic energy of the muon in the decay $\pi^+ \rightarrow \mu^+ + \nu_\mu$ assuming that the neutrino is massless. For a neutrino of finite but very small mass m_ν show that, compared with the case of a massless neutrino, the muon momentum would be reduced by the fraction

$$\frac{\Delta p}{p} = -\frac{m_\nu^2(m_\pi^2 + m_\mu^2)}{(m_\pi^2 - m_\mu^2)^2} \simeq -\frac{4m_\nu^2}{10^4}$$

where m_ν is in MeV.

1.4 Deduce an expression for the energy of a γ-ray from the decay of the neutral pion, $\pi^0 \rightarrow 2\gamma$, in terms of the mass m, energy E and velocity βc of the pion and the angle of emission θ in the pion rest frame. Show that if the pion has spin zero, so that the angular distribution is isotropic, the laboratory energy spectrum of the γ-rays will be flat, extending from $E(1+\beta)/2$ to $E(1-\beta)/2$. Find an expression for the disparity D (the ratio of energies) of the γ-rays and show that $D > 3$ in half the decays and $D > 7$ in one quarter of them.

1.5 (a) A negative muon, when brought to rest in liquid hydrogen, can form a molecular ion H_2^+ by displacing an electron. Why? (b) Hydrogen contains a small amount of the heavier isotope deuterium, and it is found that negative muons stopping in hydrogen eventually form molecular ions HD^+. Why? (c) What is the typical internuclear distance in such an ion? (d) If the two nuclei fuse to form ^{3}He, what may happen to the muon?

1.6 The ρ meson is a particle of spin $J = 1$ and mass 770 MeV/c^2 occurring in three charge states ρ^+, ρ^0, ρ^-. It decays to a pair of spinless pions. Show that while $\rho^\pm \rightarrow \pi^0\pi^\pm$ and $\rho^0 \rightarrow \pi^+\pi^-$ are allowed, $\rho^0 \rightarrow \pi^0\pi^0$ is forbidden.

1.7 State which of the following reactions are allowed by the conservation laws and which

are forbidden, giving the reasons:

$$\begin{aligned} \pi^0 &\rightarrow e^+ + e^- \\ e^- + p &\rightarrow n + \nu_e \\ \mu^+ &\rightarrow e^+ + e^- + e^+ \\ K^0 + n &\rightarrow \Lambda + \pi^0 \\ \Xi^0 &\rightarrow \Lambda + \pi^0. \end{aligned}$$

1.8 The solar constant (the rate at which energy is incident on the Earth) is about 2 cals cm^{-2} each minute. The fusion of hydrogen to helium in the Sun produces 26 MeV energy for every helium atom formed, plus two neutrinos carrying only a small percentage of the energy. Calculate the expected solar neutrino flux at the Earth.

1.9 (a) Show that a negative muon captured in an S-state by a nucleus of charge Ze and mass A will spend a fraction $f \simeq 0.25A(Z/137)^3$ of its time inside the nuclear matter, and that in time t it will travel a total distance $fct(Z/137)$ in the nuclear matter. (b) The law of radioactive decay of free muons is $dN/dt = -\lambda_d N$, where $\lambda_d = 1/\tau$ is the decay constant and the lifetime is $\tau = 2.16$ μs. For a negative muon captured in an atom Z the decay constant is $\lambda = \lambda_d + \lambda_c$, where λ_c is the probability per unit time of nuclear capture. For aluminium ($Z = 13, A = 27$) the mean lifetime of negative muons is 0.88 μs. Calculate λ_c and, using the expression for f in (a), compute the interaction mean free path Λ for a muon in nuclear matter. (c) From the magnitude of Λ estimate the magnitude of the weak coupling constant in the reaction $\mu^- + p \rightarrow n + \nu$, assuming that a coupling constant of unity corresponds to a mean free path equal to the range (1 fm) of the nuclear forces.

1.10 In the following reaction in hydrogen,

$$\pi^- + p \rightarrow X^- + p,$$

a boson X is observed with mass 2.4 GeV. (a) If the incident pion beam momentum is 12 GeV/c, calculate the maximum angle of emission of the recoil proton with respect to the beam direction, and its momentum. (b) Calculate the angle and momentum of the proton when the 4-momentum transfer is a maximum, and compute the value of q^2_{max}.

Hints: First write down the relativistic relation between angles in the cms and in the lab system, using the Lorentz transformations in subsection 1.1.3, and the fact that $\tan\theta = p_y/p_x$ etc. Next, find the condition that the lab system and cms angles of emission of the recoil proton are maximal, in terms of the velocity of the cms in the lab system and the velocity of the proton in the cms. Calculate the cms momentum of the proton in terms of M_X and the total cms energy. Finally, from the γ factor of the cms in the lab system, compute the lab system momentum and angle of the recoil proton. The value of q^2 is a maximum when the proton recoils in the forward direction.

2

Interactions and fields

2.1 Classical and quantum pictures of interactions

Classically, interaction at a distance, e.g. in electromagnetism, is described in terms of a potential or field due to one charged particle acting on another, the field permeating the whole of space around the source charge. A conceptually more appealing idea, perhaps, is that of an *exchange* interaction, where the object exchanged carries momentum from one charge to the other, the rate of exchange of momentum providing the force. A frequently quoted everyday example is of two ice-skaters travelling side by side, initially moving parallel, who start to diverge as they repel one another by throwing a ball back and forth.†

In quantum theory, action at a distance is indeed viewed in terms of an exchange interaction, the exchange being of a specific quantum (a boson) associated with the particular type of interaction. Since the quantum carries momentum and energy, say ΔE, the conservation laws can only be satisfied if the process takes place within a timescale Δt limited by the Uncertainty Principle, i.e. $\Delta E\, \Delta t \simeq \hbar$. Such transient quanta are said to be *virtual.*

The quantum concept of an electromagnetic interaction is of the continual exchange (emission and absorption) of virtual photons by the charges, which is no more or less fictitious than the classical concept of an all-pervading field surrounding a source charge. Neither the field nor the virtual quanta are directly observable; it is the force that is the measured quantity. Since, however, it is observed that propagating electromagnetic fields are quantised in the form of free photons, the quantum description of virtual photon exchange in the static case is appropriate for interactions on a microscopic scale.

† This example might suggest, quite wrongly, that exchange interactions in quantum mechanics must be repulsive. Classical mechanical models help us to visualise events but must never be taken literally as representing quantum phenomena. In the exchange process describing the electromagnetic interaction, the photon does not possess a classical trajectory, and the momentum it carries may have either positive or negative sign.

2.2 The Yukawa theory of quantum exchange

Yukawa (1935), in seeking to describe the short-range nature of the force between neutrons and protons in the nucleus, postulated that the interaction was due to exchange of massive quanta. Referring to the Klein–Gordon equation (1.13),

$$\frac{1}{c^2}\frac{\partial^2\psi}{\partial t^2} = \nabla^2\psi - \frac{m^2c^2}{\hbar^2}\psi$$

we note that, if we set $m = 0$, it becomes the familiar wave equation describing the propagation of an electromagnetic wave, with ψ interpreted either as the potential $U(\mathbf{r})$ at a point in space or as the wave amplitude of the associated free, massless photons. For a static potential, we drop the time-dependent term; then the above equation assumes the spherically symmetric form

$$\nabla^2 U(r) = \frac{1}{r^2}\frac{\partial}{\partial r}\left(r^2\frac{\partial U}{\partial r}\right) = \frac{m^2c^2}{\hbar^2}U(r) \tag{2.1}$$

for values of $r > 0$ from a point source at the origin, $r = 0$. Integration gives

$$U(r) = \frac{g_0}{4\pi r}e^{-r/R} \tag{2.2}$$

where

$$R = \frac{\hbar}{mc} \tag{2.3}$$

Here, the quantity g_0 is a constant of integration identified with the strength of the point source. The analogous equation in electromagnetism is $\nabla^2 U(r) = 0$ for $r > 0$, with solution

$$U = \frac{Q}{4\pi r}$$

where Q is the charge at the origin. Thus, g_0 can be interpreted as the 'strong nuclear charge'.

Historically, for nuclear forces with a range $R \simeq 10^{-15}$ m the Yukawa hypothesis predicted a spinless quantum of mass $mc^2 = \hbar c/R \simeq 100$ MeV. The pion observed in 1947 (see subsection 1.9.1) had mass 140 MeV, spin 0 and strong nuclear interactions, i.e. more or less exactly the properties required. However, although pion exchange is still recognised as accounting for the longer-range part of the nuclear potential, the full details of this interaction turn out to be very much more complicated than was realised 50 years ago.

It should also perhaps be noted here that Yukawa was in a sense fortunate in making a simple connection between the range of the field and the mass of the associated quantum. As we shall see in Section 2.7 and in more detail in Chapters 4 and 6, what we believe to be *the* elementary strong interactions, those occurring

between the constituent quarks in the nucleon, are mediated by massless gluons but nevertheless have a very short range, of order 1 fm. The interquark potential in this case is more complex than that of Yukawa and is represented as containing two terms, one corresponding to the form (2.2) with $m = 0$ and a second term proportional to r and responsible for quark confinement.

2.3 The boson propagator

Consider a particle being scattered by a potential provided by an infinitely massive source, the effect of which is observed through the angular deflection of the particle or, equivalently, the momentum transfer $\mathbf{q}$. The potential $U(\mathbf{r})$ in coordinate space will have an associated amplitude, $f(\mathbf{q})$, for scattering of the particle; this is simply the Fourier transform of the potential, in just the same way that the angular distribution of light diffracted from an obstacle in classical optics is the Fourier transform of the spatial extent of the obstacle (see Problem 5.1). So we may write

$$f(\mathbf{q}) = g \int U(\mathbf{r}) e^{i\mathbf{q}\cdot\mathbf{r}} dV \tag{2.4}$$

where g is the intrinsic coupling strength of the particle to the potential. For a central potential, such that $U(\mathbf{r}) = U(r)$, the integration over volume V is easily performed, setting

$$\mathbf{q}\cdot\mathbf{r} = qr\cos\theta, \qquad dV = r^2 d\phi \sin\theta d\theta dr,$$

where θ and ϕ are the polar and azimuthal angles. If we now substitute the Yukawa potential above, and for convenience use units such that $\hbar = c = 1$, we find after integration over ϕ and θ

$$\begin{aligned} f(\mathbf{q}) &= 4\pi g \int_0^\infty U(r) \frac{\sin qr}{qr} r^2 dr \\ &= g_0 g \int_0^\infty e^{-mr} \left(\frac{e^{iqr} - e^{-iqr}}{2iq} \right) dr \end{aligned}$$

which gives

$$f(\mathbf{q}) = \frac{g_0 g}{|\mathbf{q}|^2 + m^2} \tag{2.5}$$

This equation describes, in momentum space, the potential (2.2) in coordinate space; the two descriptions are equivalent. The discussion here has been of the scattering of a particle of coupling g by the static potential U provided by a massive source of strength g_0. The incident particle has been scattered elastically, but, in an actual collision between two particles, energy ΔE as well as 3-momentum $\Delta\mathbf{p} = \mathbf{q}$ will be transferred. The components of the 3-momentum transfer and the energy transfer together form a 4-vector. As in subsection 1.1.3 we define the square of

the 4-momentum transfer as $q^2 = \Delta\mathbf{p}^2 - \Delta E^2$, which for a massive source gives $q^2 \equiv |\mathbf{q}|^2$. The result in (2.5) indeed holds in general if we replace the integral (2.4) by one over both space and time and $\mathbf{q}^2$ is replaced by the relativistically invariant quantity q^2. In summary, the scattering amplitude or matrix element for a single boson-exchange process is the product of two *vertex factors* g_0, g describing the coupling of the boson to the scattered and scattering particles, and a *propagator* term $(q^2 + m^2)^{-1}$:

$$f(q^2) = \frac{g_0 g}{q^2 + m^2} \tag{2.6}$$

The rate W of a particular reaction mediated by boson exchange is proportional to $|f|^2$ multiplied by a phase-space factor, as discussed below, and determines the rate of decay of an unstable state, or the cross-section for a collision process. Large values of $|f|^2$ correspond to high rates of decay or large collision cross-sections. Extra factors associated with particle spin will also have to be introduced later as necessary. Nevertheless (2.6) is the basic formula describing the interaction of two particles via single-boson exchange; it will be used frequently throughout the text.

2.4 Feynman diagrams

Feynman diagrams are a graphical way of displaying the interactions between particles and fields. Examples are shown in Figure 2.1, referring to electromagnetic interactions. Solid straight lines represent fermions (electrons in the figure) while wavy, curly or broken lines represent bosons (photons in electrodynamics). Arrows along the lines indicate the time sense, with time increasing from left to right, i.e. the arrow indicates the direction of fermion number flow. An arrow indicating motion of an electron backwards in time is equivalent to a positron moving forwards in time; the convention for antiparticles uses such time-reversed arrows.

Fermion and boson lines meet at vertices where charge, energy and momentum are conserved, and the strength of the interaction is represented by a coupling constant (the fine structure constant α in Figure 2.1). Lines entering or leaving the boundaries of a diagram represent real, or free, particles, while those joining vertices represent virtual particles. Virtual particles have energy and momentum such that the rest mass does not correspond to that of a real, free particle.

There is a set of algebraic rules for Feynman diagrams that allows the detailed calculation of the matrix elements of the interaction, but we shall not discuss these here. The main points for our purpose are that coupling constants are involved at the vertices, and that propagators are associated with the virtual particles running between the vertices. We now discuss briefly the various forms of fundamental interaction in terms of these graphical representations.

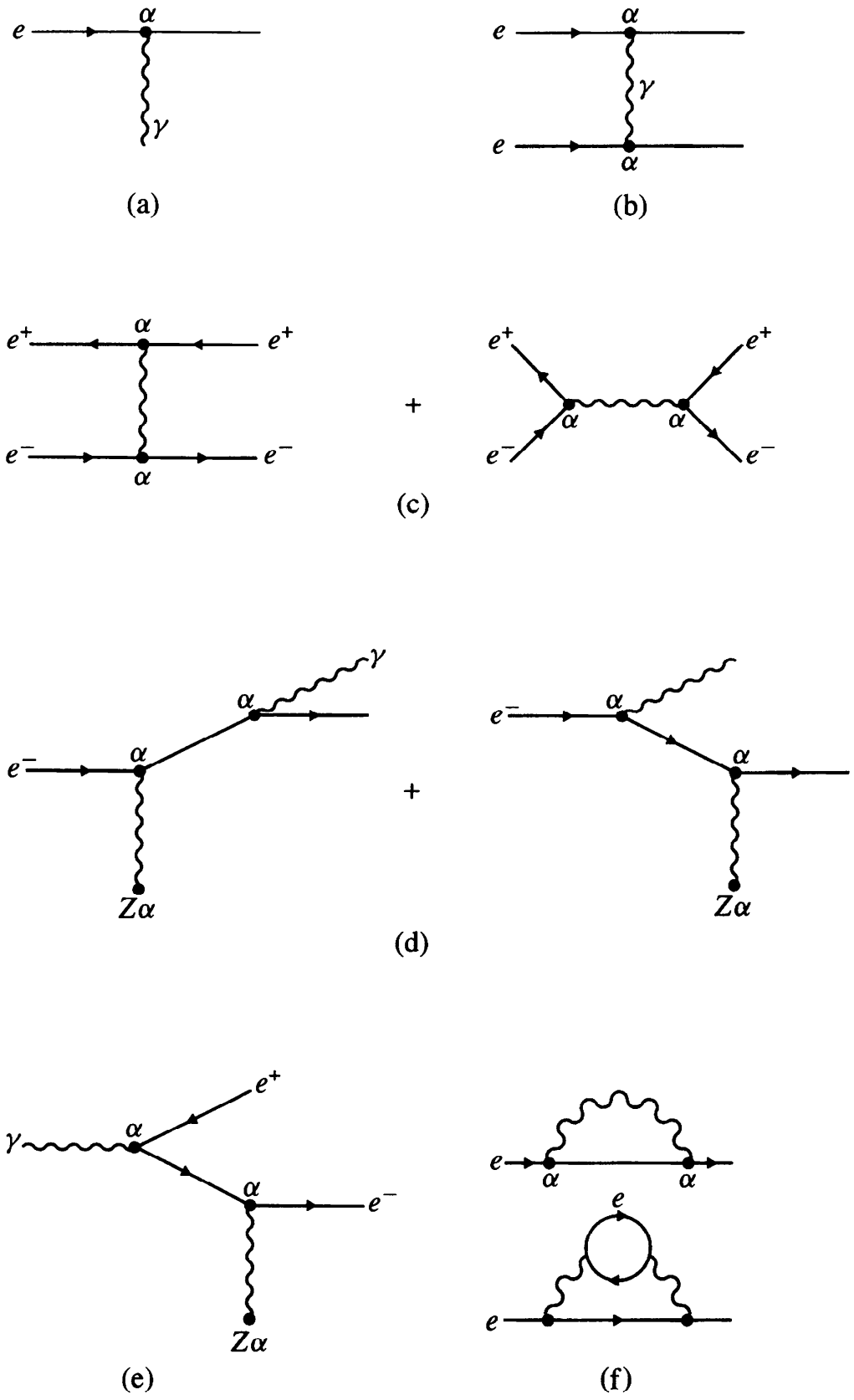

Fig. 2.1. Feynman diagrams depicting some basic electromagnetic processes. (a) basic electron–photon vertex; (b) electron–electron scattering via photon exchange; (c) e^+e^- scattering via photon exchange with two diagrams contributing in first order; (d) bremsstrahlung or photon emission in the field of a nucleus; (e) pair production; (f) self-energy terms.

2.5 Electromagnetic interactions

The coupling constant specifying the strength of the interaction between charged particles and photons is the dimensionless quantity

$$\alpha = \frac{e^2}{4\pi\hbar c} = \frac{1}{137.0360\cdots} \tag{2.7}$$

called the fine structure constant, because it determines the fine structure (spin–orbit splitting) in atomic spectra. Electromagnetic fields have vector transformation properties and the photon, which mediates the interaction, is a vector particle. As will be explained in Chapter 3, it has spin-parity $J^P = 1^-$.

Figure 2.1 depicts various electromagnetic processes. Figure 2.1(a) shows the basic electromagnetic vertex, i.e. the process of absorption (or emission) of a photon by an electron. The photon couples to the electron with amplitude $\sqrt{\alpha}$ (or e, in units $\hbar = c = 1$). This process cannot occur for free particles, since an electron cannot absorb or emit a massless photon while conserving energy and momentum. The photoelectric effect of photon absorption by an electron involves momentum conservation *by the whole atom.* The cross-section, which equals the matrix element squared, is proportional to the square of the amplitude, i.e. to α or e^2. Since α occurs to the first power, this is called a first-order process.

Figure 2.1(b) shows Coulomb scattering between two electrons, via the exchange of a single virtual photon of momentum q, say, coupling at the two vertices. The product of the coupling amplitudes is $\sqrt{\alpha}\sqrt{\alpha} = \alpha$, while the virtual photon (with zero mass if it were a free particle, but with an actual mass given by $m^2 = -q^2$) introduces a propagator factor $1/q^2$ as in (2.6). The matrix element is proportional to α/q^2 and the differential scattering cross-section $d\sigma/dq^2$ is proportional to α^2/q^4 (the Rutherford scattering formula).

Figure 2.1(c) shows the corresponding first-order diagram for e^+e^- scattering (Bhabha scattering). In addition to the first diagram, which is akin to that in Figure 2.1(b), there is also a second, so-called 'annihilation' diagram that has to be included.

Figure 2.1(d) shows the emission of a real photon by an electron that has undergone acceleration in the electric field of a nucleus, charge Ze (the bremsstrahlung process). A virtual photon has to be exchanged with the nucleus in order to conserve momentum, and the cross-section is of order α^3. Note that an intermediate virtual electron state is also involved, since an electron cannot emit a real photon and conserve energy and momentum without reducing its rest mass (it is said to go 'off mass shell'). Again, two leading-order diagrams are involved.

Figure 2.1(e) depicts the process of e^+e^- pair creation by a photon in the field of a nucleus, also of magnitude α^3. The diagrams in (d) and (e) are obviously closely related, and can be obtained from each other by reversing the time sense of the

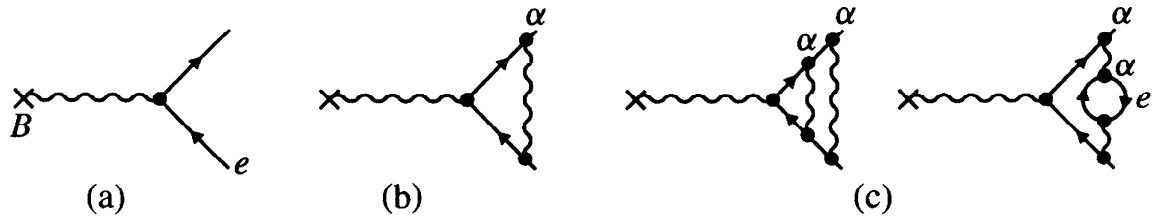

Fig. 2.2. Some leading diagrams contributing to the magnetic moment of the electron.

incoming electron line. They will therefore have the same matrix element and the cross-sections will only differ by kinematic factors. They are said to be *crossed diagrams*.

Finally, Figure 2.1(f) shows two 'self-energy' diagrams, to be discussed in the next section.

The diagrams of Figure 2.1(a)–(d) represent leading order processes, but there will be, in addition to these, further diagrams for contributions of higher order in α. As an example, Figure 2.2 shows some of the diagrams contributing to the magnetic moment of the electron. Figure 2.2(a) indicates the leading interaction of the external magnetic field B with a 'bare' electron, yielding a calculated value for the magnetic moment equal to one Bohr magneton, $\mu_B = e\hbar/(2mc)$, as given by the Dirac theory of a literally pointlike electron. Figure 2.2(b) shows the next-to-leading-order correction. Here, the electron is shown temporarily dissociated into a 'bare' electron, with which the field interacts, and a virtual photon. This so-called radiative correction to the moment will clearly be of magnitude e^2 or α. Qualitatively, we can see that although the charge resides on the electron, part of the mass–energy is carried by the virtual photon, and hence the value of e/m for the electron itself will be slightly increased. Figure 2.2(c) shows two possible corrections of order α^2. The second diagram involves the formation of a virtual electron–positron pair. Because of the Coulomb field of the electron, the vacuum containing the virtual e^+e^- pair becomes polarised, and the effect is referred to as 'vacuum polarisation'.

These diagrams of higher and higher order are a graphical representation of the perturbation series in powers of α that predicts the correction to, or anomaly in, the magnetic moment of the 'Dirac' electron. Defining the magnetic moment as $\mu = g\mu_B s$, where $s = \frac{1}{2}$ is the spin in units of $\hbar$, then $g = 2$ in the Dirac theory and the quantity $(g-2)/2$ represents the anomaly, with a calculated value

$$\left(\frac{g-2}{2}\right)^{\text{theory}} = 0.5\left(\frac{\alpha}{\pi}\right) - 0.32848\left(\frac{\alpha}{\pi}\right)^2 + 1.19\left(\frac{\alpha}{\pi}\right)^3 + \cdots$$
$$= (115\,965\,230 \pm 10) \times 10^{-11}$$

This may be compared with the experimental value

$$\left(\frac{g-2}{2}\right)^{\text{expt}} = (115\,965\,219 \pm 1) \times 10^{-11}$$

Incidentally, the reason for the larger error in the predicted number is experimental uncertainty in the value of α. In any case, the agreement between experiment and theory at the level of 1 in 10^8 is quite convincing evidence of the predictive power of quantum field theory.

2.6 Renormalisation and gauge invariance

Quantum electrodynamics (QED), some processes in which we have discussed above, is the prototype quantum field theory. It is characterised by two crucial properties, *renormalisability* and *gauge invariance*, which we mention briefly here. Figure 2.1(f) shows a single electron emitting and reabsorbing a virtual photon or a virtual electron–positron pair. The electron line itself in a Feynman diagram represents a 'bare' electron, whereas the real observable particles are the 'bare' particles 'dressed' by these virtual processes, the so-called 'self-energy' terms which contribute to the mass and charge of the electron that the experimentalist measures. There is no restriction on the momentum k of particles in such virtual states, and such terms are of the form $\int dk/k$ and thus logarithmically divergent.

Divergent terms of this type are present in all QED calculations, e.g. in all the other processes shown in Figure 2.1. Fortunately, it is found possible to redefine the mass or charge as follows. The 'bare' mass or charge m_0 or e_0 (the purely fictitious and unmeasurable value that would obtain in the absence of the self-interaction terms) is always found to be multiplied by a dimensionless term containing the divergent integral; since this combination occurs in all calculations, it is therefore replaced by the physical values e, m as determined from experiment. This process is called *renormalisation*. The procedure is highly technical and beyond the scope of this text. We simply remark that it results in predictions that are, as we have seen, in incredibly good agreement with experiment.

The other important point to emerge from the renormalisation procedure is that the coupling 'constants' such as α are not in fact constant but depend (logarithmically) on the energy scale at which measurements are being made: for example, the usually quoted value of α applies at the frequency of the Hall junction with which it is measured. Its value at the mass of the Z^0 is 1/128 instead of 1/137. These running coupling constants are discussed in more detail in Chapter 6.

The vital feature necessary for renormalisability is that the theory should be formulated so that it has the property of *gauge invariance*. We know that in electrostatics, for example, the energy of a system depends only on *changes*

Table 2.1. *Decays of* Σ *baryons. The Q-value gives the total kinetic energy liberated in the decay*

Baryon	Composition	Q-value, MeV	Decay mode	Lifetime, s
$\Sigma^0(1192)$	uds	74	$\Lambda\gamma$	10^{-19}
$\Sigma^+(1189)$	uus	189	$p\pi_0$	10^{-10}
$\Sigma^0(1385)$	uds	208	$\Lambda\pi^0$	10^{-23}

in the static potential and not on its absolute magnitude, so that it is invariant under arbitrary redefinitions of the global potential scale or gauge. In quantum mechanics, the phase of a fermion field, e.g. the wavefunction of an electron, is likewise arbitrary, and one could demand the freedom to change the phase at will, not just globally but at any local point in space–time, without changing the physics. By demanding such local gauge invariance one is led to conserved currents and to the conservation of electric charge (see Section 3.7).

A mention of renormalisability, running coupling constants and gauge invariance in quantum electrodynamics has been made here because they are closely related and we shall be referring to them again. They seem to be essential ingredients of any successful quantum field theory, e.g. of the theories of the strong and weak interactions which we now present briefly.

2.7 Strong interactions

Table 2.1 lists some of the decays of unstable baryons generically labelled Σ, standing for states made up of three quarks u, d, s in the form of charge triplets of nearly equal mass. In the table, the numbers in parentheses give the central mass values in MeV. The Q-value is the total kinetic energy liberated in the decay. The first two entries, $\Sigma^0(1192)$ and $\Sigma^+(1189)$ are spin $\frac{1}{2}$ baryons, while $\Sigma^0(1385)$ has spin $\frac{3}{2}$ and is a first orbital excitation of the ground state. The decay mode $\Sigma^0(1192) \rightarrow \Lambda\gamma$ involves no change in quark flavour; Λ has spin $\frac{1}{2}$ and is also a uds combination, but it is a charge singlet state, and strong decay is forbidden (as we shall see later, by conservation of isospin). This decay proceeds by an electromagnetic transition, with a lifetime of 10^{-19} s. By contrast, $\Sigma^0(1385) \rightarrow \Lambda\pi^0$ is a strong, isospin-conserving decay. It is a broad state with width $\Gamma = 36$ MeV and a calculated lifetime $\tau = \hbar/\Gamma = 10^{-23}$ s. Disregarding the factor 3 difference in the Q values in the two cases, and with the decay rate for a leading-order process proportional to the square of the coupling constant, we

estimate that the strong coupling α_s analogous to α in QED will be given by

$$\frac{\alpha_s}{\alpha} \sim \sqrt{\frac{10^{-19}}{10^{-23}}} \sim 100$$

This is a crude estimate, but clearly shows that, while $\alpha = e^2/(4\pi) = 1/137$, $\alpha_s = g_s^2/(4\pi) \sim 1$. Here, g_s is defined as the strong charge of the constituent quarks.

The interaction between quarks proceeds via an appropriate mediating boson called a *gluon*, the neutral, massless carrier of the strong force analogous to the photon in QED. Like the photon, the gluon is a vector particle of spin-parity $J^P = 1^-$. In QED, there are just two types of charge, historically denoted by the symbols $+$ and $-$. In the theory of strong interquark forces, quantum chromodynamics (QCD), there are six types of strong charge, called colour charges; 'colour' is just a name for an internal degree of freedom. A quark can carry one of three primary colours (say red, blue and green), and its antiquark then carries the corresponding anticolour. Colour symmetry is supposed exact, so that the interquark force is independent of the colours involved. An example of colour-force exchange is shown in Figure 2.3(b), where a red quark interacts with a blue quark via exchange of a red–antiblue gluon. Note that the gluon carrier itself is endowed with a colour charge ($r\bar{b}$ in the case shown). On this account, gluons have self-interaction, with triple (and quadruple) gluon vertices; see Figure 2.3(c). This marks a crucial difference from QED, where the photon is uncharged and there is no first-order photon–photon interaction. In the jargon, QED is said to be an Abelian, and QCD a non-Abelian, theory. Since the gluons carry one colour and one anti-colour, there should be $3^2 = 9$ possible colour combinations. However, one of these turns out to be a colourless singlet (in the form $r\bar{r} + b\bar{b} + g\bar{g}$), leaving eight active gluon states.

The diagrams in Figure 2.3 are drawn for the case of single-gluon exchange, but if, as indicated above, $\alpha_s \sim 1$, multiple exchanges, involving terms in $\alpha_s^2, \alpha_s^3, \ldots$, must also be very probable. However, it turns out that for violent 'close' collisions at very high q^2, $\alpha_s \ll 1$ and single-gluon exchange is a good approximation, while at low q^2 or, equivalently, larger distances, the coupling becomes very large and the theory is uncalculable. This large-distance behaviour is presumably linked with the confinement of quarks and gluons inside hadrons.

Since gluons are massless, one might expect the static QCD potential to have a similar, $1/r$, form to that in QED. In fact the quark–antiquark potential is often taken to be of the form

$$V_s = -\frac{4}{3}\frac{\alpha_s}{r} + kr \tag{2.8}$$

where the first term, dominating at small r, arises from single-gluon exchange. It

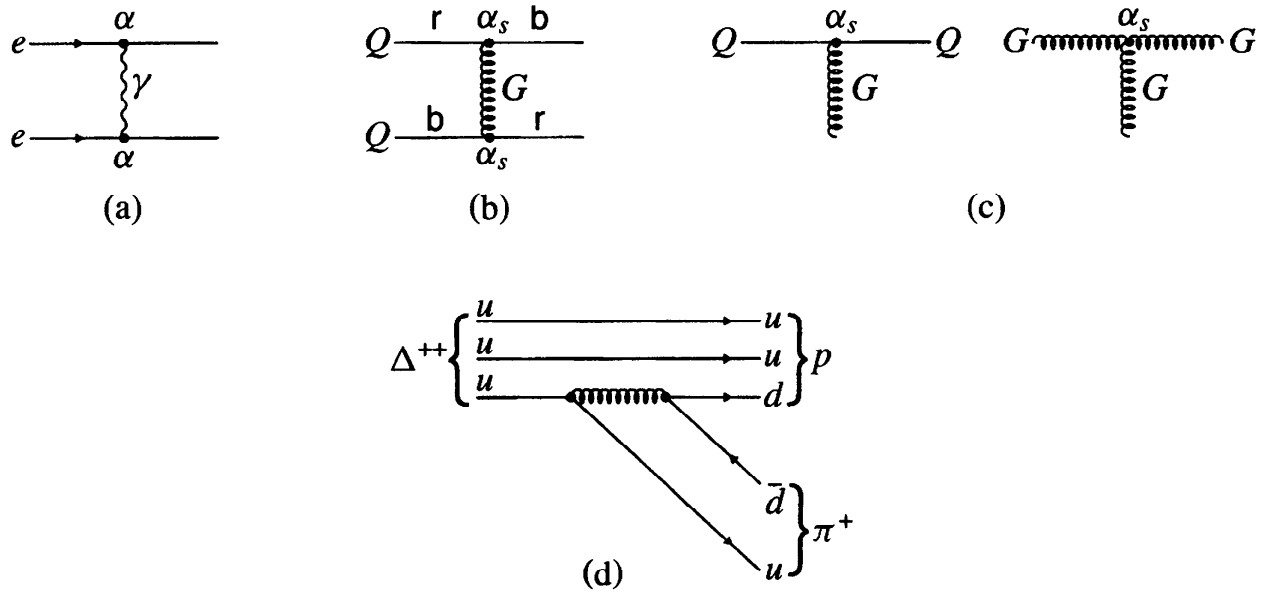

Fig. 2.3. Comparison of an electromagnetic interaction between charges via one-photon exchange in (a), with a strong interaction between quarks via one-gluon exchange in (b). The diagrams in (c) show the basic quark–gluon and gluon–gluon vertices in QCD. Finally (d) shows the strong decay of the $\Delta^{++} \rightarrow p+\pi^+$ resonance (see subsection 2.11.1 below), in terms of quarks and antiquarks and a 'gluon string' (see also Figure 2.4).

is similar to the Coulomb potential between elementary charges

$$V_{\text{em}} = -\frac{\alpha}{r}$$

The factor $\frac{4}{3}$ in (2.8) is plausible in view of the fact that there are eight colour gluon states, to be averaged over three quark colours, giving a factor $\frac{8}{3}$ as compared with QED (one 'colour' of photon and one fermion charge). This has to divided by 2 because, for historical reasons, a factor 2 enters into the definition of α_s in terms of the square of the strong colour charge.

The second, linear term in (2.8) is associated with confinement at large r. As discussed later, there is experimental evidence for both terms in the above potential. Because of the linear term, attempts to free a quark from a hadron simply result in the production of fresh $Q\bar{Q}$ pairs, i.e. mesons. One can imagine that the lines of force of the colour field are pulled together by the gluon–gluon interaction, so that they form a tube or string. Pulling out this string, the stored energy kr eventually reaches the point where it is energetically more favourable to create a new $Q\bar{Q}$ pair, so that there are now two short strings rather than one long one (see Figure 2.4). From the sizes and masses of hadrons we can expect that, in order of magnitude, $k \sim 1$ GeV fm^{-1}. In fact the usually quoted value of k is 0.85 GeV fm^{-1}, which, as the reader can readily verify, corresponds to a force between those tiny quarks of 14 tonnes weight!

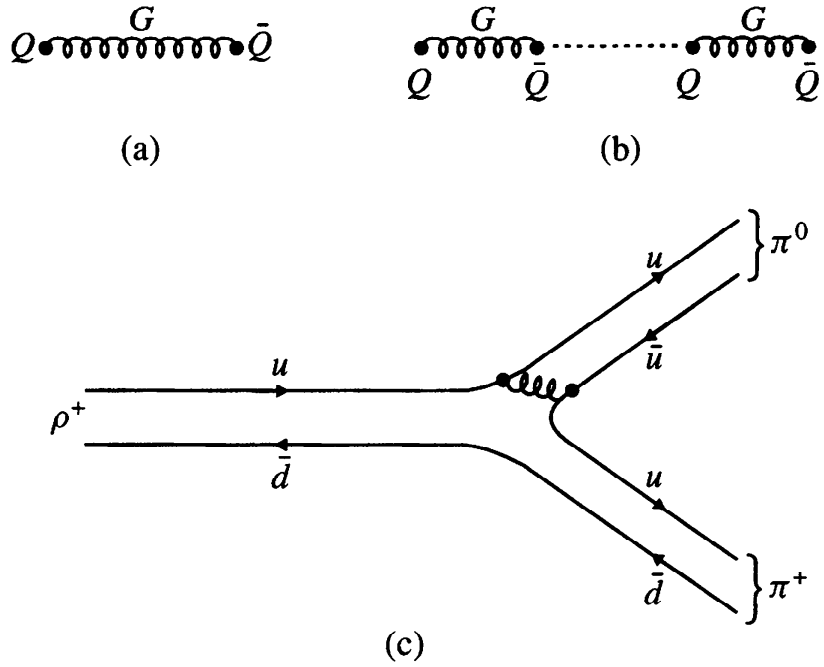

Fig. 2.4. Diagram (a) shows a gluon 'string' connecting two quarks. Pulling out the string costs energy proportional to the string length, and eventually, as in (b), it is more favourable to create a quark–antiquark pair involving two short strings. Diagram (c) depicts the decay of a ρ meson, consisting of the combination $u\bar{d}$, to $\pi^+\pi^0$ via a gluon 'string'.

In the limit of high quark energies, the confining potential has dramatic effects. The process $e^+e^- \rightarrow$ hadrons is viewed as the elementary process

$$e^+e^- \rightarrow Q\bar{Q}$$

followed by 'fragmentation' of the quarks to hadrons via the above string processes. Since the transverse momenta of the created mesons are set by the large distance ($\sim$1 fm) behaviour at about 0.3 GeV/c, one obtains two collimated 'jets' of hadrons travelling in opposite directions and following the momentum vectors of the original quarks, as shown in Figure 2.5.

2.8 Weak and electroweak interactions

Comparison of the strangeness-changing weak decay $\Sigma^+(1189) \rightarrow p\pi_0$ and the electromagnetic decay $\Sigma^0(1192) \rightarrow \Lambda\gamma$ in Table 2.1 shows that the weak coupling is smaller by a factor of order $\sqrt{10^{-19}/10^{-10}} \sim 10^{-5}$ than the electromagnetic coupling, α. Weak interactions take place between all quark and lepton constituents: each of them has to be assigned a weak charge g. Usually, the weak interaction is completely swamped by the much greater strong and electromagnetic interactions, unless these are forbidden by some conservation rule. Observable weak interactions consequently involve either neutrinos (with no electric or strong

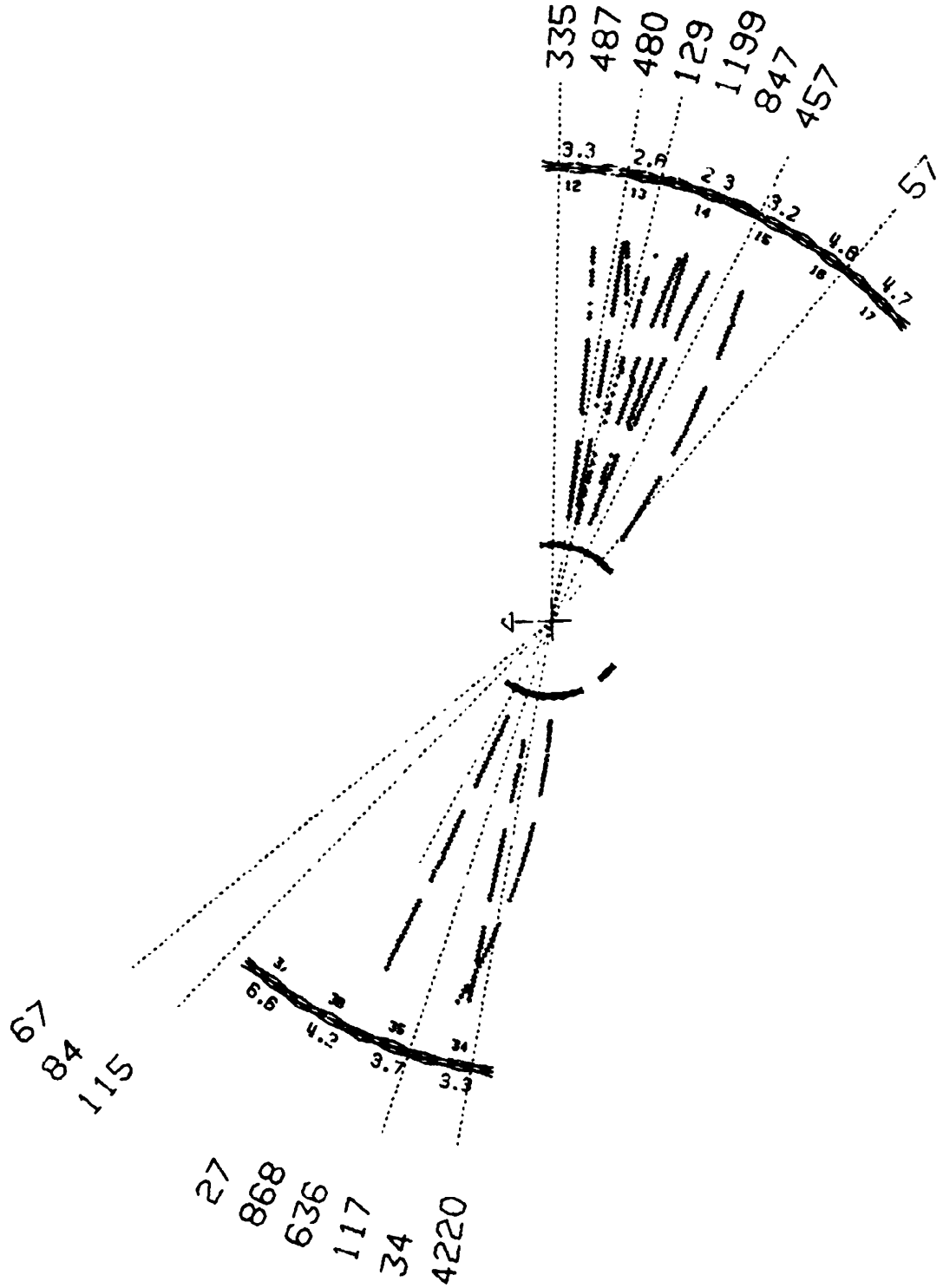

Fig. 2.5. Example of hadron production in e^+e^- annihilation in the JADE detector at the PETRA e^+e^- collider at DESY, Hamburg. The total (centre-of-momentum) energy is 30 GeV. Computer reconstruction shows the trajectories of charged particles (pions) as lines of crosses where they traverse gas ionisation detectors (drift chambers). A solenoidal magnet provides a field of 0.5 tesla, so that particle momenta can be measured from track curvature. Gamma-rays from neutral pion production and decay ($\pi_0 \rightarrow 2\gamma$) are recorded as electron–photon cascades as they traverse lead-glass counters, where the electrons produce Čerenkov light recorded by photomultipliers. The γ-ray trajectories are shown by dotted lines. The event demonstrates the collimation of the hadrons into two oppositely directed jets, from the fragmentation of quarks created in the elementary process $e^+e^- \rightarrow Q\bar{Q}$.

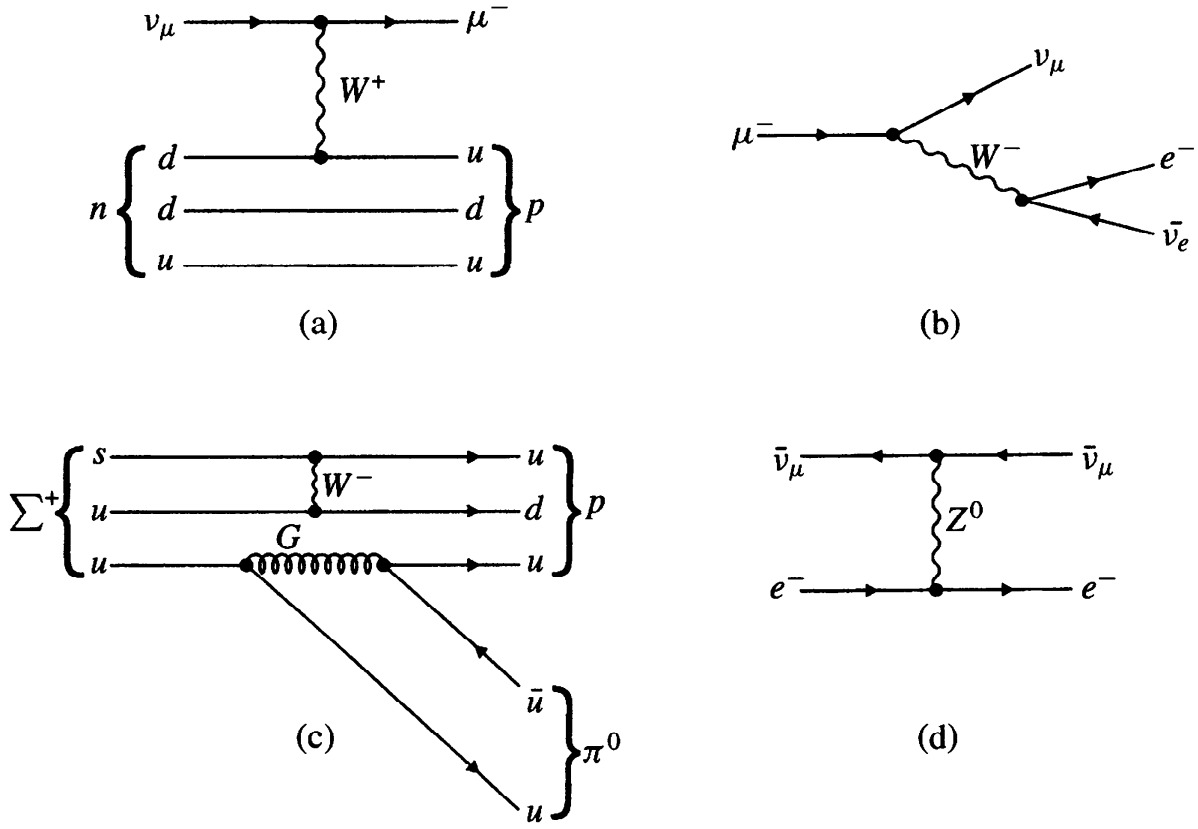

Fig. 2.6. (a) $\nu_\mu + n \rightarrow \mu^- + p$, (b) $\mu^- \rightarrow e^- + \bar{\nu}_e + \nu_\mu$; (c) $\Sigma^+ \rightarrow p + \pi^0$ ($\Delta S = 1$), (d) $\bar{\nu}_\mu + e^- \rightarrow \bar{\nu}_\mu + e^-$. Diagrams (a), (b) and (c) indicate charged-current weak interactions, mediated by $W^\pm$ exchange. In contrast to the strong decay of Figure 2.3(d), Figure 2.6(c) shows a weak hadronic decay, involving a change in strangeness. Finally (d) shows an example of a neutral-current weak interaction, mediated by Z^0 exchange.

charges) or quarks with a flavour change ($\Delta S = 1$, $\Delta C = 1$ etc.) that is forbidden for strong interactions.

Nuclear β-decay and its inverse are the prototype weak interactions involving neutrinos:

$$n \rightarrow p + e^- + \bar{\nu}_e$$
$$\bar{\nu}_e + p \rightarrow n + e^+$$

Lepton conservation requires the total lepton number to be the same on both sides (see Section 1.7), which with charge conservation then requires both a neutral and a charged lepton of the same flavour to appear together. A second example, not involving a neutrino, is the above decay $\Sigma^+ \rightarrow p\pi_0$, where we have the exchange of a strange quark for a non-strange one.

The weak interactions are weak principally because they are mediated by charged and neutral vector bosons, $W^\pm$, Z^0, which are very massive and hence give rise to interactions of very short range. Figure 2.6 shows some examples of weak boson exchanges, at the quark or lepton level.

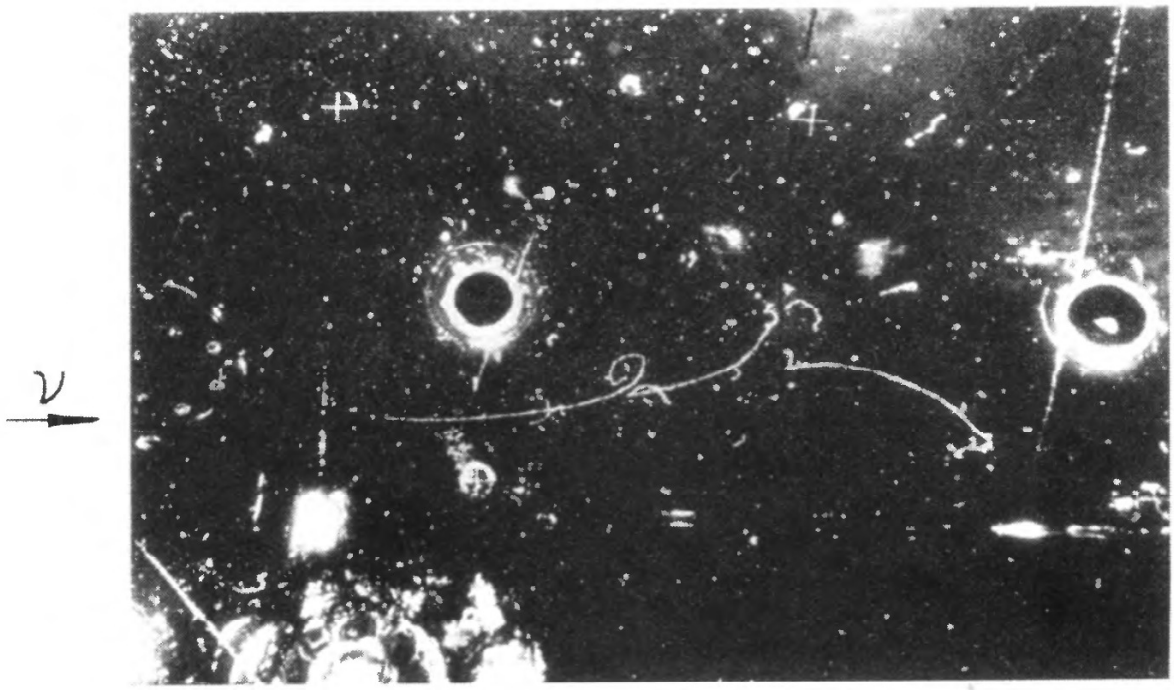

Fig. 2.7. First example of the neutral weak current process $\bar{\nu}_\mu + e \to \bar{\nu}_\mu + e$ observed in the bubble chamber Gargamelle at CERN, filled with heavy freon and irradiated with a $\bar{\nu}_\mu$ beam, from the decay in flight of negative pions. A single electron of 400 MeV energy is projected at an angle $1.5 \pm 1.5°$ to the beam, and is identified by the bremsstrahlung and pair production along the track. About 10^9 $\bar{\nu}_\mu$'s traversed the chamber in each pulse, and three such events were found in 1.4 million pictures (after Hasert *et al.* 1973a).

The masses of the bosons are $M_W = 80$ GeV and $M_Z = 91$ GeV. $W^\pm$ exchange results in a change of charge of the lepton or quark, while Z^0 exchange does not. These reactions are called – rather inexactly – charged-current and neutral-current weak interactions respectively. Figure 2.7 shows the first example of neutral-current $\bar{\nu}_\mu e^-$ elastic scattering, and Figure 2.8 an early example of W production and decay, $W^+ \to e^+ \nu_e$, in a high energy $p\bar{p}$ collision.

If we oversimplify the picture somewhat by denoting the W, Z couplings to quarks and leptons by a single number, the weak charge g, we would get from (2.6)

$$f(q^2) = \frac{g^2}{q^2 + M_{W,Z}^2} \tag{2.9}$$

to be compared with e^2/q^2 for the electromagnetic scattering of Figure 2.3(a). For $q^2 \ll M_{W,Z}^2$, the amplitude (2.9) is independent of q^2, i.e. the interaction is pointlike. Fermi had postulated just such an interaction, of strength G, between four fermions to describe nuclear β-decay back in 1934. Thus at low q^2 we can

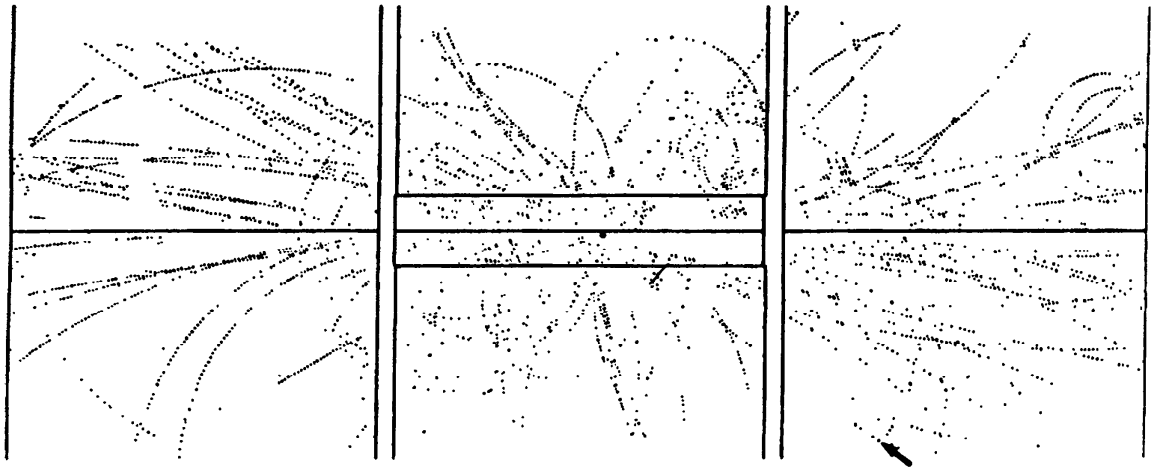

Fig. 2.8. One of the first events attributed to production and decay of a W boson, $W^+ \to e^+ + \nu_e$. The picture shows a reconstruction of the drift chamber signals in a large detector, UA1, surrounding the beam pipe of the CERN proton–antiproton collider. These signals originated in the collision of a 270 GeV proton (from the right) with a 270 GeV antiproton (from the left). Among the 66 tracks observed, one, shown by the arrow, is a very energetic (42 GeV) positron identified in a surrounding electromagnetic calorimeter. The transverse momentum of the positron is 26 GeV/c, while the missing transverse momentum in the whole event is 24 GeV/c, consistent with that of the neutrino (from Arnison *et al.* 1983).

write

$$G \equiv \frac{g^2}{M_{W,Z}^2} \simeq 10^{-5}\ \text{GeV}^{-2} \tag{2.10}$$

where the number on the right comes from measured β-decay rates. In this expression, we have employed units such that $\hbar = c = 1$. If one were to retain these constants, they enter as the relation $G/(\hbar c)^3 \simeq 10^{-5}\ \text{GeV}^{-2}$ (see Table 2.2).

The *electroweak theory* of Glashow, Weinberg and Salam proposed over the period 1961–8 that the coupling g of the $W^{\pm}$ and Z^0 to leptons and quarks should be *the same as that of the photon*, i.e. $g = e$; the weak and electromagnetic interactions are thus *unified*, with the same coupling. Here we have omitted certain numerical factors, mixing angles etc.; these are discussed at length in Chapter 8. Then, from the measured value of G in (2.10) it was expected that

$$M_{W,Z} \sim \frac{e}{\sqrt{G}} \sim \sqrt{\frac{4\pi\alpha}{G}} \sim 90\ \text{GeV} \tag{2.11}$$

in rough agreement with the values measured when the W and Z particles were first observed in 1983.

2.9 Gravitational interactions

Gravity is not an important effect in particle physics at accelerator energies, but we mention it briefly for completeness. It is described in terms of the Newtonian constant, G_N, the force between two equal point masses M being given by $G_N M^2/r^2$, where r is their separation. Comparing with the electrostatic force between singly charged particles, e^2/r^2, the quantity $G_N M^2/(\hbar c)$ is seen to be dimensionless. If we take as the unit of mass $Mc^2 = 1$ GeV, then

$$\frac{G_N M^2}{4\pi\hbar c} = 5.34 \times 10^{-40} \tag{2.12}$$

which may be compared with

$$\frac{e^2}{4\pi\hbar c} = \frac{1}{137.036}$$

Thus for the mass scales common in high energy physics the gravitational coupling is negligibly small. It would approach unity only for hypothetical elementary particles of mass equal to the Planck mass, defined as $(\hbar c/G_N)^{1/2} = 1.22 \times 10^{19}$ GeV. The Planck length is defined in terms of the Planck mass M_P by $l_P = \hbar/(M_P c)$. Two pointlike particles, each having the Planck mass and separated by the Planck length, will have a gravitational potential energy $G_N M_P^2/l_P = M_P c^2$ equal to their rest mass. Thus quantum gravitational effects become important at the Planck scale. *Supergravity* theories are theories of the Planck scale and seek to unify the other fundamental interactions with gravity. These matters are discussed briefly in Chapter 9.

We may remark here that gravity is important in the everyday world because it is *cumulative*. There is only one sign of gravitational charge (negative mass does not exist), so the gravitational potential experienced by a proton is the sum of the potentials due to all nucleons and electrons in the Earth. However, there are two signs of electric charge, the world is electrically neutral, and the enormously greater electrical force on a proton due to all other protons in the Earth is exactly cancelled by that due to the electrons.

To summarise the results of the last few sections, we list in Table 2.2 the fundamental interactions and their principal characteristics.

2.10 The interaction cross-section

The strength of a particular interaction between two particles is specified by the *interaction cross-section*, defined as follows. Imagine a two-body to two-body reaction of the form

$$a + b \rightarrow c + d \tag{2.13}$$

Table 2.2. *Fundamental interactions ($Mc^2 = 1$ GeV)*

	Gravitational	Electromagnetic	Weak	Strong
field boson	graviton	photon	$W^{\pm}$, Z	gluon
spin-parity	2^+	1^-	1^-, 1^+	1^-
mass, GeV	0	0	$M_W = 80.2$ $M_Z = 91.2$	0
range, m	∞	∞	10^{-18}	$\leq 10^{-15}$
source	mass	electric charge	'weak charge'	'colour charge'
coupling constant	$\frac{G_N M^2}{4\pi\hbar c}$ $= 5 \times 10^{-40}$	$\alpha = \frac{e^2}{4\pi\hbar c}$ $= \frac{1}{137}$	$\frac{G(Mc^2)^2}{(\hbar c)^3}$ $= 1.17 \times 10^{-5}$	$\alpha_s \leq 1$
typical cross-section, m^2		10^{-33}	10^{-39}	10^{-30}
typical lifetime, s		10^{-20}	10^{-10}	10^{-23}

in which a well-defined parallel beam of particles of type a impinges normally on a target of thickness dx containing n_b particles of type b per unit volume, and c and d are the product particles. If the density of particles in the incident beam is n_a, the flux through the target will be

$$\phi = n_a v_i \tag{2.14}$$

particles per unit area and per unit time, where v_i is the velocity of the incident beam relative to the target. If each of the target particles has an effective cross-section σ, the probability that any particle a will hit a target particle is $\sigma n_b dx$, since this is the fraction of the target area obscured by the b particles (see Figure 2.9). The number of reactions per unit time is therefore

$$\phi \sigma n_b dx$$

and the reaction rate per target particle will be

$$W = \phi\sigma \tag{2.15}$$

Thus the cross-section per target particle is equal to the reaction rate per unit incident flux. The unit of cross-section is defined as the barn: 1 b $= 10^{-28}$ m^2. This is roughly the geometrical cross-section of a nucleus of mass number $A = 100$. More appropriate units in particle physics are the millibarn, microbarn, nanobarn

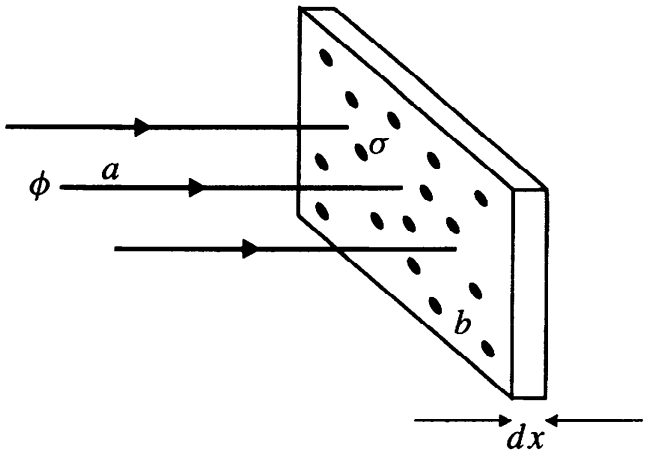

Fig. 2.9. The sketch of reaction of a particle beam with a target of thickness dx.

Table 2.3. *Units of cross-section and energy*

Cross-section σ	Energy E
1 barn $= 10^{-28}$ m^2	1 MeV $= 10^6$ eV
1 millibarn $=$ 1 mb $= 10^{-3}$ b	1 GeV $= 10^3$ MeV
1 microbarn $=$ 1 μb $= 10^{-6}$ b	1 TeV $= 10^3$ GeV
1 nanobarn $=$ 1 nb $= 10^{-9}$ b	
1 picobarn $=$ 1 pb $= 10^{-12}$ b	
$(= 10^{-40}$ m$^2)$	

and picobarn, as defined in Table 2.3 together with the commonly used units of energy.

The reaction rate W is given by an expression from (non-relativistic) perturbation theory, popularly known as Fermi's Second Golden Rule and derived in most standard texts on quantum mechanics:

$$W = \frac{2\pi}{\hbar}|M_{if}|^2\rho_f \tag{2.16}$$

Here M_{if} is the matrix element between initial and final states. Effectively it is the overlap integral over volume, $\int \psi_f^* U \psi_i dV$, between the initial-state and final-state wavefunctions, brought about by the interaction potential U. M_{if} will include the coupling constants involved, propagator terms and any angular dependence of the reaction rate. ρ_f is the energy density dN/dE of final states, i.e. the number of states in phase space available to the product particles, per unit interval of the total energy. M_{if} has dimensions of energy E, ρ_f those of E^{-1}, while $\hbar$ has dimensions of E times t. Thus W measures a rate per unit time. If we temporarily neglect the effects of spin, the expression for the number of states in phase space available

to a particular final-state particle, directed into solid angle $d\Omega$ and enclosed in a physical volume V, is given by

$$dN = \frac{V}{(2\pi\hbar)^3} p^2 dp d\Omega \tag{2.17}$$

where p is the value of the 3-momentum.

Turning to the reaction (2.13), we have to normalise the wavefunctions of the particles correctly. The final state will contain the product wavefunction $\psi_f = \psi_c \psi_d$, and for each particle wavefunction we need to insert a normalisation factor $1/\sqrt{V}$, to ensure that after volume integration for M_{if} we end up with just one particle. The resulting V^{-1} factor cancels with the V factor in the expression (2.17) for the phase space per particle. Similarly, the normalisation factors for the wavefunctions of the initial-state particles a and b cancel with the factors proportional to V for the incident particle flux and the number of target particles. Hence, the arbitrary normalisation volume V cancels out in the expression for the cross-section, as indeed it must. In practice, one simply sets $V = 1$ and forgets about it.

It is most convenient to calculate the cross-section by expressing all quantities in the centre-of-momentum system (cms) of the reaction. Then from (2.14)–(2.17) we get

$$\frac{d\sigma}{d\Omega} = \frac{W}{\phi_i} = \frac{W}{v_i} = \frac{2\pi}{\hbar} \frac{|M_{if}|^2}{v_i} \frac{1}{(2\pi\hbar)^3} p_f^2 \frac{dp_f}{dE_0} \tag{2.18}$$

where $p_f = |\mathbf{p}_c| = |\mathbf{p}_d|$ is the cms momentum of each of the final-state particles, and $E_0 = E_c + E_d$ is the total cms energy. Conservation of energy gives

$$\sqrt{p_f^2 + m_c^2} + \sqrt{p_f^2 + m_d^2} = E_0$$

or

$$\frac{dp_f}{dE_0} = \frac{E_c E_d}{E_0 p_f} = \frac{1}{v_f}$$

The quantities v_i, v_f are the relative velocities in the cms of a and b and of c and d respectively. So finally we have

$$\frac{d\sigma}{d\Omega}(a + b \to c + d) = \frac{1}{4\pi^2\hbar^4} |M_{if}|^2 \frac{p_f^2}{v_i v_f} \tag{2.19}$$

What about spin? Suppose the initial-state particles a and b are unpolarised. If the final-state particles c and d have spins s_c and s_d, the total number of spin substates available to them will be given by the multiplicity factor

$$g_f = (2s_c + 1)(2s_d + 1) \tag{2.20}$$

For the initial-state particles it is

$$g_i = (2s_a + 1)(2s_b + 1) \tag{2.21}$$

As a given reaction must proceed through a particular spin configuration, one must average the transition probability over all possible initial states, all equally probable, and sum over all final states. This amounts to multiplying (2.19) by the factor g_f/g_i.

We have, in the foregoing, computed the cross-section for the process $a + b \to c + d$, but, replacing incoming (outgoing) particles by outgoing (incoming) antiparticles, the so-called *crossed reactions* are also allowed. Moreover they are described by the same matrix element but, of course, different kinematic constraints:

$$\begin{aligned} a + b &\to c + d \\ a + \bar{c} &\to \bar{b} + d \\ a + \bar{d} &\to c + \bar{b} \\ a &\to \bar{b} + c + d \\ c + d &\to a + b \end{aligned} \tag{2.22}$$

The last reaction is the inverse of the first. The equality in matrix elements follows in this case from the principle of detailed balance (itself a consequence of microscopic reversibility).

2.11 Decays and resonances

The mean lifetime of a decaying state is $\tau = 1/W$, with W as defined in (2.16). In calculating W (as distinct from the cross-section) relativistic versions of (2.16)–(2.19) are needed. See Appendix E and Problem 8.8. For strong decays, τ is unmeasurably short and instead one quotes a width Γ, i.e. the natural spread in energy of the decaying state, where

$$\Gamma = \frac{\hbar}{\tau} = \hbar W = 2\pi |M|^2 \int \rho_f d\Omega \tag{2.23}$$

The connection between the lifetime and width of a decaying state follows from the Uncertainty Principle, $\Delta E \Delta t \simeq \hbar$. The decay rate for a particle A will be equal to the fractional number of decays of an assembly of A particles per unit time, i.e.

$$\Gamma = -\hbar \frac{dN_A}{dt} \frac{1}{N_A}$$

giving the exponential decay rate

$$N_A(t) = N_A(0)\exp\left(-\frac{\Gamma t}{\hbar}\right) \tag{2.24}$$

Frequently, a particle may decay via several different channels. Then the total width is the sum of the partial widths for each channel,

$$\Gamma = \sum_i \Gamma_i \tag{2.25}$$

Broad states with finite widths and lifetimes, which can be formed by collision between the particles into which they decay, are referred to as *resonances*. The exponential time dependence (2.24) determines the form of the line shape of the resonance: the energy dependence of the cross-section for creating the resonant state from its constituents is simply the Fourier transform of the time pulse, in the same way that the angular distribution of light diffracted by a slit system in optics is equal to the Fourier transform of the slit profile. The wavefunction describing a non-stationary decaying state of central angular frequency $\omega_R = E_R/\hbar$, where E_R is the resonance energy, and lifetime $\tau = \hbar/\Gamma$ can be written

$$\psi(t) = \psi(0)e^{-i\omega_R t}e^{-t/2\tau} = \psi(0)e^{-t(iE_R+\Gamma/2)} \tag{2.26}$$

in units $\hbar = c = 1$, so that the intensity $\psi(t)^*\psi(t)$ obeys the radioactive decay law (2.24), where the asterisk denotes the complex conjugate wavefunction. The Fourier transform of the expression (2.26) is

$$g(\omega) = \int_0^\infty \psi(t)e^{i\omega t}dt$$

with $\omega = E/\hbar = E$. The amplitude as a function of E is then

$$\chi(E) = \int \psi(t)e^{iEt}dt = \psi(0)\int e^{-t[(\Gamma/2)+i(E_R-E)]}dt = \frac{K}{(E-E_R)-i\Gamma/2} \tag{2.27}$$

where K is some constant and E_R is the central value of the energy of the state. Thus the cross-section $\sigma(E)$ measuring the probability of two particles a and b forming a resonant state c will be proportional to $\chi^*(E)\chi(E)$:

$$\sigma(E) = \sigma_{\max}\frac{\Gamma^2/4}{(E-E_R)^2+\Gamma^2/4} \tag{2.28}$$

which is called the Breit–Wigner resonance formula. The shape of the resonance curve is shown in Figure 2.10. The cross-section falls to half of its peak value when $E - E_R = \pm\Gamma/2$.

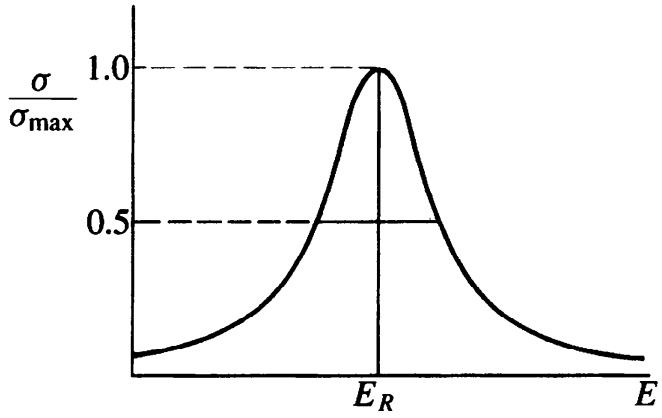

Fig. 2.10. Shape of the Breit–Wigner resonance curve. The width of the curve at $\sigma/\sigma_{max} = 0.5$ is Γ.

The value of the peak cross-section σ_{max} in (2.28) can be found using arguments from wave optics. First, the plane wave describing the incident particles of momentum p is a superposition of waves of different angular momentum l with respect to the scattering centre, where $l\hbar = pb$ and b is the 'impact parameter'. Particles of angular momentum in the range $l \to l + 1$ therefore impinge on an annular ring of cross-sectional area

$$\sigma = \pi\left(b_{(l+1)}^2 - b_l^2\right) = \pi\lambda\!\!\!^{-2}(2l + 1) \tag{2.29}$$

where $\lambda\!\!\!^{-} = \hbar/p$. If the scattering centre is totally absorbing, $\sigma = \sigma_r$ is the absorption or reaction cross-section (for the lth partial wave). The elastic cross-section in this case is also $\sigma_{el} = \sigma_r$, and corresponds to the elastically diffracted beam from the absorbing obstacle. The other extreme case is that of pure scattering without absorption but simply with a phase shift. The maximum effect is for a phase shift of π, which clearly leads to a scattered amplitude just twice that for total absorption (again for the lth partial wave), and hence a cross-section

$$(\sigma_{el})_{max} = 4\pi\lambda\!\!\!^{-2}(2l + 1) \tag{2.30}$$

Here, $\lambda\!\!\!^{-}$ is the wavelength of the scattered and scattering particles in their common centre-of-momentum frame, and $l\hbar$ the angular momentum of these particles with respect to each other (see also Problem 2.7).

So far, we have not considered particle spin. The appropriate spin multiplicity factors were given in the previous section. Putting all these things together, we finally get for the complete Breit–Wigner formula,

$$\sigma = \frac{4\pi\lambda\!\!\!^{-2}(2J + 1)}{(2s_a + 1)(2s_b + 1)} \frac{\Gamma^2/4}{[(E - E_R)^2 + \Gamma^2/4]} \tag{2.31}$$

where s_a and s_b are the spins of the incident and target particles and J is the spin of the resonant state (all in units of $\hbar$).

Often the resonant state c made in the reaction $a+b \rightarrow c$ can decay in a number of modes, the total width being the sum of the partial widths as in (2.25). The 'elastic' channel of decay, $c \rightarrow a + b$, is that by which the resonant state was formed. In this case, the cross-section for both formation and decay through this elastic channel is obtained by multiplying the cross-section (2.31) by the factor $(\Gamma_{\text{el}}/\Gamma)^2$. In general, if the state is formed through channel i and decays through channel j, the cross-section is given by multiplying (2.31) by a factor $\Gamma_i\Gamma_j/\Gamma^2$.

It will be noticed that (2.28) and (2.31) are not in a relativistically invariant form. The so-called relativistic Breit–Wigner formula replaces (2.28) by

$$\sigma(s) = \sigma_{\max}\frac{M_0^2\Gamma^2}{(s-M_0^2)^2+\Gamma^2M_0^2} \tag{2.32}$$

Here s $(= E^2)$ is the cms energy squared and M_0 $(= E_R)$ is the central resonance mass. One can reproduce (2.32) by multiplying (2.28) at top and bottom by $(E + E_R)^2$ and using the approximation $E \simeq E_R$ $(= M_0)$. Generally, (2.28) or (2.32) give equally good fits, with slightly different resonance parameters.

2.11.1 The Δ^{++} pion–proton resonance

As an example of a resonance we show in Figure 2.11 the cross-section for production of the pion–nucleon resonant state $\Delta^{++}(1232)$, formed when pions are incident on a proton target:

$$\pi^+ + p \rightarrow \Delta^{++}(1232) \rightarrow \pi^+ + p$$

This resonance was the first in a long list of baryon and meson resonant states found in the 1950s and 1960s, which, through their symmetry properties, paved the way for the quark concept to emerge. The Δ is an elastic resonance with $J = \frac{3}{2}$ and width $\Gamma = 120$ MeV. With $s_a = s_p = \frac{1}{2}$ and $s_b = s_\pi = 0$, the maximum cross-section $8\pi\lambda\!\!\!^{-2}$ in (2.30) is seen to be reached just above the resonance peak.

2.11.2 The Z^0 resonance

As a second example of a resonance, we consider the Z^0 intermediate vector boson responsible for mediating the neutral weak current interactions (see Figure 2.6). This has a central mass $M_Z = 91$ GeV and a total width $\Gamma = 2.5$ GeV. Figure 2.12 shows the cross-section for the reaction $e^+e^- \rightarrow$ anything, plotted against the cms energy in e^+e^- annihilation. The Z^0, once formed, can decay to hadrons via $Q\bar{Q}$ pairs, into charged leptons e^+e^-, $\mu^+\mu^-$, $\tau^+\tau^-$ or into neutral lepton pairs $\nu_e\bar{\nu}_e$,

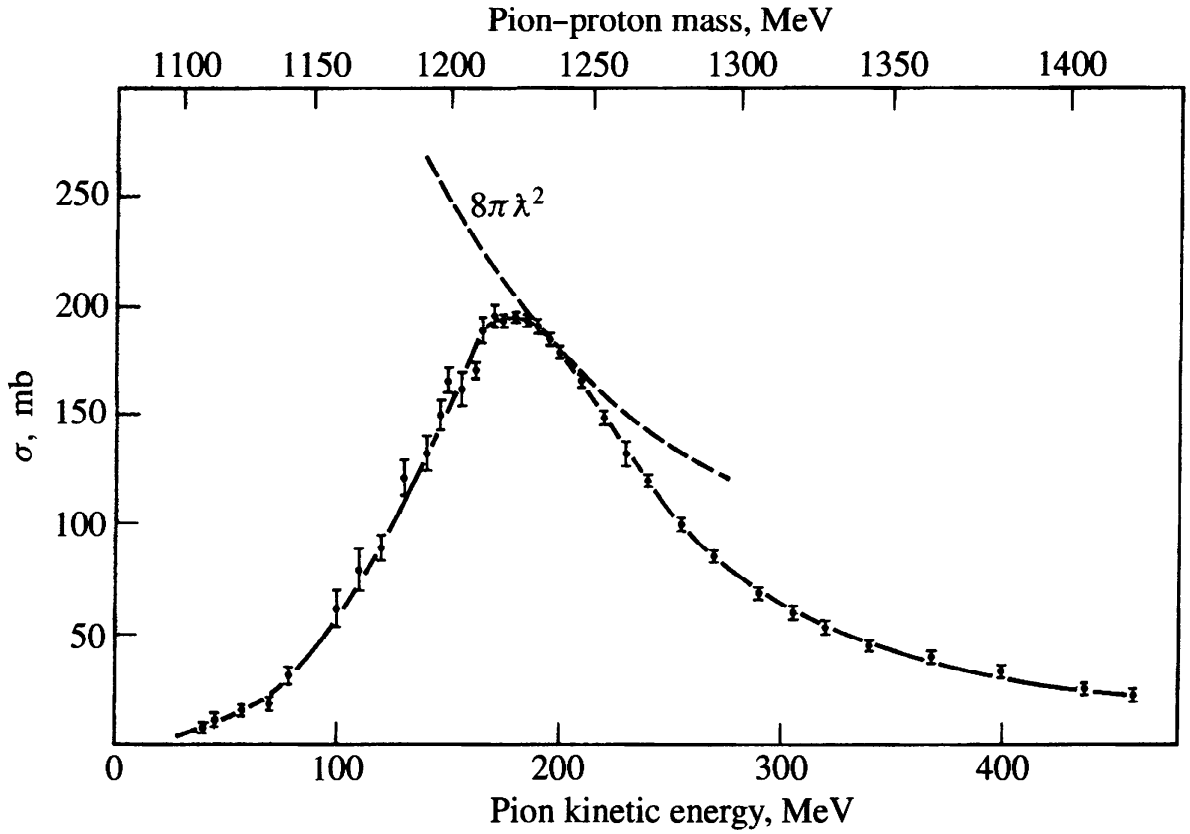

Fig. 2.11. The $\pi^+ p$ elastic scattering cross-section in the region of the $\Delta^{++}(1232)$ resonance. The central mass is 1232 MeV and the width is $\Gamma = 120$ MeV. Note that the formula (2.28) holds strictly for a narrow resonance. For a broad resonance with width comparable with the central mass, such as the Δ^{++}, the final-state phase-space factor varies appreciably over the width so that, in comparison with Figure 2.10, the resonance curve appears asymmetric.

$\nu_\mu \bar{\nu}_\mu$ and $\nu_\tau \bar{\nu}_\tau$. The total width is the sum of the individual partial widths for each decay mode. The curves show the effect on the width of assuming two, three or four flavours of neutrino. The observed width gives for the number of flavours

$$N_\nu = 2.99 \pm 0.01 \tag{2.33}$$

Thus there are three and only three types of neutrino. The observation of many millions of Z^0 decays at e^+e^- colliders has made possible intensive studies of the electroweak sector that have helped to establish in great detail the validity of the Standard Model, as discussed in Chapter 8.

2.11.3 Resonances in astrophysics

It is appropriate here to mention that resonances in atomic nuclei play an important role on the cosmic scale. A famous example of such a resonance level is the 7.654 MeV excited state of ^{12}C, with width about 10 eV. The production of ^{12}C in helium-burning red-giant stars is achieved through the so-called triple alpha

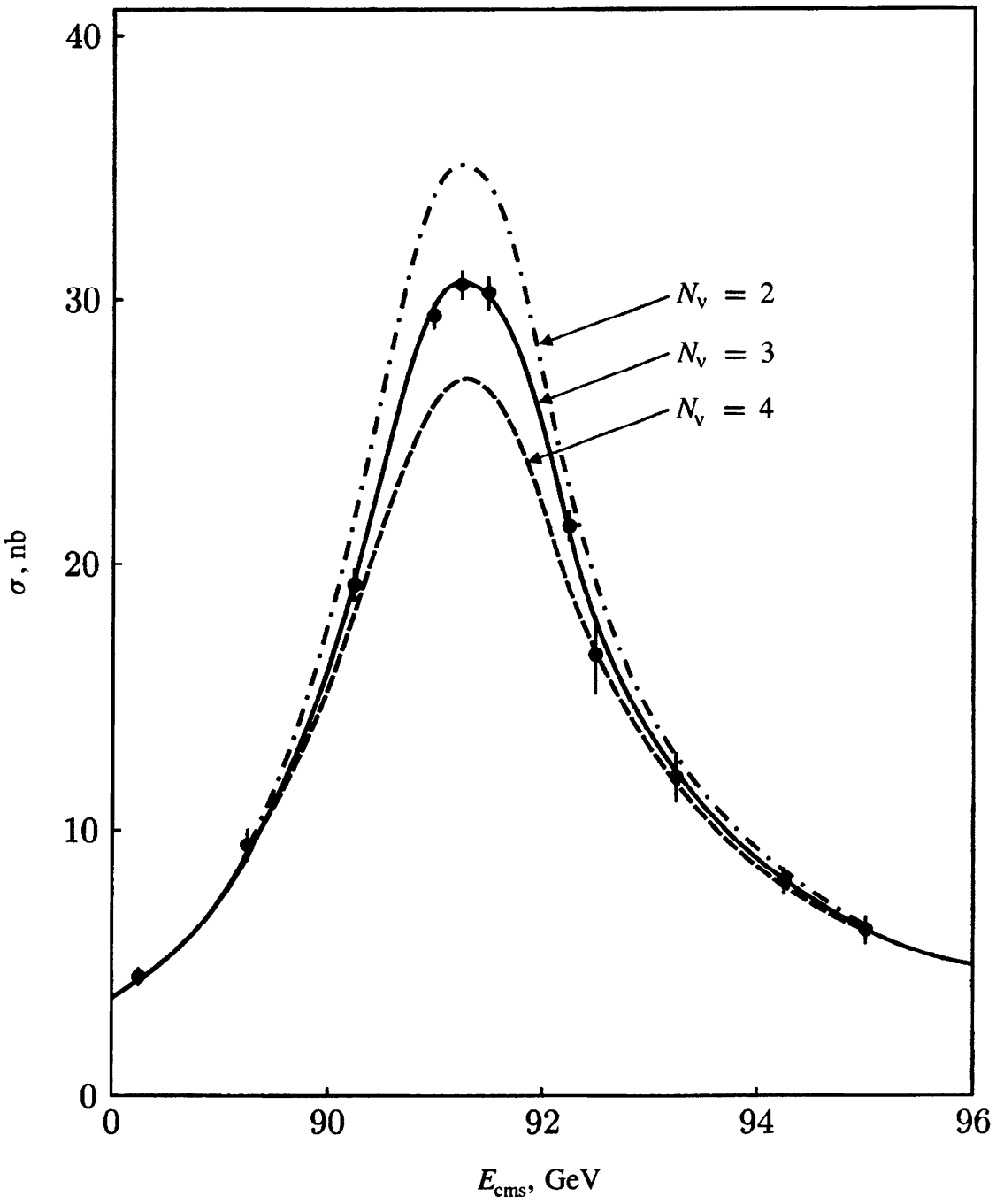

Fig. 2.12. The cross-section for the reaction $e^+e^- \rightarrow$ anything, in the neighbourhood of the Z^0 resonance, plotted against cms energy. The data is a collection from experiments at the CERN LEP collider. The three curves are the (Standard Model) predictions for the total width, for two, three or four flavours of neutrino. Clearly for the data $N_\nu = 3$ is indicated, as in (2.33).

process, $3\alpha \rightarrow {}^{12}C$. First, two α-particles combine to form the ground state of ^8Be, which is unstable with a lifetime of only 10^{-16} s. The ^8Be may nevertheless capture an α-particle to form ^{12}C in the above s-wave resonance; the ^{12}C usually decays back to $^8Be + \alpha$ but can, with low (4×10^{-4}) probability, decay by γ-emissions to form the ^{12}C ground state. The rate of ^{12}C generation depends crucially on the

existence of this resonance at the right energy, and indeed Hoyle had predicted the need for it and its properties in 1953, before it was finally found in laboratory experiments. Of course, were it not for the existence of this resonance in carbon, the whole of the biological evolution of the universe (if indeed there were any such evolution) would have been totally different.

It is also of interest to remark here that a further stage of stellar fusion is α-capture by ^{12}C, which in turn leads to ^{16}O formation, and that it is the *absence* of an appropriate resonance level in ^{16}O that ensures that not all the carbon disappears, and that it remains an abundant element in our universe.

Problems

2.1 The cross-section for the reaction $\pi^- + p \rightarrow \Lambda + K^0$ at 1 GeV/c incident momentum is about 1 mb (10^{-27} cm^2). Both the Λ and K^0 particles decay with a mean lifetime of order 10^{-10} s. From this information, estimate the relative magnitude of the couplings responsible for the production and decay, respectively, of these strange particles.

2.2 It was once suggested that the numerical values of the charge of the electron and the proton might differ by a small amount $|\Delta e|$, so that the expansion of the universe could be attributed to the electrostatic repulsion between hydrogen atoms in space. Estimate the minimum value of $|\Delta e/e|$ required for this hypothesis.

(*Note*: This hypothesis was disproved in a brilliant experiment at AERE Harwell, within 10 days of its being proposed! The proposal was made by Bondi and Littleton (1959) and the experimental disproof was the work of Cranshaw and Hillas (1959). Their experiment was a development of an earlier one by Piccard. It consisted essentially of the very precise measurement of any charge induced on the neck of a cylinder of gas at high pressure as the valve was opened and the gas surged out. By comparing gases with different neutron-to-proton ratios, the net charge of a proton plus an electron, and of a neutron, could be separately measured. For both, the limit $|\Delta e/e| < 10^{-20}$ was obtained. This also sets the same limit on the neutrino charge, from charge conservation in the decay $n \rightarrow p + e^- + \nu_e$.)

2.3 From equation (2.8) with $k = 0.85$ GeV fm^{-1}, show that the QCD potential leads to a value for the confining force between a pair of quarks equal to 14 tonnes weight.

2.4 Several broad $\pi^+ p$ resonant states Δ^{++} are found with invariant masses ranging from 1.2 to 2.5 GeV/c^2. One state has a central mass of 1.62 GeV and a width $\Gamma = 150$ MeV. If it has spin $J = \frac{1}{2}$, what would be the peak cross-section for $\pi^+ p$ scattering via this resonant state?

2.5 Draw Feynman diagrams (in terms of transitions at the quark level if hadrons are

involved) for the following weak decays:

$$\begin{aligned} \pi^+ &\rightarrow \mu^+ + \nu_\mu \\ \Lambda &\rightarrow p + e^- + \nu_e \\ K^0 &\rightarrow \pi^+ + \pi^- \\ \pi^+ &\rightarrow \pi^0 + e^+ + \nu_e \end{aligned}$$

Draw Feynman diagrams for the following strong decays:

$$\begin{aligned} \omega^0 &\rightarrow \pi^+ + \pi^- + \pi^0 \\ \rho^0 &\rightarrow \pi^+ + \pi^- \\ \Delta^{++} &\rightarrow p + \pi^+ \end{aligned}$$

2.6 Show that, in the process of pair conversion $\gamma \rightarrow e^+e^-$, it is impossible to conserve energy and momentum without the participation of another particle (a nucleus), as in Figure 2.1(e). Calculate the minimum momentum transfer from this extra particle, for a 1 GeV γ-ray.

2.7 In the optical model of scattering in Section 2.11, the amplitude of the radial outgoing wave (for fixed angular momentum l) can be written as $A = \exp(ikr)$ before scattering, and as $A' = \eta \exp[i(kr + \delta)]$ after scattering, where $k = p/\hbar$ is the wavenumber, $\eta \leq 1$ and δ is the phase shift. Show that the reaction or absorption cross-section $\sigma_r \propto 1 - \eta^2$ and that the elastic cross-section $\sigma_{el} \propto 1 + \eta^2 - 2\eta \cos\delta$. Hence verify the expression (2.30) for the maximum value of the elastic cross-section in a particular partial wave.

3

Invariance principles and conservation laws

A very important concept in physics is the symmetry or invariance of the equations describing a physical system under an operation – which might be, for example, a translation or rotation in space. Intimately connected with such invariance properties are conservation laws – in the above cases, conservation of linear and angular momentum. Such conservation laws and the invariance principles and symmetries underlying them are the very backbone of particle physics. However, one must remember that their credibility rests entirely on experimental verification. A conservation law can be assumed to be absolute if there is no observational evidence to the contrary, but this assumption has to be accompanied by a limit set on possible violations by experiment.

The transformations to be considered can be either continuous or discrete. A translation or rotation in space is an example of a continuous transformation, while spatial reflection through the origin of coordinates (the parity operation) is a discrete transformation. The associated conservation laws are additive and multiplicative, respectively.

3.1 Translation and rotation operators

In an isolated physical system, free of any external forces, the total energy must be invariant under translations of the whole system in space. Since there are no external forces, the rate of change of momentum is zero and the momentum is constant. So invariance of the energy of a system under space translations corresponds to conservation of linear momentum. Similarly, invariance of the energy of a system under spatial rotations corresponds to conservation of angular momentum.

The effect of an infinitesimal translation δr in space on a wavefunction ψ will be that it becomes

$$\psi' = \psi(r + \delta r) = \psi(r) + \delta r \frac{\partial \psi(r)}{\partial r} = D\psi$$

where

$$D = 1 + \delta r \frac{\partial}{\partial r} \tag{3.1}$$

is an infinitesimal space translation operator. Since the momentum operator is $p = -i\hbar\partial/\partial r$, we can write this as

$$D = 1 + ip\delta r/\hbar$$

A finite translation Δr can be obtained by making n steps in succession ($\Delta r = n\delta r$), giving as $n \to \infty$

$$D = \lim_{n\to\infty} \left(1 + \frac{ip\Delta r}{n\hbar}\right)^n = e^{ip\Delta r/\hbar} \tag{3.2}$$

In complete analogy with the translation operator D, the generator of an infinitesimal rotation about some axis may be written

$$R = 1 + \delta\phi \frac{\partial}{\partial \phi}$$

The operator for the z-component of angular momentum is†

$$J_z = -i\hbar \left(x\frac{\partial}{\partial y} - y\frac{\partial}{\partial x}\right) = -i\hbar \frac{\partial}{\partial \phi} \tag{3.3}$$

where ϕ measures the azimuthal angle about the z-axis. So

$$R = 1 + iJ_z\delta\phi/\hbar$$

Again, a finite rotation $\Delta\phi$ is obtained by repeating the infinitesimal rotation n times, where $n \to \infty$ as $\delta\phi \to 0$. Then

$$R = \lim_{n\to\infty} \left(1 + \frac{iJ_z\Delta\phi}{n\hbar}\right)^n = e^{iJ_z\Delta\phi/\hbar} \tag{3.4}$$

Note that the operators D and R in (3.2) and (3.4) are unitary operators. The inverse operators $D^* = D^{-1}$ have the property $D^*D = D^{-1}D = 1$, preserving the norm of the state.

† See Appendix C.

3.2 The parity operation

The operation of the spatial inversion of coordinates $(x, y, z \rightarrow -x, -y, -z)$ is an example of a discrete transformation. This transformation is produced by the parity operator P, where

$$P\psi(\mathbf{r}) = \psi(-\mathbf{r})$$

Repetition of this operation clearly implies $P^2 = 1$, so that P is a unitary operator. The eigenvalue of the operator (if there is one) will be ± 1, and this is also called the parity P of the system. A wavefunction may or may not have a well-defined parity, which can be even ($P = +1$) or odd ($P = -1$). For example,

$$\text{for } \psi = \cos x, \quad P\psi = \cos(-x) = \cos x = +\psi; \quad \psi \text{ is even } (P = +1)$$
$$\text{for } \psi = \sin x, \quad P\psi = \sin(-x) = -\sin x = -\psi; \quad \psi \text{ is odd } (P = -1)$$

while

$$\text{for } \psi = \cos x + \sin x, \qquad P\psi = \cos x - \sin x \neq \pm\psi,$$

so the last function has no definite parity eigenvalue. A spherically symmetric potential $V(\mathbf{r})$ has the property that $V(-\mathbf{r}) = V(\mathbf{r})$, so that one expects states bound by a central potential, such as a hydrogen atom, to have a definite parity. The H-atom wavefunctions can be described by a product of radial and angular functions, the latter in the form of spherical harmonics $Y_m^l(\theta, \phi)$ with θ and ϕ as polar and azimuthal angles.†

$$\begin{aligned}\psi(r, \theta, \phi) &= \chi(r) Y_l^m(\theta, \phi) \\ &= \chi(r) \sqrt{\frac{(2l+1)(l-m)!}{4\pi(l+m)!}} P_l^m(\cos\theta) e^{im\phi}\end{aligned} \tag{3.5}$$

The spatial inversion $\mathbf{r} \rightarrow -\mathbf{r}$ is equivalent to

$$\theta \rightarrow \pi - \theta, \qquad \phi \rightarrow \pi + \phi$$

with the result that

$$e^{im\phi} \rightarrow e^{im(\pi+\phi)} = (-1)^m e^{im\phi}$$
$$P_l^m(\cos\theta) \rightarrow P_l^m(\cos(\pi - \theta)) = (-1)^{l+m} P_l^m(\cos\theta)$$

or

$$Y_l^m(\theta, \phi) \rightarrow Y_l^m(\pi - \theta, \pi + \phi) = (-1)^l Y_l^m(\theta, \phi) \tag{3.6}$$

Thus, the spherical harmonic functions have parity $(-1)^l$. So s, d, g, ... atomic states have even parity, while p, f, h, ... have odd parity. Electric dipole transitions

† A list of spherical harmonics is given in Appendix D.

between states are characterised by the selection rule $\Delta l = \pm 1$, so that as a result of the transition, the parity of the atomic state must change. The parity of the electromagnetic (E1) radiation (photons) emitted in this case must be -1, so the parity of the whole system (atom + photon) is conserved.

Parity is a multiplicative quantum number, so the parity of a composite system $\psi = \phi_a \phi_b \cdots$ is equal to the product of the parities of the parts.

In strong as well as electromagnetic interactions, parity is found to be conserved. This is true, for example, in the strong reaction $p + p \rightarrow \pi^+ + p + n$ in which a single boson (pion) is created. In such a case, it is necessary to assign an *intrinsic parity* to the pion in order to ensure the same parity in initial and final states, in just the same way that we assign a charge to the pion in order to ensure charge conservation in the same reaction. As shown below, the intrinsic parity is $P_\pi = -1$.

What about the intrinsic parities of the proton and neutron? By convention, neutrons and protons are assigned the same value, $P_n = +1$. The sign here *is* simply due to convention, because baryons are conserved and the nucleon parities cancel in any reaction.

While the intrinsic parity assignment for the pion arises because pions can be created or destroyed singly, strange particles, i.e. those containing an s quark or antiquark, must be created in association, e.g. in a reaction such as $p + p \rightarrow K^+ + \Lambda + p$ involving particles with strangeness $S = +1$ and -1. Thus only the parity of the ΛK pair, relative to the nucleon, can be measured, and it is found to be odd. By convention, the hyperon Λ is assigned the same (even) parity as the nucleon, so that of the kaon is odd.

3.3 Pion spin and parity

As an example of the application of symmetry principles, we discuss the determination of the spin and parity of the charged and neutral pions.

3.3.1 Spin of the pion

For charged pions, the spin was originally determined by measurement of the cross-section for the reversible reaction

$$p + p \rightleftharpoons \pi^+ + d \tag{3.7}$$

If the forward and backward reactions are compared at the same energy in the centre-of-momentum system, then by the principle of detailed balance, which involves invariance under time reversal and space inversion, both of which hold in a strong interaction, the forward and backward matrix elements will be the same,

$|M_{if}|^2 = |M_{fi}|^2$. Hence from (2.19)

$$\sigma_{pp\to\pi^+d} \propto (2s_\pi + 1)(2s_d + 1)p_\pi^2 \tag{3.8a}$$

where $p_\pi = p_d$ is the arithmetic value of the cms momentum and the deuteron spin is $s_d = 1$. For the back reaction

$$\sigma_{\pi^+d\to pp} \propto \tfrac{1}{2}(2s_p + 1)^2 p_p^2 \tag{3.8b}$$

where the factor $\frac{1}{2}$ arises since the two protons in the final state are identical, so that a solid angle integration over 2π, rather than 4π, gives the full reaction rate. The ratio of the cross-sections (3.8a) and (3.8b) was first measured in 1951–3 and gave $s_\pi = 0$ for the spin of the charged pion.

For neutral pions, the existence of the decay

$$\pi^0 \to 2\gamma$$

proves that the pion spin must be integral (since $s_\gamma = 1$) and that $s_\pi \neq 1$, from the following argument. It can be proved as a consequence of relativistic invariance that for any massless particle of spin s, there are only two possible spin substates, $s_z = \pm s$, where z is the direction of motion. Taking the common line of flight of the photons in the pion rest frame as the quantisation axis, the z-component of total photon spin in the above decay can thus have the values $S_z = 0$ or 2. Suppose $s_\pi = 1$; then only $S_z = 0$ is possible, and the two-photon amplitude must behave under rotation like the polynomial $P_1^m(\cos\theta)$ with $m = 0$, where θ is the angle of the photon relative to the z-axis. Under a 180° rotation about an axis normal to z, $\theta \to \pi - \theta$, and since $P_1^0 \propto \cos\theta$ it therefore changes sign. For $S_z = 0$, the situation corresponds to two right-circularly polarised (or two left-circularly polarised) photons travelling in opposite directions. So the above rotation is equivalent to interchange of the two photons, for which, however, the wavefunction, describing two identical bosons, must be symmetric. Hence $s_\pi \neq 1$, and therefore $s_\pi = 0$ or $s_\pi \geq 2$. In high energy interactions, it is observed that positive, negative and neutral pions are produced in equal numbers, indicating that the neutral pion spin is zero, with the same spin multiplicity as its charged counterparts.

3.3.2 *Parity of the charged pion*

The parity of the charged pion was deduced from observation of the following reaction of slow negative pions captured in deuterium:

$$\pi^- + d \to n + n \tag{3.9}$$

Capture takes place from an atomic S-state of the pion with respect to the deuterium nucleus (as is proved by studies of the mesic X-rays emitted following capture). Since the spin of the deuteron is $s_d = 1$ and that of the pion is $s_\pi = 0$, the initial state has total angular momentum $J = 1$. If the two neutrons have orbital angular momentum **L**, and **S** is their total spin, then $\mathbf{J} = \mathbf{L} + \mathbf{S}$.

The wavefunction of the two neutrons, which are non-relativistic, may be written as the product of space and spin functions:

$$\psi = \phi(\text{space})\,\alpha(\text{spin}) \tag{3.10}$$

We label the spin function $\alpha(S, S_z)$ where S, S_z refer to the total spin and its z-component and obviously $S = 0$ or 1. Using an up or down arrow to denote a neutron state with z-component of spin $+\frac{1}{2}$ or $-\frac{1}{2}$, the four possible combinations of two neutrons, each with two spin substates can be written

$$\alpha(1, 1) = \uparrow\uparrow \tag{3.11a}$$

$$\alpha(1, 0) = \tfrac{1}{\sqrt{2}}(\uparrow\downarrow + \downarrow\uparrow) \tag{3.11b}$$

$$\alpha(1, -1) = \downarrow\downarrow \tag{3.11c}$$

$$\alpha(0, 0) = \tfrac{1}{\sqrt{2}}(\uparrow\downarrow - \downarrow\uparrow) \tag{3.11d}$$

These functions have well-defined exchange symmetry; the first three form a spin triplet with $S = 1$ and $S_z = +1, 0, -1$, which is seen to be *symmetric* under interchange of the spin labels of the neutrons, i.e. $\alpha \rightarrow +\alpha$. The last state, (3.11d), is a singlet with $S = S_z = 0$, which is *antisymmetric* under spin-label interchange, $\alpha \rightarrow -\alpha$. Thus the symmetry of the spin function is $(-1)^{S+1}$. For the spatial function ϕ in (3.10), the symmetry under interchange of space coordinates is $(-1)^L$, as in (3.6). Hence the overall symmetry of the wavefunction ψ under total interchange (space and spin) will be $(-1)^{L+S+1}$. Since we are dealing with identical fermions then ψ must be antisymmetric, so that $L + S$ must be even.

The requirement $J = 1$ alone allows $L = 0$, $S = 1$, or $L = 1$, $S = 0$ or 1, or $L = 2$, $S = 1$. Of these possibilities, only $L = S = 1$ has $L+S$ even. Thus the two neutrons are in a $^3P_1$ state, with parity $(-1)^L = -1$. Since both the neutron and the deuteron have intrinsic parity $+1$, it follows† that the only way to obtain negative parity in the initial state is to assign to the pion an intrinsic parity $P_\pi = -1$.

3.3.3 *Parity of the neutral pion*

The parity of the neutral pion is found from considerations of the polarisation of the two photons in the decay $\pi^0 \rightarrow 2\gamma$. Suppose **k**, $-\mathbf{k}$ represent the momentum

† We have defined the nucleon parity to be $+1$, but since two nucleons appear on each side of the equation, the choice of nucleon parity is irrelevant.

vectors of the photons in the pion rest frame, ϵ_1 and ϵ_2 their polarisation vectors (**E**-vectors) which, because electromagnetic fields in free space are transverse, are perpendicular to **k**. The initial state π^0 has $J = 0$, and the final state consists of identical bosons. The simplest wavefunctions describing the two-photon system, with even exchange symmetry, can be written in terms of **k**, ϵ_1, ϵ_2 as follows:

$$\psi_1(2\gamma) = A(\epsilon_1 \cdot \epsilon_2) \propto \cos\phi \tag{3.12a}$$

$$\psi_2(2\gamma) = B(\epsilon_1 \times \epsilon_2) \cdot \mathbf{k} \propto \sin\phi \tag{3.12b}$$

where A and B are constants and ϕ is the angle between the planes of polarisation. The quantity ψ_1 is a scalar and therefore even under space inversion, and thus requires positive parity for the pion and preferentially parallel polarisations for the photons, with intensity $I(\phi) \propto \cos^2\phi$. The second function, ψ_2, is the product of an axial vector with a polar vector, and is therefore a pseudoscalar quantity, changing sign under inversion. It corresponds to a pion of negative parity, preferentially orthogonal polarisation vectors and a rate $I(\phi) \propto \sin^2\phi$.

It is not feasible to measure the polarisation vectors of the photons directly. Observations were made on rare decays of the type

$$\pi^0 \rightarrow (e^+ + e^-) + (e^+ + e^-)$$

in which each photon internally converts to an electron pair, with a branching ratio, compared with $\pi^0 \rightarrow 2\gamma$, of order $\alpha^2 \simeq 10^{-4}$. The plane of each pair is predominantly in that of the **E**-vector, so that the measurement of the angles between the planes of the pairs allows one to infer the pion's parity. The results are shown in Figure 3.1. As in the case of the charged pion, the parity is found to be $P_\pi = -1$.

The angular momentum and parity of particle states is described by the notation J^P. Thus the pion has $J^P = 0^-$. The pion is called a *pseudoscalar* particle, because it is described by a wavefunction with the spatial transformation properties of a pseudoscalar. Similarly, a particle with $J^P = 0^+$ is called *scalar*, one with $J^P = 1^-$ is *vector* and one with $J^P = 1^+$ is an *axial vector*.

3.4 Parity of particles and antiparticles

While the intrinsic parity of a fermion is a matter of convention, the *relative* parity of a fermion and antifermion is not. Fermion–antifermion pairs (e.g. $\bar{p}p$) can be created in a reaction so that, just as for the creation of a single pion, the intrinsic parity of the pair must be a measurable quantity.

The Dirac theory of fermions requires *particle and antiparticle to have opposite intrinsic parity*. This prediction was checked experimentally by Wu and Shaknov in their observations on positronium, an 'atomic' bound state of e^+ and e^- with

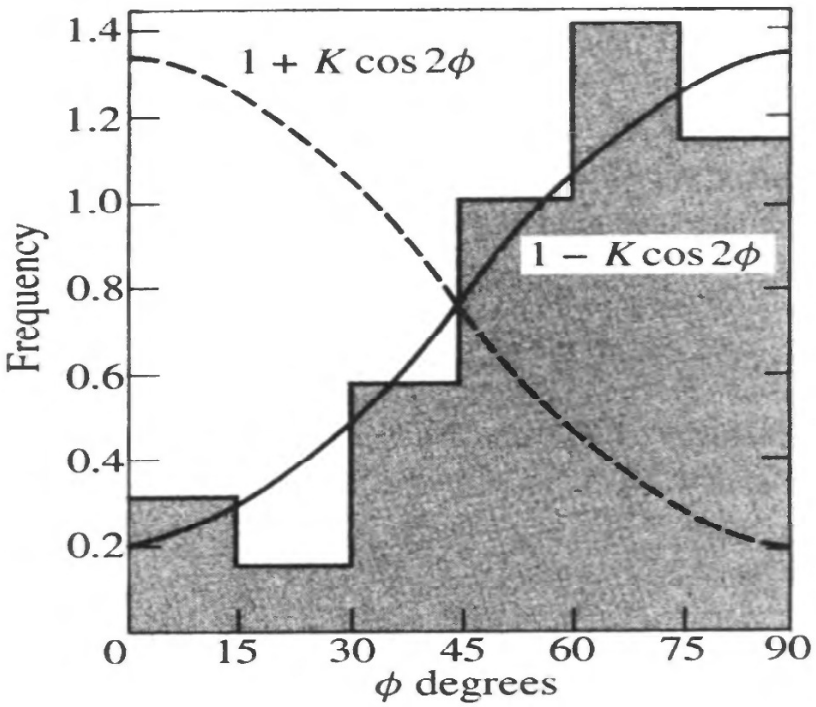

Fig. 3.1. Plot of the weighted frequency distribution of the angle ϕ between the planes of pairs in the rare decays $\pi^0 \rightarrow (e^+ + e^-) + (e^+ + e^-)$. For a scalar pion this should be of the form $1 + K \cos 2\phi$ (broken curve), while for a pseudoscalar pion it should follow $1 - K \cos 2\phi$ (solid curve), where the constant K is close to unity (after Plano *et al.* 1959).

principal energy levels akin to those of the hydrogen atom, but with almost exactly half the spacing because of the factor 2 in the reduced mass.† The spin-singlet ground state of positronium, $^1S_0$ (analogous to the spin-singlet state of two neutrons in (3.11d)) decays to two photons:

$$e^+e^-(^1S_0) \rightarrow 2\gamma$$

and, exactly as in the case of π^0 decay to two photons discussed above, negative parity of the two-photon state – because of the opposite parities of e^+ and e^- – will imply preferentially orthogonal polarisation of the photons. That means that the distribution of the azimuthal angle ϕ between the polarisation vectors must have a $\sin^2\phi$ dependence. The photon polarisation can be measured indirectly by observing the angular distribution in Compton scattering of the γ-rays, which depends strongly on the polarisation, being more probable in a plane normal to to the **E**-vector. This is clear if one considers that the incident photon will set up oscillations of the target electron in the direction of the **E**-vector. Recalling the distribution in polar angle of radiation from an oscillating electric dipole, the scattered intensity will be greatest normal to **E**.

† The energy levels and other properties of positronium are discussed in Section 4.1.

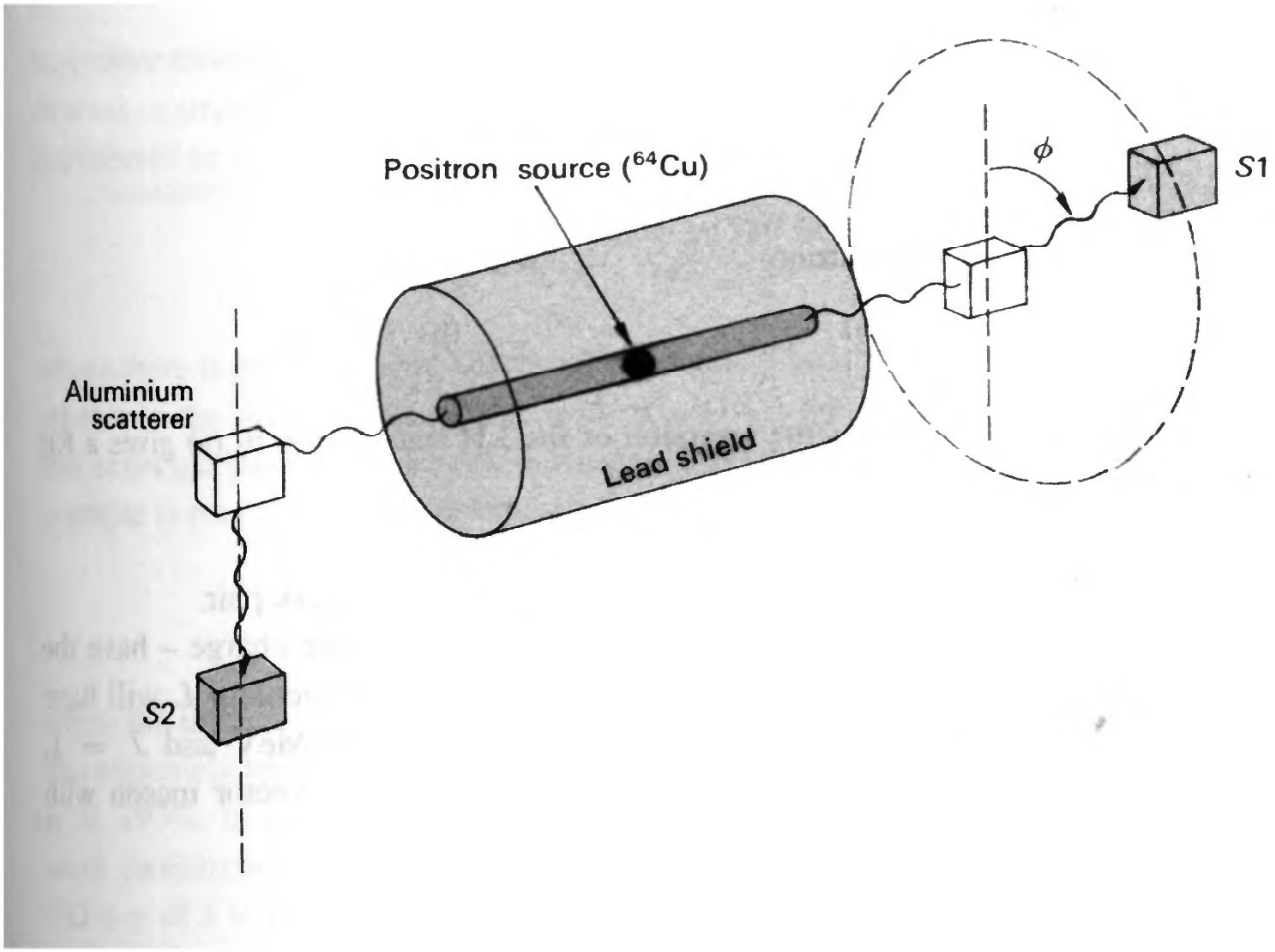

Fig. 3.2. Sketch of the method used by Wu and Shaknov (1950) to measure the relative orientation of the polarisation vectors of the two photons emitted in the decay of S_0-positronium. $S1$ and $S2$ are anthracene counters recording the γ-rays after scattering by aluminium cylinders. The results proved that fermion and antifermion have opposite intrinsic parity, as predicted by the Dirac theory.

The experimental set-up used by Wu and Shaknov (1950) is shown in Figure 3.2. The coincidence rate of γ-rays scattered by aluminium cylinders was measured in the anthracene counters $S1$ and $S2$ as a function of their relative azimuthal angle ϕ. The expected anisotropy depends on the polar angle of scattering and is greatest for $\theta = 81°$. The observed ratio was

$$\frac{\text{rate } (\phi = 90°)}{\text{rate } (\phi = 0°)} = 2.04 \pm 0.08 \tag{3.13}$$

compared with a theoretically expected ratio of 2.00. This experiment therefore confirms the prediction of preferentially orthogonal polarisation of the γ-rays, and thus proves that fermions and antifermions have opposite intrinsic parities.

If orbital angular momentum L is involved in the two-particle system, it follows that the parity of the fermion–antifermion pair will be $(-1)^{L+1}$. Thus a pion, which we shall see later is considered to be an S-state combination $\pi^+ = u\bar{d}$, has $L = 0$

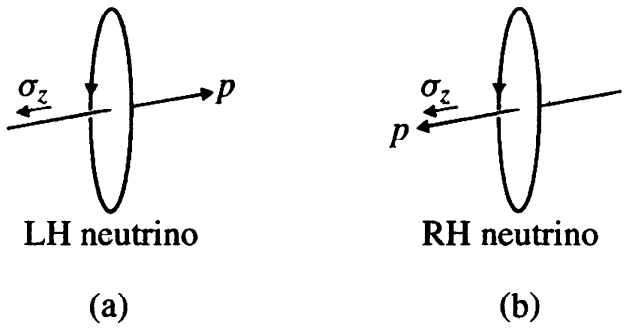

Fig. 3.3. (a) LH neutrino state; (b) inversion of the LH state shown in (a) gives a RH neutrino, not observed in nature.

and intrinsic parity (-1) arising from that of the quark–antiquark pair.

However, a boson and 'antiboson'– i.e. one of the opposite charge – have the same parity. Thus a $\pi^+\pi^-$ system in a state of angular momentum L will have parity $(-1)^L$. As an example, the ρ meson, of mass 770 MeV and $J = 1$, undergoes decay to two pions, $\rho \rightarrow \pi^+\pi^-$, and thus is a vector meson with $J^P = 1^-$.

3.5 Tests of parity conservation

While the strong and electromagnetic interactions are parity-conserving, the weak interactions are not. Indeed, it turns out that weak decays contain almost equal proportions of even and odd parity amplitudes – the principal of maximal parity violation, to be discussed in Chapter 7. This situation can be illustrated by the specific example of the neutrino, which as mentioned in Section 1.7 has spin $\frac{1}{2}$ but is found to exist in only one of the two possible polarisation states; as follows. The spin vector σ and the momentum vector $\mathbf{p}$ define a left-handed screw sense as in Figure 3.3. Upon spatial inversion, i.e. reflection in a mirror with plane normal to $\mathbf{p}$, the axial vector σ is unchanged, while $\mathbf{p}$ is reversed. So, the parity operation results in a RH neutrino state, which is not, however, observed in nature. Thus weak interactions are not invariant under spatial inversion and do not conserve parity.

In experimental studies of both strong and electromagnetic interactions, tiny degrees of parity violation are in fact observed. These arise not from the breakdown of parity conservation in these interactions as such but because the Hamiltonian or energy operator (which, acting on the wavefunction of a bound state system, generates the energy eigenvalues of the state) also contains contributions from the weak interactions between the particles involved:

$$H = H_{\text{strong}} + H_{\text{electromagnetic}} + H_{\text{weak}}$$

In nuclear transitions, the degree of parity violation will be of the order of the ratio of weak to strong couplings, i.e. 10^{-7} typically. For example, a fore–aft asymmetry is observed in the γ-decay of polarised ^{19}F nuclei:

$$\begin{array}{ccc} ^{19}\mathrm{F}^* & \rightarrow & ^{19}\mathrm{F} + \gamma(110\,\mathrm{keV}) \\ J^P = \frac{1}{2}^- & & J^P = \frac{1}{2}^+ \end{array}$$

where there is parity mixing between the states. The observed fore–aft asymmetry, relative to the polarisation vector, is $\Delta = -(18 \pm 9) \times 10^{-5}$, in good accord with that expected from weak neutral-current effects (Adelberger *et al.* 1975). Another example is provided by the α-decay of the 8.87 MeV excited state of ^{16}O:

$$\begin{array}{ccc} ^{16}\mathrm{O}^* & \rightarrow & ^{12}\mathrm{C} + \alpha \\ J^P = 2^- & & J^P = 2^+ \end{array}$$

where the initial state is known to have odd parity and the final state, even parity. The extremely narrow width for this decay, $\Gamma_\alpha = (1.0 \pm 0.3) \times 10^{-10}$ eV (Neubeck *et al.* 1974), is consistent with the magnitude expected from the parity-violating weak contribution and may be contrasted with the width for the γ-decay $^{16}\mathrm{O}^* \rightarrow {}^{16}\mathrm{O} + \gamma$ of 3×10^{-3} eV.

Parity violation in hadronic interactions has also been detected from the polarisation asymmetry in nucleon–nucleon scattering. One measures the fractional difference in the scattering cross-sections for positive or negative helicity beams, $A = P^{-1}(\sigma^+ - \sigma^-)/(\sigma^+ + \sigma^-)$, where P is the degree of longitudinal polarisation. At 45 MeV incident proton energy, $A \simeq -3 \times 10^{-7}$, in approximate agreement with the expected weak interaction contribution. For a detailed discussion of such parity violation experiments, see the review by Adelberger and Haxton (1985).

In atomic as well as in nuclear transitions, tiny degrees of parity violation can also be detected in favourable circumstances (see Chapter 8).

3.6 Charge conjugation invariance

As the name implies, the operation of charge conjugation reverses the sign of the charge and magnetic moment of a particle, leaving all other coordinates unchanged. Symmetry under charge conjugation in classical physics is evidenced by the invariance of Maxwell's equations under change in sign of the charge and current density and also of **E** and **H**. In relativistic quantum mechanics the term 'charge conjugation' also implies the interchange of particle and antiparticle, e.g. $e^- \rightarrow e^+$. For baryons and leptons, a reversal of charge will entail a change in the sign of the baryon or lepton number, and is of course forbidden if lepton number and baryon number are strictly conserved.

Strong and electromagnetic interactions are found experimentally to be invariant under the charge conjugation operation. For example, in strong interactions comparisons have been made of the rates of positive and negative mesons in the reactions

$$\begin{aligned} p + \bar{p} &\to \pi^+ + \pi^- + \cdots \\ &\to K^+ + K^- + \cdots \end{aligned}$$

and any possible violation has been found to be well below the 1% level.

Only neutral bosons that are their own antiparticles can be eigenstates of the C(charge conjugation) operator. If we were to operate on the wavefunction for a charged pion, which we here denote by the Dirac convention $|\pi\rangle$, we would get

$$C|\pi^+\rangle \to |\pi^-\rangle \neq \pm|\pi^+\rangle$$

An arbitrary phase may be included in this operation. This is not important for the present discussion. We see that charged pions π^+ and π^- cannot be C eigenstates. For a neutral pion however, the C operator has a definite eigenvalue, since the neutral pion state transforms into itself. Thus

$$C|\pi^0\rangle = \eta|\pi^0\rangle$$

where η is some constant. Repeating the operation gives $\eta^2 = 1$, so that

$$C|\pi^0\rangle = \pm 1|\pi^0\rangle$$

To find the sign, note that electromagnetic fields are produced by moving charges that change sign under C. Hence, the photon has $C = -1$. Since the charge conjugation quantum number is multiplicative, a system of n photons has C eigenvalue $(-1)^n$. The neutral pion undergoes the decay

$$\pi^0 \to 2\gamma$$

and thus has even C-parity,

$$C|\pi^0\rangle = +|\pi^0\rangle \tag{3.14}$$

It follows that the decay $\pi^0 \to 3\gamma$ will be forbidden if electromagnetic interactions are C-invariant. The limit on the branching ratio is as follows:

$$\frac{\pi^0 \to 3\gamma}{\pi^0 \to 2\gamma} < 3 \times 10^{-8}$$

Other tests of C symmetry in electromagnetic interactions are provided by the decay of the η meson (a particle with $J^P = 0^-$ and $C = +1$ like the neutral

pion, but with mass 550 MeV instead of 135 MeV). For example, the branching ratio for the C-violating decay

$$\frac{\eta \to \pi^0 e^+ e^-}{\eta \to \text{anything}} < 4 \times 10^{-5}$$

Whilst C invariance holds in strong and electromagnetic interactions, it, like invariance under the parity operation, is broken in weak interactions. Under the C operation, a LH neutrino ν will transform into a LH antineutrino $\bar{\nu}$. Such a state is not found in nature. However, under the *combined* operation CP, a LH neutrino ν_L transforms into a RH antineutrino $\bar{\nu}_R$ (see Figure 3.4). So, while the weak interactions respect neither P nor C invariance separately, they are eigenstates of the product CP:

$$CP|\nu_L\rangle \to |\bar{\nu}_R\rangle \tag{3.15}$$

Actually, this statement is only very nearly true: CP violation in weak interactions does occur at the 10^{-4} level (see Chapter 7).

3.7 Charge conservation and gauge invariance

Electric charge is known to be accurately conserved and we assume this to be exact. For, recalling that the attractive gravitational force on an electron in the laboratory due to all the other electrons in the earth is only 10^{-38} of their repulsive electrical force – which is, however, exactly balanced by the attraction of the protons – we can appreciate that even a tiny degree of charge non-conservation could have major effects. Experimental limits have been set by searching for a possible charge nonconserving decay mode of the neutron, for which the limit on the branching ratio is given by

$$\frac{n \to p\nu_e\bar{\nu}_e}{n \to pe^-\bar{\nu}_e} < 9 \times 10^{-24} \tag{3.16}$$

The conservation of a quantity is connected with an invariance principle, and that involved in the case of charge conservation is the property of *gauge invariance* of the electromagnetic field. The connection may be introduced using an argument of Wigner (1949). In electrostatics, the potential ϕ is arbitrary. The equations are concerned with *changes* in potential and are independent of the absolute value of ϕ at any point. Suppose, now, that charge is not conserved, that it can be created by some magic process and that to create a charge Q work W is required, which can be recovered later when the charge is destroyed. Let the charge be created at a point where the potential on the chosen scale is ϕ. The work done will be W, and independent of ϕ since by hypothesis no physical process can depend on the absolute potential scale. If the charge is now moved to a point

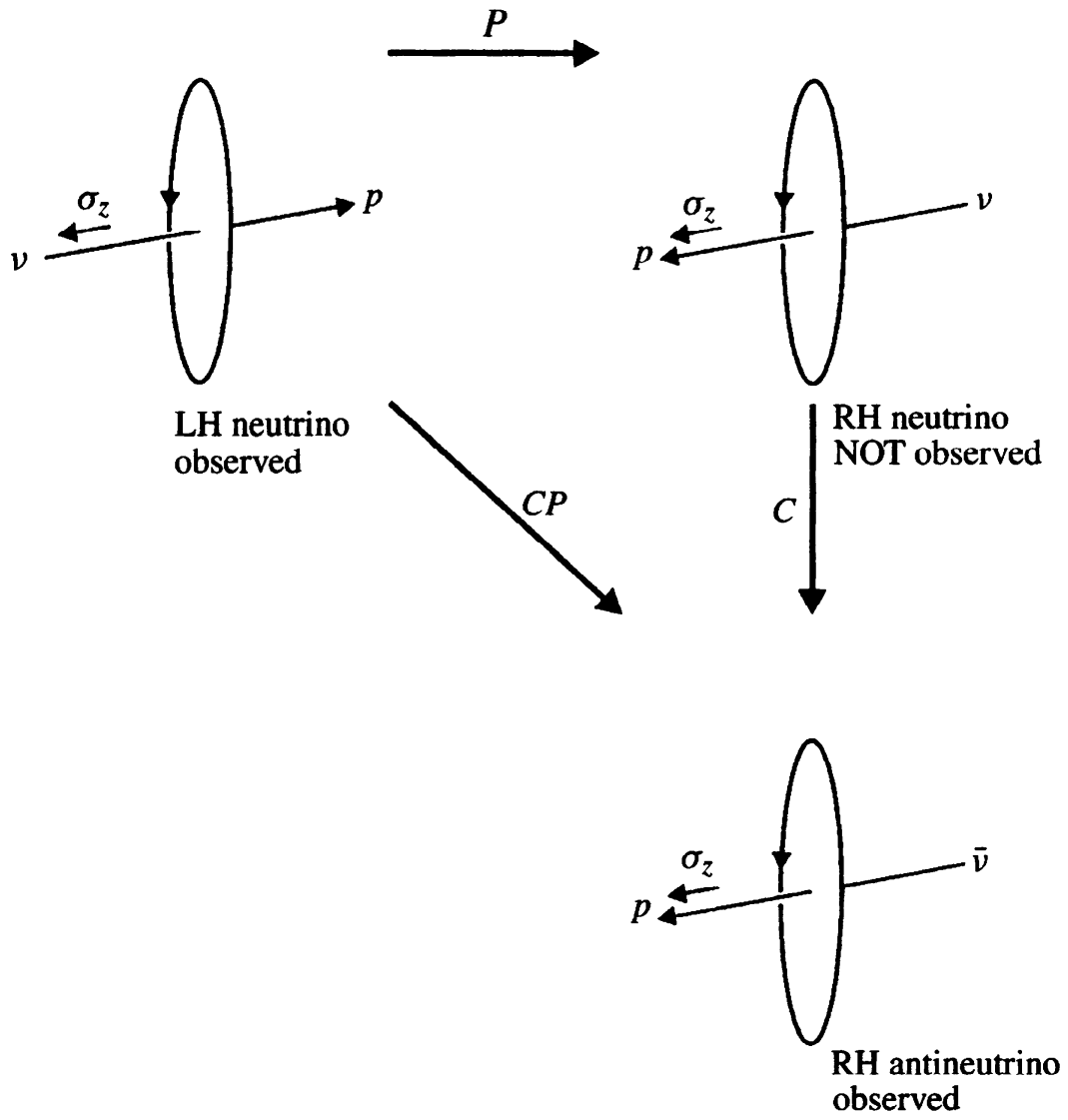

Fig. 3.4. Result of C, P and CP operations on neutrino or antineutrino states. Only the states connected by the CP operation exist in nature.

where the potential is ϕ', the energy change will be $Q(\phi - \phi')$, so that when the charge is destroyed we recover the original system but have gained a net energy $W - W + Q(\phi - \phi')$. So, conservation of energy implies that we cannot create or destroy charge if the potential scale is arbitrary. Hence, if the theory of electromagnetism is formulated in such a way that the scale or gauge of potential can be arbitrary, charge conservation is a necessary consequence.

In quantum mechanics, we can see the effect of a gauge transformation using a simple example. Imagine, as in Figure 3.5, a parallel beam of low energy electrons incident on and scattered by a 'double slit' AB (which might be provided by points on a crystal lattice) and detected at the plane C, where a characteristic diffraction pattern is observed. The incident wave is described by a wavefunction that, in units

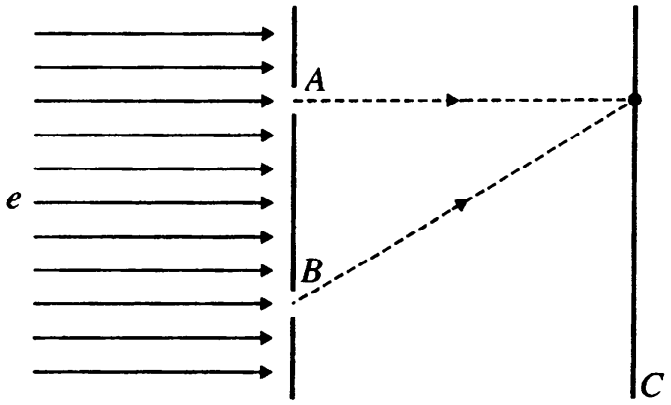

Fig. 3.5. Diffraction of an electron beam by a slit AB, observed in plane C.

such that $\hbar = c = 1$, will be of the form

$$\psi = e^{i(\mathbf{p}\cdot\mathbf{x}-Et)} = e^{ipx} \tag{3.17}$$

where $p = (\mathbf{p}, iE)$ is the 4-momentum of the electron and $x = (\mathbf{x}, it)$ is the space–time coordinate. In general we can include a constant phase factor, which, for reasons that will become clear later, we write as $e\theta$, where e is the elementary charge, so that

$$\psi \rightarrow \psi e^{ie\theta} \tag{3.18}$$

The intensity at C depends on the *difference* in phase of the waves from A and from B, and is independent of the *global* (same over all space) phase $e\theta$, which is arbitrary and unobservable. Suppose, however, that the phase is chosen differently at different points: $e\theta = e\theta(x)$. Then the space–time gradient of the overall phase is

$$\frac{\partial}{\partial x} i(px + e\theta) = i\left(p + e\frac{\partial\theta}{\partial x}\right) \tag{3.19}$$

As θ depends on x, the relative phase difference in the waves from A and from B will change and the predicted pattern at C will be altered, so the physical result would not be invariant under arbitrary *local* phase transformations. The electrons, however, are charged and they interact via an electromagnetic potential, which we write as the 4-vector $A = (\mathbf{A}, i\phi)$ where $\mathbf{A}$ is the vector and ϕ the scalar potential. The effect of the electrostatic potential ϕ on the energy of a singly charged particle is to change it from E to $E - e\phi$. In 4-vector notation, the effect of the potential A is therefore to change the phase of the electron wavefunction by the substitution in (3.17)

$$p \rightarrow p - eA \tag{3.20}$$

so that the derivative (3.19) becomes

$$\frac{\partial}{\partial x} i(px - eAx + e\theta) = i\left(p - eA + e\frac{\partial\theta}{\partial x}\right) \tag{3.21}$$

Let us recall that the magnetic and electric fields $\mathbf{B}, \mathbf{E}$ can be expressed as derivatives of the vector and scalar potentials,

$$\mathbf{B} = \nabla \times \mathbf{A} \tag{3.22}$$

$$\mathbf{E} = -\nabla\phi - \frac{\partial \mathbf{A}}{\partial \mathrm{t}} \tag{3.23}$$

and that the physical fields are unaltered if one changes the potential by adding to it the gradient of any scalar function. Identifying this with $\theta(x)$ as defined above, the gauge transformation on the potential is

$$A \to A + \frac{\partial\theta}{\partial x} \tag{3.24}$$

One can verify that this transformation leaves unaltered the fields in (3.22) and (3.23). When applied to (3.21), the derivative becomes

$$i\left[p + e\frac{\partial\theta}{\partial x} - e\left(A + \frac{\partial\theta}{\partial x}\right)\right] = i(p - eA) \tag{3.25}$$

which is independent of θ. Thus, the combined effects of the phase transformation (3.18) on the electron wavefunction and the gauge transformation (3.24) on the field now leave the previous derivative (3.19) independent of θ; hence the diffraction pattern is unaltered, and the physical result is invariant under this *local* gauge transformation.

The quantity $i(p - eA)$ or, in operator notation,

$$D = \frac{\partial}{\partial x} - ieA \tag{3.26}$$

is called the *covariant derivative*. We shall refer to covariant derivatives again in discussing electroweak interactions in Chapter 8. While the effects of the local phase transformation on the electron wavefunction and the local gauge transformation on the potential acting on the electron cancel exactly, it is important to note that this cancellation depends on two things. First, there has to be a long-range field (the electromagnetic field in this case) acting on the electrons and changing their phases. It has to be long range because our slit separation can be arbitrarily large, and this infinite field range in turn implies from (2.2) a zero photon mass. Second, charge has to be conserved: the cancellation clearly would not work if the electron were suddenly to lose, and later regain, its charge, in traversing the slit system.

To summarise: it is possible to describe charged particles by wavefunctions with phases chosen arbitrarily at different times and places, and this makes no difference to the predicted physical results provided the charges are coupled to a long-range field (the electromagnetic field) to which is applied a simultaneous local gauge transformation *and* provided the charge is conserved.

As mentioned in Chapter 2, loops in Feynman diagrams in QED give rise to divergent integrals. In a field theory with gauge invariance however, there is a high degree of symmetry, and this results in the systematic cancellation of divergences between different diagrams, order by order. Such a renormalisable theory predicts cross-sections and decay rates that are finite and calculable to all orders in the coupling constant. On the contrary, theories without the property of gauge invariance do not give finite and calculable results.

3.8 Baryon and lepton conservation

In the previous section an invariance principle, in this case gauge invariance, led to a conservation law, that of the conservation of charge. In field theories with local gauge symmetry, an absolutely conserved quantity like electric charge implies the existence of a long-range field – in this case, the electromagnetic field – coupled to the charge. Similarly, if baryon number were absolutely conserved as a result of a local gauge symmetry, one might expect that there should exist a long-range field coupled to it. There is, however, no evidence for such a field. Limits have been set as follows. The Equivalence Principle of general relativity states that the ratio R of inertial mass to gravitational mass should be the same for all substances. If one compares the same mass of, say, aluminium and platinum, they will have slightly different baryon numbers (by about 1 part in 2000) because the mass per baryon differs on account of the different neutron-to-proton ratio and the different binding energy per nucleon in the two cases. Hence, a field coupled to baryon number should be manifested as a tiny difference in R for the two substances. In a series of experiments starting with those by Eötvös in 1922 and spanning over 50 years, the values of R have been compared by placing the same mass of two different materials on the arms of a torsion balance. The most precise experiments, by Braginsky and Panov in 1972, used the fact that the inertial force due to the Earth's motion (at 30 km s^{-1}) around the Sun balances the force due to the Sun's gravity. Any discrepancy in the ratio of inertial to gravitational mass for the two substances would lead to a couple on the suspension, which would vary sinusoidally, with a 24 hour period, owing to the Earth's rotation. In the experiment, the (very slow, typically 5 hour) natural oscillations of the suspension system were Fourier analysed to detect any 24 hour period. The observed limit

$\Delta R/R < 10^{-12}$ implies a coupling for a field coupled to baryon number of less than 10^{-9} of the gravitational coupling.

It is instructive to compare and contrast some of the experimental limits on the non-conservation of charge Q, lepton number L and baryon number B, as indicated by the limits on the mean lifetime τ for different decay processes:

charge conservation,	$\tau(n \to p\nu_e\bar{\nu}_e) > 10^{18}$ yr
lepton conservation,	$\tau(^{76}\text{Ge} \to {}^{76}\text{Se} + 0\nu + e^- + e^-) > 10^{26}$ yr
baryon conservation,	$\tau(p \to e^+\pi^0) > 10^{33}$ yr

Thus, remarkably enough, the highest limits are on the conservation of baryon number and lepton number, neither of which appears to be protected by any gauge principle. Apart from the absence of any long-range field coupled to baryon number there are other, more cogent, reasons for actually postulating baryon non-conservation. The most obvious one is the huge baryon–antibaryon asymmetry of the universe, implying that if one started with the Big Bang scenario and net baryon number zero (compared with $N_B \sim 10^{79}$ today!), baryon-number-violating interactions must have taken place, as will be discussed in Chapter 10. Grand unification models in fact postulate that, at extremely high energies, possibly 10^{16}–10^{17} GeV, the weak, electromagnetic and strong interactions will be unified, with a single coupling. In such models, quarks and leptons appear in supermultiplets and transitions between them can occur. While of course we cannot reach such energies today, virtual processes involving such massive bosons could occur, and this means that even at normal energies protons may decay, albeit with a very long lifetime (for example, $p \to e^+\pi^0$). Baryon non-conservation, in the form of proton decay, has however not yet been observed; the present lifetime limit is given above.

Searches have also been made for the non-conservation of lepton number. The limit for lepton number non-conservation as exemplified by neutrinoless double beta decay in ^{76}Ge is quoted above; a fuller discussion is given in Chapter 9. Nor is there any evidence for the instability of other leptons. For example, the neutrino pulse from the supernova SN1987A in the Large Magellanic Cloud covered the 170 000 light-year journey to Earth without significant attenuation (see Section 10.9). For all practical purposes, therefore, in our present cold universe baryon and lepton number are conserved; equally, there are no deep theoretical reasons to suppose that this conservation rule is absolute.

Finally, it may be remarked that while total lepton number seems to be conserved, weak transitions between leptons of different flavours (e.g. $\nu_e \to \nu_\mu$) may have been detected. Such oscillations of neutrino flavour have indeed been postulated to account for the solar neutrino deficit. Remarkably enough, possible evidence for oscillations has also been found in the interactions of atmospheric

Table 3.1. *Tests of the CPT theorem*

Measured quantity	Limit or value
$(M_{K^0} - M_{\bar{K}^0})/(M_{K^0} + M_{\bar{K}^0})$	$< 10^{-19}$
$(M_{e^+} - M_{e^-})/(M_{e^+} + M_{e^-})$	$< 4 \times 10^{-8}$
$(M_\Lambda - M_{\bar{\Lambda}})/(M_{\bar{\Lambda}} + M_\Lambda)$	$(-5 \pm 5) \times 10^{-6}$
$(Q_p - Q_{\bar{p}})/e$	$< 2 \times 10^{-5}$
$\left(\frac{Q_p}{M_p} - \frac{Q_{\bar{p}}}{M_{\bar{p}}}\right) \Big/ \left(\frac{Q_p}{M_p} + \frac{Q_{\bar{p}}}{M_{\bar{p}}}\right)$	$(8 \pm 6) \times 10^{-10}$
$(\mu_{e^+} - \mu_{e^-})/(\mu_{e^+} + \mu_{e^-})$	$-(3 \pm 5) \times 10^{-13}$
$(\tau_{\mu^+} - \tau_{\mu^-})/(\tau_{\mu^+} + \tau_{\mu^-})$	$< 10^{-4}$

neutrinos, investigated as a 'background' or by-product of experiments originally searching for (the unobserved) proton decay!

3.9 *CPT* invariance

In the following section we mention the phenomenon of *CP* violation. This is also linked to violation of invariance under time reversal, *T*, through the very important *CPT* theorem. This theorem states that *all* interactions are invariant under the successive operation of *C* (= charge conjugation), *P* (= parity operation) and *T* (= time reversal) taken in any order.

The proof of the *CPT* theorem is based on very general assumptions and impacts the whole of particle physics, for example, the spin-statistics relation, that integral and half-integral spin particles obey Bose and Fermi statistics respectively (see Section 1.2). Consequences of the *CPT* theorem that may be verified experimentally relate to the properties of particles and antiparticles: they must have the same mass and lifetime and equal and opposite electric charges and magnetic moments. These results would follow from *C* invariance alone, if it held universally, but since weak interactions violate *C* and *CP* symmetry the prediction rests on the more general theorem.

The expected experimental consequences of the *CPT* theorem seem to be well verified, as shown by the examples in Table 3.1.

3.10 *CP* violation and *T* violation

Until 1964, it was believed that, although weak interactions were known to violate *C* and *P* invariance separately, *CP* symmetry was respected. However, in that year Christenson *et al.* discovered that the long-lived neutral kaon, normally decaying

Table 3.2. *Effect of T and P operations*

Quantity		Effect of T	Effect of P
position	$\mathbf{r}$	$\mathbf{r}$	$-\mathbf{r}$
momentum	$\mathbf{p}$	$-\mathbf{p}$	$-\mathbf{p}$
spin	$\boldsymbol{\sigma}$, axial vector $(\mathbf{r} \times \mathbf{p})$	$-\boldsymbol{\sigma}$	$\boldsymbol{\sigma}$
electric field	$\mathbf{E}\ (= -\nabla V)$	$\mathbf{E}$	$-\mathbf{E}$
magnetic field	$\mathbf{B}$, axial vector	$-\mathbf{B}$	$\mathbf{B}$
magnetic dipole moment	$\boldsymbol{\sigma} \cdot \mathbf{B}$	$\boldsymbol{\sigma} \cdot \mathbf{B}$	$\boldsymbol{\sigma} \cdot \mathbf{B}$
electric dipole moment	$\boldsymbol{\sigma} \cdot \mathbf{E}$	$-\boldsymbol{\sigma} \cdot \mathbf{E}$	$-\boldsymbol{\sigma} \cdot \mathbf{E}$
longitudinal polarisation	$\boldsymbol{\sigma} \cdot \mathbf{p}$	$\boldsymbol{\sigma} \cdot \mathbf{p}$	$-\boldsymbol{\sigma} \cdot \mathbf{p}$
transverse polarisation	$\boldsymbol{\sigma} \cdot (\mathbf{p}_1 \times \mathbf{p}_2)$	$-\boldsymbol{\sigma} \cdot (\mathbf{p}_1 \times \mathbf{p}_2)$	$\boldsymbol{\sigma} \cdot (\mathbf{p}_1 \times \mathbf{p}_2)$

into three pions with CP eigenvalue -1, could also, with probability 2×10^{-3}, decay to two pions with $CP = +1$. These results are discussed in detail in Chapter 7.

The origin of CP violation in K^0 decay is not presently known. In the Standard Model, incorporating six fundamental quark flavours, weak transitions occur between flavours and a CP-violating phase angle can be involved. CP violation is a necessary prerequisite to the development of a universal baryon–antibaryon asymmetry (see Section 7.16).

CP violation implies T violation through the CPT theorem; consequently, searches for T-violating processes have acquired great importance. The transformations of common quantities under the T and P operations are given in Table 3.2. We note that in elementary weak decay processes, e.g. $\mu^+ \rightarrow e^+ + \nu_e + \bar{\nu}_\mu$ or $n \rightarrow p + e^- + \bar{\nu}_e$, observation of the polarisation transverse to a plane defined by the momentum vectors of the secondary particles is a signal for T violation. Limits to such T-violating contributions are below the 10^{-3} level.

Direct searches for T violation in strong interactions have been made by application of the principle of detailed balance to forward and backward reactions. If the interactions are invariant under the T and P operations then the matrix elements for the forward and backward reactions will be identical. Figure 3.6 shows the result of such a test in the reversible reactions

$$p + {}^{27}\mathrm{Al} \rightleftharpoons \alpha + {}^{24}\mathrm{Mg}$$

from which it was concluded that the amplitude of any T violation was less than 5×10^{-4}.

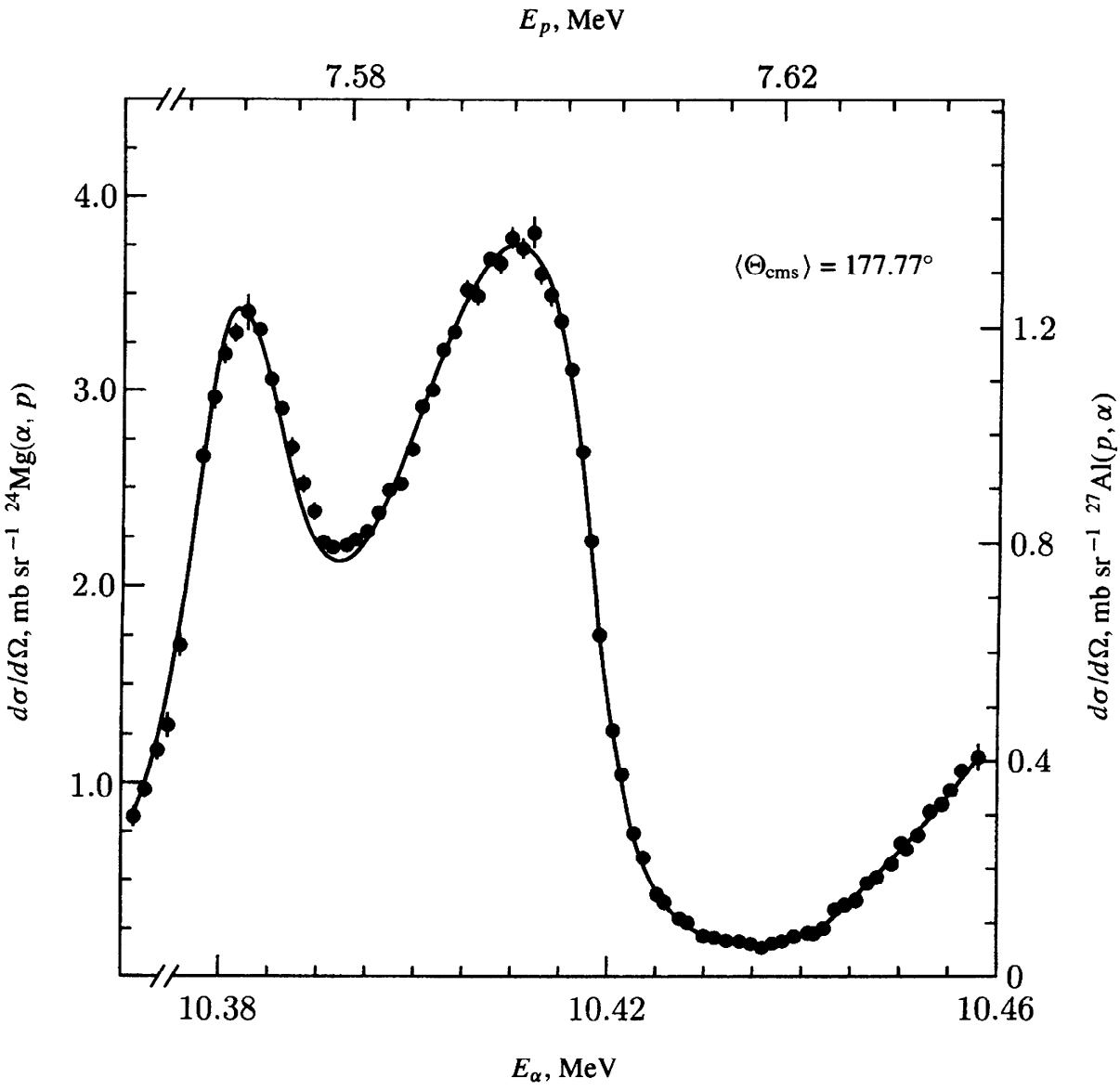

Fig. 3.6. The differential cross-sections for the reaction ^{24}Mg(α, p)^{27}Al (solid points) and its inverse (curve), as measured by Blanke *et al.* (1983).

3.11 Neutron electric dipole moment

To date, the most sensitive tests of T violation have been made in searches for electric dipole moments of the neutron and the electron. From Table 3.2 we see that an electric dipole moment (EDM) for an elementary particle violates both P and T symmetry. Since it turns out that such an EDM is in principle sensitive to new physics beyond the Standard Model, we describe these investigations in a little detail.

First, let us try to guess the magnitude of any EDM, on dimensional grounds. One can write

$$\text{EDM} = \text{charge } (e) \times \text{length } (l) \times T\text{-violating parameter } (f) \qquad (3.27)$$

The EDM for the neutron will arise from an asymmetry in the spatial distribution of the electric charge (carried by the quarks) relative to the neutron's spin axis. The fact that P invariance is violated means that the weak interaction is involved, with a coupling $G = g^2/M_W^2$ where $g^2 \sim e^2$ in the electroweak model (see (2.10) and (2.11)) and $M_W = 80$ GeV. To obtain the dimensions of a length we need to introduce an arbitrary mass, which we can take as that of the neutron, M. Hence, recalling that, in units such that $\hbar = c = 1$ we have 1 GeV$^{-1} = 2 \times 10^{-14}$ cm, we might expect that

$$l \sim e^2 M/M_W^2 = 4\pi\alpha M/M_W^2 = 1.4 \times 10^{-5}\ \text{GeV}^{-1} \simeq 10^{-19}\ \text{cm}$$

For the T-violating parameter we could take $f = 10^{-3}$, the level of CP $(= T)$ violation in K^0 decay. Then (3.27) gives us as an estimate

$$\text{EDM} \sim 10^{-22} e\ \text{cm}$$

The length here is very short compared with the radius (10^{-13} cm) of a neutron. Actual theoretical estimates of the EDM vary from the above figure down to $10^{-34} e$ cm. Experiments to measure the EDM over recent years have been carried out at reactors at Grenoble and St Petersburg.

The basic method (as employed at ILL, Grenoble) is to store 'ultra-cold' neutrons in a totally reflecting metallic 'bottle' for as long as possible, and to measure any change in the neutron spin precession frequency ($\nu = \mu B/h$) in a weak magnetic field B when a strong, parallel electric field is reversed in sign – thus indicating an electric dipole interaction.

A reactor provides the primary neutron source, a liquid deuterium moderator being placed in the core so that neutrons thermalised by collisions with cold deuterons achieve a roughly Maxwellian spectrum with a temperature of order 25 K (average velocity 500 m s^{-1}). Neutrons at the low velocity end of the spectrum can be transported through polished metal tubes by successive internal reflections, which occur for angles of incidence (relative to the surface) less than the critical angle θ_c, where

$$\sin^2\theta_c = 1 - n^2 = \lambda^2 N a/\pi \tag{3.28}$$

Here, n is the refractive index of the 'mirror', λ is the neutron wavelength, N is the number of scattering nuclei per unit volume and 'a' is a quantity called the coherent nuclear scattering length. The neutron velocity is further reduced by reflection from the (retreating) polished nickel blades of a high speed turbine (see Figure 3.7). Ultra-cold neutrons have such low velocity (of order 5 m s^{-1}) that θ_c in (3.28) reaches 90° and total reflection occurs for any angle of incidence. Such neutrons can be stored in a highly polished cylindrical metallic 'bottle' of beryllium.

Access to the bottle is via a thin magnetised iron foil. If a field B' is applied normally to the foil surface, it adds a term $\pm\mu B'/T$ to the right-hand side of (3.28), where T is the neutron kinetic energy and μ is the magnetic moment. The parameters are chosen so that neutrons entering the bottle are polarised, i.e. the foil reflects one orientation of neutron spin and transmits the other. A uniform steady magnetic field of 10 milligauss and a reversible electric field of 15 kV cm^{-1} are applied along the bottle axis. The neutrons precess about the magnetic field with a frequency $\nu \simeq 30$ Hz. After the bottle is full and the door closed, an oscillating magnetic field of 30 Hz is applied in two separate pulses in a perpendicular direction, so that resonant depolarisation of the neutrons takes place. After about three minutes, the door is opened and those neutrons with the correct polarisation pass out through the foil, now acting as an analyser.

The count of neutrons leaving the bottle is made as a function of the spin precession frequency ν (see Figure 3.7(b)). When the EDM is being measured, measurements are confined to working points where the variation of count rate with frequency is a maximum.

The present (1998) limit is

$$\text{EDM (neutron)} < 1.0 \times 10^{-25} e \text{ cm} \tag{3.29}$$

Over the last 40 years, the experimental limit has been progressively improved, by a steady factor of 20 per decade – a remarkable technical achievement.

On the theoretical side, several sources of CP or T violation have been considered. That observed in K^0 decay (Section 7.16) is usually ascribed to CP violation in the Standard Model, which is second order in the weak interaction and predicts an EDM $\simeq 10^{-32} e$ cm.† Such a level is, however, much too small to account for the cosmological matter–antimatter asymmetry, which would imply an EDM $> 3 \times 10^{-28} e$ cm. Enlargement of the Standard Model with supersymmetric or left–right symmetric models could give first-order CP-violating effects, with a predicted EDM as high as $10^{-26} e$ cm. It is clear therefore that the search for the neutron EDM is of profound importance and a good test of new physics beyond the Standard Model (see also Chapter 9).

The limit on the EDM of the electron is $< 4 \times 10^{-27} e$ cm, an order of magnitude below that of the neutron. However, the expected EDM of the electron – a lepton rather than an assembly of quarks – is some orders of magnitude less than that of the neutron.

† This very low value arises partly because of the large mass (180 GeV) of the top quark. For CP violation in the Standard Model, all three quarks (u, c, t) of charge $\frac{2}{3}$ must be involved in a so-called 'penguin diagram' (see Section 7.16).

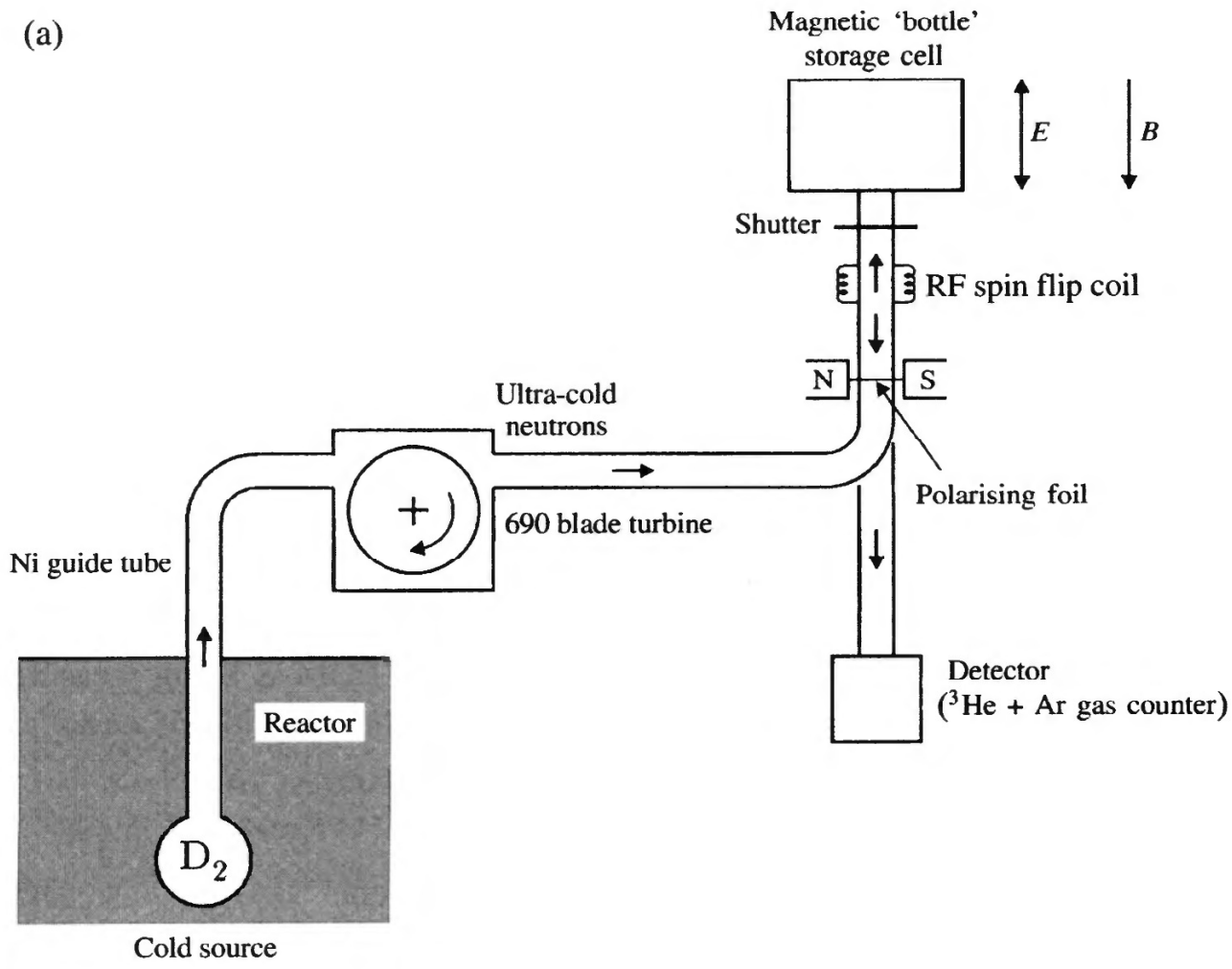

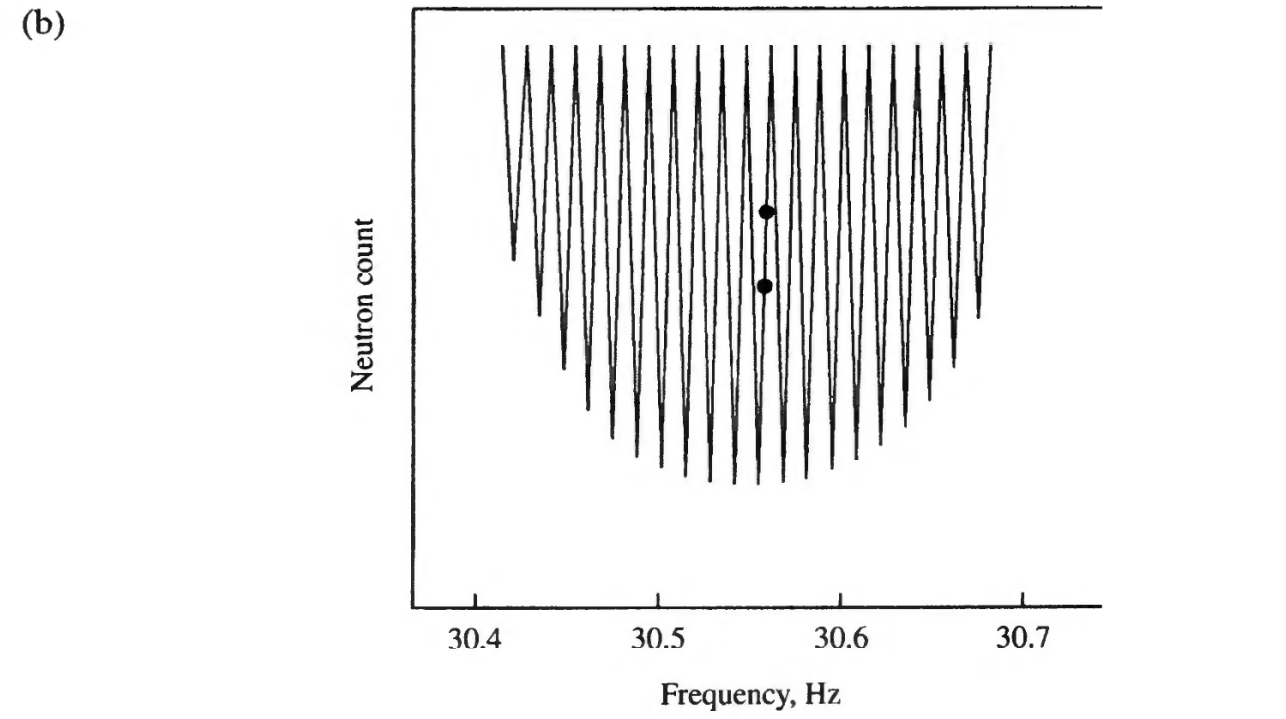

Fig. 3.7. (a) The apparatus at Grenoble for measuring the EDM of the neutron. (b) Neutron count rate as a function of precession frequency. To measure the EDM, the operations are confined to the two working points shown by the dots (after Pendlebury 1993).

3.12 Isospin symmetry

Heisenberg suggested in 1932 that neutron and proton might be treated as different charge substates of one particle, the nucleon. A nucleon is ascribed a quantum number, isospin, denoted by the symbol I, with value $I = \frac{1}{2}$; there are two substates with I_z, or I_3, equal to $\pm\frac{1}{2}$. The charge is then given by $Q/e = \frac{1}{2} + I_3$, if we assign $I_3 = +\frac{1}{2}$ to the proton and $I_3 = -\frac{1}{2}$ to the neutron. This purely formal description is in complete analogy with that of a particle of ordinary spin $\frac{1}{2}$, with substates $J_z = \pm\frac{1}{2}$ (in units of $\hbar$).

Isospin is a useful concept because it is a conserved quantum number in strong interactions. Consequently these depend on I and not on the third component, I_3. The strong interactions between nucleons, for example, are determined by I and we do not distinguish between neutron and proton – they are degenerate states. A pictorial way to visualise isospin is as a vector, **I**, in a three-dimensional 'isospin space', with Cartesian coordinates I_x, I_y, I_z – or, as they are more usually denoted, I_1, I_2, I_3. Isospin conservation corresponds to invariance of the length of this vector under rotation of the coordinate axes in isospin space. Electromagnetic interactions do not conserve **I** and are not invariant under such rotation. Because they couple to electric charge Q, they single out the I_3-axis in isospin space.

The earliest evidence for isospin conservation in strong interactions came from the observation of the charge symmetry and charge independence of nuclear forces, i.e. the equivalence of n–p, p–p and n–n forces in the same angular-momentum states once Coulomb effects had been subtracted. This equality followed from the remarkable similarity in the level schemes of mirror nuclei, i.e. nuclei with similar configurations of nucleons but with a neutron replaced by a proton or vice versa.

Where does isospin symmetry come from? In the context of the quark model, the proton consists of uud, while the neutron is a udd combination. Since one is obtained from the other by exchanging a u quark for a d quark or vice versa, the closeness in mass of neutron and proton must reflect the near equality of u and d quark masses.

Of course, there will be a Coulomb energy term (the energy required to put the charge on the proton) which – all else being equal – would make the proton heavier than the neutron. As we find later (Chapter 5) protons and neutrons have a finite size, with rms radius of the charge distribution of order $r \sim 1$ fm. The Coulomb energy difference is then clearly of order $e^2/(4\pi r) \simeq \alpha$ fm$^{-1} \approx 1$ MeV (recalling that $\hbar c = 197$ MeV fm and that in units $\hbar = c = 1$, $e^2 = 4\pi\alpha$ and 1 fm$^{-1} = 197$ MeV). So, the neutron being heavier by $M_n - M_p = 1.3$ MeV, we conclude that $M_d > M_u$ by 2 or 3 MeV. Since the constituent mass of each quark is of order 300 MeV (one third of the nucleon mass), the u and d quark masses come

out equal within 1% or so. This apparently accidental near equality in mass of the lightest quarks is *the sole reason for isospin symmetry.*

Isospin symmetry will apply between all baryons and mesons which transform one to another by interchange of u and d quarks. The lightest meson, the pion, exists in three charge states. Anticipating the discussion of the quark model of hadrons in Chapter 4, these may be written as

$$\begin{aligned} \pi^+ &= u\bar{d} && (I_3 = +1) \\ \pi^- &= d\bar{u} && (I_3 = -1) \\ \pi^0 &= \tfrac{1}{\sqrt{2}}(d\bar{d} - u\bar{u}) && (I_3 = 0) \end{aligned} \tag{3.30}$$

The masses of the pions are $m_{\pi^+} = 140$ MeV ($\equiv m_{\pi^-}$ from C symmetry), and $m_{\pi^0} = 135$ MeV. Again, a few MeV separate the masses of the members of this triplet, which we identify as an $I = 1$ multiplet, with third components $I_3 = +1, -1$ and 0 as above.

3.13 Isospin in the two-nucleon and the pion–nucleon systems

The isospin states of a system of two nucleons, each with $I = \frac{1}{2}$, can be written down in complete analogy with the combination of two states of spin $\frac{1}{2}$ in (3.11), which gives us (labelling the wavefunctions n and p to denote neutron and proton states):

$$\chi(1,1) = p(1)p(2) \tag{3.31a}$$

$$\chi(1,0) = \tfrac{1}{\sqrt{2}}[p(1)n(2) + n(1)p(2)] \tag{3.31b}$$

$$\chi(1,-1) = n(1)n(2) \tag{3.31c}$$

$$\chi(0,0) = \tfrac{1}{\sqrt{2}}[p(1)n(2) - n(1)p(2)] \tag{3.31d}$$

The first three states are members of an $I = 1$ triplet, symmetric under label interchange $1 \leftrightarrow 2$, while the last is an $I = 0$ singlet, antisymmetric under label interchange.

In the language of group theory, these isospin multiplets, just like the spin multiplets (3.11), are representations of the group SU(2), which involves transformations in a complex, two-dimensional space. The '2' of SU(2) in this case arises because the fundamental representation of isospin is a two-component doublet. The $I = 1$ triplet (3.31a)–(3.31c) forms a '3' representation of SU(2) while the $I = 0$ singlet (3.31d) forms a '1' representation. Symbolically this is written as

$$2 \otimes 2 = 1 \oplus 3$$

where, as is clear in (3.31), the singlet is antisymmetric and the triplet symmetric under label interchange.

The total wavefunction for a two-nucleon state may be written

$$\psi(\text{total}) = \phi(\text{space})\alpha(\text{spin})\chi(\text{isospin}) \tag{3.32}$$

provided orbital and spin angular momentum can be separately quantised (i.e. the system is non-relativistic). Applying (3.32) to a deuteron, which has spin 1, we see that α is symmetric under interchange of the two nucleons. The space wavefunction ϕ has symmetry $(-1)^l$ under interchange, from (3.6). The two nucleons in the deuteron are known to be in an $l = 0$ state (with a few per cent $l = 2$ admixture). Thus ϕ is symmetric, and so finally χ must be antisymmetric in order to satisfy overall antisymmetry of the total wavefunction ψ. From (3.31) it follows that $I = 0$: the deuteron is an isosinglet.

As an example, consider the reactions

$$\begin{array}{llll} \text{(i)} & p + p \to d + \pi^+, & \text{(ii)} & p + n \to d + \pi^0 \\ I = & 1 \quad 0 \quad 1 & I = & 0 \text{ or } 1 \quad 0 \quad 1 \end{array}$$

In each case the final state has $I = 1$. Considering the left-hand sides, we have a pure $I = 1$ state in reaction (i), but 50% $I = 0$ and 50% $I = 1$ in reaction (ii). Conservation of isospin means that either reaction can proceed only through the $I = 1$ channel. Consequently, $\sigma(\text{ii})/\sigma(\text{i}) = \frac{1}{2}$, as is observed.

An important application of isospin conservation arises in the strong interactions of non-identical particles, which will generally consist of mixtures of different isospin states. The classical example of this is pion–nucleon scattering. Since $I_\pi = 1$ and $I_N = \frac{1}{2}$, one can have $I_{\text{total}} = \frac{1}{2}$ or $\frac{3}{2}$. If the strong interactions depend only on I and not on I_3, then the $3 \times 2 = 6$ pion–nucleon scattering processes can all be described in terms of two isospin amplitudes.

Of the six elastic scattering processes,

$$\pi^+ p \to \pi^+ p \tag{3.33a}$$

and

$$\pi^- n \to \pi^- n \tag{3.33b}$$

have $I_3 = \pm\frac{3}{2}$, and are therefore described by a pure $I = \frac{3}{2}$ amplitude. Clearly, at a given bombarding energy, (3.33a) and (3.33b) will have identical cross-sections, since they differ only in the sign of I_3.

The remaining interactions,

$$\pi^- p \to \pi^- p \tag{3.33c}$$

$$\pi^- p \to \pi^0 n \tag{3.33d}$$

$$\pi^+ n \to \pi^+ n \tag{3.33e}$$

$$\pi^+ n \to \pi^0 p \tag{3.33f}$$

Table 3.3. *Clebsch–Gordan coefficients in pion–nucleon scattering*

		$I=\frac{3}{2}$				$I=\frac{1}{2}$	
Pion	Nucleon	$I_3=\frac{3}{2}$	$\frac{1}{2}$	$-\frac{1}{2}$	$-\frac{3}{2}$	$\frac{1}{2}$	$-\frac{1}{2}$
π^+	p	1					
π^+	n		$\sqrt{\frac{1}{3}}$			$\sqrt{\frac{2}{3}}$	
π^0	p		$\sqrt{\frac{2}{3}}$			$-\sqrt{\frac{1}{3}}$	
π^0	n			$\sqrt{\frac{2}{3}}$			$\sqrt{\frac{1}{3}}$
π^-	p			$\sqrt{\frac{1}{3}}$			$-\sqrt{\frac{2}{3}}$
π^-	n				1		

have $I_3=\pm\frac{1}{2}$ and therefore $I=\frac{1}{2}$ or $\frac{3}{2}$. The weights of the two amplitudes in the mixture are given by Clebsch–Gordan coefficients (see Table 3.3). Their derivation is given in Appendix C.

Let us use Table 3.3 to calculate the relative cross-sections for the following three processes, at a fixed energy:

$$\pi^+ p \to \pi^+ p \qquad \text{(elastic scattering)} \tag{3.34a}$$

$$\pi^- p \to \pi^- p \qquad \text{(elastic scattering)} \tag{3.34b}$$

$$\pi^- p \to \pi^0 n \qquad \text{(charge exchange)} \tag{3.34c}$$

The cross-section is proportional to the square of the matrix element connecting initial and final states. Using the Dirac notation $\langle\,|$ and $|\,\rangle$ for the 'in' and 'out' wavefunctions, we can write

$$\sigma \propto \langle\psi_f|H|\psi_i\rangle^2 = M_{if}^2$$

where H is an isospin operator equalling H_1 if it operates on initial and final states with $I=\frac{1}{2}$ and H_3 for states with $I=\frac{3}{2}$. By conservation of isospin, there is no operator connecting initial and final states of different isospin. Let

$$M_1 = \langle\psi_f(\tfrac{1}{2})|H_1|\psi_i(\tfrac{1}{2})\rangle$$
$$M_3 = \langle\psi_f(\tfrac{3}{2})|H_3|\psi_i(\tfrac{3}{2})\rangle$$

The reaction (3.34a) involves a pure state with $I=\frac{3}{2}$, $I_3=+\frac{3}{2}$. Therefore

$$\sigma_a = K|M_3|^2,$$

where K is some constant.

Referring again to Table 3.3, in the reaction (3.34b) we may write

$$|\psi_i\rangle = |\psi_f\rangle = \sqrt{\tfrac{1}{3}}\,|\chi(\tfrac{3}{2}, -\tfrac{1}{2})\rangle - \sqrt{\tfrac{2}{3}}\,|\chi(\tfrac{1}{2}, -\tfrac{1}{2})\rangle$$

Therefore

$$\begin{aligned}\sigma_b &= K|\langle\psi_f|H_1 + H_3|\psi_i\rangle|^2 \\ &= K|\tfrac{1}{3}M_3 + \tfrac{2}{3}M_1|^2\end{aligned}$$

For the reaction (3.34c), one has

$$\begin{aligned}|\psi_i\rangle &= \sqrt{\tfrac{1}{3}}\,|\chi(\tfrac{3}{2}, -\tfrac{1}{2})\rangle - \sqrt{\tfrac{2}{3}}\,|\chi(\tfrac{1}{2}, -\tfrac{1}{2})\rangle \\ |\psi_f\rangle &= \sqrt{\tfrac{2}{3}}\,|\chi(\tfrac{3}{2}, -\tfrac{1}{2})\rangle + \sqrt{\tfrac{1}{3}}\,|\chi(\tfrac{1}{2}, -\tfrac{1}{2})\rangle\end{aligned}$$

and thus

$$\sigma_c = K\left|\sqrt{\tfrac{2}{9}}M_3 - \sqrt{\tfrac{2}{9}}M_1\right|^2$$

The cross-section ratios are then

$$\sigma_a : \sigma_b : \sigma_c = |M_3|^2 : \tfrac{1}{9}|M_3 + 2M_1|^2 : \tfrac{2}{9}|M_3 - M_1|^2 \tag{3.35}$$

The limiting situations, if one or other isospin amplitude dominates under the experimental conditions, are

$$\begin{aligned}M_3 \gg M_1, &\qquad \sigma_a : \sigma_b : \sigma_c = 9 : 1 : 2 \\ M_1 \gg M_3, &\qquad \sigma_a : \sigma_b : \sigma_c = 0 : 2 : 1\end{aligned}$$

Numerous experimental measurements have been made of the total and differential pion–nucleon cross-sections. The earliest and simplest experiments measured the attenuation of a collimated, monoenergetic $\pi^{\pm}$ beam in traversing a liquid hydrogen target. The results of such measurements are shown in Figure 3.8. For both positive and negative pions, there is a strong peak in σ_{total} at a pion kinetic energy of 200 MeV. The ratio $(\sigma_{\pi^+p}/\sigma_{\pi^-p})_{\text{total}} = 3$, proving that the $I = \frac{3}{2}$ amplitude dominates this region. This bump is the $\Delta(1232)$ resonance previously discussed in subsection 2.11.1.

3.14 Isospin, strangeness and hypercharge

In the foregoing discussion of pions and nucleons, the relation between electric charge Q, third component of isospin I_3 and baryon number B can be compactly expressed as

$$\frac{Q}{|e|} = I_3 + \frac{B}{2} \tag{3.36}$$

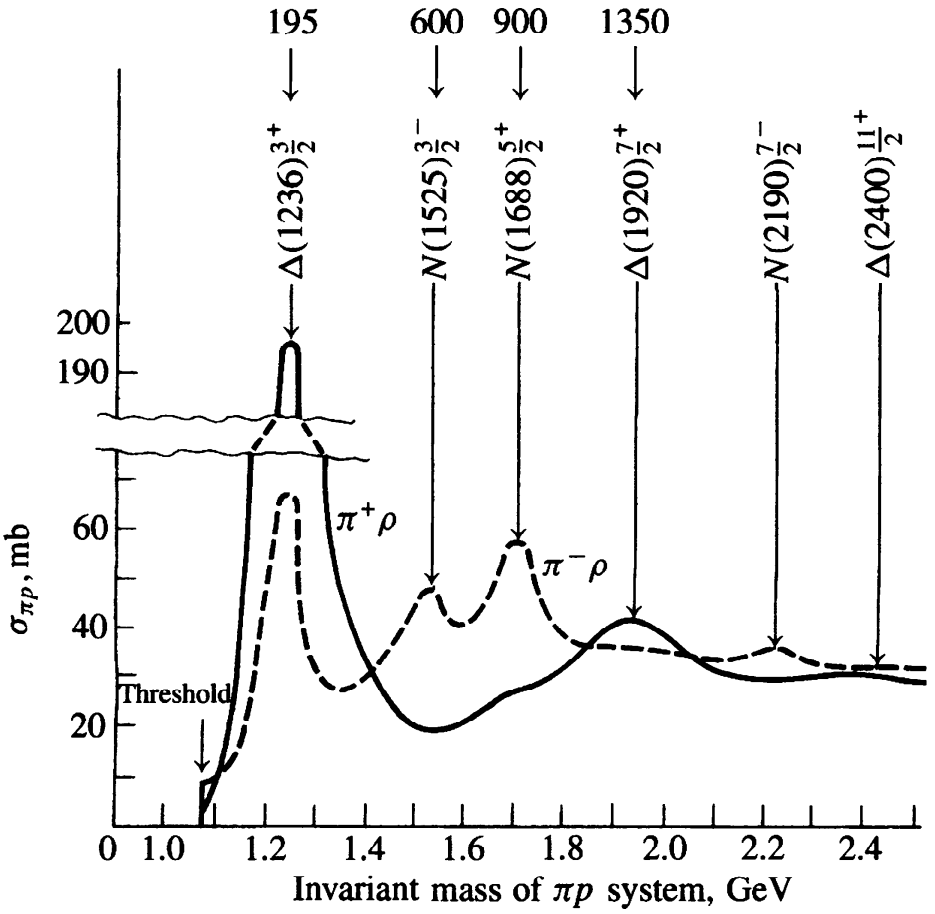

Fig. 3.8. The total cross-section for π^+ and π^- mesons on protons, as a function of pion energy or invariant mass of the pion–nucleon system. The symbol Δ refers to $I = \frac{3}{2}$ resonances, while N refers to $I = \frac{1}{2}$ states. The positions of a few of the known states, together with spin-parity assignments, are given. The four numbers at the top give the pion kinetic energy in MeV.

so that the nucleon isospin doublet with $B = 1$ and $I_3 = \pm\frac{1}{2}$ has $Q/|e| = 0$ or 1. The formula can be extended to include strange particles with quantum number S as follows:

$$\frac{Q}{|e|} = I_3 + \frac{B+S}{2} = I_3 + \frac{Y}{2} \tag{3.37}$$

where the quantity $Y = B + S$ is called the *hypercharge*. As examples, the kaons of $S = +1$ and $B = 0$ form a doublet with $Y = 1$, $I_3 = \pm\frac{1}{2}$ and $Q/|e| = 1$ and 0, for K^+ and K^0. Likewise the $S = -1$ isospin doublet consists of K^- and $\bar{K}^0$, while the isosinglet Λ hyperon, with $B = +1$, $S = -1$, $I_3 = 0$, has $Q/|e| = 0$.

Finally, to summarise this chapter, Table 3.4 gives a list of the conservation rules in the various fundamental interactions.

Table 3.4. *Conservation rules*

	Interaction		
Conserved quantity	strong	electromagnetic	weak
energy–momentum, charge, baryon number, lepton number	yes	yes	yes
CPT	yes	yes	yes
P (parity)	yes	yes	no
C (charge conjugation parity)	yes	yes	no
CP (or T)	yes	yes	10^{-3} violation
I (isospin)	yes	no	no

Problems

3.1 Show that the reaction $\pi^- + d \to n + n + \pi^0$ cannot occur for pions at rest.

3.2 What restrictions does the decay mode $K^0 \to 2\pi^0$ place on (a) the kaon spin, (b) the kaon parity?

3.3 Show that, for pions with zero relative orbital angular momentum, the combination $\pi^+\pi^-$ is an eigenstate of CP with eigenvalue $+1$, and $\pi^+\pi^-\pi^0$ is an eigenstate of CP with eigenvalue -1.

3.4 Show that a scalar meson cannot decay to three pseudoscalar mesons in a parity-conserving process.

3.5 (a) Find a relation between the total cross-sections (at a given energy) for the reactions

$$\pi^- p \to K^0\Sigma^0$$
$$\pi^- p \to K^+\Sigma^-$$
$$\pi^+ p \to K^+\Sigma^+$$

At a given centre-of-momentum energy, what is the ratio of cross-sections for the reactions $p + d \to {}^3\mathrm{He} + \pi^0$ and $p + d \to {}^3\mathrm{H} + \pi^+$?

3.6 Deduce through which isospin channels the following reactions may proceed: (a) $K^+ + p \to \Sigma^0 + \pi^0$, (b) $K^- + p \to \Sigma^+ + \pi^-$. Find the ratio of the cross-sections for (a) and (b), assuming that one or other isospin channel dominates.

3.7 As shown in Chapter 7, the neutral kaons decay from the states K_1^0 and K_2^0 with CP eigenvalues $+1$ and -1 respectively. If $p\bar{p}$ annihilation at rest takes place from an S-state only, show that $p\bar{p} \to K_1^0 + K_2^0$ occurs but that $p\bar{p} \to 2K_1^0$ and $p\bar{p} \to 2K_2^0$ do not.

3.8 In which isospin states can (a) $\pi^+\pi^-\pi^0$, (b) $\pi^0\pi^0\pi^0$ exist?

(*Hint*: First write the isospin functions for a pair of pions, and then combine each with a third pion. Refer to Appendix C for the Clebsch–Gordan coefficients required.)

3.9 The ω meson has isospin $I = 0$ and the ρ meson has $I = 1$. They have the same spin and parity (1^-). The ρ meson has central mass 775 MeV and width $\Gamma \simeq 120$ MeV, overlapping the ω state with mass 783 MeV and width $\Gamma \simeq 10$ MeV. Would you expect the ω and ρ states to interfere, and what qualitative effects would any interference have on the $\pi^+\pi^-$ and $\pi^+\pi^-\pi^0$ mass spectra in reactions where both ω and ρ can be produced?

3.10 State which of the following decays of the ρ meson ($J^P = 1^-$, $I = 1$) are allowed by the strong or electromagnetic interactions:-

$$\begin{aligned}\rho^0 &\to \pi^+\pi^- \\ &\to \pi^0\pi^0 \\ &\to \eta^0\pi^0 \\ &\to \pi^0\gamma\end{aligned}$$

where the η meson is an isosinglet.

3.11 The intrinsic parity of the hyperon Ξ^- with $S = -2$, can in principle be determined from observations on capture in hydrogen from an S-state:

$$\Xi^- + p \to \Lambda + \Lambda$$

The polarisation of the Λ hyperons produced can be found from the angular asymmetry of the products in the weak decay $\Lambda \to p + \pi^-$. State what is the polarisation (if any) of the Λ particles produced in the above reaction and how the relative polarisations are determined from the parity of the Ξ^-.

3.12 Capture of negative kaons in helium sometimes leads to the formation of a hypernucleus (one in which a neutron is replaced by a Λ hyperon) according to the reaction

$$K^- + {}^4\mathrm{He} \to {}^4\mathrm{H}_\Lambda + \pi^0$$

Study of the branching ratios of ${}^4\mathrm{H}_\Lambda$ and the isotropy of the decay products establish that this hypernucleus has spin zero. Show that this implies negative parity for the K^-, independently of the orbital angular momentum state from which the K^- is captured.

3.13 Both the neutral mesons $\rho^0(770)$, with $J = 1$, and $f^0(1275)$, with $J = 2$, decay to $\pi^+\pi^-$. What are their C and P parities? State which of the decays $\rho^0 \to \pi^0 + \gamma$ and $f^0 \to \pi^0 + \gamma$ is or are allowed, and estimate the branching ratio.

4

Quarks in hadrons

During the great accumulation of data on baryon and meson resonances in the 1960s, regularities or patterns were noted among these hadron states and interpreted in terms of an approximate symmetry, called unitary symmetry. This description was soon superseded by one in which the patterns or multiplets of states could be simply accounted for in terms of quark constituents, a baryon consisting of three quarks and a meson of a quark–antiquark pair. This evidence is especially compelling in the level systems of bound states formed from heavy quark–antiquark pairs, which we discuss first.

4.1 Charm and beauty; the heavy quarkonium states

4.1.1 Charmonium states, ψ

Very massive meson states were observed in the 1970s as sharp resonances in e^+e^- annihilation at high energy. Their fine structure in several energy levels bore a remarkable resemblance to the levels of positronium, a non-relativistic bound state of e^+ and e^- that decays to two or three γ-rays. It was a natural inference that, if positronium were a bound state of particle and antiparticle, these heavy mesons must be evidence of bound states of massive fundamental fermion–antifermion pairs.

Table 4.1 gives a list of the six flavours of quark that have been observed. The u, d, s quarks were introduced in Chapter 1. Here we want to concentrate on the c and b quarks, where the symbols stand for 'charm' and 'bottom' (or 'beauty').

The ψ series of resonances, observed in e^+e^- annihilation, correspond to quark–antiquark ($c\bar{c}$) bound states. They were first observed in 1974 in e^+e^- collisions at SLAC (Stanford), using the e^+e^- collider SPEAR (Augustin *et al.* 1974); and the lowest-lying state, called ψ or J/ψ, was simultaneously observed in experiments at the Brookhaven alternating gradient synchrotron (AGS) in collisions of 28 GeV

Table 4.1. *Quark quantum numbers*
$Q/e = I_3 + \frac{1}{2}(B + S + C + B^* + T)^a$

Flavour	I	I_3	S	C	B^*	T	Q/e
u	$\frac{1}{2}$	$\frac{1}{2}$	0	0	0	0	$+\frac{2}{3}$
d	$\frac{1}{2}$	$-\frac{1}{2}$	0	0	0	0	$-\frac{1}{3}$
s	0	0	-1	0	0	0	$-\frac{1}{3}$
c	0	0	0	1	0	0	$+\frac{2}{3}$
b	0	0	0	0	-1	0	$-\frac{1}{3}$
t	0	0	0	0	0	1	$+\frac{2}{3}$

[a] B denotes baryon number, which is $\frac{1}{3}$ for all quarks; B^* here denotes the bottom or beauty quantum number.

protons on a beryllium target (Aubert *et al.* 1974), leading to a massive e^+e^- pair:

$$\text{SLAC} \qquad e^+e^- \rightarrow \psi \rightarrow \text{hadrons} \quad \hookrightarrow e^+e^-, \mu^+\mu^- \tag{4.1}$$

$$\text{BNL} \qquad p + \text{Be} \rightarrow \psi/J + \text{anything} \quad \hookrightarrow e^+e^- \tag{4.2}$$

The original data on the reaction (4.1) are shown in Figure 4.1 and on (4.2) in Figure 4.2. In both cases, a sharp resonance ψ is observed, peaking at a mass of 3.1 GeV. In (4.2), massive electron pairs were detected by means of a magnet spectrometer and detectors downstream of the target, electrons and positrons being recorded in coincidence at large angles on either side of the incident proton beam axis. In the e^+e^- experiment, the reaction rate in the beam intersection region was measured as the beam energies were increased in small steps. In addition to the particle ψ a second resonance ψ' of mass 3.7 GeV was also found in this first SPEAR experiment (Abrams *et al.* 1974).

The observed widths of the peaks in Figures 4.1 and 4.2 are dominated by the experimental resolution, on the secondary-electron momentum in the Brookhaven experiment and on the circulating-beam momentum in the SLAC experiment. The true width of the ψ is much smaller and can be determined from the total reaction rate and the leptonic branching ratio, both of which have been measured. Recalling the Breit–Wigner formula (2.31) for the formation of a resonance of spin J from

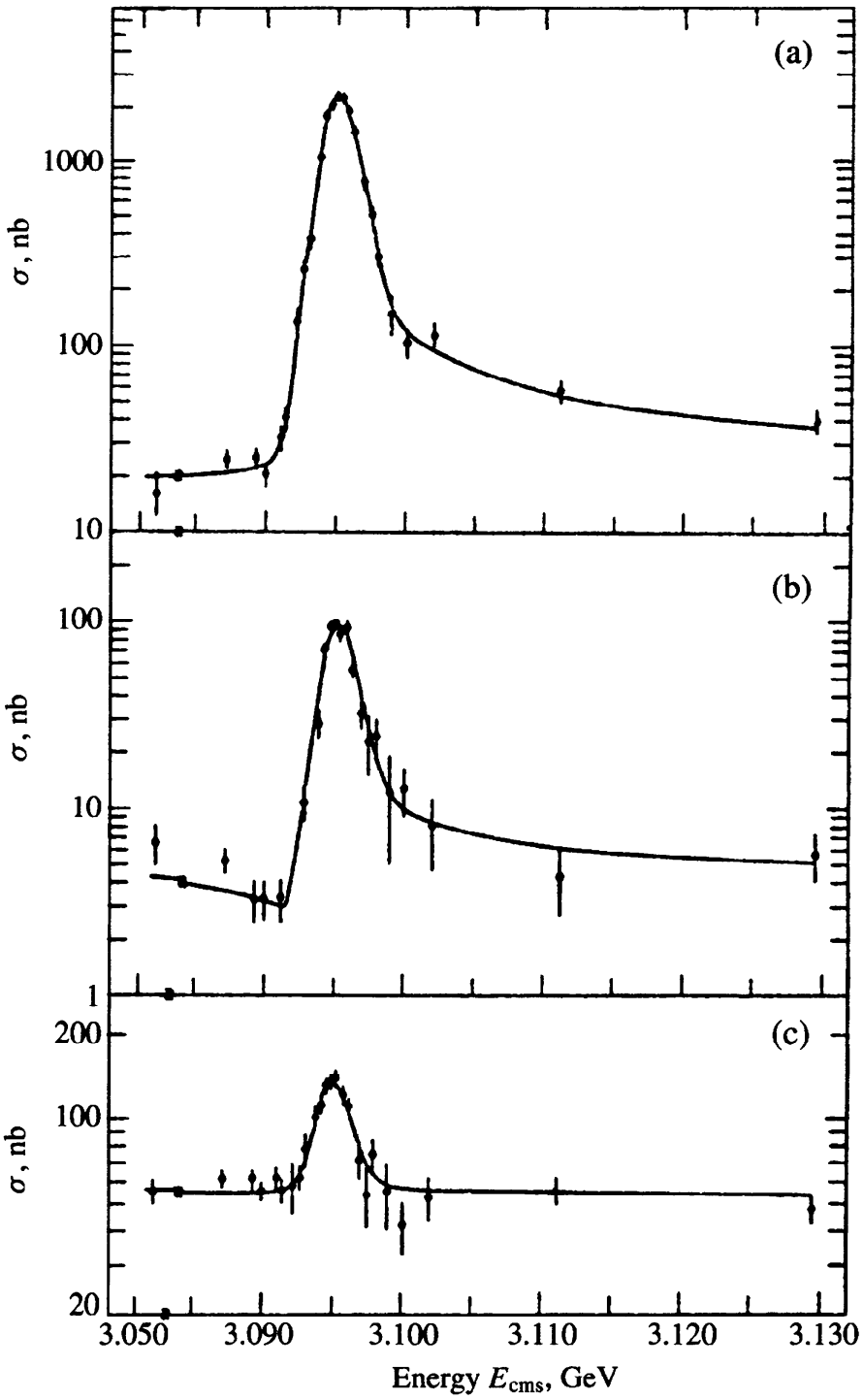

Fig. 4.1. Results of Augustin *et al.* (1974) showing the observation of the J/ψ resonance of mass 3.1 GeV, produced in e^+e^- annihilation at the SPEAR storage ring, SLAC. (a) $e^+e^- \to$ hadrons; (b) $e^+e^- \to \mu^+\mu^-$, $|\cos\theta| \leq 0.6$; (c) $e^+e^- \to e^+e^-$, $|\cos\theta| \leq 0.6$.

two particles of spin s_1 and s_2, we can write

$$\sigma(E)_{e^+e^- \to \psi \to e^+e^-} = \frac{4\pi\lambda\!\!\!^{-2}(2J+1)\Gamma^2_{e^+e^-}/4}{(2s_1+1)(2s_2+1)[(E-E_R)^2+\Gamma^2/4]} \tag{4.3}$$

where $\lambda\!\!\!^{-}$ is the de Broglie wavelength of the e^+ and e^- in the cms, E is the cms energy, E_R is the energy at the resonance peak, Γ is the total width of the resonance

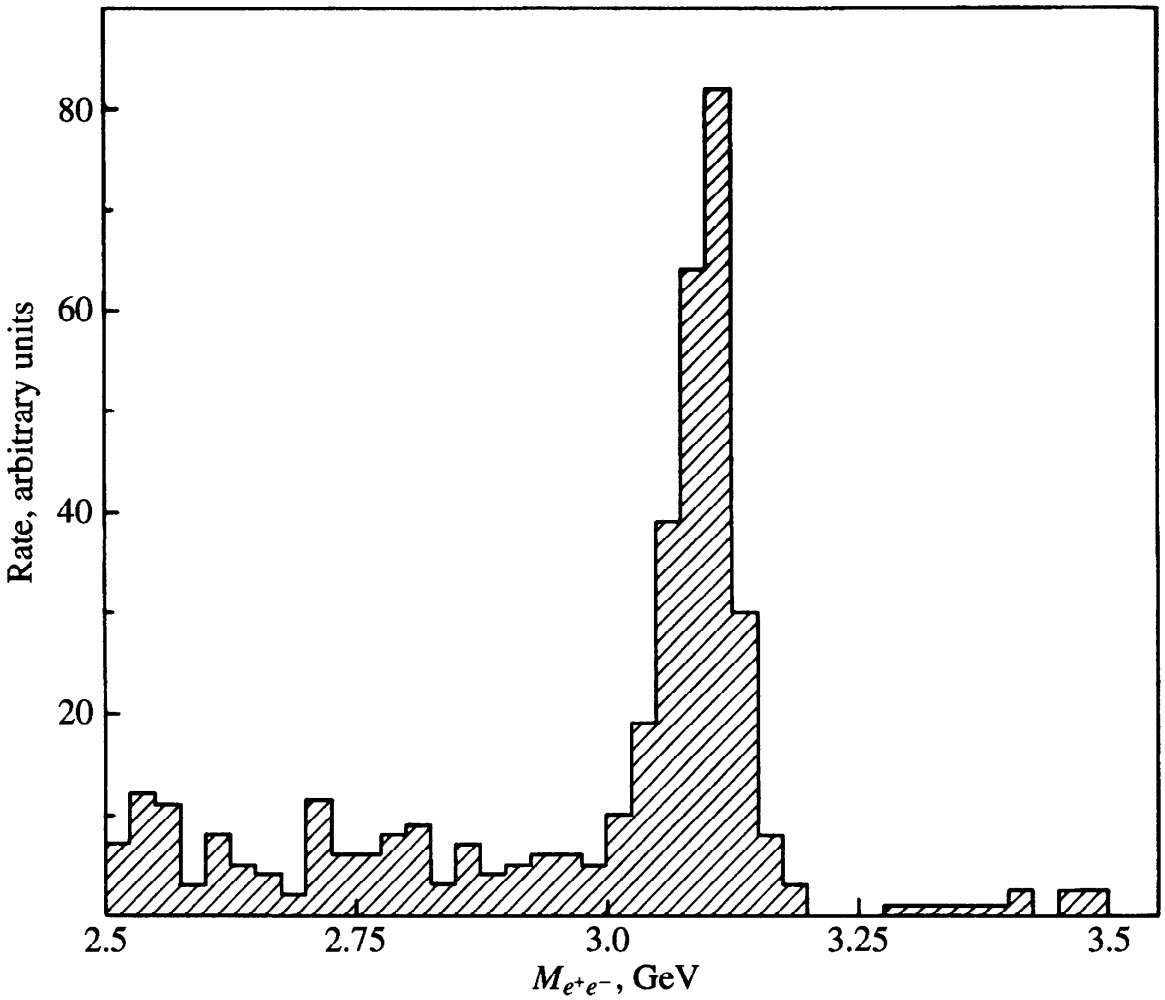

Fig. 4.2. Results of Aubert *et al.* (1974) indicating the narrow resonance J/ψ in the invariant-mass distribution of e^+e^- pairs produced in inclusive reactions of protons with a beryllium target, $p + \text{Be} \rightarrow e^+ + e^- + X$. The experiment was carried out with the 28 GeV AGS at Brookhaven National Laboratory.

and $\Gamma_{e^+e^-}$ is its partial width for $\psi \rightarrow e^+e^-$. With $s_1 = s_2 = \frac{1}{2}$ and the assumption $J = 1$, the total integrated cross-section is readily found from (4.3) using the substitution $\tan\theta = 2(E - E_R)/\Gamma$:

$$\int_0^\infty \sigma(E)dE = \frac{3\pi^2}{2}\lambda\!\!\!^{-2}\left(\frac{\Gamma_{e^+e^-}}{\Gamma}\right)^2\Gamma \tag{4.4}$$

The integrated cross-section in Figure 4.1 must be equal to $\int \sigma(E)dE$, and experimentally is 800 nb MeV. The branching ratio $\Gamma_{e^+e^-}/\Gamma = 0.06$, and $\lambda\!\!\!^{-} = \hbar c/pc$, where $pc = 1500$ MeV and $\hbar c = 197$ MeV fm. Inserting these numbers in (4.4), we obtain $\Gamma = 0.087$ MeV for the true width of the ψ, which is much smaller than the experimental width, of order several MeV. In comparison with other vector mesons formed from light (u, d or s) quarks such as the ρ(776 MeV) with $\Gamma = 150$ MeV or ω(784 MeV) with $\Gamma = 8.4$ MeV, the ψ(3100 MeV) has an

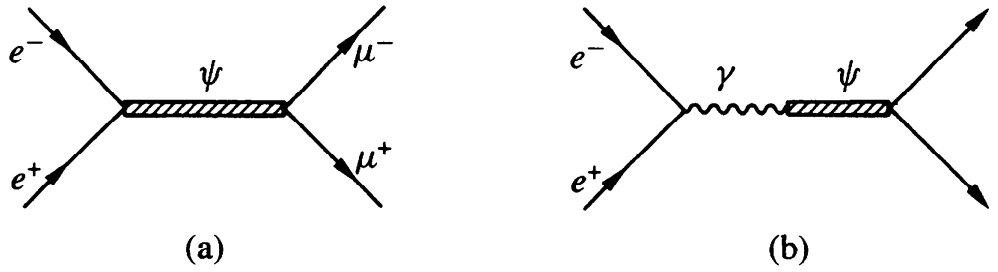

Fig. 4.3.

extremely small width, and the purely electromagnetic decay $\psi \rightarrow e^+e^-$ competes with decay into hadrons. Note that the partial width $\Gamma(\psi \rightarrow e^+e^-) = 5$ keV and is not so different from that of the other vector mesons. For example, $\Gamma(\omega \rightarrow e^+e^-) = 0.6$ keV and $\Gamma(\phi \rightarrow e^+e^-) = 1.4$ keV.

The assumption $J^P = 1^-$, i.e. the vector nature of the ψ particle, is justified by observing the shape of the resonance curve in Figure 4.1(b). This has the characteristic dispersion-like appearance characteristic of two interfering amplitudes; these are the amplitudes for the production of ψ via the direct channel (Figure 4.3(a)) and via an intermediate virtual photon (Figure 4.3(b)). The interference between these diagrams is proof that ψ must have the same quantum numbers as the photon. The isospin assignment $I = 0$ is based on the characteristics of hadronic decays, e.g. by observations on the decay mode $\psi \rightarrow \rho\pi$: the various charge states $\rho^+\pi^-$, $\rho^0\pi^0$, $\rho^-\pi^+$ are found to be equally populated. Reference to the Clebsch–Gordan coefficient (Appendix C) for combining the two states ρ and π, each with $I = 1$, then shows that $I = 0$ is the correct assignment for ψ.

In summary, some properties of the particles ψ and ψ' are listed in Table 4.2. An example of the decay $\psi' \rightarrow \psi + \pi^+\pi^-$, $\psi \rightarrow e^+e^-$ is shown in Figure 4.4. As indicated in a later section, these states are often referred to by the spectroscopic nomenclature $\psi(1S)$ and $\psi(2S)$.

The extreme narrowness of the ψ and ψ' states in comparison with those of other meson resonances indicated that there was no possibility of understanding them in terms of u, d and s (and $\bar{u}$, $\bar{d}$ and $\bar{s}$) quarks. A new type of quark had in fact been postulated some years before by Glashow, Iliopoulos and Maiani (1970), in connection with the non-existence of strangeness-changing neutral weak currents (see Section 7.11). This carried a new quantum number, C for *charm*, which, like strangeness, would be conserved in strong and electromagnetic interactions. The large masses of the ψ, ψ' mesons implied that, if they contain such charmed quarks, these in turn must be massive. It was therefore postulated that ψ, ψ' consisted of vector combinations of $c\bar{c}$, called *charmonium*.

Other combinations with a net charm number, e.g. $c\bar{d}$, form the so-called charmed mesons, identified by a generic code 'D'; these had been observed

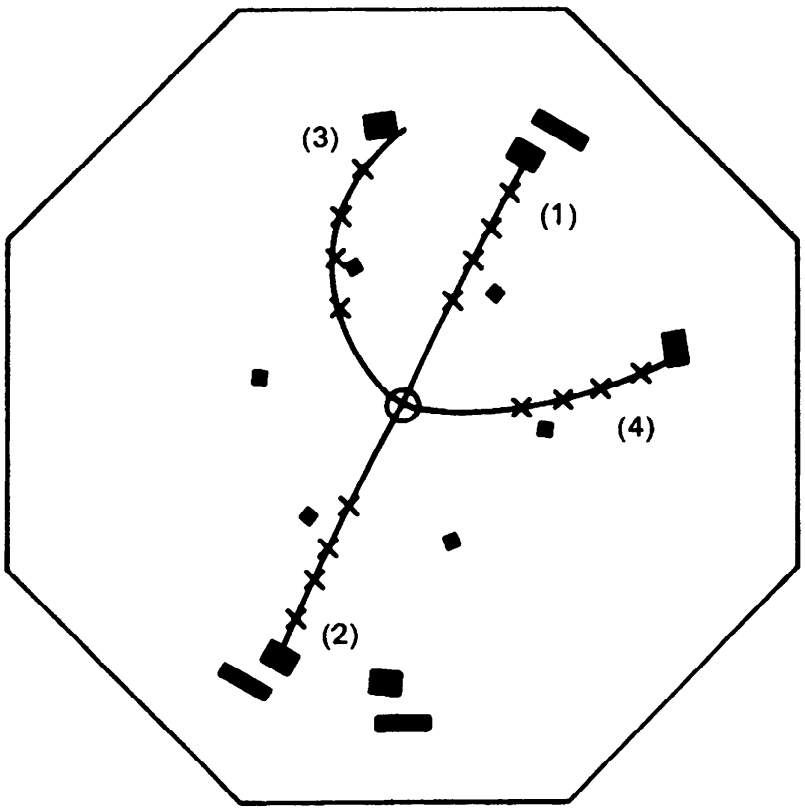

Fig. 4.4. Example of the decay $\psi(3.7) \rightarrow \psi(3.1) + \pi^+ + \pi^-$ observed in a spark chamber detector. The $\psi(3.1)$ decays to $e^+ + e^-$. Tracks (3) and (4) are due to the relatively low energy (150 MeV) pions, and (1) and (2) to the 1.5 GeV electrons. The magnetic field and the SPEAR beam pipe are normal to the plane of the figure. The trajectory shown for each particle is the best fit through the sparks, indicated by crosses. (From Abrams *et al.* 1975.)

previously in neutrino experiments (but not clearly identified) and were soon to be catalogued in SLAC experiments. The lowest-lying D meson has mass 1870 MeV and decays weakly in a $\Delta C = 1$ transition.

In addition to the $\psi(3100)$ and $\psi(3700)$ states at least four more vector meson states – presumably higher excitations $\psi(3S)$, $\psi(4S)$ and $\psi(5S)$ of the $c\bar{c}$ system – have been observed in e^+e^- annihilation. They have masses ranging from 3770 to 4415 MeV and are all broad states, with widths between 24 and 78 MeV. For all these states, the decay $\psi \rightarrow D\bar{D}$ is energetically possible, while for $\psi(3100)$ and $\psi(3700)$ it is not. Thus, the broadness of the higher-mass ψ states can be associated with decay to hadrons containing c and $\bar{c}$ quarks, while the two-orders-of-magnitude-smaller widths of $\psi(3100)$ and $\psi(3700)$ is a consequence of the fact that the $c\bar{c}$ combination can only decay to u, d or s quarks and antiquarks, involving a change in quark flavour. This is known as the OZI rule:† decay rates described by diagrams with unconnected quark lines are suppressed. Thus $\psi(3770) \rightarrow D\bar{D}$ is allowed by this rule, while $\psi(3100) \rightarrow \pi^+\pi^0\pi^-$ is suppressed.

† After its proposers Okubo, Zweig and Iizuka.

Table 4.2. *Charmonium states and decay modes*

State	Mass, MeV	J^P, I	Γ, MeV	Branching ratio	
J/ψ (3100)	3097.88 ± 0.04	$1^-, 0$	0.087	hadrons	88%
$= \psi(1S)$				e^+e^-	6%
				$\mu^+\mu^-$	6%
$\psi(3700)$	3686 ± 0.1	$1^-, 0$	0.28	$\psi + 2\pi$	50%
$= \psi(2S)$				$\chi + \gamma$	24%
				e^+e^-	0.9%
				$\mu^+\mu^-$	0.8%

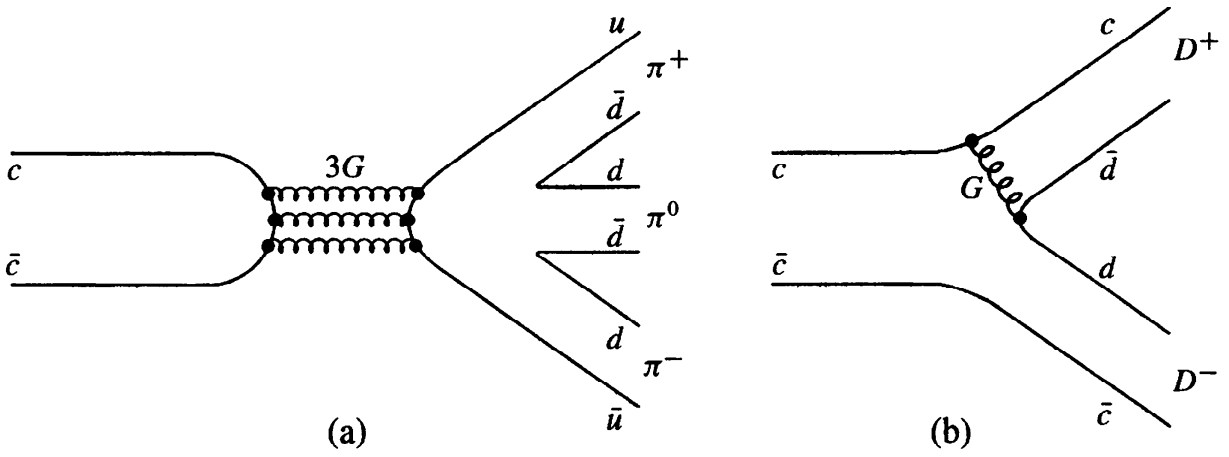

Fig. 4.5. Quark diagrams for charmonium decay. (a) $\Psi(3100) \rightarrow 3\pi$, $\Gamma = 0.076$ MeV; (b) $\Psi(3770) \rightarrow D\bar{D}$, $\Gamma = 24$ MeV. Diagram (b) is favoured but forbidden by energy conservation for charmonium states $\psi(3.1)$ and $\psi(3.7)$ with masses below threshold $2M_D = 3.75$ GeV. The 'OZI forbidden' diagram (a) is therefore the only one allowed for hadronic decay of these low-mass states.

In quantum chromodynamics (QCD) the explanation for this rule is given in terms of gluon exchange. In Figure 4.5(b) only a single-gluon exchange is necessary to connect the $c, \bar{d}$ quark lines. In Figure 4.5(a), however, no colour can be transmitted from the (colour-singlet) $\psi(3100)$ meson to the (colour-singlet) 3π state. Hence a colourless combination of at least two coloured gluons is necessary. However, the $\psi(3100)$ is a quark spin triplet state ($^3S_1$) and therefore, by the same argument (using C-parity) leading to the annihilation of $^3S_1$ positronium to three photons (see (4.8) below), the $\psi(3100)$ must decay through an odd number of gluons. Thus, triple 'hard' gluon exchange is the most likely process, and this is strongly suppressed relative to the single 'soft' gluon exchange of Figure 4.5(b).

Table 4.3. *Upsilon states* $\Upsilon(= b\bar{b})$

	$\Upsilon(1S)$	$\Upsilon(2S)$	$\Upsilon(3S)$	$\Upsilon(4S)$
Mass, MeV	9460.4 ± 0.2	10023.3 ± 0.3	10355.3 ± 0.5	10580.0 ± 3.5
$\Gamma_{e^+e^-}$, keV	1.32 ± 0.05	0.52 ± 0.03	—	0.25 ± 0.03
Γ_{tot}, MeV	0.053 ± 0.002	0.044 ± 0.007	0.026 ± 0.004	10 ± 4

4.1.2 Upsilon states Υ

The discovery of the narrow charmonium ($\psi = c\bar{c}$) states in 1974 was followed in 1977 by the observation of similar narrow resonances in the mass region 9.5–10.5 GeV, attributed to bound states of still heavier 'bottom' quarks with charge $-\frac{1}{3}$ and generically named $\Upsilon = b\bar{b}$ – see Table 4.3.

Figure 4.6 shows the results on the mass spectrum of muon pairs produced in the 400 GeV proton–nucleus collisions

$$p + \text{Be, Cu, Pt} \rightarrow \mu^+ + \mu^- + \text{ anything}$$

as observed in a two-arm spectrometer by Herb *et al.* (1977) and Innes *et al.* (1977) in an experiment at Fermilab. A broad peak centred around 10 GeV is apparent against the falling continuum background. Since the total width ($\simeq$ 1.2 GeV) was greater than that arising from the apparatus resolution (0.5 GeV), it was deduced that two or three resonances were present, with masses of 9.4, 10.0 and possibly 10.4 GeV – named Υ, Υ' and Υ'', respectively.

As in the case of charmonium, the states Υ, Υ' were later observed in e^+e^- experiments at the DORIS storage ring in Hamburg, where they could be clearly resolved, and at CESR, Cornell, where the narrow state Υ'' and a fourth state Υ''' were identified (see Figure 4.7). As for charmonium, the apparent widths of the three lightest Υ states are determined by the beam energy resolution. Their masses and leptonic widths are given in Table 4.3. Note that, as for charmonium, the $\Upsilon(1S)$, $\Upsilon(2S)$ and $\Upsilon(3S)$ states are narrow because of the OZI rule, while the $\Upsilon(4S)$ state and two higher levels are above the threshold (10558 MeV) for decay into a pair of $B\bar{B}$ mesons made up of $b\bar{u}$ and $b\bar{d}$ combinations and their antiparticles.

4.2 Comparison of quarkonium and positronium levels

Figure 4.8 shows, side by side, the level schemes of positronium, charmonium and the upsilon states of 'bottomonium'.

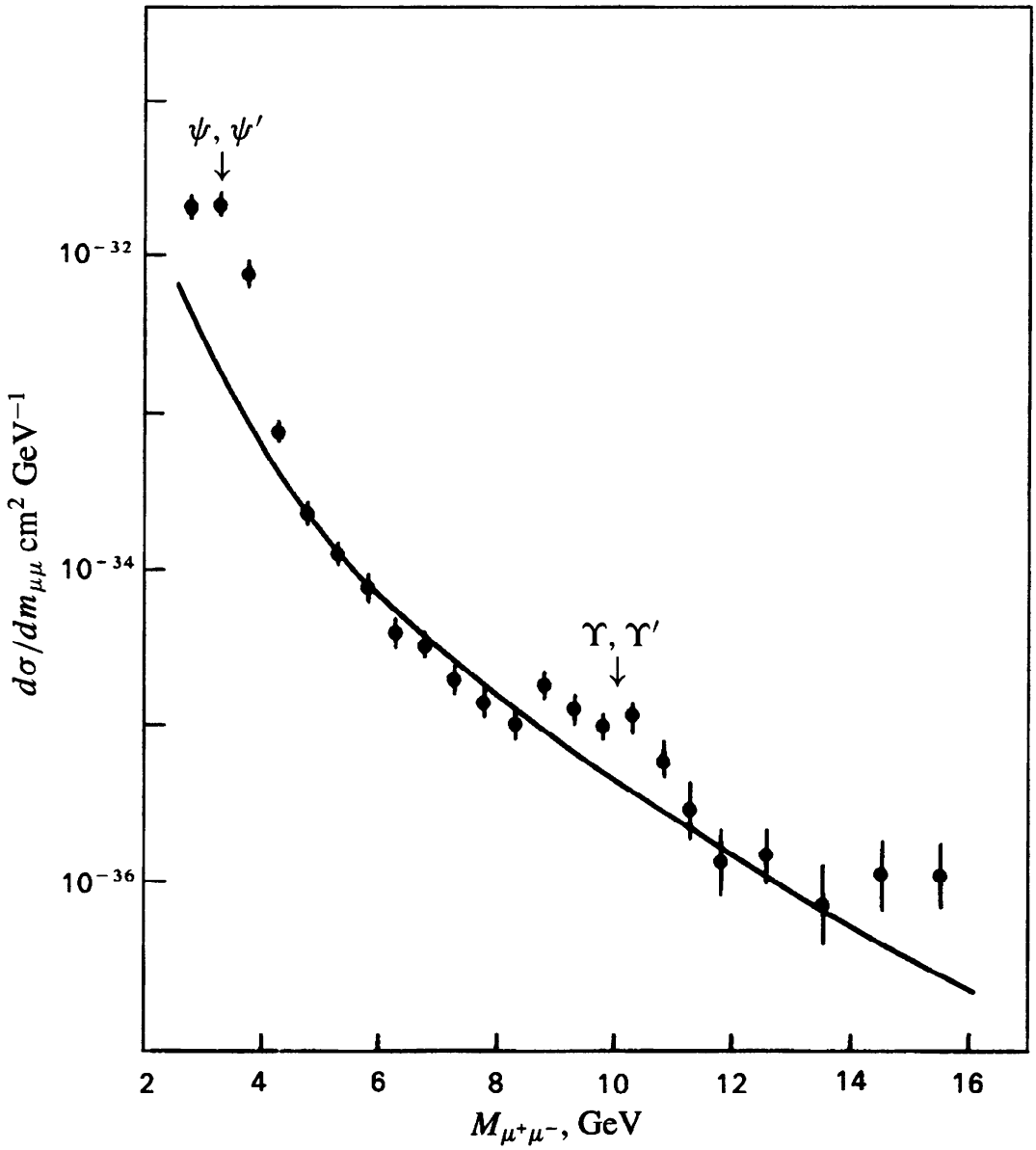

Fig. 4.6. First evidence for the upsilon resonances Υ, Υ', obtained by Herb *et al.* (1977) from the spectrum of muon pairs observed in 400 GeV proton–nucleus collisions at Fermilab, near Chicago. The enhancement due to these resonances stands out against the rapidly falling continuum background. The individual states Υ, Υ' are not resolved.

4.2.1 Positronium states

First let us recall some of the salient features of the positronium states. When a positron comes to rest in matter, it forms with an electron an 'atom' called positronium, which decays into γ-rays with two distinct lifetimes. The short one is associated with 2γ and the longer with 3γ decay. Bose symmetry of the two-photon system shows that it must result from decay of a state of even angular momentum, identified with the spin singlet state of the e^+e^- system, with $J = 0$, as in (3.11d), and with $C = +1$ since $C = (-1)^n$ for a system of n photons. The 3γ decay is ascribed to the triplet state $J = 1$ with $C = -1$.

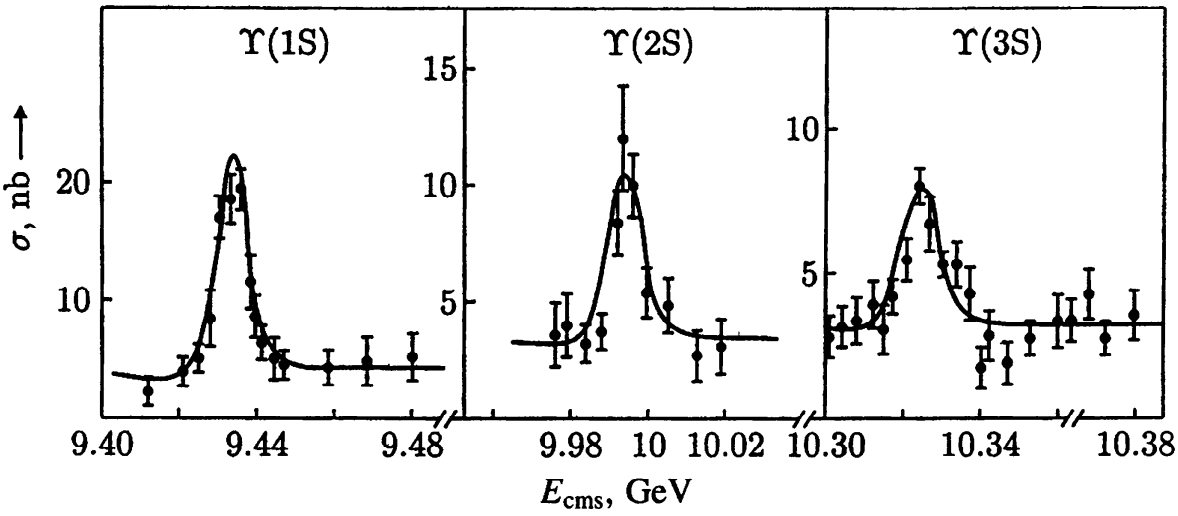

Fig. 4.7. The narrow Υ(1S), Υ(2S) and Υ(3S) resonances observed with the CLEO detector at the CESR storage ring. The data have not been corrected for radiative effects, which would bring up the masses to the values in Table 4.3 (from Andrews *et al.* 1980).

The principal level energies of positronium, assuming that it can be described using the non-relativistic Schrödinger equation in a Coulomb potential, can be found from those of the hydrogen atom,

$$E_n = -\frac{\alpha^2 \mu c^2}{2n^2}$$

where n is the principal quantum number and $\mu = mM/(M+m)$ is the reduced mass of the proton, mass M, and the electron, mass m. For positronium, it follows that $\mu = m/2$ and thus

$$E_n = -\frac{\alpha^2 mc^2}{4n^2} \tag{4.5}$$

Relativistically, the levels are split, first by the spin–orbit interaction into S, P, ... states of different orbital angular momentum l ($< n$), and secondly by the spin–spin (magnetic moment) interaction into triplet ($^3S_1$) and singlet ($^1S_0$) states. In atomic spectroscopy these splittings are called fine structure and hyperfine structure, respectively, but in positronium (where both constituents have magnetic moments equal to a Bohr magneton), both are of similar magnitude,

$$\Delta E \text{ (fine structure)} \sim \frac{\alpha^4 mc^2}{n^3}. \tag{4.6}$$

The triplet and singlet states are called ortho- and para-positronium respectively.

The lifetime of the singlet state can be easily estimated by dimensional analysis. Clearly, the decay rate contains a factor α^2 since two photons are coupled, and it is

also proportional to the square of the e^+e^- wavefunction at the origin, where the e^+ and e^- must coincide if they are to annihilate. This has the value

$$|\psi(0)|^2 = \frac{1}{\pi a^3}$$

where the Bohr radius in positronium (double that in hydrogen) is

$$a = \frac{2\hbar}{mc\alpha}$$

Since the radius has dimensions (energy)$^{-1}$ or (mass)$^{-1}$, a decay width Γ in energy units can be obtained by dividing the product $\alpha^2|\psi(0)|^2$ by m^2 (in units $\hbar = c = 1$). Thus, the dimensional argument gives $\Gamma \sim \alpha^5 m$: an actual calculation yields, to leading order in α,

$$\Gamma(2\gamma) = \frac{\alpha^5 m}{2} \tag{4.7}$$

The 3γ decay from the spin triplet state will obviously be slower by a factor of order α, and the calculated width is

$$\Gamma(3\gamma) = \frac{2(\pi^2 - 9)}{9\pi}\alpha^6 m \tag{4.8}$$

As shown in Table 4.4, both of the calculated lifetimes are in good agreement with experiment.

Figure 4.8 gives the calculated energy levels of the singlet and triplet S-states as well as those of the P-states, from an exact quantum-electrodynamic treatment. From (4.5) we expect the 2S $\rightarrow$ 1S level separations to be, to first order, $\Delta E \simeq 3\alpha^2 mc^2/16 = 5.1$ eV. In contrast, the triplet-singlet fine structure separation for $n = 1$ ($1^3S_1 \rightarrow 1^1S_0$) is calculated to be $\Delta E \simeq 7\alpha^4 mc^2/12 = 8.4 \times 10^{-4}$ eV only, and the energy difference, $\Delta E \simeq 23\alpha^4 mc^2/960 \simeq 3.5 \times 10^{-5}$ eV, of the ($2^3S_1 \rightarrow 2^3P_2$) transition is even smaller. The theoretical and observed frequencies of these two transitions – the only ones measured so far – are compared in Table 4.4. Again, the good agreement between experiment and calculation is a triumph for quantum electrodynamics.

It is customary to label the various levels according to the charge and space parities C and P. For a non-relativistic system e^+ and e^-, with total spin S and orbital angular momentum L, the symmetry under particle interchange is $(-1)^{S+1}$ for the spin function (see (3.11)) and $(-1)^{L+1}$ for the space wavefunction (3.5), after taking account of the opposite intrinsic parities of particle and antiparticle. So the overall symmetry under interchange of both space and spin acquires the factor $(-1)^{L+S}$; but this is equivalent to the C operation, interchanging the charges of the particles, $e^+ \leftrightarrow e^-$, and leaving all other coordinates alone. Hence the charge conjugation parity of the system is $C = (-1)^{L+S}$ while the space parity

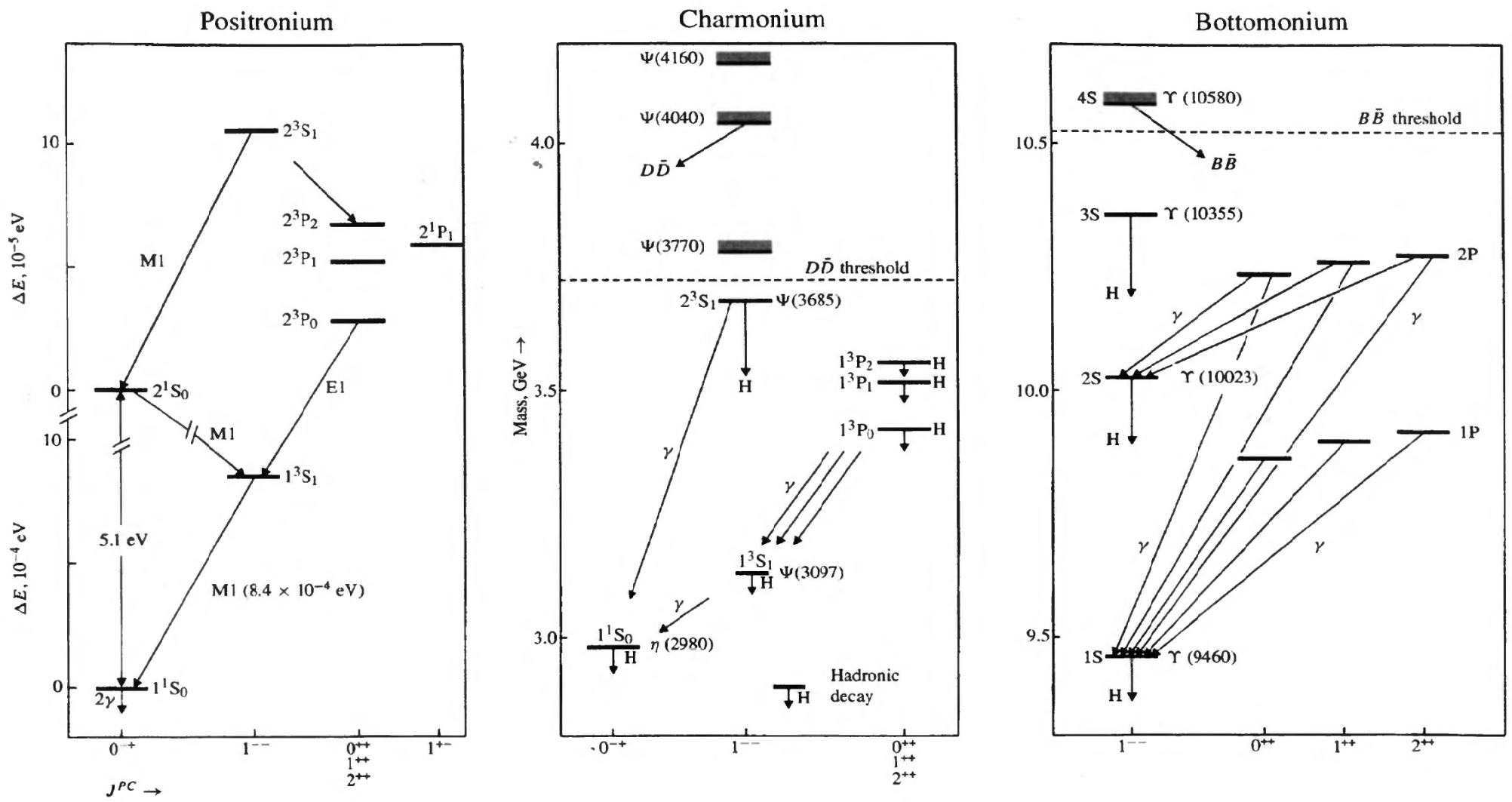

Fig. 4.8. The energy-level diagrams for positronium, charmonium and bottomonium. Note the changes in scale for positronium. Only states with $J^{PC} = 1^{--}$ can be accessed in e^+e^- annihilation experiments. Note that the atomic physics convention is to label the lowest-lying P states of positronium as 2P, while for the charmonium and bottomonium states the nuclear physics nomenclature 1P is employed. The shading indicates broad states.

Table 4.4. *Positronium lifetimes and level spacings*

	Theory	Experiment
$e^+e^- \to 2\gamma$ rate	$(7.985 \pm 0.002) \times 10^9\ s^{-1}$	$(7.99 \pm 0.11) \times 10^9\ s^{-1}$
$e^+e^- \to 3\gamma$ rate	$(7.0386 \pm 0.0004) \times 10^6\ s^{-1}$	$(7.05 \pm 0.01) \times 10^6\ s^{-1}$
$(\Delta E/h)(1^3S_1–1^1S_0)$	$203\,400 \pm 10$ MHz	$203\,386 \pm 2$ MHz
$(\Delta E/h)(2^3S_1–2^3P_2)$	8625 ± 10 MHz	8629 ± 6 MHz

is $P = (-1)^{L+1}$. The abscissae in Figure 4.8 are labelled with the values of J^{PC} for the various states, which are individually prefixed with the principal (radial) quantum number n; the letter S, P, ... indicates the value of orbital momentum L, the upper index gives the value of $2S + 1$, where S is the total spin, and the lower index gives the value of $J = L + S$.

4.2.2 Quarkonium levels

A brief inspection of the level schemes of charmonium ($c\bar{c}$) and bottomonium ($b\bar{b}$) in Figure 4.8 shows striking similarities with positronium and is compelling evidence for the view that, like positronium, the ψ and Υ series can be ascribed to the quantum states of a bound fermion–antifermion (i.e. quark–antiquark) pair. Let us now discuss this more quantitatively.

For positronium, we know the potential has the Coulomb form

$$V_{\text{em}} = -\frac{\alpha}{r}$$

where r is the separation of e^+ and e^-. The exact form of the potential in the heavy $Q\bar{Q}$ systems is, however, unknown. In the field theory of quark–quark interactions, quantum chromodynamics (QCD), the strong colour field is mediated by massless vector gluons, just as in QED it is mediated by massless vector photons. Hence the potential might be expected to be of Coulomb form, and this has been verified experimentally from the two-jet cross-section at hadron colliders (see Section 6.2). At large r, the quarks are subject to confining forces, and from the linearity of the plot of J versus squared mass for baryons and mesons it is deduced that the potential at large r is linear (see Section 6.3). Thus a favoured QCD potential as in (2.8) is

$$V_{\text{QCD}} = -\frac{4}{3}\frac{\alpha_s}{r} + kr \tag{4.9}$$

where α_s is the quark–gluon coupling, analogous to α in the case of positronium, and $\frac{4}{3}$ is a colour factor. The relationship is plotted in Figure 4.9, for $\alpha_s = 0.2$ and $k = 1$ GeV fm^{-1}.

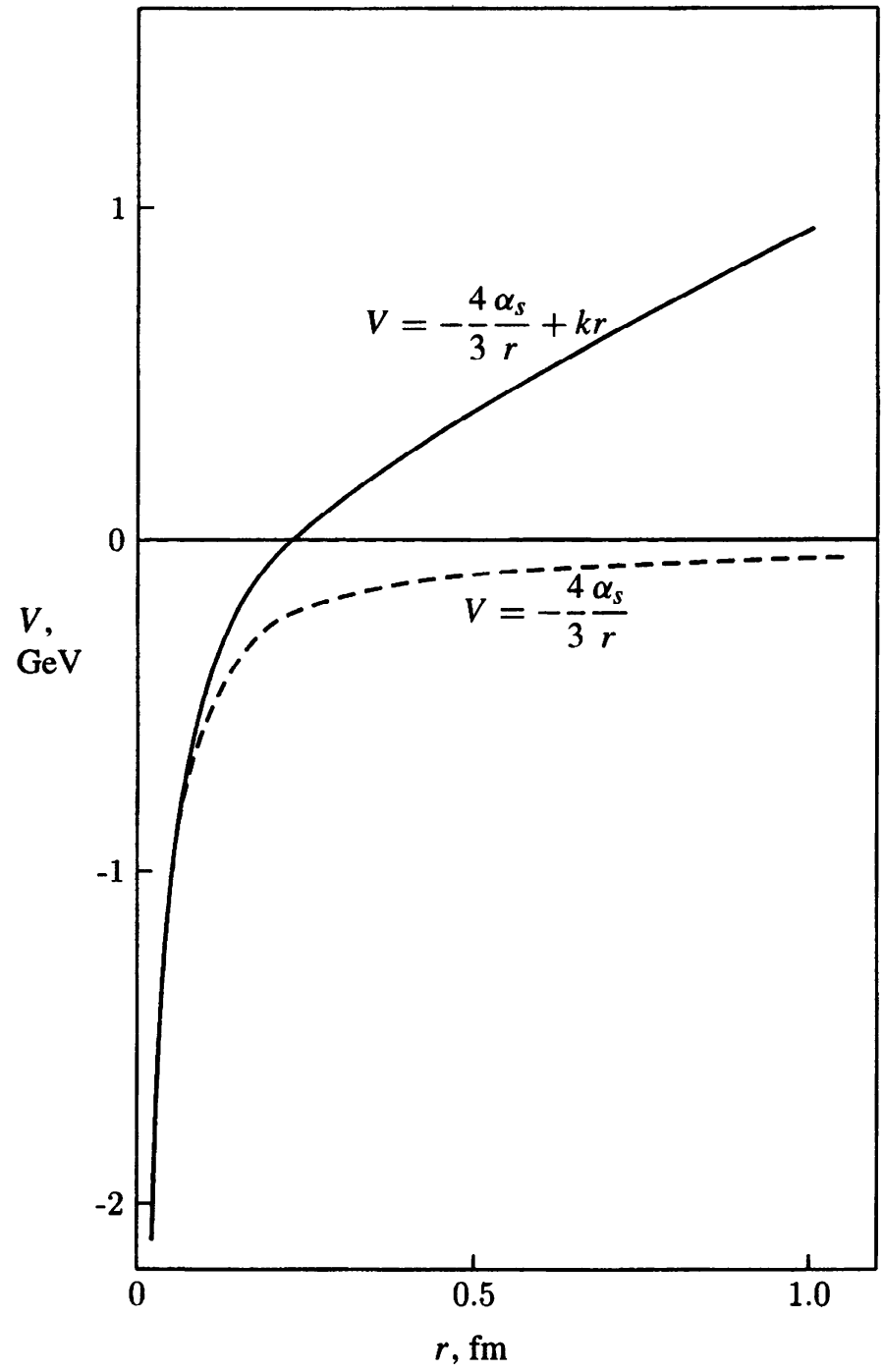

Fig. 4.9. Plot of the QCD potential (4.9), for quark–gluon coupling $\alpha_s = 0.20$ and $k = 1$ GeV fm^{-1}.

In the case of positronium, the principal energy levels are given, as in the case of the H atom, by solving the non-relativistic Schrödinger equation. This is justified because the momentum of each of the particles for a state of principal quantum number n is p where

$$\frac{p}{mc} = \frac{\alpha}{2n} \tag{4.10}$$

as is easily demonstrated from the formula for the Bohr radius 'a' and the condition

on the quantisation of angular momentum, $pa = n\hbar$. Thus $p \ll mc$ and relativistic effects enter only in the fine structure.

For quarkonium at small r, where the Coulomb-like term in (4.9) dominates, it is expected, from studies of deep inelastic lepton scattering (discussed in Chapter 6), that $\alpha_s \simeq 0.2$; thus, replacing α by $\frac{4}{3}\alpha_s$ gives $p/(mc) \simeq 0.13$ for $n = 1$, so that the non-relativistic approximation for heavy quark systems can also be justified. This may not be so obviously the case for light $Q\bar{Q}$ systems, discussed later, where the value of α_s could even be of order unity.

Regardless of the masses involved, (4.5) and (4.6) indicate that the *relative* magnitude of the fine structure will be of order α_s^2 and thus much coarser for quarkonium – as is observed. The existence of the second term in the potential (4.9) has two effects. First, the 2S and 2P states are no longer practically degenerate as in positronium, but the P states of given n are shifted in energy, particularly in bottomonium. Second, while the Coulomb-like term in (4.9) gives a 2S $\rightarrow$ 1S separation proportional to particle mass m, as in (4.5), the second term kr gives a separation proportional to $m^{-1/3}$. Because of the interplay of these two terms the 2S–1S separation in the $c\bar{c}$ system, 589 MeV, turns out to be almost the same as its value, 565 MeV, in the $b\bar{b}$ system, despite the factor 3 difference in particle mass. Another effect of the linear term kr is to make the number of narrow $Q\bar{Q}$ states, below the threshold for decay to $Q\bar{u}$, $\bar{Q}u$ mesons, an increasing function of mass. For the $t\bar{t}$ system (with $m \sim 175$ GeV) the number of narrow bound states could be of order 10 or more, except that, see Section 4.13, it is too short-lived to form them.

By optimising the values of the coefficients in (4.9), numerical calculations are able to account quite well for the observed charmonium and bottomonium levels. Best-fit values of $\alpha_s \simeq 0.20$ are obtained. Qualitatively, we can get rough values for α_s from the hadronic widths of the $^3S_1$ states, treating the decay $\psi \rightarrow$ hadrons as proceeding through a triple gluon decay $\psi \rightarrow 3G \rightarrow$ hadrons, as in Figure 4.5(a) and in exact analogy with the width for ortho-positronium decay to three photons in (4.8). Using the widths and hadronic branching ratios in Table 4.2 and replacing α in (4.8) by $\frac{4}{3}\alpha_s$, a charmed quark mass $m = 1.6$ GeV yields $\alpha_s \simeq 0.23$ (see Problems 4.5 and 4.6). The same exercise for the triplet $b\bar{b}$ states (Table 4.3) gives $\alpha_s \simeq 0.18$. These values ($\alpha_s \simeq 0.2$) are in fair agreement with those deduced from deep inelastic lepton scattering and high energy e^+e^- annihilation to hadrons, described in Chapter 6.

4.3 The baryon decuplet

The quark model had its origins in the 1960s, when it was found that regularities among the baryon and meson states could be neatly accounted for if it was assumed that they were built from u, d, s quark constituents. Quarks are not observed as

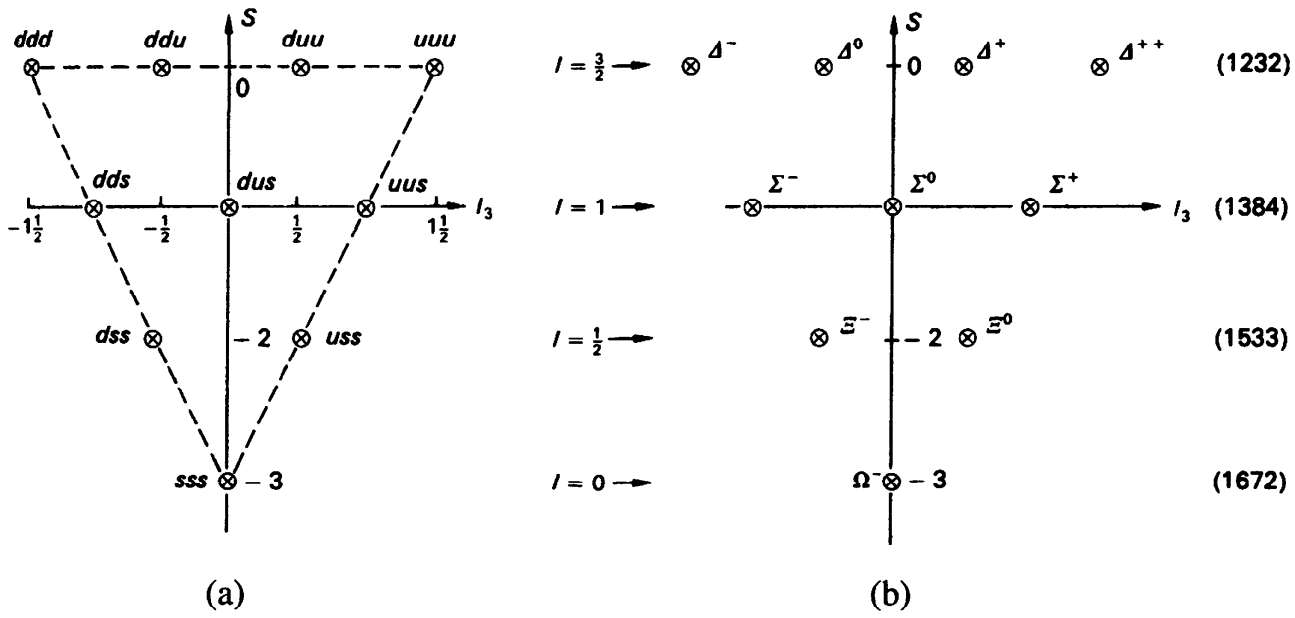

Fig. 4.10. (a) Quark label assignments in the baryon decuplet. (b) The observed decuplet of baryon states of spin-parity $\frac{3}{2}^+$. The mean mass of each isospin multiplet is given in parentheses.

free particles and hence must be confined in hadrons by the interquark potential. Although the quark model was first formulated in 1964, it was to take 10 years before it would be accepted as an actual dynamical model of hadron structure. The reasons are worth spelling out.

As soon as quarks were proposed by Gell-Mann and by Zweig, the experimentalists began exhaustive searches for these objects, at accelerators and in cosmic rays, and even as deposits in substances ranging from oyster shells to moon rocks. Despite the unique properties of the quarks, of fractional charge and of forming peculiar chemical combinations with atoms, all searches were to no avail. Free quarks simply did not seem to exist. The initial conclusion was that quarks must be *extremely massive* – many times the proton mass – and very tightly bound, so that it would be very hard to kick them out of the nucleon. The impasse was resolved, in the late 1960s and early 1970s, with the discovery that, in deep inelastic lepton scattering by nucleons, the nucleon appeared to be built from *light, quasi-free* pointlike constituents, called *partons* – the complete antithesis of the assumed massive, strongly bound quarks. The revelation turned out to be that the partons were indeed the quarks (see Chapters 5 and 6), but that they were confined inside the nucleon by a special confining potential, which increased as one attempted to separate them, as in (4.9).

Within the quark confinement potential, the quarks were considered as being quasi-free particles of effective mass m^* (of order one third of the baryon mass) with a momentum of order R_0^{-1}, where R_0 is the typical hadron size (about 1 fm).

The early calculations assumed the quarks to be in non-relativistic motion, i.e. that $m^* \gg R_0^{-1}$. As stated in the previous section, this may be a somewhat marginal assumption for the light quarks (u, d, s) but seems to work. The best tests of the non-relativistic quark model in fact apply to hadrons containing the heavier quarks (c, b), as described above.

Figure 4.10 indicates the 10 baryon states of lowest mass and of spin-parity $J^P = \frac{3}{2}^+$, where we plot the strangeness S against the third component of isospin, I_3, for each of the 10 members.† Working downward, these consist of an $S = 0, I = \frac{3}{2}$ isospin quadruplet, the $\Delta(1232)$, existing in the charge substates Δ^{++}, Δ^+, Δ^0, Δ^-. The number 1232 in parentheses indicates the central resonance mass in MeV. Next come an $I = 1$ isospin triplet with $S = -1$, the $\Sigma(1384)$; an $S = -2, I = \frac{1}{2}$ isospin doublet, the $\Xi(1533)$; and finally an $I = 0$ singlet of $S = -3$, the $\Omega^-(1672)$. The members of each isospin multiplet have essentially the same central mass, differing only by a few MeV, which is characteristic of electromagnetic mass splittings in isospin multiplets. The states of different strangeness differ considerably in mass, but the mass difference for each increment of strangeness is roughly the same. This surely could not be an accident; indeed, the Ω^- baryon was predicted on this basis three years before it was observed (see Figure 4.11).

The regularities such as that in the decuplet could be accounted for by postulating three types of fermion constituent in a baryon, called *quarks*, with the quantum numbers shown in Table 4.5. The quarks involved here consisted of an $S = 0$ isospin doublet, labelled u and d (standing for $I_3 = +\frac{1}{2}$ (up) and $I_3 = -\frac{1}{2}$ (down)), and a $S = -1$ isosinglet, labelled s (strange). The assignments u, d, s were called the *flavour* of the quark.

Baryons were postulated to consist of three quarks and the most reasonable assignment of baryon number was to allot $B = \frac{1}{3}$ to each. The relation between baryon number, strangeness and charge, (3.37), was worked out by Gell-Mann and Nishijima in 1955, to accommodate two isospin $I = \frac{1}{2}$ kaon doublets, one with strangeness $S = +1$ (K^0, K^+) and another with $S = -1$ $(K^-, \bar{K}^0)$:

$$Q/e = \tfrac{1}{2}(B + S) + I_3 \tag{4.11}$$

It follows that the $B = \frac{1}{3}$ assignment leads to fractional charge $Q/e = +\frac{2}{3}$ for the u quark $(I_3 = +\frac{1}{2})$, $Q/e = -\frac{1}{3}$ for the d quark $(I_3 = -\frac{1}{2})$ and $Q/e = -\frac{1}{3}$ for the $I = 0$ s quark, with strangeness $S = -1$. The appropriate combinations of quarks, indicated in Figure 4.10, could then account for the quantum numbers I, I_3, S of

† Note that convention dictates that the same symbol, S, is used for strangeness and for total spin – beware!

the members of the decuplet, and of course their electric charges. The progressive increase in mass of the decuplet members with decreasing S was simply ascribed to a difference in mass of the s quark, as compared with the u and d quarks, $m_s - m_{u,d}$, in the region of 150 MeV. The masses of the u and d quarks were expected to be nearly equal, since any difference must be of the order of the electromagnetic mass differences among the members of an isospin multiplet, typically 3–5 MeV.

Given that a baryon is to consist of three quarks chosen from any three flavours, 27 combinations are possible; so what is special about only 10 of them? We have to introduce some symmetry principle peculiar to members of a particular multiplet. Such symmetry will concern quark spin as well as quark flavour. First, with regard to flavour, we can require that the flavour part of the baryon wavefunction should have a definite symmetry under interchange of any pair of quarks. The corner states uuu, ddd and sss of Figure 4.10 are clearly symmetric under interchange, so it is natural to require the same symmetry for the other states. We have indicated these as ddu, duu, uss etc., as shorthand for the properly symmetrised expressions. For example, the full form of the ddu state is

$$\tfrac{1}{\sqrt{3}}\,(ddu + udd + dud) \tag{4.12}$$

which is symmetric under interchange of any two quarks; the numerical factor is for normalisation. Similarly, dus is shorthand for

$$\tfrac{1}{\sqrt{6}}\,(dsu + uds + sud + sdu + dus + usd) \tag{4.13}$$

and so on. The different states in the multiplet can be obtained from each other, horizontally, by applying the isospin shift operators $I_\pm$ successively (cf. Appendix C). Thus,

$$I_-(uuu) = [I_-(u)](uu) + (u)[I_-(u)](u) + (uu)[I_-(u)] = duu + udu + uud.$$

Similarly, successive rows are constructed by replacing u quarks with s quarks.

These 10 states are the *only* completely symmetric combinations we can make. Of the remaining 17 of the total of 27, one is completely antisymmetric; the wavefunction

$$dsu + uds + sud - usd - sdu - dus \tag{4.14}$$

describes this state, changing sign under interchange of any two quarks, for example $1 \leftrightarrow 2$ or $2 \leftrightarrow 3$. It is easily constructed by adding an s quark to an antisymmetric u, d combination, i.e. $(ud - du)s$, plus cyclic permutations thereof. This leaves 16 states, which turn out to consist of two octets of mixed symmetry.

Table 4.5. *Quark quantum numbers (as of 1964)*[a]

Flavour	B	J	I	I_3	S	Q/e
u	$\frac{1}{3}$	$\frac{1}{2}$	$\frac{1}{2}$	$+\frac{1}{2}$	0	$+\frac{2}{3}$
d	$\frac{1}{3}$	$\frac{1}{2}$	$\frac{1}{2}$	$-\frac{1}{2}$	0	$-\frac{1}{3}$
s	$\frac{1}{3}$	$\frac{1}{2}$	0	0	-1	$-\frac{1}{3}$

[a] Antiquarks $\bar{u}$, $\bar{d}$ and $\bar{s}$ have the signs of B, I_3, S and Q/e reversed.

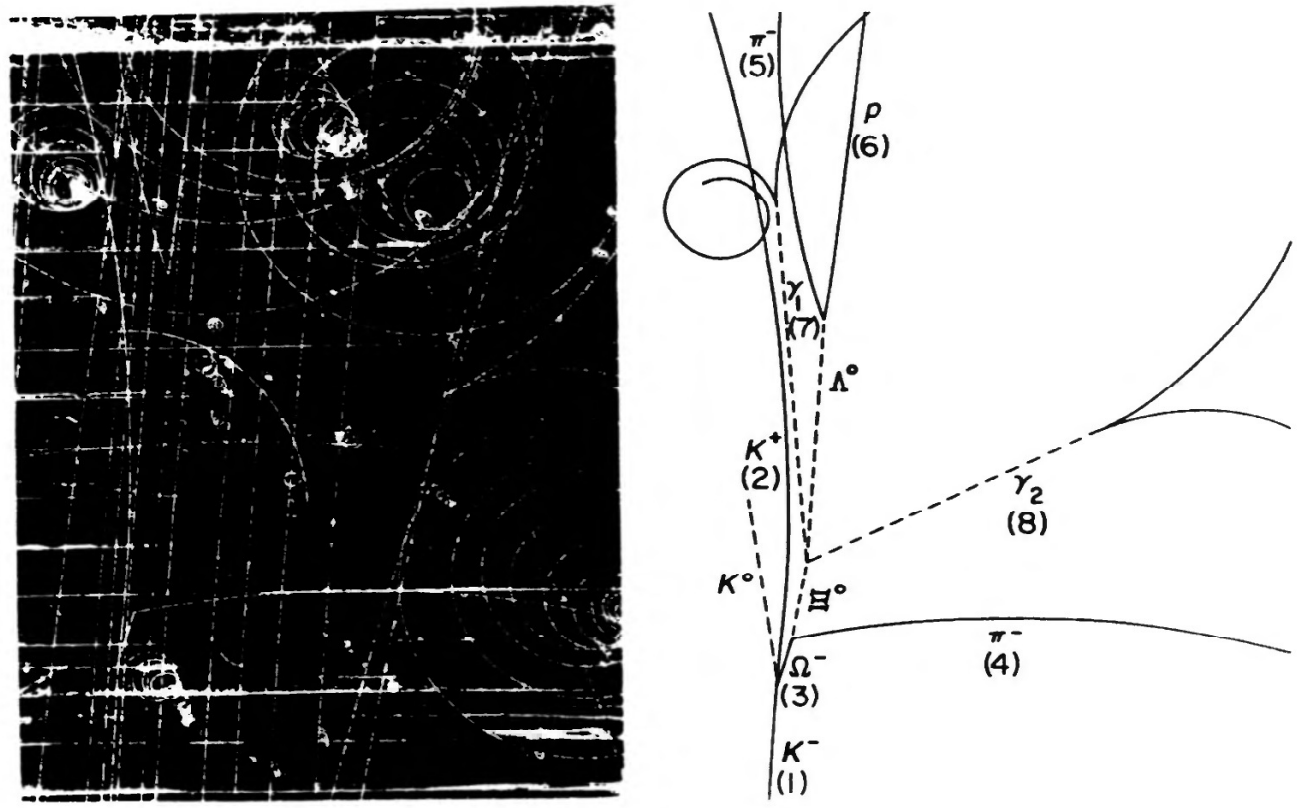

Fig. 4.11. The first Ω^- event (Barnes *et al.* 1964), courtesy Brookhaven National Laboratory). It depicts the following chain of events:

$$K^- + p \to \Omega^- + K^+ + K^0$$
$$\hookrightarrow \Xi^0 + \pi^- \ (\Delta S = 1 \text{ weak decay})$$
$$\hookrightarrow \pi^0 + \Lambda \ (\Delta S = 1 \text{ weak decay})$$
$$\hookrightarrow \pi^- + p \ (\Delta S = 1 \text{ weak decay})$$
$$\hookrightarrow \gamma + \gamma \text{ (electromagnetic decay)}$$
$$\downarrow \quad \downarrow$$
$$e^+e^- \quad e^+e^-$$

Historically, in the 1960s, the patterns of meson and baryon multiplets were first interpreted in terms of group theory, as representations of a unitary symmetry group SU(3). The '3' here stands for the fact that the fundamental representation of the group was a triplet (the u, d, s quarks, which were the only ones known at that time). Transformations between members of multiplets then occur in a three-dimensional complex space (in complete analogy to the group SU(2) of spin or isospin with group transformations in a two-dimensional complex space; see Section 3.13). Thus, combining any two of the basic quark states Q_1, Q_2 or Q_3, each a fundamental '3' representation of SU(3), would give us a sextet and a triplet:

$$3 \otimes 3 = 6 \oplus 3$$

Thus Q_3Q_3 and $(Q_1Q_2 + Q_2Q_1)$ are members of the '6', symmetric under label interchange, while $(Q_2Q_3 - Q_3Q_2)$ is antisymmetric and a member of the '3'. Bringing in a third quark gives us, as described above, decuplets, octets and singlets of baryon (QQQ) states:

$$3 \otimes 3 \otimes 3 = 27 = 1 \oplus 8 \oplus 8 \oplus 10$$

where the singlet state (4.14) is antisymmetric under interchange of any two quark labels, the '10' is symmetric as in (4.13), while the two octets have mixed symmetry. This flavour symmetry is approximate, as the decuplet members do not have equal masses.

4.4 Quark spin and colour

Since the members of the decuplet consist of the spin $\frac{3}{2}$ baryons of lowest mass, we assume that the quarks sit in the spatially symmetric ground state ($l = 0$). The value $J = \frac{3}{2}$ is then obtained by having the quarks in a symmetric spin state, with spins 'parallel', as in $\Delta^{++} = u\uparrow u\uparrow u\uparrow$, for example. Hence the $\frac{3}{2}^+$ decuplet is characterised by *symmetry of the three-quark wavefunction in both flavour and spin, as well as space.* This clearly violates the Pauli principle, that two or more identical fermions may not exist in the same quantum state. Subsequently, it turned out that another degree of freedom, called *colour*, was necessary. It is postulated that quarks exist in three colours – say red, green, blue – and that baryons and mesons built from quarks have zero net colour, i.e. they are *colour singlets.* (The hadrons must be colourless, otherwise colour would be a necessary and measurable property of hadrons.) So Δ^{++} consists of one red, one green and one blue u quark, which makes them in this respect non-identical. The three colours specify the 'strong charges' of the quarks, in just the same way that the signs + and − specify their electric charges. The interquark force is independent of the colours involved, so there is an SU(3) symmetry of colour which is exact.

The evidence for the colour quantum number comes from a number of sources. Most dramatic is the measured cross-section ratio at high energy

$$\frac{\sigma(e^+e^- \to \text{hadrons})}{\sigma(e^+e^- \to \mu^+\mu^-)}$$

described in Chapter 5. The observed ratio requires that expected for fractionally charged quarks to be multiplied by a factor $N_c = 3$. As described in Section 5.6, a first stage of the process is $e^+e^- \to Q\bar{Q}$, followed by $Q\bar{Q} \to$ hadrons, on a much longer timescale. Thus in principle the quark colours involved are distinguishable and the amplitudes for the different colours add incoherently, giving a factor $N_c = 3$ in the rate.

Another example of the effect of colour is in the neutral pion decay $\pi^0 \to 2\gamma$. It turns out that the dominant graph is the triangle diagram shown in Figure 4.12, with u quarks (or it could be d quarks, or antiquarks) running around the sides of the triangle (a pion, as we shall see below, consists of a $Q\bar{Q}$ pair). In this case the colours involved are not distinguishable, the three amplitudes must be added coherently and the rate acquires a factor $N_c^2 = 9$. A calculation gives

$$\Gamma(\pi^0 \to 2\gamma) = \left(\frac{N_c}{3}\right)^2 \frac{\alpha^2 m_\pi^3}{64\pi^3 f_\pi^2} = 7.73\left(\frac{N_c}{3}\right)^2 \text{ eV}$$

where the pion decay constant $f_\pi = 92.4$ MeV is known from the charged pion decay rate. The observed width

$$\Gamma(\text{obs}) = 7.7 \pm 0.6 \text{ eV}$$

thus gives

$$N_c = 2.99 \pm 0.12$$

As mentioned in subsection 1.2.1, a triangle diagram as in Figure 4.12 is a source of so-called *anomalies*, which spoil the renormalisability of the Standard Model. The condition that such anomalies should disappear is that the sums of the electrical charges of the quarks and leptons should be zero. This is the case, since the charged leptons give a charge of -3, the neutrinos give zero, the charge $+\frac{2}{3}$ quarks give $+6$ and the charge $-\frac{1}{3}$ quarks give -3, but one only gets this result if the quarks come in three colours.

4.5 The baryon octet

We noted that the baryon decuplet members have wavefunctions that are symmetric in both spin and flavour as well as in space. It is plausible that we can also form three-quark states that are symmetric under *simultaneous* interchange of flavour

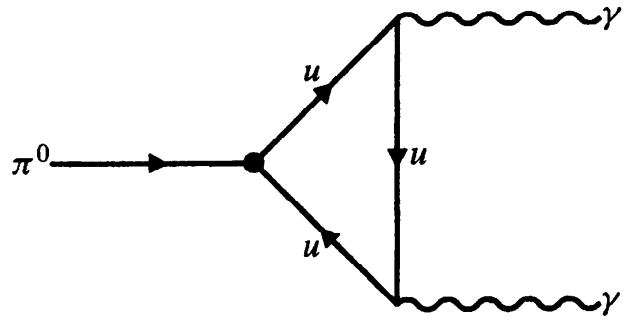

Fig. 4.12. The dominant Feynman diagram describing $\pi^0 \to 2\gamma$ decay.

and spin of any quark pair, although not, as in the decuplet, under each separately. These states are identified with the members of the lowest-lying baryon states of $J^P = \frac{1}{2}^+$, the baryon octet that includes the proton and neutron as members.

To construct the baryon octet wavefunctions we first start with a proton (uud) and put two quarks in the spin singlet state (see (3.11d)).

$$\tfrac{1}{\sqrt{2}}(\uparrow\downarrow - \downarrow\uparrow)$$

which is antisymmetric. To make the overall state symmetric, we need a flavour-antisymmetric combination of u and d (since u and u cannot achieve this), which is the isosinglet

$$\tfrac{1}{\sqrt{2}}(ud - du)$$

We then add the third quark u, with spin up, to obtain

$$(u\uparrow d\downarrow - u\downarrow d\uparrow - d\uparrow u\downarrow + d\downarrow u\uparrow)u\uparrow$$

Although the expression in parentheses is symmetric under interchange of the first and second quarks (flavour and spin), the whole expression has to be symmetrised by making a cyclic permutation, involving 12 terms in all, giving finally

$$\begin{aligned}\phi(p, J_z = +\tfrac{1}{2}) = \tfrac{1}{\sqrt{18}}\big(&2u\uparrow u\uparrow d\downarrow + 2d\downarrow u\uparrow u\uparrow + 2u\uparrow d\downarrow u\uparrow \\ &-u\downarrow d\uparrow u\uparrow - u\uparrow u\downarrow d\uparrow - u\downarrow u\uparrow d\uparrow \\ &-d\uparrow u\downarrow u\uparrow - u\uparrow d\uparrow u\downarrow - d\uparrow u\uparrow u\downarrow\big)\end{aligned} \tag{4.15}$$

The other members of the $J^P = \frac{1}{2}^+$ baryon octet can be worked out in similar fashion. This octet is depicted in Figure 4.13, where the wavefunctions have been indicated as uud, uus etc., but it should be understood that these are abbreviations for the properly symmetrised expressions. The eight members consist of the n and

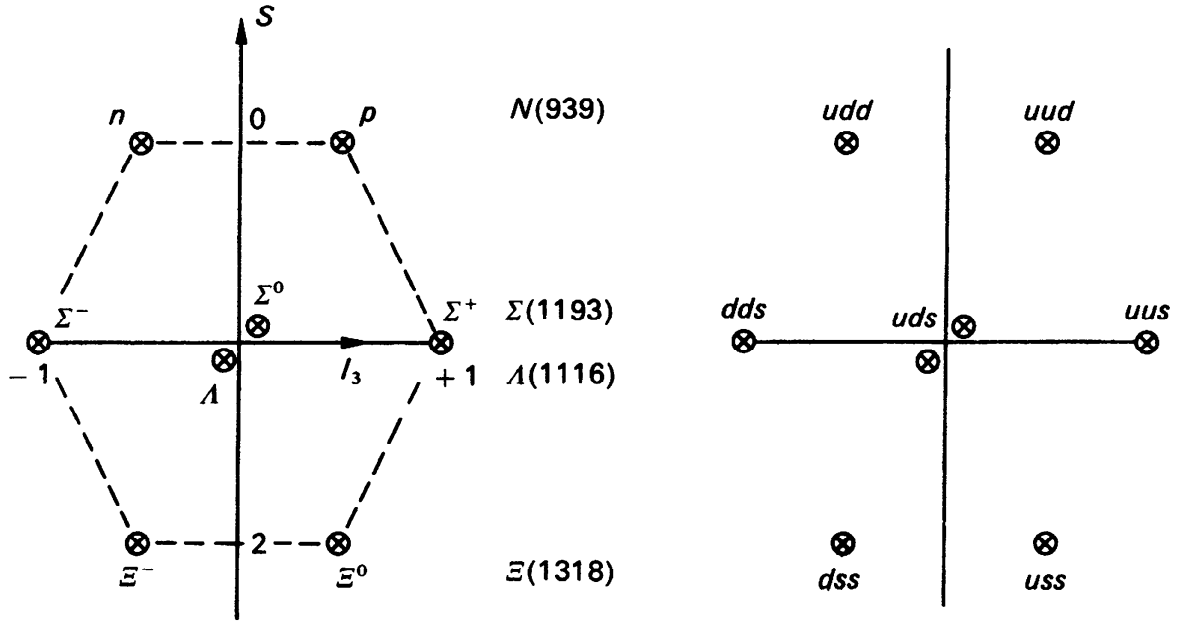

Fig. 4.13. The baryon octet with spin-parity $\frac{1}{2}^+$. The observed states are given on the left, and quark flavour assignments on the right.

$p(939)$ nucleon isospin doublet ($I = \frac{1}{2}, S = 0$), the $\Sigma(1193)$ isotriplet ($I = 1, S = -1$), the $\Xi(1318)$ isodoublet ($I = \frac{1}{2}, S = -2$), and the $\Lambda(1116)$ isosinglet ($I = 0, S = -1$).

The hypothesis that baryon masses differ because of differences in the strange quark content gives for the $J^P = \frac{3}{2}^+$ decuplet

$$\underset{152\text{ MeV}}{\Sigma(1384) - \Delta(1232)} = \underset{149\text{ MeV}}{\Xi(1533) - \Sigma(1384)} = \underset{139\text{ MeV}}{\Omega^-(1672) - \Xi(1533)} \tag{4.16}$$

In the $\frac{1}{2}^+$ octet, the same hypothesis gives

$$\underset{1193\text{ MeV}}{M_\Sigma} = \underset{1116\text{ MeV}}{M_\Lambda} \tag{4.17}$$

$$\underset{177\text{ MeV}}{M_\Lambda - M_N} = \underset{203\text{ MeV}}{M_\Xi - M_\Lambda} \tag{4.18}$$

Evidently there is rather poor agreement among the three expected equalities in (4.16) as well as a large discrepancy between the average masses in the decuplet and the octet. As discussed below, a more quantitatively correct description of baryon and meson masses is obtained in terms of the 'hyperfine splitting' effects of the interquark interactions.

Baryon multiplets of higher spin are also observed, and these can be accounted for in terms of the u, d, s quark combinations, three at a time, introducing the relative orbital angular momentum l of the quarks as necessary to account for the

Table 4.6.

	Nucleons		Quarks	
I_3	particle	antiparticle	particle	antiparticle
$+\frac{1}{2}$	p	$+\bar{n}$	u	$+\bar{d}$
$-\frac{1}{2}$	n	$-\bar{p}$	d	$-\bar{u}$

states of high J. This separate quantisation of orbital and spin angular momentum of the quarks is in fact valid only in the approximation of non-relativistic motion.

4.6 Quark–antiquark combinations: the light pseudoscalar mesons

As indicated before, the states observed in nature consist of three-quark combinations (the baryons) and quark–antiquark combinations (the mesons). Restricting ourselves to three flavours, we expect families of mesons containing $3^2 = 9$ states, or nonets. Given spin $\frac{1}{2}$ for quarks and antiquarks, we might expect both spin-triplet ($\uparrow\uparrow$) states with $J = 1$ and spin-singlet ($\downarrow\uparrow$) states with $J = 0$. These are displayed in Figure 4.14.

In discussing the baryon multiplets, emphasis was placed on the quark-exchange symmetry. But now we are dealing with quarks and antiquarks, and thus the interchange $u \rightarrow \bar{u}$, for example. It is necessary therefore to consider the effect of charge conjugation applied to quark wavefunctions. If the baryon number B is conserved, there is no actual physical process corresponding to $Q \leftrightarrow \bar{Q}$: thus, as a result of the operation of charge conjugation, or particle–antiparticle conjugation, an arbitrary and unobservable phase occurs. We can write for the result of the C operation, $u \rightarrow \bar{u}$ or $u \rightarrow \bar{u}e^{i\phi}$. The phase ϕ is generally chosen according to the Condon–Shortley convention, which actually introduces a minus sign in some places. In Table 4.6, the arrows denote the C operation.

Assuming that our quark–antiquark combinations are in the $l = 0$ singlet spin state and recalling the opposite intrinsic parity of fermion and antifermion, the quantum numbers will be $B = 0$, $J^P = 0^-$. These correspond to *pseudoscalar mesons*, so-called because the wavefunctions have $J = 0$ and odd parity (they change sign under spatial inversion).

With only u and d quarks and antiquarks we can make $2^2 = 4$ isospin combinations, in exact analogy with the spin combinations in (3.11), as in Table 4.7. The four combinations consist of the $I = 1$ triplet, identified with the π^+, π^0 and π^- mesons, and an $I = 0$ singlet, η. One can check this identification by applying the isospin shift operators $I^{\pm}$, in exact analogy with the angular-momentum operators

Table 4.7.

I	I_3	Wavefunction	Q/e
1	1	$u\bar{d} = \pi^+$	+1
1	−1	$-\bar{u}d = \pi^-$	−1
1	0	$\frac{1}{\sqrt{2}}(d\bar{d} - u\bar{u}) = \pi^0$	0
0	0	$\frac{1}{\sqrt{2}}(d\bar{d} + u\bar{u}) = \eta$	0

$J^{\pm}$ (see Appendix C):

$$I^{\pm}\Psi(I, I_3) = \sqrt{I(I+1) - I_3(I_3 \pm 1)}\,\Psi(I, I_3 \pm 1) \tag{4.19}$$

Thus, for single-quark states,

$$I^+ d = u, \qquad I^+ \bar{u} = -\bar{d}, \qquad I^+ u = I^+ \bar{d} = 0$$

Furthermore,

$$I^-\Psi(1,1) = I^+\Psi(1,-1) = \sqrt{2}\Psi(1,0)$$

$$I^+\Psi(1,0) = \sqrt{2}\Psi(1,1), \qquad I^+\Psi(1,1) = I^-\Psi(1,-1) = 0$$

Applying these results to the quark–antiquark combinations in Table 4.7 we obtain, for example,

$$I^+\pi^- = I^+(-d\bar{u}) = -u\bar{u} + d\bar{d} = \sqrt{2}\pi^0$$

$$I^+\pi^0 = I^+\frac{d\bar{d} - u\bar{u}}{\sqrt{2}} = \frac{u\bar{d} + 0 - 0 + u\bar{d}}{\sqrt{2}} = \sqrt{2}u\bar{d} = \sqrt{2}\pi^+$$

The $I = 1$ combinations are thus identified with π^+, π^-, π^0, the lowest-mass pseudoscalar mesons. The fourth combination has the property

$$I^{\pm}\eta = I^+\frac{d\bar{d} + u\bar{u}}{\sqrt{2}} = \frac{u\bar{d} - u\bar{d}}{\sqrt{2}} = 0.$$

Thus η is an isospin singlet, which does not transform under an isospin transformation into any other state; it is orthogonal to the $I = 1$ combinations. With the phase convention under C conjugation which we have adopted, the singlet state is *symmetric* with respect to the interchange of quark labels ($d \to u, \bar{d} \to \bar{u}$), whereas the π^+, π^-, π^0 states all change sign. The singlet is identified with the η meson, of mass 550 MeV.

Table 4.8. *Pseudoscalar meson states as quark–antiquark combinations*

	I	I_3	S	Meson	Quark combination	Decay	Mass, MeV
octet	1	1	0	π^+	$u\bar{d}$	$\pi^\pm \to \mu\nu$	140
	1	−1	0	π^-	$d\bar{u}$		
	1	0	0	π^0	$\frac{1}{\sqrt{2}}(d\bar{d} - u\bar{u})$	$\pi^0 \to 2\gamma$	135
	$\frac{1}{2}$	$\frac{1}{2}$	+1	K^+	$u\bar{s}$	$K^+ \to \mu\nu$	494
	$\frac{1}{2}$	$-\frac{1}{2}$	+1	K^0	$d\bar{s}$	$K^0 \to \pi^+\pi^-$	498
	$\frac{1}{2}$	$-\frac{1}{2}$	−1	K^-	$\bar{u}s$	$K^- \to \mu\nu$	494
	$\frac{1}{2}$	$\frac{1}{2}$	−1	$\bar{K}^0$	$\bar{d}s$	$\bar{K}^0 \to \pi^+\pi^-$	498
	0	0	0	η_8	$\frac{1}{\sqrt{6}}(d\bar{d} + u\bar{u} - 2s\bar{s})$	$\eta \to 2\gamma$	549
singlet	0	0	0	η_0	$\frac{1}{\sqrt{3}}(d\bar{d} + u\bar{u} + s\bar{s})$	$\eta' \to \eta\pi\pi$	958
						$\to 2\gamma$	

Introduction of s quarks in addition to u and d gives us a total of $3^2 = 9$ states, which are listed in Table 4.8 together with their assignment to the pseudoscalar mesons. In analogy with the singlet state obtained with the u, d quark–antiquark combinations, these nine states built from u, d and s quarks break down into a singlet – the symmetric $Q\bar{Q}$ combination η_0 in the last line of Table 4.8 – plus eight states that can be transformed one into another by interchange of the u, d and s quarks. Note that the eighth member, η_8, is $\frac{1}{\sqrt{6}}(d\bar{d} + u\bar{u} - 2s\bar{s})$, orthogonal to η_0. The square-root factors are inserted where appropriate so that all states are normalised to unity. The approximately linear mass relations found for the baryon multiplets do not work for mesons. An empirical mass formula (due originally to Gell-Mann and Okubo) can be applied to mesons if the squared mass is used:

$$\begin{array}{lcc} 2(M^2_{K^0} + M^2_{\bar{K}^0}) = & 4M^2_{K^0} & = M^2_{\pi^0} + 3M^2_{\eta} \\ & 0.988\ \text{GeV}^2 & 0.924\ \text{GeV}^2 \end{array} \qquad (4.20)$$

However, the actual states η and η' observed in nature appear to be linear combinations of the wavefunctions η_8 and η_0 in the last two lines of Table 4.8, if one assumes that the Gell-Mann and Okubo mass formula is valid. Such mixing is discussed more fully below, for the vector meson nonet.

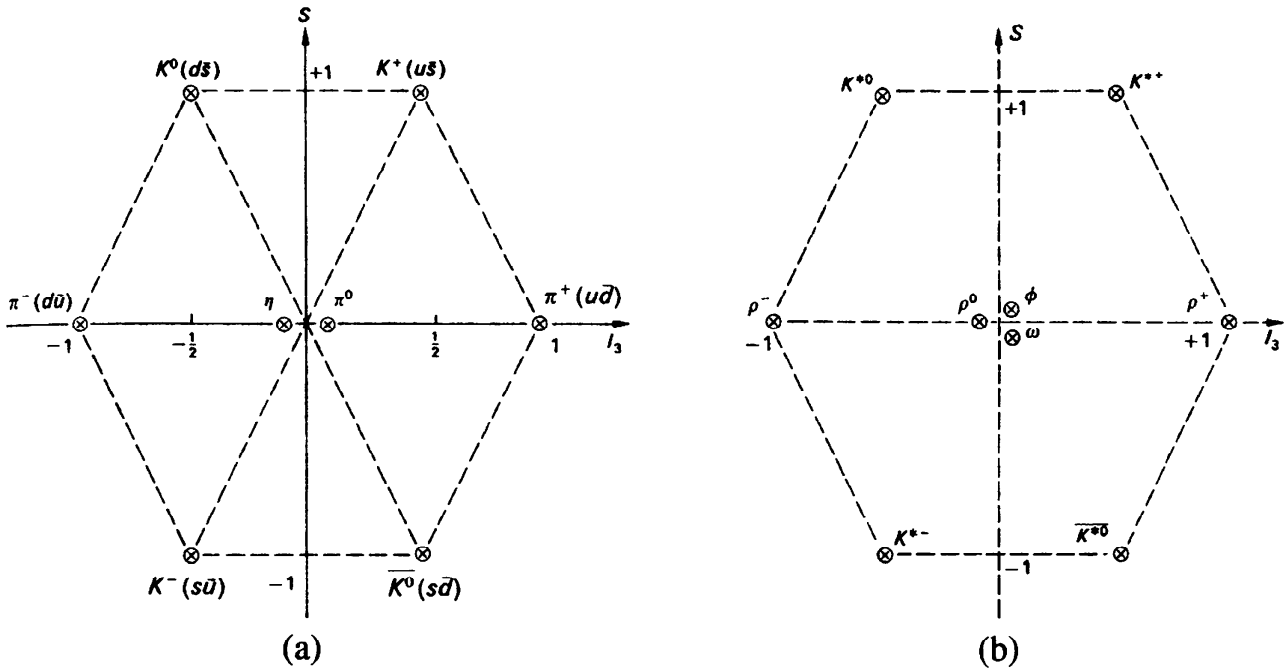

Fig. 4.14. (a) The lowest-lying pseudoscalar meson states ($J^P = 0^-$). Quark flavour assignments are indicated. (b) The vector meson nonet ($J^P = 1^-$). The quark assignments are the same as in (a).

4.7 The light vector mesons

The $l = 0$ spin triplet combinations ($\uparrow\uparrow$) of Q and $\bar{Q}$ give us the vector mesons ($J^P = 1^-$); see Figure 4.14(b). To get satisfactory results, it is necessary to assume that the octet and singlet states are mixed. Let θ be the octet–singlet mixing angle. Formally we can write

$$\begin{aligned} \phi &= \phi_0 \sin\theta - \phi_8 \cos\theta \\ \omega &= \phi_8 \sin\theta + \phi_0 \cos\theta \end{aligned} \tag{4.21}$$

where ϕ, ω denote the physical vector meson states and ϕ_0, ϕ_8 the singlet and octet states, respectively, with $I = S = 0$. Assuming that the matrix element of the energy operator between the states yields the squared mass, as above, we obtain from (4.21)

$$M_\phi^2 = M_0^2 \sin^2\theta + M_8^2 \cos^2\theta - 2M_{08}^2 \sin\theta\cos\theta \tag{4.22a}$$

$$M_\omega^2 = M_8^2 \sin^2\theta + M_0^2 \cos^2\theta + 2M_{08}^2 \sin\theta\cos\theta \tag{4.22b}$$

in an obvious notation. Further, since ϕ and ω are orthogonal, we obtain

$$M_{\phi\omega}^2 = 0 = (M_0^2 - M_8^2)\sin\theta\cos\theta + M_{08}^2(\sin^2\theta - \cos^2\theta). \tag{4.23}$$

Eliminating M_{08} and M_0 between these three equations gives

$$\tan^2\theta = \frac{M_\phi^2 - M_8^2}{M_8^2 - M_\omega^2} \tag{4.24}$$

Table 4.9. *Vector meson nonet*

State	I	Y	Mass, MeV	Dominant decay mode
ρ	1	0	776	$\rho \to 2\pi$
K^*	$\frac{1}{2}$	± 1	892	$K^* \to K\pi$
ω	0	0	783	$\omega \to 3\pi$
ϕ	0	0	1019	$\phi \to K\bar{K}$

Using an analogue of (4.20), we get

$$M_8^2 = \tfrac{1}{3}(4M_{K^*}^2 - M_\rho^2) \tag{4.25}$$

so that the observed masses (Table 4.9) give $\theta \simeq 40°$. For the particular case $\sin\theta = \frac{1}{\sqrt{3}}$, $\theta \simeq 35°$, (4.21) would give

$$\phi = \tfrac{1}{\sqrt{3}}(\phi_0 - \sqrt{2}\phi_8)$$

$$\omega = \tfrac{1}{\sqrt{3}}(\phi_8 + \sqrt{2}\phi_0)$$

where from Table 4.8

$$\begin{aligned} \phi_0 &= \tfrac{1}{\sqrt{3}}(d\bar{d} + u\bar{u} + s\bar{s}) \\ \phi_8 &= \tfrac{1}{\sqrt{6}}(d\bar{d} + u\bar{u} - 2s\bar{s}) \end{aligned} \tag{4.26}$$

so that

$$\begin{aligned} \phi &= s\bar{s} \\ \omega &= \tfrac{1}{\sqrt{2}}(u\bar{u} + d\bar{d}) \end{aligned} \tag{4.27}$$

In this case of 'ideal mixing' – which is almost true in practice – ϕ is composed entirely of s quarks, and ω of u and d quarks. We note that these simple expressions predict similar masses for ω and ρ as well as a larger mass for the ϕ – as is observed. Even more importantly, they allow some understanding about the decay modes of ω and ϕ. These are

$$\begin{aligned} \phi(1020) &\to K^+K^- \\ &\to K^0\bar{K}^0 \end{aligned} \Bigg\} \ 84\% \qquad \begin{aligned} \omega(783) &\to \pi^+\pi^-\pi^0 \quad 90\% \\ &\to \pi^+\pi^- \\ &\to \pi^0\gamma \end{aligned} \Bigg\} \ 10\%$$

$$\phi(1020) \to \pi^+\pi^-\pi^0 \quad 15\% \tag{4.28}$$

The phase-space factors favour 3π decay of the ϕ, since the Q-value is 600 MeV compared with $Q = 24$ MeV for $K\bar{K}$ decay. Yet the $K\bar{K}$ decay is dominant. Here is another example of the OZI rule we met earlier in charmonium decay.

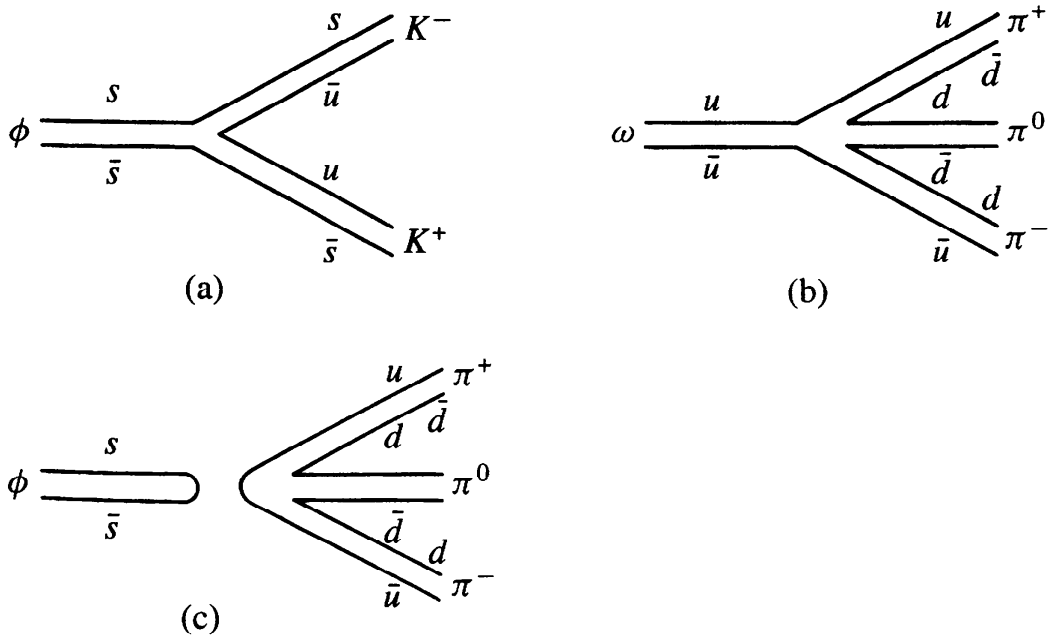

Fig. 4.15. Quark flow diagrams for ϕ and ω decay. (a) $\phi \to K^+K^-$; (b) $\omega \to \pi^+\pi^-\pi^0$; (c) $\phi \to \pi^+\pi^-\pi^0$.

Figure 4.15 shows the appropriate quark flow diagrams for ϕ and ω decay. The $\phi \to 3\pi$ decay is suppressed because it involves unconnected quark lines, just as in Figure 4.5.

4.8 Other tests of the quark model

The quark model makes a large number of predictions that can be verified experimentally. We mention briefly a few of them.

4.8.1 Pion–nucleon cross-sections

High energy hadron–hadron cross-sections can be interpreted as due to the additive effects of the scattering amplitudes in collisions between the individual constituent quarks. Then simple quark counting in the pion–nucleon case would suggest that

$$\frac{\sigma(\pi N)}{\sigma(NN)} = \frac{2}{3} \tag{4.29}$$

For example, at a beam energy of 60 GeV, $\sigma(\pi^+ p)$ and $\sigma(\pi^- p)$ are nearly equal, with an average of 25 mb, while $\sigma(pp) \simeq \sigma(pn) = 38$ mb in an equivalent energy range. This ratio is indeed approximately $\frac{2}{3}$.

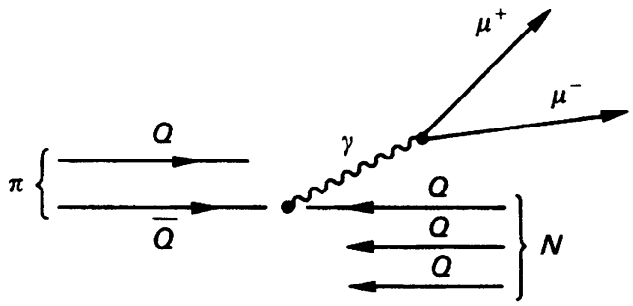

Fig. 4.16. The Drell–Yan mechanism for the production of lepton pairs is viewed as the fusion of quark and antiquark to a virtual photon, decaying to the pair.

4.8.2 *Lepton pair production on isoscalar targets*

This provides a test of the quark charge assignments. As shown in Figure 4.16, the production of a lepton pair in a pion–nucleon collision is interpreted as the annihilation of the antiquark from the pion with a quark from the nucleon, giving a virtual photon that transforms to a muon pair. The cross-section for such an electromagnetic process is proportional to the square of the quark charge. For $\pi^-(=\bar{u}d)$ on an isoscalar ^{12}C nucleus $(= 18u + 18d)$ we expect annihilation of $u\bar{u}$; thus

$$\sigma(\pi^-\mathrm{C} \to \mu^+\mu^- + \cdots) \propto 18Q_u^2 = 18(\tfrac{4}{9})$$

while for incident $\pi^+(= u\bar{d})$,

$$\sigma(\pi^+\mathrm{C} \to \mu^+\mu^- + \cdots) \propto 18Q_d^2 = 18(\tfrac{1}{9}).$$

The cross-section ratio $\sigma(\pi^-\mathrm{C})/\sigma(\pi^+\mathrm{C})$ is indeed 4 : 1 in the region well away from any heavy meson resonances (e.g. $\psi \to \mu^+\mu^-$).

4.8.3 *Vector meson decay to leptons*

The quark–antiquark assignments for the vector mesons, as well as the fractional values for the quark charges, may be tested from the values of their partial widths $\Gamma(e^+e^-)$ for decay to electron pairs.

In the non-relativistic quark model, the leptonic decay width $\Gamma(e^+e^-)$ of a vector meson depends on its coupling to a single exchange photon and is expected to be proportional to the square of the quark charges (Rutherford scattering; see Figure 4.17). Empirically, as seen in Table 4.10, the ratios $\Gamma_{e^+e^-}/|\Sigma a_i Q_i|^2$ of the leptonic width to the square of the mean quark charge are closely similar for the ρ, ω, ϕ, ψ and Υ. Here $|\Sigma a_i Q_i|^2$ is the squared sum of the charges of the quarks in the meson.

Table 4.10. *Leptonic widths of vector mesons*

Meson	Quark wavefunction	$\lvert\Sigma a_i Q_i\rvert^2$	$\Gamma_{e^+e^-}$, keV	$\Gamma_{e^+e^-}/\lvert\Sigma a_i Q_i\rvert^2$
ρ	$\frac{1}{\sqrt{2}}(u\bar{u}-d\bar{d})$	$\frac{1}{2}$	6.8 ± 0.3	13.6 ± 0.6
ω	$\frac{1}{\sqrt{2}}(u\bar{u}+d\bar{d})$	$\frac{1}{18}$	0.60 ± 0.02	10.8 ± 0.4
ϕ	$s\bar{s}$	$\frac{1}{9}$	1.37 ± 0.05	12.3 ± 0.5
ψ	$c\bar{c}$	$\frac{4}{9}$	5.3 ± 0.4	11.9 ± 0.9
Υ	$b\bar{b}$	$\frac{1}{9}$	1.32 ± 0.05	11.9 ± 0.5

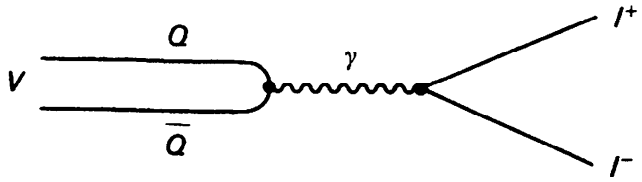

Fig. 4.17. Decay of a vector meson to an e^+e^- pair via a virtual photon.

The absolute values of the leptonic widths are given by the Van Royen–Weisskopf formula (1967);

$$\Gamma(V \to l^+l^-) = \frac{16\pi\alpha^2 Q^2}{M_V^2}|\psi(0)|^2 \tag{4.30}$$

where $Q^2 = |\Sigma a_i Q_i|^2$, $\psi(0)$ is the amplitude of the $Q\bar{Q}$ wavefunction at the origin and M_V is the meson mass. Apart from numerical factors, the form of this expression follows in straightforward fashion. The square of the propagator of the single-photon exchanged introduces a factor q^{-4} (where $|q|^2 = M_V^2$), and the phase-space factor for the two-body final state introduces a factor q^2. The quantity $\sqrt{\alpha}Q_i$, where Q_i is the quark charge, measures the coupling amplitude to the photon, and we take a superposition of amplitudes a_i from all quarks in the meson. Including the coupling of the photon to the lepton pair gives a total amplitude $\sqrt{\alpha}\sqrt{\alpha}\sum a_i Q_i$, which has to be squared to get the decay rate. Finally, $|\psi(0)|^2$ is the probability that the quark and antiquark will interact with the photon at a point in space–time (the origin of their relative coordinates). The quantity $|\psi(0)|^2$ is simply V^{-1}, where V is the volume occupied by the meson. For the lighter vector mesons (ρ, ω, ϕ), the rms radius of the charge distribution is known to be about 0.6 fm. This may be measured by firing a high energy pion beam at a target and selecting pion–electron scatters. Neglecting the binding energy of the electrons in the atoms of the target, the recoil electron distribution gives the values

of q^2 (see (5.31a)), and thence the root mean square radius of the pion's charge distribution.

It is left as an exercise to show that the observed leptonic widths are in approximate agreement with the above formula (see Problems 4.3 and 5.13).

4.9 Mass relations and hyperfine interactions

So far, mass differences in hadron multiplets have been simply ascribed to those between the constituent u, d and s quarks. These alone, however, cannot account for the observed differences, especially those between baryon octet and decuplet members having the same quark constitution. The discrepancy has to be attributed to the effects of quark–quark interactions, for which there is a theory called quantum chromodynamics, discussed in Chapter 6. Here, we shall only sketch out briefly how the most important new contribution, the hyperfine splitting of the hadron energy levels, can be described in terms of the colour force between quarks.

First, let us recall that in the energy-level diagram of the hydrogen atom, each level of given n, l and j quantum numbers is split into two very close hyperfine levels, owing to the interactions of the magnetic moments of the constituent proton and electron. In the ground (1S) state, the transition between the two states gives rise to the famous 1420 MHz (21 cm) radio-frequency spin-flip line, which has been used to map the distribution of atomic hydrogen on a cosmic scale. Now consider two charged point fermions with magnetic dipole moments $\boldsymbol{\mu}_i$ and $\boldsymbol{\mu}_j$. Suppose the two particles are in a relative S-state. Dipole j is in the field due to dipole i, which can be calculated assuming that this dipole is located at random inside a sphere of arbitrary volume V centred on $\boldsymbol{\mu}_j$. The field at the centre of a uniformly magnetised sphere is $B = 2M/3$, where $M = \mu/V$ is the magnetic moment per unit volume, and in turn $V^{-1} = |\psi(0)|^2$, the square of the amplitude of the two-particle wavefunction at the origin of relative coordinates ($r_{ij} = 0$). So, the spin–spin magnetic interaction energy (applicable only to S-states, since for all others $|\psi(0)|^2 = 0$) is

$$\begin{aligned} \Delta E = \boldsymbol{\mu} \cdot \mathbf{B} &= \tfrac{2}{3}\boldsymbol{\mu}_i \cdot \boldsymbol{\mu}_j |\psi(0)|^2 \\ &= \frac{2\pi}{3}\frac{\alpha}{m_i m_j}|\psi(0)|^2 \boldsymbol{\sigma}_i \cdot \boldsymbol{\sigma}_j \end{aligned} \tag{4.31}$$

where in units such that $\hbar = c = 1$ the Dirac moment is $\boldsymbol{\mu}_i = (e_i/2m_i)\boldsymbol{\sigma}_i$, $\boldsymbol{\sigma}$ being the Pauli spin vector ($\boldsymbol{\sigma}^2 = 1$), and we set $e_i e_j = 4\pi\alpha$.

Turning now to quarks, the normal magnetic interaction associated with the electric charge and spin of the quarks is small on the scale of hadron masses; it is of the order of the electromagnetic mass differences ($\sim$ 1 MeV). But quarks carry a strong colour charge, and at small interquark separation the colour potential is

assumed to have the same $(1/r)$ form as the Coulomb potential. Associated with the colour charges of spinning quarks is a colour magnetic interaction, of the same form as (4.31) but with electric charges replaced by colour charges. The numerical coefficient in the expression for ΔE depends on whether the interaction is between a quark pair or a quark–antiquark pair. From (4.9), we replace α by $4\alpha_s/3$ for a $Q\bar{Q}$ pair, while for a QQ pair in a baryon (QQQ) it is found that the factor is half this, i.e. $2\alpha_s/3$. Here we simply state these results without proof. Then from (4.31)

$$\Delta E(Q\bar{Q}) = \frac{8\pi\alpha_s}{9m_i m_j}|\psi(0)|^2 \boldsymbol{\sigma}_i \cdot \boldsymbol{\sigma}_j \tag{4.32}$$

$$\Delta E(QQ) = \frac{4\pi\alpha_s}{9m_i m_j}|\psi(0)|^2 \boldsymbol{\sigma}_i \cdot \boldsymbol{\sigma}_j \tag{4.33}$$

The product of the Pauli vectors $\boldsymbol{\sigma}_i$, $\boldsymbol{\sigma}_j$ depends in magnitude and sign on the relative quark spin orientations, just as for two bar magnets the force depends on orientation. Denoting the spin vectors of the quarks by $\mathbf{s}_i$, $\mathbf{s}_j$, where $s_z = \pm\frac{1}{2}$, and the total spin by $\mathbf{S} = \mathbf{s}_i + \mathbf{s}_j$, one obtains (recalling that the eigenvalue of the operator $\mathbf{S}^2$ is $S(S+1)$; see also Appendix C),

$$\begin{aligned}\boldsymbol{\sigma}_i \cdot \boldsymbol{\sigma}_j = 4\mathbf{s}_i \cdot \mathbf{s}_j &= 2[S(S+1) - s_i(s_i+1) - s_j(s_j+1)] \\ &= \begin{cases} +1 & \text{for } S = 1 \\ -3 & \text{for } S = 0 \end{cases}\end{aligned} \tag{4.34}$$

Turning to baryons, consisting of three quarks, we have to sum (4.34) over the quark spins to obtain, with $\mathbf{S} = \mathbf{s}_i + \mathbf{s}_j + \mathbf{s}_k$,

$$\begin{aligned}\sum \boldsymbol{\sigma}_i \cdot \boldsymbol{\sigma}_j = 4\sum \mathbf{s}_i \cdot \mathbf{s}_j &= 2[S(S+1) - 3s(s+1)] \\ &= \begin{cases} +3 & \text{for } S = \frac{3}{2} \\ -3 & \text{for } S = \frac{1}{2} \end{cases}\end{aligned} \tag{4.35}$$

This formula will be satisfactory for the nucleon N or the Δ states, where the three (u and d) quark masses in the denominator of (4.33) are very nearly equal. For a $\Sigma^+(1193)$ hyperon (uus) in the octet, the difference in mass of s and u quarks has to be taken into account in summing over the three-quark state. The like pair is $u\uparrow u\uparrow$, in a triplet spin state with $\boldsymbol{\sigma}_u \cdot \boldsymbol{\sigma}_u = 1$, so that from (4.35)

Table 4.11. *Baryon masses predicted from hyperfine splitting*

Baryon and mass (MeV)	Quark composition (n denotes u or d)	$\Delta E/K$	Predicted mass, MeV
$N(939)$	$3n$	$-3/m_n^2$	939
$\Lambda(1116)$	$2n, 1s$	$-3/m_n^2$	1114
$\Sigma(1193)$	$2n, 1s$	$1/m_n^2 - 4/(m_n m_s)$	1179
$\Xi(1318)$	$1n, 2s$	$1/m_n^2 - 4/(m_n m_s)$	1327
$\Delta(1232)$	$3n$	$3/m_n^2$	1239
$\Sigma(1384)$	$2n, 1s$	$1/m_n^2 + 2/(m_n m_s)$	1381
$\Xi(1533)$	$1n, 2s$	$1/m_s^2 + 2/(m_n m_s)$	1529
$\Omega(1672)$	$3s$	$3/m_s^2$	1682

$2\boldsymbol{\sigma}_u \cdot \boldsymbol{\sigma}_s = \sum \boldsymbol{\sigma}_i \cdot \boldsymbol{\sigma}_j - \boldsymbol{\sigma}_u \cdot \boldsymbol{\sigma}_u = -4$. Thus we find, for example,

$$\begin{aligned}(\Delta E)_\Delta &= +\frac{3}{m_u^2}K \\ (\Delta E)_N &= -\frac{3}{m_u^2}K \\ (\Delta E)_\Sigma &= \left(\frac{1}{m_u^2} - \frac{4}{m_u m_s}\right)K\end{aligned} \tag{4.36}$$

where $K = 4\pi\alpha_s|\psi(0)|^2/9$. From the eight isomultiplets of baryons in the decuplet and octet, we are thus able to fit the unknown parameters K, m_u and m_s. Taking

$$\begin{aligned}m_n(= m_u = m_d) &= 363 \text{ MeV} \\ m_s &= 538 \text{ MeV} \\ K/m_n^2 &= 50 \text{ MeV}\end{aligned} \tag{4.37}$$

we obtain the values for the baryon masses shown in Table 4.11. The agreement between observed and expected masses is at the level of 1% or better. The hyperfine splitting due to the colour magnetic interaction successfully accounts for the 300 MeV mass difference between the Δ and N states.

For the pseudoscalar and vector meson states, discussed in Sections 4.6 and 4.7, a similar treatment is possible. In particular, the large mass difference between the $\pi(140)$ and $\rho(776)$, representing singlet and triplet spin combinations of u and d quarks and antiquarks, is ascribed to the hyperfine interaction. The fitted values of quark mass are somewhat smaller than in (4.37), while $K/m_n^2 \simeq 90$ MeV is larger. This is expected: from the scattering of high energy charged pion and

kaon beams by atomic electrons, it is known that the rms radius of the charge distribution of mesons is smaller ($R_0 \simeq 0.6$ fm) than it is for baryons ($R_0 \simeq 0.8$ fm), so that $|\psi(0)|^2$, which is proportional to $1/R_0^3$, will be more than a factor 2 larger. Together with the factor 2 in the expression for ΔE in (4.32) as compared with (4.33), we can therefore understand the much larger mass splitting between π and ρ as compared with that between Δ and N states.

4.10 Electromagnetic mass differences and isospin symmetry

The actual mass of a charged hadron can be thought of as made up of two components. First there is a sort of 'bare' mass m originating from that of the quark constituents and from their strong mutual interactions, of the type described in the previous section. Second, there will be a contribution Δm due to the electric charge of the hadron – basically equal to the work required to put the charge on the previously uncharged particle. If all baryons in the $\frac{1}{2}^+$ octet have similar charge distributions, then we might reasonably expect similar values of Δm for similarly charged hadrons:

$$\Delta m_p = \Delta m_{\Sigma^+}, \qquad \Delta m_{\Sigma^-} = \Delta m_{\Xi^-}, \qquad \Delta m_{\Xi^0} = \Delta m_n$$

Adding the 'bare' masses to each side and summing these equations gives

$$m_p + m_{\Sigma^-} + m_{\Xi^0} = m_{\Sigma^+} + m_{\Xi^-} + m_n$$

or

$$(m_p - m_n) = (m_{\Sigma^+} - m_{\Sigma^-}) + (m_{\Xi^-} - m_{\Xi^0}) \tag{4.38}$$

$$-1.3 \text{ MeV} \qquad \underbrace{-8.0 \text{ MeV} \qquad +6.4 \text{ MeV}}_{-1.6 \text{ MeV}}$$

This formula was due originally to Coleman and Glashow and is approximately verified. The individual mass differences are associated with isospin symmetry breaking, which has already been discussed in Section 3.12. In the context of the quark model, there are several distinct effects to consider in accounting for the mass differences.

(i) Difference in masses of the u and d quarks. The sign of each term in (4.38) indicates $m_d > m_u$.

(ii) Coulomb energy difference associated with the electrical energy between pairs of quarks. This will be of order $e^2/R_0 = e^2/(\hbar c)(\hbar c/R_0)$, where R_0 is the size of a baryon. With $\hbar c = 197$ MeV fm, $R_0 \simeq 0.8$ fm, we have $e^2/R_0 \simeq 2$ MeV.

(iii) Magnetic energy difference associated with the magnetic-moment (hyperfine) interaction between quark pairs. From (4.31) this will be of order $[e\hbar/(mc)]^2(1/R_0)^3$, where m is the quark mass and $|\psi(0)|^2 \simeq R_0^{-3}$. Since $\hbar/(mc)$ is of order R_0, the magnetic energy is also in the region of e^2/R_0, i.e. 1 or 2 MeV.

Fitting the exact forms of these terms to the numbers in (4.38), it is found that $m_d - m_u = 2$ MeV. While, given the values of the spins, charges and radii of baryons, any model must predict Coulomb and magnetic energy differences of the above magnitudes, the closeness in mass of the u and d quarks could not have been foreseen. Thus the property of approximate isospin invariance of the interactions between hadrons and in atomic nuclei can be associated simply with the near equality of m_u and m_d (which, however, is not presently understood).

4.11 Magnetic moments of baryons

If the quarks behave as pointlike Dirac particles, each will have a magnetic dipole moment as above:

$$\boldsymbol{\mu}_i = \left(\frac{e_i}{2m_i}\right)\boldsymbol{\sigma}_i \tag{4.39}$$

where e_i, m_i and σ_i are the charge, mass and spin. From the symmetry properties of the three-quark wavefunction in the baryons, we should then be able to compute their magnetic moments, as vector sums of the moments of the constituent quarks. For the proton p $(= uud)$, we have already noted that the two u quarks will be in a symmetric (triplet) spin state described by a spin function $\chi(J = 1, m = 0, \pm 1)$, while the third (d) quark can be denoted by $\phi(J = \frac{1}{2}, m = \pm\frac{1}{2})$. The total-angular-momentum function for a spin-up proton will be $\psi(J = \frac{1}{2}, m = \frac{1}{2})$, and the Clebsch–Gordan coefficients for combining $J = 1$ and $J = \frac{1}{2}$ give us (see Appendix C)

$$\psi(\tfrac{1}{2}, \tfrac{1}{2}) = \sqrt{\tfrac{2}{3}}\,\chi(1, 1)\phi(\tfrac{1}{2}, -\tfrac{1}{2}) - \sqrt{\tfrac{1}{3}}\,\chi(1, 0)\phi(\tfrac{1}{2}, \tfrac{1}{2}) \tag{4.40}$$

For the first combination, the moment will be $\mu_u + \mu_u - \mu_d$, and for the second, just μ_d. Hence we get for the proton moment

$$\mu_p = \tfrac{2}{3}(2\mu_u - \mu_d) + \tfrac{1}{3}\mu_d = \tfrac{4}{3}\mu_u - \tfrac{1}{3}\mu_d. \tag{4.41}$$

The result for the neutron is the same but with the labels u and d interchanged. For Σ^+ one replaces μ_d by μ_s in (4.41), and for Σ^-, μ_d by μ_s and μ_u by μ_d. For the Λ hyperon, which is a uds combination with $I = 0$, the pair u and d must be in an $I = 0$ (i.e. antisymmetric) isospin state. So as shown in Section 4.5, they must be in an antisymmetric spin state $(J = 0)$. Hence the u and d in the Λ make no

Table 4.12. *Baryon magnetic moments in nuclear magnetons (n.m.), normalised to proton and lambda moments*

Baryon	Magnetic moment in quark model	Predicted, n.m.	Observed, n.m.
p	$\frac{4}{3}\mu_u - \frac{1}{3}\mu_d$	+2.79	+2.793
n	$\frac{4}{3}\mu_d - \frac{1}{3}\mu_u$	−1.86	−1.913
Λ	μ_s	−0.61	-0.614 ± 0.005
Σ^+	$\frac{4}{3}\mu_u - \frac{1}{3}\mu_s$	+2.68	$+2.46 \pm 0.01$
Σ^-	$\frac{4}{3}\mu_d - \frac{1}{3}\mu_s$	−1.04	-1.16 ± 0.03
Ξ^0	$\frac{4}{3}\mu_s - \frac{1}{3}\mu_u$	−1.44	-1.25 ± 0.014
Ξ^-	$\frac{4}{3}\mu_s - \frac{1}{3}\mu_d$	−0.51	-0.65 ± 0.01
Ω^-	$3\mu_s$	−1.84	-2.02 ± 0.05

contribution to the moment, and $\mu_\Lambda = \mu_s$. Values of μ for Σ^0, Ξ^0 and Ξ^- can be worked out in similar fashion.

Assuming, as before, that the u and d quarks have approximately the same mass m_n, an immediate result of (4.41) and the quark charge assignments applied to (4.39) is the ratio of neutron to proton moments:

$$\mu_n = -\tfrac{2}{3}\mu_p$$

in impressive agreement with the observed ratio, −0.685.

For the absolute values, the measured moments of proton and Λ hyperon can be used to estimate the values of m_n and m_s, using (4.39) and the formulae for the moments given in Table 4.12. All the numbers in this table are quoted in units of the nuclear magneton (n.m.), which has the value $\mu = e\hbar/(2Mc)$ where M is the nucleon mass. After normalising to the proton and lambda moments, the calculated moments of the other baryons then agree with observation within discrepancies at the 10%–20% level. The masses deduced in this way are

$$\begin{aligned} m_n (= m_u = m_d) &= 336 \text{ MeV} \\ m_s &= 509 \text{ MeV} \end{aligned} \tag{4.42}$$

to be compared with the values (4.37) from the mass splittings. These different estimates of quark mass, although not in precise agreement, are sufficiently close to give confidence in the basic correctness of the quark model of hadrons and in the quark quantum numbers. Of course our model of baryon moments, as the sum of three constituent quark moments, is very simplistic and takes no account of the

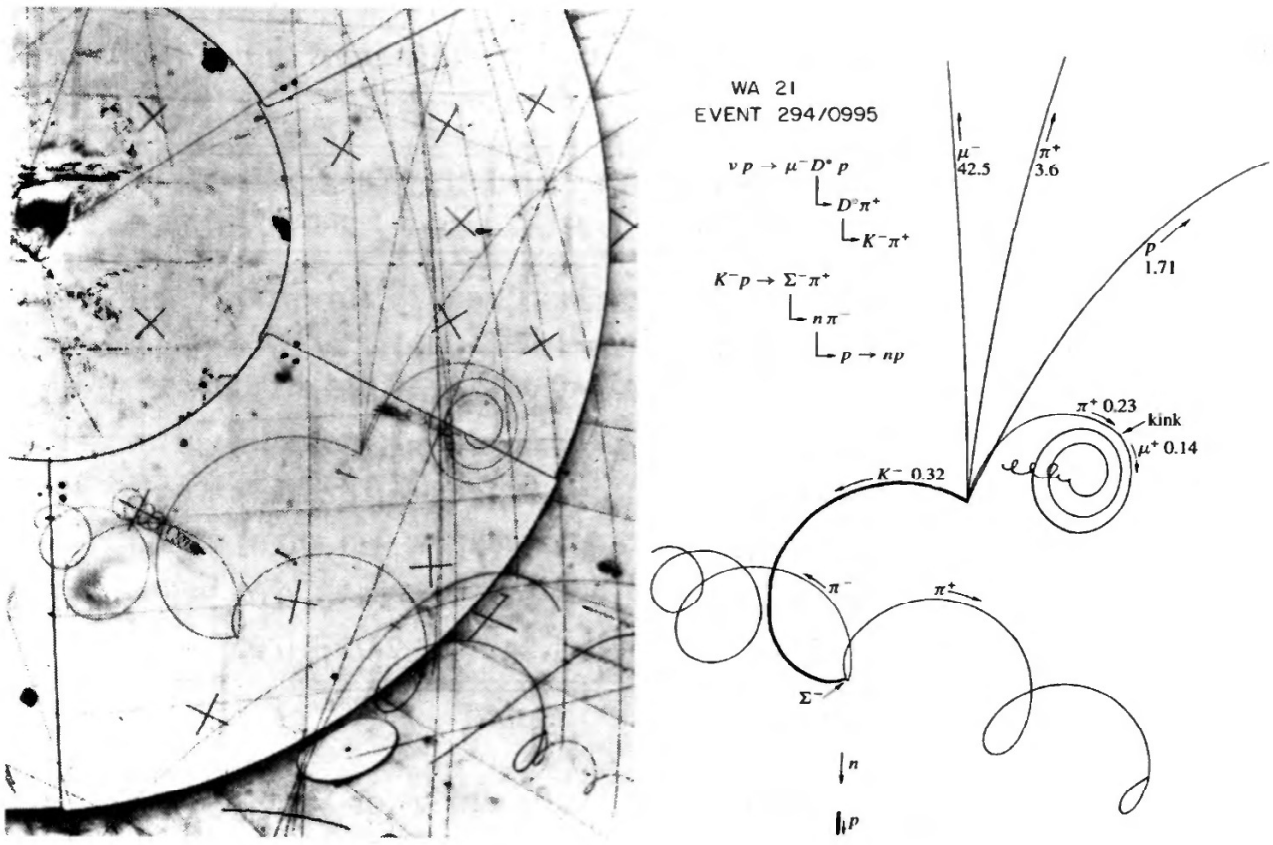

Fig. 4.18. Example of charmed-particle production and decay in the hydrogen bubble chamber BEBC exposed to a neutrino beam at the CERN SPS. It gives an almost complete pictorial representation of the production and decay of a charmed particle D^*. The figures on the facsimile drawing give the particle momenta in GeV/c.

dynamics of the quark interactions, including the magnetic effects of currents due to quark–antiquark pairs. It is surprising that it works so well.

4.12 Mesons built of light and heavy quarks

Shortly after the discovery of charmonium in 1974, combinations of light and heavy quarks were observed. These consisted of charmed pseudoscalar ($J^P = 0^-$) D mesons, D^+ ($= c\bar{d}$), D^0 ($= c\bar{u}$), D_s^+ ($= c\bar{s}$), ..., and vector ($J^P = 1^-$) mesons, D^{*0} ($= c\bar{u}$), D_s^{*+} ($= c\bar{s}$), ..., plus states corresponding to radial excitations ($J^P = 2^+$ etc.). The pseudoscalars decay by weak ($\Delta C = \pm 1$) interactions with a lifetime $\tau \simeq 10^{-12}$ s, into non-charmed states, with decays to strange mesons (e.g. $D^0 \to K^-\pi^+$ etc.) favoured by the Cabibbo suppression factor (see Section 7.14).

Similarly, bottom quark combinations with light quarks form the pseudoscalar B mesons and vector B^* mesons ($B^+ = u\bar{b}$, $B^0 = d\bar{b}$, $B_s^0 = s\bar{b}$ etc.). Again, the pseudoscalars decay by weak interactions ($\tau \simeq 10^{-12}$ s), predominantly to the

Table 4.13. *Hyperfine splitting for D and B mesons*

Heavy quark mass	Triplet–singlet difference	Product
$M_c \simeq 1.86$ GeV	$M_{D^*} - M_D = 0.14$ GeV	$M_c(M_{D^*} - M_D) = 0.26$ GeV^2
$M_b \simeq 5.28$ GeV	$M_{B^*} - M_B = 0.046$ GeV	$M_b(M_{B^*} - M_B) = 0.24$ GeV^2

Cabibbo-favoured charmed mesons (e.g. $B^0 \to D^-\pi^+$). Over the years, a huge amount of information has been compiled on the many decay modes of these exotic meson states, but we cannot go into details here. Figure 4.18 shows a beautiful example, in a bubble chamber, of the decay of a D^* meson produced in a neutrino interaction.

Mesons consisting of one heavy (mass M) and one light (mass m) quark have some aspects in common with a hydrogen atom, where most of the mass is in the nucleus, i.e. the proton (the analogue of the heavy quark) to which is bound the much lighter electron (the analogue of the light quark). The chemistry of an atom depends on the number and masses of its electrons and their energy levels, and hardly at all on the nuclear mass; whether the nucleus of a hydrogen atom is a proton or a deuteron, it is still hydrogen.

Quantitatively, the atomic wavefunction is, to first order, independent of the nuclear mass; corrections are of order m(electron)/M(nucleus) or atomic binding energy/M(nucleus). Similarly, in a heavy quark–light quark system, the effect of the heavy quark on the energy levels is of order Λ/M, where $\Lambda \sim 0.2$ GeV is the strong-interaction scale parameter, representing the light quark mass and the gluon binding potential (see Section 6.5).

We give here two examples of these effects. First, the hyperfine splitting of the pseudoscalar (quark spin singlet) and vector (quark spin triplet) states discussed in Section 4.9 above arises from the colour magnetic interaction, as in (4.32), and is therefore proportional to M^{-1}. Since M is large, we expect this splitting to be small (as compared with the large $\pi - \rho$ mass difference for the light quark combinations). Furthermore, as shown in Table 4.13, the hyperfine splitting is indeed inversely proportional to the heavy quark mass.

As a second example, let us compare the masses of D and B mesons with different flavours of light quark. The mass difference for the pseudoscalar states D_s $(= c\bar{s})$ and D $(= c\bar{u})$ is $M_{D_s} - M_D = 99 \pm 1$ MeV, while the corresponding value for the B mesons is $M_{B_s} - M_B = 90 \pm 3$ MeV. Here, the difference in each case depends on the light quark flavours and hardly at all on the heavy quark mass, which enters only as a small perturbation, of order Λ/M.

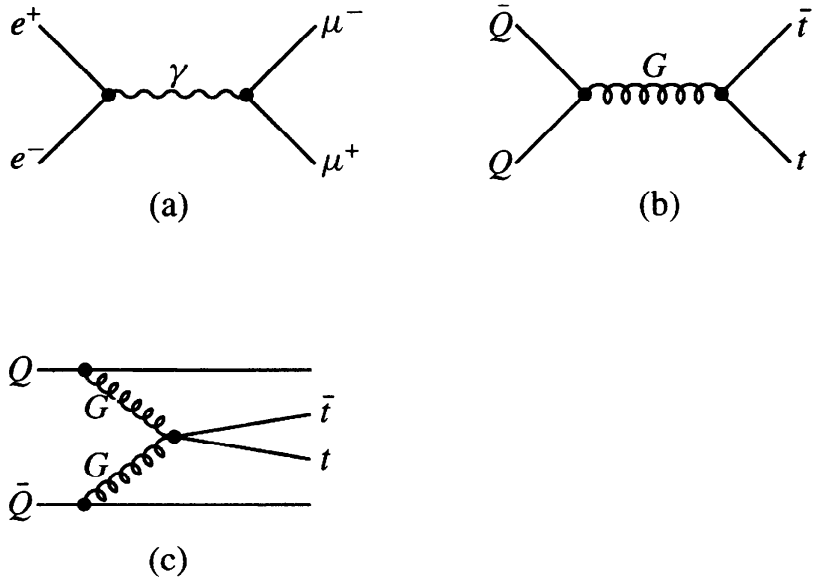

Fig. 4.19. (a) The process $e^+e^- \to \mu^+\mu^-$ via single-photon exchange: (b) the analogous process $Q\bar{Q} \to t\bar{t}$ via single-gluon exchange: (c) $t\bar{t}$ production via gluon fusion.

4.13 The top quark

The top quark, the sixth member of the three quark pairs listed in Table 4.1, was not observed until 1995, almost 20 years after the discovery in 1977 of the previously heaviest quark, the b quark. The top quark is unexpectedly massive, with $M \simeq 175$ GeV, and was finally discovered at the Fermilab $p\bar{p}$ collider with 1.8 TeV cms energy, being produced there in only about 1 in 10^{10} of all collisions. The experimental detection of the top quark is worth describing in some detail, not only because of its intrinsic importance but also because the detection methods had many features in common with practically all major detectors used at high energy $p\bar{p}$, e^+e^- and ep colliders.

Figures 4.19(b) and (c) show the dominant diagrams for the production of a $t\bar{t}$ quark–antiquark pair in a $p\bar{p}$ collision. After production, the pair is expected to undergo weak decay, predominantly in the mode

$$t\bar{t} \to W^+b + W^-\bar{b} \tag{4.43}$$

where, of course, the t quark mass exceeds that of the b quark and W boson. In this process, the b, $\bar{b}$ quarks will each generally fragment into a jet of hadrons, while the W's may decay into leptons ($W \to e\nu, \mu\nu, \tau\nu$) or into hadronic jets ($W \to Q\bar{Q}$). Thus, the detector must be capable of identifying charged leptons and hadrons and measuring their energies and directions in space. While the lifetimes of both t and W are unmeasurably short, B mesons formed from the b quarks have a lifetime 1.6×10^{-12} s, or $c\tau_B = 0.45$ mm. Thus the B decay may be identified as a secondary vertex separated from the main vertex of the primary collision. The

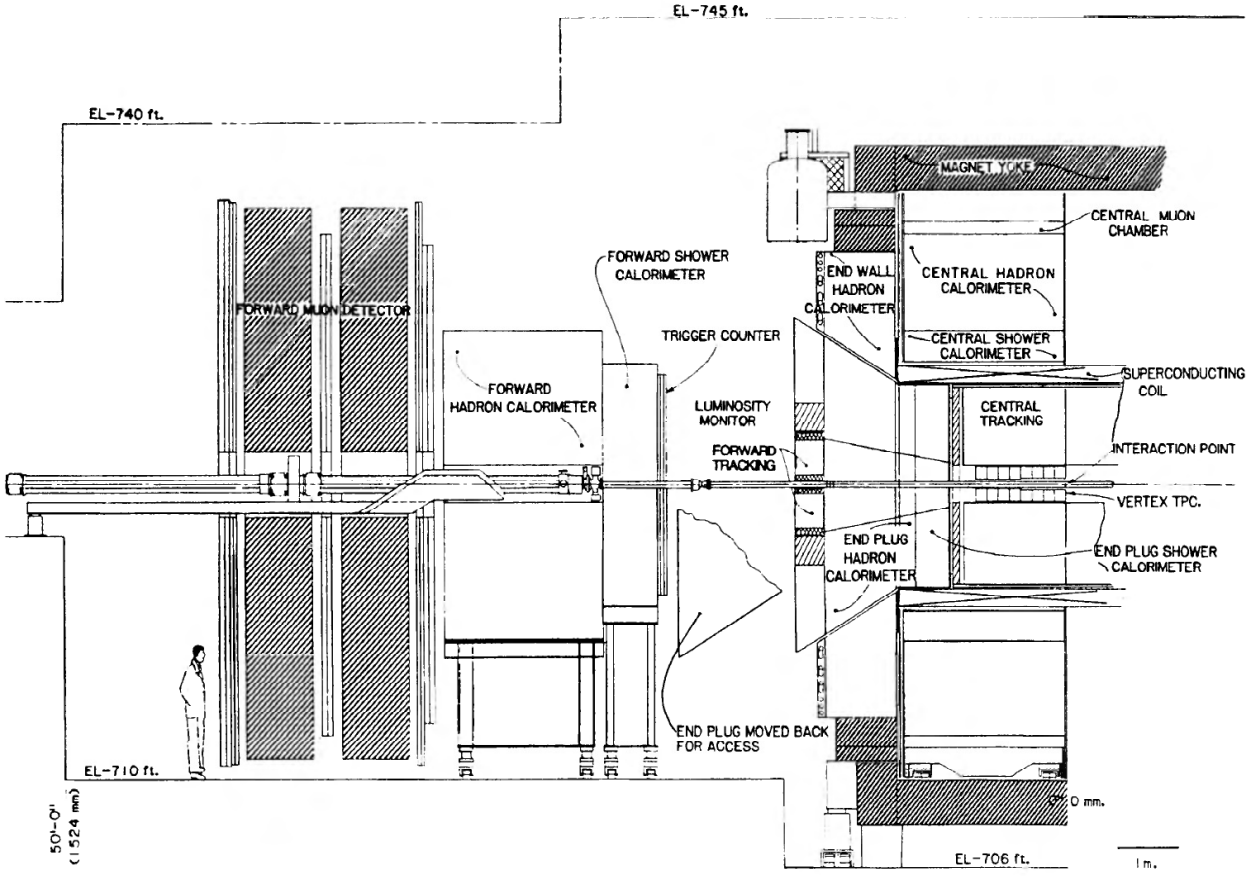

Fig. 4.20. Schematic drawing of one half of the CDF detector (the other half is a mirror image of that shown, about the interaction point at the right-hand side). The main features are: a superconducting solenoid surrounding drift chambers for tracking particles from the interaction point; electromagnetic and hadron showering calorimeter units, to identify and measure the energies of electrons (photons) and hadrons from total energy deposition: muon chambers to identify and measure the momenta of muons, via their penetration through iron and their magnetic deflection: and, close to the beam pipe, silicon strip detectors to give precision track trajectories and identify secondary vertices from B decay. The total length of the detector is 26 m, and the height is 10 m.

distance between the two vertices in a direction perpendicular to the beam axis is clearly $\Delta z = (p_T/m_B c)c\tau_B$ where p_T is the transverse momentum of the B meson. The kinematics of the decay $t \to Wb$ make for large values of p_T, and a transverse momentum cut is applied so that Δz is much larger than the transverse spread (~ 50 μm) of the colliding beams.

The observation of the t quark was made with two detectors, CDF (Abe *et al.* 1994, 1995) and D-zero (Abachi *et al.* 1995). Figure 4.20 shows a schematic drawing of the CDF detector. Basically this consists of a superconducting solenoid 5 m long by 3 m diameter, providing an axial field of 1.4 tesla and enclosing a cylindrical drift chamber to measure the coordinates and momenta of charged particles. Outside the coil is a finely segmented electromagnetic-shower detector and a hadronic-shower 'calorimeter' detector (see Section 11.7), to measure total energies of electrons, photons and hadrons. In turn, the calorimeters are enclosed by muon detectors consisting of iron absorber instrumented with drift

chambers. The overall detector is divided into three sections: a central unit covering particles at angles 10°–170° to the axis, and forward and backward regions to intercept secondaries within 10° of the beam. The secondaries of leptonic W decay ($W \rightarrow e\nu, \mu\nu$) include neutrinos, whose presence is inferred from the missing energy and transverse momentum. It is therefore important that the calorimeters have essentially 4π solid angle coverage, without cracks, so that an apparent missing energy signal is not due to any failure to detect all charged secondaries. Finally, high resolution silicon strip detectors are mounted around the beam pipe, to give precision measurements on particle trajectories close to the beam intersection point and allow the measurement of secondary vertices due to B decay. Figure 4.21 shows a photograph of the detector during assembly.

In the reaction (4.43), the process with lowest background is that in which both W's decay leptonically, $W \rightarrow e\nu$ or $W \rightarrow \mu\nu$. The di-lepton signature also requires two jets from the hadronic decay of the B mesons. Both leptons are required to have $p_T > 20$ GeV/c. From the measured energy and direction of a secondary particle i, a quantity called the transverse energy E_T, of magnitude $E_i \sin\theta_i$, can be constructed in space. The total transverse energy in the event is the sum $E_T = \sum_i (E_T)_i$. If all particles are detected $E_T = 0$, and the existence of an imbalance, or 'missing' transverse energy E_T(missing), is an indication of non-interacting secondaries (neutrinos). Thus another requirement is E_T(missing) > 25 GeV. Opposite charges for the leptons and isolation from other tracks are also required, as is the exclusion of events with $75 < M_{ee,\mu\mu} < 105$ GeV, in order to remove the background due to Z production and decay ($Z^0 \rightarrow \mu^+\mu^-, e^+e^-$).

A second selection of $t\bar{t}$ events was made, in which one W decays leptonically while the other decays to $Q\bar{Q}$ pairs (hadrons); this configuration has a 30% probability compared with only 5% for di-lepton events. The second selection thus requires one lepton plus $\geq$ three jets from W, B and $\bar{B}$ decays. The potentially greater background is reduced by requiring at least one distinct secondary vertex from B decay. Yet a third selection was of events with one 'hard' lepton ($p_T >$ 20 GeV/c) from W decay, $\geq$ three jets from W or B decay and a 'soft' lepton ($p_T > 2$ GeV/c) from leptonic B decay.

In the first experimental runs of the two detectors together, a total of 12 (di-lepton plus two-jet) events were observed, against a calculated background of 2.5 events; some 86 events had a single hard lepton and at least three jets, plus a secondary vertex or soft additional lepton, against a background of 37 events. The fitted mass from these events was $m_t = 180 \pm 12$ GeV. As indicated in Chapter 8, the value of m_t deduced from radiative corrections to the electroweak model is in amazingly good agreement with this direct measurement.

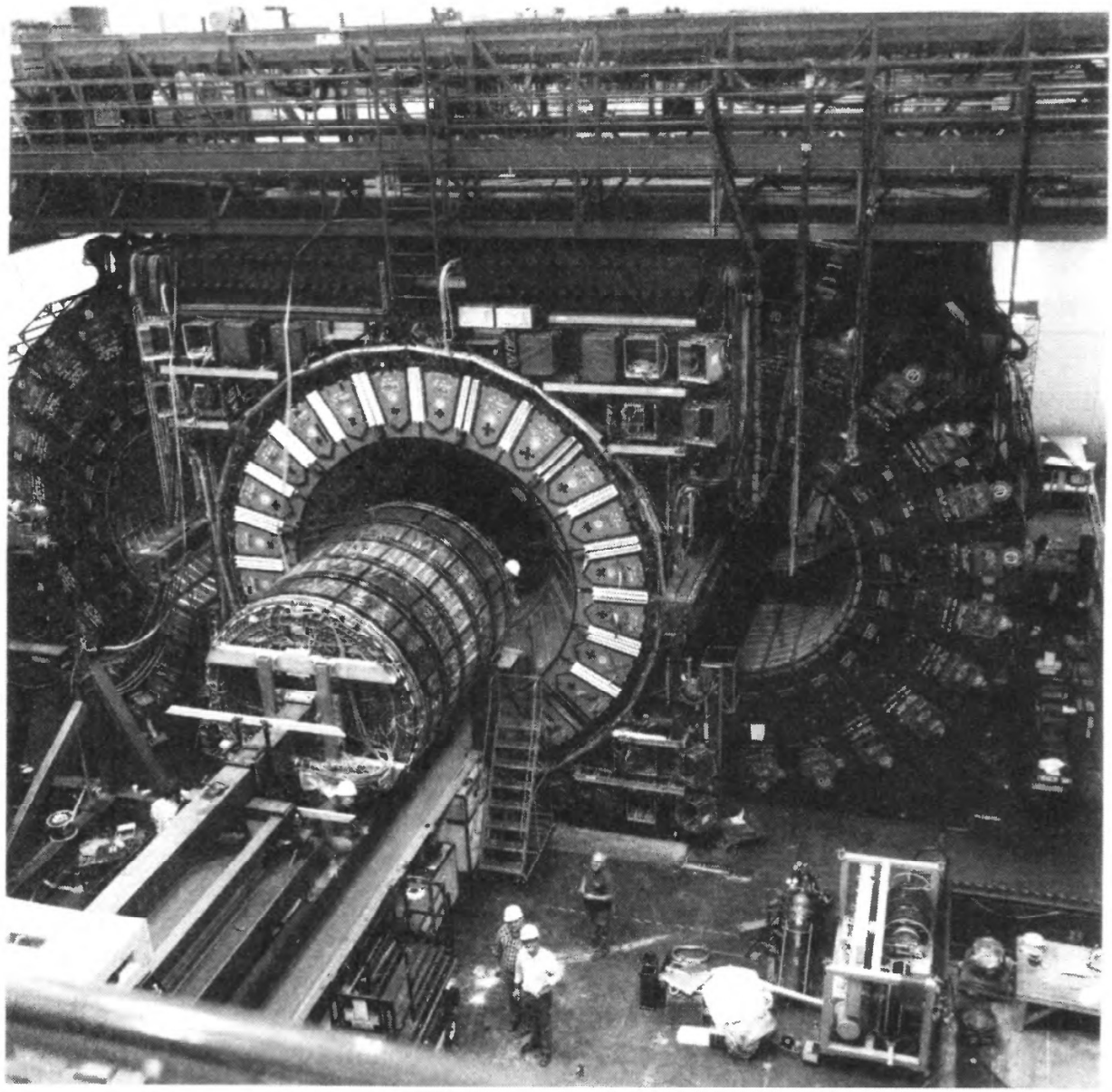

Fig. 4.21. Central part of the CDF detector during assembly, with calorimeter arches retracted and the central tracking detector (drift chamber) about to be installed in the solenoid (courtesy Fermilab Visual Media Services).

From the known momentum distribution of the quarks and antiquarks in the colliding protons and antiprotons (see Section 6.6) it should be possible to calculate the $t\bar{t}$ production cross-section as a function of m_t. Here we just try to get a rough estimate of the numbers involved. Figures 4.19(a) and (b) show the analogous processes $e^+e^- \to \mu^+\mu^-$ and $Q\bar{Q} \to t\bar{t}$. The first goes (to leading order) via single-photon exchange and the second by single-gluon exchange. As shown in (5.5a), in the extreme relativistic limit

$$\sigma(e^+e^- \to \mu^+\mu^-) = \frac{4\pi\alpha^2}{3s} \tag{4.44}$$

where $s = (\text{cms energy})^2 \gg 4m_\mu^2$. So we expect that

$$\sigma(Q\bar{Q} \to t\bar{t}) = \frac{4\pi\alpha_s^2}{3\hat{s}}\frac{2}{9} \tag{4.45}$$

where $\hat{s}$ is the squared quark–antiquark cms energy, α_s is the strong quark–gluon coupling and $\frac{2}{9}$ is a factor due to colour. If the t and $\bar{t}$ are not extreme relativistic – and they are certainly not at 1.8 TeV $p\bar{p}$ cms energy – there is a correction factor, of order 0.75 (see (5.5b), with m_μ replaced by m_t), which we shall just ignore. It is easy to show that, if s is the squared cms energy in the $p\bar{p}$ collision, the threshold for $t\bar{t}$ production is given by

$$x_1 x_2 = \frac{\hat{s}}{s} \geq \frac{4m_t^2}{s} \tag{4.46}$$

where x_1 and x_2 are the fractional momenta of the proton (and antiproton) carried by the quark (and antiquark) involved. To find the $t\bar{t}$ cross-section, one has to integrate (4.45) numerically over the quark densities $f(x_1)$, $f(x_2)$, subject to the condition (4.46). For guidance, let us just take $\hat{s} = 4m_t^2$ and $\alpha_s = 0.10$ (from Figure 6.12), when we find, with $m_t = 0.18$ TeV,

$$\sigma(p\bar{p} \to t\bar{t}) = 0.07F \text{ TeV}^{-2} = 28F \text{ pb} \tag{4.47}$$

where we have used the fact that, in units $\hbar = c = 1$, $1 \text{ TeV}^{-1} = 1.97 \times 10^{-17}$ cm and $1 \text{ pb} = 10^{-36} \text{ cm}^2$. The quantity F is the probability that in the proton and antiproton the u and $\bar{u}$ quarks have $x_1 x_2 s > 4m_t^2$ or $x_1 x_2 > 0.04$ for the Fermilab collider. Judging from measured quark density distributions in the nucleon (see for example Figure 5.14) one can guess therefore that the cross-section will be a few pb. One also has to include another, less important, diagram shown in Figure 4.19(c) of $t\bar{t}$ production via gluon fusion. A full calculation gives $\sigma \simeq 6$ pb, in excellent agreement with the value, $\sigma(t\bar{t}) = 7.6 \pm 2.2$ pb, actually measured.

Finally, we remark that the top quark is unique in that, unlike all the other quarks, it is massive enough to decay to a real W boson. On dimensional grounds, it is then expected that $\Gamma(t \to bW) \sim Gm_t^3$; the large value of m_t in fact results in a calculated width $\Gamma \simeq 1.4$ GeV. The decay time $\hbar/\Gamma$ is therefore much shorter than the typical timescale of hadronic interactions, of order $\hbar/\Lambda$ where $\Lambda \simeq 0.2$ GeV. In particular, the $t\bar{t}$ interaction will be determined mostly by single-gluon exchange, without the second confinement term in (4.9). The $t\bar{t}$ system is so short-lived that no discrete bound states, such as are met with in charmonium and bottomonium, have time to form.

Problems

4.1 Show that the additive quark model predicts the following cross-section relations:

$$\sigma(\Lambda p) = \sigma(pp) + \sigma(K^- n) - \sigma(\pi^+ p)$$
$$\sigma(\Sigma^- p) = \sigma(pp) + \sigma(K_p) - \sigma(\pi^- p) + 2[\sigma(K^+ n) - \sigma(K^+ p)]$$
$$\sigma(\Sigma^- n) = \sigma(pp) + \sigma(K^- p) - \sigma(\pi^- p)$$

4.2 Discuss the possible decay modes of the Ω^- hyperon allowed by the conservation laws, and show that weak decay is the only possibility.

4.3 Evaluate $|\psi(0)|^2$ in (4.30) from the typical size of a hadron, and hence estimate the absolute values of the leptonic widths of the vector mesons ρ, ω, ϕ.

4.4 Verify the expressions for the magnetic moments of baryons in Table 4.12. The magnetic moments of the proton and neutron, as well as certain combinations of those of the hyperons, will depend only on the magnetic moments of the u and d quarks. Assuming each has one third of the mass of the nucleon, calculate the baryon moments (or those combinations of baryon moments that do not depend on the moment of the s quark) and compare with the experimental values.

The anomalous moments of the proton and neutron are nearly equal in magnitude but opposite in sign. Show how this result was originally explained (before the advent of quarks) by considering the nucleon to consist for part of the time as a Dirac (pointlike) nucleon and for the rest of the time as a pointlike core with a charged circulating pion in a P-state, contributing to the overall moment as a circulating current.

4.5 The state $J/\psi(3100)$ has a full width $\Gamma = 87$ keV and 88% of the decays are to a hadronic final state. Assume that the hadronic decay proceeds via three gluons, $\psi \to 3G$, with a rate given by the same formula as that for triplet positronium decay (4.8), but with $\frac{4}{3}\alpha_s$ replacing α. Estimate a value for α_s from this data.

4.6 The radiative decay $\Upsilon(9460) \to \gamma +$ hadrons has a branching ratio of about 0.3%. The total width of the Υ is 53 keV. Using the same approach as in Problem 4.5 estimate a value for α_s, assuming that radiative decays proceed via $\Upsilon \to GG\gamma$.

4.7 The 1^3S_1–1^1S_0 level separations in the ground states of the hydrogen atom, positronium e^+e^- and muonium μ^+e^- are proportional to the product of the magnetic moments of the fermions involved. From the transition frequency (1420 MHz) in hydrogen, calculate that in muonium and compare with the experimentally observed value (4463.30 MHz). For positronium, an extra factor $\frac{7}{16}$ is present because of the contribution from an annihilation diagram not present in the other systems. Remembering to allow for the reduced-mass-effects, calculate the value of the splitting in positronium and compare with the result in Table 4.4. (Your calculation should be within 1% of the observed value; what is the reason for any discrepancy?)

5

Lepton and quark scattering

A dynamical (rather than a static) understanding of quark substructure had its origins in the late 1960s, when new evidence for quarks started to come from experiments on deep inelastic lepton–nucleon scattering. These showed that the complicated process of leptoproduction of many hadrons in such collisions could be simply interpreted as elastic scattering of the lepton by a pointlike (or nearly pointlike) constituent of the nucleon, soon to be identified as a quark. Furthermore, the analysis of precise and detailed lepton–nucleon scattering experiments gave the first information on the nature of quark–quark interactions. This evidence was soon reinforced and greatly strengthened and enlarged by studies of e^+e^- annihilation to hadrons at high energy.

So much for history. We shall not proceed in historical fashion, but consider first the evidence from e^+e^- annihilation, starting with the simpler process $e^+e^- \to \mu^+\mu^-$.

5.1 The process $e^+e^- \to \mu^+\mu^-$

The annihilation process $e^+e^- \to \mu^+\mu^-$ is considered as an electromagnetic interaction mediated by single-photon exchange. The annihilation diagram is shown in Figure 5.1(b). First let us neglect the effects of spin. Then from (2.6) the matrix element to first order in α is

$$M_{if} = \frac{e^2}{q^2} = \frac{4\pi\alpha}{q^2} \tag{5.1}$$

The quantity q^2 is the squared 4-momentum of the virtual photon, i.e. $q^2 = -E_0^2 = -s$, where s denotes the square of the total energy in the centre-of-momentum (cms) frame, in which the net 3-momentum is zero. We assume this energy is so large that the electron and muon masses can be neglected in comparison. Then the relative velocities in the initial and final states are $v_i = v_f = 2c$ and $E_0 = 2p_f c$,

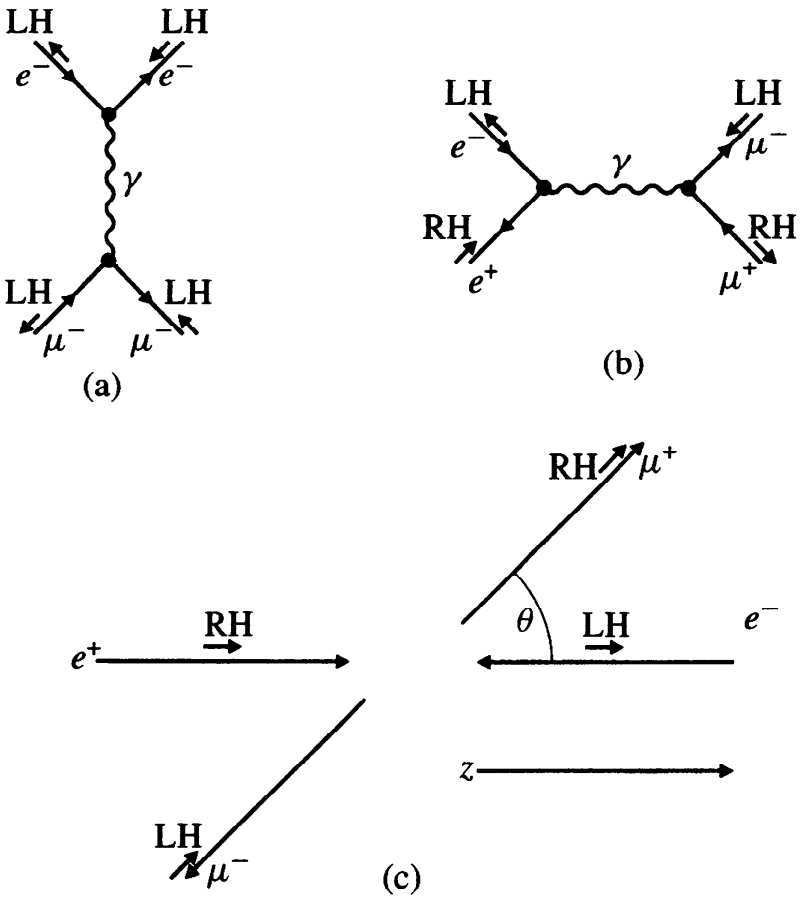

Fig. 5.1. (a) Diagram for electron–muon scattering via single-photon exchange. In the relativistic limit, the helicity (LH in the case shown) is preserved for each particle. (b) If outgoing particles are replaced by incoming antiparticles, only particles of opposite helicities (LR or RL) are coupled in the annihilation process $e^+e^- \to \mu^+\mu^-$. (c) The annihilation process viewed in the cms.

where p_f is the cms momentum of either particle. Inserting these quantities and (5.1) into (2.19), we obtain, in units $\hbar = c = 1$

$$\frac{d\sigma}{d\Omega} = \frac{\alpha^2}{4s} \tag{5.2}$$

Now we have to sum over final-state spins and average over those in the initial state. From Section 1.6 we know that in a vector or axial vector interaction between extreme relativistic particles helicity is conserved. Thus, in the scattering of an electron, $e_L^- \to e_L^-$ and $e_R^- \to e_R^-$; see e.g. Figure 5.1(a). The process for e^-e^+ is represented by the crossed diagram, obtained by replacing the outgoing electron in Figure 5.1(a) by an ingoing positron with the opposite helicity, as in Figure 5.1(b). Thus for example e_L^- and e_R^+ are coupled, but not e_L^- and e_L^+.

Figure 5.1(c) shows the collision in the cms, with the z-axis defining the incident direction. Clearly the initial state is either the combination RL with $J_z = +1$ or LR

with $J_z = -1$, so that the exchanged photon is transverse.† Equally the final state can be RL or LR. For the RL combination in both the initial and final states (where the first symbol, R, refers to the positively charged lepton), let θ be the angle of emission of the $\mu^+\mu^-$ pair with respect to the z-axis. The probability amplitude for this pair to have $J_z = +1$, as in the initial state, is given by the d-function (see Appendix C):

$$A_{RL\to RL} = d^J_{m,m'}(\theta) = d^1_{1,1}(\theta) = \frac{1+\cos\theta}{2} \tag{5.3a}$$

If we started with an e^+e^- combination LR, with $J_z = -1$, that goes to final state RL then we would need to replace θ, defined relative to the positive z-direction, by $\pi - \theta$, so the amplitude is then

$$A_{LR\to RL} = d^1_{1,-1}(\theta) = \frac{1-\cos\theta}{2} \tag{5.3b}$$

Squaring and summing these orthogonal states, which by parity conservation must have equal intensity, we get for the angular dependence

$$P(\theta) = \frac{1+\cos^2\theta}{2} \tag{5.3c}$$

Finally, we sum over the final spin states (four in number) and average over the initial spins involved (two in number, out of a possible four). In other words, to include the cases RL $\to$ LR and LR $\to$ LR, we have to double (5.3c), so that the differential cross-section becomes from (5.2)

$$\frac{d\sigma}{d\Omega}(e^+e^- \to \mu^+\mu^-) = \frac{\alpha^2}{4s}(1+\cos^2\theta) \tag{5.4}$$

Integration over angle, with $d\Omega = 2\pi d(\cos\theta)$, then gives

$$\sigma(e^+e^- \to \mu^+\mu^-) = \frac{4\pi\alpha^2}{3s} \tag{5.5a}$$

This cross-section, we must emphasise, applies to pointlike leptons annihilating via single-photon exchange, at energies where the lepton masses can be neglected. Numerically, the cross-section (5.5a) has the value 86.8 nb/s (GeV^2).

Perhaps, for completeness, we should state here that, if the muon mass is not neglected, the effect is to multiply (5.5a) by the factor

$$(1+z/2)\sqrt{1-z} \tag{5.5b}$$

where $z = 4m_\mu^2/s$. The square root factor allows for the reduction in the phase space available to the final-state muons (giving zero at the threshold $z = 1$), while

† A transverse photon has the associated **E** and **B** field vectors perpendicular to each other and to the 3-momentum vector **k**. Transverse photons are a superposition of $J_z = +1$ and $J_z = -1$ spin substates of equal amplitude.

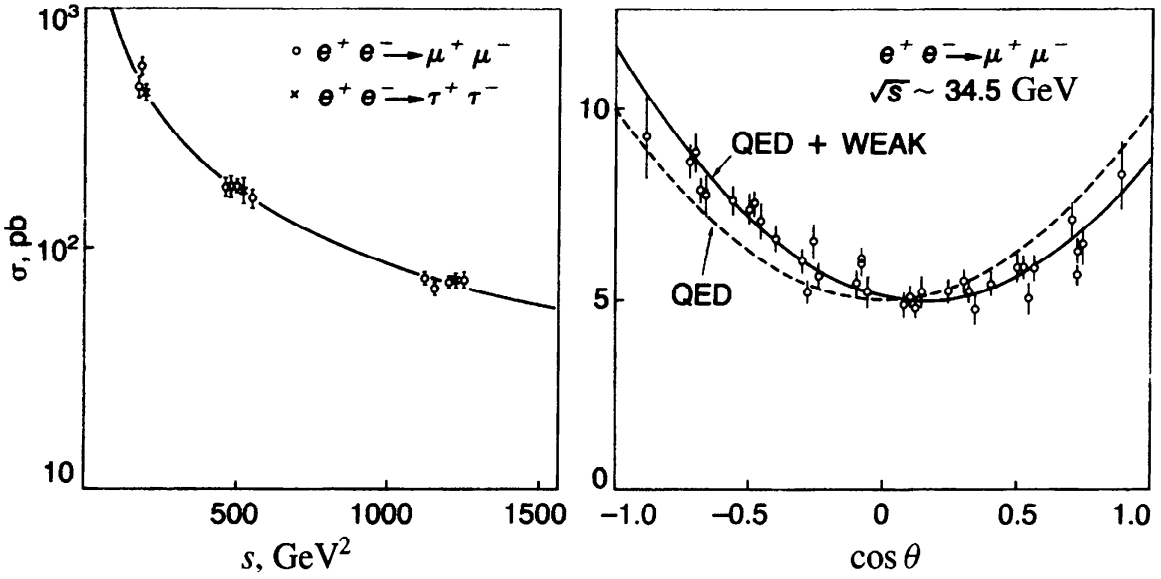

Fig. 5.2. Results on total and differential cross-sections for $e^+e^- \to \mu^+\mu^-$ and $e^+e^- \to \tau^+\tau^-$ from the PETRA collider at DESY. The curve on the left shows the QED prediction for the total cross-section, on which neutral currents due to Z^0 exchange have small and unmeasurable effects. On the right is given the cms angular distribution. The broken curve shows the pure QED prediction (5.4), while the solid curve indicates the small forward–backward asymmetry expected from the combination of Z^0 and γ exchange.

the factor in parentheses allows for the extra 'wrong' helicity amplitude that enters when the muons are not extreme relativistic. The product of these two factors varies between 0 and 1 but always lies between 0.95 and 1 for $s > 10m_\mu^2$. The experimental data on the total and differential cross-sections at high energy for the processes $e^+e^- \to \mu^+\mu^-$ and $e^+e^- \to \tau^+\tau^-$ are shown in Figure 5.2. The total cross-section is in good accord with the prediction (5.5a). The angular distribution has the general $1 + \cos^2\theta$ form (5.4), but with a marked backward–forward asymmetry. This arises because, in addition to the photon-exchange diagram, there is also a parity-violating weak amplitude arising from Z^0 exchange, which we have neglected in our calculation (see Figure 8.6). Since the weak matrix element is of order G, the Fermi constant, compared with $4\pi\alpha/s$ for the electromagnetic matrix element in (5.1), the γ–Z^0 interference term is expected to make a relative contribution of magnitude $f = a_{\text{weak}}a_{\text{em}}/a_{\text{em}}^2$, i.e.

$$f \sim Gs/(4\pi\alpha) \sim 10^{-4}s$$

where s is in GeV^2 and $G \simeq 10^{-5}$ GeV^{-2}. Thus the expected asymmetry $(B - F)/(B + F) = f \simeq 10\%$ at $s = 1000$ GeV^2, as observed. Such asymmetries are important tests of the electroweak theory, as discussed in detail in Chapter 8.

5.2 e^+e^- annihilation to hadrons

Figure 2.5 shows the reconstruction of an event recorded at the e^+e^- collider PETRA at the DESY laboratory. Charged and neutral mesons are produced and appear in the form of two oppositely directed 'jets'. These are interpreted as due to a two-stage process involving the production and subsequent 'fragmentation' of a quark–antiquark pair:

$$e^+e^- \to Q\bar{Q}, \qquad Q, \bar{Q} \to \text{hadrons} \tag{5.6}$$

The cross-section for this process as a function of cms energy is shown in Figure 5.3. One observes a general fall-off of the cross-section as $1/s$, just as in the case $e^+e^- \to \mu^+\mu^-$, with peaks due to various boson resonances (e.g. ρ, J/ψ, Υ, Z^0). The evidence for the process (5.6) becomes even more apparent upon plotting the cross-section ratio

$$R = \frac{\sigma(e^+e^- \to \text{hadrons})}{\sigma(\text{point})} \tag{5.7}$$

where σ(point) is the cross-section (5.5); see Figure 5.4. We see that over large ranges in collision energy, R is constant. The results shown in Figures 5.3 and 5.4 mean that the annihilation of e^+e^- to hadrons must proceed as a *pointlike* process, as does $e^+e^- \to \mu^+\mu^-$.

The magnitude of R is easily calculated if the pointlike constituents are taken to be quarks, acting independently. In the crossed channel of electron–quark scattering, the cross-section will be proportional to $\sum e_i^2$, the square of the quark charges summed over all the contributing quark flavours i. Replacing incoming (outgoing) fermions by outgoing (incoming) antifermions for the process $e^+e^- \to Q\bar{Q}$ we obtain

$$R = \frac{\sum e_i^2}{1} \tag{5.8}$$

At low s-values, below the $c\bar{c}$ threshold, only u, d, s quarks are involved and thus we expect

$$R_{\text{th}}(\sqrt{s} < 3\ \text{GeV}) = \left(\tfrac{1}{3}\right)^2 + \left(\tfrac{1}{3}\right)^2 + \left(\tfrac{2}{3}\right)^2 = \tfrac{2}{3} \tag{5.9}$$

while at high s-values, where u, d, s, c, b quarks can contribute, we expect

$$R_{\text{th}}(\sqrt{s} > 10\ \text{GeV}) = \left(\tfrac{1}{3}\right)^2 + \left(\tfrac{1}{3}\right)^2 + \left(\tfrac{1}{3}\right)^2 + \left(\tfrac{2}{3}\right)^2 + \left(\tfrac{2}{3}\right)^2 = \tfrac{11}{9} \tag{5.10}$$

It is obvious from Figure 5.4 that these predictions are a long way below the data, and indeed this conflict was one of the primary reasons for introducing the *colour* degree of freedom mentioned in Section 2.7. Quarks are endowed with three possible values of the strong colour charge: a common choice is red, green and blue (r, g, b). Antiquarks are assigned the corresponding anticolour. Thus, any given

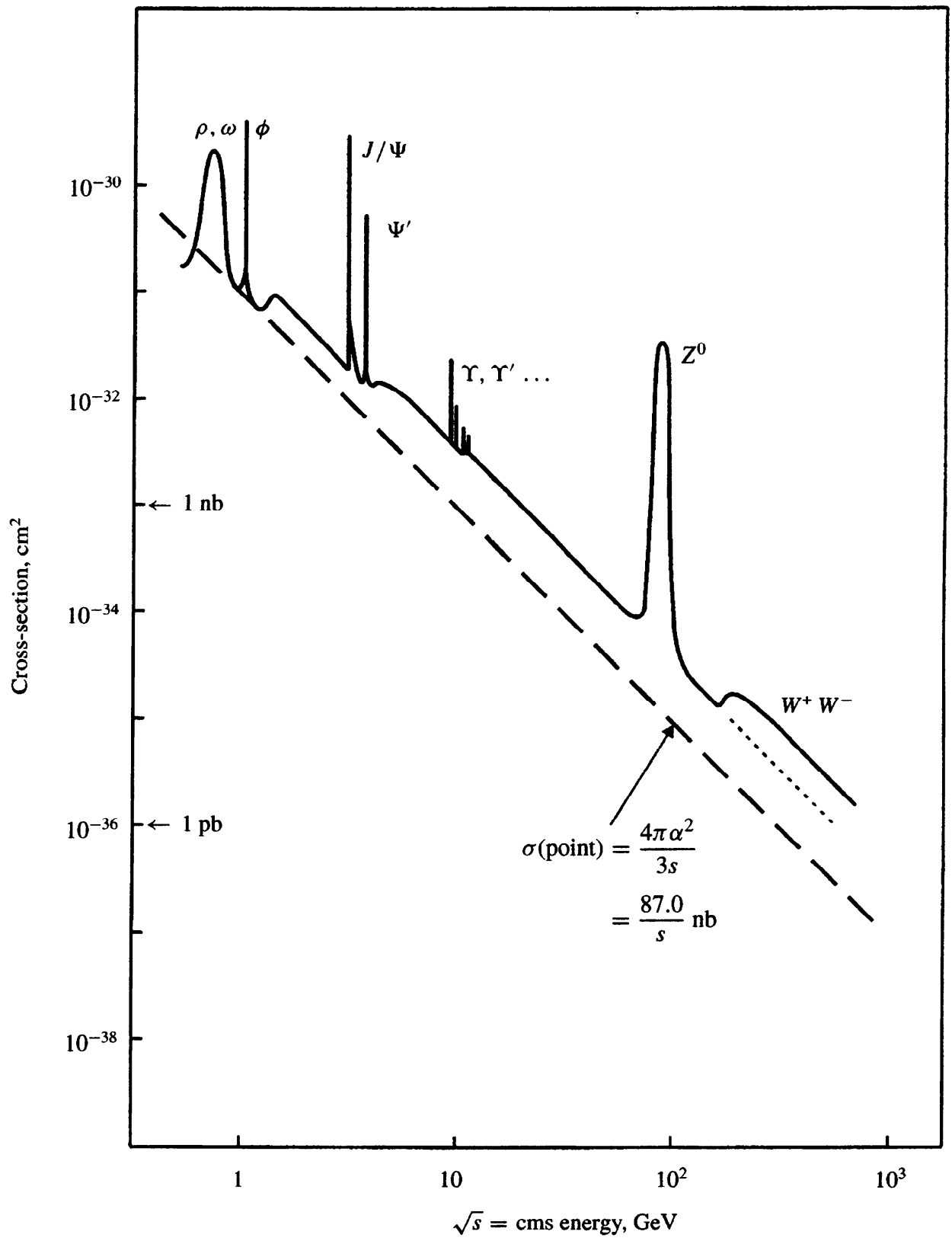

Fig. 5.3. The cross-section σ for the annihilation process $e^+e^- \rightarrow$ anything, as a function of cms energy. The prominent peaks are due to various boson resonances, but the general $1/s$ dependence of the cross-section, typical of a pointlike process, is clear.

$Q\bar{Q}$ flavour combination occurs in three substates $r\bar{r}$, $g\bar{g}$ and $b\bar{b}$, and the expected R-values must be multiplied by a factor 3, in good agreement with experiment.

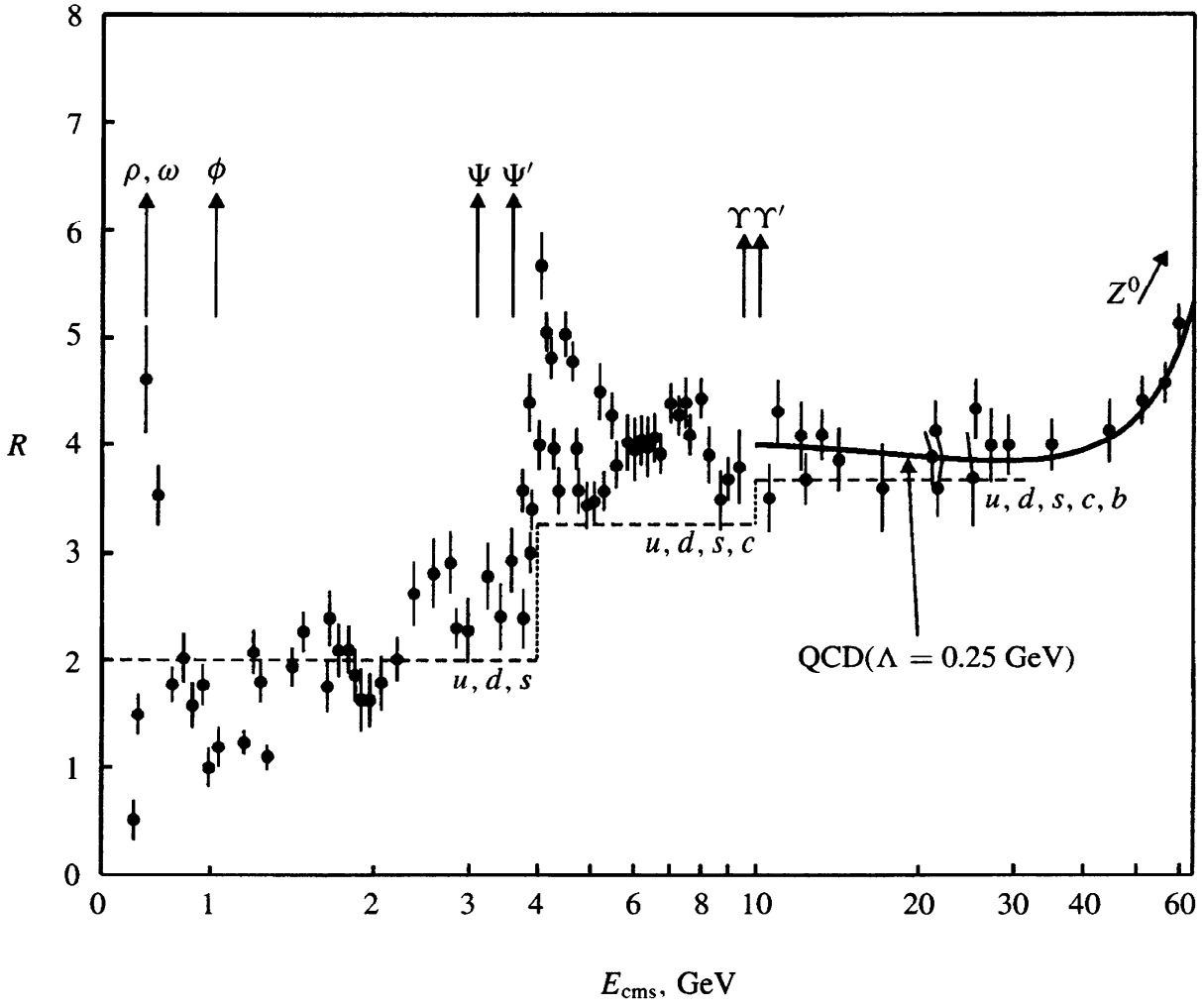

Fig. 5.4. The ratio R of the cross-section in Figure 5.3 to the pointlike cross-section (5.5a), $R = \sigma(e^+e^- \to \text{hadrons}/\sigma(\text{point}))$. The 'steps' in R correspond to excitation of various quark quantum numbers. The QCD correction to R is discussed in Section 6.5.

At high energies, it is observed that the hadrons from the process $e^+e^- \to Q\bar{Q} \to$ hadrons are collimated into two oppositely directed 'jets', and presumably the jet axis must be approximately the axis of emission of the primary $Q\bar{Q}$ pair. The angular distribution in the process $e^+e^- \to Q\bar{Q}$ will depend on the spin of the quark constituents. Again, in the prototype process $e^+e^- \to \mu^+\mu^-$ involving spin $\frac{1}{2}$ particles, the angular distribution has the form (see (5.4)):

$$\frac{dN}{d\Omega} \propto 1 + \cos^2\theta$$

where θ is the angle between the $\mu^\pm$ and beam directions. Figure 5.5 shows the results for the angular distributions in the process $e^+e^- \to$ two hadron jets; it is indeed consistent with that expected for spin $\frac{1}{2}$ quark constituents.

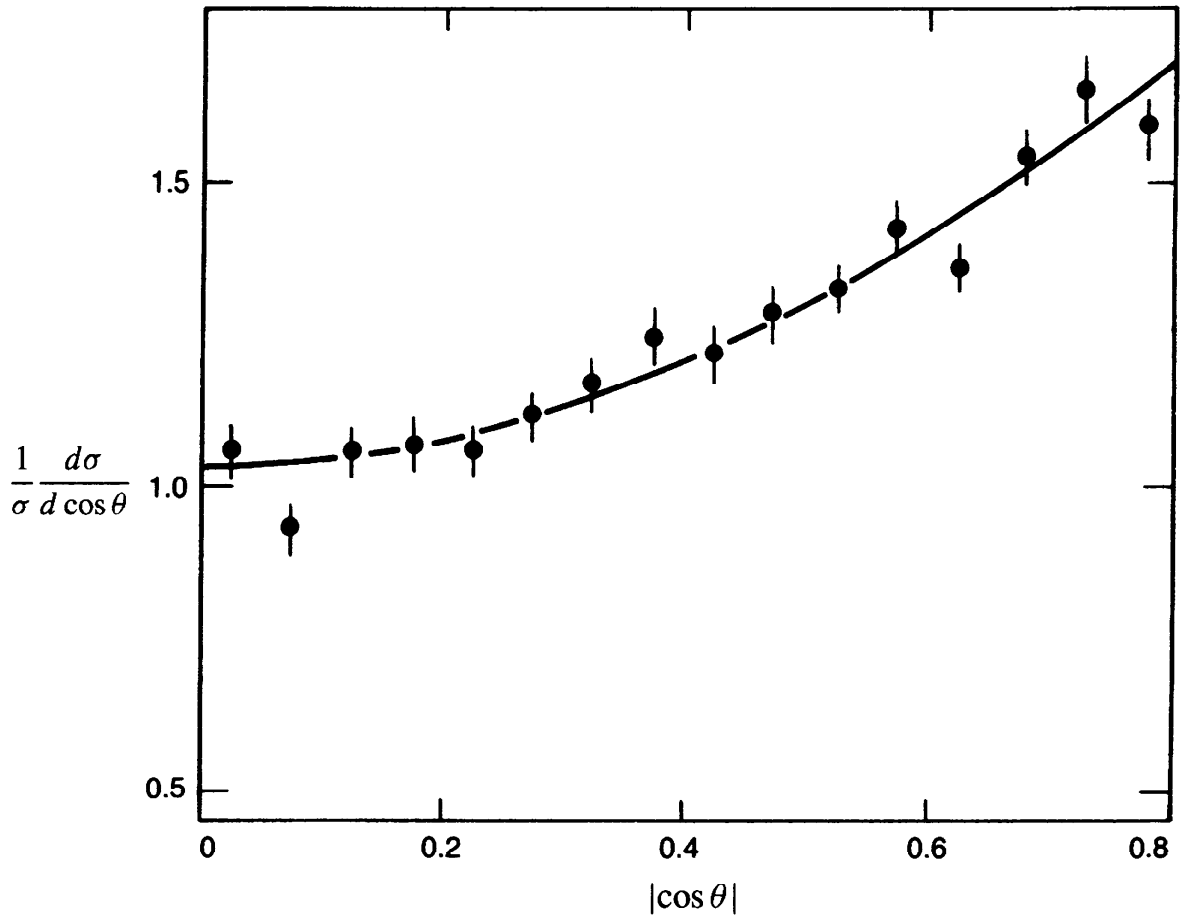

Fig. 5.5. Centre-of-momentum angular distribution of the two hadron jets (as in Figure 2.5) relative to the beam axis in e^+e^- annihilation at cms energy $W = 34$ GeV. The data are consistent with a $1 + \cos^2\theta$ distribution, as expected if the fundamental process is $e^+e^- \to Q\bar{Q}$. Since it is not possible to say which jet corresponds to Q and which to $\bar{Q}$, only half the angular distribution can be plotted. The asymmetry visible in Figure 5.2 is therefore not apparent.

To summarise the results from the process $e^+e^- \to$ hadrons:

(i) The constancy of R is evidence for the pointlike (parton) constituents of hadrons.

(ii) The angular distribution of the two hadron jets is proof of spin $\frac{1}{2}$ for the partons.

(iii) The value of R is equal to that expected if the charged partons are quarks, with fractional charges and the colour quantum number.

5.3 Electron–muon scattering, $e^-\mu^+ \to e^-\mu^+$

As a preliminary to discussing lepton–nucleon scattering, we consider first the simpler process of pointlike electromagnetic scattering, as exemplified by $e^-\mu^+ \to e^-\mu^+$. Let us first recall the results of the crossed process $e^+e^- \to \mu^+\mu^-$ in equation (5.4). Denoting the 4-momenta of the particles involved by k_1, k_2, k_3,

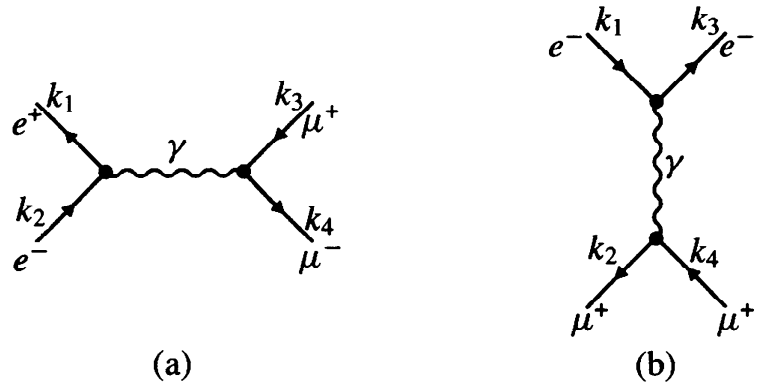

Fig. 5.6. (a) The 4-momenta of the leptons involved in the annihilation process $e^+e^- \to \mu^+\mu^-$; (b) the 4-momenta involved in the crossed diagram for $e^-\mu^+ \to e^-\mu^+$, related to those in (a) by the substitution $k_3 \leftrightarrow -k_2$.

k_4, as in Figure 5.6(a), we can express the cross-section in terms of relativistic invariants, known as the *Mandelstam variables* s, t, u. These are, respectively, the cms energy squared, the 4-momentum transfer squared and the crossed momentum transfer squared, defined as follows:

$$\begin{aligned} s &= -(k_1 + k_2)^2 = -(k_3 + k_4)^2 = -2k_1k_2 = -2k_3k_4 \\ t &= q^2 = (k_1 - k_3)^2 = (k_2 - k_4)^2 = -2k_1k_3 = -2k_2k_4 \\ u &= (k_2 - k_3)^2 = (k_1 - k_4)^2 = -2k_2k_3 = -2k_1k_4 \end{aligned} \tag{5.11}$$

In the final expressions on the right, the lepton rest masses have been neglected, i.e. we have taken $k^2 = 0$. The variables s, t and u defined here are all positive quantities. They are not independent; in fact $s - t - u = \sum m^2$, the sum of the squared masses of the particles involved. If we neglect the masses, $s = u + t$.

Evaluating these quantities in the cms (see Figure 5.1(c)), in which the 3-momentum of each particle has magnitude p and the angle between the e^- and μ^- lines of flight is θ,

$$\begin{aligned} s &= 4p^2 \\ t &= q^2 = 2p^2(1 - \cos\theta) = 4p^2 \sin^2(\theta/2) \\ u &= 2p^2(1 + \cos\theta) = 4p^2 \cos^2(\theta/2) \end{aligned} \tag{5.12}$$

In terms of the Mandelstam variables the annihilation cross-section (5.4) becomes

$$\frac{d\sigma}{d\Omega}(e^+e^- \to \mu^+\mu^-) = \frac{\alpha^2}{8p^2}\left(\frac{t^2 + u^2}{s^2}\right) \tag{5.13}$$

By crossing symmetry, the scattering process in Figure 5.6(b) can be obtained from the annihilation process of Figure 5.6(a) simply by replacing an incoming e^+ by

an outgoing e^- and an outgoing μ^+ by an incoming μ^-, and rotating the entire diagram through 90°. Thus $q = k_1 + k_2$ in Figure 5.6(a) is replaced by $q = k_1 - k_3$ in Figure 5.6(b), since k_2 replaces $-k_3$; this amounts to the interchange $s \to -t$ in (5.11), so that from (5.13) the scattering cross-section will be, using (5.12),

$$\frac{d\sigma}{d\Omega}(e^-\mu^+ \to e^-\mu^+) = \frac{\alpha^2}{8p^2}\left(\frac{s^2+u^2}{t^2}\right)$$
$$= \frac{\alpha^2}{8p^2\sin^4(\theta/2)}[1+\cos^4(\theta/2)] \qquad (5.14)$$

In making the substitution $k_2 \to -k_3$ described above, to transform from the annihilation process to the scattering process, the 4-momentum of the virtual photon has changed from being *timelike*, i.e. $q = k_1 + k_2$ and $q^2 = -s < 0$, to *spacelike*, i.e. $q = k_1 - k_3$ with $q^2 = t > 0$.†

Equation (5.14) is the prediction from quantum electrodynamics (QED) to leading order in the coupling and is valid, we emphasise, for the case where the lepton masses may be neglected in comparison with the momenta involved. All quantities refer to cms variables. It is also useful to express the cross-section in terms of laboratory quantities, i.e. those measured in the rest frame of the target muon. Suppose E_e is the incident electron energy in the laboratory system (LS) and E_μ that of the recoiling muon after the collision. If γ is the Lorentz factor of the cms in the laboratory, then the Lorentz transformations in Section 1.1 give, in terms of the cms quantities p and θ (where θ denotes the angle with respect to the x-axis):

$$E_\mu = \gamma p(1-\cos\theta), \qquad E_e = 2\gamma p, \qquad y = \frac{E_\mu}{E_e} = \frac{1-\cos\theta}{2} \qquad (5.15)$$

where $0 < y < 1$. Then

$$\cos^2\frac{\theta}{2} = \frac{1+\cos\theta}{2} = 1-y$$
$$d\Omega = 2\pi d(\cos\theta) = 4\pi dy$$

Hence (5.14) becomes, in terms of the fraction y of the incident electron's energy acquired by the recoil muon,

$$\frac{d\sigma}{dy}(e^-\mu^+ \to e^-\mu^+) = \frac{2\pi\alpha^2 s}{q^4}[(1+(1-y)^2] \qquad (5.16)$$

where $s = 4p^2$ is the squared total cms energy, which in the laboratory system will have the value $s = 2m_\mu E_e + m_\mu^2 + m_e^2 \simeq 2m_\mu E_e$. The two terms, 1 and $(1-y)^2$

† This is our convention. In most texts on field theory, however, the sign of q^2 is reversed, i.e. $q^2 > 0$ is timelike and $q^2 < 0$ is spacelike.

in the square bracket correspond to scattering between particles of the same and opposite helicities respectively. From (5.12), it is easy to show that $y = q^2/(4p^2)$. Thus we note that as $y \to 0$, i.e. the muon recoil energy becomes small, the above formula reverts to the small-θ approximation

$$\frac{d\sigma}{dq^2}(y \to 0) = \frac{16\pi\alpha^2}{q^4} p^2 \frac{dy}{dq^2} = \frac{4\pi\alpha^2}{q^4} \tag{5.17}$$

which is the famous Rutherford formula for the case where spins can be neglected.

The y-distribution in (5.16) is typical of the scattering between two spin $\frac{1}{2}$ particles. For scattering of an electron by a particle of spin 0, the y-distribution would have the form $1-y$ instead of $[1+(1-y)^2]$; see Problem 5.9. This is known as *Mott scattering*. The difference is in the absence of any spin–spin (magnetic as opposed to electric or Coulomb) scattering. Magnetic-moment scattering involves a flip-over of the two spins which, because of helicity conservation, is a maximum in the backward direction, $\theta = \pi$ and $y = 1$.

Measurement of the scattering of an electron by a muon – which has a lifetime of only 2.2 microseconds – is obviously impractical. We have taken this case merely as an example of the scattering of two pointlike fermions via photon exchange. The serious application is to the scattering of electrons by quarks, which we discuss in Section 5.5 below.

5.4 Neutrino–electron scattering, $\nu_e e \to \nu_e e$

As another preliminary to our discussion of deep inelastic lepton–nucleon scattering, we consider the pointlike scattering of neutrinos by charged leptons, which is an example of a weak interaction. Specifically, let us consider the scattering of ν_e by e via $W^{\pm}$ exchange, as in Figure 5.7(a). Here, we use g to denote the weak coupling of the W boson to the leptons. In fact, νe scattering will receive a contribution from Z^0 exchange as well as from $W^{\pm}$ exchange but at present we consider only the latter, i.e. the so-called charged-current reaction. In place of the matrix element (5.1) we expect from (2.6) that

$$\mathcal{M}(\nu e \to \nu e) = \frac{(g/\sqrt{2})^2}{q^2 + M_W^2} \tag{5.18}$$

where the finite boson mass appears in the propagator. The $1/\sqrt{2}$ factor inserted here in the coupling is a conventional factor (Clebsch–Gordan coefficient) arising from the particular way that g has been defined in the electroweak theory – see Section 7.9. Assume first that the electron of mass m is stationary in the laboratory system, in which the incident neutrino has energy E_ν. Since $M_W = 80$ GeV and

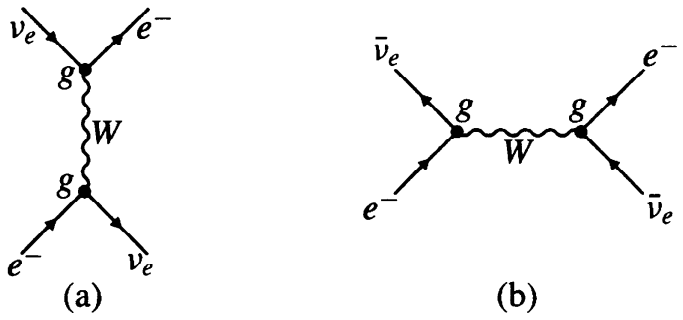

Fig. 5.7. Feynman diagrams for (a) neutrino ν_e and (b) antineutrino $\bar{\nu}_e$ scattering from an electron via W boson exchange, with coupling g.

$q^2(\max) \simeq 2mE_\nu$, $q^2 \ll {M_W}^2$ for neutrino energies in the GeV (or even TeV) range and the matrix element will simply be a constant:

$$\mathcal{M}(\nu e \to \nu e) = \frac{g^2}{2{M_W}^2} \tag{5.19}$$

The differential cross-section will have the usual form, cf. (2.18),

$$\frac{d\sigma}{dq^2} = \frac{2\pi}{v}|\mathcal{M}|^2 p^2 \frac{dp}{dE_f}\frac{d\Omega}{dq^2}\frac{2}{(2\pi)^3} \tag{5.20}$$

where we assume again that the leptons are extreme relativistic so that in the centre-of-momentum frame, the relative velocity $v = 2c$ and $dp/dE_f = \frac{1}{2}$. Summing over final-state spins and averaging over initial-state spins gives the factor 2 indicated: as described below, the incident neutrino can have $j_z = -\frac{1}{2}$ only, while in the final state it can have either $j_z = -\frac{1}{2}$ or $j_z = +\frac{1}{2}$. With $q^2 = 2p^2(1 - \cos\theta)$, the quantity $d\Omega/dq^2 = \pi/p^2$ so that the above equation becomes

$$\frac{d\sigma}{dq^2} = \frac{2}{\pi}\left(\frac{g^2}{8M_W^2}\right)^2$$

Historically, the parameters of the prototype weak interaction found in nuclear β-decay were defined long before the $W^\pm$ boson was observed or indeed postulated. The process was treated as a pointlike i.e. s-wave, interaction of the four fermion states involved, and the decay rate was specified by the Fermi constant G, defined for vector transitions. In the way in which G and g are defined (see (7.20)), it turns out that

$$\frac{G}{\sqrt{2}} \equiv \frac{g^2}{8M_W^2} \tag{5.21}$$

and hence that

$$\frac{d\sigma}{dq^2}(\nu_e e \to \nu_e e) = \frac{G^2}{\pi} \tag{5.22}$$

Let us now look at spin effects. As mentioned in Chapter 1, the leptons participating in weak interactions are *longitudinally polarised.* The polarisation is defined as the number I_+ of leptons with spin vector $\boldsymbol{\sigma}$ and momentum $\mathbf{p}$ parallel minus the number I_- with $\boldsymbol{\sigma}$ and $\mathbf{p}$ antiparallel, divided by their sum. The $V - A$ theory of weak interactions, which appeared in the mid-1950s and is discussed in Section 7.7, predicts the following dependence:

$$P = \frac{I_+ - I_-}{I_+ + I_-} = \alpha \frac{p}{E} = \alpha \frac{v}{c} \tag{5.23}$$

where v, p and E are the values of the velocity, 3-momentum and total energy of the lepton. The constant $\alpha = -1$ for leptons and $+1$ for antileptons; see (7.16) and Figure 7.6.

Thus, relativistic leptons emitted in charged-current weak interactions (those mediated by $W^{\pm}$ exchange) will be almost completely polarised, with $P \simeq \pm 1$, i.e. they are in nearly pure helicity states as described in Section 1.6. Leptons of *exactly* zero mass (neutrinos) have $v = c$ and *are* in pure helicity eigenstates. The classic measurement of the neutrino helicity is described in Section 7.10. It was found that for neutrinos $H = -1$ (i.e. LH helicity) while antineutrinos have $H = +1$ (i.e. RH helicity). In the high energy collisions we are considering here, both charged and neutral leptons are extreme relativistic, so that they are, near enough, in pure helicity states. So, in the case of $\nu_e e$ scattering in the cms, as in Figure 5.8(a), both leptons are LH and the total angular momentum $J = 0$. The angular distribution must therefore be isotropic, so that the differential cross-section is just given by (5.22). The total cross-section is obtained by integrating from $q^2 = 0$ to $q^2{}_{\max} = s = 4p^2$:

$$\begin{aligned} \frac{d\sigma}{dq^2} &= \frac{G^2}{\pi} \\ \sigma(\nu e \to \nu e) &= \frac{G^2 s}{\pi} \end{aligned} \tag{5.24}$$

Thus the cross-section in the LS rises linearly with incident neutrino energy, since $s \simeq 2mE_\nu$. For antineutrinos, however, the diagram of Figure 5.8(b) shows that $J_z = +1$, $J = 1$. Angular momentum conservation requires $J_z = +1$ in the final state also, and the d-function giving the probability amplitude for a scatter through angle θ is, as in 5.3(a),

$$d^1_{1,1} = \tfrac{1}{2}(1 + \cos\theta)$$

Multiplying the neutrino cross-section (5.22) by the square of this factor gives the

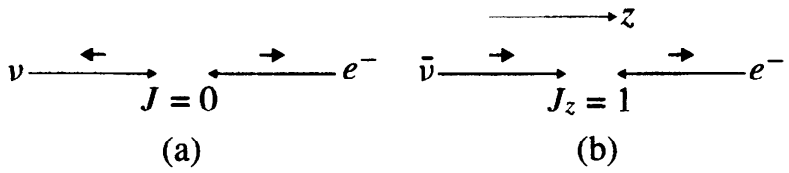

Fig. 5.8. The momentum vectors and spin vectors in (a) neutrino–electron scattering, and (b) antineutrino–electron scattering in the cms. In both cases, only the charge-changing ($W^{\pm}$ exchange) process is considered.

antineutrino cross-section:

$$\frac{d\sigma}{d\cos\theta}(\bar{\nu}_e e \to \bar{\nu}_e e) = \frac{G^2}{8\pi} s(1+\cos\theta)^2$$
$$\sigma(\bar{\nu}_e e \to \bar{\nu}_e e) = \frac{G^2 s}{3\pi} \tag{5.25}$$

where we have used the relation $d\sigma/d(\cos\theta) = 2\pi d\sigma/d\Omega = (s/2)d\sigma/dq^2$. The fact that both the cross-sections (5.24) and (5.25) are proportional to s also follows from dimensional analysis. From (5.21), $G^2 \propto (\text{energy})^{-4}$, since g is dimensionless. Since a cross-section has dimensions $(\text{energy})^{-2}$, it is clear that we need to multiply G^2 by $(\text{energy})^2$, i.e. by s, to obtain the right dimensions.

The smaller cross-section for antineutrinos can be understood simply, as follows. The initial state has $J = 1$, but there is the requirement that $J_z = +1$ in both initial and final states. So, of the $2J + 1 = 3$ possible final substates, only one is allowed, reducing the cross-section by a factor 3 as compared with the neutrino case, for which $J = 0$ and only one spin substate is involved.

The differential cross-sections may again be expressed in terms of $y = E_e/E_\nu$, the fraction of the neutrino's energy acquired in the LS by the recoil electron. From (5.15),

$$(1+\cos\theta)^2 = 4(1-y)^2$$

so that (5.24) and (5.25) become

$$\frac{d\sigma}{dy}(\nu_e e \to \nu_e e) = \frac{G^2 s}{\pi} \tag{5.26}$$

$$\frac{d\sigma}{dy}(\bar{\nu}_e e \to \bar{\nu}_e e) = \frac{G^2 s}{\pi}(1-y)^2 \tag{5.27}$$

These equations show that, while the laboratory energies of electrons scattered from a monoenergetic beam of neutrinos form a flat distribution with an average value $E_\nu/2$, electrons scattered from antineutrinos are peaked to low values (small y) with an average $E_\nu/4$.

The formulae in Sections 5.3 and 5.4 are for lepton scattering via vector or axial vector (γ or $W^{\pm}$) exchange. They will now be used as prototypes to study

lepton–quark scattering and quark–quark scattering, also via vector exchanges in electromagnetic, weak and strong interactions.

5.5 Elastic lepton–nucleon scattering

The evidence for quarks from the annihilation of e^+e^- to hadronic two-jet events emerged in the late 1970s, but the first evidence for quarks as real dynamical constituents of hadrons was found 10 years before, in studies of deep inelastic lepton–nucleon scattering. Early experiments with electron (and neutrino) beams from accelerators, incident on nucleon targets, had concentrated on the study of so-called *exclusive* processes, i.e. those in which the final hadron state is well defined. In particular, measurements were made of the elastic or quasi-elastic processes

$$e + p \to e + p, \qquad \nu_\mu + n \to \mu^- + p$$

where the nucleon recoils elastically from the impact. These reactions are dominated by *form factors*, which determine how the scattering is reduced from its value for a pointlike nucleon. The latter is described in the electromagnetic case and for small scattering angles by the Rutherford formula (5.17). We can generically label the form factor as $F(q^2)$, which is found to be a rapidly decreasing function of squared momentum transfer, q^2. Essentially, $|F(q^2)|^2$ measures the probability that the nucleon 'holds together' and recoils intact under the impact q. At high momentum transfers, this is found to be very improbable. Empirically, the elastic scattering form factors are fitted by the so-called 'dipole formula'

$$F(q^2) \simeq \frac{1}{(1 + q^2/M_V^2)^2} \tag{5.28}$$

where the quantity $M_V \simeq 0.9$ GeV. The observed variation with q^2 in electron–proton scattering is shown in Figure 5.9(a). We see for example that for $q^2 = 25\ \text{GeV}^2$, $|F(q^2)|^2 \sim 10^{-6}$ only.

The weak quasi-elastic scattering $\nu_\mu + n \to \mu^- + p$ is again dominated by form factors, as in (5.28). There are actually two sets of form factors, one for vector coupling (specified by M_V) and one for axial vector coupling (specified by M_A). Both M_V and M_A as measured in neutrino scattering are close to the value 0.9 GeV found for the electromagnetic case, and clearly both electrons and neutrinos are probing a similar structure. For neutrino scattering a consequence is that the total elastic cross-section (above the threshold energy $E_\nu(\text{min}) \simeq m_\mu c^2$) will initially rise with LS neutrino energy, since $\sigma \sim G^2 q^2_{\text{max}}/\pi$ as in (5.24) and q^2_{max} rises with E_ν. However, this rise is halted by the strong q^2 dependence in the form

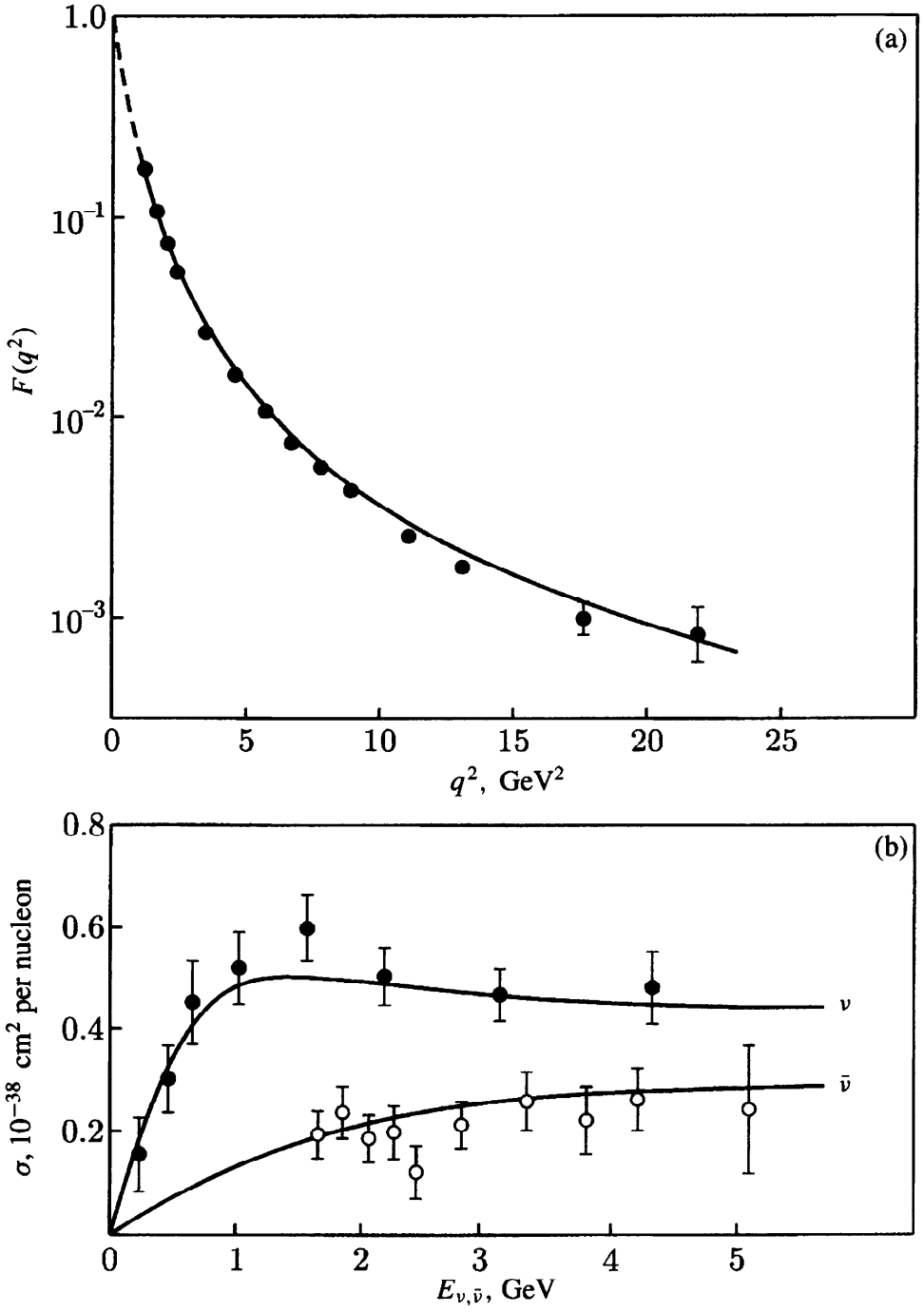

Fig. 5.9. (a) The form factor of the proton as measured in electron–proton scattering. At high q^2, this is dominated by the distribution of magnetic moment, rather than charge, on the proton. The curve represents the dipole formula (5.28) with $M_V = 0.9$ GeV. (b) The cross-section for the quasi-elastic reactions $\nu_\mu + n \to \mu^- + p$ (solid circles) and $\bar{\nu}_\mu + p \to \mu^+ + n$ (open circles). The data comes from measurements in bubble chambers at CERN with freon fillings and from the Argonne National Laboratory (ANL) with deuterium fillings. The curves are for $M_A = M_V = 0.9$ GeV.

factor and the cross-section tends to a constant value as shown in Figure 5.9(b); see Problem 5.1.

At present, there is no detailed theoretical model of form factors; the above formula can be interpreted in terms of an exponential distribution of charge and

magnetic moment in the nucleon (see also Problem 5.1). In terms of the quark model, the form factor just measures the amplitude that under an impact, the three 'valence' quarks, plus the other constituents – gluons and quark–antiquark pairs as described below – hold together and recoil coherently, as opposed to going their separate ways and forming a completely different hadronic final state.

5.6 Deep inelastic scattering and partons

Now we turn to *inclusive* processes, i.e. lepton–nucleon scattering in the deep inelastic region of high energy and momentum transfers when there is no restriction on the type of hadronic final state. An example of a deep inelastic collision (in this case initiated by a neutrino) is shown in Figure 5.10.

It is found that the cross-sections for deep inelastic scattering, in contrast to the elastic cross-sections, are large and only weakly q^2-dependent – see Figure 5.11. This is a signal of *elastic* scattering by *pointlike* constituents inside the nucleon. Initially these constituents were called *partons*, subsequently to be identified with quarks and gluons (Feynman 1969).

Imagine a reference frame in which the target proton has very large 3-momentum – the so-called infinite-momentum frame (Figure 5.12). The proton's mass can be neglected, so it has 4-momentum $P = (p, 0, 0, ip)$ and is visualised as consisting of a parallel stream of quasi-free partons, each with 4-momentum xP, where $0 < x < 1$. Again, if P is large, the masses and transverse momentum components of the partons can be neglected. Suppose now that one parton of mass m is scattered elastically by absorbing the 4-momentum q of the scattered lepton. Then

$$\begin{aligned} (xP + q)^2 &= -m^2 \simeq 0 \\ x^2P^2 + q^2 + 2xPq &\simeq 0 \end{aligned} \tag{5.29}$$

If $|x^2P^2| = x^2M^2 \ll q^2$, we obtain

$$x = \frac{-q^2}{2Pq} = \frac{q^2}{2M\nu} \tag{5.30}$$

where the invariant scalar product Pq has been evaluated in the laboratory system, in which the energy transfer is ν and the nucleon is at rest, and where x in (5.30) represents the fractional momentum of the parton in the infinite-momentum frame. If a free pointlike particle of mass m, *stationary* in the laboratory system, undergoes an elastic collision in which it receives an energy transfer ν and 3-momentum $q' = \sqrt{(\nu + m)^2 - m^2}$, the 4-momentum transfer is given by the elastic relation

$$q^2 = q'^2 - \nu^2 = 2m\nu \tag{5.31a}$$

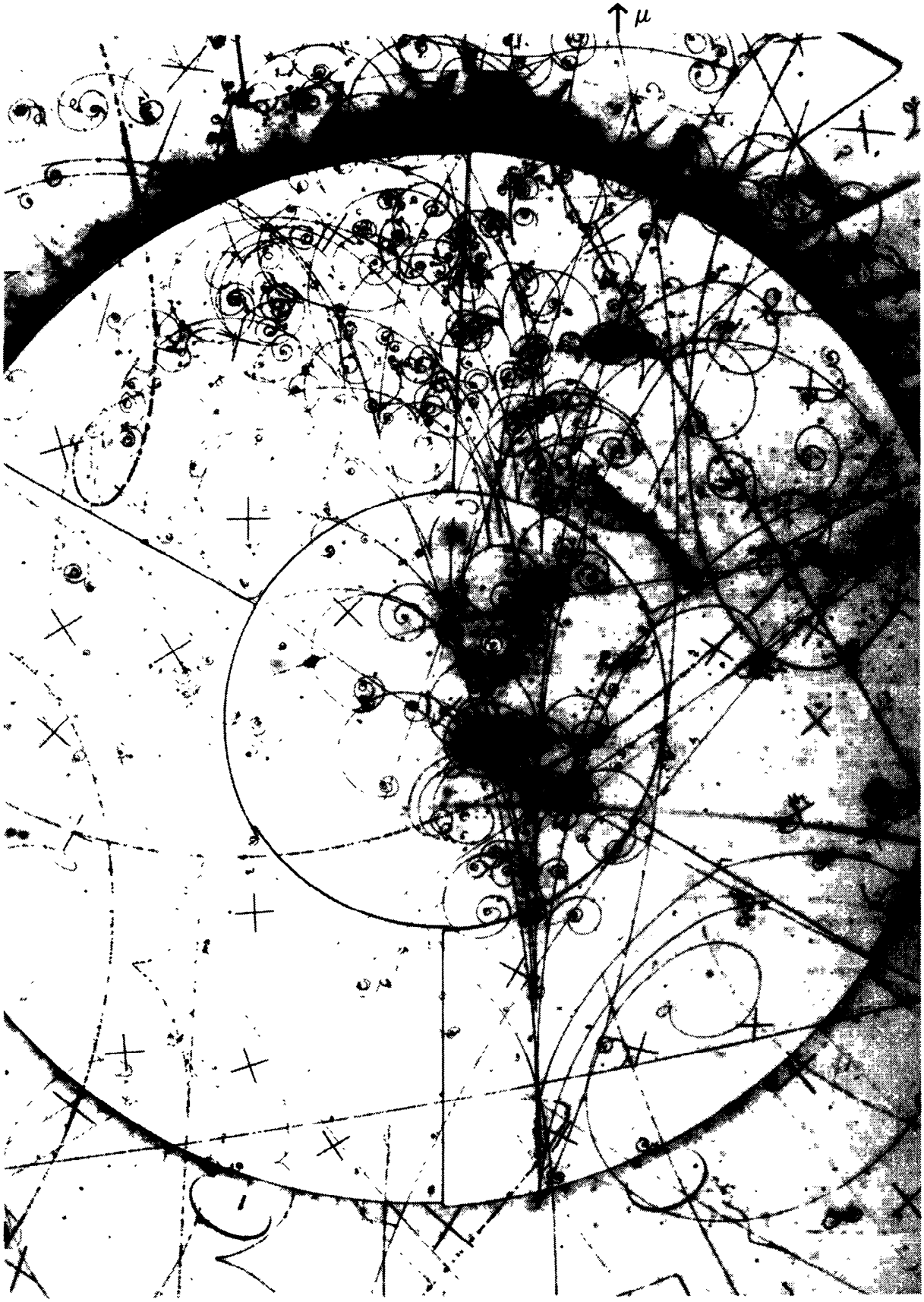

Fig. 5.10. Example of neutrino–nucleon deep inelastic interaction in the BEBC bubble chamber (see Figure 11.13) filled with a liquid-neon–hydrogen mixture and exposed to a narrowband neutrino beam. A neutrino ν_μ enters from the bottom and interacts, transforming to a negative muon (the track curving slowly anticlockwise at 1 o'clock, and reaching the top of the picture at the arrow), the remaining energy going to the creation of secondary pions and other hadrons. Neutral pions decay to γ-rays which in turn convert to e^+e^- pairs in the heavy liquid, creating the electromagnetic shower in the upper half of the picture.

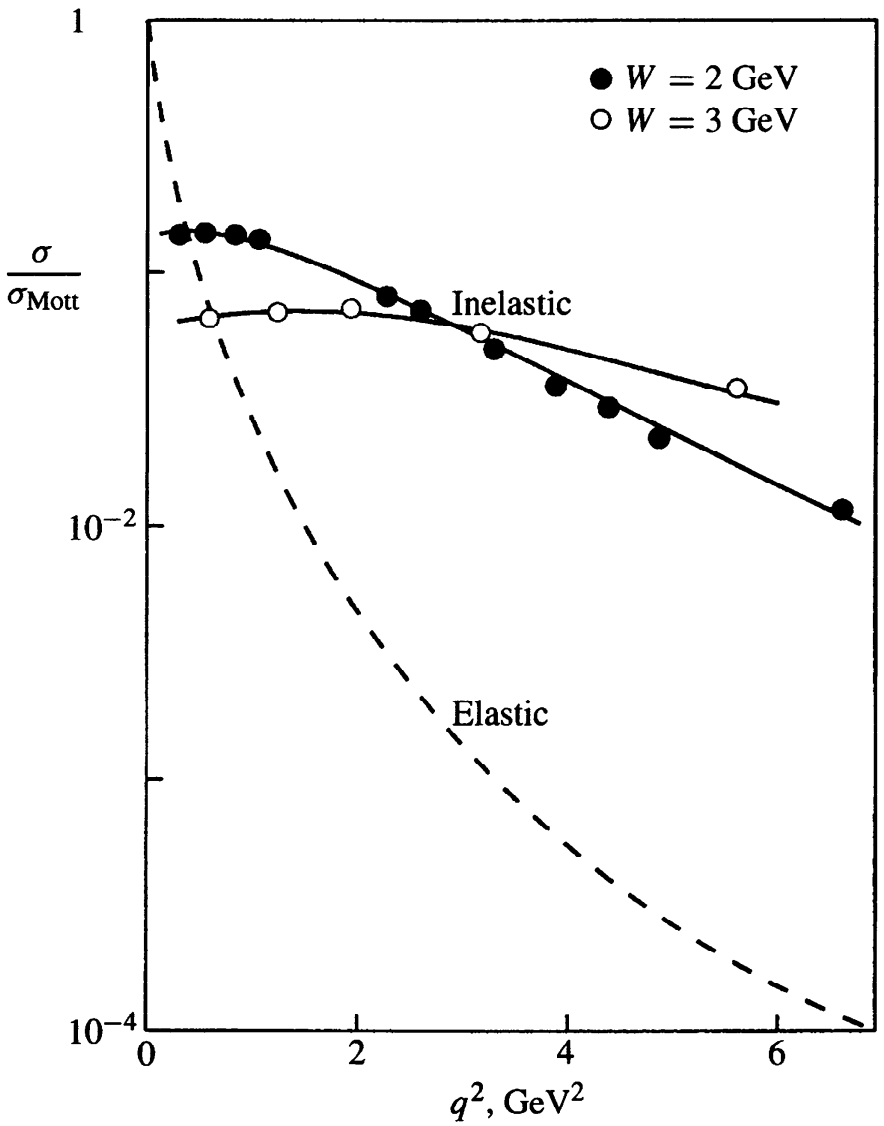

Fig. 5.11. Early SLAC measurements of the inelastic electron–proton scattering cross-section divided by the Mott (pointlike) cross-section, for two values of the invariant mass W of the hadronic final state. The ratio is seen to be only weakly q^2-dependent, in contrast with the strong q^2 dependence of the elastic scattering process, taken from Figure 5.9.

so that

$$x = \frac{q^2}{2Mv} = \frac{m}{M} \tag{5.31b}$$

So in a sense x could also be interpreted as the fractional mass of the nucleon carried by such a hypothetical free parton initially at rest in the laboratory system.

Of course, we do not observe partons in the final state, but hadrons. Somehow the scattered and unscattered partons have to recombine to form hadrons. The basic assumption is that the collision occurs in *two independent stages*. First, one parton is scattered, the collision time being that required to define the energy transfer, i.e. $t_1 \simeq \hbar/\nu$. Over a much longer time, the partons recombine to form the final hadronic state, of mass W. Clearly the proper lifetime of this state must be

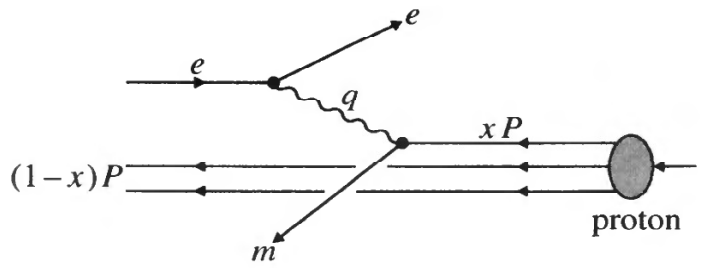

Fig. 5.12. Electron–parton collision via single-photon exchange, seen in the infinite-momentum frame of the target proton.

$t_2 > \hbar/W$, or, transformed into the laboratory frame, $t_2 > \gamma\hbar/W = \nu\hbar/W^2$, so that since $W^2 \simeq 2M\nu$, we have finally $t_2 \simeq \hbar/M \gg t_1$ for $\nu \gg M$. The recombination therefore takes place over a long timescale and can be treated separately from the initial collision. Thus the cross-section will depend first and foremost on the dynamics of the initial stage, and only weakly or not at all on the complexities of the final-state interaction. This turns out to be a good guess except in the low energy region ($\nu \simeq M$), where there are significant resonance effects.

5.7 Deep inelastic scattering and quarks

5.7.1 Electron–nucleon scattering

First we note that early evidence from the deep inelastic electron–proton scattering experiments demonstrated from the angular distributions that the partons had spin $\frac{1}{2}$. The elastic scattering between two spin $\frac{1}{2}$ particles is characterised by two terms in the angular distribution. One, the electric or Mott scattering, varies with cms angle as $\cos^2(\theta/2)$, with a maximum in the forward direction. The second, the magnetic or spin-flip term, varying as $\sin^4(\theta/2)$, has a maximum in the backward direction (the overall angular dependence $1 + \cos^4(\theta/2)$ in (5.14) can be resolved into the combination $2\cos^2(\theta/2) + \sin^4(\theta/2)$). It was found that the empirical coefficients in the angular distribution were indeed exactly those for spin $\frac{1}{2}$–spin $\frac{1}{2}$ scattering. So this was a first indication that partons were fermions. Let us now try to make the identification of partons with quarks.

Although we know that quarks are bound inside nucleons, we shall for the time being continue treating them as free pointlike particles. Let $u(x)dx$ and $d(x)dx$ be the number of u and d quarks in the proton that carry a fractional momentum in the range $x \to x + dx$. As shown below, we also have to allow for the possibility of antiquarks and strange quarks, in the form of pairs $u\bar{u}, d\bar{d}, s\bar{s}, \ldots$. Since the cross-section will be proportional to the square of the quark charges, we expect,

from (5.16),

$$\frac{d^2\sigma(ep)}{dydx} = \frac{4\pi\alpha^2}{q^4} xs \frac{F_2^{ep}(x)}{x} \left[\frac{1+(1-y)^2}{2}\right] \tag{5.32}$$

where the *structure function* $F_2^{ep}(x)$ involves the quark density weighted by the squares of the quark charges,

$$\frac{F_2^{ep}(x)}{x} = \tfrac{4}{9}[u(x)+\bar{u}(x)] + \tfrac{1}{9}\left[d(x)+\bar{d}(x)+s(x)+\bar{s}(x)\right] \tag{5.33}$$

and where in place of s in (5.16) we use xs, the electron–quark cms energy squared.

The scattering of electrons by neutrons can be determined experimentally by a comparison of electron–proton and electron–deuteron scattering. By isospin invariance, we expect the u, $\bar{u}$ population in the neutron to equal the d, $\bar{d}$ population in the proton and vice versa. Hence

$$\frac{F_2^{en}(x)}{x} = \tfrac{4}{9}[d(x)+\bar{d}(x)] + \tfrac{1}{9}[u(x)+\bar{u}(x)+s(x)+\bar{s}(x)] \tag{5.34}$$

For a nucleon target that has an equal admixture of protons and neutrons

$$\frac{F_2^{eN}(x)}{x} = \tfrac{5}{18}[u(x)+\bar{u}(x)+d(x)+\bar{d}(x)] + \tfrac{1}{9}[s(x)+\bar{s}(x)] \tag{5.35}$$

5.7.2 *Neutrino–nucleon scattering*

For neutrino–nucleon collisions, let us recall (5.26) and (5.27), the cross-sections for neutrinos and antineutrinos on electron and positron targets:

$$\frac{d\sigma}{dy}(\nu e \to \nu e) = \frac{G^2 s}{\pi} = \frac{d\sigma}{dy}(\bar{\nu}\bar{e} \to \bar{\nu}\bar{e}) \tag{5.36}$$

$$\frac{d\sigma}{dy}(\bar{\nu} e \to \bar{\nu} e) = \frac{G^2 s}{\pi}(1-y)^2 = \frac{d\sigma}{dy}(\nu\bar{e} \to \nu\bar{e}) \tag{5.37}$$

For neutrino–quark scattering via W exchange the reactions will be

$$\nu_\mu + d \to \mu^- + u, \qquad \nu_\mu + \bar{u} \to \mu^- + \bar{d}$$

while for antineutrinos they are

$$\bar{\nu}_\mu + u \to \mu^+ + d, \qquad \bar{\nu}_\mu + \bar{d} \to \mu^+ + \bar{u}$$

Interactions with s, $\bar{s}$ quarks are suppressed by the Cabibbo angle factor (see Section 7.14) and can be neglected here. Hence, treating the quarks as pointlike

particles, just like the electrons in (5.36) and (5.37), we get

$$\frac{d\sigma(\nu p)}{dydx} = \frac{G^2xs}{\pi}\left[d(x) + \bar{u}(x)(1-y)^2\right] \tag{5.38}$$

$$\frac{d\sigma(\nu n)}{dydx} = \frac{G^2xs}{\pi}\left[u(x) + \bar{d}(x)(1-y)^2\right] \tag{5.39}$$

On an isoscalar target, with equal numbers of neutrons and protons, one thus obtains

$$\frac{d\sigma(\nu N)}{dydx} = \frac{G^2xs}{2\pi}\left\{[u(x)+d(x)] + [\bar{u}(x)+\bar{d}(x)](1-y)^2\right\} \tag{5.40}$$

For antineutrinos, the corresponding expressions are obtained by interchanging the factors $(1-y)^2$ and 1:

$$\frac{d\sigma(\bar{\nu}N)}{dydx} = \frac{G^2xs}{2\pi}\left\{[u(x)+d(x)](1-y)^2 + [\bar{u}(x)+\bar{d}(x)]\right\} \tag{5.41}$$

We define structure functions in analogy with those in electron scattering:

$$\frac{F_2^{\nu N}(x)}{x} = u(x) + d(x) + \bar{u}(x) + \bar{d}(x) \tag{5.42}$$

$$F_3^{\nu N}(x) = u(x) + d(x) - \bar{u}(x) - \bar{d}(x) \tag{5.43}$$

Then the foregoing equations become

$$\frac{d^2\sigma^{\nu N,\bar{\nu}N}}{dydx} = \frac{G^2ME}{\pi}\left\{\left[\frac{F_2(x) \pm xF_3(x)}{2}\right] + \left[\frac{F_2(x) \mp xF_3(x)}{2}\right](1-y)^2\right\} \tag{5.44}$$

where $s \simeq 2ME$. For the integrals over $x = 0 \to 1$ of the quark and antiquark momentum fractions (i.e. the densities multiplied by x), let us write the quantities

$$Q = \int x[u(x)+d(x)]dx, \qquad \bar{Q} = \int x[\bar{u}(x)+\bar{d}(x)]dx$$

Then, integrating (5.40) and (5.41) over $x, y = 0 \to 1$, one finds for the total cross-sections

$$\sigma(\nu N) = \frac{G^2ME}{\pi}\left(Q + \tfrac{1}{3}\bar{Q}\right) \tag{5.45}$$

$$\sigma(\bar{\nu}N) = \frac{G^2ME}{\pi}\left(\bar{Q} + \tfrac{1}{3}Q\right) \tag{5.46}$$

giving as the expected ratio of antineutrino to neutrino cross-sections

$$R = \frac{1 + 3\bar{Q}/Q}{3 + \bar{Q}/Q} \tag{5.47}$$

5.8 Experimental results on quark distributions in the nucleon

Experimental studies of deep inelastic lepton–nucleon scattering have been carried out with electron beams from the SLAC 20 GeV electron linac and with muon and neutrino beams, principally from the Fermilab Tevatron and the CERN SPS. High energy protons are focussed onto an external pencil target, and the secondary $\pi^{\pm}$, $K^{\pm}$ beams that are produced traverse a decay tunnel where a fraction decay to $\mu^{\pm}$ and (principally) $\nu_{\mu}, \bar{\nu}_{\mu}$. More details of neutrino beams are given in Section 7.11. The muon and neutrino interactions have been recorded in large electronic detector arrays (see Figure 11.16 for example) and in large bubble chambers (see Figure 5.10 and Figure 11.13 for example).

The equations in the last section lead to a number of predictions for comparison with experiment. The more important of these are as follows.

(i) The total neutrino–nucleon cross-sections should be proportional to energy. This is well verified; see Figure 5.13. The linear rise is of course a direct consequence of pointlike scattering, for which the cross-section is determined by phase space, as in (2.18) with M_{if} constant.

(ii) The observed ratio $R \simeq 0.45$ derived from the results in Figure 5.13 indicates, from (5.47), that the nucleon contains antiquarks as well as quarks, with $\bar{Q}/Q \simeq 0.15$.

(iii) Comparing (5.35) and (5.42) we see that if the tiny $s, \bar{s}$ quark population is ignored, one expects the following relation between electron–nucleon and neutrino–nucleon scattering:

$$F_2^{eN}(x) = \tfrac{5}{18} F_2^{\nu N}(x) \tag{5.48}$$

where the factor $\frac{5}{18}$ is simply the mean square quark charge per nucleon. Figure 5.14 shows early (1973) data from Stanford (eN) and CERN (νN) experiments. The prediction (5.48) is well verified. This comparison provided at that time the most convincing evidence that nucleons contained fractionally charged quarks as real dynamical entities.

(iv) From (5.35) and (5.42) we obtain

$$\int_0^1 x[u(x) + \bar{u}(x) + d(x) + \bar{d}(x)]dx = \int F_2^{\nu N}(x)dx \simeq \tfrac{18}{5} \int F_2^{eN}(x)dx \approx 0.50 \tag{5.49}$$

as the total momentum fraction carried by quarks and antiquarks, and the value of $\simeq$ 0.50 for the integral is obvious from Figures 5.14(a) and (b). Thus, 50% of the nucleon momentum is carried by partons *without* weak or electromagnetic coupling. In fact this fraction is carried by the strongly

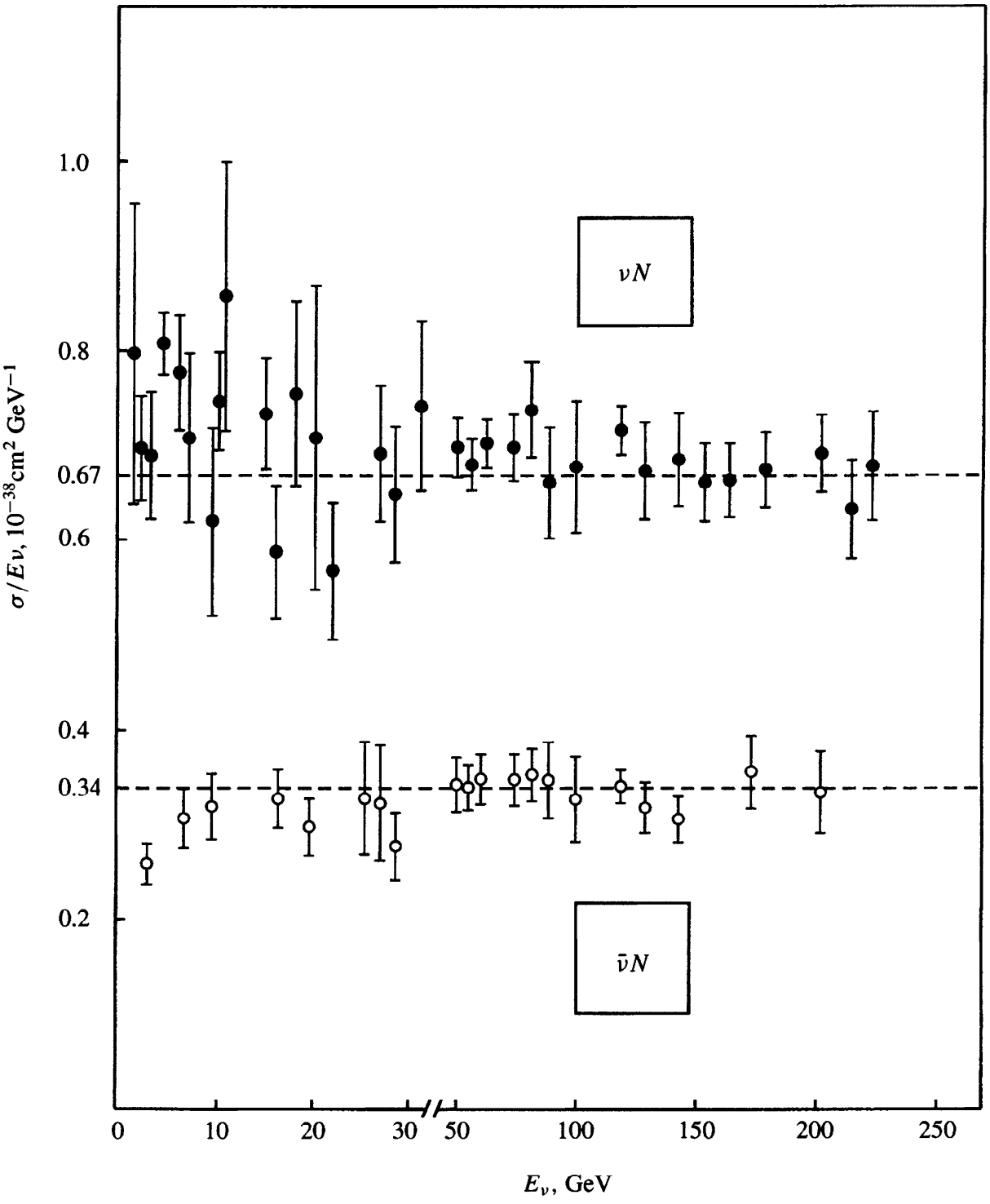

Fig. 5.13. Neutrino and antineutrino cross-sections on nucleons. The ratio σ/E_ν is plotted as a function of energy and is indeed a constant, as predicted in (5.45) and (5.46).

interacting neutral *gluons* that mediate the quark interactions, as discussed in more detail in Chapter 6.

From the values for $xF_3(x)$ and $F_2(x)$ defined above, the separate x-distributions for quarks and antiquarks can be found, as shown in Figure 5.14(b). Note that both Q and $\bar{Q}$ are finite as $x \to 0$, while the valence quark distribution $Q - \bar{Q}$ tends to zero there.

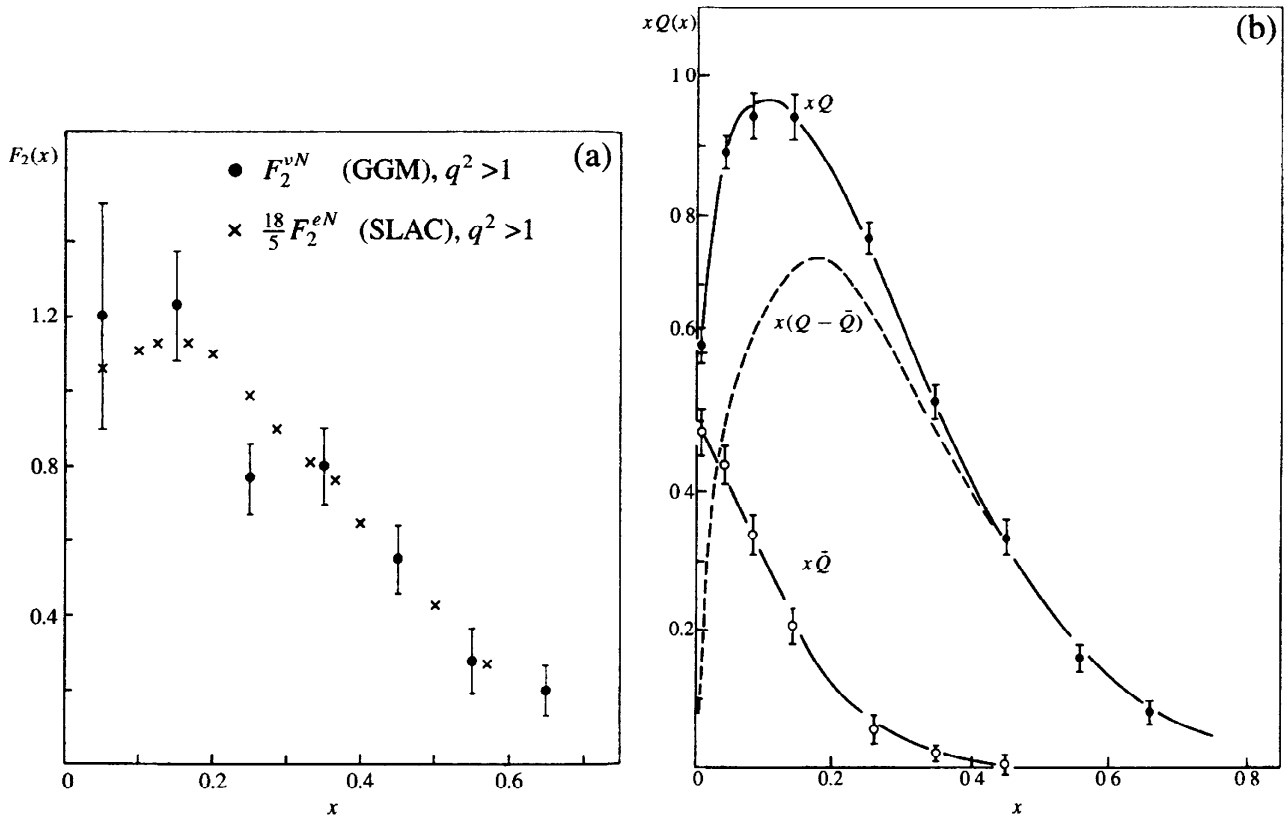

Fig. 5.14. (a) Early data on $F_2^{\nu N}(x)$ measured at CERN in the Gargamelle bubble chamber, compared with $\frac{18}{5} F_2^{eN}(x)$ measured from *ep* and *ed* scattering at SLAC. (b) Momentum distributions of quarks and antiquarks in the nucleon, at a value of $q^2 \simeq 10$ GeV^2, from neutrino experiments at CERN and Fermilab.

The observed distribution in x of the valence quarks is quite broad, peaking at $x \simeq 0.15$. Clearly, if the nucleon had consisted only of three quasi-free valence quarks, we would have expected a narrow distribution centred around $x = \frac{1}{3}$. The broad distribution and smaller x-value at the peak arises because the nucleon momentum is shared between valence quarks, quark–antiquark pairs and gluons. Furthermore, the quarks are not free but confined within the nucleon radius $R_0 \sim 1$ fm. The Fermi momentum $p_f \simeq h/R_0 \simeq 0.2$ GeV/c therefore also contributes a spread in x.

In fixed-target experiments at the CERN 400 GeV SPS and the Fermilab Tevatron proton accelerators, the maximum value of q^2 available with the secondary muon and neutrino beams produced from $\pi^{\pm}$ and $K^{\pm}$ decay in flight is of order 200 GeV^2. Since the early 1990s, much higher values of q^2, of up to 20 000 GeV^2, have been obtained at the HERA electron–proton collider. This accelerates electrons to 28 GeV in one ring, 6.2 km in circumference, and protons in the

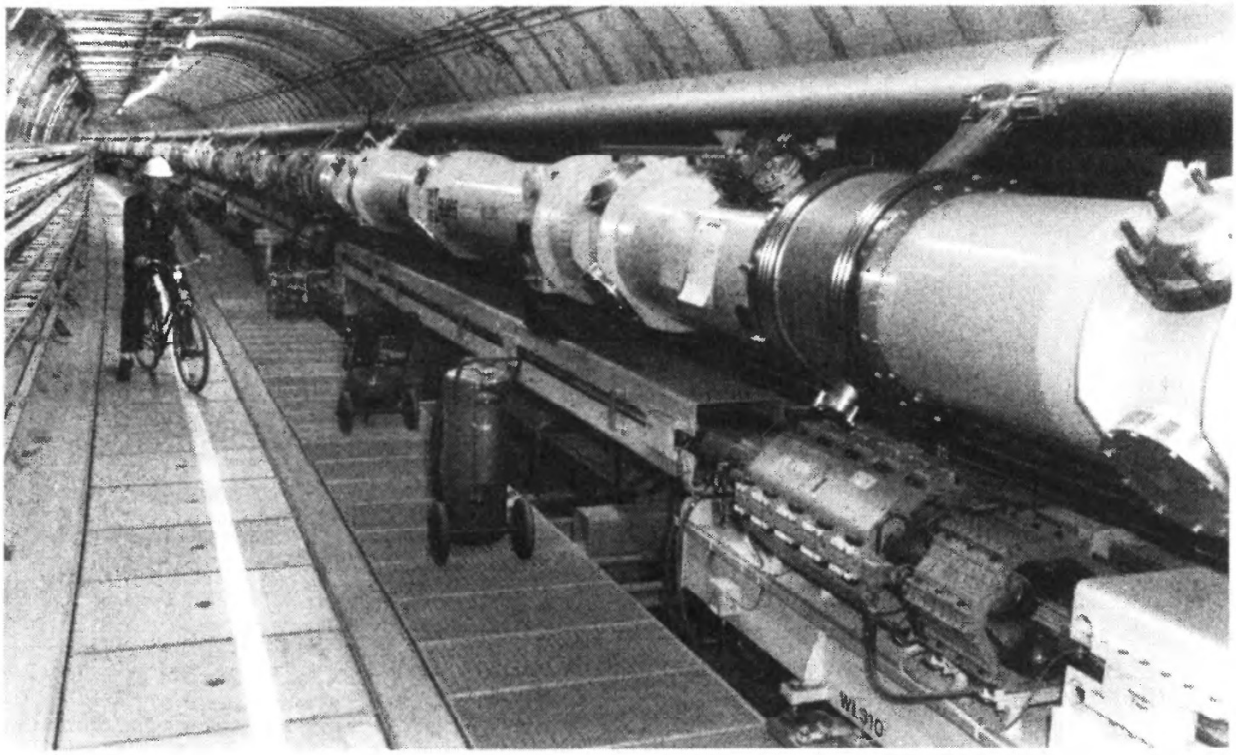

Fig. 5.15. The underground tunnel of the HERA electron–proton collider at DESY, Hamburg. The lower ring includes conventional (warm) bending and focussing magnets for accelerating the electron beam to 28 GeV, while the upper ring consists of superconducting magnets, with coils at liquid helium temperatures, for accelerating protons to 820 GeV. Above the proton ring is the liquid helium supply piping.

opposite direction to 820 GeV in a second ring placed above it (see Figure 5.15), the total cms energy squared being $s = 4E_1E_2 \simeq 10^5$ GeV^2. Both neutral-current events

$$e + p \rightarrow e + \text{hadrons}$$

and charged-current events

$$e + p \rightarrow \nu_e + \text{hadrons}$$

are observed (see Figure 5.16 for an example, also Problem 5.11). In the electroweak theory, to be discussed in Chapter 8, the neutral-current and charged-current (CC) couplings are comparable, but the $W^{\pm}$ propagator in (2.9) suppresses the charged-current cross-section relative to the neutral-current cross-section at moderate values of q^2. Only when $q^2 \sim M_W^2$ do the two rates become roughly equal (see Problem 8.7). Details of the most recent results obtained in both fixed-target and collider experiments, and their comparison with the predictions of QCD, are given in Section 6.6.

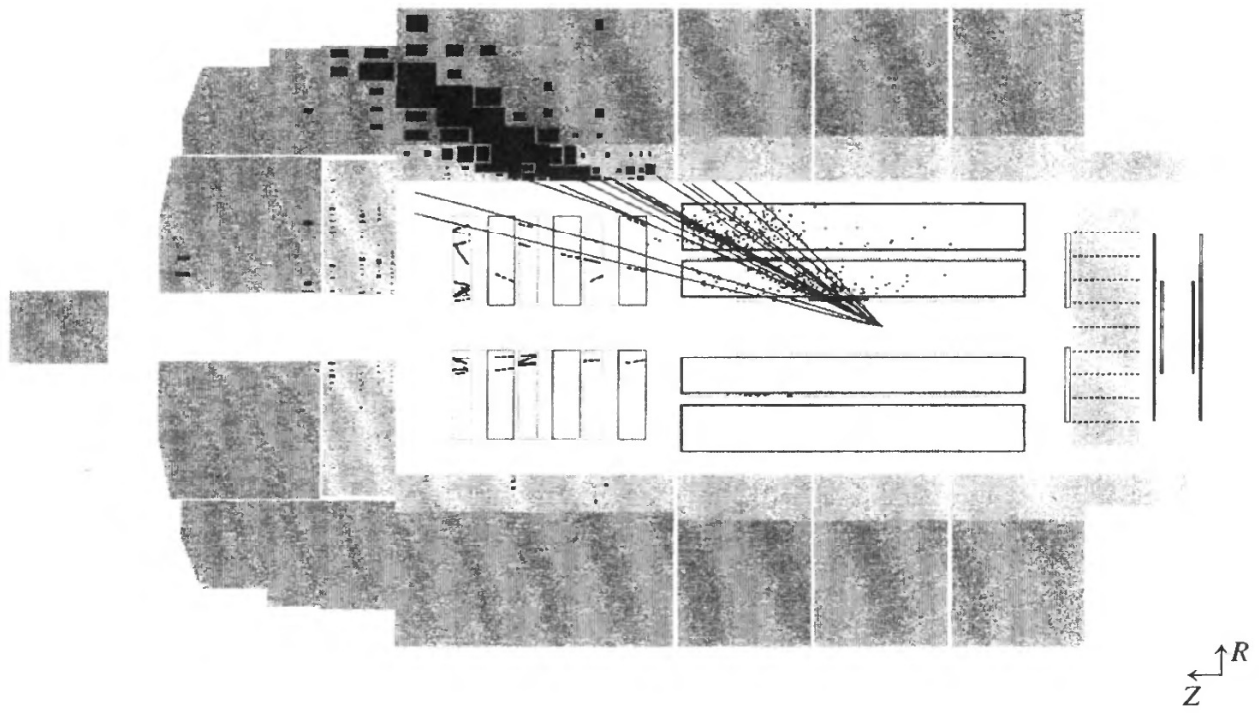

Fig. 5.16. Computer reconstruction of a charged-current event, $e + p \rightarrow \nu_e +$ hadrons, recorded in the H1 detector placed in one of the four beam-intersection regions of the HERA collider. The electron beam comes in from the left and the proton beam from the right. A high energy jet of hadrons is shown emerging from the intersection region in the beam pipe. In such events, much of the energy of the incident proton goes down the beam pipe, and, like the neutrino, is invisible. The value of q^2 in this event was of order 15 000 GeV^2.

5.9 Sum rules

The integrals over the structure functions F_2 and F_3 give rise to sum rules, that basically express the conservation of quark quantum numbers in the nucleon. The quark charge relation (5.48) and the momentum sum (5.49) are examples. Other examples are as follows.

5.9.1 Gottfried sum rule

From the relations (5.33) and (5.34) it is left as an exercise (Problem 5.8) to show that

$$\int_0^1 \left[F_2^{ep}(x) - F_2^{en}(x)\right]\frac{dx}{x} = \frac{1}{3} + \frac{2}{3}\int_0^1 \left[\bar{u}(x) - \bar{d}(x)\right]dx \qquad (5.50)$$

The observed value for this sum, 0.24 ± 0.03 shows, that the quark–antiquark sea is not flavour symmetric and that in the proton there are more $\bar{d}$ quarks than $\bar{u}$ quarks.

5.9.2 Gross Llewellyn Smith sum rule

From (5.43) it follows that

$$\int_0^1 x F_3^{\nu N}(x)\frac{dx}{x} = \int_0^1 [u_V(x) + d_V(x)]dx = 3 \tag{5.51}$$

where $u_V = u - \bar{u}$ and $d_V = d - \bar{d}$ are the numbers of valence quarks in the proton. This prediction is for the naive 'free' parton model, and would be literally true only for $q^2 \to \infty$. At finite q^2, it is modified by a factor $\simeq 1 - \alpha_s(q^2)/\pi$, where $\alpha_s(q^2)$ is the strong QCD coupling (analogous to α in QED) and is a slow function of q^2, as described in Chapter 6. The sum rule is verified in practice to an accuracy $\sim 10\%$.

5.9.3 Spin structure functions: Bjorken sum rule

The foregoing discussion of inelastic electron scattering was for unpolarised beams on unpolarised targets. Experiments have also been carried out using longitudinally polarised electron or muon beams (with typically 80% polarisation) incident on longitudinally polarised hydrogen and deuterium targets. One can define unpolarised and polarised structure functions as follows:

$$\begin{aligned} F_1(x) &= \frac{1}{2}\sum z^2 [q\uparrow(x) + \bar{q}\uparrow(x) + q\downarrow(x) + \bar{q}\downarrow(x)] \\ g_1(x) &= \frac{1}{2}\sum z^2 [q\uparrow(x) + \bar{q}\uparrow(x) - q\downarrow(x) - \bar{q}\downarrow(x)] \end{aligned} \tag{5.52}$$

where ze is the quark charge, and the sum is over all quark flavours. $q\uparrow$ and $q\downarrow$ refer to quarks with spin parallel or antiparallel to the proton spin. The polarisation asymmetry is defined as

$$A(x) = \frac{d\sigma^{\uparrow\uparrow}(x) - d\sigma^{\uparrow\downarrow}(x)}{d\sigma^{\uparrow\uparrow}(x) + d\sigma^{\uparrow\downarrow}(x)}$$

where $d\sigma^{\uparrow\uparrow}$ and $d\sigma^{\uparrow\downarrow}$ respectively refer to cross-sections for parallel and antiparallel lepton and proton spins. Allowance must be made for the degree of polarisation of both lepton and nucleon. The expected asymmetry $g_1(x)/F_1(x)$ is easily calculated from (4.15) for the particular case where sea quarks are neglected, when $A_p = \frac{5}{9}$ and $A_n = 0$.

The most important sum rule for polarised scattering is that due to Bjorken (1967) for the difference

$$I = \int_0^1 (g_1^p - g_1^n)dx = \frac{1}{6}\left(\frac{g_A}{g_V}\right)\left(1 - \frac{\alpha_s}{\pi} + \cdots\right) \tag{5.53}$$

where $g_A/g_V = 1.26$ is the ratio of axial to vector coupling in neutron decay (see

Section 7.8). A recent measurement at $q^2 = 5$ GeV^2 gave $I = 0.16$, within about 10% of the estimate 0.18 from (5.53). (In all evaluations of sum rules, inherent uncertainties arise because, at fixed q^2 and finite beam energy, one cannot reach $x = 0$ and extrapolations are necessary.)

Separate sum rules for g_1^p and g_1^n have also been proposed, but unlike the Bjorken sum rule these depend on assumptions about gluon and strange-quark–antiquark contributions to the polarisation asymmetry (i.e. to the nucleon spin). The results suggest that much of the angular momentum is carried by the gluons (and strange quarks). In Chapter 4, we found that the static magnetic moments (and hence the spin) of baryons were reasonably well accounted for in terms of those of the three constituent (valence) quarks, each of mass $\sim M_N/3$. In high q^2 collisions, however, the instantaneous state of a nucleon is a seething mass of gluons, quarks and antiquarks and it is not very surprising that the valence quarks account for only a small part of the total angular momentum.

5.10 Summary

Let us finally try to summarise the results on deep inelastic lepton–nucleon scattering and e^+e^- annihilation to hadrons.

The data are broadly in agreement with the predictions of the parton model, i.e. of a nucleon or other hadron built from pointlike, quasi-free constituents, with quantum numbers (for spin and charge) identifying them as fractionally charged quarks and antiquarks. In addition, both direct and indirect evidence is found for the existence of neutral gluons among the parton constituents; neutral gluons appear in three-jet events in e^+e^- annihilation (see Section 6.4) and account for some 50% of the nucleon momentum in deep inelastic scattering. The quark quantum numbers give rise to several sum rules, which are all verified within the attainable accuracies, of order 10%.

We have also noted significant departures from the predictions of the parton model; these departures are associated with the interactions between the quarks, formally described by quantum chromodynamics, the subject of the next chapter.

Problems

5.1 Show that an exponential charge distribution in the proton of the form $\rho(R) = \rho(0)\exp(-M_V R)$ leads to a dipole form factor of the form (5.28), and that a value $M_V = 0.84$ GeV leads to an rms radius of the charge distribution of the proton of 0.8 fm. Show also that for the quasi-elastic process $\nu_\mu + n \to \mu^- + p$, the total cross-section tends to a constant as $E_\nu \to \infty$.

(*Hint*: Use equation (2.4).)

5.2 Show that in a reaction of the form $a + b \to c + d$ the Mandelstam variables defined in (5.11) are connected by the relation $s - t - u = m_a^2 + m_b^2 + m_c^2 + m_d^2$.

5.3 Draw a Feynman diagram to demonstrate that the process $e^+e^- \to \pi^+\pi^-$ measures the electromagnetic form factor of the pion in the timelike region of momentum transfer. If this process is dominated by the $\rho(\to \pi^+\pi^-)$ intermediate state, show that the rms radius of the pion is 0.64 fm ($m_\rho c^2 = 769$ MeV).

5.4 In an e^+e^- colliding-beam experiment, the ring radius is 10 m and each beam forms a 10 mA current, with a cross-sectional area of 0.1 cm^2. Assuming that the electrons and positrons are bunched and that the two bunches meet head-on twice per revolution, calculate the luminosity in cm^{-2} s^{-1} (a luminosity L provides a reaction rate of σL per second for a process of cross-section σ). From the Breit–Wigner formula (2.28) calculate the cross-section for the reaction $e^+e^- \to \pi^+\pi^-\pi^0$ at the peak of the ω resonance, assuming that the branching ratio for $\omega \to e^+e^-$ is simply α^2. Hence deduce the event rate per hour for this process with the above luminosity ($m_\omega c^2 = 783$ MeV, $J_\omega = 1$.)

5.5 A neutrino of energy E_0 and negligible mass collides with a stationary electron. Find an expression for the laboratory angle of emission of the electron in terms of its recoil energy E and calculate its value when $E_0 = 1$ GeV and $E = 0.5$ GeV. Calculate the maximum momentum transfer to the electron when $E_0 = 1$ GeV ($m_e c^2 = 0.51$ MeV.)

5.6 Show that if sea quarks are neglected, the polarisation asymmetries from (5.52) for proton and neutron targets are $A_p = \frac{5}{9}$ and $A_n = 0$.

5.7 Assume that the quark momentum distribution in the nucleon is of the form $A(1-x)^3$ and that the antiquark momentum distribution in the pion is of the form $B(1 - \bar{x})$, where A and B are constants and x, $\bar{x}$ are the fractional momenta of the quarks in the hadrons. Find an expression for the cross-section for the production of muon pairs ($u\bar{u} \to \mu^+\mu^-$) in a pion–proton collision as a function of $\tau = m_\mu^2/s = x\bar{x}$, where s is the square of the pion–proton cms energy. Show that

$$\frac{d\sigma}{dm} = \frac{8\pi\alpha^2}{180m^3} AB \sum e_i^2 (1-\tau)^5$$

where e_i is the charge, in units of $|e|$, of a quark i.

5.8 Derive the Gottfried sum rule (5.50).

5.9 Show that in the Mott scattering of an electron by a pointlike, spinless target, the y distribution has the form $d\sigma/dy \propto (1 - y)$, where $y = \nu/E$ and E, ν are the incident electron energy and the energy transfer to the target.

5.10 Express the variables x and y defined in (5.30) and (5.15) in relativistically invariant form. Show that

$$x = -q^2/(2Pq)$$
$$y = -2Pq/s$$

where the 4-momenta P, q are defined in Figure 5.12 and s is the squared total cms energy in the collision.

5.11 In the electron–proton collider HERA, electrons of energy $E_e = 30$ GeV collide head-on with protons of energy $E_p = 820$ GeV. In a neutral-current event of the type $e + p \to e +$ hadrons, the secondary electron is emitted with energy $E'_e = 90$ GeV at angle 120° with respect to the incident electron, and the visible hadrons appear in the form of a jet on the opposite side of the beam pipe, with total energy $E_H = 250$ GeV and with resultant momentum at angle $\theta = 18°$ relative to the incident proton direction.

Show that, in the context of the parton model, the squared momentum transfer calculated solely from the hadronic jet will be

$$q_H^2 = \frac{E_H^2 \sin^2\theta}{1 - (E_H/2E_e)(1 - \cos\theta)}$$

Compare the value of q^2 obtained from this formula with that computed from the secondary electron variables. Is there a discrepancy between the two values and, if so, why?

5.12 Starting from the matrix element (5.1) and the expression (2.18) for the differential cross-section, derive the formula (5.14) for electron–muon scattering directly, without recourse to the Mandelstam variables and crossing symmetry.

5.13 After reading the discussion of the summation over spin states in the process $e^+e^- \to Q\bar{Q}$ in Section 5.1, deduce the Van Royen–Weisskopf formula (4.30) for the width for the leptonic decay of a vector meson, $V \to e^+e^-$, starting from the formulae (2.16) and (2.17) for the transition rate.

(*Hint*: The rate will contain a factor $N_c = 3$ for colour and a factor 8/3 from integration over the angular distribution of the leptons, described by the d-functions in Appendix C.)

6

Quark interactions and QCD

6.1 The colour quantum number

The colour quantum number has already been introduced as an extra degree of freedom in the quark model of hadrons and in describing the process $e^+e^- \rightarrow$ hadrons. Recall that the introduction of three colours for quarks increases the expected e^+e^- cross-section by a factor 3 and brings it into line with experiment. Quantum chromodynamics (QCD) is the formal theory of the strong colour interactions between quarks. The colour charge of a quark has three possible values, say red, blue, or green. Antiquarks carry anticolour, and the interquark interactions are assumed to be invariant under colour interchange. The bosons mediating the quark–quark interactions are called *gluons*, each carrying a colour and an anticolour and postulated to belong to an octet of states. In analogy with the flavour octet of mesons in Table 4.8 we can write these as

$$\mathrm{r\bar{b}},\ \mathrm{r\bar{g}},\ \mathrm{b\bar{g}},\ \mathrm{b\bar{r}},\ \mathrm{g\bar{r}},\ \mathrm{g\bar{b}},\ \frac{1}{\sqrt{2}}(\mathrm{r\bar{r}}-\mathrm{b\bar{b}}),\ \frac{1}{\sqrt{6}}(\mathrm{r\bar{r}}+\mathrm{b\bar{b}}-2\mathrm{g\bar{g}}) \tag{6.1}$$

With three colours and three anticolours, we expect $3^2 = 9$ combinations, but one is a colour singlet $\frac{1}{\sqrt{3}}(\mathrm{r\bar{r}}+\mathrm{g\bar{g}}+\mathrm{b\bar{b}})$ and, since it carries no net colour, has to be excluded. As an example, Figure 6.1 depicts the colour interaction between a red quark and a blue quark via exchange of a single $\mathrm{r\bar{b}}$ gluon.

The colour charge of the strong quark interactions is analogous to the electric charge in electromagnetic interactions. Both forces are mediated by a massless, vector particle (a gluon or a photon). However, whereas in electromagnetism there are two types of charge and an uncharged mediating boson, in QCD there are six types of charge (colour and anticolour) and a charged (i.e. coloured) mediating boson. This difference turns out to be crucial in understanding the features of quark interactions at short distances and the success of the parton model in describing deep inelastic scattering in terms of quasi-free, non-interacting constituents.

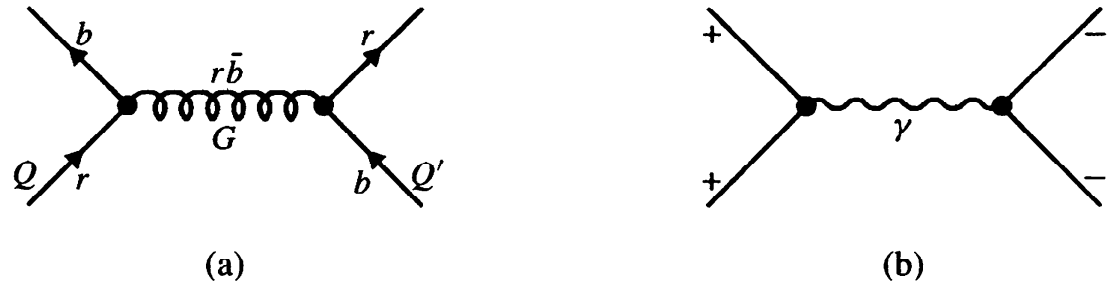

(a) (b)

Fig. 6.1. (a) QQ interaction via (colour-charge) gluon exchange, compared with (b) interaction between charges via (uncharged) photon exchange.

The colour quantum number does not enter our description of hadrons, so that both baryons and mesons must be colourless. If we write down the various contributions due to exchange of gluons between the quarks, those quark configurations of lowest energy are found to consist of the colour-singlet QQQ state (baryon) and the colour-singlet $Q\bar{Q}$ state (meson). Other possible combinations (e.g. QQ or $QQ\bar{Q}\bar{Q}$) are not bound, i.e. the interaction is found to be repulsive, so that QCD correctly predicts that only two of all the possible quark combinations should exist in nature.

The actual form of the potential between quarks was described in Section 2.7. At small distances the interaction is assumed to be of the Coulomb type, in analogy with electromagnetism, while at larger distances the potential must increase indefinitely, so as to confine the quarks inside a hadron. The form

$$V = -\frac{4}{3}\frac{\alpha_s}{r} + kr \tag{6.2}$$

was given in (2.8). In Chapter 4, we saw that this form of the potential successfully accounts for the energy levels in charmonium and bottomonium bound states. However, we now discuss the direct experimental evidence for it.

6.2 The QCD potential at short distances

Direct evidence supporting the form (6.2) at short distances was first obtained in experiments at the CERN $p\bar{p}$ collider (Arnison *et al.* 1984, Bagnaia *et al.* 1984). In this accelerator, protons of energy 315 GeV circulate in one direction around a magnet ring and antiprotons of energy 315 GeV circulate in the other direction. The two beams intersect in two positions, large detectors being placed at the intersection points to record the secondaries produced. Rare events (about 10^{-6} of all collisions) are found to consist of two high energy jets of hadrons at an angle to the beams, as in Figure 6.2. The selection of such events is based firstly on the requirement that the transverse energy $E_T = \sum E_i \sin\theta_i > 15$ GeV, where the

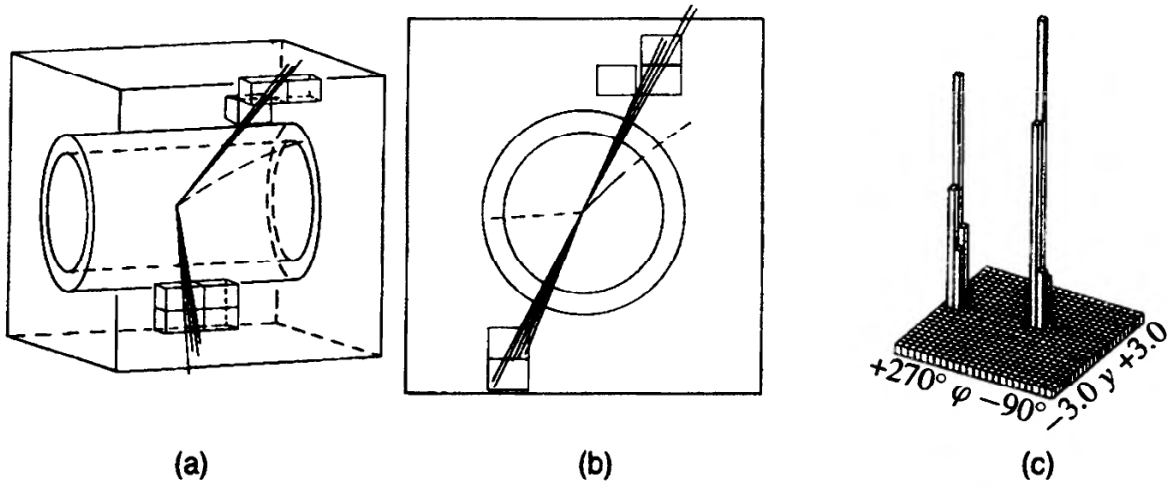

Fig. 6.2. Displays of a two-jet event in the UA1 detector at the CERN $p\bar{p}$ collider (315 GeV protons on 315 GeV antiprotons). In (a) the event is shown in perspective. After traversing an inner cylindrical tracking detector, the hadrons in the jets enter a calorimeter-type detector that measures the total energy deposited. Activated calorimeter modules are shown as blocks; (b) shows the view down the beam pipe, demonstrating the back-to-back nature of the jets in azimuth; (c) is a plot of transverse energy as a function of azimuth and polar angle, showing that the energy is concentrated in two well-collimated jets, with total energies of 93 GeV and 84 GeV and transverse energies of 81 GeV and 78 GeV respectively.

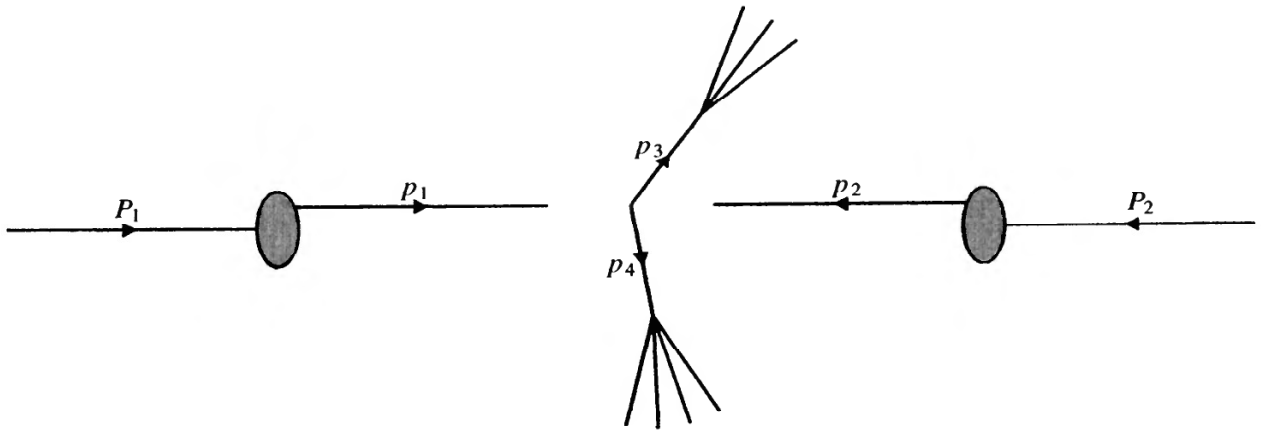

Fig. 6.3. Kinematics of a parton–parton collision in a proton–antiproton collider. P_1, P_2 are respectively the proton and antiproton momenta.

sum is made over local energy depositions in the calorimeter cells and θ_i is the angle to the incident beam direction. Most of these events consist of two jets with approximate momentum balance (as evidenced by the back-to-back configuration in azimuthal angle in Figure 6.2). The remainder are principally three-jet events, although four-jet and one-jet events also occur.

The two-jet events (Figure 6.3) are interpreted in terms of the elastic scattering of a parton (quark or gluon) in the proton from one in the antiproton, each scattered

parton giving rise to a hadron jet in the manner familiar from the process $e^+e^- \rightarrow$ hadrons. The kinematics of the collision are shown in the figure; p_3, p_4 are the 4-momenta of the observed jets and p_1, p_2 are the (unknown) momenta of the partons before the collision. Then energy–momentum conservation gives

$$p_1 + p_2 = p_3 + p_4 \tag{6.3}$$

while 3-momentum conservation along the beam (z-axis) gives

$$p_{1z} + p_{2z} = p_{3z} + p_{4z} \tag{6.4}$$

The 4-momentum transfer is

$$q = p_3 - p_1 = p_2 - p_4 \tag{6.5}$$

In terms of the x-variable, (5.30),

$$p_1 = x_1 P_1 \qquad p_2 = x_2 P_2 \tag{6.6}$$

where P_1 and P_2 are the 4-momenta of the proton and antiproton. Let E be the energy in each beam. Then from (6.4), neglecting all particle masses, we can define

$$x_1 - x_2 = (p_{3z} + p_{4z})/E = x_F \tag{6.7}$$

whereas from (6.3) and (6.6)

$$(p_3 + p_4)^2 = (x_2 P_2 + x_1 P_1)^2 = -4x_1 x_2 E^2$$

We then define

$$x_1 x_2 = -(p_3 + p_4)^2/(4E^2) = \tau \tag{6.8}$$

The Feynman x_F and τ variables defined in this way give the values of the fractional momenta x_1 and x_2,

$$x_1, x_2 = \tfrac{1}{2}\left(x_F \pm \sqrt{x_F^2 + 4\tau}\right) \tag{6.9}$$

and therefore p_1, p_2 in terms of the known quantities E, p_3 and p_4. Thus the 4-momentum transfer q in (6.5) can also be calculated. The direction of the equal and opposite 3-momentum vectors of the scattered partons in their common cms frame is clearly given by $\mathbf{p}_3 - \mathbf{p}_4$, so that the cms scattering angle of the partons relative to the beam direction is

$$\cos\theta = \frac{(\mathbf{p}_3 - \mathbf{p}_4) \cdot (\mathbf{p}_1 - \mathbf{p}_2)}{|\mathbf{p}_3 - \mathbf{p}_4||\mathbf{p}_1 - \mathbf{p}_2|}$$

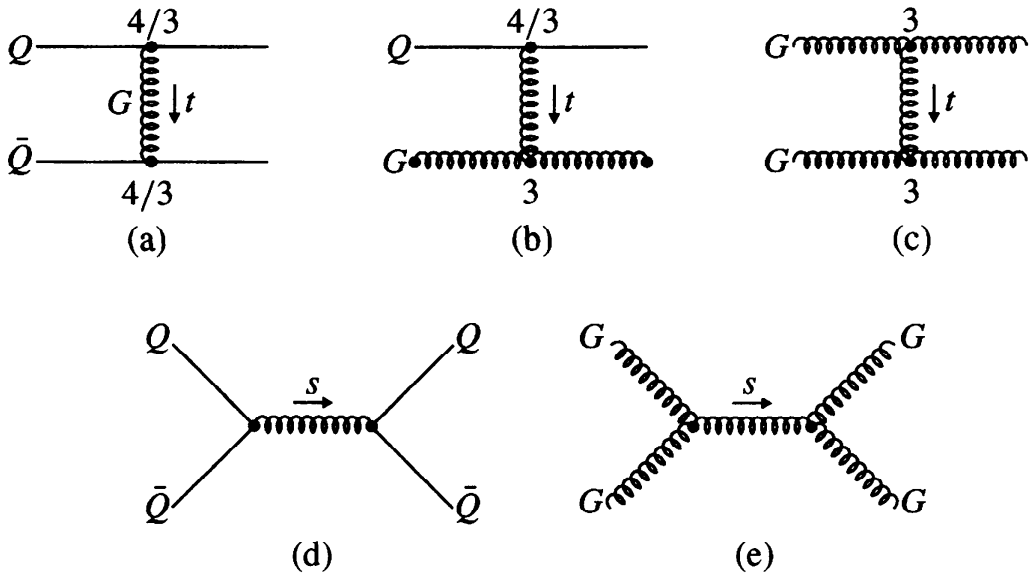

Fig. 6.4. Quark–quark, quark–gluon and gluon–gluon scattering via single-gluon exchange, in the t- and s-channels. Q denotes a quark, $\bar{Q}$ an antiquark and G a gluon. (a), (b), (c) show t-channel exchanges and (d), (e) show s-channel exchanges.

Note that since we do not know which incident parton (p_1 or p_2) belongs to which jet (p_3 or p_4), there is an ambiguity between θ and $\pi - \theta$. In the analysis, the smaller of the two values of θ was assumed, as it was also for the predicted distribution when comparing with theory. The expected cross-section for the proton–antiproton scattering to two jets will be

$$\frac{d^3\sigma(p\bar{p} \to 2\,\text{jets})}{dx_1 dx_2 d(\cos\theta)} = \sum_{i,j} \left[\frac{F_i(x_1)}{x_1}\right]\left[\frac{F_j(x_2)}{x_2}\right]\frac{d\sigma_{ij}}{d(\cos\theta)} \tag{6.10}$$

where $F_i(x_1)/x_1$, $F_j(x_2)/x_2$ are the densities of partons of type i, j in the proton and antiproton, with fractional momenta x_1 and x_2, and $d\sigma_{ij}/d(\cos\theta)$ is the elementary parton–parton cross-section. The contributions to the cross-section through the process of single-gluon exchange are shown in Figure 6.4. Scattering may proceed through momentum transfer in the so-called t-channel, where

$$t = q^2 = (p_1 - p_3)^2 \tag{6.11}$$

and p_1 and p_3 are defined in Figure 6.3, or through the s-channel, where

$$s = -(p_1 + p_2)^2 = 4x_1x_2E^2 \tag{6.12}$$

is the square of the cms energy of the partons. Figures 6.4(a), (b), (c) show t-channel exchanges, and (d), (e) show s-channel processes. Broadly, the t-channel cross-sections vary as $d\sigma/dt \simeq 1/t^2$ (or $1/q^4$), whereas the crossed, s-channel

cross-sections go as $d\sigma/ds \simeq 1/s^2$, as is clear on dimensional grounds. Provided $t \ll s$, the t-channel exchanges dominate, which is the case in the experimental conditions. The actual numbers multiplying the coupling parameter α_s at each vertex, as predicted by QCD, are indicated. As previously stated in Chapter 2 and in (6.2), the QQG or $\bar{Q}\bar{Q}G$ coupling factor is $\frac{4}{3}\alpha_s$, while for the GGG vertex it is $3\alpha_s$. Thus, in the approximation that all three processes have a similar angular distribution, we see that the cross-section effectively measures the combination of structure functions

$$F(x) = G(x) + \tfrac{4}{9}[Q(x) + \bar{Q}(x)] \tag{6.13}$$

where now $Q(x)$, $\bar{Q}(x)$ and $G(x)$ represent momentum densities, i.e. the quark, antiquark and gluon densities weighted by the momentum fraction, x.

The different processes in Figure 6.4 involve particles with different spins and hence, in principle, different angular distributions. However, if $t \ll s$, the typical cms scattering angle θ is small and all processes will then display the same angular distribution as in (5.14), which for $t \ll s$ gives

$$\frac{d\sigma}{d\Omega} \propto \frac{\alpha_s^2}{4p_0^2 \sin^4(\theta/2)} \tag{6.14}$$

where $p_0 = \sqrt{s/2}$ is the cms momentum of each parton. This is, of course, the famous Rutherford formula for scattering via a $1/r$ potential, with the replacement of α by α_s. It assumes of course that $\alpha_s \ll 1$ so that double-gluon exchange can be neglected.

The observed angular distribution in the early $p\bar{p}$ experiments is shown in Figure 6.5. If we parameterise it in the form $[\sin(\theta/2)]^{-n}$, then the data give $n = 4.16 \pm 0.20$. We note that deviations from the straight line are expected near $\theta = \pi/2$, both because the full relativistic formula for single-vector-gluon exchange must be used and because of the ambiguity between θ and $\pi - \theta$ mentioned before.

It is instructive to compare these results for (predominantly) gluon–gluon scattering, typically at $q^2 \simeq 2000$ GeV^2, with the results of Geiger and Marsden (1909) on the scattering of α-particles by silver and gold nuclei at $q^2 \simeq 0.1$ GeV^2. The linearity of the plots in both cases is evidence that a $1/r$ potential is involved. In the case of the scattering of spinless, non-relativistic α-particles, the Rutherford formula applies at all angles (if the nuclei act as point charges). In parton–parton scattering, the Rutherford formula is a small-angle approximation for the full relativistic formula including spin effects.

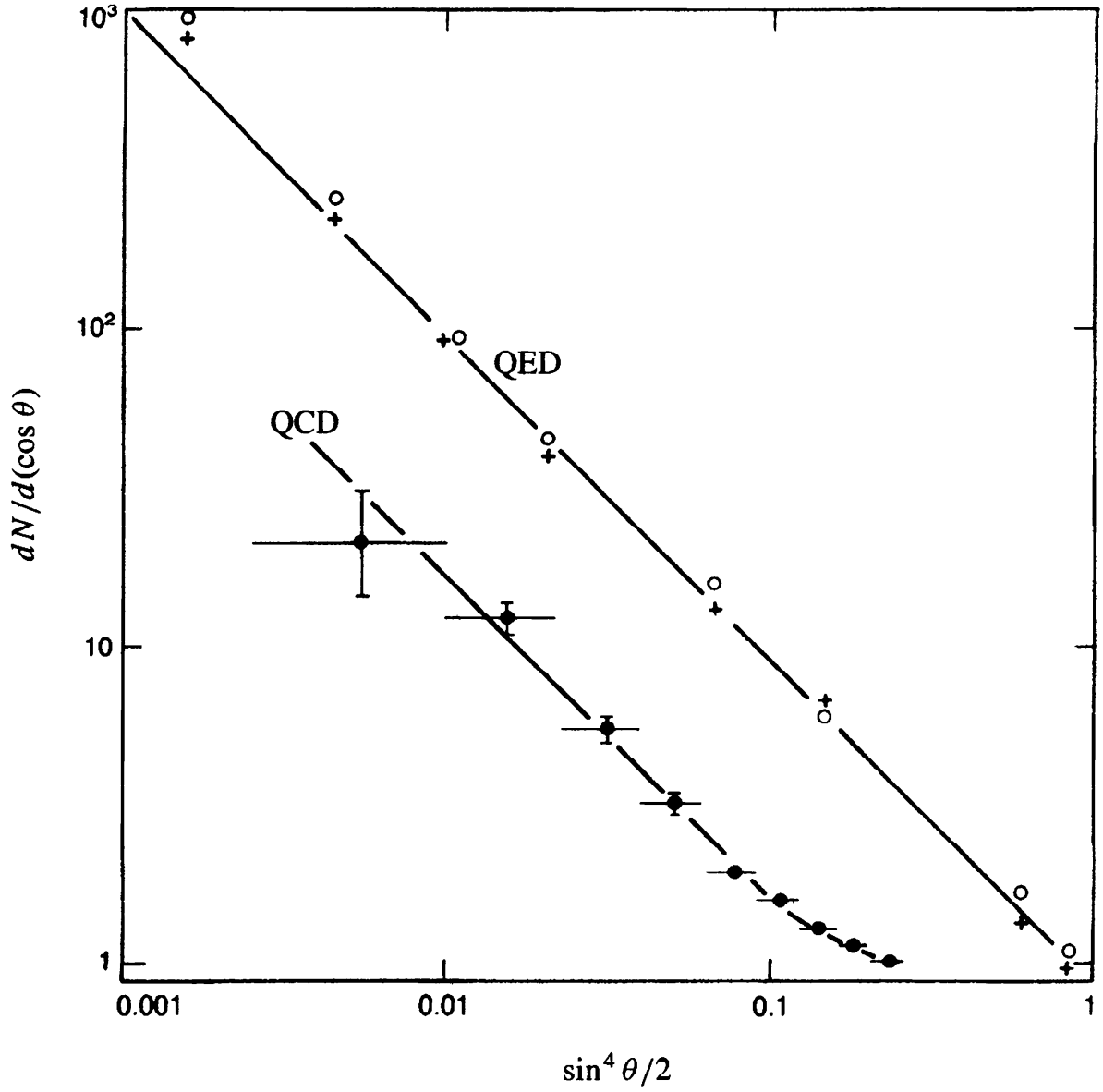

Fig. 6.5. Examples of differential cross-sections for pointlike scattering via a $1/r$ potential. The upper plot shows the results of Geiger and Marsden (1909) for the scattering of α-particles from radioactive sources by gold (crosses) and silver (open circles) foils, demonstrating the existence of a nucleus to the atom that scatters the α-particles through the Coulomb field. Their results involved momentum transfers $\simeq 0.1$ GeV^2 and are consistent with the Rutherford formula $dN/d\Omega \propto \sin^{-4}(\theta/2)$ (solid line). The lower plot is the two-jet angular distribution found at the CERN $p\bar{p}$ collider, at $q^2 \simeq 2000$ GeV^2, showing that the scattering of pointlike (quark or gluon) constituents in the nucleon also obeys the Rutherford law at small angles, and hence that the QCD potential varies as $1/r$ at small distances. At large angles, deviations from the straight line occur because of relativistic (spin) effects and because scatters of $\theta > \pi/2$ have to be folded into the distribution for $\theta < \pi/2$. The solid curve is the QCD prediction for single vector gluon exchange. Scalar (spin 0) gluons are excluded, as they predict a very much weaker angular dependence.

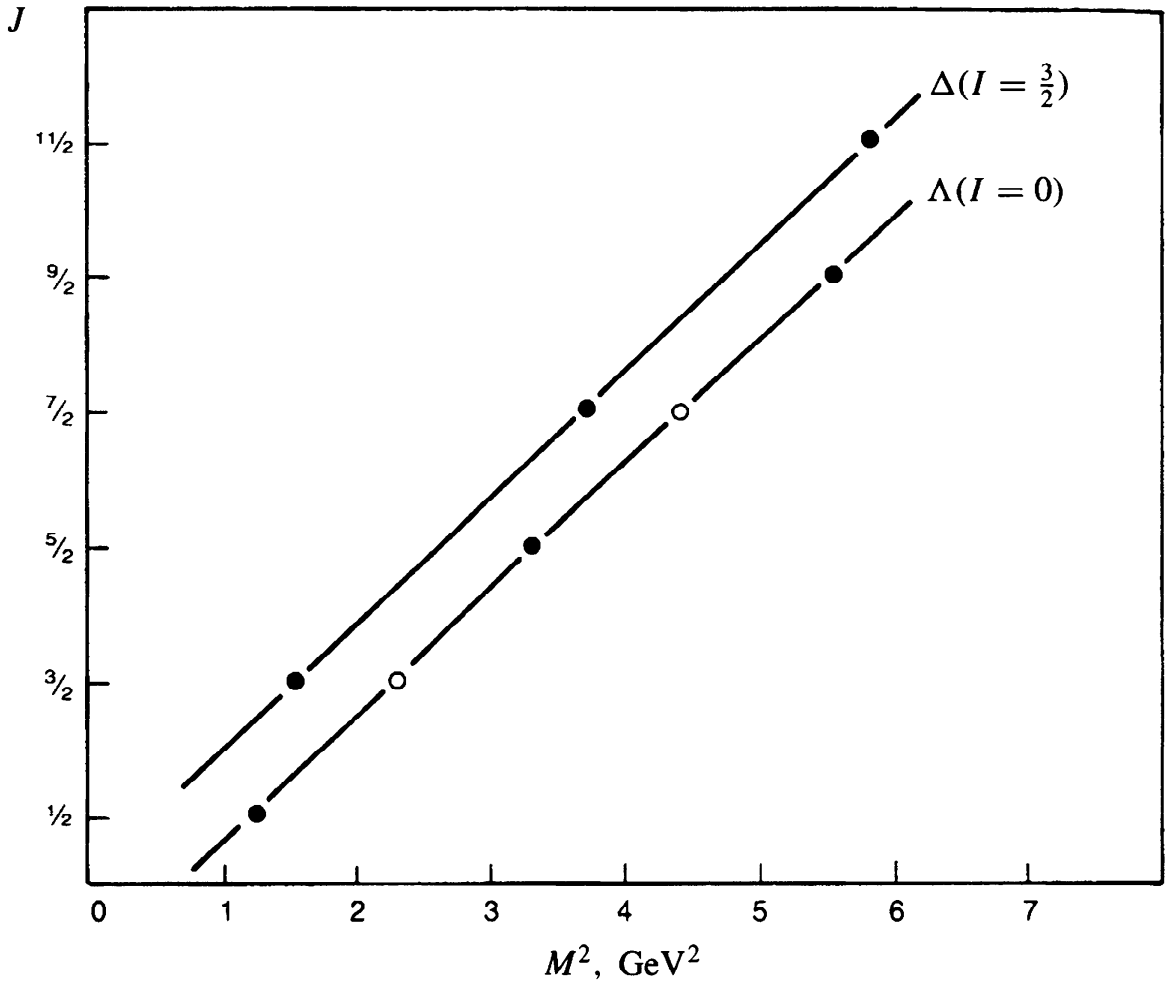

Fig. 6.6. Plots of spin J against squared mass for baryon resonances of the Δ family ($S = 0, I = \frac{3}{2}$) and the Λ family ($S = -1, I = 0$). Positive- and negative-parity states are shown as full and open circles.

6.3 The QCD potential at large distances: the string model

One of the most remarkable empirical results of the study of baryon and meson resonances is that observed for states with a given isospin I, charge parity C, strangeness S etc., but with different angular momentum J and mass M. There appears to be a simple linear dependence of the J value of those states of highest angular momentum on the square of the mass. Examples of the plots for the Δ and Λ baryon resonances are shown in Figure 6.6. Such a plot is called a Chew–Frautschi plot (and was originally of interest in Regge pole theory, which we shall not discuss). Here we show its relevance to the form of the QCD potential at large distances.

In QCD, a characteristic feature of the gluon mediators of the colour force is their strong self-interaction, because the gluons themselves are postulated to carry colour charges. In analogy with the electric lines of force between two electric charges, as in Figure 6.7(a), we can imagine that quarks are held together by

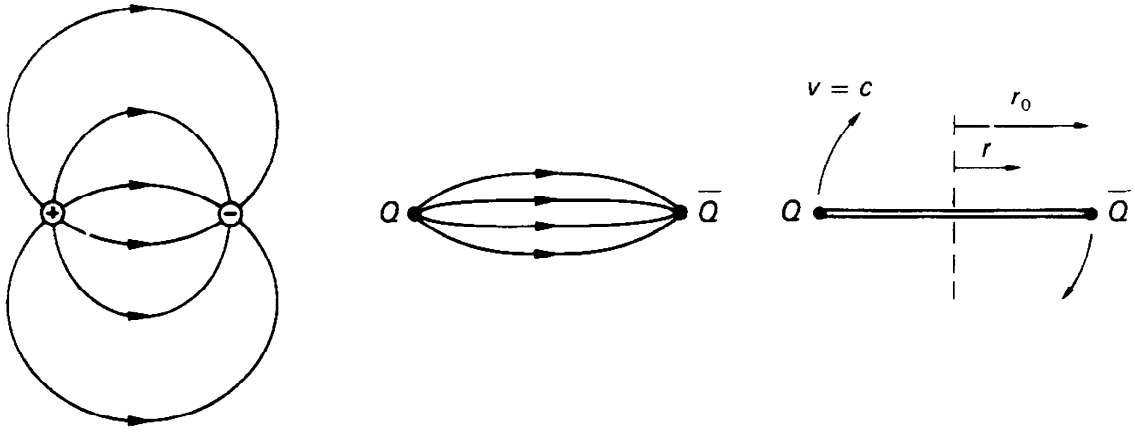

(a) (b) (c)

Fig. 6.7. (a) Electric lines of force between two charges. (b) Colour lines of force between quarks are pulled together into a tube or string, because of the strong self-interaction between the gluons, which are the carriers of the colour field. (c) String model used in calculating the relation between the angular momentum and mass of a hadron.

colour lines of force as in Figure 6.7(b), but the gluon–gluon interaction pulls these together into the form of a tube or string.

Suppose that k is the energy density per unit length of such a string and that it connects together two massless quarks as in Figure 6.7(c). The orbital angular momentum of the quark pair will then be equal to the angular momentum of the gluon tube, and we can calculate this if we assume that the ends of the tube rotate with velocity $v = c$. Then the local velocity at radius r will be

$$\frac{v}{c} = \frac{r}{r_0}$$

where r_0 is half the length of the string. The total mass is then (relativistically)

$$E = Mc^2 = 2\int_0^{r_0} \frac{kdr}{\sqrt{1 - v^2/c^2}} = kr_0\pi$$

and its orbital angular momentum will be

$$J = \frac{2}{\hbar c^2}\int_0^{r_0} \frac{krvdr}{\sqrt{1 - v^2/c^2}} = \frac{kr_0^2\pi}{2\hbar c}$$

Eliminating r_0 between these equations and including the quark spins we therefore expect for the observed relation between the angular momentum quantum number and energy of a hadron state $J = \alpha' E^2 +$ constant.

This result holds for the case of constant energy density k of the string, i.e. for a potential of the form $V = kr$. Generally, for a potential of the form $V = kr^n$ it is

easy to show that the relation acquires the form

$$J \propto E^{(1+1/n)} \tag{6.15}$$

so the observed linear dependence of J on M^2 is evidence for the linear potential (6.2). The value of k is obtained from the slope α' of the plot (Figure 6.6) which in our model is given by

$$\alpha' = 1/(2\pi k\hbar c)$$

Inserting the observed value, $\alpha' = 0.93\ \text{GeV}^{-2}$, we find

$$k = 0.87\ \text{GeV fm}^{-1} \tag{6.16}$$

This number also comes from consideration of the sizes of hadrons. A typical hadron mass is about 1 GeV and its radius, as measured in electron scattering is about 1 fm, so the linear energy density will be $k \simeq 1\ \text{GeV fm}^{-1}$.

6.4 Gluon jets in e^+e^- annihilation

Dramatic demonstrations of quark substructure are obtained in e^+e^- annihilation to hadrons at very high energy. As noted previously the elementary process is annihilation to a $Q\bar{Q}$ pair, followed by 'fragmentation' of the quarks to hadrons. At cms energies of 30 GeV or more, typically about 10 hadrons (mostly pions) are produced. The average hadron momentum along the original quark direction is therefore large compared with its transverse momentum p_T, which is limited to $p_T \simeq 0.5\ \text{GeV}/c$, i.e. a magnitude $\sim 1/R_0$, where R_0 is a typical hadron size ($\sim$ 1 fm). Hence, the hadrons appear in the form of two 'jets' collimated around the $Q\bar{Q}$-axis (see Figures 6.8(a) and 2.5). Occasionally, one might expect a quark to radiate a 'hard' gluon, carrying perhaps half of the quark energy, at a large angle (Figure 6.8(b)), the gluon and quark giving rise to separate hadronic jets. Such processes are observed (Figure 6.9(a)). The rate of three-jet compared with two-jet events is clearly determined by α_s, which gives the probability of radiating a gluon. The results of the analyses in four detectors at the PETRA e^+e^- collider at DESY gave, for cms energy 30–40 GeV, a value $\alpha_s \simeq 0.14$.

The angular distribution in the three-jet events also allows a determination of the gluon spin. First the jets are ordered in energy, $E_1 > E_2 > E_3$. Then a transformation is made to the cms frame of jets 2 and 3, and the angle $\tilde{\theta}$ calculated for jet 1 (of highest energy) with respect to the common line of flight of jets 2 and 3. Jet 3 (that of lowest energy) is most likely to be produced by the gluon, and the distribution in $\tilde{\theta}$ is sensitive to the gluon spin. Figure 6.9(b) shows data from the TASSO detector together with the predictions for scalar and vector gluons.

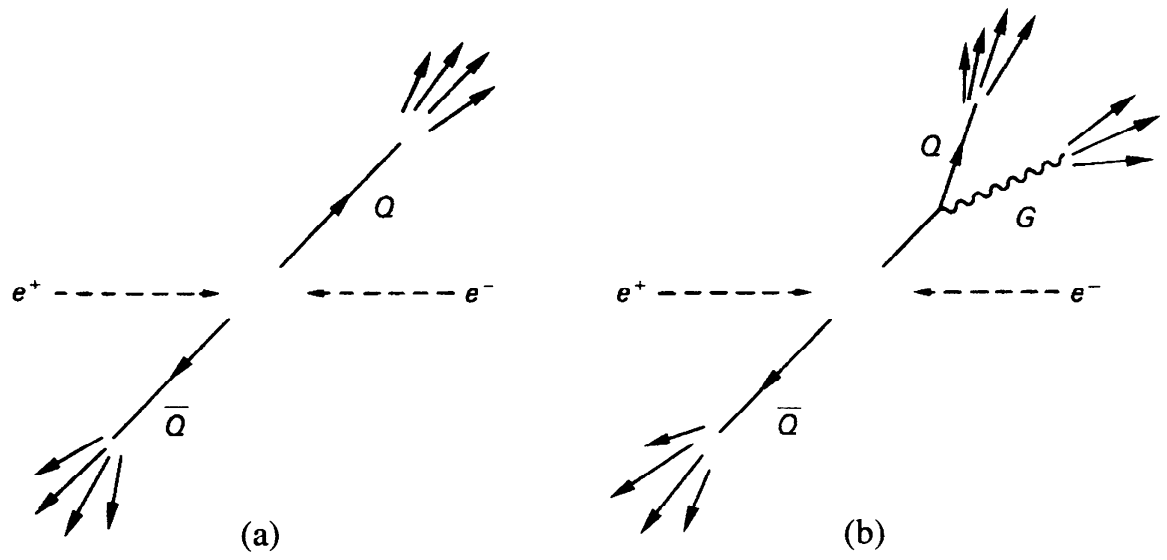

Fig. 6.8.

The data strongly favour the vector gluon hypothesis, i.e. the gluon has spin-parity $J^P = 1^-$, like the photon.

6.5 Running couplings in QED and QCD

We saw in Section 2.5 that the departure of the observed magnetic moment of the electron from the Dirac value $e\hbar/(2mc)$ is correctly predicted in quantum electrodynamics (QED). The so-called anomaly for the electron and muon is expressed in terms of the departure of the gyromagnetic ratio g from 2 and appears in the form of a perturbation expansion in powers of α, obtained by summing the relevant Feynman graphs:

$$\left(\frac{g-2}{2}\right)^{\text{electron}} = 0.5\left(\frac{\alpha}{\pi}\right) - 0.32848\left(\frac{\alpha}{\pi}\right)^2 + 1.19\left(\frac{\alpha}{\pi}\right)^3 + \cdots \quad (6.17a)$$

$$\left(\frac{g-2}{2}\right)^{\text{muon}} = 0.5\left(\frac{\alpha}{\pi}\right) + 0.76578\left(\frac{\alpha}{\pi}\right)^2 + 24.45\left(\frac{\alpha}{\pi}\right)^3 + \cdots \quad (6.17b)$$

The observed and predicted numbers are given in Table 6.1. Note that in the above expressions the leading correction $0.5(\alpha/\pi)$ is the same for electron and muon, while the vacuum polarisation term discussed below, of order α^2, differs in both magnitude and sign and is much larger for the muon, since the momenta of the particles in the intermediate virtual states or loops (see Figure 6.11) scale in proportion to the parent particle mass. The fact that the error on the predicted number exceeds that of the observed value (see Table 6.1) is just a reflection of the error in the experimental value of α measured from the Hall effect and used in the theoretical prediction (6.17).

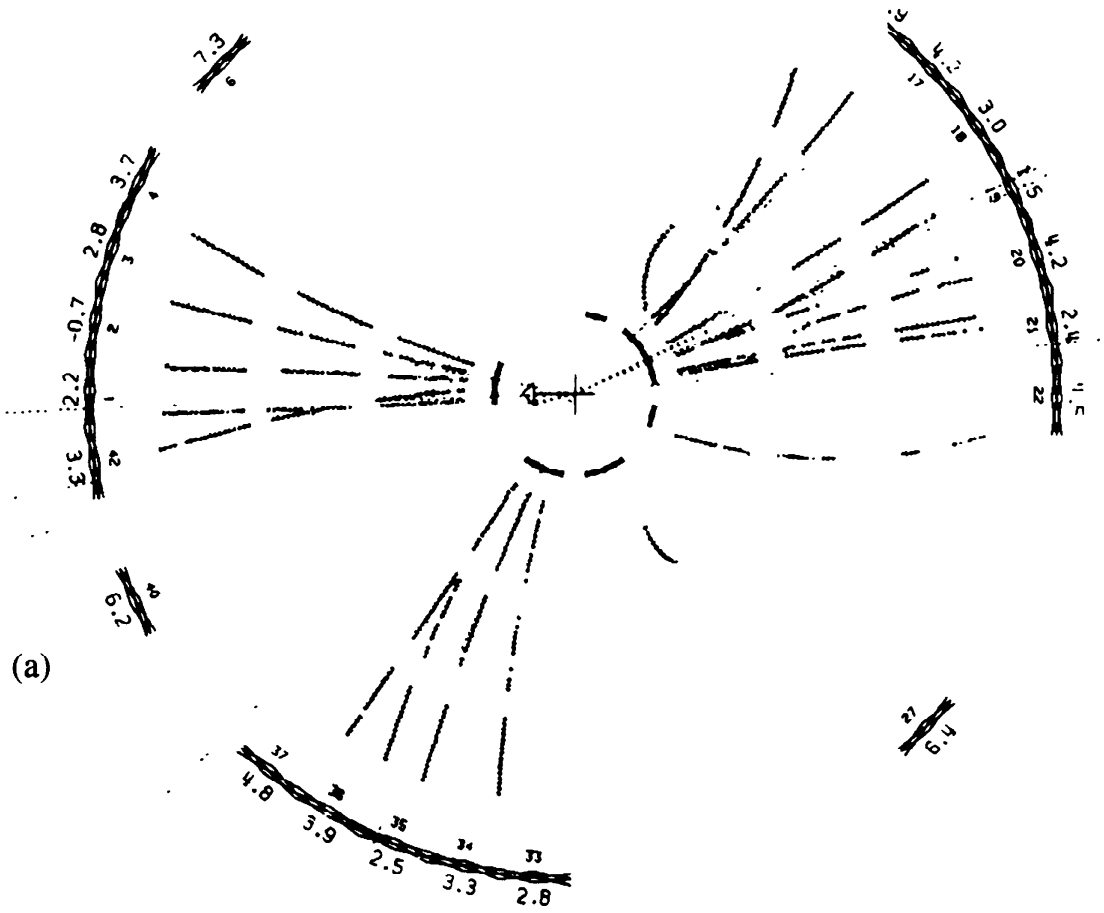

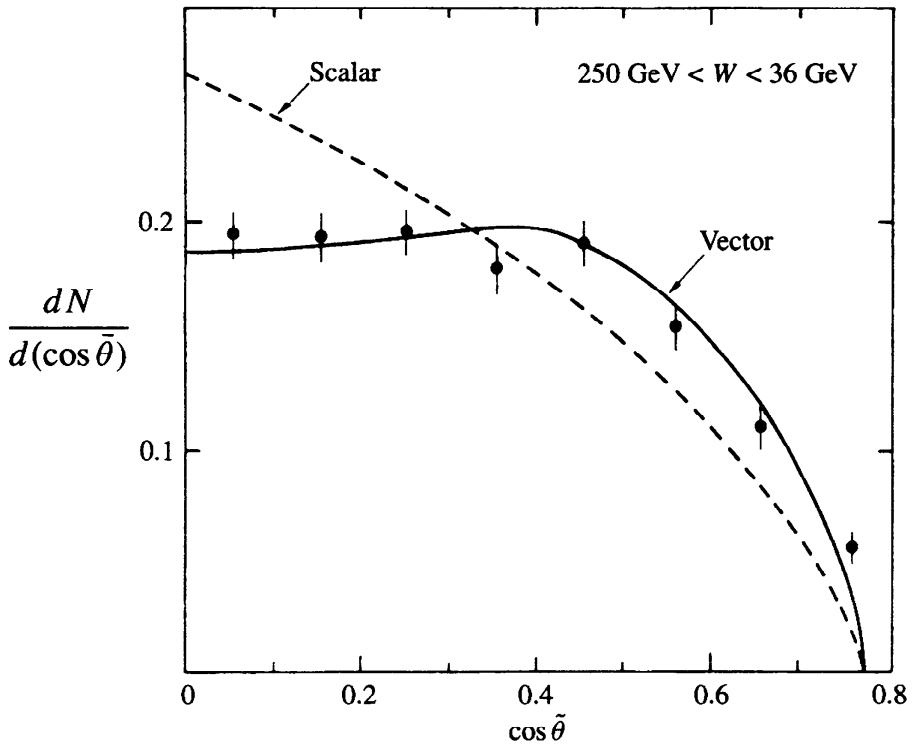

Fig. 6.9. (a) Example of a three-jet event observed in the JADE detector at the PETRA e^+e^- collider (DESY, Hamburg). The total cms energy in the event is 31 GeV. Such events are suggestive of the process in Figure 6.8(b) (compare with the more common two-jet event of Figure 2.5). (b) Distribution in angle $\tilde{\theta}$ of the highest energy jet in three-jet events, with respect to the line of flight of the other two jets in their cms frame. The curves show predictions for spin 1 (vector) and spin 0 (scalar) gluons. Data from the TASSO detector at PETRA.

Table 6.1. $(g-2)/2$ *anomaly for leptons* ($\times 10^{10}$)

	Electron	Muon
predicted	$11\,596\,524 \pm 4$	$11\,659\,180 \pm 100$
observed	$11\,596\,521.9 \pm 0.1$	$11\,659\,230 \pm 80$

The above results can also be described in terms of a single, first-order correction, with α depending on the masses or momentum transfers in the virtual processes involved, so that we can write for the anomaly

$$\left(\frac{g-2}{2}\right) = \frac{0.5}{\pi}\alpha_{\text{eff}} \tag{6.18}$$

where α_{eff} is slightly larger for the muon than for the electron. In fact we are treating α as a 'running coupling constant' dependent on the masses or momentum transfers involved in any particular case. This is not so arbitrary as it sounds. We noted previously that attempts to define 'bare' couplings, charges or masses – α_0, e_0, m_0 – in QED led to infinities associated with self-energy terms, arising from the fact that the momenta of virtual particles in loop diagrams can go to infinity. We have to replace such quantities by the renormalised, physically measured values. The running coupling constant expresses the value of α at one value of q^2 in terms of that at another value, say $q^2 = \mu^2$ (and thus avoids the problem of the coupling at $q^2 = \infty$). This relation is given in (6.21) below. Notice that according to (6.21) the effective coupling gets smaller as q^2 decreases, or the typical distance involved in the interaction, $r \sim 1/q$, increases. This is a well-known effect in a polarisable (dielectric) medium. A test charge immersed in a dielectric exerts a potential, at distances comparable with or larger than molecular dimensions, that is smaller than the Coulomb potential in free space. The dielectric produces a *shielding* effect (see Figure 6.10). Even in a vacuum, a test charge is continually emitting and reabsorbing virtual photons that can temporarily produce e^+e^- pairs, again producing a shielding effect, the so-called *vacuum polarisation*; see Figure 6.11.

Here we state without proof some results from field theory and the renormalisation procedure. The general dependence of the coupling on momentum transfer is expressed by the so-called renormalisation group equation, in which the coupling is expanded in powers of $\ln(q^2/\mu^2)$:

$$\frac{1}{\alpha(\mu^2)} = \frac{1}{\alpha(q^2)} + \beta_0 \ln\left(\frac{q^2}{\mu^2}\right) + \cdots \tag{6.19}$$

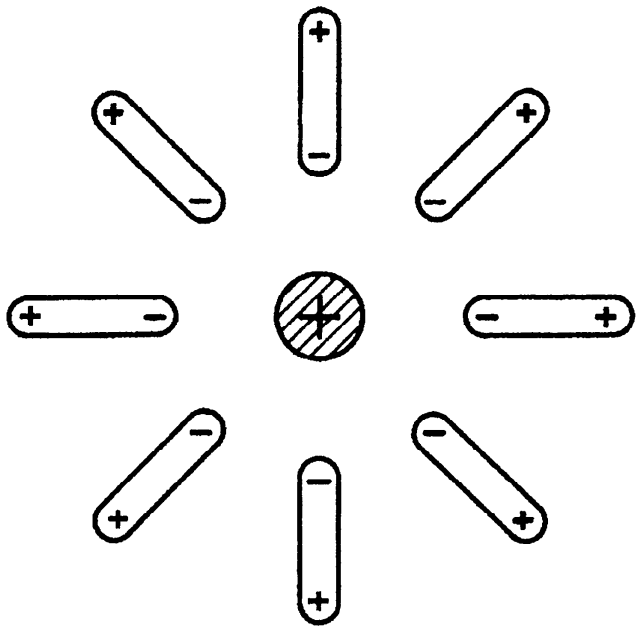

Fig. 6.10.

and where as a first approximation just the first two terms are considered. The quantity β_0 depends on the number of degrees of freedom, n_b for bosons and n_f for fermions, in the loops of the vacuum polarisation terms:

$$\beta_0 = \frac{1}{12\pi}(4n_f - 11n_b) \tag{6.20}$$

For the electromagnetic interaction (or any other Abelian field, i.e. one without self-interaction) there can be no loops containing photons, so that in this case $n_b = 0$. At high energies we can take the number of fermion families as $n_f = 3$, so that $\beta_0 = 1/\pi$. Inserting this in (6.19) we get for the QED coupling parameter

$$\alpha_{\text{em}}(q^2) = \frac{\alpha(\mu^2)}{\left[1 - \frac{1}{\pi}\alpha(\mu^2)\ln\left(\frac{q^2}{\mu^2}\right)\right]} \tag{6.21}$$

For example, if we take $\alpha_{\text{em}} = 1/137$ at $\mu = 1$ MeV, then near the Z^0 mass, at $q \simeq 100$ GeV, the effective value will be $\alpha(M_Z) \simeq 1/129$. The effective coupling *increases* (very slowly) with energy–momentum transfer.

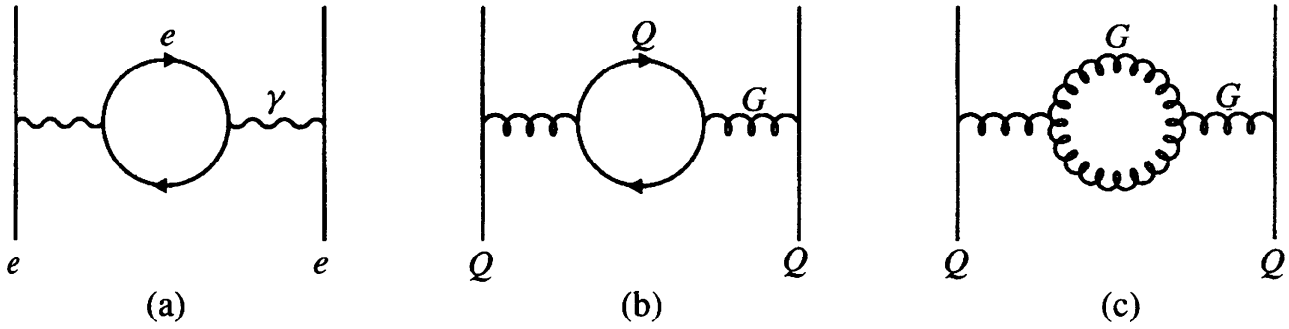

Fig. 6.11. Diagrams involving loops (vacuum polarisation effects) (a) in QED, where loops contain fermions only, (b) in QCD for a loop containing quarks and (c) in QCD for a gluon loop, involving gluon–gluon coupling, absent in QED.

For QCD, described by an SU(3) colour symmetry, $n_b = 3$ so that with $n_f = 3$ we find $\beta_0 = -7/(4\pi)$ in (6.20) and thus

$$\alpha_s(q^2) = \frac{\alpha_s(\mu^2)}{1 + \frac{7}{4\pi}\alpha_s(\mu^2)\ln\left(\frac{q^2}{\mu^2}\right)} \tag{6.22}$$

This can be put in the simpler form

$$\alpha_s(q^2) = \frac{1}{B\ln(q^2/\Lambda^2)} \tag{6.23}$$

where the positive quantity $B = -\beta_0$ and $\Lambda^2 = \mu^2 \exp\{-1/B\alpha_s(\mu^2)\}$. Here we see that α_s *decreases* with increasing q^2. This is typical of a non-Abelian field, i.e. one in which the field particles, in this case the gluons, themselves carry a colour charge and thus have self-coupling. The fermions as well as the transverse components of the gluon field exert a shielding effect, just as in QED, but the longitudinal gluons have an *antishielding* effect that dominates the situation and 'spreads out' the colour charge, resulting in weaker coupling as q^2 increases. Historically, this behaviour was first predicted by Politzer, Gross and Wilczek in 1973, and the first experimental support for it came from detailed studies of deep inelastic lepton–nucleon scattering in the period 1973–8. Observed were 'scaling deviations', i.e. small departures from the pure partonlike behaviour of non-interacting, free quark constituents; see the next section.

Clearly, (6.22) and (6.23) show that at asymptotically large q^2, the coupling $\alpha_s(q^2) \to 0$, i.e. the quarks behave as if free, a phenomenon known as *asymptotic freedom* and precisely what is expected in the naive, free parton, model. At low q^2, such that $q \sim \Lambda$, however, $\alpha_s(q^2)$ becomes very large and the perturbation expansion (6.19) becomes meaningless. Such large interquark coupling is presumably connected with the confinement of quarks at large distances, as for the potential

(6.2). The main point here is that, like QED, QCD has the form of a perturbation theory and applies only for $q^2 \gg \Lambda^2$.

Figure 6.12 shows experimental data on α_s as a function of q^2, to be compared with the dependence (6.23). The 'running' of the coupling is clearly visible. The data shown comes from a variety of sources.

(i) The widths of the $c\bar{c}$ and $b\bar{b}$ bound states ψ, ψ', Υ, Υ' etc. depend on α_s in the ways described in Sections 4.1 and 4.2.

(ii) In the continuum, the ratio $R = \sigma(e^+e^- \to \text{hadrons})/\sigma(\text{point})$ includes a factor $1+\alpha_s/\pi$ (see Figure 5.4). The extra term is there because, for example, an $r\bar{r}$ colour state of $Q\bar{Q}$ can also arise from a $g\bar{g}$ state which has undergone $\bar{r}g$ gluon exchange with probability of order α_s.

(iii) Event shapes in e^+e^- annihilation to hadrons, which are essentially the ratio of three-jet ($= Q\bar{Q}G$) to two-jet ($= Q\bar{Q}$) events, measure the gluon radiation probability, proportional to α_s.

(iv) Scaling deviations in deep inelastic lepton–nucleon scattering, measuring the departures in the structure functions from the naive, free parton, model, gave the first measurements of α_s and of Λ. In particular, the fundamental sum rules in such scattering have QCD corrections, e.g. the GLS sum rule (Section 5.9) includes a correction term $1 - \alpha_s/\pi$ at finite q^2.

(v) Finally, the most precise data on α_s comes from the QCD corrections to the hadronic width of the Z^0 resonance, which has been measured with great accuracy, as described in Chapter 8.

The curve in Figure 6.12 shows the variation predicted by (6.23), but in a somewhat more sophisticated form (taking some account of second-order terms). The usually quoted value of the parameter is $\Lambda \simeq 200$ MeV, but it is not very well determined and the most recent data from the HERA ep collider suggest a larger value, $\Lambda \simeq 300$ MeV. These numbers include estimates of the effects of higher-order terms in the expansion (6.19): the actual value depends on the exact prescription adopted for minimising the uncertainties from higher-order effects.

6.6 Evolution of structure functions in deep inelastic scattering

The q^2 evolution of the quark distributions (structure functions) in deep inelastic lepton–nucleon scattering formed one of the first tests of quantum chromodynamics.

Suppose that $u(x, q^2)dx$ denotes the density in a nucleon of the valence u quarks with momentum fraction $x \to x + dx$ at a particular value of q^2. Since there is no

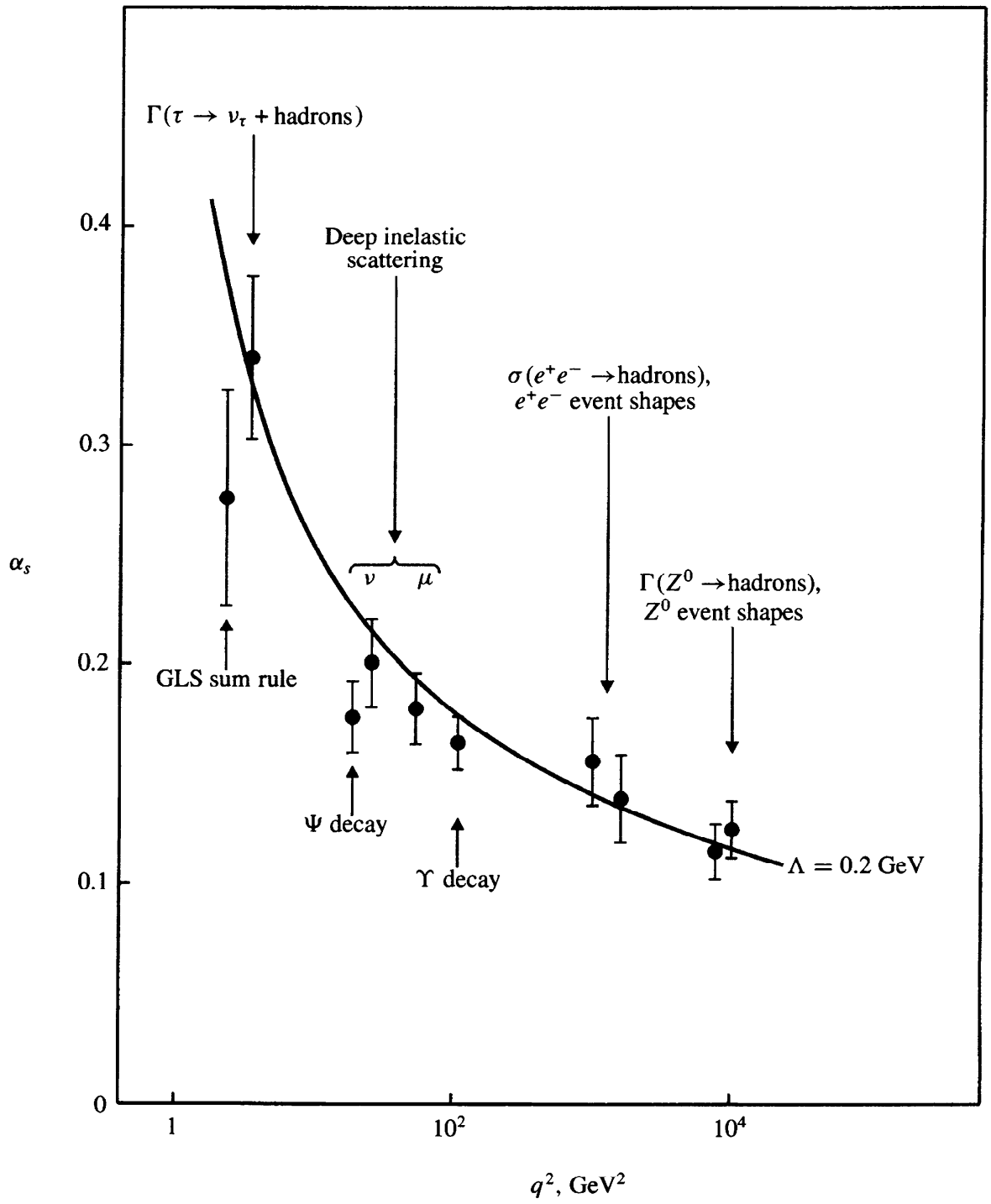

Fig. 6.12. Variation of the QCD coupling parameter α_s with q^2. The data come from various sources, as described in the text. The curve is the prediction (6.23) for $\Lambda \simeq 200$ MeV.

mass scale in the problem, any fractional change in $u(x, q^2)$ as a result of a change in q^2 can only be proportional to the fractional change dq^2/q^2, so that we can write

$$\frac{du(x,q^2)}{d(\ln q^2)}dx = \frac{\alpha_s(q^2)}{2\pi}\left[\int_{y=x}^{y=1} u(y,q^2)P_{QQ}\left(\frac{x}{y}\right)\frac{dy}{y}\right]dx \qquad (6.24)$$

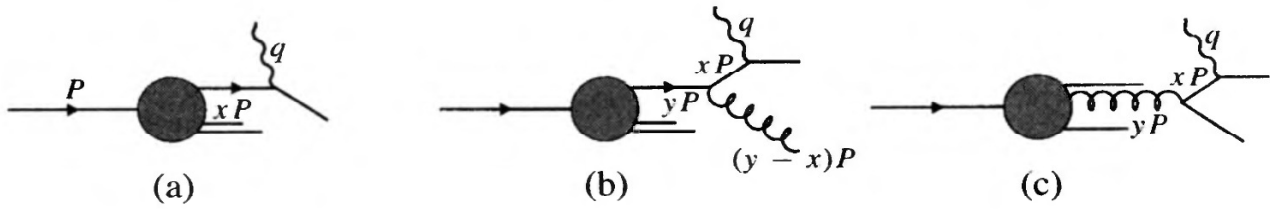

Fig. 6.13. Diagrams illustrating the absorption of a momentum transfer q in deep inelastic scattering by (a) a quark with momentum fraction x, (b) a quark with momentum fraction x which has radiated a gluon and which had originally a momentum fraction y, (c) a quark of momentum fraction x created by a gluon with momentum fraction greater than x.

known as the Altarelli–Parisi equation. The meaning of this equation is clear from Figure 6.13(b). Here, a quark with momentum fraction x, which absorbs a momentum transfer q, is shown originating from a quark with momentum fraction $y > x$, which has previously radiated a gluon with fraction $y - x$. The probability of such gluon emission is clearly given by α_s, and the probability that the quark retains a fraction $z = x/y$ of its momentum is given by the splitting function $P_{QQ}(z)$, describing the radiation of a vector particle by a fermion:

$$P_{QQ}(z) = \frac{4}{3}\frac{(1+z^2)}{(1-z)} \tag{6.25}$$

This z dependence was originally written down by Williams and Weizsacker in 1934, for the radiation of a virtual photon by an electron (so that, with $1 - z$ as the photon fraction, the equivalent spectrum of photon frequencies is $\sim dk/k$). The quantity $\frac{4}{3}$ is a colour factor. Equation (6.24) therefore simply states that the increase du in u is proportional to α_s and to the integrated number of quarks with $y > x$ that can radiate a gluon in such a way that they then fall into the interval $x \to x + dx$.

So much for the valence quarks. If 'sea quarks' ($Q\bar{Q}$ pairs) are also included, there will be an additional term in (6.24) since, as shown in Figure 6.13(c), gluon constituents can transform to $Q\bar{Q}$ pairs with probability $\alpha_s(q^2)$ and thus also contribute to the quark density. Both terms have the effect that, as q^2 increases, the quark (predominantly valence quark) distribution shrinks to smaller x, i.e. the density at large x progressively decreases while that at small x is enhanced.

From (6.24) and similar equations it is possible, given a value for the parameter Λ in (6.23) and the quark distributions $u(x)$, $d(x)$ etc. at one value of q^2, to predict how these distributions will change with q^2.

Figure 6.14 shows results for the structure function $F_2(x, q^2)$ measured from muon and electron scattering off nucleon (deuterium) targets. (F_2, it will be recalled, measures the sum of the Q and $\bar{Q}$ momentum fractions; see (5.35)). The decrease in F_2 with increasing q^2 for $x > 0.2$, and its increase for smaller x-values,

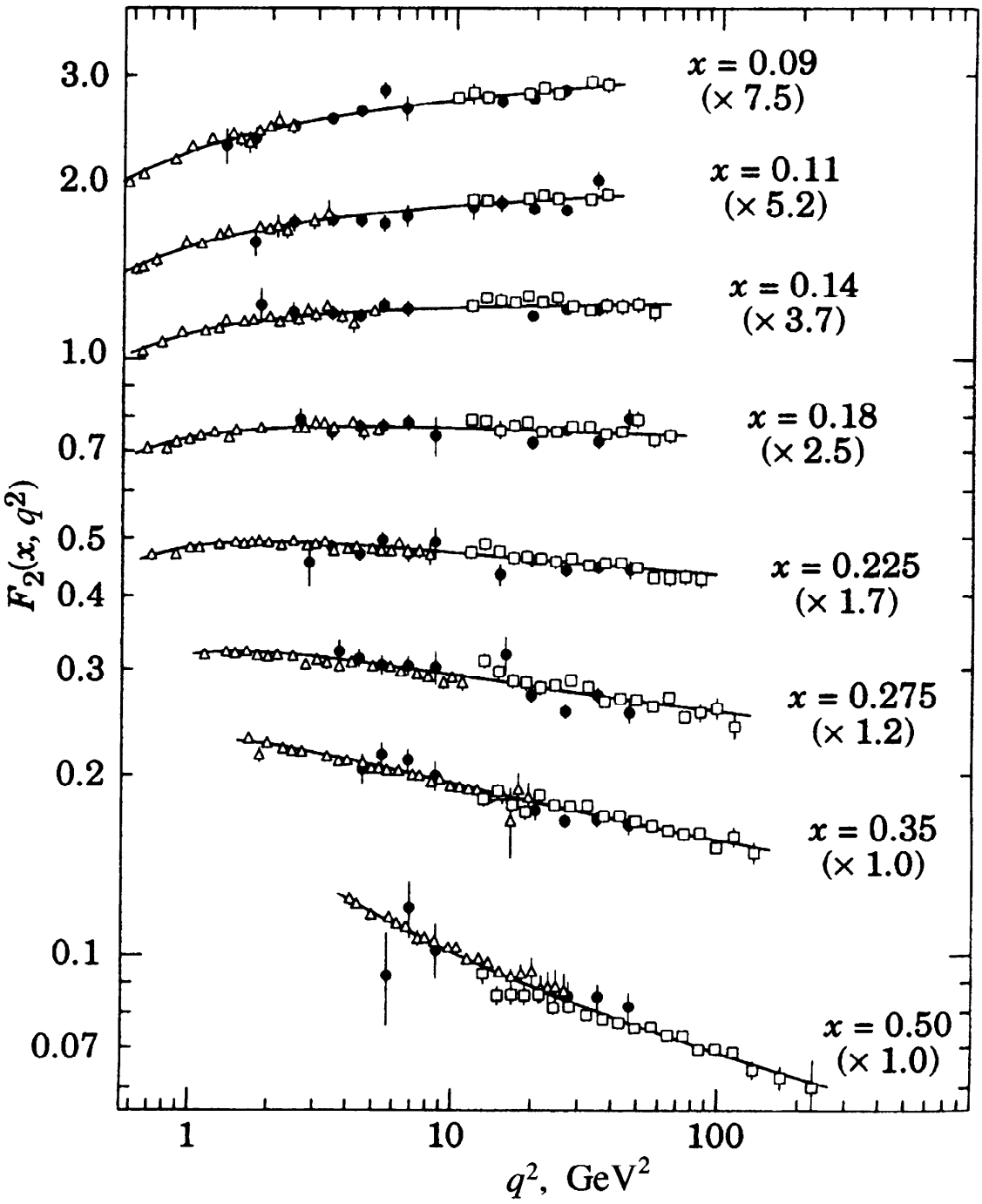

Fig. 6.14. The nucleon structure function $F_2(x, q^2)$ measured in deep inelastic muon and electron scattering off a deuterium target. The curves show the dependence expected from QCD, with $\Lambda = 0.2$ GeV. For clarity, the different curves have been multiplied by the factors shown in brackets. ●, NMC; △, SLAC; □, BCDMS. (After Montanet *et al.* 1994.)

is well displayed. The curves give the predicted variation for $\Lambda = 0.2$ GeV. An empirical fit, in the form of a polynomial in x and $1 - x$, is made to the structure function at one value of q^2 (5 GeV^2 in this case) and the evolution with q^2 is then computed.

Figure 6.15 includes data on lepton–proton scattering at small x that extend to much higher values of q^2, from the HERA ep collider. Collisions take place between 28 GeV $e^{\pm}$ circulating in one direction and 820 GeV protons circulating in the other. The cms energy squared is $4E_1E_2 \simeq 90\,000$ GeV^2. To achieve a similar energy in a fixed-target experiment would require a 50 TeV lepton beam incident on a stationary proton target. The enormous increase of the quark density at very small values of x in Figure 6.15 is especially notable. There is not space here to discuss these interesting phenomena, which many years ago, Feynman alluded to as 'the secrets of wee x'.

From detailed studies of the structure functions for protons and neutrons, found using targets of hydrogen and deuterium as well as heavier elements bombarded by secondary electron, muon and neutrino beams from fixed-target accelerators, and from experiments at the HERA ep collider, the x-distributions of the valence quarks, sea quarks and gluons can be evaluated as a function of q^2. The valence quark distribution, as might be expected, extends to the largest values of x, with an approximate form $x^{1/2}(1-x)^3$. The sea quarks and gluons are more prominent at small x, the gluon distribution dominating for $x < 10^{-2}$.

6.7 Gluonium and the quark–gluon plasma

Because of the strong gluon–gluon interaction, it can be expected that, in addition to the colour-singlet QQQ and $Q\bar{Q}$ quark composites – the hadrons – bound colour-singlet states of gluons, GG and GGG will occur. It is extremely difficult to disentangle these states and identify them uniquely, because of the much more prolific $Q\bar{Q}$ states. However, there now appears to be quite convincing evidence that a few such gluonium states (commonly called 'glueballs') have been identified. This is one more piece of evidence in support of QCD.

Somewhat more speculative at the present time is the hypothesis of a quark–gluon plasma. The basic idea is that, at sufficiently high energy densities of hadronic matter, perhaps for example in an extremely high energy nucleus–nucleus collision, quarks and gluons could become de-confined. A phase change is predicted to take place, the low energy phase of quarks and gluons permanently confined in hadrons being replaced by a quark–gluon plasma extending through the bulk of the nuclear matter. Clearly the temperature of this plasma must be large compared with the scale parameter $\Lambda \simeq 0.2$ GeV, but the exact parameters necessary to realise such a state are unknown. The signatures of such a state could be, for example, that strange quark pairs should exist in comparable numbers to those of up and down quarks. Indeed, there is evidence for a considerable increase in the amount of Ξ hyperon and Ω hyperon production in nucleus–nucleus, as compared with proton–nucleus, collisions at the same cms energy. However,

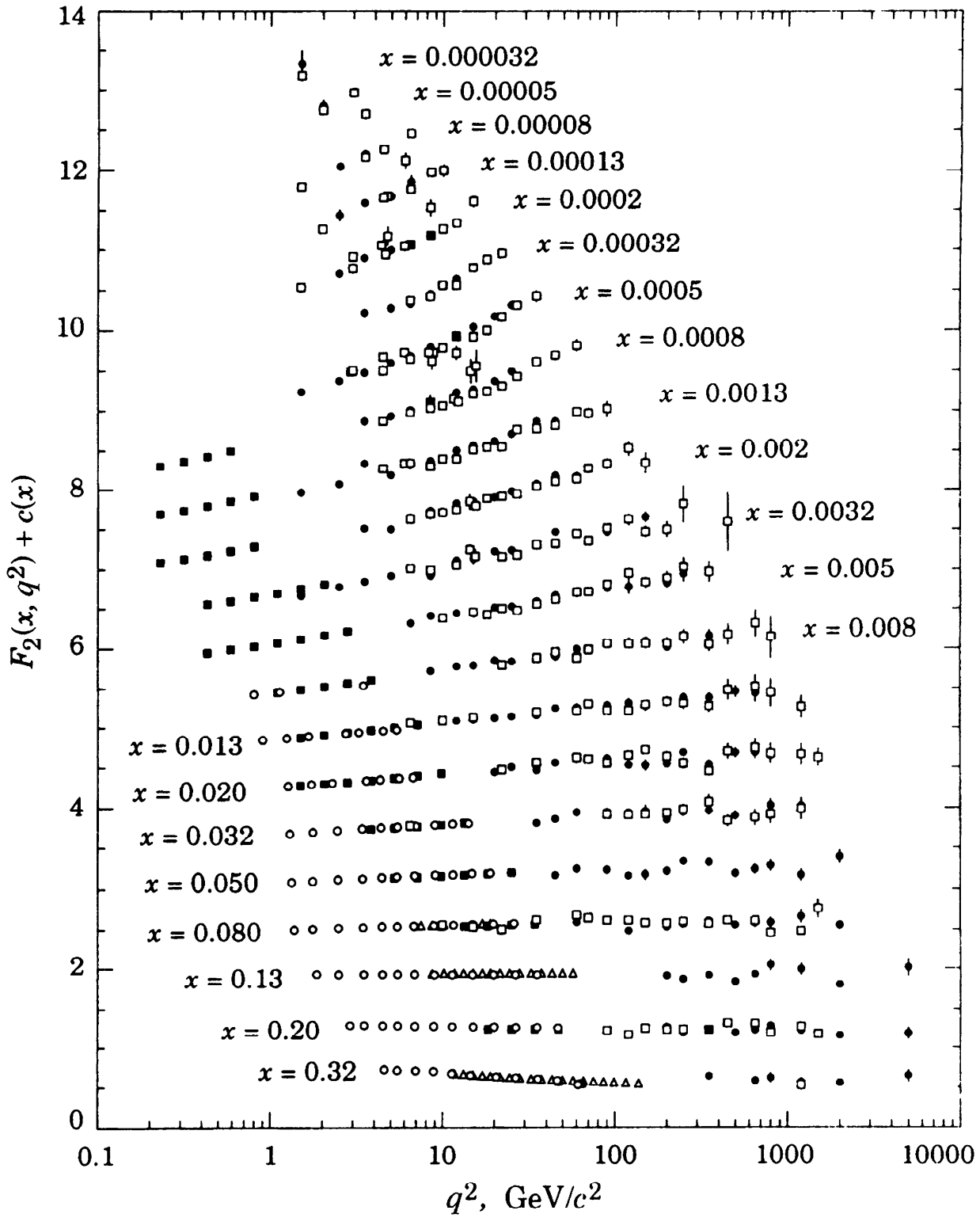

Fig. 6.15. The proton structure function measured at the HERA ep collider at DESY (colliding 28 GeV $e^{\pm}$ with 820 GeV protons). The data are from the two principal large detectors, H1 and ZEUS, for the neutral-current reaction $e + p \rightarrow e +$ hadrons. The detectors can also select the charged-current reaction $e + p \rightarrow \nu_e +$ hadrons. This is a weak reaction (via $W^{\pm}$ exchange) but at high $q^2 \sim 10^4$ GeV^2 competes with the neutral-current reaction due to γ and Z^0 exchange, with γ exchange dominating. Also shown are the results from fixed target experiments using high energy muon beams at CERN and Fermilab. For clarity, as in Figure 6.14 the various distributions have been displaced vertically relative to one another. The increase of the structure function $F_2(x, q^2)$ with q^2 at small x, and, in Figure 6.14, the decrease at large x, are well displayed. ●, H1; □, ZEUS; ■, E665; ○, NMC; △, BCDMS. (After Barnett *et al.* 1996.)

while such interesting and suggestive results have been obtained, there is as yet (1999) no conclusive evidence that a quark–gluon plasma state has been realised in practice. If such a quark–gluon plasma were demonstrated in the laboratory, it would presumably be the first time that such a state had existed since the first few microseconds of the Big Bang described in Chapter 9.

Problems

6.1 Assume that the momentum distributions of u quarks in the proton and of $\bar{d}$ quarks in the antiproton have the forms

$$F_u(x) = xu(x) = a_1(1-x)^3$$

$$F_{\bar{d}}(x) = x\bar{d}(x) = a_2(1-x)^3$$

where x is the Bjorken variable (the fraction of the momentum of a nucleon carried by a quark). If the quarks account in total for half the nucleon momentum, find a_1 and a_2.

Using the value of the peak cross-section σ_0 for the process $u\bar{d} \to W^+$ as deduced from (7.28), integrate the cross-section over the above quark distributions to calculate the cross-section σ for the process $p\bar{p} \to W^+ + \cdots$ as a function of the $p\bar{p}$ cms energy, $\sqrt{s}$. Express σ in terms of σ_0, $p = M_W^2/s$ and the total width Γ_W and mass M_W. Evaluate σ for $\sqrt{s} = 0.3$, 1.0 and 10 TeV. ($M_W = 80$ GeV, $\Gamma_W = 2.0$ GeV.)

6.2 Show that at high q^2 the elastic form factor of the nucleon has the form naively expected in QCD, if the 'struck' quark and the two 'spectator' quarks are to recoil coherently, and their interactions are mediated by single gluon-exchanges.

6.3 Show that, for a confining potential of the form $V = kr^n$, the dependence of J on E will be given by (6.15).

6.4 If one multiplies both sides of the Altarelli–Parisi equation (6.24) for the valence quark distribution by x^n (where n is any integer above 1) and integrates from $x = 0$ to $x = 1$, the right-hand side factorises into a product of integrals over z (= 0 to 1), and over y (= 0 to 1). Show that the nth moment of the quark distribution

$$M(n, q^2) = \int_0^1 x^n u(x, q^2) dx$$

will have the following simple q^2 dependence:

$$M(n, q^2) = \frac{C_n}{\left(\ln q^2/\Lambda^2\right)^{d_n}}$$

where C_n is a constant and where the so-called anomalous dimension

$$d_n = -\frac{1}{2\pi B} \int_0^1 z^n P_{QQ}(z) dz$$

and $P_{QQ}(z)$, B and Λ are defined in (6.23), (6.24) and (6.25). Hence show that the relative variation with q^2 of two different moments is given by

$$d[\ln M(n, q^2)]/d[\ln M(m, q^2)] = d_n/d_m$$

(the dependence of d_n on n is characteristic of the vector coupling of the gluon to the quark. The experimental determination of $d_{n,m}$ from the measured moments of valence quarks in neutrino interactions gave the first quantitative support for QCD in 1978).

7

Weak interactions

7.1 Classification

The weak interactions between quarks and leptons are those mediated by the so-called intermediate bosons $W^{\pm}$ and Z^0, with a coupling which we generically label g. As indicated in Figure 7.1, there is a strong similarity between the Feynman diagrams for electromagnetic interactions mediated by photon exchange and weak interactions mediated by the intermediate bosons.

A familiar interaction is that between two straight wires hanging close together when electric currents – i.e. a flow of electrons and ions – pass through them. So, we can view the interaction of Figure 7.1(a) as that of two conserved electric currents $j_{\rm em}$, carried in this case by the electron e and the quark Q. Similarly, the interactions shown in Figures 7.1(b) and (c) can be viewed as between *weak currents* $j_{\rm weak}$. The difference is that these currents consist of a flow of conserved *weak charge* g rather than electric charge, e. In either case, these currents will contain the product of the (normalised) wavefunctions of the 'in' and 'out' particles that occur in the matrix element (2.16) for the interaction. Thus $j \propto \psi^*\psi$, where ψ^* denotes an incoming and ψ an outgoing amplitude.

In Figure 7.1(b) one sees that the electric charges associated with the weak current actually change in the interaction, while in Figure 7.1(c) they do not. Rather inaccurately, these two are referred to as charged-current weak interactions (those in which the electric charge of each weak current changes) and neutral-current weak interactions (those in which the electric charges do not change). Often these are referred to as CC and NC interactions respectively. The two types of weak interaction exist because the weak force can be carried by either a charged ($W^{\pm}$) or neutral (Z^0) boson.

Weak interactions take place between all types of leptons and quarks. However, they are normally masked by the much stronger electromagnetic and strong interactions and are usually observable only when the stronger interactions are

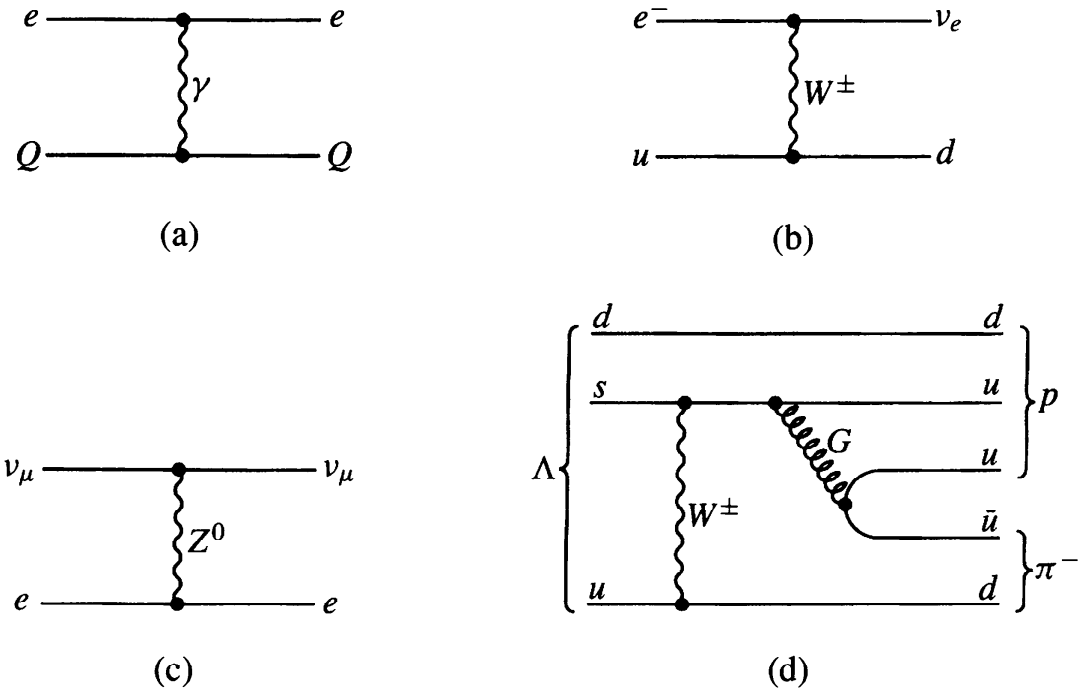

Fig. 7.1. (a) Electromagnetic interaction between lepton and quark mediated by single-photon exchange. (b) Weak charged-current interaction between lepton and quark mediated by $W^{\pm}$ exchange. (c) Weak neutral-current interaction between two leptons mediated by Z^0 exchange. (d) A non-leptonic weak interaction, the decay of a Λ hyperon, mediated by $W^{\pm}$ exchange. This changes the quark flavour, as it does also in (b).

forbidden by an energy or other conservation rule or when, as in the case of neutrinos, a particle carries no strong or electric charge. Weak interactions may occur between leptons and quarks as in Figure 7.1(b) – when they are referred to as semi-leptonic – or between leptons only as in Figure 7.1(c) – when they are referred to as leptonic – or between quarks as in Figure 7.1(d) – when they are referred to as non-leptonic. Although $W^{\pm}$ exchange does not change lepton flavour, it *can* change quark flavour, as in Figure 7.1(d) showing Λ decay, where an s quark transforms to a u quark and a u quark to a d quark.

7.2 Lepton universality

Is the weak coupling, say to the $W^{\pm}$ boson, the same for all elementary fermions or, equivalently, do all leptons and quarks carry the same unit of weak charge? The answer is yes for leptons and no for quarks.

Let us start with purely leptonic weak interactions. Examples are muon decay and tauon decay. As indicated in Chapter 2, for such low energy processes (low in comparison with the $W^{\pm}$, Z^0 masses) the weak coupling, being of very short range, is effectively pointlike and is specified by the Fermi constant G; this is related to g

as in (2.10) by

$$G \sim \frac{g^2}{M_W^2}$$

Since by hypothesis g, the weak charge or coupling amplitude to the $W^{\pm}$, is dimensionless, G must have dimensions E^{-2}. The decay amplitude is proportional to G and the rate to G^2. It follows that, on dimensional grounds, the width or inverse of the mean lifetime τ for muon decay has to be (in units $\hbar = c = 1$)

$$\begin{aligned}\Gamma(\mu \to e\nu_e\bar{\nu}_\mu) = \frac{1}{\tau} &\propto G^2 m_\mu^5 \\ &= \frac{G^2 m_\mu^5}{192\pi^3}\end{aligned} \tag{7.1}$$

Since the electron and neutrino masses are negligible compared with that of the muon, m_μ can be the only mass determining the decay rate, and it must enter to the fifth power. In the second line the numbers come from a full (and quite lengthy) calculation, using the so-called $V-A$ theory of weak interactions discussed below.

The τ lepton has a number of decay modes. The measured branching ratio B for the decay

$$\tau \to e\nu_e\bar{\nu}_\tau$$

is $17.80 \pm 0.06\%$. From the τ lepton lifetime and the formula (7.1) for the dependence on parent particle mass, we can test the universality of the couplings g_μ and g_τ to the W boson:

$$\left(\frac{g_\tau}{g_\mu}\right)^4 = B(\tau \to e\nu_e\bar{\nu}_\tau)\left(\frac{m_\mu}{m_\tau}\right)^5\left(\frac{\tau_\mu}{\tau_\tau}\right)$$

With $\tau_\mu = 2.197 \times 10^{-6}$ s, $\tau_\tau = (291.0 \pm 1.5) \times 10^{-15}$ s, $m_\mu = 105.658$ MeV and $m_\tau = 1777.0$ MeV we get

$$\frac{g_\tau}{g_\mu} = 0.999 \pm 0.003 \tag{7.2}$$

From the relative branching ratios for $\tau \to e\nu_e\bar{\nu}_\tau$ and $\tau \to \mu\nu_\mu\bar{\nu}_\tau$, one can also test the universality of electron and muon weak couplings:

$$\frac{g_\mu}{g_e} = 1.001 \pm 0.004 \tag{7.3}$$

in agreement with the independent result from the $\pi \to e\nu$ and $\pi \to \mu\nu$ branching ratios discussed below (Section 7.10), which yields

$$\frac{g_\mu}{g_e} = 1.001 \pm 0.002 \tag{7.4}$$

These results prove rather convincingly that different flavours of lepton have identical couplings to the weak $W^{\pm}$ bosons.

This universality holds equally for the Z^0 coupling to the different lepton flavours. At the LEP e^+e^- collider, the partial widths for these decay modes were found to be equal within experimental error:

$$Z^0 \to e^+e^- : \mu^+\mu^- : \tau^+\tau^- = 1 : 1.000 \pm 0.004 : 0.999 \pm 0.005 \qquad (7.5)$$

In contrast to the universality of the lepton couplings, those of the quarks to the weak bosons *do* depend on the quark flavours involved. We shall discuss these matters in detail in Section 7.14 below.

From the observed muon decay rate, the width Γ can be calculated using the relation $\Gamma = \hbar c/(c\tau)$, where $\hbar c = 197.327$ MeV fm, giving $\Gamma_\mu = 2.996 \times 10^{-19}$ GeV. Then from (7.1) we can compute the Fermi constant G. Including small radiative corrections at the 0.2% level, the result is

$$G/(\hbar c)^3 = 1.1664 \times 10^{-5}\ \text{GeV}^{-2} \qquad (7.6)$$

7.3 Nuclear β-decay: Fermi theory

Historically, the prototype weak interaction was nuclear β-decay, e.g. the decay of a free or bound neutron,

$$n \to p + e^- + \bar{\nu}_e$$

or in terms of quark constituents

$$d \to u + e^- + \bar{\nu}_e \qquad (7.7)$$

This process is described by virtual W exchange as in Figure 7.1(b) and again, at the low momentum transfers involved, $q^2 \ll M_W^2$, the interaction is effectively pointlike and described by the apparent four-fermion coupling $G = g^2/M_W^2$ as before. Such a coupling was postulated by Fermi in 1934.

The transition probability or decay rate per unit time will be given by (2.16), taking G out of the matrix element:

$$W = \frac{2\pi}{\hbar} G^2 |M|^2 \frac{dN}{dE_0} \qquad (7.8)$$

where E_0 is the energy in the final state, dN/dE_0 is the density of final states per unit energy interval and $|M|^2$ is the square of the matrix element, involving integration over angles and spin directions of the particles concerned. It will be a constant of order unity. In fact if the total angular momentum, summed over the lepton spins, is $J(\text{leptons}) = 0$ then $|M|^2 \simeq 1$, while if $J(\text{leptons}) = 1$ then $|M|^2 \simeq 3$, the spin multiplicity factor. These two types of nuclear β-decay

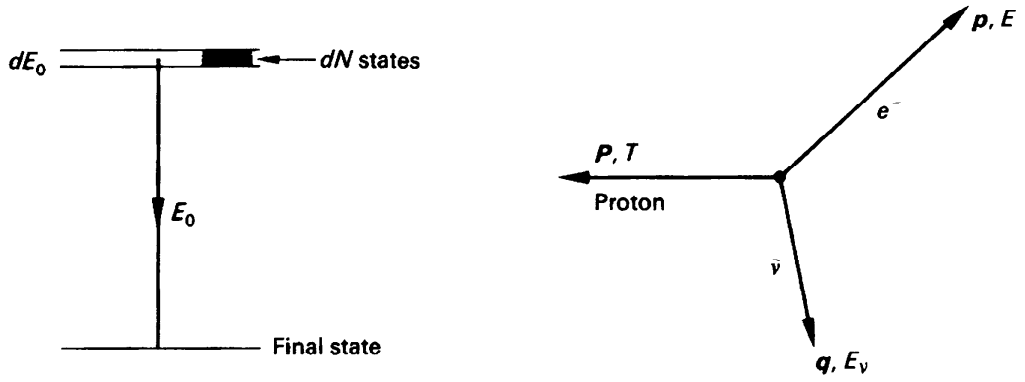

Fig. 7.2. (a) An initial state with a spread in energy dE_0 decays to a final (stable) state of unique energy, with energy release E_0. (b) The momentum vectors in neutron decay.

transition are referred to as Fermi and Gamow–Teller transitions respectively (the free neutron decay in (7.7) is a combination of both types).

The density-of-states factor is determined by the number of ways of sharing out the available energy in the range $E_0 \rightarrow E_0 + dE_0$ between the secondary particles, the quantity dE_0 arising from the spread in energy of the final state corresponding to the finite lifetime of the initial state. In Figure 7.2, $\mathbf{p}$, $\mathbf{q}$ and $\mathbf{P}$ are the momenta of the electron, neutrino and proton, while E, E_ν and T are their kinetic energies. Then in the rest frame of the initial state (the neutron)

$$\mathbf{P} + \mathbf{q} + \mathbf{p} = 0$$

$$T + E_\nu + E = E_0$$

Assume $m_\nu = 0$, so that $E_\nu = qc$. In order of magnitude $E_0 \simeq 1$ MeV, so that $Pc \simeq 1$ MeV. If the recoiling nucleon mass is M, its kinetic energy will be $T = P^2c^2/(2Mc^2) = P^2/(2M) \simeq 10^{-3}$ MeV only, and can be neglected. The nucleon serves to conserve momentum, but we can regard the energy E_0 as shared entirely between electron and neutrino. Thus $qc = E_0 - E$.

The number of states available to an electron of momentum in the range $p \rightarrow p + dp$ confined to a volume V inside an element of solid angle $d\Omega$ is

$$\frac{V d\Omega}{(2\pi)^3 \hbar^3} p^2 dp$$

Normalising wavefunctions to unit volume, integrating over space angles and ignoring the effects of spin on angular distributions, the electron phase-space factor is

$$\frac{4\pi p^2 dp}{(2\pi)^3 \hbar^3}$$

while for the neutrino it is

$$\frac{4\pi q^2 dq}{(2\pi)^3 \hbar^3}$$

We disregard possible correlation between **p** and **q** and treat these two factors as independent, the proton taking up any resultant momentum. There is no phase-space factor for the proton, since its momentum is fixed:

$$\mathbf{P} = -(\mathbf{p} + \mathbf{q})$$

So the number of final states is

$$dN = \frac{(4\pi)^2}{(2\pi)^6 \hbar^6} p^2 q^2 dp dq$$

For given values of p and E the neutrino momentum is fixed,

$$q = (E_0 - E)/c$$

within the range $dq = dE_0/c$. Hence the energy density of final states is

$$\frac{dN}{dE_0} = \frac{1}{4\pi^4 \hbar^6 c^3} p^2 (E_0 - E)^2 dp \tag{7.9a}$$

Since, when integrated over angle, $|M|^2$ in (7.8) is some constant factor, this last expression gives the electron spectrum

$$N(p)dp \propto p^2 (E_0 - E)^2 dp \tag{7.9b}$$

and thus if we plot $[N(p)/p^2]^{1/2}$ against E, a straight line cutting the energy axis at $E = E_0$ should result. This is called a Kurie plot. Experimentally, for the so-called 'allowed' transitions, the observed Kurie plots are linear, if one includes a correction factor $F(Z, p)$ to allow for the energy gained or lost by the electron from the Coulomb field of the daughter nucleus (important only for low energy electrons and nuclei of large Z). Nuclear β-decays in which a large change in angular momentum is involved, so that the leptons must carry $J(\text{lepton}) > 1$, have much lower decay rates, are referred to as 'forbidden' transitions and do not give straight-line Kurie plots. Figure 7.3 shows an example of a Kurie plot for the allowed tritium β-decay transition, $^3\text{H} \rightarrow {}^3\text{He} + \text{e}^- + \bar{\nu}_\text{e}$.

For a non-zero neutrino mass, it is straightforward to show that the effect is to modify the above expression to

$$N(p)dp \propto p^2 (E_0 - E)^2 \sqrt{1 - \left(\frac{m_\nu c^2}{E_0 - E}\right)^2}\, dp \tag{7.9c}$$

In this case the Kurie plot turns over, to cut the axis vertically at $E = E_0 - m_\nu c^2$, and this provides a method of determining the neutrino mass, or a limit to it.

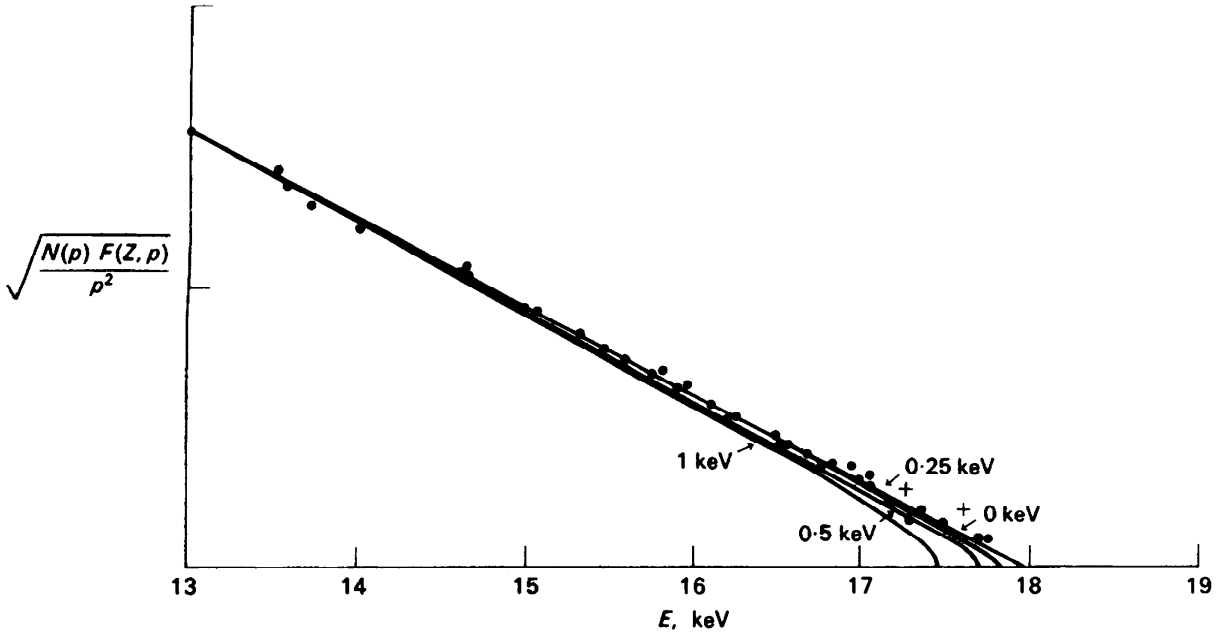

Fig. 7.3. An early plot of the energy spectrum in tritium β-decay, by Langer and Moffatt (1952), showing the linearity of the Kurie plot and the turnover expected for various neutrino masses.

Tritium decay is the most suitable example, since the end-point energy is small ($E_0 = 18.6$ keV). Over the last 40 years, the upper limit on m_ν from this transition has improved from 10 000 eV to about 10 eV.

The total decay rate is found by integrating the spectrum (7.9). Although this can be done exactly, in many decays the electrons are relativistic and we can use the approximation $pc \simeq E$. In that case we obtain the simple formula

$$N \simeq \int_0^{E_0} E^2(E_0 - E)^2 dE = \frac{E_0^5}{30} \tag{7.10}$$

Then the disintegration constant is proportional to the fifth power of the disintegration energy – the *Sargent rule*. We have already met this dependence in three-body decay of the muon; see the dimensional arguments leading to (7.1). To be more specific, if we retain all the various constants in the above expressions, the decay rate from (7.8) and integration of (7.9a) will be, for $E_0 \gg m_e c^2$,

$$W = \frac{G^2|M|^2 E_0^5}{60\pi^3(\hbar c)^6 \hbar}$$

so that with the value of G in (7.6) we find

$$W = \frac{1.11}{10^4} E_0^5 |M|^2 \mathrm{s}^{-1}$$

for E_0 in MeV. For example, with $E_0 \simeq 100$ MeV as in muon decay and assuming

$|M|^2 = 1$, then $\tau_\mu = 1/W \simeq 10^{-6}$ s (the muon lifetime is actually 2.2 μs as given above).

7.4 Inverse β-decay: neutrino interactions

In a famous letter to colleagues in 1930, Pauli presented the hypothesis of the neutrino as a 'desperate remedy' to account for the energy and momentum missing in β-decay. However, the neutrino could only be finally accepted as a real particle if one could demonstrate the interaction of free neutrinos, i.e. the inverse of the reaction (7.7),

$$\bar{\nu}_e + p \rightarrow n + e^+ \tag{7.11}$$

with a threshold of 1.80 MeV. The cross-section can be computed from (2.19) with $\hbar = c = 1$:

$$\sigma(\bar{\nu}_e + p \rightarrow n + e^+) = \frac{G^2}{\pi}|M|^2\frac{p^2}{v_i v_f} \tag{7.12}$$

Here, $v_i \simeq v_f \simeq c\ (= 1)$ are the relative velocities of the initial- and final-state particles and p is the value of the cms 3-momentum of neutron and positron. As defined here, $|M|$ is dimensionless while G^2 has dimensions E^{-4} and p^2 has dimensions E^2. Thus the overall dimensions are E^{-2}, or length squared. For a Fermi transition $|M_F|^2 \simeq 1$, while for a Gamow–Teller transition $|M_{GT}|^2 \simeq 3$. Thus for a mixed transition, as in this case, $|M|^2 \simeq 4$. Inserting the value of G from (7.6) and using the fact that 1 $\text{GeV}^{-1} = 1.975 \times 10^{-14}$ cm (see Table 1.1), we obtain

$$\sigma(\bar{\nu}_e + p \rightarrow e^+ + n) \simeq 10^{-43} E^2 \text{ cm}^2 \tag{7.13}$$

where $E \simeq pc$ is the energy above the threshold in MeV. This is an exceedingly small cross-section. The corresponding mean free path for an antineutrino in water for $E = 1$ MeV is about 10^{20} cm or 50 light years!

The first observation of neutrino interactions was made by Reines and Cowan in 1956. They employed a reactor as the source. The uranium fission fragments are neutron-rich and undergo β-decay, emitting electrons and antineutrinos (on average, about six per fission, with a spectrum peaking at a few MeV). For a 1000 MW reactor, the useful flux at a few metres from the core is of order $10^{13}\ cm^{-2}\ s^{-1}$. *Thus the low cross-section can be compensated by the very high* flux. The reaction (7.13) was observed, at a rate of a few events per hour above background, using a target of cadmium chloride ($CdCl_2$) and water. The positron produced in reaction (7.13) rapidly comes to rest by ionisation loss and forms positronium, which annihilates to γ-rays, in turn producing fast electrons by the Compton effect. These electrons are recorded in liquid scintillator viewed by

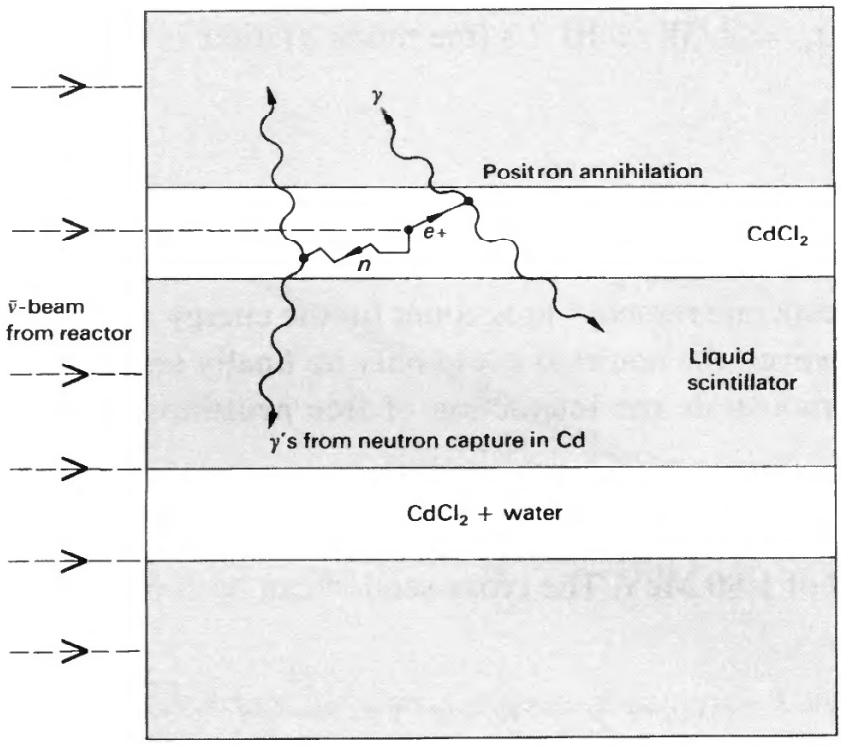

Fig. 7.4. Schematic diagram of the experiment of Reines and Cowan (1956), which demonstrated for the first time the interaction of antineutrinos produced in β-decays of the fission products in a nuclear reactor.

photomultipliers. The time scale for this process is about 10^{-9} s, so the positron gives a so-called prompt pulse. The function of the cadmium is to capture the neutron after it has been moderated, i.e. reduced to thermal energy by successive elastic collisions with protons in the water, a process that delays by several microseconds the γ-rays coming from eventual radiative capture of the neutron by a cadmium nucleus. Thus the signature of an event is two pulses microseconds apart. Figure 7.4 shows schematically the experimental arrangement employed.

7.5 Parity nonconservation in β-decay

In 1956, following a critical review of the experimental data then available, Lee and Yang came to the conclusion that weak interactions were not invariant under spatial inversion, i.e. they did not conserve parity. This was largely on the basis of the fact that the K^+ meson could decay in two modes, $K^+ \to 2\pi$, $K^+ \to 3\pi$, in which the final states have opposite parities (even and odd respectively).

To test parity conservation, an experiment was carried out by Wu *et al.* in 1957, employing a sample of ^{60}Co at 0.01 K inside a solenoid. At this low temperature, a high proportion of the ^{60}Co nuclei (spin $J = 5$) are aligned with the field. The cobalt undergoes β-decay to ^{60}Ni* ($J = 4$), a pure Gamow–Teller transition. The

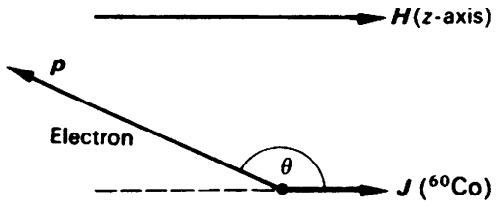

Fig. 7.5.

relative electron intensities along and against the field direction were measured (see Figure 7.5). The degree of ^{60}Co alignment could be determined from the angular distribution of the γ-rays from ^{60}Ni*. The results found for the electron intensities were consistent with a distribution of the form

$$I(\theta) = 1 + \alpha \frac{\boldsymbol{\sigma} \cdot \mathbf{p}}{E}$$
$$= 1 + \alpha \frac{v}{c} \cos\theta \tag{7.14}$$

where $\alpha = -1$. $\boldsymbol{\sigma}$ is a unit spin vector in the direction of $\mathbf{J}$; $\mathbf{p}$ and E are the momentum and energy of the electron and θ is the angle of emission of the electron with respect to $\mathbf{J}$.

The fore–aft asymmetry of the intensity in (7.14) implies that the interaction as a whole violates parity conservation. For imagine the whole system reflected in a mirror normal to the z-axis. The first term (unity) does not change sign under reflection – it is *scalar* (even parity). $\boldsymbol{\sigma}$, being an axial vector, does not change sign either, while the polar vector $\mathbf{p}$ does. So the product $\boldsymbol{\sigma} \cdot \mathbf{p}$ changes sign under reflection. It is a *pseudoscalar*, with odd parity, and the presence of both terms in the intensity implies a parity mixture. Conservation of the z-component of angular momentum in the above transition implies that the electron spin must also point in the direction of $\mathbf{J}$, so that if now $\boldsymbol{\sigma}$ denotes the electron spin vector, the intensity is again

$$I = 1 + \alpha \frac{\boldsymbol{\sigma} \cdot \mathbf{p}}{E} \tag{7.15}$$

Representing the intensities for $\boldsymbol{\sigma}$ parallel and antiparallel to $\mathbf{p}$ by I^+ and I^-, the net longitudinal polarisation is

$$P = \frac{I^+ - I^-}{I^+ + I^-} = \alpha \frac{v}{c}$$

Experimentally,

$$\alpha = \begin{cases} +1 & \text{for } e^+, \text{ thus } P = +v/c \\ -1 & \text{for } e^-, \text{ thus } P = -v/c \end{cases} \tag{7.16}$$

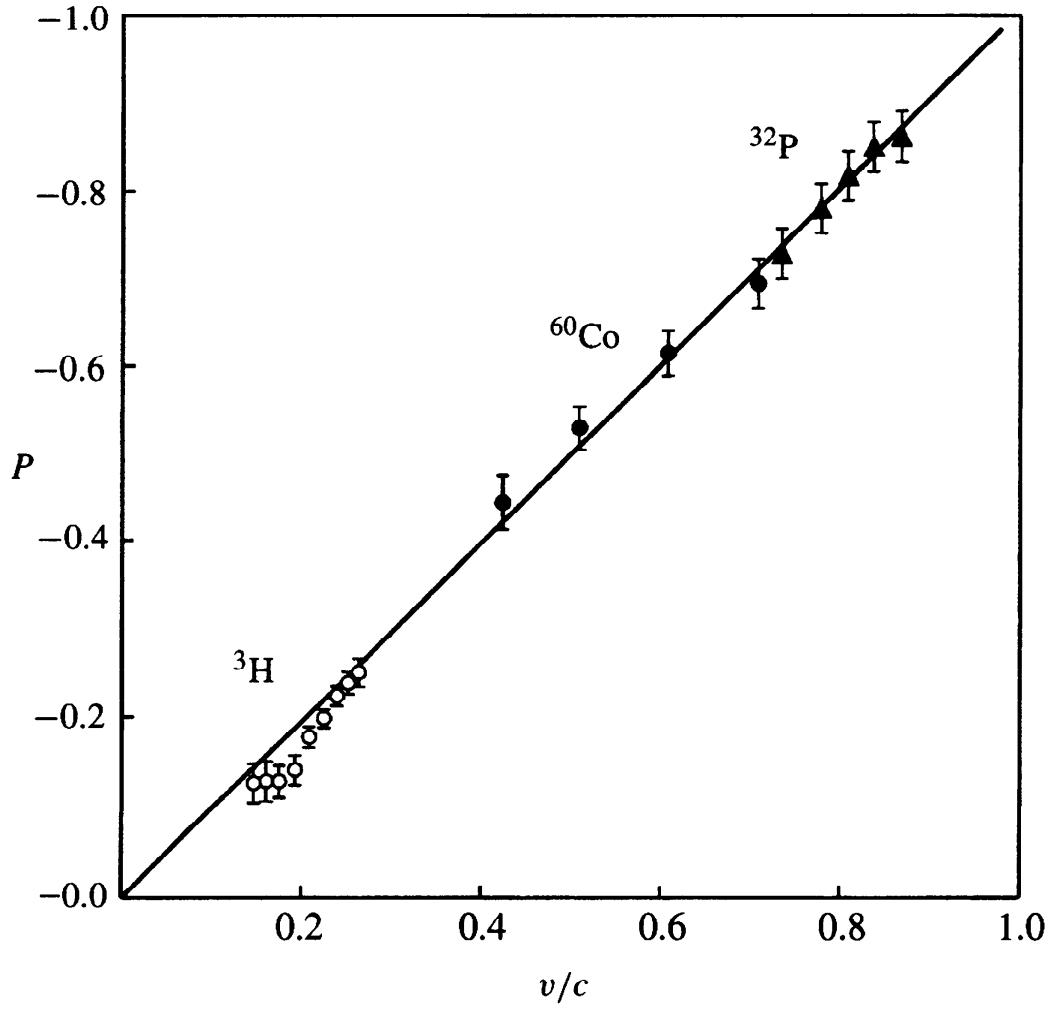

Fig. 7.6. The polarisation P of electrons emitted in nuclear β-decay, plotted as a function of electron velocity. The results demonstrate that $P = -v/c$, as in (7.16). After Koks and Van Klinken (1976).

The experimental determination of P can be achieved, for example, by passing the electrons through an electric or magnetic field, in such a way as to turn the longitudinal polarisation to a transverse polarisation; this can be measured from the right–left asymmetry in scattering of the electrons from a foil of heavy element. Or the longitudinal polarisation can be found directly by electron–electron (Møller) scattering by a magnetised iron foil. The scattering is greatest when incident and target electron spins are parallel, and the scattering ratio on reversing the magnetic field gives a measure of the degree of longitudinal polarisation.

Figure 7.6 shows measurements of the polarisation P for electrons produced in nuclear β-decay, as a function of v/c, justifying the relations (7.16).

7.6 Helicity of the neutrino

The result (7.16), if applied to a neutrino ($m = 0$), implies that such a particle must be fully polarised, $P = +1$ or -1. Here $E = |\mathbf{p}|$ and the neutrino, as explained in (1.22), is in a pure helicity state, $P \equiv H = \pm 1$. The sign of the neutrino helicity turned out to be crucial in deciding which operators occur in the matrix element describing β-decay. The neutrino here is defined as the neutral particle emitted together with the positron in β^+ decay, while the antineutrino denotes the particle accompanying the electron in β^- decay. The neutrino helicity was determined in a classic and beautiful experiment by Goldhaber, Grodzins and Sunyar in 1958. The steps in the experiment are indicated in Figure 7.7.

(i) ^{152}Eu undergoes K-capture to an excited state of ^{152}Sm with $J = 1$ (Figure 7.7(a)). To conserve angular momentum, **J** must be parallel to the spin of the electron but opposite to that of the neutrino, so the recoiling ^{152}Sm* has the same polarisation sense as the neutrino (Figure 7.7(b)).

(ii) In the transition $^{152}\text{Sm}^* \rightarrow {}^{152}\text{Sm} + \gamma$, those γ-rays emitted in the forward (backward) direction with respect to the line of flight of the ^{152}Sm* will be polarised in the same (opposite) sense to the neutrino, as in Figure 7.7(c). Thus the polarisation of the 'forward' γ-rays is the same as that of the neutrino.

(iii) The next step is to observe resonance scattering of the γ-rays in a ^{152}Sm target. Resonance scattering is possible with γ-rays of just the right frequency to 'hit' the excited state:

$$\gamma + {}^{152}\text{Sm} \rightarrow {}^{152}\text{Sm}^* \rightarrow \gamma + {}^{152}\text{Sm} \tag{7.17}$$

To produce such resonance scattering, the γ-ray energy must slightly exceed the 960 keV energy of the excited state, to allow for nuclear recoil. It is precisely the 'forward' γ-rays, carrying with them a part of the neutrino's recoil momentum, which are able to do this and which are therefore automatically selected in the resonance scattering.

(iv) The last step is to determine the polarisation sense of the γ-rays. To do this, they are passed through magnetised iron before impinging on the ^{152}Sm absorber. An electron in the iron with spin σ_e opposite to that of the photon can absorb a unit of angular momentum by spin-flip; if the spin is parallel it cannot. This is indicated in Figure 7.7(d). If the γ-ray beam is in the same direction as the field **B**, the transmission of the iron is greater for left-handed than for right-handed γ-rays.

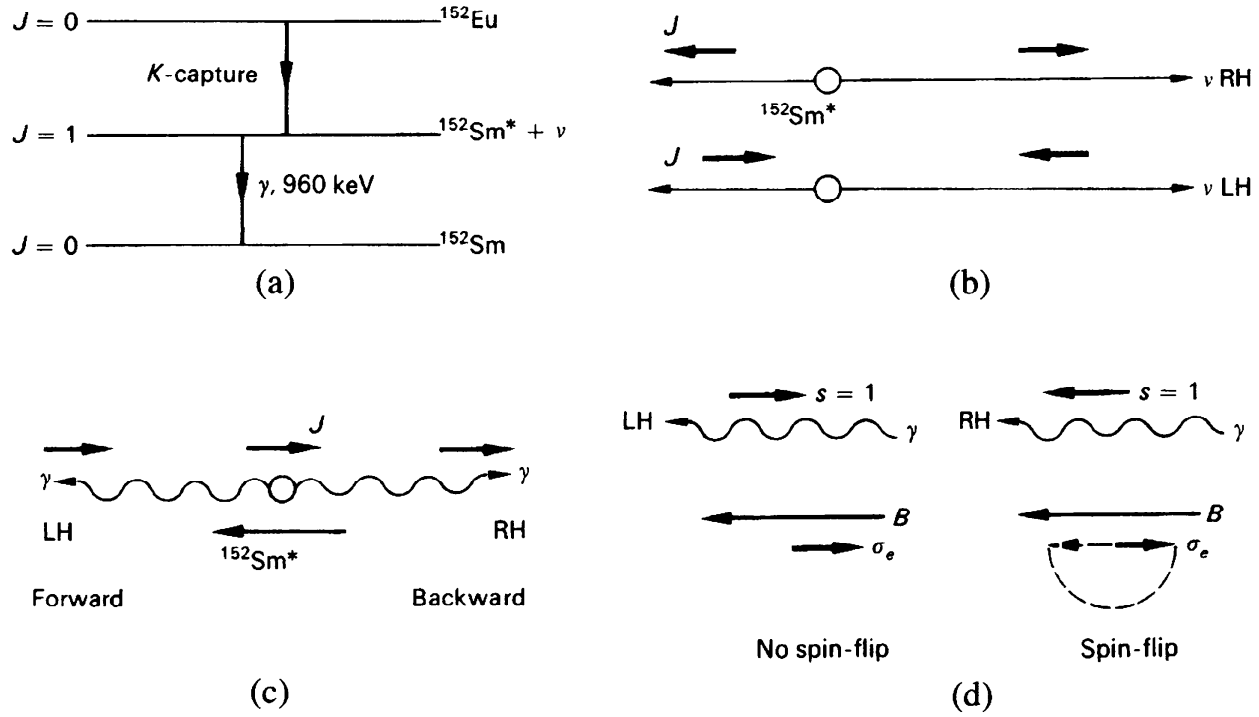

Fig. 7.7. Principal steps in the experiment to determine the neutrino helicity, as described in the text.

A schematic diagram of the apparatus is shown in Figure 7.8. By reversing the field **B**, the sense of polarisation could be determined from the change in the counting rate. When allowance was made for various depolarising effects, it was concluded that neutrinos have left-handed helicity, $H = -1$.

In conclusion, the polarisation assignments for leptons emitted in nuclear β-decay are as follows:

$$\begin{array}{lcccc} \text{particle} & e^+ & e^- & \nu & \bar{\nu} \\ \text{polarisation} & +v/c & -v/c & -1 & +1 \end{array} \tag{7.18}$$

7.7 The $V - A$ interaction

The results (7.14), (7.16) and (7.18) have been presented from a purely empirical viewpoint. The theoretical description of nuclear β-decay can be introduced by referring to Sections 1.5 and 1.6 (equations (1.19) and (1.21)), from which it can be deduced that, for *massless* fermions, the operator $P_{R,L} = \frac{1}{2}(1 \pm \boldsymbol{\sigma} \cdot \mathbf{p}/E)$ acting on two-component spinors will project out states of particular helicity from an arbitrary superposition of positive and negative helicity states:

$$\begin{aligned} P_R\psi &= \frac{1}{2}\left(1 + \frac{\boldsymbol{\sigma} \cdot \mathbf{p}}{E}\right)(\psi_L + \psi_R) = \psi_R \\ P_L\psi &= \frac{1}{2}\left(1 - \frac{\boldsymbol{\sigma} \cdot \mathbf{p}}{E}\right)(\psi_L + \psi_R) = \psi_L \end{aligned} \tag{7.19}$$

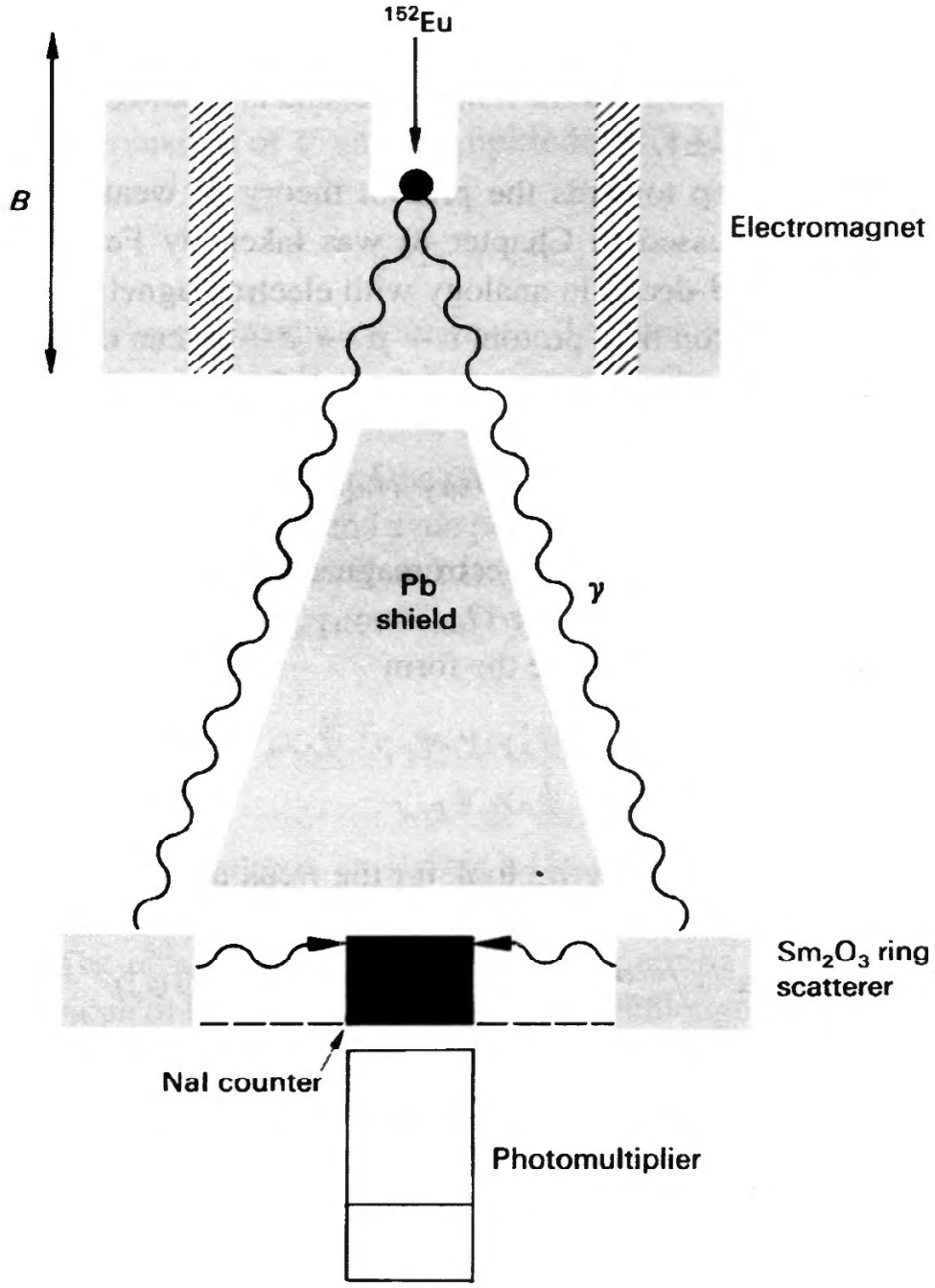

Fig. 7.8. Schematic diagram of the apparatus used by Goldhaber *et al.*, in which γ-rays from the decay of ^{152}Sm*, produced following K-capture in ^{152}Eu, undergo resonance scattering in Sm_2O_3 and are recorded by a sodium iodide scintillator and photomultiplier. The transmission of photons through the iron surrounding the source depends on their helicity and the direction of the magnetic field **B**.

For massive fermions, the analogous operators, which act on four-component Dirac spinors, are denoted

$$\tfrac{1}{2}(1 \pm \gamma_5)$$

and are 4×4 matrices replacing the above 2×2 matrices in the massless case, with $\gamma_5 = i\gamma_1\gamma_2\gamma_3\gamma_4$ and the $\gamma_{1,2,3,4}$ matrices defined in (1.20c). The effect of the

operator $1 \pm \gamma_5$ on fermion wavefunctions is to project out a state of polarisation $P = \pm v/c$, exactly as found empirically in (7.18). Clearly the result (7.19) is the extreme case where the lepton is ultra-relativistic, and is produced in a pure helicity state, i.e. with $P \equiv H = \pm 1$.

Historically, a first step towards the present theory of weak interactions (the electroweak theory discussed in Chapter 8) was taken by Fermi in 1934. He developed his model of β-decay in analogy with electromagnetism. For example, the scattering of an electron by a proton, $e + p \rightarrow e + p$, can be described as the interaction of two *currents*, as mentioned in Section 7.1, with matrix element

$$M \propto \frac{e^2}{q^2} J_{\text{baryon}} J_{\text{lepton}}$$

where q is the momentum transfer. Electromagnetic currents are described in the Dirac theory by the 4-vector operator $O_{\text{em}} = \gamma_4 \gamma_\mu$ (where $\mu = 1, 2, 3, 4$, and a summation is made over μ) and have the form

$$J_{\text{lepton}} = \psi_e^* \gamma_4 \gamma_\mu \psi_e \equiv \bar{\psi}_e \gamma_\mu \psi_e$$
$$J_{\text{baryon}} = \bar{\psi}_p \gamma_\mu \psi_p$$

where $\bar{\psi} = \psi^* \gamma_4$. By analogy, Fermi took for the weak process, e.g. for $\nu_e + n \rightarrow p + e^-$,

$$M = G J_{\text{baryon}}^{\text{weak}} J_{\text{lepton}}^{\text{weak}} = G(\bar{\psi}_p O \psi_n)(\bar{\psi}_e O \psi_\nu)$$

Fermi assumed the operator O would again be a vector operator, as in electromagnetism, the main difference in the two expressions being due to the fact that the weak process is a point four-fermion interaction specified by the Fermi coupling constant G and that the electric charge of the lepton and baryon changes in the interaction.

The discovery of parity violation in 1957 implied a combination of two types of interaction with opposite parities. In principle, up to five different types of operator in the matrix element are allowed by relativistic invariance. These operators are named according to their transformation properties under spatial reflection: vector (V), axial vector (A), scalar (S), pseudoscalar (P) and tensor (T).

The early experimental results described above showed that leptons and antileptons involved in weak decays have opposite longitudinal polarisations, i.e. helicities, and this narrowed the choice of operators down to two – the V and A operators. It will be recalled from Section 1.6 that for massless fermions the helicity is conserved in V or A interactions, with the result, as described in Section 5.1, that in a process involving production of a lepton pair, as in β-decay, the lepton and antilepton must have opposite helicities. Massive fermions are not produced in pure helicity states but again experiments showed that *opposite*

helicities are favoured over those with the same helicity (net polarisation $\pm v/c$). However, S, P and T interactions would favour the *same* helicities for fermion and antifermion and are therefore discounted.

A general combination of V and A amplitudes would correspond to an operator of the form

$$\tfrac{1}{2}(C_V + \gamma_5 C_A)$$

where C_A and C_V are constant coefficients. The fact that a neutrino is produced in a pure helicity eigenstate $H = -1$ requires that $C_A = -C_V$, giving the $\frac{1}{2}(1 - \gamma_5)$ operator. For a massless fermion the result of applying this operator to the wavefunction is identical to that of the operator P_L in (7.19). In this case the V and A amplitudes, which have odd and even parities under space inversion, are equal in magnitude but opposite in sign. Hence the term '$V - A$ theory', and the principal of 'maximal parity violation', postulated by Feynman and Gell-Mann (1958).

7.8 Conservation of weak currents

The equality $C_A = -C_V$ holds for leptonic weak interactions such as muon decay but not for weak interactions involving hadrons. We of course accept without demur that the electric charge of the proton has the same magnitude as that of the electron. The proton, unlike the electron, has strong interactions but these do not affect the value of the proton charge, e. Thus, although protons are complicated objects, which through the strong interactions are, for example, continually emitting and re-absorbing quark–antiquark pairs (pions), these processes, remarkably enough, leave the total charge unaltered. We can say that the electric current is conserved by the strong interaction.

However, this is not the case for the weak charge g. While the vector part (V) of the weak charge *is* conserved (a fact enshrined in the 'conserved vector current hypothesis'), the axial part (A) is not, and the measured ratio $C_A/C_V \neq -1$. For example, for baryons it is found that in neutron β-decay $C_A/C_V = -1.26$, in Λ β-decay $C_A/C_V = -0.72$, while in $\Sigma^- \to n + e^- + \bar{\nu}_e$, $C_A/C_V = +0.34$.

As discussed in Section 5.7, the deep inelastic scattering of neutrinos by the quark constituents of hadrons *is* described exactly by the $V - A$ theory, with $C_A = -C_V$. In these circumstances the quarks are quasi-free, pointlike particles, just like the leptons. However, when the strong quark–quark interactions are dominant, as for the bound hadronic states, the above equality is broken, at least for the A part of the weak coupling. Many years ago, Goldberger and Treiman discovered that the difference $|C_A/C_V| - 1$ in neutron decay could be almost exactly accounted for in terms of a model of virtual emission and re-absorption of pions by the nucleon, $n \to p + \pi^-$. However, a general theoretical treatment of the relative magnitudes

of the V and A couplings in hadronic β-decay would be very complicated and has not been possible.

7.9 The weak boson and Fermi couplings

As stated in Section 5.4, there are some conventional factors which have arisen historically and which enter into the definition of the coupling of the leptons to the intermediate weak bosons $W^{\pm}$, modifying the simple expression $G = g^2/M_W^2$ in (2.10). Originally, G was defined for Fermi (that is, pure vector) transitions. Since however we have in general both V and A amplitudes, the extra term in the matrix element was compensated by replacing G by $\frac{1}{\sqrt{2}}G$ so that G retained its meaning as the coupling for a general β-transition. Furthermore, at the time of the $V - A$ theory the helicity operator was defined as $1 - \gamma_5$ instead of the quantity $\frac{1}{2}(1 - \gamma_5)$ as used above. Applied at both vertices, this gives an overall factor of 4 by which g^2 should be divided.

In the electroweak theory to be discussed in Chapter 8, the weak amplitude g is defined for the generic coupling of a lepton to a W boson – see (8.7) – the latter consisting of a 'weak isospin' triplet of fields $W^{(1)}$, $W^{(2)}$, $W^{(3)}$. The charged-current interaction involves the physical charged boson $W^{\pm} = \frac{1}{\sqrt{2}}(W^{(1)} \pm iW^{(2)})$, where the $\sqrt{2}$ is a conventional normalisation factor (Clebsch–Gordan coefficient, see Appendix C). Finally therefore, the coupling g of a lepton to the $W^{\pm}$ boson is related to the Fermi constant G by the expression

$$\frac{g^2}{8M_W^2} \equiv \frac{G}{\sqrt{2}} \tag{7.20}$$

7.10 Pion and muon decay

The lepton helicities first observed in 1957 in nuclear β-decay were detected simultaneously in the decays of pions and muons. We recall that the pion and muon decay schemes are

$$\pi^+ \to \mu^+ + \nu_\mu$$
$$\mu^+ \to e^+ + \nu_e + \bar{\nu}_\mu$$

Since the pion has spin zero, the neutrino and muon must have antiparallel spin vectors, as shown in Figure 7.9. If the neutrino has helicity $H = -1$, as in β-decay, the μ^+ must also have negative helicity. In the subsequent muon decay, the positron spectrum is peaked in the region of maximum energy, so the most likely configuration is that shown, where the positron has positive helicity. The positron spectrum is shown in Figure 7.10.



Fig. 7.9. The spin polarisation in pion and muon decay.

In the experiments, positive pions decayed in flight, and those muons projected in the forward direction in the pion rest frame – and thus with the highest energies and with negative helicity – were selected. These μ^+ were stopped in a carbon absorber, and the angle θ of the e^+ momentum vector relative to that of the original muon momentum $\mathbf{p}_\mu$ was measured. The muon spin $\boldsymbol{\sigma}$ should be opposite to $\mathbf{p}_\mu$ if there is no depolarisation of the muon in coming to rest (true in carbon). The angular distribution observed was of the form

$$\frac{dN}{d\Omega} = 1 - \frac{\alpha}{3}\cos\theta \tag{7.21}$$

where it was found that $\alpha = 1$ within the errors of measurement. This is exactly the form predicted by the $V - A$ theory, and the result provided strong support for it.

Pion decay is possible for two different modes, $\pi^+ \to \mu^+ + \nu_\mu$ and $\pi^+ \to e^+ + \nu_e$, and the ratio of the two provided a very stringent test of the theory. Pion decay is a transition from a hadronic state with $J^P = 0^-$ to the vacuum, $J^P = 0^+$. Of the five operators mentioned above, only the A and P interactions could be involved in such a transition. The $V - A$ theory predicts, from (7.16), that the polarisation of the charged (anti)lepton, e^+ or μ^+, expressed in terms of the number of particles with RH and LH helicity, N_R and N_L is

$$P = \frac{N_R - N_L}{N_R + N_L} = +\frac{v}{c}$$

where v is the charged lepton velocity. The probability that this lepton will emerge with the same helicity as the neutrino – as it must do in order to conserve angular momentum – i.e. left-handed, must be

$$\frac{N_L}{N_R + N_L} = \frac{1}{2}\left(1 - \frac{v}{c}\right)$$

However, P coupling would favour the *same* helicity for lepton (ν_e or ν_μ) and antilepton (e^+ or μ^+), and the probability for this configuration would be

$$\frac{N_L}{N_R + N_L} = \frac{1}{2}\left(1 + \frac{v}{c}\right)$$

So, the zero spin of the pion and conservation of angular momentum together result in a factor in the decay rate of $1 - v/c$ for A coupling and $1 + v/c$ for P coupling.

The other factor determining the rate will be the phase-space factor. If p denotes the momentum of either lepton in the cms, m denotes the mass of the charged lepton and the neutrino mass is taken as zero, the total energy (in units where $\hbar = c = 1$) is

$$E_0 = m_\pi = p + \sqrt{p^2 + m^2}$$

Hence the phase-space factor is

$$p^2 \frac{dp}{dE_0} = \frac{(m_\pi^2 + m^2)(m_\pi^2 - m^2)^2}{4m_\pi^4}$$

while

$$1 + \frac{v}{c} = \frac{2m_\pi^2}{m_\pi^2 + m^2}$$

$$1 - \frac{v}{c} = \frac{2m^2}{m_\pi^2 + m^2}$$

Thus for A coupling the decay rate is proportional to

$$p^2 \frac{dp}{dE_0}\left(1 - \frac{v}{c}\right) = \frac{m^2}{2}\left(1 - \frac{m^2}{m_\pi^2}\right)^2$$

and for P coupling it is proportional to

$$p^2 \frac{dp}{dE_0}\left(1 + \frac{v}{c}\right) = \frac{m_\pi^2}{2}\left(1 - \frac{m^2}{m_\pi^2}\right)^2$$

The predicted branching ratios become, with the approximation $m_e^2/m_\pi^2 \ll 1$,

$$\begin{aligned} &\text{for } A \text{ coupling, } R = \frac{\pi \to e + \nu}{\pi \to \mu + \nu} = \frac{m_e^2}{m_\mu^2} \frac{1}{(1 - m_\mu^2/m_\pi^2)^2} = 1.28 \times 10^{-4} \\ &\text{for } P \text{ coupling, } R = \frac{\pi \to e + \nu}{\pi \to \mu + \nu} = \frac{1}{(1 - m_\mu^2/m_\pi^2)^2} = 5.5 \end{aligned} \tag{7.22}$$

The dramatic difference in the branching ratio for the two types of coupling just stems from the fact that angular-momentum conservation compels the electron or muon to have the 'wrong' helicity for A coupling. The phase-space factor is larger for the electron decay, but the factor $1 - v/c$ strongly inhibits decay to the lighter lepton. The measured value of the ratio R is

$$R_{\text{exp}} = 1.23 \times 10^{-4} \tag{7.23}$$

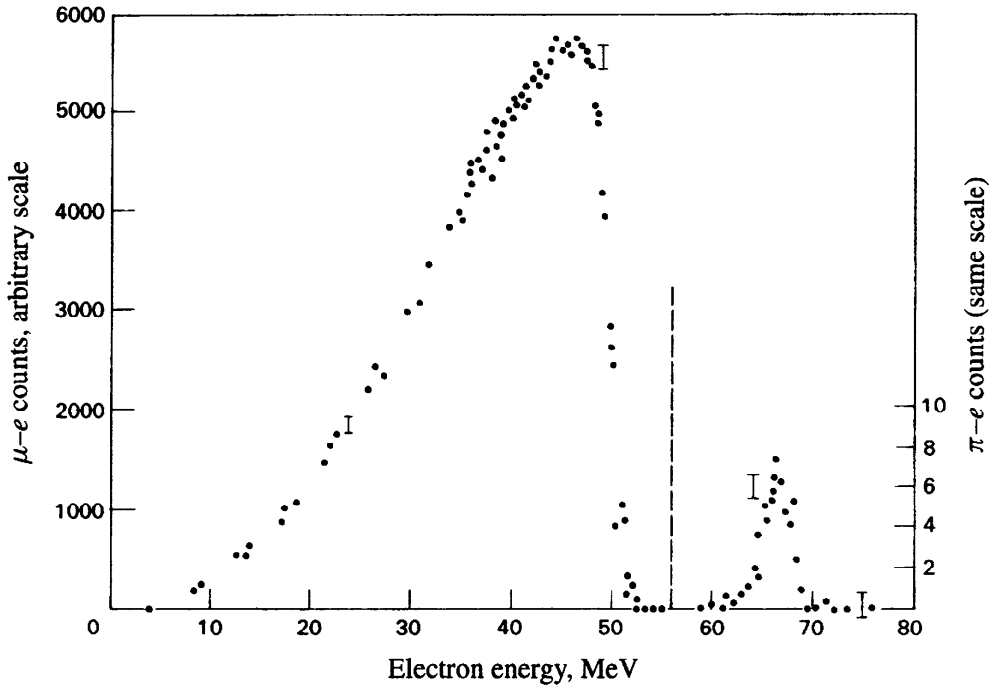

Fig. 7.10. Positron spectrum from positive pions coming to rest in an absorber. It shows at the right a narrow peak around 70 MeV, from the rare $\pi^+ \to e^+ + \nu_e$ decay, standing out above the broad spectrum from the muon decay, $\mu^+ \to e^+ + \nu_e + \bar{\nu}_\mu$, that follows, subsequent on the predominant $\pi^+ \to \mu^+ + \nu_\mu$ decay. Note the change in vertical scale for these rare events.

This result is in exact agreement with the prediction of A coupling, after small radiative corrections to (7.22), and was a major triumph for the $V - A$ theory. Figure 7.10 shows a typical positron spectrum observed from positive pions stopped by an absorber. The rare $\pi \to e + \nu$ process yields positrons of unique energy, about 70 MeV. They are accompanied by the much more numerous positrons from the decay sequence $\pi^+ \to \mu^+ + \nu_\mu$ followed by $\mu^+ \to e^+ + \nu_e + \bar{\nu}_\mu$. The spectrum from muon decay extends to 50 MeV. Rejection of electrons from muon decay is based on momentum and on the timescale (the mean life of the pion is 25 ns, that of the muon 2200 ns), as well as the absence of a muon pulse in the counters.

Today the $V - A$ nature of the (charged-current) weak interaction is accepted, and the above branching ratio provides a test of the universality of the $W^\pm$ coupling to the electron and the muon, as given in (7.4). Of course this universality was tacitly assumed in deriving (7.22).

7.11 Neutral weak currents

The production at accelerators of intense beams of high energy neutrinos and antineutrinos, from the early 1960s onwards, led to dramatic developments in our

understanding of weak interactions. The layout of a neutrino beam is sketched in Figure 7.11(a). The basic principle is to produce secondary pions and kaons from high energy proton collisions in a target T. Secondaries of one sign of charge and in a small band of momentum can be selected by means of dipole bending magnets, collimating slits and quadrupole focussing magnets. The pions and kaons then enter a decay tunnel, where a fraction of them decay to muons and neutrinos ($\pi^+, K^+ \rightarrow \mu^+ + \nu_\mu$ and $\pi^-, K^- \rightarrow \mu^- + \bar{\nu}_\mu$). The muons are ranged out by a thick iron and earth shield, and the interactions of the neutrinos are observed in the detector. This arrangement gives a 'narrowband' neutrino beam. It also possible to produce a 'wideband' beam delivering a much wider range of neutrino energies, and thus higher fluxes, by using one or more 'horn' conductors. These carry very large (100 kA) pulsed currents providing toroidal magnetic fields that 'focus' the secondary pions and kaons, emitted at a range of angles and momenta from the target, into the direction of the decay tunnel.

As mentioned in Chapter 2, accelerator neutrino experiments gave the first evidence in 1962 for lepton 'flavour' and for the separate identity of electron and muon neutrinos, ν_e and ν_μ; early examples of the two types of event in spark chambers are shown in Figure 1.6. These are *charged-current* events of the form

$$\begin{aligned} \nu_\mu + N &\rightarrow \mu^- + X \\ \nu_e + N &\rightarrow e^- + X \end{aligned} \tag{7.24}$$

with corresponding interactions for antineutrinos; X denotes the final hadronic state.

In 1973, the existence of neutrino interactions without a charged lepton in the final state were demonstrated in a bubble chamber experiment at CERN. These were termed *neutral-current* events and ascribed to reactions of the form

$$\begin{aligned} \nu_\mu + N &\rightarrow \nu_\mu + X \\ \bar{\nu}_\mu + N &\rightarrow \bar{\nu}_\mu + X \end{aligned} \tag{7.25}$$

with similar processes for electron-type neutrinos and antineutrinos. They occurred at a fraction of the rate of the charged-current events. In addition to these semi-leptonic interactions, purely leptonic neutral-current interactions of the type

$$\begin{aligned} \nu_\mu + e^- &\rightarrow e^- + \nu_\mu \\ \bar{\nu}_\mu + e^- &\rightarrow e^- + \bar{\nu}_\mu \end{aligned} \tag{7.26}$$

were also observed, as shown in Figure 2.7. The first event of this type was in fact found before the evidence for the semi-leptonic neutral currents had been established. Figure 7.12 shows examples of charged- and neutral-current events involving hadrons in the Gargamelle bubble chamber. The discovery of neutral-current events was important in providing the first evidence in favour of

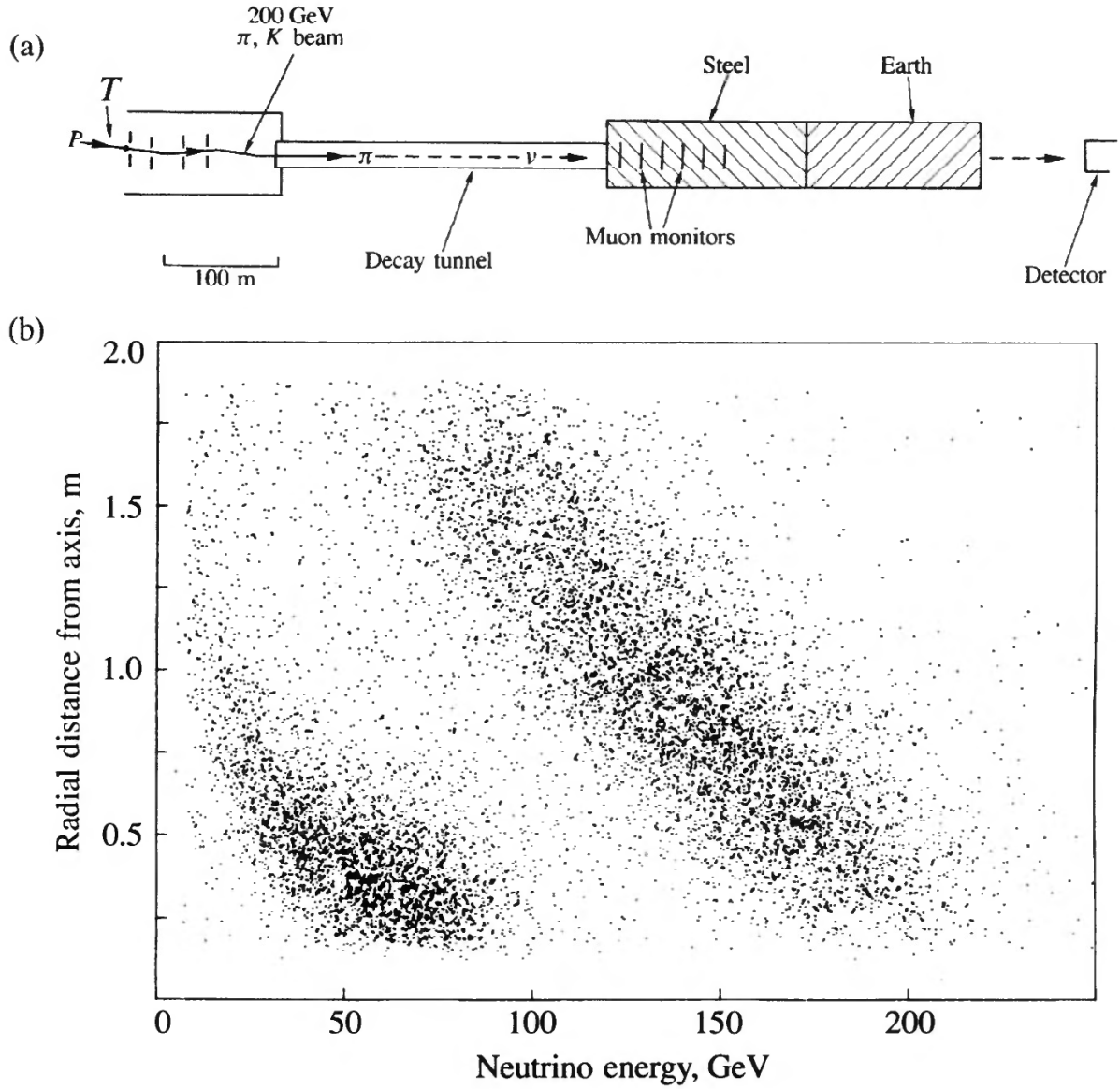

Fig. 7.11. (a) Layout of the CERN 200 GeV narrowband neutrino beam. (b) There is a kinematic relation between the energy and direction of the neutrinos from decay of pions or kaons of a particular momentum (in this case 200 GeV/c), for the dominant two-body decay modes $\pi \rightarrow \mu + \nu$, $K \rightarrow \mu + \nu$. Hence the energies of neutrino events are correlated with distance from the beam axis, the high energy band coming from kaon decay and a lower energy band coming from pion decay (see Problem 7.2).

the unified model of weak and electromagnetic interactions, as described in detail in Chapter 8. This led directly to estimates for the masses of the $W^{\pm}$ and Z^0 mediating bosons and to experiments designed to detect them, as described in the next section.

7.12 Observation of the $W^{\pm}$ and Z^0 bosons in $p\bar{p}$ collisions

The masses and decay characteristics of the vector bosons $W^{\pm}$ and Z^0, mediating the charged- and neutral-current weak interactions, are predicted in the electroweak

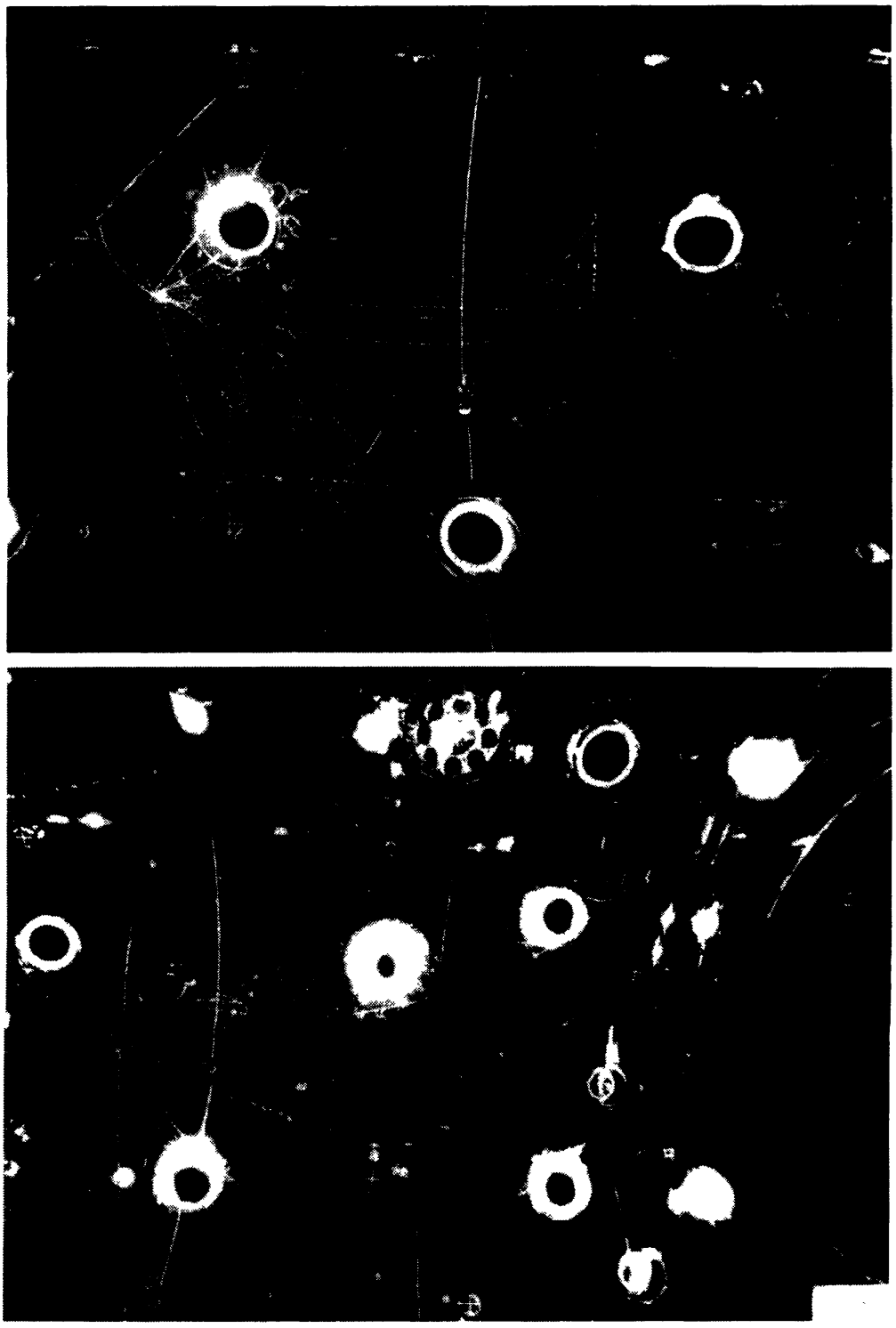

Fig. 7.12. Example (top) of a charged-current neutrino interaction in the Gargamelle bubble chamber, containing some 15 tons of freon (CF_3Br) as the liquid filling. The neutrino (ν_μ) enters from the left and in the collision transforms to a charged muon leaving the chamber at the right. Several pions and other hadrons are also produced. The bottom picture is of a neutral-current interaction where all the charged secondaries are identified as hadrons by decays or interactions. One can distinguish two e^+e^- pairs at 2–3 o'clock, close to the origin of the interaction and due to $\pi^0 \rightarrow 2\gamma$ decay; a stopping proton at 1 o'clock; a π^- at 3 o'clock interacting in the chamber liquid; and a π^+ at 4 o'clock undergoing charge exchange to a π^0, as is evident from the Compton electron knocked out by a γ-ray from π^0 decay, which points at the charge exchange vertex. (Photograph courtesy of CERN.)

theory (discussed in detail in Chapter 8) in terms of the parameter $\sin^2\theta_W$, which was first measured in neutrino experiments, as above. Among the decay modes should be the leptonic decays $W \to l + \nu_l$, $Z^0 \to l\bar{l}$ and $Z^0 \to \nu_l\bar{\nu}_l$ (where $l = e, \mu, \tau$), as well as the more numerous decays to hadrons via quark pairs, $W, Z \to Q\bar{Q} \to$ hadrons.

Such bosons were first observed at the CERN $p\bar{p}$ collider in 1983 via the elementary production and decay processes

$$u + \bar{d} \to W^+ \to e^+ + \nu_e,\ \mu^+ + \nu_\mu \tag{7.27a}$$

$$\bar{u} + d \to W^- \to e^- + \bar{\nu}_e,\ \mu^- + \bar{\nu}_\mu \tag{7.27b}$$

$$\left.\begin{matrix} u + \bar{u} \\ d + \bar{d} \end{matrix}\right\} \to Z^0 \to e^+e^-,\ \mu^+\mu^- \tag{7.27c}$$

The cross-section for (7.27a), the production of a W boson at rest in the cms, will be given by the usual Breit–Wigner resonance formula (2.31):

$$\sigma(u\bar{d} \to W^+ \to e^+\nu_e) = \frac{1}{N_c}\frac{4\pi\lambda\!\!\!^{-2}\Gamma_{u\bar{d}}\Gamma_{e\nu}/4}{(2s_d+1)(2s_u+1)[(E-M_W)^2+\Gamma^2/4]}\frac{2J+1}{3} \tag{7.28}$$

where E is the invariant mass of the $u\bar{d}$ system, $\lambda\!\!\!^{-} = 2/E$ is the de Broglie cms wavelength of the colliding particles and Γ, $\Gamma_{u\bar{d}}$, $\Gamma_{e\nu}$ are the total and partial widths for decay. $s_d = s_u = \frac{1}{2}$ are the quark spins. In the $V - A$ theory, only LH (RH) helicity states of the u ($\bar{d}$) are involved, so the spin-multiplicity factor for the W is $\frac{1}{3}(2J+1) = 1$ (see Figure 7.13). The colour factor $1/N_c = \frac{1}{3}$ is the probability of matching, say, a red quark with an antired antiquark. The peak cross-section is then

$$\begin{aligned}\sigma_{\max}(u\bar{d} \to W^+ \to e^+\nu_e) &= \frac{4\pi}{3M_W^2}\frac{\Gamma_{ud}\Gamma_{e\nu}}{\Gamma^2} = \frac{4\pi}{81M_W^2} \\ &= 9.2\ \text{nb}\end{aligned} \tag{7.29}$$

where we have assumed the value $M_W = 80$ GeV. Each of the decays to quarks $W \to u\bar{d}$, $W \to c\bar{s}$ carries a colour factor 3, while decay to the third pair of quarks $t\bar{b}$ is forbidden by energy conservation. Each of the decays $W \to e\nu_e, \mu\nu_\mu, \tau\nu_\tau$ has weight 1, so that $\Gamma_{u\bar{d}}/\Gamma = \frac{1}{3}$ and $\Gamma_{e\nu}/\Gamma = \frac{1}{9}$. The cross-section for (7.27c) involves the weak mixing parameter $\sin^2\theta_W$ discussed in Chapter 8, and turns out to be a factor of 10 smaller.

The cross-sections for the reactions $p\bar{p} \to W^+ + \cdots$, $W^+ \to e^+\nu$ and $p\bar{p} \to Z^0 + \cdots$, $Z^0 \to e^+e^-$ result from integrating the elementary quark cross-section (7.28) over the boson width and the momentum distributions of the quarks inside the nucleon. For 270 GeV protons on 270 GeV antiprotons, as employed in the pioneer experiments at the CERN $p\bar{p}$ collider in 1983, $\sigma(p\bar{p} \to W \to e\nu)$ is

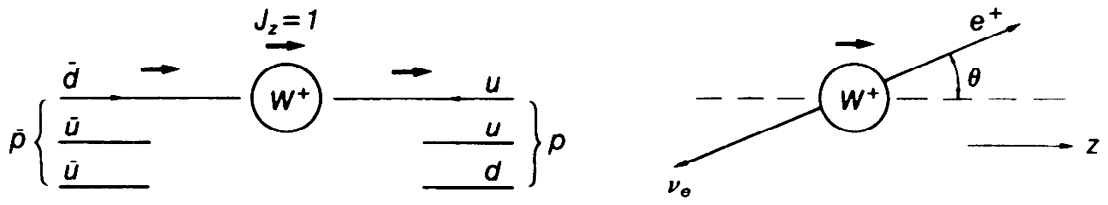

Fig. 7.13.

of order 1 nb (10^{-33} cm^2) and $\sigma(p\bar{p} \rightarrow Z^0 \rightarrow e^+e^-)$ of order 0.1 nb, to be compared with a value of $\sigma(\text{total}) = 40$ mb $= 4 \times 10^7$ nb for the total $p\bar{p}$ cross-section. The extraction of such rare events, at the level of 10^{-8}–10^{-9} of the total, was possible because the electrons, muons and neutrinos from the decays have very high transverse momenta: $p_T \leq M_W/2 \simeq 40$ GeV/c. Other sources of leptons, e.g. from hadron decay, give much smaller p_T values.

The detectors employed in these experiments consisted of central tracking chambers to detect individual secondary particles, surrounded by an electromagnetic calorimeter (to detect showers due to electrons and photons), a much larger calorimeter used in the measurement of hadron jets and an external muon detector. The calorimeters were segmented in intervals of polar and azimuthal angles, θ and ϕ. Apart from the difference in detail, the principles are, however, much the same as those in the CDF detector described in Section 4.13.

Figure 2.8 shows a reconstruction of a typical $W \rightarrow e\nu$ event. The signature is:

(i) a high p_T electron, appearing as a single isolated track of high momentum in the central tracking detector, pointing to

(ii) a shower in the electromagnetic calorimeter, with no significant energy deposition in the nearby hadronic calorimeter segments, and

(iii) missing p_T in the event overall, when a summation is made over all secondaries produced (clearly, the other quarks involved in the collision generate secondary hadrons, mostly of low p_T). The missing p_T is associated with the neutrino from the W-decay.

Figure 7.14(a) is of a plot of the missing p_T in the electron-beam plane against the p_T of the electron, showing that the neutrino and electron have approximately equal and opposite p_T values, as expected (the W bosons themselves are produced with values of p_T relative to the beam of order 5 GeV/c only). Decays to muons, $W \rightarrow \mu\nu$, $Z^0 \rightarrow \mu^+\mu^-$ were also observed, the requirement being of one (or two) particles of high p_T that penetrate the hadron calorimeter (of order six nuclear interaction lengths) and are detected in the external muon chambers.

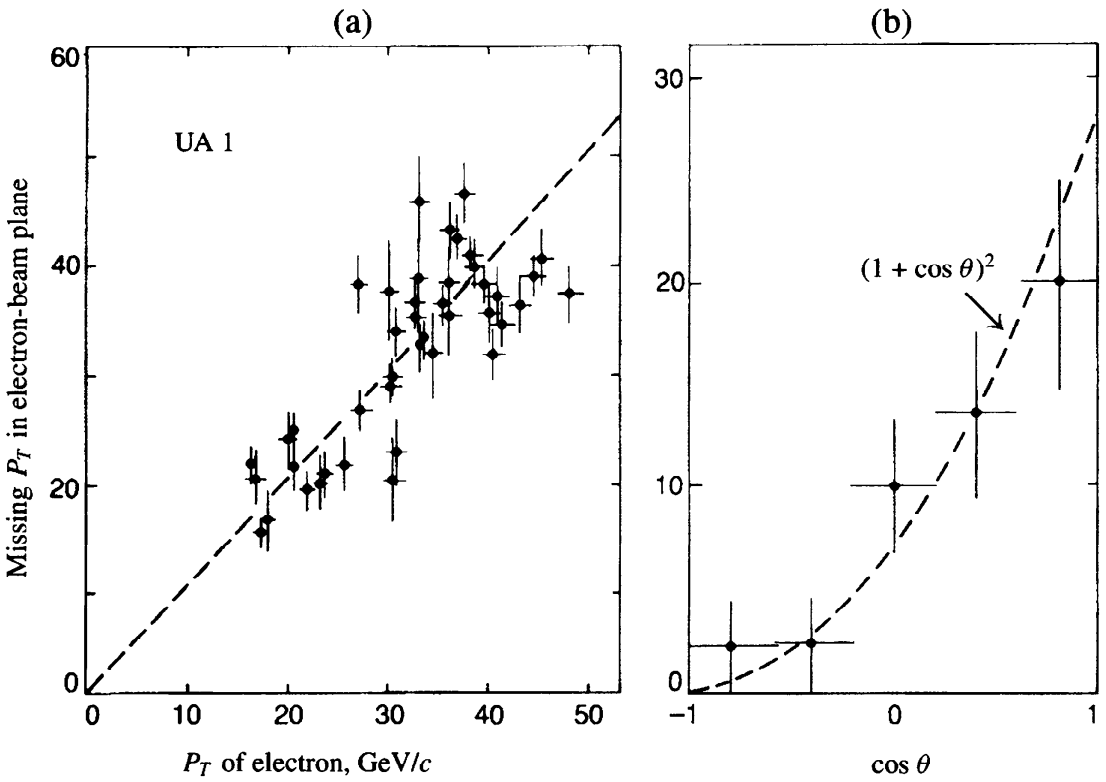

Fig. 7.14. (a) Missing p_T in the electron–beam plane, plotted against the p_T of the electron in 43 events attributed to $W \rightarrow e + \nu_e$, in the 1983 CERN experiment. The p_T of the W boson and the net p_T of the other particles produced in the event is small, so the missing p_T has to be ascribed to the neutrino. (b) Angular distribution of the decay electrons in the rest frame of the W boson. The angle θ is that between the e^- and the proton-beam direction, or between the e^+ and the antiproton direction.

Figure 7.13 shows that in the $V - A$ theory, the W's are polarised, so we expect a parity-violating asymmetry in the decay, with the e^+ from W^+ decay pointing preferentially in the same direction as the incident antiproton, while for reaction (7.27b) the e^- (or μ^-) from the W^- decay points preferentially in the direction of the incident proton. The angular distribution in the W rest frame is easily obtained. If the antiproton beam in Figure 7.13 defines the z-axis, then the W^+ is produced in the state $J_z = +1$ only. The probability that the e^+ and ν_e, with helicities $+1$ and -1 respectively, emerge at angles θ and $\pi - \theta$ and with $J_z = +1$ is clearly given by the square of the appropriate d-function (see Appendix C):

$$\frac{dN}{d(\cos\theta)} = |d^1_{1,1}|^2 = (1 + \cos\theta)^2 \tag{7.30}$$

Here θ is the angle between the positron and antiproton directions. The same distribution applies for W^- decays if θ is the angle between electron and proton directions. This angular distribution is well verified experimentally (Figure 7.14b).

7.13 Z^0 production at e^+e^- colliders

Following the observation of the W and Z bosons at the CERN $p\bar{p}$ collider in 1983, the Z boson was observed as a prominent resonance in the high energy e^+e^- colliders LEP at CERN and SLC at Stanford, from 1989 onwards. Figure 7.15 shows the Z^0 produced as an e^+e^- resonance at the appropriate cms energy $E \simeq M_Z$. From (2.31) the cross-section for $e^+e^- \to Z^0 \to$ anything is expected to be

$$\sigma = \frac{4\pi \lambda\!\!\!^{-2}(2J+1)}{(2s+1)^2} \frac{\Gamma_e \Gamma/4}{[(E-E_0)^2 + \Gamma^2/4]} \tag{7.31}$$

where E is the cms collision energy, $E_0 = M_Z$, $\lambda\!\!\!^{-} = 2/E$ is the de Broglie wavelength of the colliding particles, $s = \frac{1}{2}$ is the electron spin and $J = 1$ is the Z^0 spin. Γ is the total width, Γ_e the partial width for the decay $Z^0 \to e^+e^-$. There are also non-resonant contributions to the cross-section from the photon exchange process $e^+e^- \to \gamma \to$ anything, but these are small and we neglect them here.

Thus at the resonance peak

$$\sigma_{\max}(e^+e^- \to Z^0 \to \text{anything}) = \frac{12\pi}{M_Z^2}\left(\frac{\Gamma_e}{\Gamma}\right) \tag{7.32}$$

The result is the same if we use the relativistic Breit–Wigner formula (2.32). In comparison, the cross-section for the pointlike, non-resonant reaction $e^+e^- \to \mu^+\mu^-$ via single-photon exchange is, from (5.5a)

$$\sigma(\text{point}) = \frac{4\pi\alpha^2}{3E^2}$$

where E is the collision energy. Thus we expect that for $E = M_Z$

$$R = \frac{\sigma_{\max}(e^+e^- \to Z^0)}{\sigma(\text{point})} = \frac{9}{\alpha^2}\left(\frac{\Gamma_e}{\Gamma}\right) \tag{7.33}$$

Here, the masses m_μ, m_e have been neglected in comparison with M_Z. As described in Section 8.9, $\Gamma_e/\Gamma \simeq 0.034$, leading to $R \simeq 5700$. This is an ideal value, before taking into account the effects of radiative corrections, which reduce it to $R \simeq 3200$. These corrections, which arise principally because of radiation by the initial-state e^+ and e^-, not only depress the peak but also distort the shape of the resonance curve from that of the symmetric Breit–Wigner distribution.

At sufficiently high collision energies, W^+W^- and Z^0Z^0 pairs can also be produced at e^+e^- colliders, and the cross-sections constitute a critical test of the couplings of these bosons, which are prescribed in the electroweak theory, and are discussed in the next chapter (see Section 8.11).

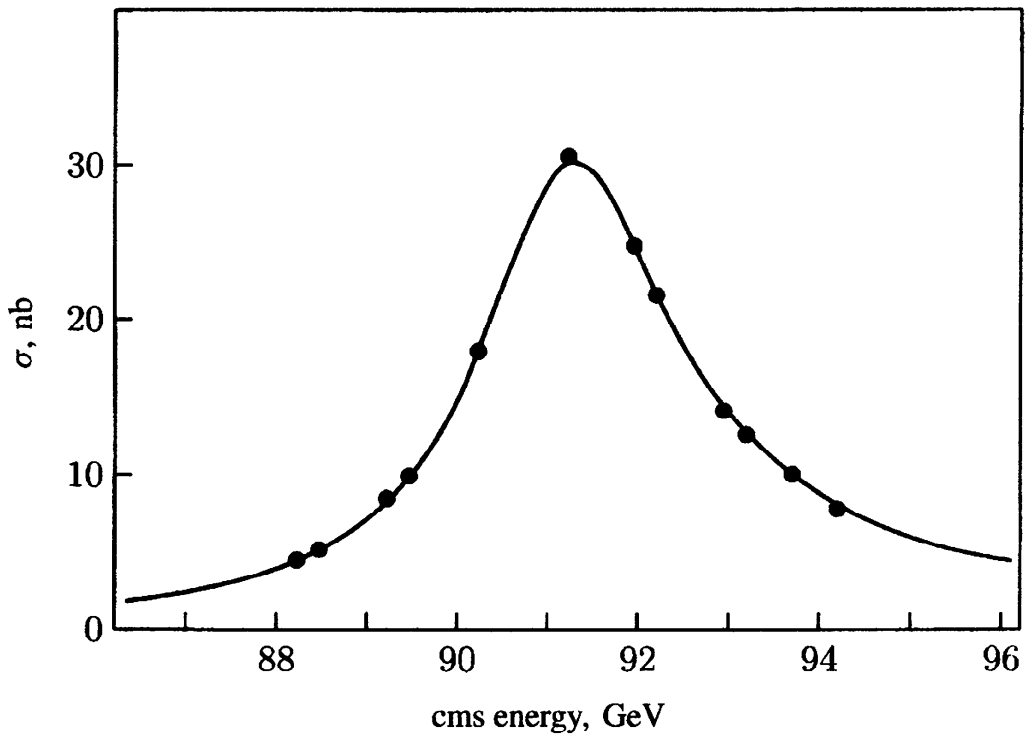

Fig. 7.15. The cross-section $\sigma(e^+e^- \to Z^0 \to \text{hadrons})$, as a function of the cms beam energy, compounded from CERN and SLAC data. The curve is the best-fit Breit–Wigner distribution and includes the effects of radiative corrections, which distort the otherwise symmetric distribution.

7.14 Weak decays of quarks. The GIM model and the CKM matrix

Early measurements of the semi-leptonic decay rates of strange particles, e.g.

$$\Sigma^- \to n + e^- + \bar{\nu}_e \tag{7.34}$$

characterised by a change in strangeness $\Delta S = 1$, indicated that they were suppressed by a factor of about 20 as compared with $\Delta S = 0$ transitions, such as

$$n \to p + e^- + \bar{\nu}_e \tag{7.35}$$

At the same time, it was noticed that the value of the Fermi constant G deduced from allowed nuclear β-decays such as (7.35) was slightly less than that deduced from muon decay, (7.1). These factors were successfully accounted for in the Cabibbo theory, in which the d and s quark states participating in a weak interaction were taken, not as pure flavour eigenstates but as having been 'rotated' by a mixing angle, called the Cabibbo angle θ_c. Thus, in analogy with the lepton doublets involved in charge-changing leptonic weak interactions, the u, d and s quarks are

organised in a doublet:

$$\begin{aligned} &\text{lepton doublets} \quad \begin{pmatrix} e \\ \nu_e \end{pmatrix}, \ \begin{pmatrix} \mu \\ \nu_\mu \end{pmatrix} \\ &\text{quark doublet} \quad \begin{pmatrix} u \\ d\cos\theta_c + s\sin\theta_c \end{pmatrix} \end{aligned} \tag{7.36}$$

At the time this scheme was proposed, only the u, d, s quarks were known, so that it was natural to write the weak eigenstate as a mixture of the two charge $-\frac{1}{3}$ quark-flavour states. However, this is just convention: now that three quarks of charge $+\frac{2}{3}$ and three of $-\frac{1}{3}$ are known, one could equally well postulate the mixture as made up of the charge $+\frac{2}{3}$ quark states.

The weak coupling G of the doublet (7.36) is exactly the same as for the leptons; but, for a $\Delta S = 0$ decay, involving u and d quarks as in (7.35), the effective coupling will be $G\cos\theta_c$ while for a $\Delta S = 1$ transition as in (7.34) it will be $G\sin\theta_c$, where experiments give $\theta_c \simeq 12°$.

As previously stated, neutral weak current processes are characterised by the selection rule $\Delta S = 0$, or, more generally speaking, they are non-flavour-changing processes. Indeed, one of the reasons why early theories of weak interactions postulating the existence of neutral currents were discounted was that they had never been detected in the decay processes of strange particles. For example, the ratio of neutral- to charged-current decay rates in kaon decay had a very stringent upper limit:

$$\frac{K^+ \to \pi^+ + \nu + \bar{\nu}}{K^+ \to \pi^0 + \mu^+ + \nu_\mu} \leq 10^{-5} \tag{7.37}$$

The absence of $\Delta S = 1$ neutral currents in the Cabibbo model was hard to understand. Figure 7.16 shows the neutral-current (Z^0) coupling to the u quark and to the 'Cabibbo-rotated' d and s quark combination. The neutral-current interaction of the u, d and s quarks will be proportional to the product of the wavefunctions of the participating particles

$$\underbrace{u\bar{u} + (d\bar{d}\cos^2\theta_c + s\bar{s}\sin^2\theta_c)}_{\Delta S = 0} + \underbrace{(s\bar{d} + d\bar{s})\sin\theta_c\cos\theta_c}_{\Delta S = 1} \tag{7.38}$$

so that $\Delta S = 1$ neutral currents are allowed. In 1970, Glashow, Iliopoulos and Maiani (GIM) proposed the introduction of a new charge $+\frac{2}{3}$ quark, with label c for 'charm', and a second doublet consisting of the new c quark and the s, d combination orthogonal to (7.36). Thus, the two quark doublets were

$$\begin{pmatrix} u \\ d' \end{pmatrix} = \begin{pmatrix} u \\ d\cos\theta_c + s\sin\theta_c \end{pmatrix}, \qquad \begin{pmatrix} c \\ s' \end{pmatrix} = \begin{pmatrix} c \\ s\cos\theta_c - d\sin\theta_c \end{pmatrix} \tag{7.39}$$

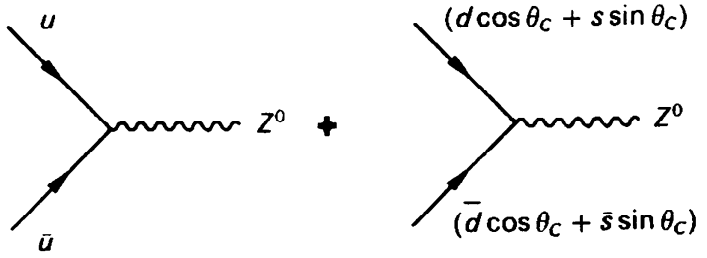

Fig. 7.16.

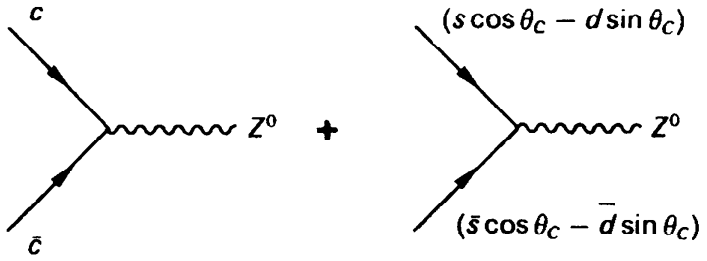

Fig. 7.17.

In this way, extra terms have to be added to Figure 7.16, as shown in Figure 7.17, and when these are included we obtain for the weak-interaction neutral-current matrix element

$$\begin{gathered}\underbrace{u\bar{u}+c\bar{c}+(d\bar{d}+s\bar{s})\cos^2\theta_c+(s\bar{s}+d\bar{d})\sin^2\theta_c}_{\Delta S=0}\\ \underbrace{+(s\bar{d}+\bar{s}d-\bar{s}d-s\bar{d})\sin\theta_c\cos\theta_c}_{\Delta S=1}\end{gathered} \tag{7.40}$$

Hence, at the price of a new quark and a second quark doublet, the unwanted $\Delta S = 1$ neutral currents have been cancelled. The GIM prediction of a second quark of charge $+\frac{2}{3}$ was a great triumph for theory, when the J/ψ state $c\bar{c}$, consisting of the new quark and antiquark was found in 1974. Indeed, just before this discovery it had been possible to estimate what the mass of the new quark should be, from the $K^0 - \bar{K}^0$ mass difference (see equation (7.59) below).

In this section we have so far restricted ourselves to u, d, s and c quarks and the Cabibbo–GIM formalism for the mixing matrix, which specifies the quark states involved in the weak interactions. These are expressed in matrix form by

$$\begin{pmatrix} d' \\ s' \end{pmatrix} = \begin{pmatrix} \cos\theta_c & \sin\theta_c \\ -\sin\theta_c & \cos\theta_c \end{pmatrix} \begin{pmatrix} d \\ s \end{pmatrix} \tag{7.41}$$

The mixing is specified here by a single parameter, the Cabibbo angle θ_c. All data on weak decays involving u, d, s and c quarks seem to be consistent with a unique value of θ_c, as described previously.

The treatment must be extended to incorporate further quarks: the b quark, with $Q = -\frac{1}{3}$, and its partner the t quark, with $Q = +\frac{2}{3}$. The existence of three pairs of quarks, in parallel with three pairs of leptons, is aesthetically attractive, and significant theoretically because of the absence of certain 'triangle anomalies'. We do not discuss these here, but remark that the condition for cancelling such anomalies is that the net charge of all fermions should be zero. The three lepton doublets $(e, \nu_e; \mu, \nu_\mu; \tau, \nu_\tau)$ contribute $-3|e|$; and the three quarks (u, c, t) with $Q = +\frac{2}{3}$ plus the three (d, s, b) with charge $Q = -\frac{1}{3}$ will contribute $+3|e|$, if allowance is made for the factor 3 for colour.

With six quark flavours, the weak currents will be described by unitary transformations among three quark doublets. Then we write, in analogy with (7.41),

$$\begin{pmatrix} d' \\ s' \\ b' \end{pmatrix} = V \begin{pmatrix} d \\ s \\ b \end{pmatrix} \tag{7.42a}$$

where the 3×3 matrix V is, in an obvious notation,

$$V = \begin{vmatrix} V_{ud} & V_{us} & V_{ub} \\ V_{cd} & V_{cs} & V_{cb} \\ V_{td} & V_{ts} & V_{tb} \end{vmatrix} \tag{7.42b}$$

This matrix is called the CKM matrix (after Cabibbo, and Kobayashi and Maskawa (1972) who developed it). An $N \times N$ matrix will have $N(N-1)/2$ real parameters (Euler angles) and $(N-1)(N-2)/2$ non-trivial phase angles. Thus the Cabibbo matrix (7.41) with $N = 2$ is specified by one real parameter (θ_c), while for the 3×3 matrix (7.42b) there are three Euler angles and one phase angle, say δ. The phase will enter the wavefunction as $\exp[i(\omega t + \delta)]$, and clearly this is not invariant under time reversal, $t \to -t$. So this phase introduces the important possibility of T-violating or, equivalently, CP-violating amplitudes in the Standard Model. CP violation is discussed below (Section 7.16).

The matrix V must be unitary ($V^\dagger V = 1$, where $V^\dagger$ is the complex transpose of V), since the couplings between u, c and t quarks and the 'rotated' states d', s' and b' are, we assume, specified by the same Fermi constant, G. The various elements of the matrix have been determined in a range of experiments.

The quantity V_{ud} $(= \cos\theta_c$ in the 2×2 Cabibbo matrix (7.41)) is determined, as described above, by comparing nuclear β-decay and μ-decay rates, while V_{us} is determined from the semi-leptonic decays of strange particles (kaons and hyperons), previously defining $\sin\theta_c$. The last entry in the top row of the

matrix, V_{ub}, can be measured by selecting semi-leptonic decays of B mesons to non-charmed particles (i.e. excluding the much more prolific $b \to clv$ decay mode) by requiring the charged lepton l to have momentum, in the B rest frame, p(lepton) > 2.30 GeV/c, the kinematic limit in the decay $B \to Dlv$. From this small region near the end of the $b \to ulv$ spectrum, an extrapolation has to be made to get the total rate. The result is quoted as the ratio $V_{ub}/V_{cb} \simeq 0.06$.

A word should be included here about the experimental methods for the identification and study of D and B mesons produced in high energy interactions. Those mesons of lowest mass decay weakly to other mesons, with a change in flavour ΔC or $\Delta B = 1$, so they have comparatively long lifetimes, ranging from 0.4 ps (4×10^{-13} s) for the D^0 meson to 1.6 ps for the $B^{0,\pm}$ mesons. Thus the decay length of a B meson is $\sim 0.5\gamma$ mm where $\gamma = E_B/(M_B c^2)$ is the time dilation factor. For the decay $Z^0 \to B\bar{B}$, for example, the mean B meson decay length is of order 1 cm, and the decay vertex may be separated from the production vertex using solid state (silicon strip) detectors; see Figure 8.5.

Coming to the second row of the CKM matrix, the parameter V_{cb} may be found from the favoured semi-leptonic B meson decay $B \to Dlv$. Treating this as a free quark decay, we obtain in analogy with (7.1) for muon decay

$$\Gamma(b \to clv) = \frac{R(b \to clv)}{\tau_B} = \frac{G^2 m_b^5}{192\pi^3} |V_{cb}|^2 f \tag{7.43}$$

where R is the branching ratio for the decay, m_b is the b quark mass and f is a correction factor allowing for the fact that the b quark is not free but bound in a meson and that the phase space is reduced compared with that for massless products. With $R(b \to clv) = 0.11 \pm 0.005$ and $\tau_B = 1.60 \pm 0.05$ ps one finds

$$V_{cb} = 0.040 \pm 0.005 \tag{7.44}$$

The quantity V_{cd} is found from the rate of single charmed particle production in high energy neutrino interactions, which in terms of quark states reads as

$$\begin{aligned} \nu_\mu + d &\to \mu^- + c \\ &\qquad \hookrightarrow s + \mu^+ + \nu_\mu \end{aligned} \tag{7.45}$$

If the charmed particle decays semi-leptonically as indicated, to a strange particle (K^- or K^0) and $\mu^+\nu_\mu$ pair, the signature of the event will be two muons of opposite sign. From the known branching ratio for the semi-leptonic decay of charmed mesons, the quantity V_{cd} may then be found from the observed di-muon rate ($d \to c$ transitions) as compared with the more usual, $\Delta C = 0$, $d \to u$ reaction. The measurements give

$$V_{cd} = 0.221 \pm 0.003 \tag{7.46}$$

The remaining element in the second row of (7.42b), V_{cs}, can be found in principle from the production of charmed particles from the $s\bar{s}$ sea quarks in the nucleon and also from semi-leptonic D decay to strange particles, $D^+ \to \bar{K}^0 e^+ \nu_e$. However, the value quoted below is obtained from the unitarity condition,

$$|V_{cd}|^2 + |V_{cs}|^2 + |V_{cb}|^2 = 1$$

Finally, since top quark events are comparatively rare, the elements V_{td} and V_{ts} are computed from virtual top quark effects in box diagrams from B^0–$\bar{B}^0$ mixing, as described in Section 7.18.

In summary, the modular values of the elements in the matrix (7.42) are (as of 1998):

$$V_{\text{CKM}} = \begin{vmatrix} V_{ud} = 0.975 & V_{us} = 0.221 & V_{ub} = 0.005 \\ V_{cd} = 0.221 & V_{cs} = 0.974 & V_{cb} = 0.04 \\ V_{td} = 0.01 & V_{ts} = 0.041 & V_{tb} = 0.999 \end{vmatrix} \tag{7.47}$$

The diagonal elements are seen to be close to unity so that, for example, top quarks decay mostly to bottom quarks and charmed mesons ($C = +1$) predominantly to strange mesons ($S = -1$); the fraction doing so is $\sim$ 95%. By contrast, the off-diagonal elements are small. Of course, these numbers are just empirical parameters among the many constants of the Standard Model; there is at present no understanding of their origins.

In terms of the four free constants of the CKM matrix, various parameterisations are possible. A popular one is that of Wolfenstein, written in the form of an expansion in $\lambda \equiv \sin\theta_c$ to terms in λ^3 and larger:

$$V_{\text{CKM}} = \begin{vmatrix} 1 - \lambda^2/2 & \lambda & A\lambda^3(\rho - i\eta) \\ -\lambda & 1 - \lambda^2/2 & A\lambda^2 \\ A\lambda^3(1 - \rho - i\eta) & -A\lambda^2 & 1 \end{vmatrix} \tag{7.48}$$

where $\lambda = 0.221 \pm 0.002$, $A = 0.8 \pm 0.1$ and η is the CP-violating parameter. η and ρ have yet to be determined.

7.15 Neutral K mesons

The K mesons, as indicated in Table 4.8, are in the form of two isospin ($I_3 = \pm\frac{1}{2}$) doublets, of strangeness $S = \pm 1$. The $S = +1$ doublet consists of K^+ ($= u\bar{s}$) and K^0 ($= d\bar{s}$), while their antiparticles, with $S = -1$, are K^- ($= s\bar{u}$) and $\bar{K}^0$ ($= \bar{d}s$) respectively. All decay to non-strange particles and/or leptons, through the $\Delta S = \pm 1$ weak interaction. Examples of quark diagrams for decay to two pions are given in Figure 7.18.

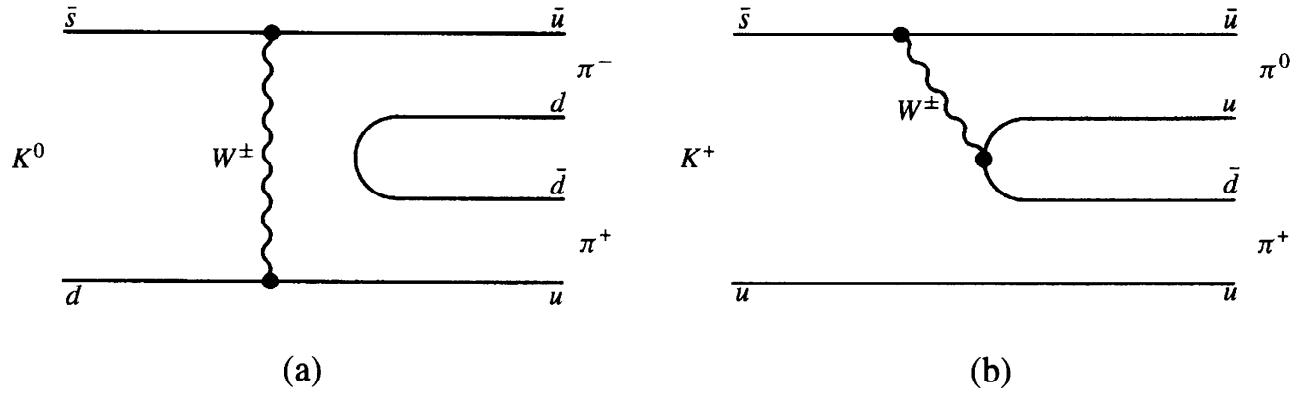

Fig. 7.18. Quark diagrams for $K \to 2\pi$ decay. (a) $K^0 \to \pi^+\pi^-$; (b) $K^+ \to \pi^+\pi^0$.

The K^0 can be produced by non-strange particles in association with a hyperon:

$$\begin{array}{cccccccc} & \pi^- & + & p & \to & \Lambda & + & K^0 \\ S & 0 & & 0 & & -1 & & +1 \end{array} \tag{7.49}$$

However, a $\bar{K}^0$ has to be produced in association with a kaon having $S = +1$:

$$\begin{array}{cccccccccc} & \pi^+ & + & p & \to & K^+ & + & \bar{K}^0 & + & p \\ S & 0 & & 0 & & +1 & & -1 & & 0 \end{array} \tag{7.50}$$

The threshold pion energy for (7.49) is 0.91 GeV, while for (7.50) it is 1.50 GeV. Thus, it is possible to produce a pure K^0 beam by choosing incident pions of suitable energy. One of the most remarkable discoveries of the early experiments on neutral kaons was that starting off with a pure K^0 beam one could end up, after a few metres, with a beam of mixed strangeness, i.e. K^0 and $\bar{K}^0$.

Pure K^0 or $\bar{K}^0$ states have also been selected in the CPLEAR experiment (1995), which uses K production in $p\bar{p}$ annihilation at rest from the CERN LEAR (low energy antiproton ring):

$$\begin{aligned} p\bar{p} &\to K^-\pi^+K^0 \\ p\bar{p} &\to K^+\pi^-\bar{K}^0 \end{aligned} \tag{7.51}$$

Although the branching fraction to these annihilation modes is only 0.2%, the high intensity, with some 10^6 antiprotons per second stopping in a high pressure hydrogen gas target, ensures a high event rate. Here, the nature of the neutral kaon produced is identified via the charged K and π secondaries produced in association.

K^0 and $\bar{K}^0$ are particle and antiparticle, and are connected by the process of charge conjugation, which involves a reversal of the value of I_3 and a change of strangeness, $\Delta S = 2$. Strong interactions conserve I_3 and S, so that as far as *production* is concerned, the separate neutral-kaon eigenstates are K^0 and $\bar{K}^0$.

Now suppose K^0 and $\bar{K}^0$ particles propagate through empty space. Since both are neutral, both can decay to pions by the weak interaction, with $|\Delta S| = 1$. Thus, *mixing* can occur via (virtual) intermediate pion states:

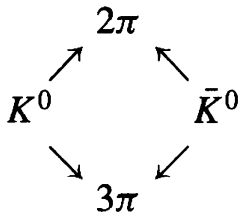

These transitions have $\Delta S = 2$ and thus are second-order weak interactions. Although extremely weak, therefore, this implies that if one has a pure K^0 state at $t = 0$ then at any later time t one will have a superposition of both K^0 and $\bar{K}^0$, so that the state can be written (using Dirac notation to indicate the wavefunction)

$$|K(t)\rangle = \alpha(t)|K^0\rangle + \beta(t)|\bar{K}^0\rangle$$

We know that objects that decay by weak interactions are eigenstates of CP, not of strangeness S. The operation of CP on the states K^0 and $\bar{K}^0$ is as follows:

$$CP|K^0\rangle \to \eta|\bar{K}^0\rangle, \qquad CP|\bar{K}^0\rangle \to \eta'|K^0\rangle \tag{7.52}$$

where η, η' are arbitrary phase factors, which we can define as $\eta = \eta' = 1$. Clearly $|K^0\rangle$ and $|\bar{K}^0\rangle$ are not CP eigenstates, but we can form the linear combinations

$$\begin{aligned} |K_S\rangle &= \sqrt{\tfrac{1}{2}}\left(|K^0\rangle + |\bar{K}^0\rangle\right), \qquad CP = +1 \\ |K_L\rangle &= \sqrt{\tfrac{1}{2}}\left(|K^0\rangle - |\bar{K}^0\rangle\right), \qquad CP = -1 \end{aligned} \tag{7.53}$$

The nomenclature K_S and K_L stands for short and long lifetimes for decay, as discussed below. We have therefore that

$$CP|K_S\rangle \to |K_S\rangle, \qquad CP|K_L\rangle \to -|K_L\rangle \tag{7.54}$$

Unlike K^0 and $\bar{K}^0$, distinguished by their mode of *production*, K_S and K_L are distinguished by their mode of *decay*. Consider the 2π and 3π decay modes.

(i) $\pi^0\pi^0$, $\pi^+\pi^-$. By Bose symmetry, the total wavefunction in either case must be symmetric under interchange of the two particles. Since no spin is involved, this is equivalent to the operation C followed by P, so that $CP = +1$.

(ii) $\pi^+\pi^-\pi^0$. The small Q-value (70 MeV) of the decay suggests $l = 0$, i.e. the three pions are in a relative S-state. By the previous arguments, the CP-parity of $\pi^+\pi^-$ is $+1$. The π^0 has $C = +1$ (since it decays to two γ-rays) and intrinsic parity $P = -1$, and thus $CP = -1$. So, combining the π^0 with the $\pi^+\pi^-$ system, we obtain one where $CP = -1$. For $l > 0$, both positive and

negative CP eigenvalues can result, but such decays are strongly suppressed by angular-momentum barrier effects.

(iii) $\pi^0\pi^0\pi^0$. Any orbital angular momentum, l, between any two pions must be even, by Bose symmetry. Hence the l-value of the remaining pion about the di-pion is also even, since $J_K = 0$. So the overall parity is the product of the *intrinsic pion parities, i.e.* $P = -1$. *Since the neutral pion has* $C = +1$, *it* follows that $CP = -1$, irrespective of the l-values involved.

Thus the 2π state has $CP = +1$, and the 3π state, including $3\pi^0$, has $CP = -1$. The two- and three-pion decay modes have different Q-values and thus different decay rates. So the hadronic (i.e. pionic) decays of neutral kaons proceed through the weak interaction CP eigenstates as follows:

$$\begin{aligned} K_S &= \sqrt{\tfrac{1}{2}}(K^0 + \bar{K}^0) \rightarrow 2\pi(CP = +1), \qquad \tau_S = 0.893 \times 10^{-10}\ \text{s} \\ K_L &= \sqrt{\tfrac{1}{2}}(K^0 - \bar{K}^0) \rightarrow 3\pi(CP = -1), \qquad \tau_L = 0.517 \times 10^{-7}\ \text{s} \end{aligned} \tag{7.55}$$

7.15.1 Strangeness oscillations

The weak-interaction kaon eigenstates are those concerned when kaons propagate through space. Because K_S and K_L have different lifetimes and decay modes, they can be expected to have a difference in mass, which will alter the relative phases of these two eigenstates.

The amplitude of the state K_S as a function of time, measured in the particle rest frame, with $E = m$, is from (2.26)

$$A_S(t) = A_S(0)e^{-(\Gamma_S/2 + im_S)t}$$

where $\Gamma_S = \hbar/\tau_s$ is the width of the K_S state and m_S is its rest mass. Similarly for K_L

$$A_L(t) = A_L(0)e^{-(\Gamma_L/2 + im_L)t}$$

Suppose we start off with a pure K^0 beam of unit intensity, created in a strong interaction at $t = 0$. Then from (7.53), $A_S(0) = A_L(0) = 1/\sqrt{2}$. After time t the K^0 intensity will be

$$\begin{aligned} I(K^0) &= \tfrac{1}{2}[A_S(t) + A_L(t)][A_S^*(t) + A_L^*(t)] \\ &= \tfrac{1}{4}\left[e^{-\Gamma_S t} + e^{-\Gamma_L t} + 2e^{-(\Gamma_S + \Gamma_L)t/2}\cos \Delta m t\right] \end{aligned} \tag{7.56}$$

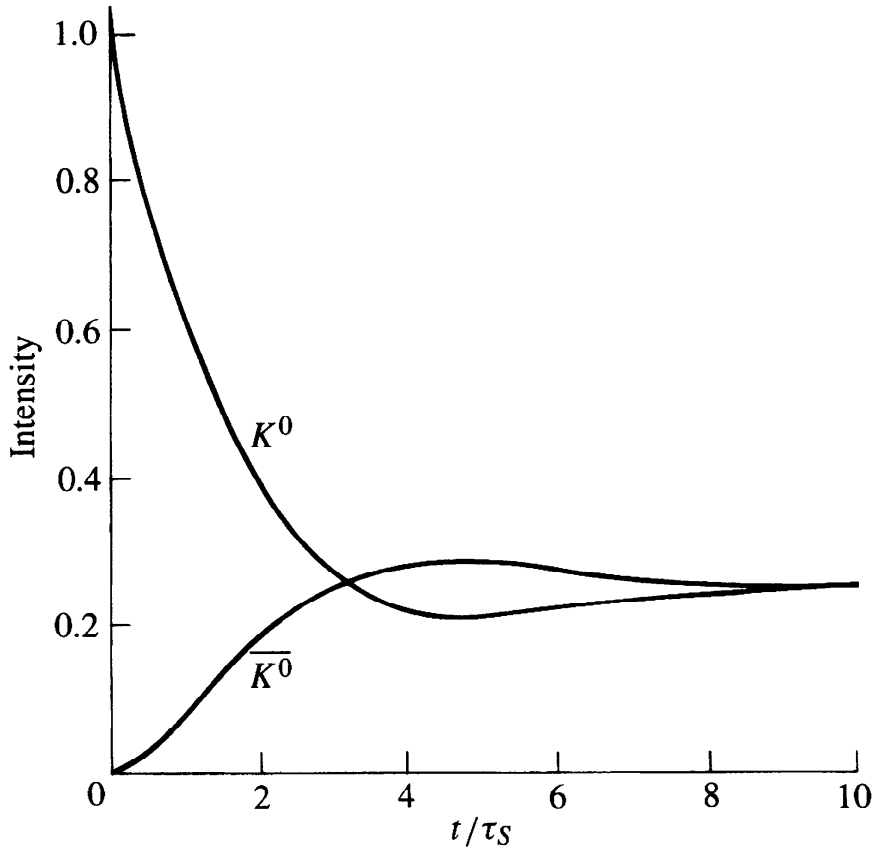

Fig. 7.19. Oscillations in K^0 and $\bar{K}^0$ intensities with time, for an initially pure K^0 beam, according to (7.56) and (7.57). The value $\Delta m\,\tau_S = 0.5$ has been assumed.

where $\Delta m = m_L - m_S$. Similarly

$$I(\bar{K}^0) = \tfrac{1}{4}[e^{-\Gamma_S t} + e^{-\Gamma_L t} - 2e^{-(\Gamma_S+\Gamma_L)t/2}\cos \Delta m t] \qquad (7.57)$$

so that the K^0, $\bar{K}^0$ intensities oscillate with frequency Δm. Figure 7.19 shows the variation to be expected for $\Delta m = 0.5/\tau_S$, and the values τ_S and τ_L given in (7.55). Observations of the number of $\bar{K}^0$ interactions (e.g. those producing hyperons with $S = -1$) lead to a measured mass difference

$$\Delta m = (3.491 \pm 0.009) \times 10^{-12}\ \text{MeV} \qquad (7.58)$$

or $\Delta m/m = 7 \times 10^{-15}$ and $\Delta m\,\tau_S = 0.474$.

The K_L–K_S mass difference or, equivalently, the rate at which K^0 oscillates to $\bar{K}^0$, is clearly due to a second-order weak interaction. Since G^2 has dimensions M^{-4}, a mass difference can be obtained by introducing the fifth power of a mass. With $M = m_K$, for example, we expect $\Delta m \sim G^2 m_K^5 \sim 10^{-9}$ MeV, while $M = m_\pi$ would give $\Delta m \sim 10^{-12}$ MeV. The actual calculation of the expected mass difference comes from the 'box diagram' in Figure 7.20. One has to integrate over the 4-momentum q of the quarks in the loop, which gives contributions proportional to the square of the quark mass. Referring to the CKM matrix (7.47)

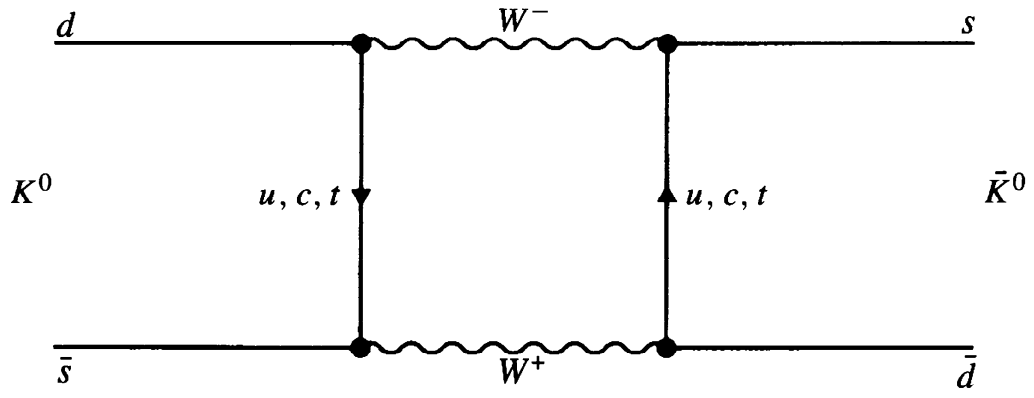

Fig. 7.20. Box diagram for $K^0 \rightarrow \bar{K}^0$ transition.

it is clear that the initial c quark will dominate over a u quark (or t quark) and will introduce a coupling $G^2 \cos^2\theta_c \sin^2\theta_c$. The actual expression for Δm is found to be

$$\Delta m = \frac{G^2}{4\pi} m_K f_K^2 m_c^2 \cos^2\theta_c \sin^2\theta_c \tag{7.59}$$

The quantity $f_K \simeq 1.2 m_\pi$ is called the kaon decay constant, m_K and m_c are the masses of the kaon and the charmed quark. The term $m_K f_K^2$ relates to the intensity $|\psi(0)|^2$ of the quark–antiquark $(d\bar{s})$ wavefunction at the origin of relative coordinates, where they undergo the pointlike W-exchange weak interaction. $|\psi(0)|^2 \simeq V^{-1}$, where the volume $V \simeq m_H^{-3}$ and m_H is some typical hadron mass, which can be estimated from the decay rate $K^+ \rightarrow \mu^+ + \nu$. The above calculation was made by Gaillard, Lee and Rosner to predict the mass of the charmed quark, just before it was discovered as a component of the so-called charmed mesons in 1975, and was used by them to estimate $m_c \simeq 1.5$ GeV.

7.15.2 K^0 regeneration

If an initially pure K^0 beam is allowed to coast *in vacuo* for many K_S mean lives, all the K_S component will have decayed and only K_L remains. If this beam traverses a slab of material, the strong interactions will pick out the $S = +1$ and $S = -1$ components of the beam, K^0 and $\bar{K}^0$:

$$K_L = \tfrac{1}{\sqrt{2}}(K^0 - \bar{K}^0) \tag{7.60}$$

This generation of particles with $S = -1$, a long way from a source of neutral kaons of $S = +1$, was confirmed in early experiments by observation of hyperon production (e.g. $\bar{K}^0 + p \rightarrow \Lambda + \pi^+$). The components K^0 and $\bar{K}^0$ in (7.60) are absorbed differently. Both K^0 and $\bar{K}^0$ can undergo charge-exchange scattering,

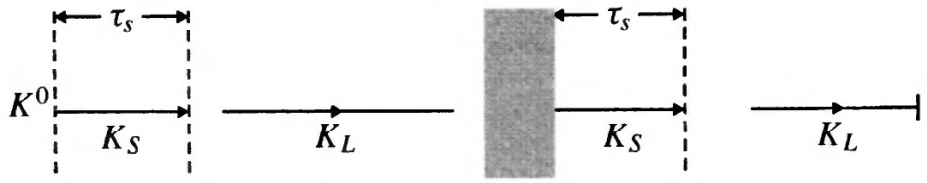

Fig. 7.21. The regeneration of K_S mesons when a pure K_L beam traverses a slab of material (shaded).

but $\bar{K}^0$ can also transform to hyperons. Thus, after emerging from the slab the amplitude of $\bar{K}^0$ will be $\bar{f}$ and that of K^0 will be f, where $\bar{f} < f < 1$. Thus, the amplitude in place of (7.60) will be

$$\tfrac{1}{\sqrt{2}}(fK^0 - \bar{f}\bar{K}^0) = \tfrac{1}{2}(f + \bar{f})K_L + \tfrac{1}{2}(f - \bar{f})K_S \tag{7.61}$$

Since $f \neq \bar{f}$, it follows that some of the short-lived weak decay eigenstate K_S has been regenerated when a K_L beam traverses a slab of material. The situation is indicated diagramatically in Figure 7.21.

7.16 CP violation in the neutral kaon system

Following the discovery of parity violation in weak decay processes in 1957, it was for some time believed that the weak interactions were at least invariant under the CP operation, and the ensuing description of the CP eigenstates of neutral kaons has been given above. In 1964, however, an experiment by Christenson, Cronin, Fitch and Turlay first demonstrated that the long-lived state we have called K_L could also decay to $\pi^+\pi^-$ with a branching ratio of order 10^{-3}. The experimental arrangement is shown in Figure 7.22.

Denoting the $CP = +1$ amplitude by K_1 and the $CP = -1$ amplitude by K_2, the K_L and K_S amplitudes are therefore the admixture

$$\begin{aligned} K_L &= \frac{1}{\sqrt{1 + |\varepsilon|^2}}(K_2 + \varepsilon K_1) \\ K_S &= \frac{1}{\sqrt{1 + |\varepsilon|^2}}(K_1 - \varepsilon K_2) \end{aligned} \tag{7.62}$$

where ε is a small parameter quantifying the CP violation. The degree of CP violation is usually quoted as the amplitude ratio

$$|\eta_{+-}| = \frac{\text{ampl}(K_L \to \pi^+\pi^-)}{\text{ampl}(K_S \to \pi^+\pi^-)} = (2.29 \pm 0.02) \times 10^{-3} \tag{7.63a}$$

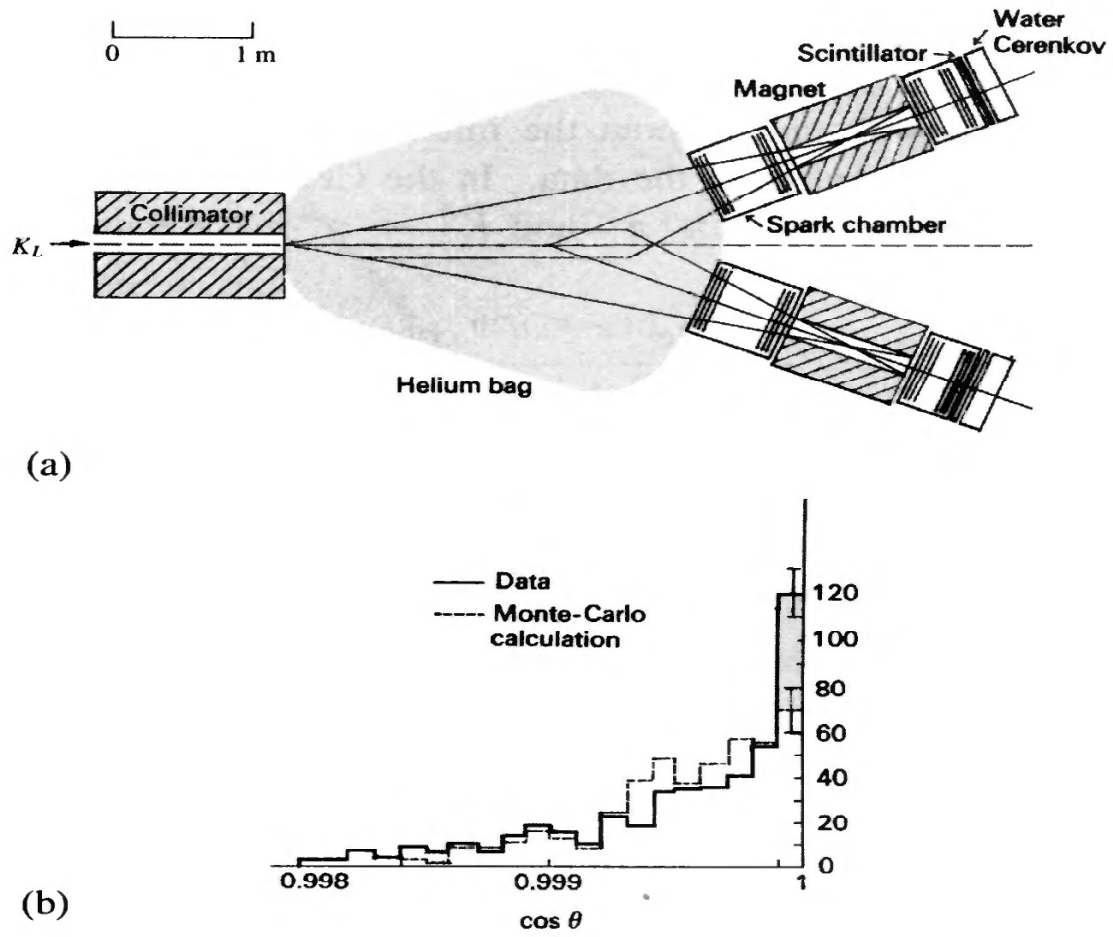

Fig. 7.22. (a) Arrangement of Christenson *et al.* (1964) demonstrating the CP-violating decay $K_L \to \pi^+\pi^-$. K_L decays are observed in a helium bag, the charged products being analysed by two magnet spectrometers instrumented with spark chambers and scintillators. (b) Rare two-pion decays are distinguished from the common three-pion decays by the invariant mass of the pair (490 MeV $< M_{\pi\pi} <$ 510 MeV) and the direction, θ, of the resultant momentum vector. The $\cos\theta$ distribution is that expected from three-body decays, plus 50 events (shaded) collinear with the beam and attributed to the two-pion decay mode.

Similarly, the measured amplitudes for $2\pi^0$ decay stand in the ratio

$$|\eta_{00}| = \frac{\text{ampl}(K_L \to \pi^0\pi^0)}{\text{ampl}(K_S \to \pi^0\pi^0)} = (2.28 \pm 0.02) \times 10^{-3} \qquad (7.63b)$$

Since both K_L and K_S can decay to two pions, interference effects in the $\pi^+\pi^-$ signal are expected as a function of the time development of an initially pure K^0 ($\bar{K}^0$) beam. From (7.56) we expect the intensity to vary as

$$\frac{I_{2\pi}(t)}{I_{2\pi}(0)} = e^{-\Gamma_S t} + |\eta_{+-}|^2 e^{-\Gamma_L t} + 2|\eta_{+-}|\, e^{-[(\Gamma_L+\Gamma_S)/2]t} \cos(\Delta m\, t + \phi_{+-}) \qquad (7.64)$$

where t measures proper time and ϕ_{+-} is an appropriate phase angle between

the $K_S \to 2\pi$ and $K_L \to 2\pi$ amplitudes. Such interference effects are indeed observed. Figure 7.23 depicts some early results using a high energy K^0 beam, showing the effects with and without the interference term in (7.64), and the interference term extracted from the data. In the CPLEAR experiment, (7.51), the asymmetry between $K^0 \to \pi^+\pi^-$ and $\bar{K}^0 \to \pi^+\pi^-$ is measured, yielding from (7.64)

$$A_{+-}(t) = \frac{2|\eta_{+-}|e^{[(\Gamma_S-\Gamma_L)/2]t}\cos(\Delta m\, t + \phi_{+-})}{1 + |\eta_{+-}|^2 e^{(\Gamma_S-\Gamma_L)t}}$$

from which the values of ϕ_{+-} and η_{+-} can be extracted, taking Δm from other measurements. The best estimates to date are

$$\phi_{+-} = 43.7° \pm 0.6° \qquad \phi_{00} = 43.5° \pm 1.0° \tag{7.65}$$

There are in fact two possible sources of CP violation in K^0 decay. That in (7.62) is called *indirect* CP violation and arises from the fact that the weakly decaying eigenstates of definite lifetime, K_S and K_L, are each an admixture of the 'wrong' CP, to a degree ε, via the box diagram of mixing in Figure 7.20. But *direct* CP violation can also occur, where a violation ε' occurs in the decay process itself. This can arise as follows. Weak hadronic decays generally obey a $\Delta I = \frac{1}{2}$ rule, for the change in isospin of the hadrons in the decay process. For example, the decay of the Λ ($I = 0$) hyperon will be to a state in which $I = \frac{1}{2}$, and the Clebsch–Gordan coefficients predict $\Gamma(\Lambda \to n\pi^0)/\Gamma(\Lambda \to p\pi^-) = \frac{1}{2}$, as observed. But $\Delta I = \frac{3}{2}$ transitions, although strongly suppressed, seem also to occur. So, in the process $K \to \pi^+\pi^-$ or $\pi^0\pi^0$ the pions can have $I = 0$ or, less probably, $I = 2$ ($I = 1$ is forbidden by Bose symmetry). The corresponding decay amplitudes A_0 or A_2 will include phase factors $A_0 e^{i\delta_0}$ or $A_2 e^{i\delta_2}$, which arise from the final-state strong pion–pion interaction. A finite difference in the phase angles, $\delta_0 - \delta_2$, would change sign under time reversal and is therefore, equivalently, CP-violating. Taking account of the Clebsch–Gordan coefficients in the coupling of $\pi^0\pi^0$ and $\pi^+\pi^-$ to $I = 0$ or $I = 2$ states, it is found that, for small values of ε and ε', and taking A_0 as real,

$$\begin{aligned} \eta_{+-} &= |\eta_{+-}|e^{i\phi_{+-}} \simeq \varepsilon + \varepsilon' \\ \eta_{00} &= |\eta_{00}|e^{i\phi_{00}} \simeq \varepsilon - 2\varepsilon' \end{aligned} \tag{7.66}$$

where

$$\varepsilon' = \frac{i}{\sqrt{2}}\left(\frac{\operatorname{Im} A_2}{A_0}\right) e^{i(\delta_2-\delta_0)}$$

If the $\Delta I = \frac{1}{2}$ rule held strictly, we would expect $A_2 = 0$, $|\eta_{+-}| = |\eta_{00}|$, $\phi_{+-} = \phi_{00}$, $\varepsilon' = 0$. Equations (7.63) and (7.65) are in fact consistent with this, at the two-standard-deviation level.

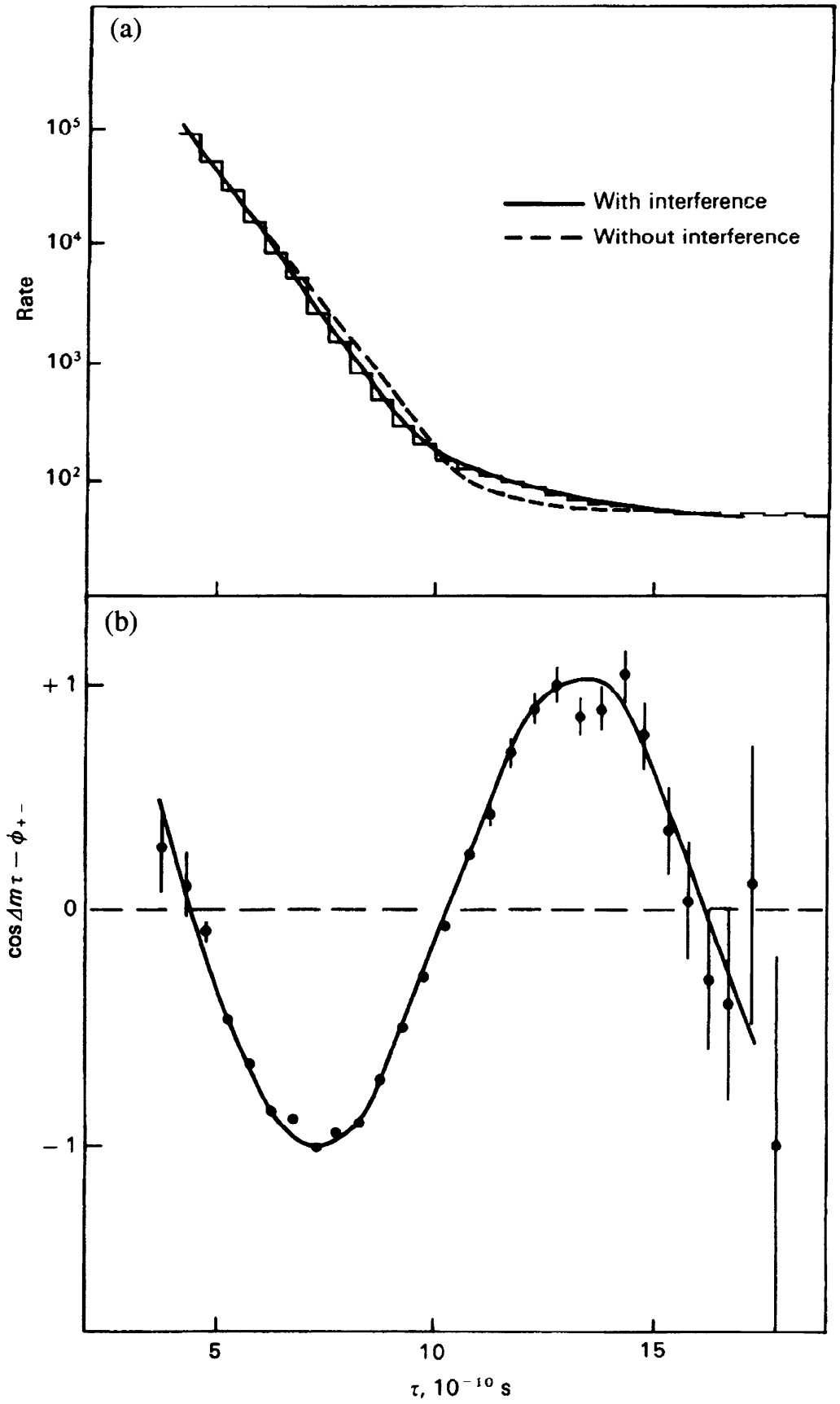

Fig. 7.23. (a) Event rates for $K^0 \to \pi^+\pi^-$ decays as a function of proper time. The best fit in the upper graph needs the existence of interference between K_L and K_S amplitudes. (b) The interference term extracted from the results: from the fit one can obtain the $K_L - K_S$ mass difference Δm and the phase angle ϕ_{+-} between the two amplitudes. (After Geweniger *et al.* 1974.)

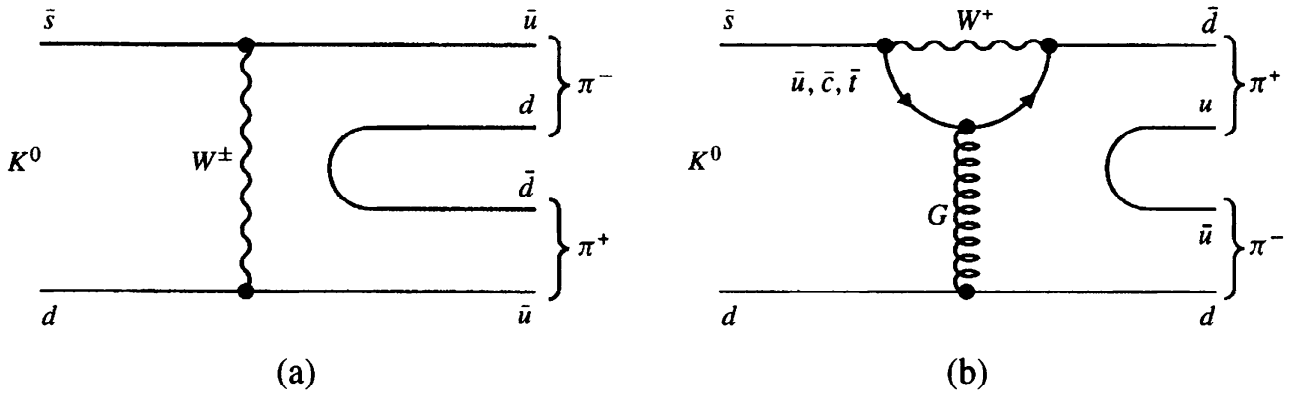

Fig. 7.24. (a) 'Tree' diagram showing $K^0 \to 2\pi$ decay via $W^\pm$ exchange; (b) 'penguin' diagram showing $K^0 \to 2\pi$ decay via the intermediary $\bar{u}$, $\bar{c}$, $\bar{t}$ quark states. The interference between diagrams (a) and (b) gives rise to a non-trivial phase factor and 'direct' CP violation shown in the decay process itself, rather than the 'indirect' CP violation shown in the 'box' diagram of Figure 7.20, where the mass eigenstates themselves are mixed states of even and odd CP.

Over the last years, major experimental attempts to determine ε'/ε have been carried out at CERN and Fermilab. The early CERN experiment measured $\pi^+\pi^-$ and $\pi^0\pi^0$ decays simultaneously and used alternate K_L and K_S beams. The regeneration target to produce K_S from the K_L beam was mounted on a train that could be moved to reproduce the K_L decay distribution as a function of distance. The Fermilab experiment generated K_L and K_S beams simultaneously using a regenerator that intercepted half of the K_L beam, but $\pi^+\pi^-$ and $\pi^0\pi^0$ decay modes were measured separately. A total of four experiments to date (1999) find when averaged an effect quoted at a significance level of over five standard deviations:

$$\frac{\varepsilon'}{\varepsilon} = (2.2 \pm 0.4) \times 10^{-3} \tag{7.67}$$

On this basis direct CP violation appears to have been established.

In the Standard Model, direct CP violation is due to interference between the 'tree' diagram of Figure 7.24(a) and the 'penguin' diagram of Figure 7.24(b). The expected value of ε' in (7.67) depends on the quark masses and for the top quark mass, 175 GeV, is extremely small.

CP non-invariance is also demonstrated in the leptonic decay modes of K_L. These modes are

$$K_L \to e^+ + \nu_e + \pi^- \tag{7.68}$$

$$K_L \to e^- + \bar{\nu}_e + \pi^+ \tag{7.69}$$

with similar ones in which muons replace electrons.

The decays (7.68) and (7.69) transform one into the other under the CP operation, and if CP invariance is violated a small charge asymmetry is expected.

The asymmetry is

$$\Delta = \frac{\text{rate}(K_L \to e^+ + \nu_e + \pi^-) - \text{rate}(K_L \to e^- + \bar{\nu}_e + \pi^+)}{\text{rate}(K_L \to e^+ + \nu_e + \pi^-) + \text{rate}(K_L \to e^- + \bar{\nu}_e + \pi^+)}$$
$$= (0.327 \pm 0.012) \times 10^{-2} \tag{7.70}$$

As can be seen from a quark flow diagram, decay into a positively charged lepton (7.68) can come only from the K^0 component of the beam, and decay into a negative lepton (7.69) only from the $\bar{K}^0$ component. Hence from (7.55) and (7.62) we expect

$$\Delta = \frac{|1+\varepsilon|^2 - |1-\varepsilon|^2}{|1+\varepsilon|^2 + |1-\varepsilon|^2} \simeq 2\,\text{Re}\,\varepsilon \tag{7.71}$$

which then gives ε from (7.70). Note that if $\varepsilon' = 0$, $\varepsilon = \eta_{+-} = \eta_{00} = \eta$ and $\phi_{+-} = \phi_{00} = \phi$ then, in (7.71),

$$\Delta(\varepsilon' = 0) = 2\eta \cos\phi = (0.332 \pm 0.004) \times 10^{-2} \tag{7.72}$$

in agreement with (7.70).

In the early days of CP violation in K^0 decay, Wolfenstein (1964) postulated that it was due to a specifically $\Delta S = 2$ *superweak* interaction. This predicted $\varepsilon' = 0$ but, as (7.67) indicates, the K^0 decay data appears not to be consistent with this prediction. In any case, rather than introduce a completely new fundamental interaction the emphasis has been on seeking to demonstrate the existence of direct CP violation, which is possible (although not inevitable) in the Standard Model with six quark flavours. This should also be detectable in other systems – bottom meson decays (see Section 7.18) and a non-zero value for the neutron electric dipole moment (see Section 3.11) – and not, as for the superweak model, be restricted to the narrow cul-de-sac of the neutral kaon system.

7.17 Cosmological CP violation

A fuller discussion of CP violation on a cosmic scale is given in Chapter 10. However, it is appropriate to mention at this point that the observed matter–antimatter asymmetry of the universe is intimately connected with CP violation.

To begin with, it must be realised that, without CP violation, it is impossible to unambiguously define what is matter and what is antimatter, on a cosmic scale. Here on Earth the anti-electron, or positron, is defined as antimatter, and it has a positive charge, e^+. But what we define as positive or negative charge is quite arbitrary, and we need an unambiguous way of defining what we call matter and antimatter, or positive and negative charge, to an intelligent being in a far corner of

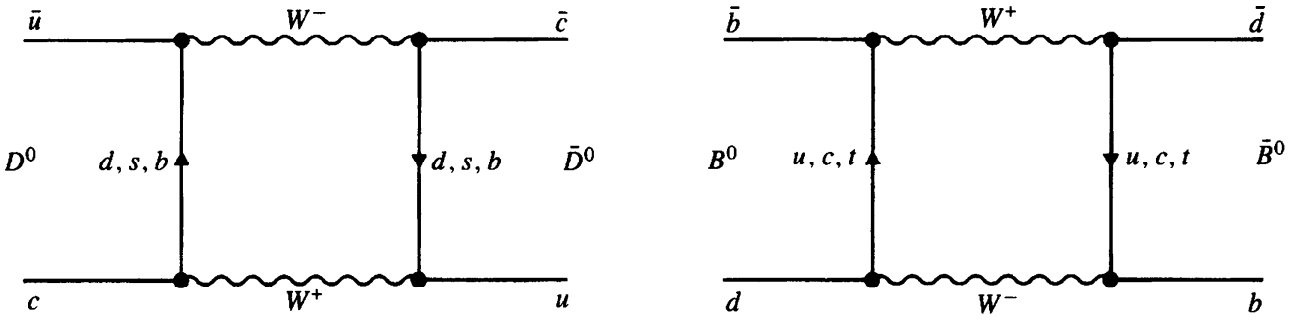

Fig. 7.25. Box diagrams for D^0–$\bar{D}^0$ mixing and B^0–$\bar{B}^0$ mixing, analogous to that for K^0–$\bar{K}^0$ in Figure 7.22.

the universe. CP violation in K decay, and in particular in the K_L semi-leptonic decays (7.68) and (7.69), now provide the answer. The positron is defined as that lepton which is more prolific (by 0.3%) in K_L decay, as in (7.70).

7.18 D^0–$\bar{D}^0$ and B^0–$\bar{B}^0$ mixing

Particle–antiparticle mixing via a common decay channel, observed in the neutral kaon system, can also apply in other neutral particle–antiparticle systems, i.e. for D^0 mesons and B^0 mesons. This mixing can be described by the box diagrams in Figure 7.25, which are analogous to Figure 7.20 for the kaon case. As before, the contributions to the rate of the different flavours of quark in the loop vary as the square of the quark mass and as the products of the vertex couplings in the CKM matrix (7.47). For the D^0 case, the dominant contribution is from b quark exchanges but the product $V_{cb}V_{ub}$ is very small, so that it turns out that the predicted D^0–$\bar{D}^0$ mixing is minute and probably unobservable.

B^0–$\bar{B}^0$ mixing (and that shown in Figure 7.25 is specifically for $\bar{B}^0_d = b\bar{d}$), is dominated by t quark exchange, and the expected level of mixing is substantial.

We can write (7.56), (7.57) for the probability that an initially pure K^0 state decays as K^0 or $\bar{K}^0$:

$$P(t)dt = \frac{\Gamma e^{-\Gamma t}}{2}\left[\frac{e^{-y\Gamma t}}{2} + \frac{e^{+y\Gamma t}}{2} \pm \cos x\Gamma t\right]dt \qquad (7.73)$$

where, with $\Delta m = m_L - m_S$ and $\Gamma = (\Gamma_S + \Gamma_L)/2 \approx \Gamma_S/2$, we define the quantities $x = \Delta m/\Gamma$ and $y = \Delta\Gamma/(2\Gamma)$; $\Delta\Gamma = \Gamma_S - \Gamma_L \simeq \Gamma_S$. For the K^0 system, $y \simeq 1$ from (7.55) and $x \simeq 0.95$ from (7.58).

For the B^0 system, one expects $\Delta\Gamma \ll \Delta m$, because $\Delta\Gamma$ is produced only in decay channels common to both B^0 and $\bar{B}^0$ and, owing to the large mass of the B^0 meson, there are scores of possible decay modes so that the branching ratio for modes common to B^0 and $\bar{B}^0$ (such as $B^0 \to J/\psi K^0_S$) is less than 10^{-3}. Putting

$y = 0$ in (7.73), the time-integrated probability that an initial B^0 ends up as $\bar{B}^0$ is

$$\chi = \frac{x^2}{2(1+x^2)}$$

from which, with χ measured to be 0.17, one obtains $x_B \simeq 0.72$. In addition to that for $\bar{B}_d^0$ $(= b\bar{d})$ mesons, of mass 5279 MeV, mixing is also observed for $\bar{B}_s^0$ $(= b\bar{s})$ mesons, of mass 5369 MeV.

Because in the B^0 system $\Delta\Gamma \ll \Delta m$, there is essentially no indirect CP violation: the quantity ε is then simply a phase factor, $e^{i\alpha}$. It is thus expected that in the B^0 system 'direct' CP violation will dominate and could be appreciable, and its importance is emphasised by the current large number of experimental projects to measure it. The problem is that, because of the very low branching ratios for decay modes common to B^0 and $\bar{B}^0$ (e.g. $B^0 \to J/\psi K_S^0$, or $B^0 \to \pi^+\pi^-$), a very large total number of B meson decays ($\sim 10^{10}$) is likely to be needed in order to obtain a meaningful measure of CP violation in the system. The very high fluxes of B mesons required give the motivation for 'B meson factories', described in Chapter 11.

The CKM matrix (7.47) is presumably unitary, i.e. the product of V with its complex transpose $V^\dagger$ is $V^\dagger V = 1$, the unit matrix. Off-diagonal elements of this unit matrix must be zero, and this leads to a set of 'unitarity' conditions, e.g.

$$V_{ud}V_{ub}^* + V_{cd}V_{cb}^* + V_{td}V_{tb}^* = 0$$

which corresponds to a (closed) triangle in the $\rho\eta$-plane, with ρ and η defined in (7.48), as shown in Figure 7.26. For example, for the modes $B_d^0(\bar{B}_d^0) \to J/\psi K_S^0$, the decay rates are

$$R \propto e^{-t/\tau}(1 \pm \sin 2\beta \sin \Delta m\, t)$$

where the second term measures the CP-violating asymmetry between B^0 and $\bar{B}^0$ decays, and thus the angle β.

Obviously, it is important in the future to establish whether the CP violation allowed in the CKM matrix is actually realised in practice. If it is, the question will then be whether this has anything to do with the CP violation observed in the universe at large.

Problems

7.1 Prove the form of the expression (7.9c) for the Kurie plot in the case of finite neutrino mass.

7.2 A 'narrowband' neutrino beam, as in Figure 7.11, is produced by bombarding a Be target with 400 GeV protons and forming a pencil secondary beam with a small spread

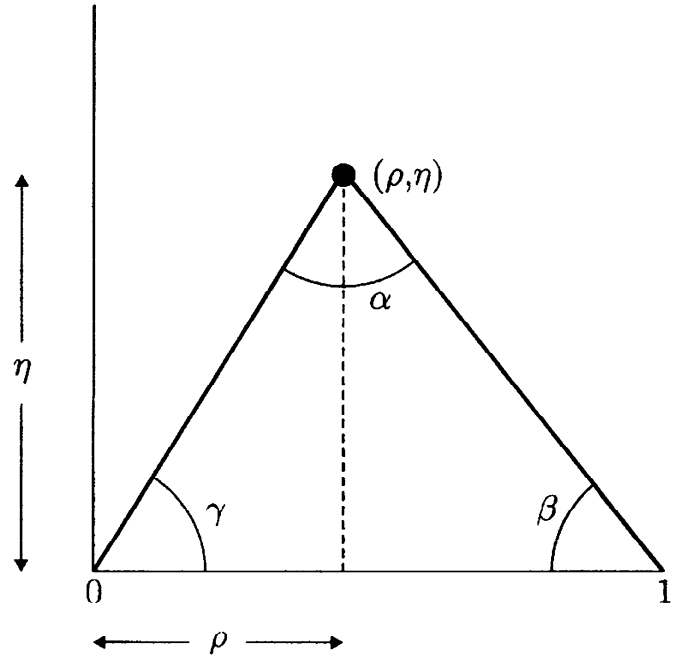

Fig. 7.26. Unitarity triangle in the $\eta\rho$-plane, which can be measured from CP asymmetries in B decays.

in momentum centred at 200 GeV/c. This beam contains charged pions and kaons with one sign of charge and it traverses an evacuated decay tunnel 300 m long, where a fraction of the mesons decay to muons and neutrinos. This is followed by an absorber consisting of 200 metres of steel and 150 metres of rock. A cylindrical detector of radius 2 m is placed 400 m beyond the end of the decay tunnel, and aligned with the beam axis. (a) Find a relation between the laboratory energy of a neutrino and its angle relative to the axis, for neutrinos from pion and from kaon decays ($\pi \to \mu + \nu$, $K \to \mu + \nu$). (b) What are the maximum and minimum energies of the neutrinos produced in the two cases? (c) Above what neutrino energy do all neutrinos from kaon decay traverse the detector? (d) If 10^{10} pions per burst enter the decay tunnel, how many neutrinos from pion decay traverse the detector? (e) If the detector has mass 100 tonne, how many neutrinos from pion decay interact in it per burst, if the cross-section per nucleon at energy E is $0.6E \times 10^{-38}$ cm^2 with E in GeV? ($m_\pi c^2 = 139$ MeV, $m_K c^2 = 494$ MeV, $m_\mu c^2 = 106$ MeV).

7.3 The neutron has a mean lifetime of 930 s, and the muon, 2.2×10^{-6} s. Show that the couplings involved in the two cases are of the same order of magnitude, when account is taken of phase-space factors ($m_n = 939.6$ MeV, $m_p = 938.3$ MeV, $m_e = 0.51$ MeV).

7.4 The ground states of $^{34}_{17}$Cl and $^{34}_{16}$S have $J^P = 0^+$ and belong to an $I = 1$ multiplet. The decay

$$^{34}_{17}\mathrm{Cl} \to {}^{34}_{16}\mathrm{S} + e^+ + \nu_e$$

has a mean lifetime of 2.3 s and a maximum positron energy of 4.5 MeV. The lifetime

of the charged pion, also of $I = 1$, is 26 ns. Estimate the branching ratio for the decay $\pi^+ \to \pi^0 + e^+ + \nu_e$ ($m_{\pi^+} = 139.6$ MeV, $m_{\pi^0} = 135.0$ MeV, $m_e = 0.51$ MeV).

7.5 Obtain an estimate for the branching ratio

$$(\Sigma^- \to \Lambda + e^- + \bar{\nu}_e)/(\Sigma^- \to n + \pi^-)$$

assuming that the matrix element for the electron decay is the same as the matrix element for the neutron β-decay and that baryon recoil can be neglected ($\tau_\Sigma = 1.5 \times 10^{-10}$ s, $m_\Sigma = 1197$ MeV, $m_\Lambda = 1116$ MeV; for other constants see Problems 7.3 and 7.4).

7.6 Given that the width of the $\Delta(1234)\pi p$ resonance is 150 MeV, estimate the branching ratio for the β-decay of Δ^{++},

$$\frac{\Delta^{++} \to p + e^+ + \nu_e}{\Delta^{++} \to p + \pi^+}$$

7.7 The muon lifetime is 2.2 μs. Calculate that of the τ lepton, given that the branching ratio for $\tau^+ \to e^+ + \nu_e + \bar{\nu}_\tau$ is 18% ($m_\tau = 1777$ MeV, $m_\mu = 105.7$ MeV).

7.8 Show why observation of the process $\bar{\nu}_\mu + e^- \to e^- + \bar{\nu}_\mu$ constitutes unique evidence for neutral currents, whereas observation of $\bar{\nu}_e + e^- \to e^- + \bar{\nu}_e$ does not. Prove that the maximum angle of emission of the recoil electron relative to the neutrino beam direction is $\sqrt{2m/E}$, where m, E are the electron mass and energy.

7.9 For heavy nuclei, the process of electron capture (principally from the K-shell),

$$e_K^- + (A, Z) \to \nu_e + (A, Z - 1)$$

competes with positron emission,

$$(A, Z) \to e^+ + \nu_e + (A, Z - 1)$$

and of course can occur when positron emission is not energetically possible.

First, find an expression for the transition rate for the case of a K-electron actually inside the nucleus (A, Z), using (7.8) and including only the phase-space factor for the neutrino, in terms of the neutrino energy E_ν. The probability of finding a K-electron at the coordinate origin (that is, in the nucleus) is $\pi^{-1}(\alpha Z mc^2/\hbar c)^3$. Multiplying this into the transition rate, calculate the ratio of rates for K capture and positron emission, for the case where the neutrino energy E_ν and the maximum positron kinetic energy $E_0 = E_\nu - 2mc^2$ are both large compared with the electron mass, mc^2. Show that

$$\frac{\Gamma_K}{\Gamma_{e^+}} = 2 \times 60\pi(\alpha Z)^3 (mc^2)^3 \frac{E_\nu^2}{E_0^5}$$

(The factor 2 arises because there are two K-electrons that can undergo capture.)

8

Electroweak interactions and the Standard Model

8.1 Introduction

As indicated in Chapters 1 and 2, we are faced in nature with several types of fundamental interaction or field between particles. Each field has its distinct characteristics, such as space–time transformation properties (vector, tensor, scalar etc.), a particular set of conservation rules that are obeyed by the interaction and a characteristic coupling constant that determines the magnitude of the collision cross-sections or decay rates mediated by the interaction.

The fact that the strength of the gravitational interaction between two protons, for example, is only 10^{-38} of their electrical interaction has always been a puzzle and a challenge, and many attempts have been made to understand the interrelation between the different fields. In the last decades, the belief has grown that the strong, weak, electromagnetic and gravitational interactions are but different aspects of a single universal interaction, which would be manifested at some colossally high energy. At the everyday energies met with in laboratory studies in particle physics, it is necessary to assume that this symmetry is badly broken, at these mass or energy scales which are puny relative to the unification energy.

The first successful attempt to unify two apparently different interactions was achieved by Clerk Maxwell in 1865. He showed that electricity and magnetism could be unified into a single theory involving a vector field (the electromagnetic field) interacting between electric charges and currents. The Maxwell equations involve the introduction of one arbitrary constant – the velocity of light, c – which is not predicted by the theory and has to be determined from experiment.

In the late 1960s Weinberg, Salam and Glashow, building on other developments, described how it would be possible to treat electromagnetic and weak interactions as different aspects of a single *electroweak interaction*, with a single coupling given by the elementary electric charge, e. They predicted that this symmetry between electromagnetic and weak interactions would be manifest at

very large momentum transfers ($q^2 \gg 10^4$ GeV^2). At low energies, it would be a *broken symmetry*: of the four mediating vector bosons involved, one (the photon) would be massless and the others, W^+, W^-, Z^0, would be massive. As a result, compared with electromagnetic interactions, weak interactions would be short-range and apparently feeble. Again, the theory contains an arbitrary constant, the weak mixing angle denoted by $\sin^2\theta_W$, which has to be determined by experiment. Over the last 25 years, this model has been verified experimentally with ever-increasing accuracy.

Building on the tremendous success of the electroweak model, ambitious attempts have been made to carry unification further, to include the strong and gravitational interactions as well. These ideas are extremely speculative, and have essentially zero direct experimental support at the present time. In this chapter, we restrict ourselves to the electroweak scenario.

8.2 Divergences in the weak interactions

In Chapters 1 and 3 we noted the desirability of formulating quantum field theories which have the property of *renormalisability*, meaning that the amplitudes for different processes associated with an interaction should be well behaved, i.e. non-divergent at high energy and to high orders in the coupling constant. The prototype field theory, that of quantum electrodynamics (QED), does in fact contain divergent terms associated with integrals over intermediate states, but it is found that these divergences can always be absorbed into a redefinition of the 'bare' lepton charges and masses, which are in any case arbitrary, as being equal to the physically measured values. Thus, we can say that a theory is renormalisable if, at the cost of introducing a finite number of arbitrary parameters (to be determined from experiment) the predicted amplitudes for physical processes remain finite at all energies and to all orders in the coupling constant. QED is an example of such a theory (and, for many years, was the only one). In it there is a small number of arbitrary constants such as c, $\hbar$, e and particle masses.

In contrast, early theories of weak interactions, while well behaved at low energy and to first order, involved divergences in higher orders that could be cancelled only at the price of introducing an indefinitely large number of arbitrary constants, thus losing essentially any predictive power. Good high energy behaviour and the cancellation of divergent terms in higher order are thus sensible demands for any physical theory. The subject of renormalisability is highly technical and outside the scope of this text, but we just remark that it is connected with the property of invariance of the interaction under gauge transformations, as discussed in Section 3.7.

We recall that in the Fermi theory of β-decay, the four fermions involved are assumed to have a contact interaction specified by the Fermi constant G. An example is the process

$$\nu_e + e^- \rightarrow e^- + \nu_e \tag{8.1}$$

The cross-section has the pointlike form given in (5.24),

$$\frac{d\sigma}{dq^2} = \frac{G^2}{\pi} \tag{8.2}$$

where q^2 is the momentum transfer squared. The total cross-section is then, as in (5.26),

$$\sigma_{\text{tot}}(\nu e) = \frac{G^2}{\pi} q^2_{\text{max}} = \frac{2G^2 mE}{\pi} = \frac{G^2 s}{\pi} \tag{8.3}$$

where m is the electron mass, E is the incident neutrino energy and s is the cms energy squared. We assume $E \gg m$ so that $s \simeq 2mE$. The cross-section depends only on G and the phase space, which rises with cms momentum p^* as $p^{*2} = s/4$.

The cross-section for such an elastic scattering process can also be found from wave theory (see (2.29)–(2.31)), which yields, for target electron spin $s = \frac{1}{2}$ and pointlike scattering ($l = 0$),

$$\sigma_{\text{max}} = \pi \lambda\!\!\!^{-2}(2l + 1)/(2s + 1) = \pi \lambda\!\!\!^{-2}/2 \tag{8.4}$$

where $\lambda\!\!\!^{-} = \hbar/p^*$ is the cms wavelength. So (8.3) predicts that $\sigma_{\text{tot}} > \sigma_{\text{max}}$ when

$$\frac{4G^2 p^{*2}}{\pi} > \frac{\pi}{2p^{*2}}$$

or when

$$p^* > (\pi/G\sqrt{8})^{1/2} \simeq 300 \text{ GeV}/c \tag{8.5}$$

At sufficiently large energy, the Fermi theory therefore predicts a cross-section exceeding the wave-theory limit, which is determined by the condition that the scattered intensity cannot exceed the incident intensity in any partial wave; frequently this is called the unitarity limit. The basic reason for the bad high energy behaviour of the Fermi theory (which becomes steadily worse if processes of higher order in G, i.e. G^2, G^4, etc., are considered) is that G has the dimensions of an inverse power of the energy. Somehow, we have to redefine the weak interaction in terms of a dimensionless coupling constant.

The intermediate vector boson $W^{\pm}$ of the weak interactions has the effect of introducing a propagator term $(1 + q^2/M_W^2)^{-1}$ into the scattering amplitude, which 'spreads' the interaction over a finite range, of order M_W^{-1}. Then σ_{tot} in (8.3) will tend to a constant value $G^2 M_W^2/\pi$ at high energy. It turns out that the unitarity limit

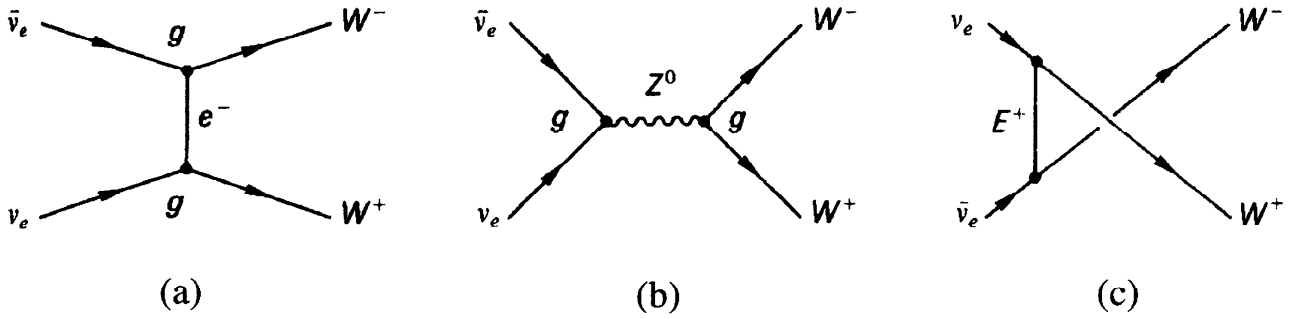

Fig. 8.1.

in a given partial wave is still broken, although only logarithmically. However, quadratic divergences still appear in other, more esoteric, processes; for example, $\nu\bar{\nu} \rightarrow W^+W^-$ is a conceivable reaction for which $\sigma_{\text{tot}} \propto s$. What is needed therefore is a mechanism to cancel the weak-interaction divergences systematically and to all orders in G.

8.3 Introduction of neutral currents

Figure 8.1(a) shows one of the recalcitrant diagrams giving a quadratic divergence (for longitudinally polarised W's). One can in principle cancel this divergence by introducing *ad hoc* either a neutral boson Z^0 or a new heavy lepton E^+ (with the same lepton number as e^- and ν_e), or both, with suitably chosen couplings. Note that diagram (b) involves a neutral current, for which there is experimental evidence, as discussed in Section 7.11. There is no evidence for a third, electron-type lepton E^+, and we do not consider this possibility (c) further.

Similarly the electromagnetic process $e^+e^- \rightarrow W^+W^-$ shown in Figure 8.2(a) is also divergent, and cancellation in this order may again be effected by postulating a neutral vector boson Z_1^0, as in (b). Although in principle the cancellations in Figures 8.1 and 8.2 could be effected with two different particles, Z^0 and Z_1^0, Nature seems to have chosen a single particle to do both jobs, in which case it is clear that the Z^0 weak coupling g will have to be similar in magnitude to the electromagnetic coupling, e. In other words, the *two fields are unified*, with (apart from numerical factors of order unity) the same intrinsic coupling strength $g \simeq e$ to leptons of the mediating bosons W, Z^0 and γ. Recall from (2.11) that, in the low-q^2 limit, where the coupling is expressed by the Fermi constant G, this hypothesis gives

$$M_W \simeq \frac{g}{\sqrt{G}} \simeq \frac{e}{\sqrt{G}} \sim 100\ \text{GeV} \tag{8.6}$$

with $e^2 = 4\pi/137$ and $G \simeq 10^{-5}\ \text{GeV}^{-2}$ (in units $\hbar = c = 1$). This is the

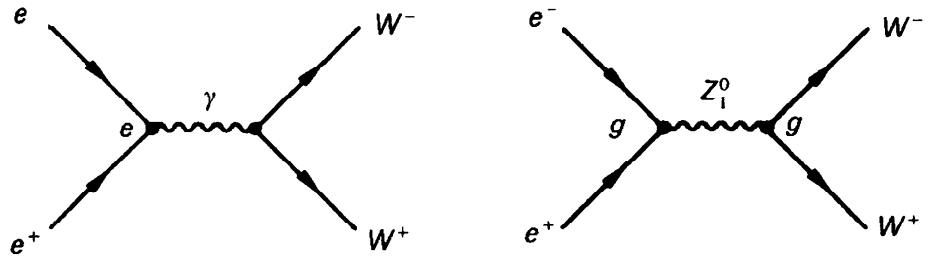

Fig. 8.2.

approximate mass required for the $W^{\pm}$ and Z^0 particles if they are to have the same coupling as in electromagnetism and are to give an effective four-fermion coupling of magnitude G in weak interactions at low energy.

Actually we have implied that by introducing a Z^0 with the right coupling, all the divergences in $e^+e^- \rightarrow W^+W^-$ would disappear. This is only true if the electron mass can be neglected. For a finite electron mass, a residual divergence exists and has to be cancelled by the introduction of further scalar particles, with special couplings proportional to the lepton mass. Such particles are called *Higgs scalars* and are discussed in Sections 8.12 and 8.13.

8.4 The Weinberg–Salam model

In the late 1960s Weinberg, Salam and Glashow proposed the electroweak theory, embracing both electromagnetic and weak interactions and postulating four massless mediating bosons, arranged in a triplet and a singlet as members of multiplets of 'weak isospin' I and 'weak hypercharge' Y. Three of the bosons, denoted $\mathbf{W}_\mu = W_\mu^{(1)}, W_\mu^{(2)}, W_\mu^{(3)}$, are the components of an $I = 1$ triplet of the group SU(2), while the fourth, B_μ, is an isoscalar ($I = 0$) belonging to the U(1) group of weak hypercharge.† For this reason, the model is often referred to by the group nomenclature SU(2) × U(1). A process called 'spontaneous symmetry breaking' is invoked, to endow the bosons with mass without spoiling the renormalisability of the theory. This is achieved by means of an $I = \frac{1}{2}$ doublet of complex fields called Higgs scalars (with four real components in total), which generate mass as a result of their self-interaction; they have been mentioned already in connection with the removal of divergences in $e^+e^- \rightarrow W^+W^-$.

The massive bosons are denoted W_μ^+, W_μ^- and Z_μ^0, while one, the photon A_μ remains massless. A_μ and Z_μ^0 are combinations of the states $W_\mu^{(3)}$ and B_μ, as

† In the notation used here, boldface type indicates isovector quantities; superscripts 1, 2, 3 indicate the components in 'isospin space'. The subscript μ signifies the space–time components of a 4-vector ($\mu = 1, 2, 3, 4$).

described below. There are no new leptons in this model, and the cancellation of divergences in Figure 8.1 is accomplished by the neutral boson Z^0.

We can write the interaction energy of leptons and quarks with these mediating bosons in a relativistically invariant form, called the Lagrangian energy density (see subsection 8.12.1)

$$L = g\mathbf{J}_\mu \cdot \mathbf{W}_\mu + g' J^Y_\mu B_\mu \tag{8.7}$$

We have already mentioned (in Section 7.7) the concept of conserved lepton currents. Here, $\mathbf{J}_\mu$ and J^Y_μ represent the weak isospin and weak hypercharge currents of the fermions, and $\mathbf{W}_\mu$ and B_μ the 4-potentials associated with the boson fields, while g and g' are coupling constants. The form (8.7) is just a generalisation of the expression for the interaction energy $e\mathbf{J}^{em}_\mu A_\mu$ of an electric current with the electromagnetic field. To avoid writing factors of 2 everywhere, we define the weak hypercharge as $Y = Q - I_3$ (rather than $2(Q - I_3)$ for the strong hypercharge, as in (3.37)), where Q is the electric charge and I_3 the third component of weak isospin. Then

$$J^Y_\mu = J^{\text{em}}_\mu - J^{(3)}_\mu \tag{8.8}$$

where J^{em}_μ is the electromagnetic current, coupling to the charge Q, and $J^{(3)}_\mu$ is the third component of the isospin current $\mathbf{J}_\mu$. The physical bosons consist of the charged particles $W^\pm_\mu$ and the neutrals Z_μ and A_μ (the photon). As stated above, the latter are taken as linear combinations of $W^{(3)}_\mu$ and B_μ. Thus, we can set (see Appendix C for the Clebsch–Gordan coefficient involved)

$$W^\pm_\mu = \frac{1}{\sqrt{2}}\left[W^{(1)}_\mu \pm i W^{(2)}_\mu\right] \tag{8.9}$$

and

$$W^{(3)}_\mu = \frac{gZ_\mu + g'A_\mu}{\sqrt{g^2 + g'^2}} \tag{8.10}$$

$$B_\mu = \frac{-g'Z_\mu + gA_\mu}{\sqrt{g^2 + g'^2}} \tag{8.11}$$

where $W^{(3)}_\mu$ and B_μ, are orthogonal as required. Hence

$$\begin{aligned} L &= g\left(J^{(1)}_\mu W^{(1)}_\mu + J^{(2)}_\mu W^{(2)}_\mu\right) + g\left(J^{(3)}_\mu W^{(3)}_\mu\right) + g'\left(J^{\text{em}}_\mu - J^{(3)}_\mu\right)B_\mu \\ &= (g/\sqrt{2})(J^-_\mu W^+_\mu + J^+_\mu W^-_\mu) + J^{(3)}_\mu\left(gW^{(3)}_\mu - g'B_\mu\right) + J^{\text{em}}_\mu g' B_\mu \end{aligned}$$

where $J_\mu^\pm = J_\mu^{(1)} \pm i J_\mu^{(2)}$. Inserting the expressions for $W_\mu^{(3)}$ and B_μ from (8.10) and (8.11) and setting

$$g'/g = \tan\theta_W \tag{8.12}$$

we get the result

$$L = \frac{g}{\sqrt{2}}(J_\mu^- W_\mu^+ + J_\mu^+ W_\mu^-) + \frac{g}{\cos\theta_W}\left(J_\mu^{(3)} - \sin^2\theta_W J_\mu^{\text{em}}\right)Z_\mu + g\sin\theta_W J_\mu^{\text{em}} A_\mu$$

$$\begin{array}{ccc} \uparrow & \uparrow & \uparrow \\ \text{weak CC} & \text{weak NC} & \text{em NC} \end{array} \tag{8.13}$$

This equation shows that the interaction energy contains the weak charge-changing current, a weak neutral current and the electromagnetic neutral current, for which we know the coupling to be e. Hence

$$e = g\sin\theta_W \tag{8.14}$$

The angle θ_W is called the weak mixing angle (or Weinberg angle).

8.5 Intermediate boson masses

As described in Section 7.9, the conventional factors associated with the coupling of the boson $W^\pm$ lead to the identification

$$\frac{G}{\sqrt{2}} = \frac{g^2}{8M_W^2} \tag{8.15}$$

as in (7.20). From (8.14) it follows that

$$M_{W^\pm} = \left(\frac{g^2\sqrt{2}}{8G}\right)^{1/2} = \left(\frac{e^2\sqrt{2}}{8G\sin^2\theta_W}\right)^{1/2} = \frac{37.4}{\sin\theta_W}\ \text{GeV} \tag{8.16}$$

to be compared with our first rough guess, (8.6).

In order to find the predicted Z^0 mass, recall that, in dealing with bosons, the Klein–Gordon equation (1.13) involves the *squares* of the boson masses (as for vector meson mixing in (4.22)). Inverting the relations (8.10) and (8.11), we find:

$$Z_\mu = W_\mu^{(3)}\cos\theta_W - B_\mu\sin\theta_W$$
$$A_\mu = W_\mu^{(3)}\sin\theta_W + B_\mu\cos\theta_W$$

so that, using the empirical fact that the photon is massless and orthogonal to the Z particle, we get for the quadratic mass relations

$$M_Z^2 = M_W^2 \cos^2\theta_W + M_B^2 \sin^2\theta_W - 2M_{BW}^2 \cos\theta_W \sin\theta_W$$
$$M_\gamma^2 = 0 = M_W^2 \sin^2\theta_W + M_B^2 \cos^2\theta_W + 2M_{BW}^2 \cos\theta_W \sin\theta_W$$
$$M_{Z\gamma}^2 = 0 = (M_W^2 - M_B^2) \sin\theta_W \cos_W + M_{BW}^2(\cos^2\theta_W - \sin^2\theta_W)$$

where M_{BW} and $M_{Z\gamma}$ are the off-diagonal mass terms. Eliminating these, we obtain

$$M_{Z^0} = \frac{M_{W^\pm}}{\cos\theta_W} = \frac{75}{\sin 2\theta_W}\ \text{GeV} \tag{8.17}$$

These predictions of boson masses are for the simplest (Salam–Weinberg) model of spontaneous symmetry breaking, which involves one weak isospin doublet of scalar (Higgs) particles. More complex isospin structure for the Higgs (e.g. an isospin triplet) is possible, with the result that additional physical Higgs mesons appear and (8.13) is no longer valid. The second term of (8.13), specifying the relative magnitude of the weak neutral-current coupling compared with that for charged currents in the first term, then acquires a factor ρ, and (8.17) is replaced by

$$M_{Z^0}^2 = \frac{M_W^2}{\rho \cos^2\theta_W} \tag{8.18}$$

However, apart from a small radiative correction of order 1%, all experiments to date find $\rho = 1$, consistent with the simplest model.†

All the mass estimates given in this section are those from first-order perturbation theory, i.e. from the so-called Born terms in tree level diagrams, without radiative loop corrections, which can be at the level of several per cent; this is discussed in more detail in Section 8.10 below.

8.6 Electroweak couplings of leptons and quarks

Let us now consider the electroweak coupling of the leptons. Just as for the gauge bosons, they will be endowed with weak isospin and weak hypercharge. Further, we know that on the one hand the weak charged-current interaction (mediated by $W^\pm$) is parity-violating and connects, for example, the left-handed states of neutrino and electron. On the other hand the electromagnetic interaction (the last

† The quantity ρ here should not be confused with that introduced in the CKM matrix (7.48).

Table 8.1. *Neutral-current Z^0 coupling of fermions*

Fermion	$2c_V$	$2c_A$
ν_e, ν_μ, ν_τ	1	1
e, μ, τ	$-1 + 4\sin^2\theta_W$	-1
u, c, t	$1 - \frac{8}{3}\sin^2\theta_W$	1
d, s, b	$-1 + \frac{4}{3}\sin^2\theta_W$	-1

term in (8.13)) is parity-conserving and involves both LH and RH states of the electron. Hence, we assign the lepton states to a LH doublet and a RH singlet, as follows:

$$\begin{aligned} \psi_L = \begin{pmatrix} \nu_e \\ e^- \end{pmatrix}_L \qquad & I = \tfrac{1}{2}, \quad I_3 = +\tfrac{1}{2}, \quad Q = 0 \\ & I = \tfrac{1}{2}, \quad I_3 = -\tfrac{1}{2}, \quad Q = -1 \end{aligned} \Bigg\} \quad Y = -\tfrac{1}{2}$$

$$\psi_R = (e^-)_R \qquad I = 0, \qquad Q = -1, \qquad Y = -1 \tag{8.19}$$

From (8.19) and (8.13), the left-handed and right-handed couplings of the fermions to the Z^0 (neutral current) have the coefficients

$$g_L = I_3 - Q\sin^2\theta_W, \qquad g_R = -Q\sin^2\theta_W \tag{8.20}$$

where Q is the electric charge in units of $|e|$ and $I_3 = \pm\frac{1}{2}$ is the third component of the weak isospin. Since vector (axial vector) interactions couple LH and RH states with the same (opposite) sign, the V and A coefficients are

$$c_V = g_L + g_R = I_3 - 2Q\sin^2\theta_W, \qquad c_A = g_L - g_R = I_3 \tag{8.21}$$

The assignment for charged leptons and neutrinos is given in (8.19). For the u quark, or the c and t quarks, with $Q = +\frac{2}{3}$, the value of $I_3 = +\frac{1}{2}$ whereas $I_3 = -\frac{1}{2}$ for the d, s and b quarks, with $Q = -\frac{1}{3}$. Thus, from (8.20) and (8.21) we can draw up the coefficients for the fermions given in Table 8.1. The couplings of the antifermions to the Z^0 are obtained from (8.20) by the interchange $g_L \leftrightarrow g_R$ or $c_A \leftrightarrow -c_A$.

8.7 Neutrino scattering via Z exchange

The observation in 1973 of neutral-current processes in neutrino–electron and neutrino–nucleon scattering, as described in Chapter 7, gave the first experimental support for the electroweak theory and the first estimates for the value of $\sin^2\theta_W$. In 1983, further dramatic proof of the intrinsic correctness of the model was provided

with the observation of the $W^{\pm}$ and Z^0 bosons at the CERN $p\bar{p}$ collider, as described in Section 7.12.

In Chapter 5 we described the charged-current scattering (via $W^{\pm}$ exchange) of high energy neutrinos and antineutrinos by electrons. We repeat here (5.26) and (5.27):

$$\begin{aligned} \frac{d\sigma}{dy}(\nu_e e \to \nu_e e)|_{\mathrm{CC}} &= \frac{G^2 s}{\pi} && (\mathrm{LL} \to \mathrm{LL}) \\ \frac{d\sigma}{dy}(\bar{\nu}_e e \to \bar{\nu}_e e)|_{\mathrm{CC}} &= \frac{G^2 s}{\pi}(1-y)^2 && (\mathrm{RL} \to \mathrm{RL}) \end{aligned} \tag{8.22}$$

where s is the cms energy squared (with $s \gg m_e^2$) and $y = E_e/E_\nu$, the fractional energy acquired by the electron. The helicities involved are indicated at the right of the equations. The second reaction would have the same cross-section as that of a neutrino ν_e on a RH electron (i.e. LR $\to$ LR) if the latter were not forbidden in the $V - A$ theory of charged-current scattering. From these relations we can therefore immediately write down the neutral-current cross-section, via Z^0 exchange, of neutrinos and antineutrinos on electrons, involving both LH and RH states of the target:

$$\frac{d\sigma}{dy}(\nu_e e \to \nu_e e)|_{\mathrm{NC}} = \frac{G^2 s}{\pi}\left[g_L^2 + g_R^2(1-y)^2\right] \tag{8.23a}$$

$$\frac{d\sigma}{dy}(\bar{\nu}_e e \to \bar{\nu}_e e)|_{\mathrm{NC}} = \frac{G^2 s}{\pi}\left[g_R^2 + g_L^2(1-y)^2\right] \tag{8.23b}$$

The values $g_L = 1$, $g_R = 0$ for the electron in $W^{\pm}$ exchange in (8.22) are here replaced by the coefficients in (8.20).

Figure 8.3 shows the diagrams for ν_μ, $\bar{\nu}_\mu$, ν_e, $\bar{\nu}_e$ scattering via Z^0 and $W^{\pm}$ exchange. The cross-sections for ν_μ, $\bar{\nu}_\mu$ scattering on electrons, which can only proceed via Z^0 exchange, are given in (8.23a) and (8.23b) respectively, with

$$\begin{aligned} g_L &= -\tfrac{1}{2} + \sin^2\theta_W \\ g_R &= \sin^2\theta_W \end{aligned} \tag{8.24}$$

For the ν_e cross-section, we have to add the Z^0 and $W^{\pm}$ exchange amplitudes, the latter having $g_L = 1$, $g_R = 0$. Hence the relevant values to insert in (8.23) to get the cross-sections for both NC and CC reactions are

$$\begin{aligned} g_L &= 1 - \tfrac{1}{2} + \sin^2\theta_W \\ g_R &= 0 + \sin^2\theta_W \end{aligned} \tag{8.25}$$

Again, the $\bar{\nu}_e$ cross-section is obtained by interchanging g_L and g_R in the formula (8.23a).

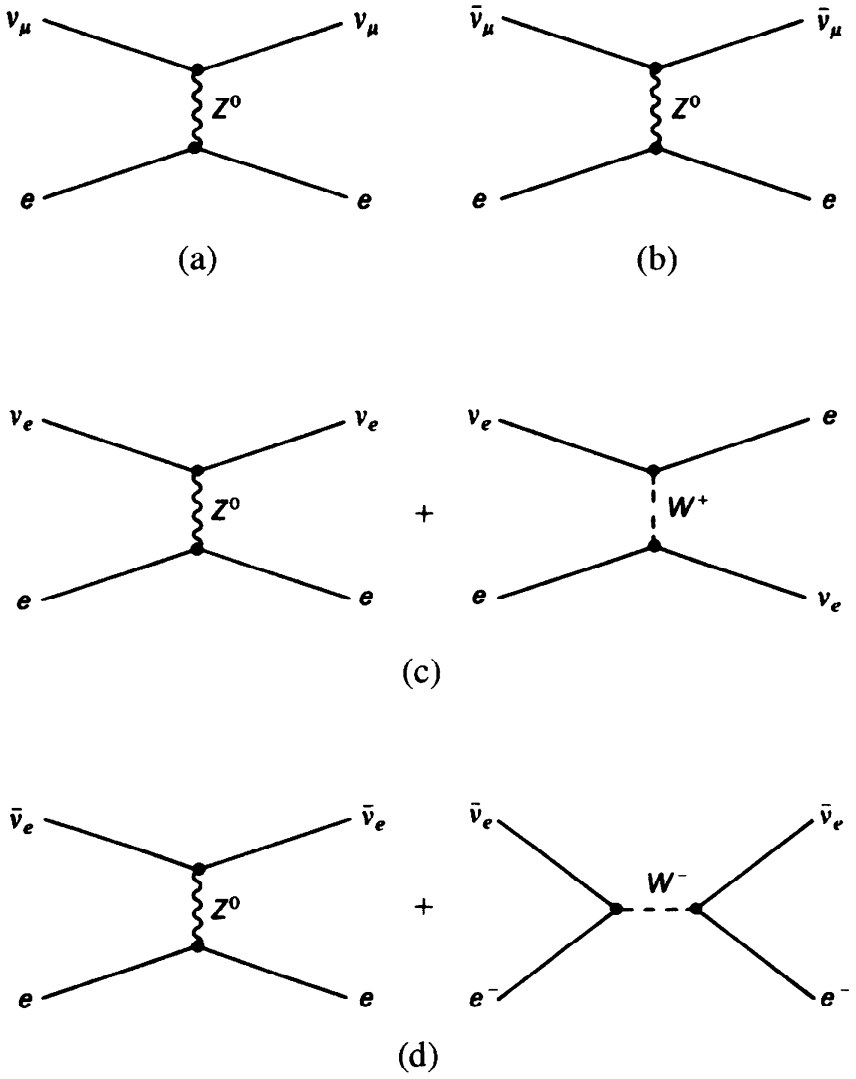

Fig. 8.3. Diagrams for the scattering of ν_μ, $\bar{\nu}_\mu$ and ν_e, $\bar{\nu}_e$ via $W^\pm$ and/or Z^0 exchange. (a) $\nu_\mu e \to \nu_\mu e$; (b) $\bar{\nu}_\mu e \to \bar{\nu}_\mu e$; (c) $\nu_e e \to \nu_e e$; (d) $\bar{\nu}_e e \to \bar{\nu}_e e$.

The measured $\nu_\mu e$ and $\bar{\nu}_\mu e$ cross-sections give values for g_L^2 and g_R^2 from (8.23). Consequently there is a four-fold sign ambiguity on the magnitudes of g_L and g_R. One must have recourse to independent data (e.g. the $e^+e^- \to \mu^+\mu^-$ forward–backward asymmetry at LEP) to resolve this ambiguity and thus obtain a value for $\sin^2\theta_W$.

Analogous formulae for deep inelastic neutrino scattering on nucleons via Z^0 exchange follow in a straightforward fashion (see Problem 8.4). The results were historically important as providing the first reliable values for $\sin^2\theta_W$ and hence estimates of the expected masses of $W^\pm$ and Z^0 bosons, several years before their observation. Present values (1999) from this method – essentially to compare the ratios of neutral-current and charged-current cross-sections – give $\sin^2\theta_W = 0.222 \pm 0.006$.

8.8 Asymmetries in the scattering of polarised electrons by deuterons

Although neutrino experiments proved the existence of neutral weak currents in 1973, independent confirmation was important and was provided in 1978 by a very delicate experiment to detect tiny parity violation effects (asymmetries) due to the interference between Z^0 and γ exchange in the inelastic scattering of polarised electrons by deuterons (see Figure 8.6). The experiment was carried out with beams of electrons of 16–22 GeV/c momentum at SLAC, the reaction being

$$e^-_{L,R} + d_{\text{unpolarised}} \rightarrow e^- + X$$

where X is any final hadron state. The electromagnetic scattering amplitude is of order e^2/q^2, where q is the 4-momentum transfer, while the weak amplitude is of order G, the Fermi constant. The parity-nonconserving asymmetry, measured by the difference in the cross-sections for LH and RH electrons, will then be

$$A = \frac{\sigma_R - \sigma_L}{\sigma_R + \sigma_L} \simeq \frac{Gq^2}{e^2} = \frac{137 \times 10^{-5}}{4\pi}\frac{q^2}{M_p^2}$$
$$\simeq 10^{-4}q^2 \qquad (q^2 \text{ in GeV}^2) \tag{8.26}$$

The method employed to measure polarisation asymmetries as small as 10^{-5} is illustrated in Figure 8.4(a). A source of electrons, either polarised or unpolarised, is accelerated in the SLAC linear accelerator to 16–22 GeV/c and impinges on a liquid deuterium target. The sign and degree of polarisation $|P_e|$ of the beam (37% for the polarised source) was measured with a polarimeter, in which one observed the left–right asymmetry in the Møller (electron–electron) scattering from a magnetised iron foil. Inelastically scattered electrons were focussed and momentum-analysed in a spectrometer and recorded in a gas Čerenkov counter followed by a lead-glass shower counter.

The polarised-electron source consisted firstly of a dye laser producing linearly polarised light, which was transformed into circularly polarised light by means of a Pockels cell, a birefringent crystal in which the sign of circular polarisation could be switched by application of a high-voltage electric field of either sign. This circularly polarised light was then used to optically pump a gallium arsenide crystal, between the valence and conduction bands, and thus provide a source of longitudinally polarised electrons. The magnitude and sign of the polarisation could also be varied by rotating the plane of polarisation of the laser light with a rotatable calcite prism. The steps in the experiment were as follows.

(i) Measurement of the asymmetry A using the unpolarised source (electron gun), yielding $A = (-2.5 \pm 2.2) \times 10^{-5}$, which is consistent with zero and proves the sensitivity of the method and the reliability of the beam monitoring.

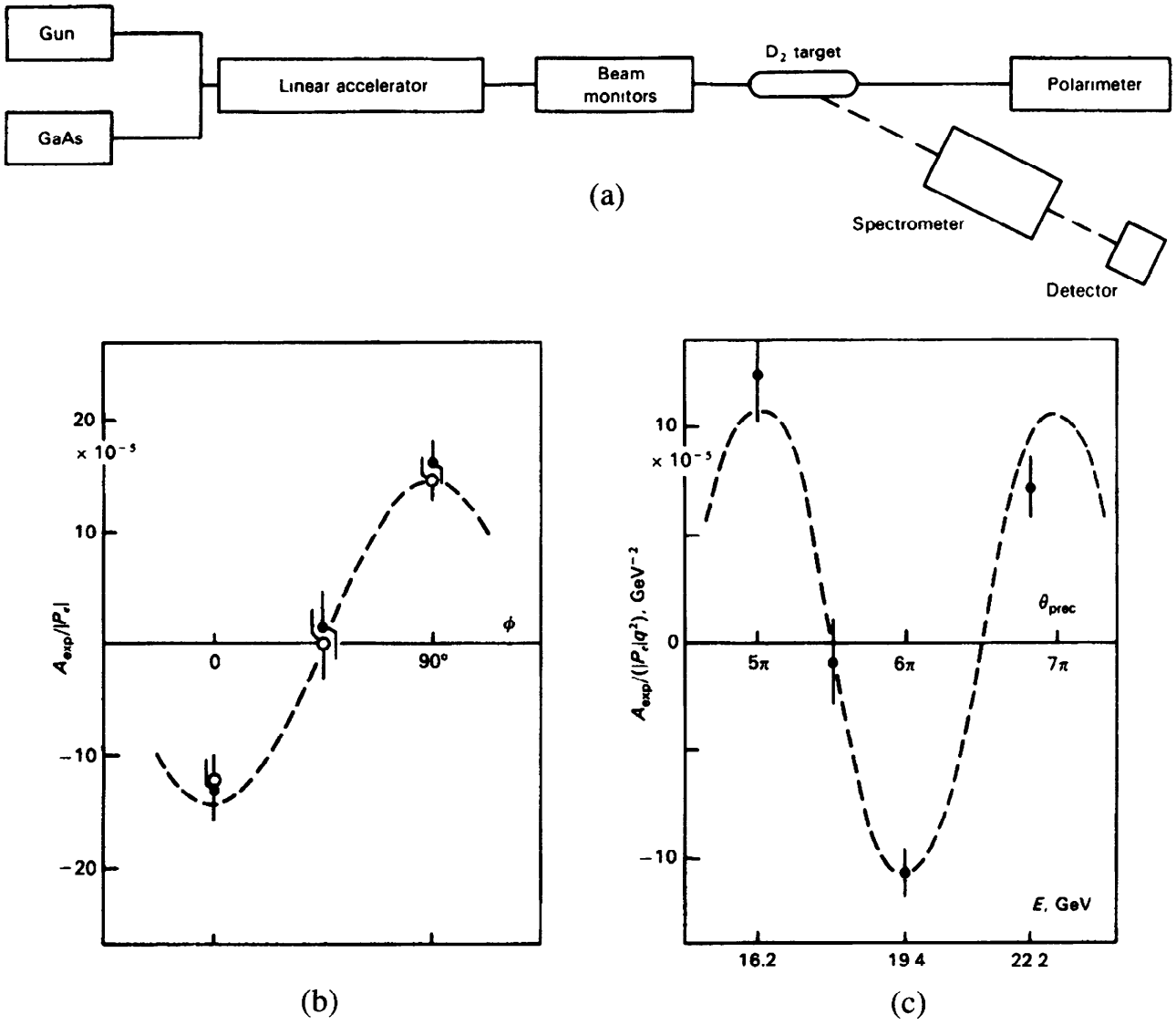

Fig. 8.4. (a) Schematic layout of the SLAC experiment on the scattering of polarised electrons on deuterons. (After Prescott *et al.* 1978.) (b) The asymmetry, as defined in (8.26), as a function of the azimuth of the calcite prism. (c) Variation of the asymmetry with electron-beam energy, showing the $g - 2$ rotation of the electron spin.

(ii) Setting the calcite prism at azimuthal angles of 0°, 45° and 90°. For $\phi = 45°$ the electrons from the GaAs source should be unpolarised, while for $\phi = 0°$ or 90° the polarisation should be R or L respectively (and L or R if the sign of the Pockels cell voltage is reversed). Figure 8.4(b) shows the measured asymmetry as a function of ϕ.

(iii) Varying the electron energy E_0 from 16 to 22 GeV/c. The beam, before hitting the target, has suffered a magnetic bending of 24.5° and, in this process, the electron spin will 'lead' over the momentum vector by an angle determined by the g-factor,

$$\theta_{\text{precession}} = \frac{E_0}{mc^2}\left(\frac{g-2}{2}\right)\theta_{\text{bend}}. \tag{8.27}$$

Thus, as the beam energy E_0 is changed, the asymmetry should vary as the degree of longitudinal polarisation is varied by the $g-2$ effect. This is demonstrated by the results in Figure 8.4(c).

The final result of this experiment was that a clear asymmetry was observed, of magnitude

$$\frac{A}{q^2} = -(9.5 \pm 1.6) \times 10^{-5}\ (\mathrm{GeV}/c)^{-2}. \tag{8.28}$$

In succeeding experiments, the variation of A was measured as a function of $y = (E_0 - E)/E_0$, the fractional energy loss of the electron in the collision. The y-dependence as well as the magnitude of A depends on the weak angle θ_W, according to

$$\frac{A}{q^2} = -\frac{9G}{20\sqrt{2}\pi\alpha}\left\{a_1 + a_2\frac{1-(1-y)^2}{1+(1-y)^2}\right\} \tag{8.29}$$

where

$$a_1 = 1 - \tfrac{20}{9}\sin^2\theta_W, \qquad a_2 = 1 - 4\sin^2\theta_W \tag{8.30}$$

These coefficients are derived from the quark model, using the appropriate values of I_3 and Q from (8.20) and Table 8.1; see also Problem 8.5. The observed y dependence was consistent with the prediction (8.29). The final result was

$$\sin^2\theta_W = 0.22 \pm 0.02 \tag{8.31}$$

agreeing with previous estimates. Historically, this SLAC experiment was crucial in support of the electroweak theory in 1978. At that time, atomic physics experiments were searching for tiny effects due to parity-violating transitions in atoms and were giving conflicting results. Four independent experiments to measure optical rotation in bismuth gave four different answers, all of them wrong! The most recent atomic experiments are in complete agreement with the Salam–Weinberg model and other measurements of $\sin^2\theta_W$ and are valuable in that the radiative corrections (see Section 8.10) are different from those in LEP experiments.

8.9 Observations on the Z resonance

The observational evidence providing the most detailed support for the electroweak model and the most accurate measurements of the various parameters comes from the study of Z^0 production and decay at the e^+e^- colliders SLC and LEP, at Stanford and CERN. The main results refer to the Z^0 mass, line shape and branching ratios to leptons and hadrons, to the angular asymmetries of the Z^0 decay products, and to the cross-section asymmetries with longitudinally polarised incident beams. This is a vast subject and we can only outline the principal results in this section.

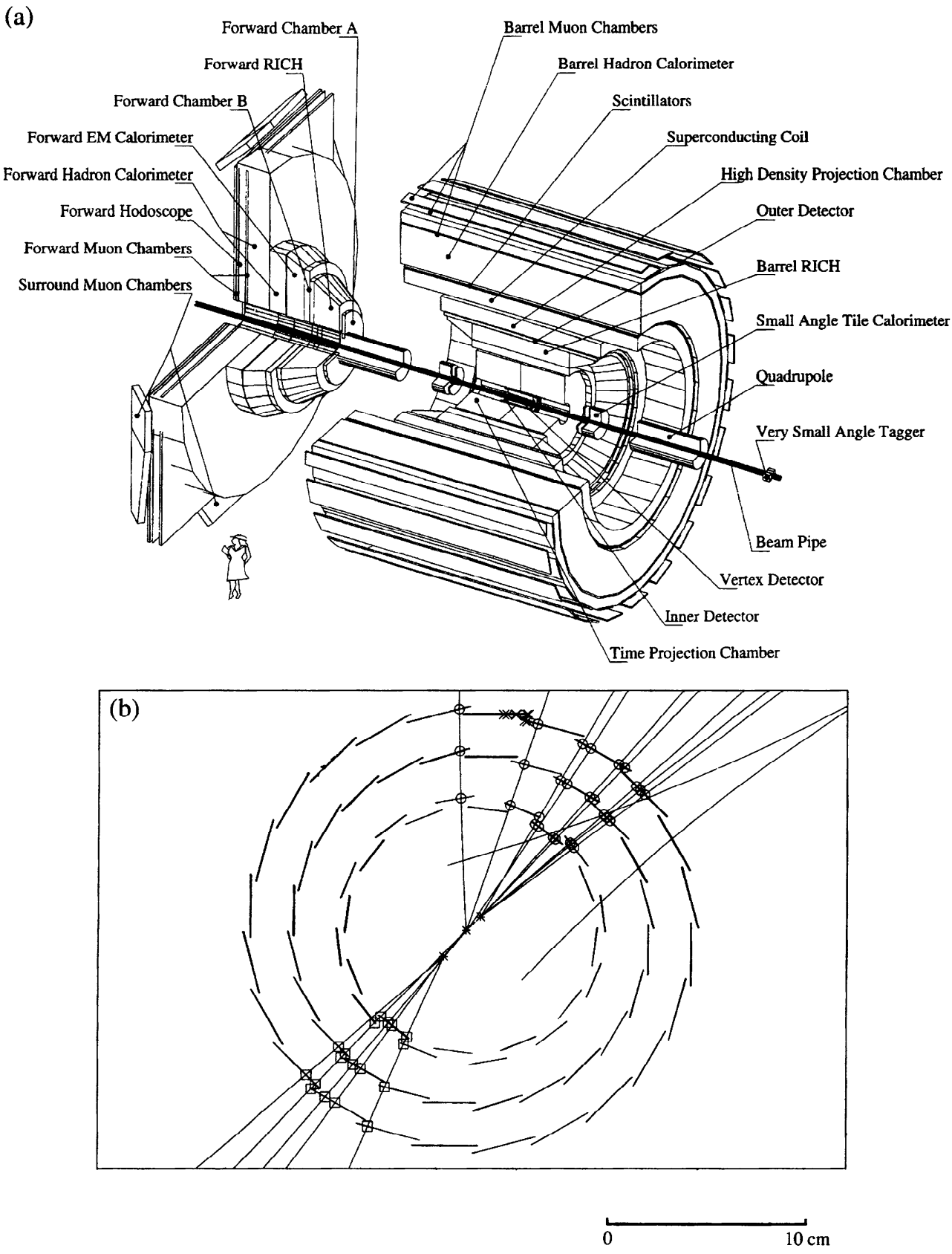

Fig. 8.5. (a) Layout of the detector DELPHI employed at the LEP collider; (b) example of $Z^0 \rightarrow b\bar{b} \rightarrow$ two jets event, showing the displaced vertices corresponding to the B meson decays.

A short description of the LEP collider is given in Chapter 11. Figure 8.5(a) shows a diagram of one of the detectors, DELPHI, used at LEP. It consists of the usual central tracking detector (drift chamber) inside the magnetic field provided by a superconducting solenoid and surrounded by sections of electromagnetic and hadronic calorimeters, the purpose of which is to measure the total energy in photons and in hadrons. Penetrating muons are recorded in arrays of muon chambers surrounding the outer part of the detector. The detector also includes ring-imaging Čerenkov (RICH) counters for particle identification, as well as semiconductor (silicon strip) micro-detectors close around the beam intersection region, to record vertices from the decay of short-lived heavy-flavour (B, D) mesons, containing bottom and charmed quarks respectively.

Figure 8.5(b) shows a reconstruction of a $Z^0 \to b\bar{b} \to$ two-jet event, achieved from the measurements of track coordinates in arrays of silicon microstrip detectors placed around the intersection region (see Figure 11.12). The displaced vertices of the B meson decays are clearly visible.

8.9.1 Total and partial widths of the Z^0

The Breit–Wigner cross-section for Z^0 production as an e^+e^- resonance was described in Section 7.13 (equations (7.31)–(7.33); see also Figure 7.16). The total width Γ is made up of contributions from decay to charged lepton pairs (e^+e^-, $\mu^+\mu^-$, $\tau^+\tau^-$), neutral lepton pairs ($\nu_e\bar{\nu}_e$, $\nu_\mu\bar{\nu}_\mu$, $\nu_\tau\bar{\nu}_\tau$) and quark–antiquark pairs ($u\bar{u}$, $d\bar{d}$, $s\bar{s}$, $c\bar{c}$, $b\bar{b}$). The partial width for any of these modes is

$$\Gamma(\text{partial}) = \frac{GM_Z^3\rho}{6\pi\sqrt{2}}\left(c_A^2 + c_V^2\right)F \tag{8.32}$$

Here, the dependence on M_Z can be easily understood on dimensional arguments: the weak coupling in the decay involves the Fermi constant G, which has dimensions (mass)$^{-2}$; hence, if M_Z is the only large mass involved the expression for the width must contain the factor M_Z^3 (see also Problem 8.8). The other parameters in (8.32) are ρ, defined in (8.18), and the axial and vector coupling factors c_A and c_V, given in Table 8.1. The quantity F takes values as follows:

$$Z^0 \to \nu\bar{\nu}, \qquad F = 1 \tag{8.33a}$$

$$Z^0 \to l\bar{l}, \qquad F = (1 + 3\alpha/4\pi) \tag{8.33b}$$

$$Z^0 \to Q\bar{Q}, \qquad F = 3(1 + \alpha_s/\pi) \tag{8.33c}$$

Here, α and α_s are the running coupling constants evaluated at the Z^0 mass as described below. For decay to charged leptons, (8.33b), the factor F is a QED correction for photon radiation in the final state, while for decay to quark–antiquark pairs in (8.33c), there is a colour factor $N_c = 3$ and another QCD factor for gluon radiation by the quarks. From (8.32) and the known approximate values of $\sin^2\theta_W = 0.23$ and $\alpha_s = 0.12$, together with the coefficients in Table 8.1, we get predictions for each of the flavours of quark or lepton (assuming $\rho = 1$):

$$\begin{aligned} \Gamma_{\nu\bar{\nu}} &= 0.166 \text{ GeV} \\ \Gamma_{l\bar{l}} &= 0.084 \text{ GeV} \\ \Gamma_{u\bar{u}} &= \Gamma_{c\bar{c}} = 0.29 \text{ GeV} \\ \Gamma_{d\bar{d}} &= \Gamma_{s\bar{s}} = \Gamma_{b\bar{b}} = 0.38 \text{ GeV} \end{aligned} \tag{8.34}$$

where quark and lepton masses and radiative corrections have only small effects on the width, and can be neglected at the 1% or 2% level.

Assuming $N_\nu = 3$ neutrino flavours, the predicted width is in good agreement with that measured:

$$\begin{aligned} \Gamma_{\text{total}}(\text{calculated}) &= 2.49 \text{ GeV} \\ \Gamma_{\text{total}}(\text{observed}) &= 2.50 \text{ GeV} \end{aligned} \tag{8.35}$$

This comparison was the basis for the estimate $N_\nu = 2.99 \pm 0.02$ for the number of neutrino flavours quoted in (2.33).

8.9.2 Forward–backward asymmetries

As pointed out in Section 5.1 (see Figure 5.2), the angular distribution for $e^+e^- \to \mu^+\mu^-, \tau^+\tau^-$, even at modest energies, does not follow exactly the pure QED prediction, since Z^0 as well as photon exchange will be involved, as shown in Figure 8.6. Since Z^0 exchange involves both V and A couplings, parity-violating forward–backward symmetries are expected. Suppose $s \ll M_Z^2$, so that the weak cross-section is very small compared with the electromagnetic, i.e. $G^2 s \ll \alpha^2/s$. The total cross-section will then be

$$\begin{aligned} d\sigma/d\Omega = (d\sigma/d\Omega)_{\text{QED}} &+ (d\sigma/d\Omega)_{\text{interf.}} + (d\sigma/d\Omega)_{\text{weak}} \\ \uparrow & \quad \uparrow \quad \uparrow \\ \alpha^2/s & \quad Gs/\alpha \quad G^2 s \end{aligned} \tag{8.36}$$

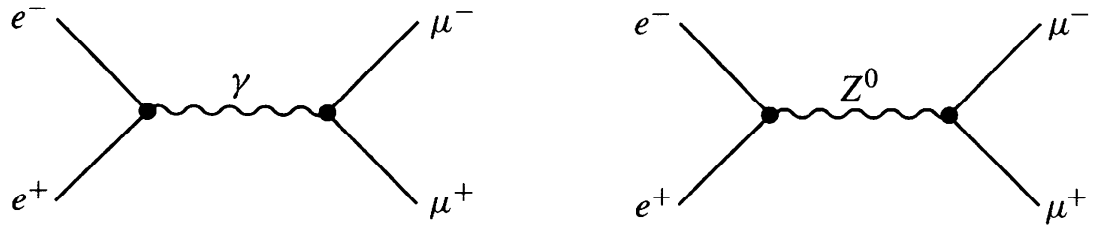

Fig. 8.6. Diagrams for $e^+e^- \to \mu^+\mu^-$ via photon exchange (left) and Z^0 exchange (right).

The only significant effect will be in the interference term. Defining F and B as the forward and backward intensities, the forward–backward asymmetry will be, in order of magnitude,

$$A_{FB} = \frac{F - B}{F + B} \simeq \frac{Gs}{\alpha} \tag{8.37}$$

Such asymmetries were first observed in the early 1980s at the PETRA and PEP colliders, with $s \simeq 10^3$ GeV^2. The full formula for the asymmetry is, for $s \ll M_Z^2$,

$$A_{FB} = -\frac{3c_A^2}{4\sqrt{2}\pi}\frac{Gs}{\alpha} \tag{8.38}$$

so that at small s, A_{FB} depends only on c_A (the dependence on c_V turns out to be very small and can be neglected) and so does not measure c_A/c_V or the parameter $\sin^2\theta_W$.

For $s \simeq M_Z^2$, the so-called pole asymmetry for $e^+e^- \to Z^0 \to f\bar{f}$ is given by

$$A_{FB}^0 = 3A_e^0 A_f^0$$

where

$$A^0 = \frac{c_V c_A}{c_V^2 + c_A^2} \tag{8.39}$$

and the subscripts e, f refer to electrons and to fermions in general. The forward–backward asymmetries can also be measured for quarks, e.g. for $b\bar{b}$ quark pairs, which can be identified via momentum cuts and from the secondary vertices in B meson decays, as described in Section 7.14.

Table 8.2. *Values of* $\sin^2\theta_W$

A^0_{FB} (leptons)	0.2309 ± 0.0006
A^0_τ (polarisation)	0.2324 ± 0.0009
$A^0_{FB}(b$ quarks)	0.2325 ± 0.0004
A^0_{LR} (SLC)	0.2306 ± 0.0005
ve or νN scattering	0.224 ± 0.004
$1 - M_W^2/M_Z^2$	0.226 ± 0.005

Using the expressions for c_V and c_A in Table 8.1, the measured values of A^0_{FB} yield values for $\sin^2\theta_W$, as in Table 8.2.

8.9.3 Left–right and polarisation asymmetries

At the SLAC linear collider, longitudinally polarised electron beams could be produced (see Section 8.8) and the pole cross-section asymmetry, using left or right circularly polarised beams, is given by

$$A^0_{LR} = \left(\frac{\sigma_L - \sigma_R}{\sigma_L + \sigma_R}\right) = A^0_e \tag{8.40}$$

giving independent measurements of $\sin^2\theta_W$ from (8.39). Obviously it is also possible to measure the forward–backward asymmetry of final-state fermions using polarised beams, which gives further information.

For unpolarised incident beams, the final-state fermions will be longitudinally polarised (just as in any other weak interaction such as nuclear β-decay), and such polarisation can be measured and clearly will depend on the ratio c_V/c_A. If the fermion is a τ lepton, the polarisation can be inferred from the angular distribution of its decay products.

From the various measurements as outlined above, estimates can be made of the Standard Model parameters. As an example, Table 8.2 shows values of $\sin^2\theta_W$ determined by different methods. Some of the values in the table differ from each other by an amount of order 1%, and they are expected to do so since the different processes are differently affected by radiative corrections, as discussed below.

8.10 Fits to the Standard Model and radiative corrections

The data on the Z^0 mass, total and partial widths and decay asymmetries obtained at LEP and SLC, as well as the measurements of the W mass and neutrino scattering cross-sections, can be used to test the predictions of the Standard Model

by verifying that the 'best-fit parameters' do in fact account satisfactorily for all the observations. These fits depend on detailed calculations of the effects of radiative corrections.

As stated before, a major (typically 30%) correction will be needed for the radiation of real photons by the incident e^+e^- beams before they actually collide. This can be made exactly and gives a precise fit to the (distorted) Breit–Wigner resonance shape, plotted as a function of the nominal energy of the circulating beams; this was shown in Figure 7.15. Other QED radiative corrections are those due to virtual photon emission by fermions, e.g. that in Figure 8.7(a); fortunately, these can be absorbed into a running of the coupling α, as discussed in Section 6.5, from $\alpha^{-1} = 137.14$ at low frequency to $\alpha^{-1}(M_Z) = 128.9$, a 6% effect. For the hadronic decays, a similar type of running, but non-Abelian, QCD coupling, α_s, has also been discussed in Section 6.5 (see equation (6.22)). The value appropriate at the Z^0 mass, $\alpha_s(M_Z)$, holds for gluon radiation by the quarks, as in (8.33(c)).

Apart from these corrections, the main radiative effects arise from the influence of loop diagrams involving virtual top quark and Higgs boson exchanges, see e.g. Figure 8.7(b), on the M_W and M_Z masses. These corrections affect the W and Z masses differently, and hence the ratio of neutral- to charged-current couplings specified by ρ in (8.18). In fact it turns out that

$$\Delta\rho \simeq +\frac{3Gm_t^2}{8\pi^2\sqrt{2}} = 0.01 \tag{8.41}$$

for $m_t = 176$ GeV, where the m_t^2 dependence is to be expected from the discussion in subsection 7.15.1. If we define

$$\sin^2\theta_W \equiv 1 - \frac{M_W^2}{M_Z^2}$$

this has the consequence that the first four entries in Table 8.2 will refer to the modified quantity

$$\sin^2\theta_W(\text{eff}) \simeq \sin^2\theta_W(1 + \cot^2\theta_W\Delta\rho)$$

obtained by expanding (8.18) for small deviations of ρ from unity.

In making the fits, one can choose a set of parameters that can be fixed by direct measurement or calculated without uncertainty and make a fit to all the data to check the validity of the model and also find the remaining unknowns. For example, one can take for the known quantities M_Z, measured very accurately ($M_Z = 91.189 \pm 0.001$ GeV), $\alpha(M_Z)$, G (from muon decay) and the known lepton and quark masses (at the time the fits were originally made, the top quark mass was unknown). The strong coupling parameter $\alpha_s(M_Z) = 0.123$ has here been taken as known, as it is determined from the ratio of hadronic to leptonic widths

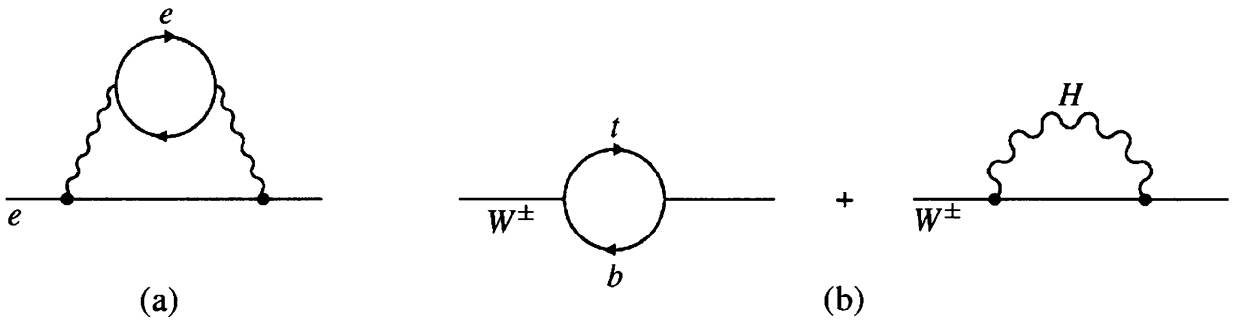

Fig. 8.7. Loop diagrams indicating various radiative corrections (a) to α from virtual fermions, and (b) to M_Z or M_W from the virtual top quark and Higgs scalar.

of the Z^0 and depends little on the remaining unknowns. These are taken as the top quark mass m_t and the Higgs mass m_H, entering the radiative corrections as in Figure 8.7(b).

Figure 8.8 shows the fitted value of $\sin^2\theta_W(\text{eff})$ at M_Z plotted as a function of m_t, for $m_H = 300$ GeV. The various shaded areas show one-standard-deviation uncertainties in $\sin^2\theta_W$. The curve marked 'M_Z', for example, shows how, for a given value of M_Z, the calculated value of $\sin^2\theta_W(\text{eff})$ depends on the assumed mass m_t of the top quark. The directly measured value of m_t from the Fermilab experiments (Section 4.13) is also shown, as a vertical band. The small black area at the centre is the best-fit value using all relevant observations, from LEP and SLC, neutrino scattering, W mass etc. Clearly, the Standard Model gives an excellent account of all the data, and the agreement between m_t deduced indirectly from radiative corrections and that found from direct measurement is very impressive.

The dependence of the above fits on the Higgs mass is much weaker. While loop corrections from the top quark vary as m_t^2, they vary only logarithmically with m_H. Present data (1999) indicate only a strong preference for the range $m_H =$ 60–300 GeV. As indicated in Section 8.13, direct searches for the Higgs presently place a lower limit $m_H > 100$ GeV.

8.11 *W* pair production

Figure 8.9 shows the three Feynman diagrams responsible for $W^\pm$ pair production in e^+e^- collisions, via neutrino, photon or Z^0 exchanges. It is noteworthy that each of these diagrams individually yields a divergent amplitude (with $\sigma \propto s$). It is only when the three are combined that the divergences cancel out and the cross-section remains finite. In fact, after an initial increase from threshold to $\sigma(\text{max}) \simeq 17$ pb, it falls off as $(\ln s)/s$. For the above cancellation to happen, the ZWW, γWW and νWW couplings have to be precisely those given by the electroweak theory. In practice, the observation of $W^\pm$ pair production has so far been limited to s-values

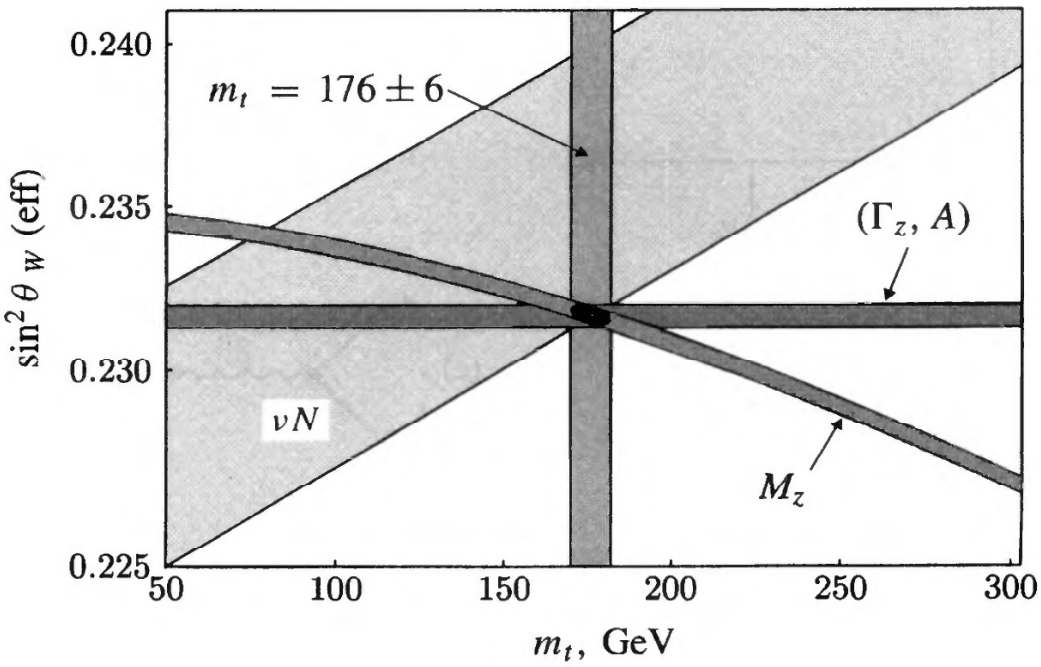

Fig. 8.8. Fitted values of $\sin^2\theta_W$(eff) as a function of the top quark mass m_t, assuming a Higgs mass $M_H = 300$ GeV. The boundaries of the shaded areas denote one-standard-deviation limits within which the value of $\sin^2\theta_W$ is calculated to lie, using that particular measurement, for example of M_Z, $\sigma(\nu N)$ or the Z^0 width and decay asymmetries Γ, A. The vertical band indicates the directly measured value, m_t from the Fermilab experiment. (Adapted from Barnett *et al.* 1996.)

below the cross-section maximum, but, as shown in Figure 8.10, the rates are in very good agreement with the calculated values and confirm the correctness of the triple boson couplings.

The cms angular distribution of W pair production is also of great interest. Different regions of angle select different fractions of transverse and longitudinally polarised W's. Recall that it is the longitudinal components that 'eat' the Higgs and are thus associated with the creation of the W mass. Again, the observed distributions are in perfect accord with the theory.

Figure 8.11 shows examples of $e^+e^- \rightarrow W^+W^-$ events in the DELPHI detector at the LEP collider, while Figure 8.12 shows an example of Z^0Z^0 pair production.

8.12 Spontaneous symmetry breaking and the Higgs mechanism

The subject of spontaneous symmetry breaking by the Higgs mechanism is somewhat beyond the scope of this text, so we include only a very brief account here to outline the basic ideas. The reader can skip this and proceed to Section 8.13 without great loss, or obtain a fuller account in a more advanced text.

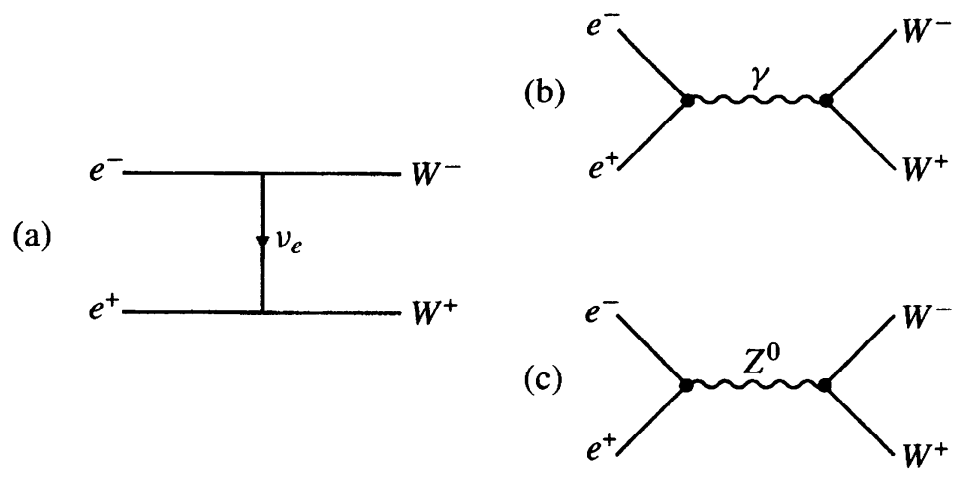

Fig. 8.9. The three Feynman graphs determining the rate of $W^{\pm}$ pair production.

8.12.1 The Lagrangian energy density

In classical mechanics, the equations of motion are most compactly expressed through Lagrange's equations. Let x, $\dot{x} = dx/dt = v$ and t be the position, velocity and time coordinates of a particle of mass m moving in one dimension. The Lagrange equation is

$$\frac{d}{dt}\left(\frac{dL}{d\dot{x}}\right) - \frac{dL}{dx} = 0 \tag{8.42}$$

where the Lagrangian is defined as the difference of kinetic and potential energies,

$$L = T - V = \tfrac{1}{2}mv^2 - V \tag{8.43}$$

Substituting in (8.42) we get Newton's second law, equating force to rate of change of momentum:

$$\frac{d}{dt}(mv) = \frac{dV}{dx} = F$$

Similarly, taking instead of x and $\dot{x}$ the angular coordinate θ and angular velocity $\dot{\theta} = \omega$, then, with I as the moment of inertia of our particle and

$$L = T - V = \tfrac{1}{2}I\omega^2 - V$$

we obtain

$$\frac{d}{dt}(I\omega) = \frac{dV}{d\theta} = G$$

equating the rate of change of angular momentum to the torque G. Generally, for a system of i particles with generalised coordinates q_i and $\dot{q}_i = dq_i/dt$, the Lagrange equation is

$$\frac{d}{dt}\left(\frac{dL}{d\dot{q}_i}\right) - \frac{dL}{dq_i} = 0 \tag{8.44}$$

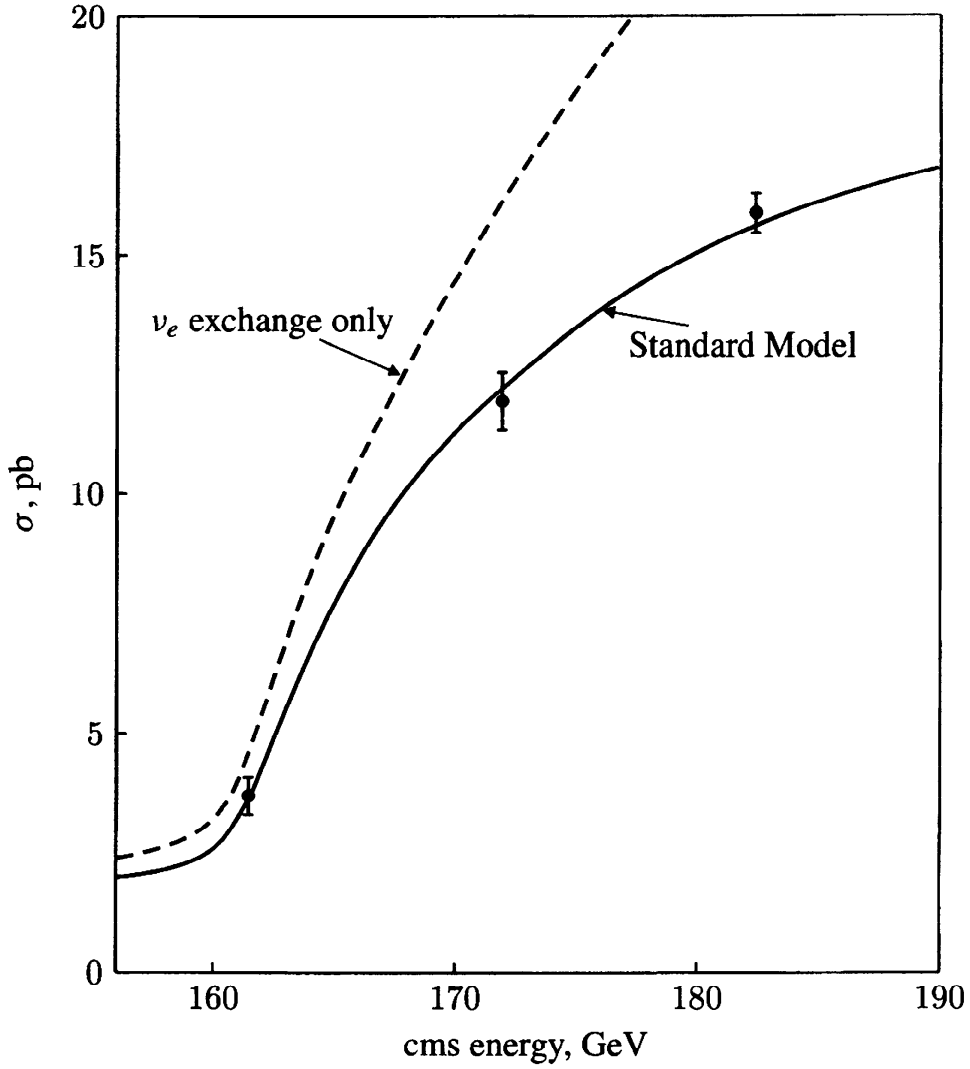

Fig. 8.10. The $W^{\pm}$ pair production cross-section $\sigma(e^+e^- \rightarrow W^+W^-)$ as a function of cms beam energy, measured at the LEP 200 e^+e^- collider. The solid curve shows the values predicted by the electroweak theory in the Standard Model. The broken curve shows the divergent cross-section expected from the graph in Figure 8.9(a), with ν_e exchange only.

Turning now to quantum mechanics, we can again define a Lagrangian energy density, and to make it relativistically invariant we replace the time derivative by the 4-vector space–time derivative $\partial/\partial x_\mu$, where $\mu = 1, 2, 3, 4$, which we write more compactly as ∂_μ. The discrete coordinates q_i of individual particles are replaced by a continuously variable wave or field amplitude, ϕ. Then the Lagrange equation becomes

$$\partial_\mu \left(\frac{\partial L}{\partial(\partial_\mu \phi)} \right) - \frac{\partial L}{\partial \phi} = 0 \tag{8.45}$$

For free scalar particles of mass μ, let us guess that the Lagrangian is

$$L = T - V = \tfrac{1}{2}(\partial_\mu \phi)^2 - \tfrac{1}{2}\mu^2 \phi^2 \tag{8.46}$$

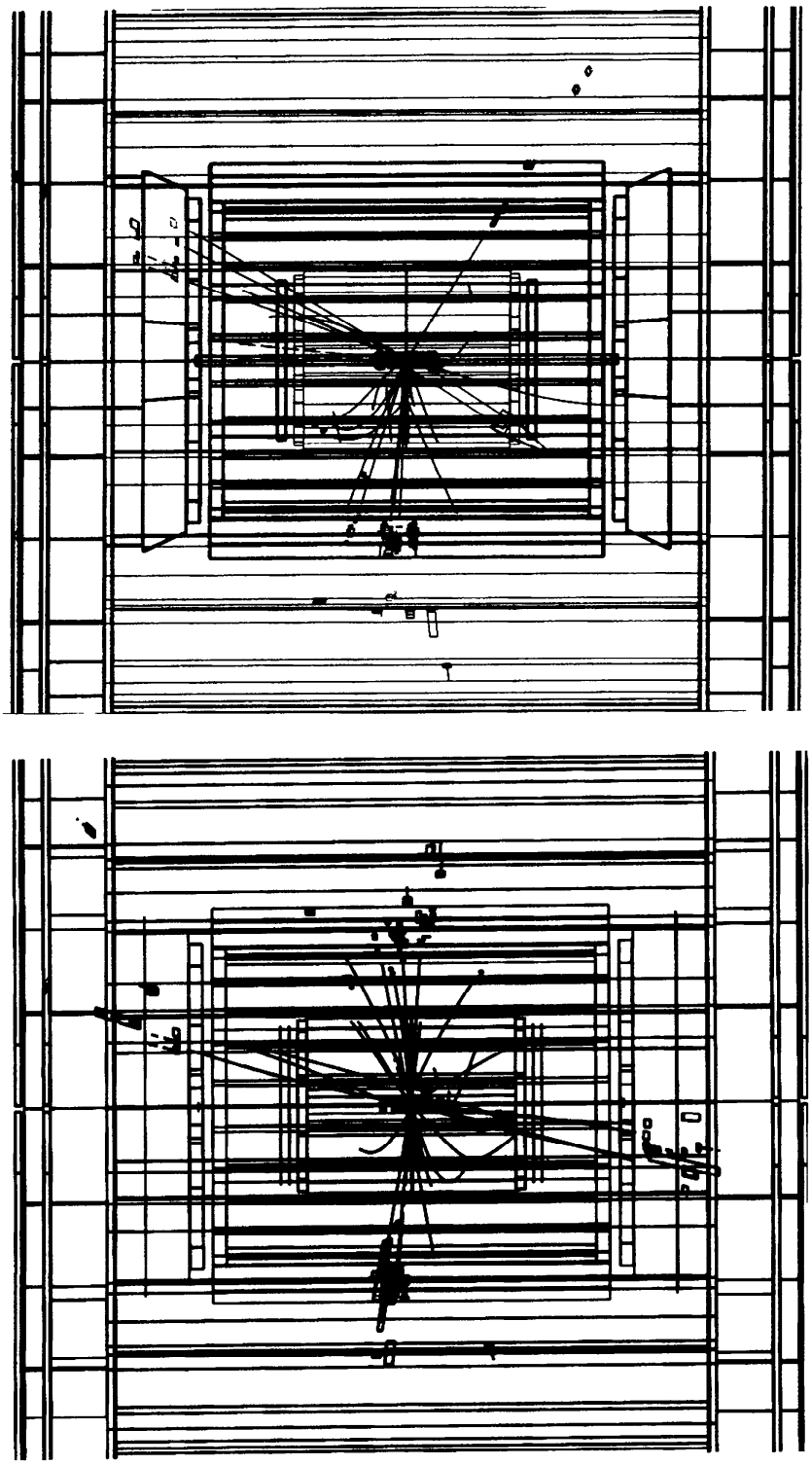

Fig. 8.11. Reconstruction of tracks due to production and decay of W^+W^- pairs in the central drift chamber of the DELPHI detector. In these pictures and the one in Figure 8.12, the beam pipe containing the colliding e^+ and e^- beams runs horizontally through the centre of the picture. The other horizontal and vertical lines are meant to depict the various components of the detector, which are itemised in the perspective drawing of Figure 8.5. In the top picture, one W decays into hadrons, i.e. $W \to \bar{Q}Q \to$ two jets, one around 6 o'clock and the other around 10 o'clock, while the other W undergoes leptonic decay $W \to \mu + \nu_\mu$. The muon track is the very straight one at 1 o'clock. The missing momentum in the event, carried by the neutrino, is indicated by the large outlined arrow at 4 o'clock. In the lower picture, both W's decay to quark–antiquark pairs, giving four jets at 10, 12, 4 and 6 o'clock, with energies 16, 33, 33 and 46 GeV respectively.

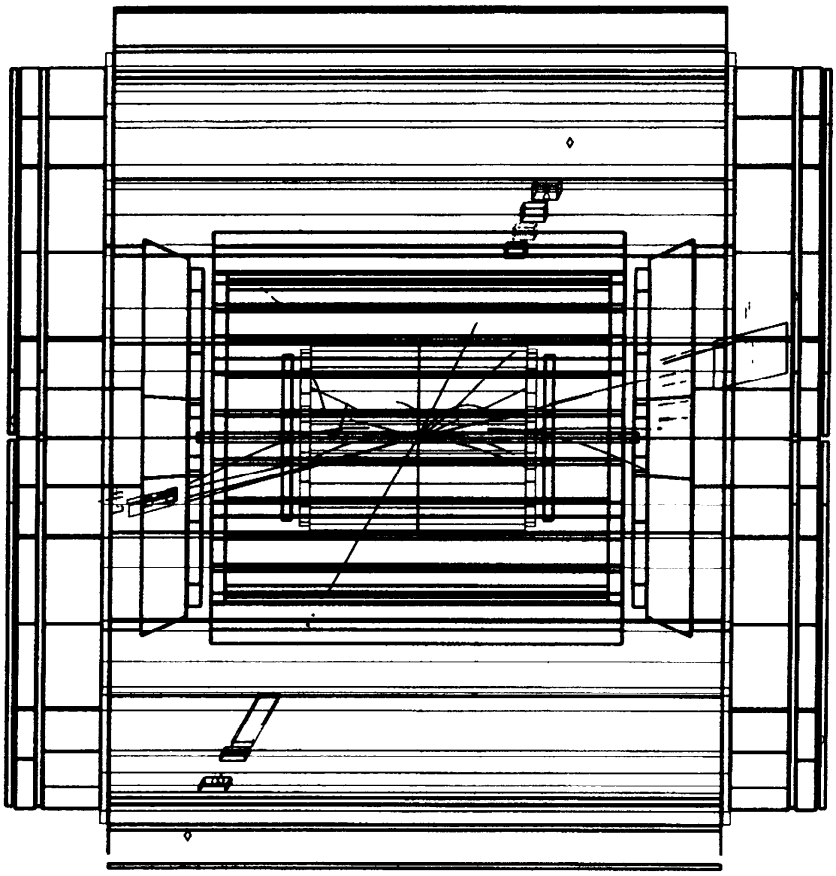

Fig. 8.12. Example of Z^0 pair production, in which one boson decays hadronically giving two jets (at 2 o'clock and 8 o'clock) while the other decays as $Z^0 \rightarrow \mu^+\mu^-$, giving the straight single tracks at 1 o'clock and 7 o'clock, with signals in the outer muon chambers. See also Problem 8.6.

which gives for the equation of motion (units $\hbar = c = 1$)

$$\partial_\mu^2 \phi + \mu^2 \phi = 0 \tag{8.47}$$

This is the Klein–Gordon equation (1.13), with $\partial_\mu^2 \equiv \partial^2/\partial t^2 - \nabla^2$. The Lagrangian (8.46) was obviously chosen to give this result.

8.12.2 The Higgs Lagrangian

Suppose now that we are dealing with scalar particles that interact with each other. Then V in (8.46) must contain an extra term of the form ϕ^4 (odd powers are excluded by symmetry under the transformation $\phi \rightarrow -\phi$, and terms in ϕ^6 or higher powers are excluded by the requirement of renormalisability). Thus the most general Lagrangian for the scalar field would be

$$L = \tfrac{1}{2}(\partial_\mu \phi)^2 - \tfrac{1}{2}\mu^2\phi^2 - \tfrac{1}{4}\lambda\phi^4 \tag{8.48}$$

where μ is the particle mass. L has dimensions of energy per unit volume, or E^4, while the boson field ϕ clearly has dimensions of E. Thus λ is a dimensionless

constant, representing the coupling of the 4-boson vertex. The minimum value of V occurs at $\phi = \phi_{\min}$, when $\partial V/\partial\phi = 0$ or

$$\phi(\mu^2 + \lambda\phi^2) = 0 \tag{8.49}$$

If $\mu^2 > 0$, the situation for a massive particle, then $\phi = \phi_{\min}$ when $\phi = 0$; this is the normal situation for the lowest energy vacuum state with $V = 0$. However, if $\mu^2 < 0$ then

$$\phi = \phi_{\min} \quad \text{when} \quad \phi = \pm v = \pm\sqrt{\frac{-\mu^2}{\lambda}} \tag{8.50}$$

Here the lowest energy state has ϕ finite, with $V = -\mu^4/4\lambda$, so that V is everywhere a non-zero constant. The quantity v is called the vacuum expectation value of the scalar boson field ϕ. Figure 8.13 shows V as a function of ϕ, both for $\mu^2 > 0$ and $\mu^2 < 0$. In either case a symmetric curve results, but for $\mu^2 < 0$ there are *two* minima, $\phi_{\min} = +v$ and $-v$. In weak interactions, we are however concerned with evaluating small perturbations about the energy minimum, so that we should expand the field variable ϕ, not about zero but about the chosen vacuum minimum v (or $-v$), i.e.

$$\phi = v + \sigma(x)$$

where $\sigma(x)$ is the (variable) value of the field over and above the constant and uniform value, v. Substituting in (8.48) we get

$$L = \tfrac{1}{2}(\partial_\mu\sigma)^2 - \lambda v^2\sigma^2 - \left(\lambda v\sigma^3 + \tfrac{1}{4}\lambda\sigma^4\right) + \text{constant} \tag{8.51}$$

where the constant refers to terms in v^2 and v^4 and the third term on the right-hand side represents the interaction of the σ field with itself. The first two terms on the right will be the same for either value of v, and when compared with (8.46), suggest that the term $-\lambda v^2\sigma^2$ is a mass term, with the positive value

$$m = \sqrt{2\lambda v^2} = \sqrt{-2\mu^2} \tag{8.52}$$

So, by making a perturbation expansion about either of the two minima $\pm v$, a real positive mass – as against an imaginary one in (8.50) – has appeared. The perturbation expansion must be made about one or other of the two minima – chosen for example by the toss of a coin – but when this is done, of course the symmetry in Figure 8.13 will be broken. This behaviour is called *spontaneous symmetry breaking*. Many examples exist in physics. A bar magnet heated above the Curie point has its elementary magnetic domains pointed in random directions, with zero net moment, and the Lagrangian is invariant under rotations of the magnet in space. On cooling, the domains will set in a particular direction, that of the resultant moment, and the rotational symmetry is spontaneously broken.

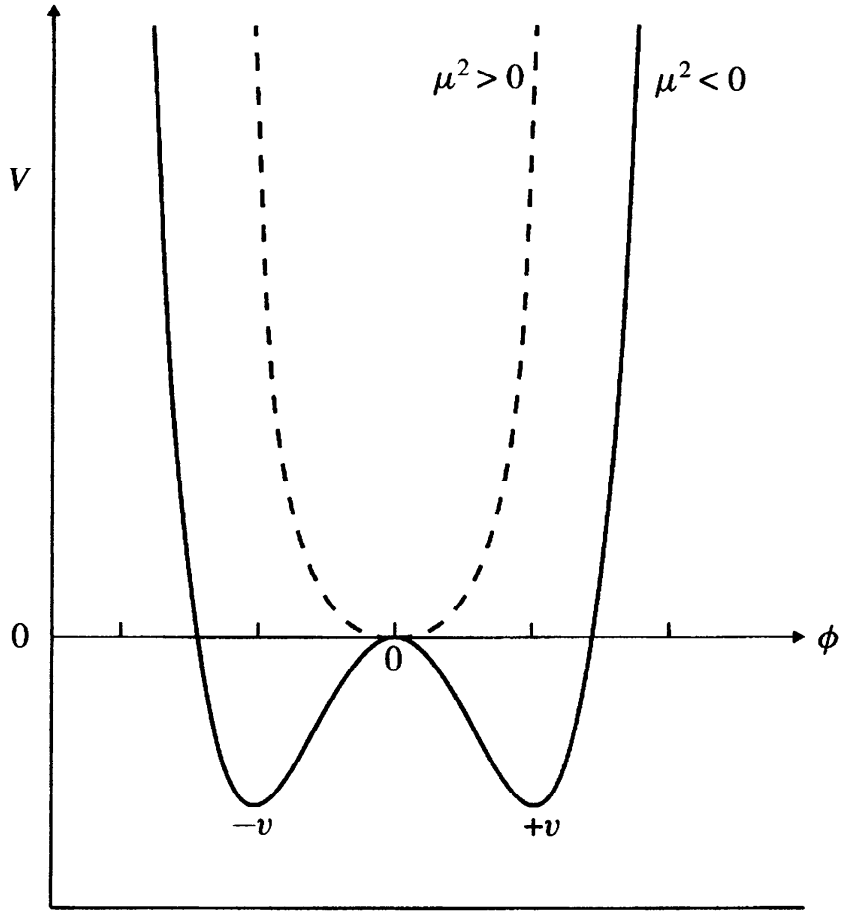

Fig. 8.13. Plot of the potential V in (8.48) as a function of a one-dimensional scalar field ϕ for the two cases $\mu^2 > 0$ and $\mu^2 < 0$.

Salam has given an amusing example of symmetry breaking on a macroscopic scale. He imagines N diners seated symmetrically around a circular table, with N bread rolls placed equidistantly between adjacent diners. Thus any diner will find a bread roll both on his left and on his right. Someone has to break the symmetry by taking a roll, say that on his left, when all the other diners will be compelled to follow suit.

8.12.3 Gauge invariance in the electroweak model

In Chapter 3 we discussed gauge invariance in QED. There we saw that the interaction (i.e. the Lagrangian energy density) would be invariant under arbitrary local phase transformations, on charged particle wavefunctions, of the form

$$\psi(x) \rightarrow e^{ie\theta(x)}\psi(x) \tag{8.53}$$

if these were accompanied by gauge transformations on a long-range field, the electromagnetic potential A_μ, to which the particles were coupled. This gauge

transformation was of the form

$$A_\mu \rightarrow A_\mu + \partial_\mu \theta(x) \tag{8.54}$$

and could be arranged by replacing the derivative ∂_μ by the covariant derivative (see (3.26))

$$D_\mu = \partial_\mu - ieA_\mu \tag{8.55}$$

where e is the particle charge.

The infinite set of phase transformations (8.53) form the unitary group called U(1), and, since $\theta(x)$ is a scalar quantity, the U(1) group is said to be Abelian. In 1954, Yang and Mills considered gauge transformations by non-Abelian operators, specifically in the group SU(2) of isospin, involving non-commuting operators $\boldsymbol{\tau} = \tau_1, \tau_2, \tau_3$, which are identical to the Pauli spin operators in (1.18).

Let us apply these ideas to the groups of weak hypercharge U(1) and weak isospin SU(2) introduced in Section 8.4. Weak hypercharge clearly behaves in the same way under gauge transformations as electric charge, described in (8.53). Conservation of weak isospin implies invariance under a rotation in weak isospin space (see (3.4)):

$$\psi \rightarrow e^{ig\boldsymbol{\tau}\cdot\boldsymbol{\Lambda}}\psi \tag{8.56}$$

where $\boldsymbol{\Lambda}$ is an arbitrary vector in isospin space about which the rotation takes place and g is the coupling constant in (8.7), analogous to e in (8.53). Again, we can require that $\boldsymbol{\Lambda}(x)$ be chosen arbitrarily at different points x in space–time. In a similar way as for electromagnetism, a gauge-invariant description can be obtained, by introducing a massless isovector (i.e. $I = 1$) field $\mathbf{W}_\mu$ having both charged and neutral components. Invariance under the transformation (8.56) is obtained by introducing a covariant derivative of the form

$$D_\mu = \partial_\mu - ig\boldsymbol{\tau} \cdot \mathbf{W}_\mu \tag{8.57}$$

where an infinitesimal gauge transformation of the field $\mathbf{W}_\mu$ is given by

$$\mathbf{W}_\mu \rightarrow \mathbf{W}_\mu + \partial_\mu \boldsymbol{\Lambda} - g\boldsymbol{\Lambda} \times \mathbf{W}_\mu \tag{8.58}$$

The extra term, as compared with (8.54), is associated with the fact that the Pauli isospin matrices do not commute. The resulting invariance under a gauge transformation can be readily verified by writing out the expression for $\psi^* D_\mu \psi$ using (8.57) and (8.58) in the case where $\boldsymbol{\Lambda}$ is infinitesimal. Note that inclusion of the vector product term in (8.58) not only leads to local gauge invariance but also implies an interaction of $\mathbf{W}_\mu$ with all particles carrying isospin and hence with itself. The bosons $\mathbf{W}_\mu$ are at one and the same time the carriers of and a part of the source of the weak isospin field. Similarly, we saw that in the non-Abelian gauge

group of colour SU(3), the quanta (gluons) of the colour field themselves carry colour and are therefore self-coupled.

The effect of the Higgs mechanism on the massless fields $\mathbf{W}_\mu$ and B_μ is found by substituting the covariant derivative for the $\mathbf{W}$ and B fields, which involves appropriate weak charges g and g' (see (8.7)). From (8.55) and (8.57), this will have the form

$$D_\mu = \partial_\mu - ig\boldsymbol{\tau} \cdot \mathbf{W}_\mu - ig'YB_\mu \tag{8.59}$$

Substituting D_μ for ∂_μ in the Lagrangian (8.48), one will then get terms quadratic in the $\mathbf{W}$ and B fields, multiplied by the Higgs vacuum term v^2, which as in (8.51) will be associated with the masses of these particles. In fact this leads to relations for the squares of the boson masses already given in (8.16) and (8.17), with $M_W = gv/2$ and $M_Z = v\sqrt{g'^2 + g^2}/2$. Thus, from the measured boson masses we find the value $v = 246$ GeV. This is then the typical scale of electroweak symmetry breaking.

The Higgs mechanism also endows the fermions with mass. As pointed out in Section 1.6, a scalar operator – and mass is such a scalar quantity – mixes LH and RH helicity states of fermions. In the limit of exact SU(2) × U(1) symmetry, i.e. conservation of weak isospin and of weak hypercharge, we see from (8.19) that such terms cannot exist since, for an electron, for example, e_L has $I = \frac{1}{2}$, $Y = -\frac{1}{2}$ while e_R has $I = 0$, $Y = -1$. However, the symmetry is broken by the Higgs particle mechanism, and the Higgs particle has exactly the right quantum numbers, $I = \frac{1}{2}$, $Y = +\frac{1}{2}$, to couple e_R with e_L and thus result in a mass term.

As indicated in Section 8.3, the Higgs was introduced in order to cancel out divergences associated with finite fermion masses, and the proportionality of the Higgs coupling (usually referred to as the Yukawa coupling) to the fermion mass is important from the point of view of Higgs particle detection. The very large value of the top quark mass, $m_t \simeq 176$ GeV, shows that its Yukawa coupling to the Higgs is near unity, i.e. $m_t \sim v$. While unit coupling may be regarded as natural, the comparative smallness of the masses of the other quarks and leptons (down to values of eV or less for neutrinos) remains one of the great mysteries of particle physics.

8.13 Higgs production and detection

As previously stated, in the Weinberg–Salam model the bosons consist of a weak isospin triplet $\mathbf{W}$ and an isospin singlet B, both space–time vector particles, plus an isospin doublet of scalar Higgs particles. These are denoted by complex fields ϕ^+, ϕ^0 with four real components such that $\phi^+ = \frac{1}{\sqrt{2}}(\phi_1 + \phi_2)$, $\phi^0 = \frac{1}{\sqrt{2}}(\phi_3 + \phi_4)$. The antiparticles are $\phi^- = (\phi^+)^*$ and $\bar{\phi}^0 = (\phi^0)^*$. Three of the four components,

ϕ^+, ϕ^- and $\frac{1}{\sqrt{2}}(\phi^0 - \bar{\phi}^0)$ are 'eaten' by the W's, giving them a mass that appears as the third, longitudinal degree of freedom of these previously massless, transverse particles. There is also W–B mixing, resulting in a massless photon – introduced as an experimental fact and not predicted by the model – and massive Z^0. This leaves one physical neutral Higgs scalar, $H = \frac{1}{\sqrt{2}}(\phi^0 + \bar{\phi}^0)$, which is predicted to exist as a free particle.

The mass of the Higgs is unknown, but $M_H \simeq 1$ TeV is considered an upper limit. To estimate this limit, we note that on dimensional grounds the width must be

$$\Gamma_H \sim G M_H^3 \tag{8.60}$$

If the Higgs self-coupling is not to be strong (recalling that in Section 8.12 the Higgs is a manifestation of perturbation theory), then we must have that $\Gamma_H < M_H$ or

$$M_H < G^{-1/2}$$

In fact the unitarity limit on WW scattering gives the more precise limit

$$M_H < (8\pi\sqrt{2}/3)^{1/2} G^{-1/2} \simeq 1 \text{ TeV} \tag{8.61}$$

The actual production of the Higgs is visualised through various diagrams, of which a sample is shown in Figure 8.14. As stated in Section 8.10, the radiative corrections to the LEP data suggest $M_H \sim$ 60–300 GeV.

A Higgs of moderate mass, up to $M_H \sim 100$ GeV, should be identifiable at an e^+e^- collider of suitable energy via the production and decay processes

$$\begin{aligned} e^+e^- &\to H^0 Z^0 \\ H^0 &\to b\bar{b}, \tau\bar{\tau}, \ldots \\ Z^0 &\to Q\bar{Q}, l\bar{l}, \nu\bar{\nu} \end{aligned}$$

Because of the proportionality of the coupling to fermion mass, the Higgs will decay preferentially to the heaviest available quark or lepton pair. In the above processes, it should be readily detectable as a spectacular mass peak recoiling from the lepton or quark pair from Z^0 decay. Absence of such effects in LEP 200 experiments to date (1999) shows that $M_H > 100$ GeV.

At a much higher energy hadron collider (LHC), the Higgs mass range explored could be greatly extended, to the region of 1 TeV. For $M_H =$ 80–150 GeV, the $H \to \gamma\gamma$ mode is favoured, while for a very massive Higgs, with $M_H \sim$ 150–1000 GeV, a search for the 'golden' decay modes $H \to l^+l^-l^+l^-$ and $l^+l^-\nu\bar{\nu}$, as well as $H \to ZZ$, $WW \to l^+l^-$ + two jets, is considered the best approach.

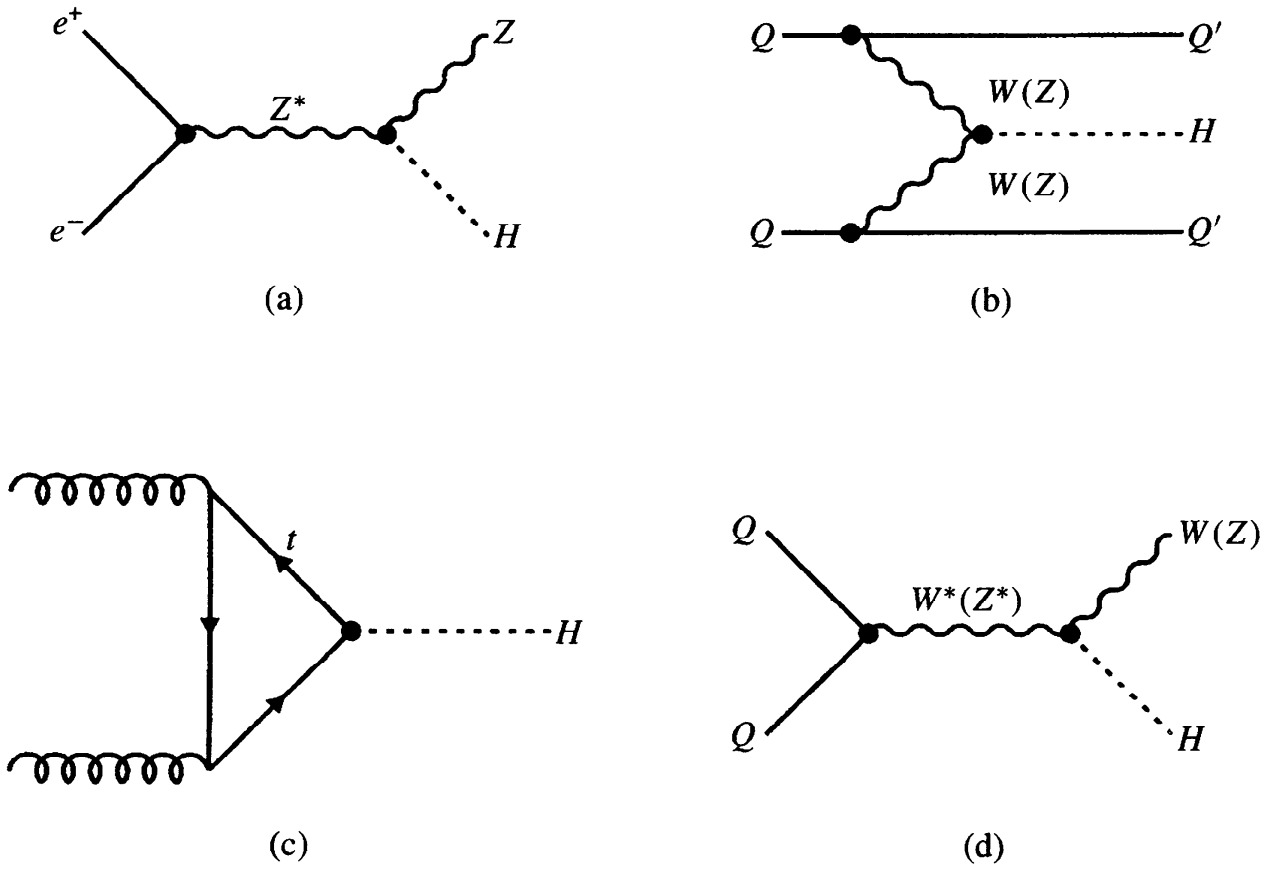

Fig. 8.14. Typical diagrams showing mechanisms for Higgs boson production in (a) e^+e^- collisions and (b), (c), (d) pp collisions. Diagrams (a) and (d) are the so-called bremsstrahlung diagrams and (b) is a $W(Z)$ fusion diagram, while (c) is a gluon fusion diagram.

Whether the Higgs is searched for at e^+e^- or pp colliders, the expected production cross-sections multiplied by the decay branching ratios are very small. Integrated luminosities of order 100 fb^{-1} are necessary,† corresponding to runs of a year or more at the highest available luminosities, of order 10^{34} cm^2 s^{-1}.

In supersymmetric models, to be discussed in the next chapter, the Higgs sector is much richer. There are two complex Higgs doublets, H_1 and H_2, and a total of five physical Higgs particles in the minimal supersymmetric Standard Model (MSSM). These consist of scalar (CP even) particles h^0 and H^0, a pseudoscalar (CP odd) neutral A^0 and two charged scalars H^+ and H^-. The masses are determined in terms of two parameters, M_A and $\tan\beta = v_2/v_1$, where v_2 and v_1 are the vacuum expectation values of the fields H_2 and H_1. The lowest-mass component is calculated to have $M_{h_0} < 130$ GeV. The search schemes for this particle are similar to those for the non-supersymmetric Standard Model Higgs.

While the electroweak theory is usually associated with spontaneous symmetry breaking via the Higgs mechanism, the Higgs does not *have* to exist. It could be

† 1 fb = 10^{-15} barns = 10^{-39} cm^2.

replaced by some other dynamical mechanism, e.g. W substructure. In any case, it seems certain that some as yet undiscovered particles or processes will occur in the cms energy region of 0.5–1 TeV, and this is the goal of present and future high energy particle colliders.

Problems

8.1 Using (8.23) and the results from Table 8.1, plot the total cross-sections σ/E_ν for ν_e, $\bar{\nu}_e$, ν_μ and $\bar{\nu}_\mu$ scattering from stationary electron targets as a function of $\sin^2\theta_W$. Where do σ_{ν_μ}, $\sigma_{\bar{\nu}_\mu}$ have minimum values? For what value of $\sin^2\theta_W$ is the coupling of $\bar{\nu}_\mu$ to electrons purely axial vector?

8.2 Using (8.23) and integrating over the electron recoil energy, plot the relation between g_V and g_A assuming that $\sigma(\nu_\mu e) = 3 \times 10^{-42} E_\nu$ cm^2 GeV. Take $G = 1.17 \times 10^{-5}$ GeV^{-2}. Show that if $\sigma(\bar{\nu}_\mu e)$ is also known, there are four possible solutions for g_A and g_V.

8.3 Using the expressions in Table 8.1 for the Z^0–fermion couplings, estimate the width of the Z^0 from (8.32), assuming $\rho = 1$, $M_Z = 91.2$ GeV and $\sin^2\theta_W = 0.23$, and compare with (8.35).

8.4 The neutral-current cross-section for neutrino scattering by nucleons via the quark constituents is readily obtained from (8.23) if we replace $s = 2mE$ by $s = 2xME$ where M is the nucleon mass and x is the momentum fraction carried by the quark, and we use the results of Table 8.1 plus (8.21) for the quark couplings to the Z^0. Neglecting sea quarks and using the analogous expressions for the charged-current cross-sections from (8.22), show that the ratios of neutral to charged-current cross-sections on nucleons are

$$R = \frac{\sigma^{\nu N}(\mathrm{NC})}{\sigma^{\nu N}(\mathrm{CC})} = \frac{1}{2} - \sin^2\theta_W + \frac{20}{27}\sin^4\theta_W$$

and

$$\bar{R} = \frac{\sigma^{\bar{\nu}N}(\mathrm{NC})}{\sigma^{\bar{\nu}N}(\mathrm{CC})} = \frac{1}{2} - \sin^2\theta_W + \frac{20}{9}\sin^4\theta_W$$

8.5 Verify (8.29) for the asymmetry in the scattering of polarised electrons by deuterons. Use (8.20) and the values in Table 8.1 for the couplings of electrons and quarks to the Z^0 and the photon. The cross-section results from the sum of the photon exchange and Z^0 exchange amplitudes. In summing these, only the pure photon exchange term and the Z^0 photon interference term will contribute, assuming $q^2 \ll M_Z^2$. Assume also equal numbers of u and d quarks in the deuteron, and neglect antiquarks. (In case of difficulty, consult, for example, Cahn and Gilman (1977).)

8.6 Draw a Feynman diagram for the process $e^+e^- \to Z^0Z^0$ shown in Figure 8.14. Why is the virtual Z^0 exchange diagram of Figure 8.9(c) not allowed for this process?

8.7 Using the expressions for deep inelastic electron–nucleon and neutrino–nucleon scattering in Section 5.7, and equations (8.15) and (5.18) relating the Fermi constant and W propagator to the weak and electromagnetic couplings, show that in the HERA ep collider, the electromagnetic cross-section ($e + p \to e +$ anything) and weak CC cross-section ($e + p \to \nu_e +$ anything) will be equal for $q^2 \sim 6000\ \text{GeV}^2$. (Neglect antiquark contributions and assume that in the proton $u(x) = 2d(x)$, $y = \frac{1}{2}$ and $\sin^2\theta_W = 0.23$.)

8.8 Calculate the partial width $\Gamma = \hbar W$ for the decay $W^\pm \to e^\pm + \nu_e$, using the formulae (2.16)–(2.19) for the transition rate W. These formulae include expressions for the matrix element, phase space and flux factors, which are not, individually, relativistically invariant. This does not affect calculation of the cross-section, which as a transverse quantity is necessarily invariant, but it can affect W. For relativistically invariant normalisation (see Appendix E), the particle density is equal to $2E$ particles per unit volume. Hence, the value of Γ calculated in the boson rest-frame from (2.16) must be divided by $2M_W$, to refer to a single particle.

Using arguments similar to those in Sections 5.3 and 5.4 for the decay angular distribution and the spin summation, show that $\Gamma = GM_W^3/6\pi\sqrt{2}$.

9

Physics beyond the Standard Model

The Standard Model incorporates the fundamental fermions – three pairs of quarks and three of leptons – with interactions between them mediated by gauge fields carried by the bosons $W^{\pm}$, Z^0 and γ of the electroweak sector, and, between the quarks only, by the gluons G of the strong sector. Recall that the electroweak sector is described by a broken SU(2) × U(1) symmetry, where SU(2) contains left-handed weak isospin doublets (such as e_L^- and ν_e) and U(1) contains right-handed isospin singlets such as e_R^-. The strong interactions are described by an (unbroken) SU(3) colour symmetry. As shown in the previous chapters, the Standard Model has been outstandingly successful in accounting for essentially all the data from laboratory experiments to date.

However, there are a number of shortcomings and problems with the Standard Model, which we discuss in this chapter. First, attempts have been made to carry unification further, by combining the electroweak and strong interactions in a higher, unified symmetry, which could be manifest at extremely high energy. The scale of *grand unified theories* – GUTs for short – is believed to be $E_{\rm GUT} \sim 10^{16}$ GeV. Such theories and their practical implications are described below.

Once, however, one admits to the possibility of higher mass scales – and we already know, for example, that a typical gravitational mass scale where quantum effects could be important is the Planck scale at 10^{19} GeV – difficulties start to arise for the Standard Model. This is called the *hierarchy problem.* In Chapter 8 we saw that the very successful calculation of the radiative corrections to the electroweak parameters arose from diagrams such as in Figure 8.7 where corrections to the boson masses come from loops with circulating virtual fermions and bosons. Clearly, if there are much more massive particles $M \simeq M_{\rm GUT}$ in the unexplored region above the electroweak mass scale of $M_W \sim G^{-1/2}$, these will inevitably occur in virtual processes at lower energy scales and can give corrections of order $M_{\rm GUT}^2$. If the mass of the (electroweak) Higgs particle (i.e. its self-energy) is driven by these more massive Higgs objects of the GUT scale, its value will

become unstable (i.e. divergent), unless we can arrange clever and quite precise cancellations at the level of $M_W/M_{\rm GUT} \simeq 10^{-14}$. *Supersymmetric models* are designed to do just that.

Another totally separate problem for the Standard Model is that neutrinos are known to exist in one helicity state (see (8.19)), and are assumed therefore to be massless. Although there is as yet no direct evidence for neutrino mass, observational phenomena such as the solar neutrino deficit and the atmospheric neutrino anomaly are suggestive of *neutrino flavour oscillations* and hence, as we shall see, of neutrino masses. A discussion of the search for neutrino oscillations is also included in this chapter.

Other shortcomings of the Standard Model are that it is both incomplete and ugly. Gravity is not included, whereas a 'theory of everything' should encompass that also, as well as account for the many arbitrary parameters in the Standard Model – some 17 or 18 empirical masses, couplings, mixing angles etc. – that have to be inserted 'by hand'. Ambitious attempts to incorporate gravity with the other fundamental interactions, the so-called *supergravity theories*, will also be mentioned briefly.

9.1 Supersymmetry

Under appropriate conditions, the hypothesis of supersymmetry can provide the cancellations of divergent amplitudes required to solve the hierarchy problem mentioned above. It postulates a fermion–boson symmetry, according to which new fermion (boson) partners are postulated for all known fundamental bosons (fermions). Of course this symmetry cannot be exact, otherwise the superpartners would have the same mass as the original particles, which is clearly not the case. The important point is that even with a broken symmetry – different masses for particles and their superpartners – the radiative corrections from virtual boson and fermion loops are of opposite sign. Thus, since the particles and their supersymmetric (SUSY) partners are assumed to have the same couplings, the one-loop divergences will cancel, provided that the SUSY particles have masses at or below the Fermi scale, i.e. $|M_F^2 - M_B^2| < 1\ \text{TeV}^2$. Indeed, the masses of the SUSY particles are expected to be of the same order as M_W, M_Z and M_H.

It is generally assumed that SUSY particles would be produced *in association*, with conservation of a special quantum number R, i.e. in pairs with $R = \pm 1$ (in much the same way that pairs of strange particles of $S = \pm 1$ are produced in strong interactions). For example, a squark–antisquark pair can be produced in quark–antiquark annihilation, $Q + \bar{Q} \rightarrow \tilde{Q} + \bar{\tilde{Q}}$. Each SUSY particle would decay, in an R-conserving cascade process or directly, to the lightest superparticle, which will be stable. If this were the photino, $\tilde{\gamma}$, production of a squark would be

Table 9.1. *Particles and SUSY partners*

Particle	Spin	Sparticle	Spin
quark Q	$\frac{1}{2}$	squark $\tilde{Q}$	0
lepton l	$\frac{1}{2}$	slepton $\tilde{l}$	0
photon γ	1	photino $\tilde{\gamma}$	$\frac{1}{2}$
gluon G	1	gluino $\tilde{G}$	$\frac{1}{2}$
$W^{\pm}$	1	wino $\tilde{W}^{\pm}$	$\frac{1}{2}$
Z^0	1	zino $\tilde{Z}^0$	$\frac{1}{2}$

manifest in the decay $\tilde{Q} \rightarrow Q + \tilde{\gamma}$, where the signature of the missing photino is indicated by acoplanarity of the decay products and momentum imbalance.

The most widely quoted scheme is that of the Minimal Supersymmetric Standard Model (MSSM). Table 9.1 gives examples of the (s)particle content in this model. It turns out that in SUSY models a minimum of two complex Higgs doublets are required, yielding eight components in all and five physical Higgs particles, as described in Section 8.13. In addition, one expects superpartners, the spin $\frac{1}{2}$ Higgsinos ($H^0_{1,2}$, $H^{\pm}$). The gauginos $\tilde{\gamma}$, $\tilde{W}^{\pm}$, $\tilde{Z}$ mix with the Higgsinos to form four mass eigenstates called *charginos* $\chi^{\pm}_{1,2}$ and four *neutralinos* $\chi^0_{1,2,3,4}$.

The masses and couplings of the SUSY particles are described in terms of four parameters – three masses and one mixing angle. The latter is denoted β, where $\tan\beta = v_2/v_1$ and v_1, v_2 are vacuum expectation values of the Higgs fields H_1 and H_2. For the Higgs sector, one further parameter is required. Generally, the cross-sections for producing SUSY particles (sleptons, squarks, charginos and neutralinos) at energies above threshold are typical of weak cross-sections, i.e. of order 0.01–0.1 pb. Thus if such particles are produced at colliders, they should be easy to find. The present (1999) lower limit on squark and slepton masses is essentially that set by the kinematics at high energy colliders, about 100 GeV/c^2.

9.2 Grand unified theories: the SU(5) GUT

The success of the electroweak model, unifying weak and electromagnetic interactions described in the previous chapter, opened the possibility that the strong interactions might also be included in a unifying scheme. The basic idea is that the SU(2) × U(1) electroweak symmetry and the SU(3) colour symmetry of the strong interactions might be encompassed by a more global symmetry at some high unification energy, well above the electroweak scale. From Chapter 6 we know that the couplings of the various interactions 'run' in different ways. The Abelian U(1)

Table 9.2. $\bar{5}$ *Multiplet in* SU(5)

		I_3	$Q/\lvert e\rvert$
W	ν_e	$+\frac{1}{2}$	0
W	e^-	$-\frac{1}{2}$	-1
X	$\bar{d}_R$	0	$+\frac{1}{3}$
G	$\bar{d}_B$	0	$+\frac{1}{3}$
G	$\bar{d}_G$	0	$+\frac{1}{3}$

coupling g' (or e) increases with energy, while the non-Abelian couplings, g of SU(2) and g_s of SU(3), decrease with increasing energy. The question then is: assuming that there is no new physics between the electroweak scale and that of grand unification, would these couplings extrapolate to a common value at some unknown energy, where the coupling would be universal?

There are many ways in which the U(1), SU(2) and SU(3) symmetries might be incorporated into a more global symmetry. The first and simplest GUT model was the SU(5) model of Georgi and Glashow in 1974. This incorporates the known fermions, i.e. both the leptons and the quarks, into multiplets, inside which, having the same universal coupling, leptons and quarks can transform one into the other. They interact via the mediation of massive bosons Y and X, with electric charges $-\frac{1}{3}|e|$ and $-\frac{4}{3}|e|$ respectively. These carry three colours and, counting both particles and antiparticles, therefore exist in 12 varieties. Including the eight gluons of SU(3) and the $W^{\pm}$, Z^0 and γ of SU(2) and U(1), there are a total of 24 gauge bosons (i.e. $N^2 - 1$ gauge bosons for SU(N) with $N = 5$).

The known fermions are split into three generations or families, each containing 15 states. For example, the first generation comprises the u and d quarks, each in three colour and two helicity states, the e^- in two helicity states and the ν_e, with one helicity only. By convention, the SU(5) multiplets are written down as LH states, the RH states of particles being replaced by LH antiparticles (since, by CP symmetry, e_L^- and e_L^+ are equivalent; the RH states of course appear in separate multiplets). The 15 LH states have to be distributed in a '$\bar{5}$' representation and in a '10' representation, where the latter is an antisymmetric combination of two '5's. As an example, Table 9.2 lists the particles and quantum numbers of the '$\bar{5}$' representation. In this table, the arrows indicate that gluon G mediates the colour force between quarks, the $W^{\pm}$ mediate the charged weak current and an X 'leptoquark' boson transforms a quark to a lepton. The electric charge is one of the generators of the SU(5) group; consequently the multiplets have the property that the total electric charge $\sum Q_i = 0$. The heavier leptons and quarks, μ, ν_μ, s, c

and τ, ν_τ, b, t, are assigned to separate (second and third) generations. Among the immediately attractive features of this model are the following.

(i) The fractional charges of the quarks occur because the quarks in a multiplet come in three colours and the electron is colourless (and $\sum Q_i = 0$). This is also, as it happens, the condition for freedom from triangle anomalies in field theory (see Section 4.4).

(ii) The equality of the baryon (proton) charge and electron charge – a historic puzzle – is accounted for.

(iii) Electric charge, originally a (continuously variable) generator of the Abelian U(1) group, now becomes a generator of the non-Abelian SU(5) group, and the commutation relations of this symmetry allow only discrete, rather than continuous, eigenvalues for the electric charge. So charge quantisation, in this model, occurs as a result of grand unification.

(iv) The strong similarity between the lepton and quark doublet patterns involved in weak interactions, e.g. $(\nu_e, e)_L$ and $(u, d_c)_L$, and the fact that $Q(\nu) - Q(e) = Q(u) - Q(d)$ occur as natural consequences of lepton–quark symmetry.

9.3 Unification energy and weak mixing angle

The bringing together of quarks and leptons into multiplets allows one to estimate the weak mixing angle, since the coupling amplitudes g and g' defined in (8.7), which determine $\sin^2\theta_W$ from (8.12), must be related by Clebsch–Gordan coefficients at the GUT scale. Consider the diagram of Figure 9.1 depicting the Z^0 mixing with a photon via a fermion loop. The Z^0 and γ are orthogonal states (weak isospin triplet and singlet) so, to first order, there should be no net coupling when summed over all fermions. The coupling of the fermions to Z^0 is proportional to $I_3 - Q\sin^2\theta_W$, and to the photon is simply Q (refer to (8.20)), where the LH states of fermions (or RH states of antifermions) have $I_3 = 0$ as explained in Chapter 8. The net coupling to both Z^0 and γ has to vanish, giving the relation

$$\sum_f Q(I_3 - Q\sin^2\theta_W) = 0 \qquad \text{or} \qquad \sin^2\theta_W = \frac{\sum QI_3}{\sum Q^2} = \frac{3}{8} \tag{9.1}$$

taking the quantum numbers from the states in Table 9.2. The same result would apply if the sum were made over the states of the '10' representation. So we can write that at unification

$$e^2 = g^2\sin^2\theta_W = \frac{3g^2}{8} \tag{9.2}$$

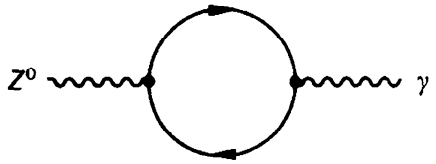

Fig. 9.1. Z^0 mixing with a photon via a fermion loop.

To conform to the usual nomenclature, we denote the U(1), SU(2) and SU(3) couplings by $\alpha_1, \alpha_2, \alpha_3$ respectively. Here we set $\alpha_1 = (5/3)g'^2/4\pi$ and $\alpha_2 = g^2/4\pi$, so that with $\alpha_{\rm em} = e^2/4\pi$ we get from (8.12) and (8.14), $1/\alpha_2 + 5/3\alpha_1 = 1/\alpha_{\rm em}$ and from (9.2), $\alpha_1 = \alpha_2 = 8\alpha_{\rm em}/3$ at $E = M_X$. With $\alpha_3 = \alpha_s$ unification implies

$$\alpha_1(M_X) = \alpha_2(M_X) = \alpha_3(M_X) = \alpha_{\rm GUT} \tag{9.3}$$

The general expression for the evolution in the so-called leading log approximation was given in (6.21):

$$\alpha(q^2) = \frac{\alpha(\mu^2)}{1 + R\alpha(\mu^2)\ln(q^2/\mu^2)} \tag{9.4}$$

where

$$R = -\beta_0 = \frac{11n_b - 4n_f}{12\pi} \tag{9.5}$$

Here, $n_b = 0$, 2 and 3 for U(1), SU(2) and SU(3) respectively, and the number of fermion generations is $n_f = 3$. When the extrapolation to high energies was first made in the 1970s, using the values of α_s, $\alpha_{\rm em}$ and $\sin^2\theta_W$ measured at low energy, the three couplings did indeed appear to meet at a unique energy, with $M_X \sim 3 \times 10^{14}$ GeV and $\alpha_{\rm GUT} \simeq \frac{1}{43}$. This was heralded as a great triumph for unification, and stimulated the search for proton decay, described in Section 9.5. The value of $\sin^2\theta_W$ extrapolated from (9.1) to laboratory energies was about 0.2, within 10% of the measured value! But later and more precise measurements of $\sin^2\theta_W$ and α_s (at $\mu = M_Z$, as described in Section 8.9) show that the couplings do not meet exactly in a point, missing it by several standard deviations, as shown in Figure 9.2(a). Put another way, if the unification energy is defined by the intersection of the extrapolated values of α_1 and α_3, then extrapolating back $\sin^2\theta_W$, i.e. α_1/α_2, gives a predicted value of $\sin^2\theta_W(M_Z) = 0.214 \pm 0.004$, significantly below the most accurately measured value of 0.2313 ± 0.0003.

In this discussion, we have neglected the role of the Higgs boson in the evolution. Its contribution is small. It would affect the computed value of $\sin^2\theta_W(M_Z)$, but not enough to alter the conclusion.

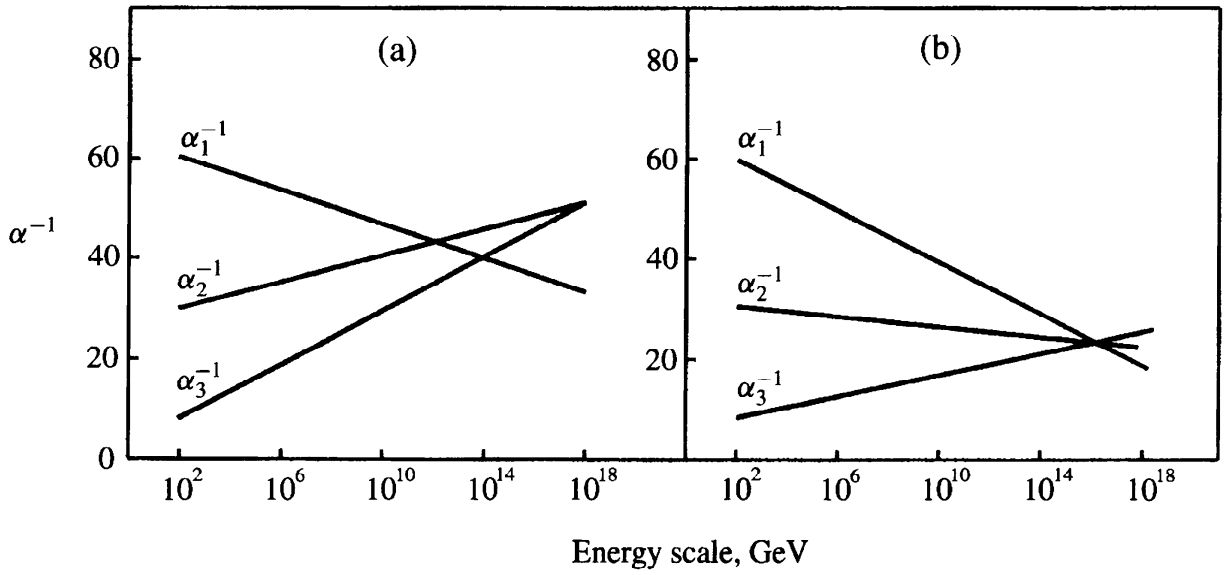

Fig. 9.2. Evolution of the couplings α_1^{-1}, α_2^{-1} and α_3^{-1} with the energy scale, for (a) non-supersymmetric SU(5) and (b) supersymmetric SU(5).

9.4 Supersymmetric SU(5)

The hypothesis of supersymmetry introduces new elementary fermions and bosons, and these extra degrees of freedom reduce the slopes of the α^{-1} dependence on $\ln(q^2/\mu^2)$. In fact the value of R in (9.5) has to be replaced by the smaller value

$$R_{\text{SUSY}} = \frac{9n_b - 6n_f}{12\pi} \tag{9.6}$$

As a result, the unification energy is increased. One can also adjust the energy scale E_{SUSY} at which the SUSY-type evolution of the couplings takes over from the non-SUSY evolution. Remarkably enough, for $E_{\text{SUSY}} \sim 1$ TeV, the three couplings appear to extrapolate to one point at $E_{\text{GUT}} \simeq 3 \times 10^{16}$ GeV, with $\alpha_{\text{GUT}} \simeq \frac{1}{24}$, as shown in Figure 9.2(b). Of course, it can be argued that two of the three couplings must meet somewhere, and the third extrapolated coupling will pass through the same point if its scale is adjustable. However, this confluence could have occurred at very small or very large values of E_{GUT} – in excess of the Planck energy of 10^{19} GeV for example – and it is remarkable that the scale required for the SUSY-type evolution is that previously foreseen in Section 9.1.

9.5 Proton decay

As shown in Table 9.2, grand unification implies that at energies $\simeq M_X$, quarks will transform to leptons via X, Y exchanges, as discussed in Section 9.2. Even at normal energies, virtual X, Y boson exchanges can take place and, although enormously suppressed on account of the propagators, will lead to the very

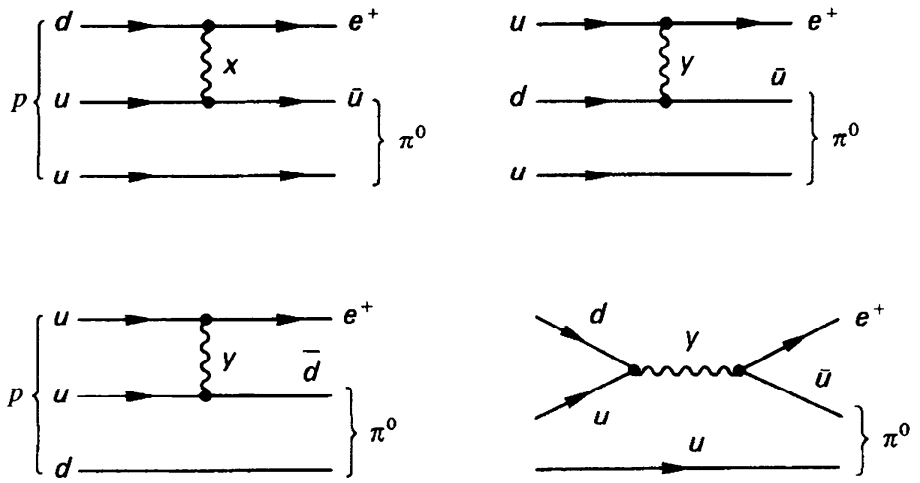

Fig. 9.3. Diagrams for proton decay via X, Y (leptoquark) boson exchanges.

important prediction of proton decay at some level. Indeed, proton decay is one of the very few tests of grand unification that would be manifest at everyday energies.

Figure 9.3 shows some possible diagrams leading to proton decay in SU(5). In analogy with muon decay (7.1), we expect the proton lifetime to be given by

$$\tau_p = \frac{A M_X^4}{\alpha_{\mathrm{GUT}}^2 M_p^5} \tag{9.7}$$

Here, A is a dimensionless quantity, of order unity, which includes a factor for the probability of finding two quarks effectively at the origin of their relative coordinates so that the very-short-range X boson can act to provide, for example, the transition $ud \to e^+\bar{u}$. The M_X^4 factor is from the X propagator and the M_p^5 factor is included to get the right dimensions.

First let us use (9.7) to compute τ_p for non-SUSY unification, i.e. with $M_X = 3\times 10^{14}$ GeV, $\alpha_{\mathrm{GUT}} = \frac{1}{43}$ and $A = 1$. One finds $\tau_p \sim 4\times 10^{29}$ yr. An exact calculation, including the various uncertainties, yields for non-supersymmetric SU(5)

$$\tau_p \simeq 10^{30\pm 1}\ \mathrm{yr} \tag{9.8}$$

It is interesting to note that, while in this process neither baryon number B nor lepton number L is conserved, the difference $B - L$ *is* conserved.

It has of course been known for a long time that in ordinary matter the constituent protons are extremely stable. The mere existence of life on Earth sets a lower limit on τ_p more than a million times the age of the universe (see Problem 9.2). Although 10^{30} yr in (9.8) is very long, a kilotonne of material contains some 3×10^{32} protons, so the above lifetime would yield about one decay per day per kilotonne of material. When this was realised in the late 1970s, several experiments were started to search for the decay, using massive (kilotonne) detectors placed deep underground to

reduce cosmic ray muon background. Figure 9.4 shows a picture of the largest of these, the Superkamiokande detector. This is a cylinder holding 50 000 tons of water, viewed by 11 000 photomultipliers placed around the water surface, with which to detect the Čerenkov light that would be emitted if relativistic products ($e^{\pm}$) from proton decay were to traverse the water. Proton decay detectors are placed deep underground (typically under 3000 m water equivalent of rock) in a mine or mountain tunnel.

No examples of proton decay have been detected so far, however. The precise limits on the lifetime depend on the decay mode assumed and on the branching ratio, BR. For the mode $p \rightarrow e^+ + \pi^0$, for which the water Čerenkov detectors are very well suited, $\tau_p/BR > 5 \times 10^{32}$ yr. One can combine the results from the Kamiokande and Irvine–Michigan–Brookhaven water Čerenkov detectors with those from electronic tracking detectors, which use an iron matrix as the source of protons, instrumented with discharge tubes or drift tubes (the Soudan 2, Frejus and Nusex experiments). The various detectors have different sensitivities to different decay modes, but taken together one can confidently place a lower limit $\tau_p > 10^{32}$ yr, well above the estimate (9.8).

As stated above, since these kilotonne and multikiloton search experiments were started much more precise values of α_s and $\sin^2\theta_W$ have been obtained, particularly at the LEP e^+e^- collider at CERN, showing that the supersymmetric version of SU(5) gives the more convincing evidence for unification, with a higher unification energy (3×10^{16} GeV) and hence, according to (9.7), a much longer expected proton lifetime. However, since supersymmetry involves also the possibility of proton decay via the exchange of Higgsinos associated with grand unified symmetry breaking, the experimental limit on the lifetime simply sets a lower limit on the GUT Higgsino mass $M_{\text{Higgsino}} > 2 \times 10^{16}$ GeV. For smaller masses, the predicted lifetime would be unacceptably short. Thus, the question of proton decay is now a purely experimental matter.

9.6 Neutrino mass: Dirac and Majorana neutrinos

In the Standard Model and the possible extensions to it discussed so far in this chapter, neutrinos occupy a unique position. They are assumed to be massless and to exist in only one (LH) helicity state: $\nu = \nu_L$ (while $\bar{\nu} = \bar{\nu}_R$).

Before discussing neutrino masses as such, we should mention that there is still, after more than 60 years, a question about the actual nature of neutrinos. The conventional description treats them as Dirac particles, i.e. spin $\frac{1}{2}$ particles with one of the two spin substates missing. A more economical description was proposed by Majorana, namely that the neutrino was *its own antiparticle*, so that $\nu \equiv \bar{\nu}$. Thus there is just one spin $\frac{1}{2}$ particle, with two substates ν_L and ν_R. The difference

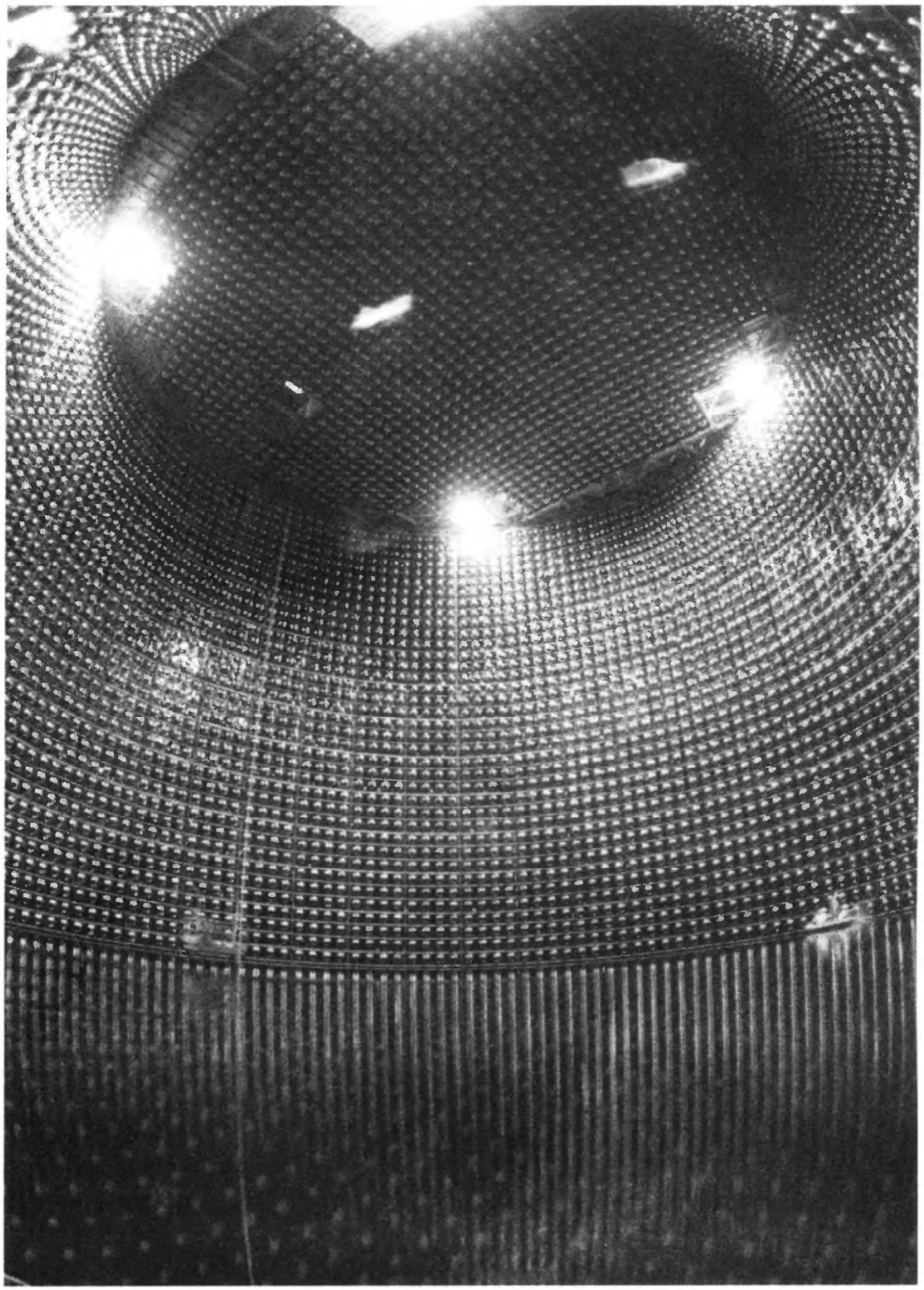

Fig. 9.4. The Superkamiokande water Čerenkov detector used to search for proton decay. It consists of a right cylinder filled with water, whose surfaces are covered with 11 000 20 inch photomultipliers, which record the Čerenkov light produced by relativistic particles traversing the water. This picture was taken during the filling of the tank with the full volume (50 000 tons) of water (courtesy Professor Y. Totsuka, Superkamiokande collaboration).

in behaviour of 'neutrino' and 'antineutrino' is then merely a consequence of the different helicities in the two cases.

The most important test of the Majorana model relates to nuclear double β-decay, where *neutrinoless* decay can occur as follows. A double β-decay results in the conversion of two neutrons to two protons, which in the Dirac description is

$$2n \rightarrow 2p + 2e^- + 2\bar{\nu}_{eR} \tag{9.9}$$

the energy being shared between electrons and antineutrinos. The subscript is put there to remind us that antineutrinos are right-handed. The above process has been observed, for example, in the decay $^{82}\mathrm{Se} \rightarrow {}^{82}\mathrm{Kr}$, with a mean lifetime of 10^{20} yr. However, if $\nu \equiv \bar{\nu}$, this process can proceed in two stages, where the neutrino generated in the first stage is absorbed in the second stage:

$$(1) \qquad n \rightarrow p + e^- + \bar{\nu}_{eR}$$

$$(2) \quad \bar{\nu}_{eR}\ (\equiv \nu_{eR}) + n \rightarrow p + e^-$$

or

$$2n \rightarrow 2p + 2e^- \tag{9.10}$$

If neutrinos are strictly massless, this process is forbidden by helicity conservation, since the neutrino from the first decay is in a pure RH helicity state and the amplitude for its absorption by the second neutron is identically zero (only $\nu_R + p \rightarrow e^+ + n$ being allowed in the $V - A$ theory). However, if the neutrino mass is small but finite, a tiny LH helicity component will also be present, and the neutrinoless process (9.10) can occur. As we know from Section 7.10, suppression of the LH helicity leads to a factor

$$1 - \frac{v}{c} = \frac{m_\nu^2}{2E_\nu} \tag{9.11}$$

in the decay rate (assuming $E_\nu \gg m_\nu$). Neutrinoless double β-decay as in (9.10) would be signalled by a unique total energy for the two electrons, and the absence of any such discrete line in the electron spectrum has been used to put an upper limit on the lifetime for this process. For example, using large (2–3 kg) crystal detectors of isotope-enriched germanium containing 86% ^{76}Ge, the limit $\tau(0\nu) > 5 \times 10^{24}$ yr has been set for the reaction $^{76}\mathrm{Ge} \rightarrow {}^{76}\mathrm{Se} + 2e^-$. From (9.11) and a calculation of the nuclear matrix elements involved, this results in a limit

$$m_\nu(0\nu\beta\beta) < 1 \text{ eV}$$

applying for the case where the neutrino is a Majorana particle. The non-observation of neutrinoless double β-decay also sets a limit on any new type of coupling, e.g. that due to an extra, massive, right-handed W boson.

To continue our discussion of neutrino mass we shall, in order to avoid possible confusion, henceforth treat neutrinos as Dirac particles. Direct measurements of the neutrino mass were already given in Table 1.4. They come from kinematic fits to the decays $^3\mathrm{H} \rightarrow {}^3\mathrm{He} + \mathrm{e}^- + \bar{\nu}_\mathrm{e}$ ($m_{\nu_e} < 10$ eV), $\pi \rightarrow \mu + \nu_\mu$ ($m_{\nu_\mu} <$ 0.17 MeV) and $\tau \rightarrow \nu_\tau + 5\pi$ ($m_{\nu_\tau} < 18$ MeV). It may be noted that, as in (7.9a), the kinematic constraints determine m_ν^2 and that in the majority of experiments this actually comes out to be negative. Thus there seem to be unknown sources of systematic error and we have therefore quoted conservative mass limits above.

9.7 Neutrino oscillations

The masslessness of neutrinos was questioned by Pontecorvo and others many years ago, in connection with the possibility of neutrino flavour oscillations. It was proposed that while neutrinos are created or annihilated as *flavour* eigenstates, they propagate through space as a superposition of *mass* eigenstates. The weak interaction eigenstates ν_e, ν_μ, ν_τ are therefore expressed as combinations of mass eigenstates ν_1, ν_2, ν_3, which propagate with slightly different frequencies due to their different masses and between which different phases develop with distance travelled, corresponding to a change or oscillation in the neutrino flavour.

In order to simplify the treatment we shall consider the case of two neutrino flavours, say ν_e and ν_μ. Each will be a linear combination of two mass eigenstates, ν_1 and ν_2, as given by the unitary transformation involving an arbitrary mixing angle θ:

$$\begin{pmatrix} \nu_\mu \\ \nu_e \end{pmatrix} = \begin{pmatrix} \cos\theta & \sin\theta \\ -\sin\theta & \cos\theta \end{pmatrix} \begin{pmatrix} \nu_1 \\ \nu_2 \end{pmatrix} \tag{9.12}$$

so that the wavefunctions

$$\nu_\mu = \nu_1 \cos\theta + \nu_2 \sin\theta$$

and

$$\nu_e = -\nu_1 \sin\theta + \nu_2 \cos\theta$$

are orthonormal states. Thus propagation in space is given by

$$\begin{aligned} \nu_1(t) &= \nu_1(0) e^{-iE_1 t} \\ \nu_2(t) &= \nu_2(0) e^{-iE_2 t} \end{aligned} \tag{9.13}$$

where we set $\hbar = c = 1$. The states ν_1 and ν_2 will have a fixed momentum p, so that if the masses are $m_i \ll E_i$ (where $i = 1, 2$)

$$E_i = p + \frac{m_i^2}{2p} \tag{9.14}$$

If we were to start off at $t = 0$ with muon-type neutrinos then $\nu_\mu(0) = 1$ and $\nu_e(0) = 0$. Hence inverting (9.12)

$$\begin{aligned} \nu_2(0) &= \nu_\mu(0) \sin\theta \\ \nu_1(0) &= \nu_\mu(0) \cos\theta \end{aligned} \tag{9.15}$$

and

$$\nu_\mu(t) = \cos\theta \nu_1(t) + \sin\theta \nu_2(t)$$

Using (9.13) and (9.15) we therefore obtain for the amplitude

$$A_\mu = \frac{\nu_\mu(t)}{\nu_\mu(0)} = \cos^2\theta\, e^{-iE_1 t} + \sin^2\theta\, e^{-iE_2 t}$$

so that the intensity is readily found to be

$$\frac{I_\mu(t)}{I_\mu(0)} = A_\mu A_\mu^* = 1 - \sin^2 2\theta \sin^2 \frac{(E_2 - E_1)t}{2}$$

Writing $\Delta m^2 = m_2^2 - m_1^2$ and with the help of (9.14) we obtain the following form for the probability of finding ν_μ or ν_e after time $t = L/c$, where L is the distance travelled:

$$P(\nu_\mu \to \nu_\mu) = 1 - \sin^2 2\theta \sin^2 \left(\frac{1.27 \Delta m^2 L}{E} \right) \tag{9.16a}$$

$$P(\nu_\mu \to \nu_e) = 1 - P(\nu_\mu \to \nu_\mu) \tag{9.16b}$$

Here, the numerical constant is obtained by retaining the $\hbar$, c terms which we set to unity in (9.13) and (9.14). When one does this the phase angle in the bracket in (9.16a) becomes

$$\frac{\Delta m^2 c^4 L}{4E\hbar c}$$

so that, expressing L in metres, $(\Delta m c^2)^2$ in $(\text{eV})^2$ and E in MeV, and with $\hbar c = 197$ MeV fm, the constant 1.27 in (9.16) follows. The above equation shows that the neutrino flavour *oscillates* with time or distance travelled by the beam. Figure 9.5 shows the situation for $\theta = 45°$. It can be seen that as it traverses space the beam, starting off as ν_μ, oscillates back and forth between a pure ν_μ and a pure ν_e eigenstate. For other values of θ, the beam will oscillate between a pure ν_μ eigenstate and a superposition of ν_e and ν_μ.

Experimental searches for neutrino oscillations have been carried out over some 25 years or more. Using man-made beams, only one laboratory at the time of writing (1998) has claimed a signal. Since, however, this has not been corroborated by other experiments, it cannot be claimed as definite. Measurements can be either

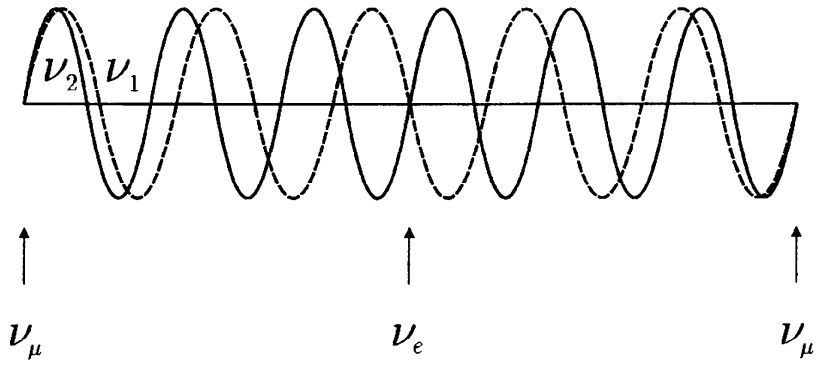

Fig. 9.5. Two-neutrino oscillation scenario, showing the amplitudes of ν_1 and ν_2 mass eigenstates for the case $\theta = 45°$. The two are in phase at the beginning and end of the plot, separated by one oscillatory wavelength, and thus from (9.12) correspond at these points to pure ν_μ flavour eigenstates. The two amplitudes are 180° out of phase in the centre of the plot, corresponding, from (9.12), to the ν_e weak eigenstate.

of the *disappearance* of an initial flavour of neutrino, as described for the two-flavour case by (9.16a), or of the *appearance* of a new flavour of neutrino in an initially one-flavour beam, as in (9.16b).

The survival probability $P(\bar{\nu}_\alpha \to \bar{\nu}_\alpha)$ equals $P(\nu_\alpha \to \nu_\alpha)$, where $\alpha = e, \mu, \tau$. This follows from the CPT theorem connecting particle and antiparticle. However, the transformation probability $P(\bar{\nu}_\alpha \to \bar{\nu}_\beta)$ is not equal to $P(\nu_\alpha \to \nu_\beta)$ and $P(\nu_\beta \to \nu_\alpha)$ is not equal to $P(\nu_\alpha \to \nu_\beta)$ in general. These relations would be equalities if CP invariance held good, but we know that in weak interactions it can be violated.

The laboratory investigations have been carried out with $\bar{\nu}_e$ beams from reactors and, principally, with $\nu_\mu, \bar{\nu}_\mu$ beams from accelerators. Solar and atmospheric neutrino experiments (both showing effects that can be interpreted as due to oscillations) are discussed below. Reactor beams are of low energy, extending to $E_\nu \simeq 10$ MeV only, with the maximum event rate for the detection process $\bar{\nu}_e + p \to n + e^+$ at 5 MeV. Thus such beams can only be used for disappearance experiments, since even if the transformation $\bar{\nu}_e \to \bar{\nu}_\mu$ occurs the energy is below the threshold to produce a charged muon.

Figure 9.6 shows a plot of the allowed and forbidden regions in the Δm^2 versus $\sin^2 2\theta$ plane for two-flavour oscillations, according to various experiments at reactors and accelerators. Also included are the positive results from solar and atmospheric neutrino experiments. Figure 9.7 shows a diagram of the CHOOZ reactor experiment, which consists of a target of 5 tonnes of Gd-loaded scintillator surrounded by a 17 tonne containment region equipped with photomultipliers to detect scintillation light and to contain γ-rays from neutron capture, plus a 90 tonne active shield, also equipped with photomultipliers, to veto the cosmic

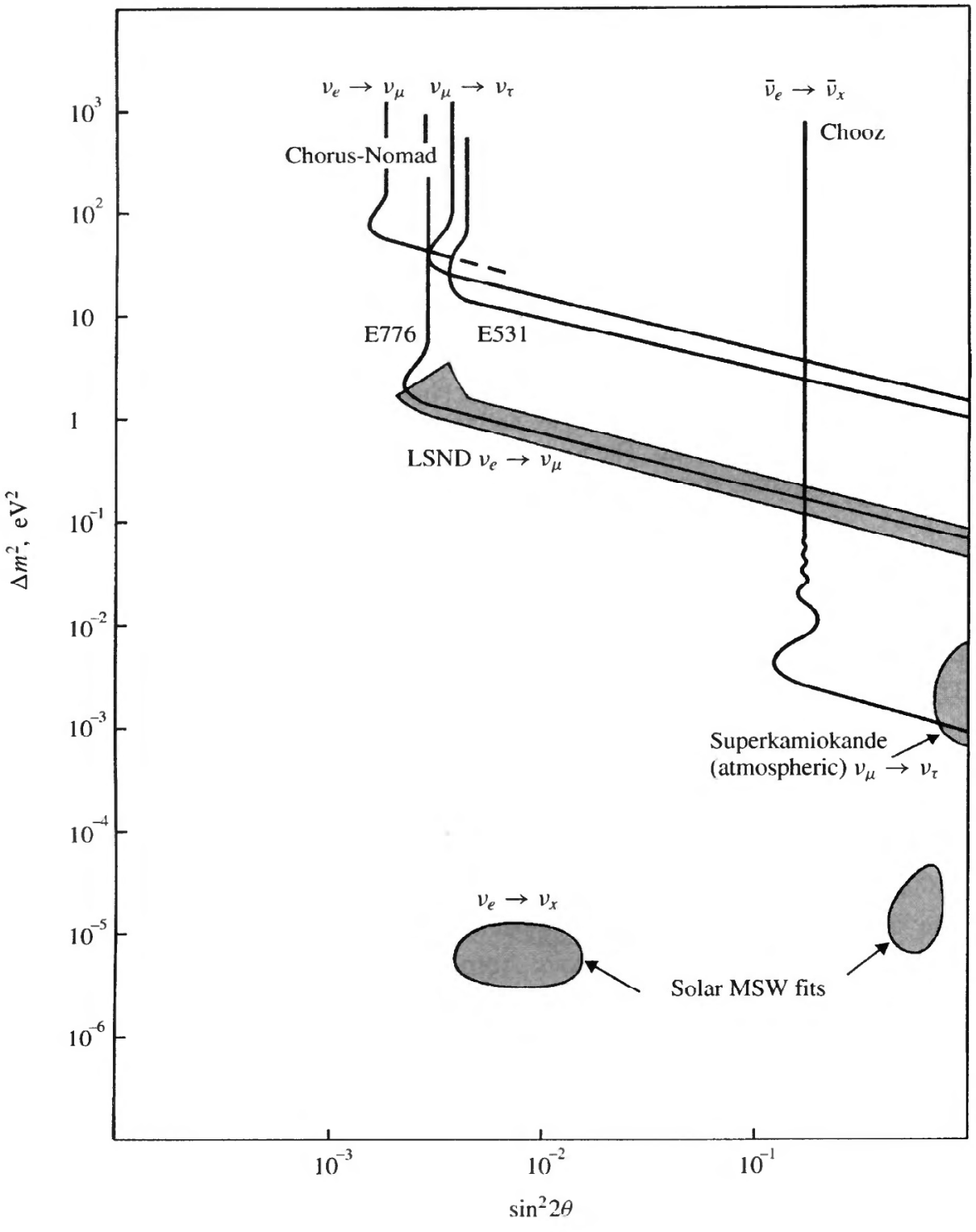

Fig. 9.6. A plot of Δm^2 versus $\sin^2 2\theta$ for two-flavour oscillations. The curves referring to reactor and accelerator-based data are 'exclusion plots' showing 90% confidence limits on these parameters, from the absence of any signal, that is, the region to the upper right of the curves is excluded. The positive results from solar and atmospheric neutrino experiments are also included, the shaded areas indicating the regions inside which the parameters must lie. The solar results are interpreted in terms of $\nu_e \rightarrow \nu_\mu$ oscillations and the atmospheric results are interpreted as $\nu_\mu \rightarrow \nu_\tau$ oscillations. The shaded area marked LSND represents a positive result from one accelerator experiment on the detection of $\bar{\nu}_\mu \rightarrow \bar{\nu}_e$ oscillations. This claim, however, has not been independently confirmed.

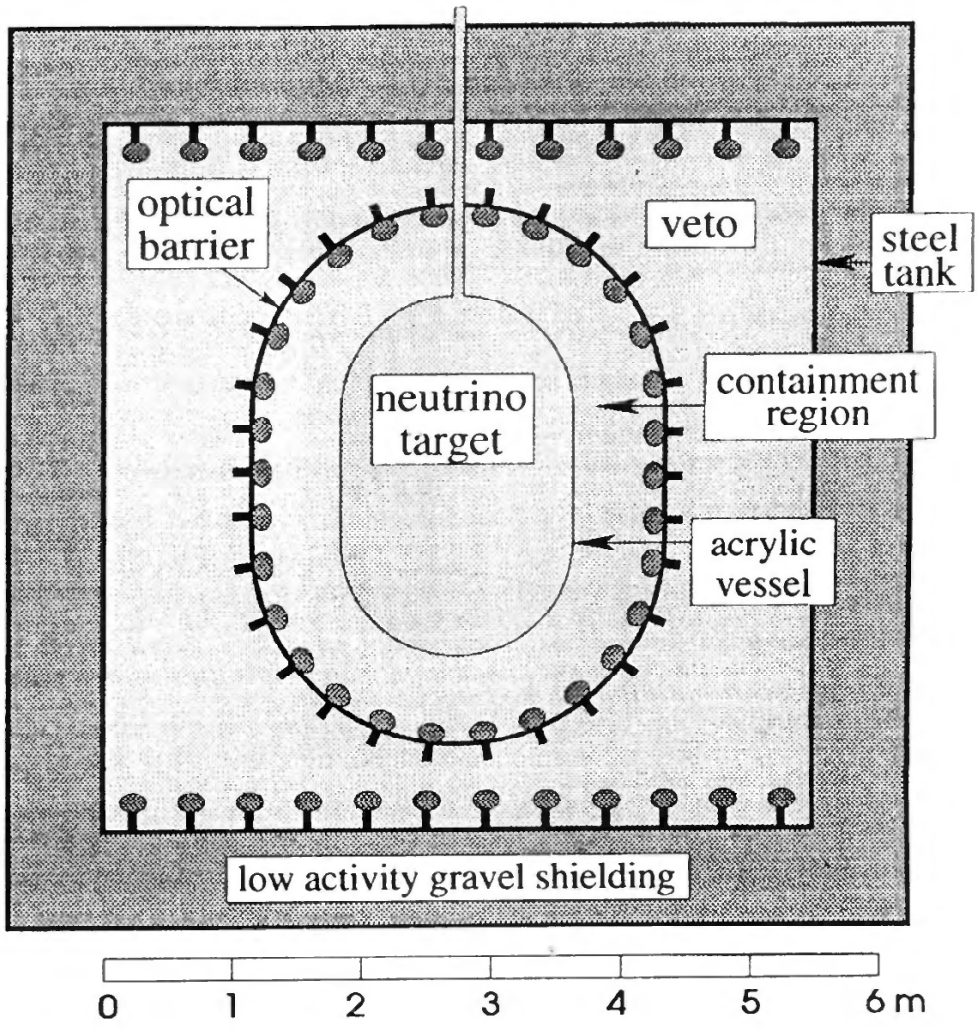

Fig. 9.7. Reactor experiment at CHOOZ (Ardennes) using a Gd-loaded scintillator to detect the reaction $\bar{\nu}_e + p \rightarrow e^+ + n$, similar to that used by Reines and Cowan (Figure 7.4) 40 years previously. (After Appolonio *et al.* 1998.)

ray muon background. The detector is contained in a steel tank buried under rock, of thickness equivalent to 300 m of water, and located 1.0 km from two reactors of total power 8 GW. Results of the experiment are shown in Figure 9.8, where the ratio of the observed and expected event rates is given as a function of energy.

Appearance experiments, where a second flavour of neutrino is detected in an initially single-flavour (or almost single-flavour) beam, can probe to much smaller mixing angles. In accelerator experiments with high energy pions and kaons as the source of neutrinos by decay in flight, for example, the beams consist of ν_μ or $\bar{\nu}_\mu$ from pion and kaon decay, with a small (0.5%) contamination of ν_e and $\bar{\nu}_e$ from $Ke3$ decay ($K^+ \rightarrow \pi^0 + e^+ + \nu_e$). For such appearance experiments, detection depends on observation of the corresponding charged lepton, and thus requires a beam energy above threshold for its creation. For example, to detect a $\nu_\mu \rightarrow \nu_\tau$ transition requires $E_\nu > 5$ GeV.

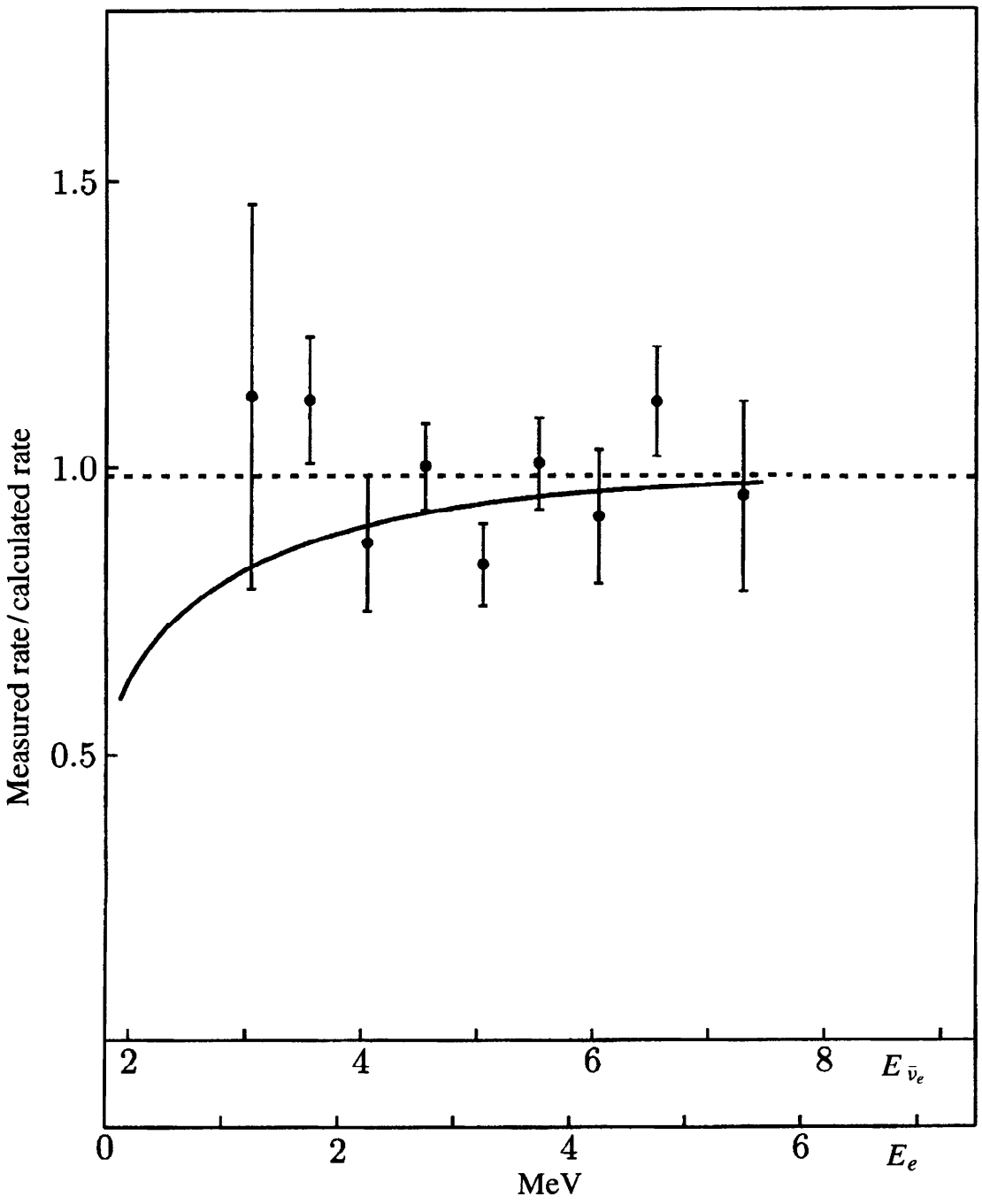

Fig. 9.8. The ratio of the observed and expected event rates for $\bar{\nu}_e + p \rightarrow n + e^+$ in the CHOOZ experiment of Figure 9.7, shown as a function of positron energy (or antineutrino energy, since $E_{\bar{\nu}_e} = E_{e^+} + 1.8$ MeV). The curve is that calculated from (9.16) for $\sin^2 2\theta = 1$, $\Delta m^2 = 10^{-3}$ eV^2 and $L = 1$ km. The average ratio is 0.98 ± 0.04 (broken horizontal line). The experiment finds no evidence for oscillations, with the limits on $\sin^2 2\theta$ and Δm^2 shown in Figure 9.6.

9.7.1 Solar neutrinos

Non-accelerator experiments, using the naturally occurring neutrinos from the sun and from the earth's atmosphere, have shown effects that can be and have been interpreted in terms of oscillations.

Figure 9.9 shows the expected flux at the Earth of neutrinos from the Sun. Solar neutrinos are emitted in a series of thermonuclear reactions in the solar core, the first and most important of which is the *pp* reaction

$$p + p \rightarrow d + e^+ + \nu_e + 0.42 \text{ MeV} \tag{9.17}$$

In addition, there are side reactions from other sources (principally from the reaction $pep \rightarrow p + n + \nu_e$ and from the production and decay of ^{7}Be and ^{8}B), which extend the spectrum to over 14 MeV energy. As can be seen from Figure 9.9, the total flux of neutrinos is dominated by the reaction (9.17). The solar energy comes from the chain

$$p + p \rightarrow d + e^+ + \nu_e + 0.42 \text{ MeV}$$

$$p + d \rightarrow {}^3\text{He} + \gamma + 5.51 \text{ MeV}$$

$${}^3\text{He} + {}^3\text{He} \rightarrow {}^4\text{He} + p + p + \gamma + 12.98 \text{ MeV}$$

so that the end result is

$$4p \rightarrow {}^4\text{He} + 2e^+ + 2\nu_e + 24.8 \text{ MeV} \tag{9.18}$$

Thus after annihilation of the positrons we expect a total of 26.9 MeV energy release. In these reactions, the neutrinos collect about 0.5 MeV on average, and the rest goes eventually to sunlight. For every 25 MeV of solar energy, therefore, two neutrinos are produced so that, from the solar constant at the Earth ($\simeq$ 2 cal cm^{-2} min^{-1}), we can immediately deduce that the total neutrino flux integrated over energy will be 6×10^{10} cm^{-2} s^{-1}. The reaction rate that one measures in a particular reaction, however, depends on the threshold energy and the cross-section above threshold as well as the flux. For the solar neutrino detection systems used to date, the cross-sections vary approximately as E_ν^3 so that, despite their much lower fluxes, the higher energy neutrinos from the *pep* reaction and from ^{7}Be and ^{8}B decay make significant contributions to the rates.

To date (1998) four major experiments have observed solar neutrino signals. The radiochemical detectors SAGE and GALLEX utilise some tens of tonnes of gallium, which has a low (0.2 MeV) threshold for the reaction

$$\nu_e + {}^{71}\text{Ga} \rightarrow {}^{71}\text{Ge} + e^- \tag{9.19}$$

Thus these detectors are sensitive to *pp* neutrinos (accounting for 60% of the expected counting rate) plus all those of higher energy (40%). The efficiency for detecting the few Ge atoms produced per day has been shown to be close to unity,

Table 9.3. *Solar neutrino experiments*

Experiment	Reaction	Observed/expected rate
SAGE	$^{71}\mathrm{Ga} + \nu_e \rightarrow {}^{71}\mathrm{Ge} + e^-$	0.56 ± 0.07
GALLEX	$^{71}\mathrm{Ga} + \nu_e \rightarrow {}^{71}\mathrm{Ge} + e^-$	0.53 ± 0.08
HOMESTAKE	$^{37}\mathrm{Cl} + \nu_e \rightarrow {}^{37}\mathrm{Ar} + e^-$	0.27 ± 0.04
KAMIOKANDE	$\nu_e + e^- \rightarrow \nu_e + e^-$	0.39 ± 0.06

using an artificial ^{51}Cr electron-capture neutrino source of known strength. The two experiments are in excellent agreement, as indicated in Table 9.3. The total event rate observed is $55 \pm 5\%$ of that expected from the 'Standard Solar Model' (SSM, see Bahcall 1989).

Another radiochemical experiment, which started 30 years ago and was the first to discover the solar neutrino deficit, uses a target of dichlorethylene (C_2Cl_4) and records the reaction

$$\nu_e + {}^{37}\mathrm{Cl} \rightarrow {}^{37}\mathrm{Ar} + e^- \tag{9.20}$$

This has a threshold of 0.8 MeV and so is not sensitive to neutrinos from the *pp* reaction. Again, the event rate is found to be low, in fact only about 30% of that expected.

Finally, the Kamiokande and Superkamiokande water Čerenkov detectors record electron recoils (in real time) from the elastic scattering process $\nu_e + e^- \rightarrow \nu_e + e^-$. With a minimum detectable electron recoil of order 5 or 6 MeV (below which background from natural radioactivity dominates), the experiment is sensitive only to ^{8}B neutrinos. Although there is still a large background due to cosmic ray muons, the signal is correlated with the Sun's direction and can be readily distinguished (see Problem 7.8 to estimate the angular correlation). The observed rate is about 40% of that expected. These results are summarised in Table 9.3.

The reason for the deficit of solar neutrinos could possibly be either some shortcoming in the SSM – for which there is absolutely no convincing evidence – or that something happens to the neutrinos in their passage from the solar core to the Earth. The favoured explanation of the effect is in terms of neutrino oscillations en route to Earth.

The fact that the observed rates are only half (or less) of the ones expected suggests that the mixing angle must be large, so that at the Earth the neutrinos should consist of about half ν_e and the rest, ν_μ or ν_τ. The latter cannot be detected in radiochemical experiments sensitive only to ν_e-induced charged-current processes. The Kamiokande experiments record both charged- and neutral-current scattering of ν_e and neutral-current scattering of ν_μ, ν_τ, but these latter only

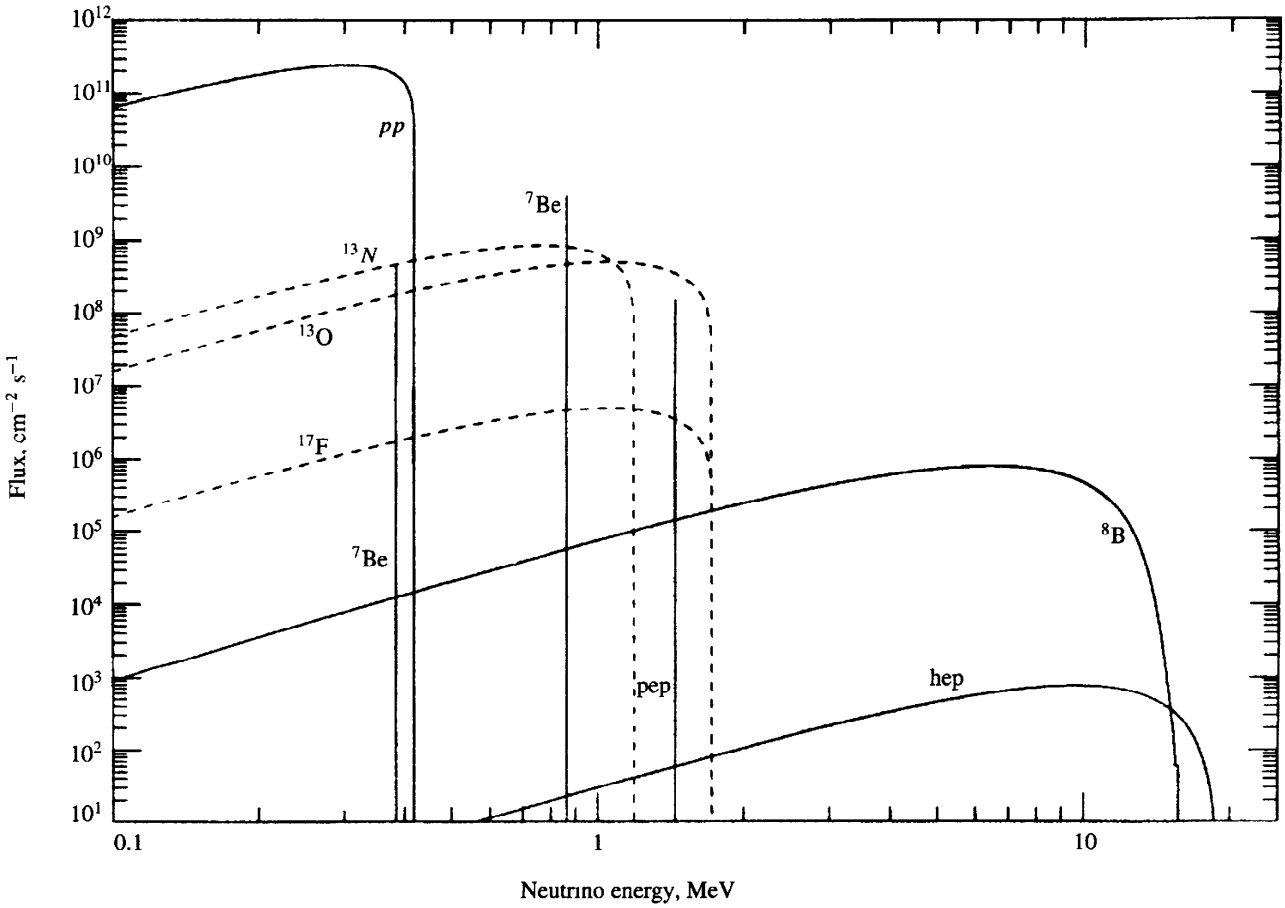

Fig. 9.9. Fluxes of solar neutrinos at the Earth from various reactions in the Sun (after Bahcall 1989).

contribute about 15% of the rate, and of course cannot be distinguished from ν_e scattering (see Problem 9.5). One experiment, called SNO, is sensitive separately to neutral-current events, since it is a heavy water Čerenkov device that records the reactions

$$\nu_e + d \rightarrow p + p + e^-$$

$$\nu_x + d \rightarrow n + p + \nu_x$$

The relative rates of these reactions should produce incontrovertible evidence that neutrinos have actually undergone flavour oscillations (rather than simply disappeared).

In a previous section we discussed neutrino flavour oscillations in vacuum. However, Wolfenstein (1978) and later Mikhaev and Smirnov (1986) pointed out that matter could modify the oscillations by what is now called the MSW effect, after the initials of its proponents. They pointed out that, while all flavours of neutrino undergo scattering from electrons via Z^0 exchange (neutral-current), in the MeV energy range only ν_e and $\bar{\nu}_e$ can scatter via $W^{\pm}$ exchange (charged-current), since ν_μ, ν_τ have insufficient energy to generate the corresponding charged leptons.

Hence the ν_e suffers an extra potential affecting the forward scattering amplitude, which leads to a change in effective mass:

$$V_e = G\sqrt{2}N_e$$

$$m^2 = E^2 - p^2 \rightarrow (E + V_e)^2 - p^2 \simeq m^2 + 2EV_e \tag{9.21}$$

$$\Delta m_m^2 = 2\sqrt{2}GN_eE$$

where N_e is the electron density, E the neutrino energy, G the Fermi constant and Δm_m^2 the shift in mass squared. Suppose now that the vacuum mixing angle θ_V is very small. Then from (9.12) in the simple case of two flavours built from two mass eigenstates, the ν_e will consist predominantly of ν_1 with a little ν_2. The matter density in the Sun (relative to water) varies from $\rho \sim 150$ at the centre to $\rho \sim 10^{-6}$ at the photosphere. If in some region, N_e and E are such that $\Delta m_m^2 \simeq \Delta m_v^2 = m_2^2 - m_1^2$, where m_m stands for matter and m_v for vacuum, it was shown that a resonant-type transition can occur. The actual condition is that

$$\Delta m_m^2 = \Delta m_v^2 \cos 2\theta_v \tag{9.22}$$

specifying from (9.21) a critical electron density for the transition. So basically what happens is that a ν_e starts out in the solar core, predominantly in what in a vacuum would be termed the ν_1 eigenstate of mass m_1, and the extra weak potential increases the effective mass of the ν_e to the mass value m_2, which is of course effectively the ν_μ flavour eigenstate in a vacuum. This mass eigenstate passes out of the sun without change provided that the interaction is adiabatic, i.e. the variation of N_e per oscillation length is small (if not, only partial conversion will take place).

So the end result is that the state of mass m_2, predominantly ν_μ, emerges from the Sun, a $\nu_e \rightarrow \nu_\mu$ conversion having taken place. Because this transition depends, from (9.21), on the neutrino energy, the suppression of the ν_e flux is also energy dependent, and it is possible to obtain differentially more suppression in the region $E = 2$–10 MeV than for $E < 2$ MeV. This was thought to provide a possible explanation of the different suppression factors in Table 9.3, with a vacuum mixing angle $\theta_v \simeq 2°$ and $\Delta m_v^2 \simeq 10^{-5}$ eV^2 as a favoured solution. Recent measurements of the electron recoil spectrum from the reaction $\nu + e \rightarrow \nu + e$ in the Superkamiokande experiment suggest however that another solution, with a much larger mixing angle is preferred.

9.7.2 Atmospheric neutrinos

The early experiments on cosmic rays in the late 1940s led to the discovery of pions and muons via their decays

$$\begin{aligned} \pi^+ &\to \mu^+ + \nu_\mu, \qquad \mu^+ \to e^+ + \nu_e + \bar{\nu}_\mu \\ \pi^- &\to \mu^- + \bar{\nu}_\mu, \qquad \mu^- \to e^- + \bar{\nu}_e + \nu_\mu \end{aligned} \tag{9.23}$$

The pions are produced by the interaction of primary protons and heavier nuclei above a few GeV energy incident on the Earth's atmosphere from outer space. Clearly, since, in terms of the amount of matter traversed, the total depth of the atmosphere is $X_0 \simeq 1030$ gm cm^{-2} and the nuclear interaction length is $\lambda \simeq 100$ gm cm^{-2}, the pions will be predominantly produced high in the atmosphere and, because of their short lifetime (26 ns), practically all charged pions (at least those with $E_\pi \ll 100$ GeV) will undergo decay in flight rather than nuclear interaction. The muon lifetime (2.2 μs) is a hundred times longer but, provided $E_\mu < 2$ GeV, practically all the muons will also decay in flight. For energies above 4 or 5 GeV, however, most of the muons have enough energy and, with $\gamma = E/(mc^2) > 50$, a sufficiently dilated lifetime that, despite the ionisation energy loss of 2 MeV per gm of air traversed, most can penetrate to sea level before decaying. Very high energy muons can of course penetrate deep underground, and solar and atmospheric neutrino experiments have therefore to be located deep underground in order to reduce this atmospheric muon flux. We expect, counting up the numbers in the pion and muon decays, that at sea level we will get approximately two ν_μ ($\bar{\nu}_\mu$) for every ν_e ($\bar{\nu}_e$); an exact calculation gives a ratio of 2.1 : 1. This ratio holds in the low energy region, $E_\nu < 1$ GeV. At higher energies, the ratio of muon to electron neutrinos is larger, since a smaller fraction of muons undergo decay in flight in the atmosphere (see also Problem 9.1).

After this preamble, let us first note that in the large (kilotonne) underground detectors built to search for proton decay (Section 9.5), atmospheric neutrino interactions, occurring at the rate of about 100 per kilotonne year, were considered to be an undesirable but ineradicable background that would set the ultimate limit on τ_p. However, this 'background' has turned out to provide very interesting results – an unexpected bonus for experiments which have so far failed to find proton decay. The ν_e and ν_μ rates, signalled by the production of electrons and muons respectively, are anomalous. The absolute values of the calculated fluxes are uncertain at the level of ±20%, but some of this uncertainty should drop out in comparing flux ratios, so what is often quoted is the ratio of ratios of event rates,

$$R = \frac{(N_\mu/N_e)_{\text{obs}}}{(N_\mu/N_e)_{\text{calc}}}$$

The results from five independent experiments all give $R < 1$, with an average value $R \simeq 0.6$. This result has been interpreted in terms of $\nu_\mu \rightarrow \nu_\tau$ oscillations, the allowed region in the Δm^2 versus $\sin^2(2\theta)$ plot being shown in Figure 9.6. More convincing evidence is provided from the zenith angle distribution of the muons produced in ν_μ events with muon energy above 1.3 GeV (see Figure 9.10). The path length L of the neutrino is a strong function of zenith angle, being typically 20 km for those coming downwards, 200 km for those travelling sideways and 10 000 km for those coming upwards from the atmosphere on the other side of the Earth. Of course, in these experiments one can only measure the zenith angle of the muon but, because of the higher neutrino energy, smearing effects resulting from the neutrino–muon angle are small, so that the muon angular distribution simulates closely that of the parent neutrino. Figure 9.10 shows the results.

The Superkamiokande experiment can also detect neutral-current events, in particular examples of single π^0 production ($\nu + N \rightarrow \nu + N + \pi^0$), by reconstructing the π^0 mass from the Čerenkov signals from $\pi^0 \rightarrow 2\gamma$. Even in the presence of oscillations no up–down asymmetry should be observed, as all flavours of neutrino will have the same neutral-current cross-sections. Indeed the observed ratio is consistent with unity.

To conclude this section: certain effects, i.e. the deficits of solar neutrinos and the anomalous flavour ratios and up–down asymmetries of atmospheric neutrinos, have been found and these can be interpreted in terms of flavour oscillations. If so, the neutrino mass differences and possibly the neutrino masses themselves are very small, of order 10^{-1}–10^{-3} eV. The very wide range in masses of the elementary particles, from 175 GeV for the top quark to only 10^{-12} GeV for neutrinos, is one of the most baffling features of high energy physics (see Figure 1.7). In grand unified theories, very massive (10^{17} GeV) RH Majorana neutrino states are postulated: these mix with the massless LH neutrinos of the Standard Model to give neutrino masses according to the so-called 'seesaw formula'

$$m_\nu \sim m_L^2 / M_{\mathrm{GUT}}$$

where m_L is some typical charged lepton or quark mass. So, on this scheme the tiny masses of (light) neutrinos are a manifestation of grand unification.

It needs to be emphasised that the actual *proof* of neutrino oscillations (as in K^0, $\bar{K}^0$ oscillations, for example) requires the observation of a *cycle* of oscillation, and this is likely to come only with the use of controlled beams from accelerators or reactors. Since the baselines involved in the atmospheric and solar experiments are 10^3–10^8 km, this proof is likely to be a formidable task.

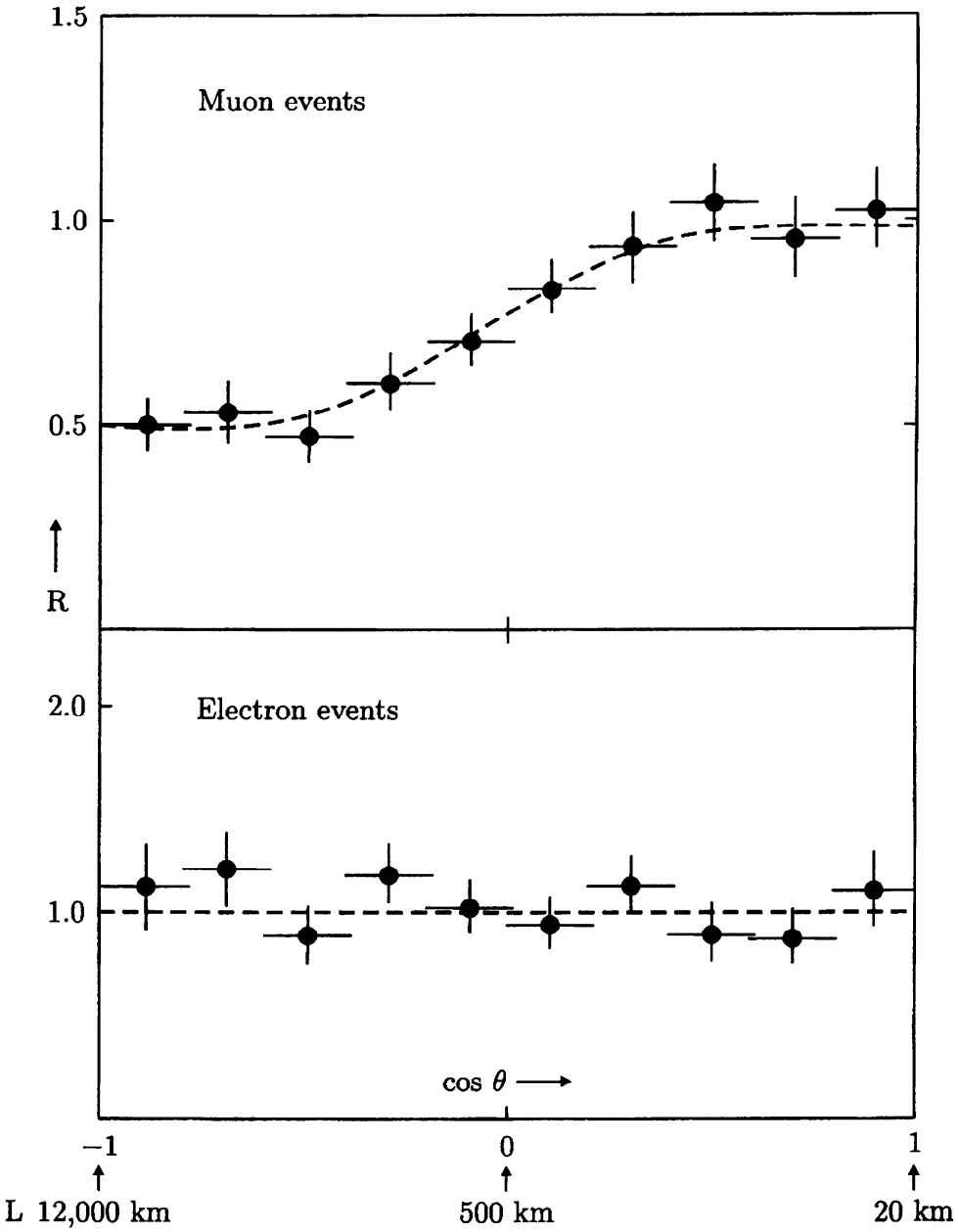

Fig. 9.10. Observed distributions in cosine of zenith angle of charged leptons produced in the interactions of atmospheric neutrinos in the Superkamiokande experiment (see Figure 9.4). The graphs indicate the ratio R of numbers of events observed with lepton momentum above 1.3 GeV/c, to the number expected in the absence of oscillations. The upper graph refers to muon events and the lower graph to electron events. The event separation is on the basis of the structure of the rings of Cerenkov light (see Figure 11.11). Muons produce rings with sharp edges, while electrons produce more diffuse rings as a result of radiation and pair production. The curves are the predictions for a model in which the ν_e component does not oscillate and where $\nu_\mu \rightarrow \nu_\tau$ oscillations are maximal, with $\sin^2(2\theta) = 1$ and $\Delta m^2 = 2 \times 10^{-3}$ eV^2. The up–down asymmetry for muons is clear evidence that the event rate is a function of zenith angle and hence of the neutrino path length L. Typical values of L are shown for $\cos\theta = +1, 0, -1$. (After Fukuda *et al.* 1998.)

9.8 Magnetic monopoles

In 1931 Dirac proposed that magnetic monopoles might exist with values of magnetic charge

$$g = n\left(\frac{4\pi\hbar c}{2e}\right) \tag{9.24}$$

where n is an integer. This formula is derived in standard texts on electromagnetism. In grand unified theories, the electric charge is one of the generators of the symmetry, and all particles must have the same unit of electric charge (or fraction of it, in the case of quarks), so charge quantisation occurs naturally. Then monopoles of charge g and mass $M_{\mathrm{GUT}}/\alpha \sim 10^{17}$ GeV are definitely predicted.

Searches for massive magnetic monopoles have been based on observing the change in flux $\Delta\phi = 4\pi g$ when a monopole traverses a (superconducting) coil, or by detecting the ionisation or excitation of atoms from the magnetic interaction of the pole with atomic electrons. Cosmological upper limits on the monopole flux are of the order of the so-called Parker bound, about 10^{-15} monopoles cm^{-2} sr^{-1} s^{-1}. This is the maximum flux that could be tolerated if monopoles were not to destroy the galactic magnetic field, of order a few microgauss.

In the Big Bang model of the universe described in Chapter 10, magnetic monopoles, if they existed, would have been produced in abundance, and with such large masses would have led to a closed universe, with an age very much less than the 10 Gyr of the actual universe. This difficulty can be avoided in the inflationary model of the early universe (Section 10.8), which predicts that the monopole density today would be infinitesimally small.

It may be noted from (9.24) that the coupling parameter α_M associated with the monopole charge g would be (for $n = 1$)

$$\alpha_M = \frac{g^2}{4\pi\hbar c} = \frac{1}{4}\left(\frac{4\pi\hbar c}{e^2}\right) = \frac{1}{4\alpha} = 34 \tag{9.25}$$

Thus, the duality of electric and magnetic charges exchanges a weakly coupled field theory, with $\alpha \ll 1$, for a strongly coupled field theory of $\alpha_M \gg 1$. There are speculations that such duality is not simply a property of electromagnetism but could hold in more general field theories, in particular in supersymmetric gauge theories and in string theories.

9.9 Superstrings

During the last decades, many attempts have been made to find a 'theory of everything', which in practice means incorporating a renormalisable field theory of gravity along with the other fundamental interactions into a single coherent model. The basic problem for a quantum field theory of gravity is that, just as in the Fermi theory of weak interactions, literally pointlike interactions lead to incurable divergences. This is overcome by replacing the point particles by *strings* of finite length. Since the only naturally occurring length in gravity is the Planck

length, the strings are expected to have dimensions of this order:

$$l_P = \frac{\hbar}{M_P c} = 1.6 \times 10^{-35}\ \text{m} \tag{9.26}$$

where the Planck mass is

$$M_P = \sqrt{\hbar c / G_N} = 1.2 \times 10^{19}\ \text{GeV}$$

as in (2.12). Elementary particles can be represented as closed strings (loops) with the different particles corresponding to different modes of oscillation of the loop. The theory, in order to be renormalisable, has to be formulated in 10 or more dimensions, all but the normal four space–time dimensions being 'curled up' or compacted within size l_P and hence undetectable. Although originally formulated in connection with strong interactions, it was found early on that the graviton, the massless spin 2 mediator of the gravitational field, occurred naturally in the supersymmetric version of the theory – called superstring theory. Since the natural energy scale is 10^{19} GeV, to get predictions within the accessible energy range of accelerators is a truly formidable task.

The known elementary particles are associated with string excitations of lowest, i.e. effectively zero, mass compared with M_P, and include those of spin $J = 0, \frac{1}{2}, 1, \frac{3}{2}$ and 2, to be identified possibly with Higgs scalars, quarks, leptons, gauge bosons and, most importantly, a graviton of spin 2 and its SUSY partner, the gravitino of spin $\frac{3}{2}$. An important feature of string theory in general is that closed strings representing the conventional elementary particles are not the only topologies that are possible. In grand unified theories, the strings can be identified with the lines of the gauge field. W's, Z's etc. correspond to simple closed loops, which can disappear by decay. But because of the non-Abelian nature of the fields, they can interact with each other and the strings can get tangled up in knots or so-called topological discontinuities, which are permanent. It is proposed that the massive GUT monopoles can be examples of such knots.

At the present time, string theory is under rapid development. Nobody yet knows, and probably will not know for some years, whether it has any relevance to the real world.

Problems

9.1 High energy pions decay in flight in the atmosphere. Calculate the mean fractional pion energy received by the muon and by the neutrino in $\pi^+ \to \mu^+ + \nu_\mu$. Estimate also the mean fractional energy of the pion carried by each of the neutrinos (antineutrinos) in the subsequent muon decay, $\mu^+ \to e^+ + \nu_e + \bar{\nu}_\mu$. Assume that all neutrinos are massless and neglect ionisation energy loss in the atmosphere and polarisation effects in muon decay.

(*Note*: Since the cosmic ray energy spectrum is steeply falling (as $E^{-2.75}$), it is not enough that the *number* of muon neutrinos is twice the number of electron neutrinos. They must have similar fractional energies, too.)

Estimate the probability of the decay in flight of a 10 GeV muon travelling vertically downwards and produced 15 km above the Earth. Take the rate of energy loss of the muon as 2 MeV g^{-1} cm^2 of matter traversed. ($m_\pi c^2 = 139.6$ MeV, $m_\mu c^2 = 105.7$ MeV; $\tau_\mu = 2.20$ μs, scale height of atmosphere = 6.5 km; atmospheric depth $=1030$ g cm^{-2}.)

9.2 The unit of radiation dosage is the rad, corresponding to an energy liberation in ionisation of 100 erg g^{-1}. The annual permissible body dose for a human is cited as 5 rad. Assuming that 100 times this dose would lead to the extinction of advanced life forms, what limit does this set on the proton lifetime, assuming that in proton decay a substantial fraction of the total energy released is deposited in body tissue?

9.3 In an experiment using a reactor as the source, the observed rate of $\bar{\nu}_e$ reactions at a distance of 250 m from the reactor core is found to be 0.95 ± 0.10 of that expected. If the mean effective antineutrino energy is 5 MeV, what limits would this place on a possible neutrino mass difference, assuming a mixing angle $\theta = 45°$?

9.4 Use (9.7) to estimate the proton lifetime, if $M_X = 3 \times 10^{14}$ GeV, $\alpha_{\text{GUT}} = \frac{1}{43}$ and $A = 1$.

9.5 Estimate the relative event rates of neutrino–electron scattering for ν_e, ν_μ and ν_τ neutrino flavours. Assume for simplicity that all electron recoils of whatever energy can be detected (take $\sin^2 \theta_W = 0.23$).

10

Particle physics and cosmology

In this chapter, we discuss the connection between particle physics and the physics of the cosmos. This is not a text on cosmology or astrophysics, and all that we shall do here is reproduce a few of the essential features of the 'Standard Model' of the early universe, insofar as they affect and are affected by particle physics.

The presently accepted cosmological model rests on four main pieces of experimental evidence:

(i) Hubble's law;
(ii) the cosmic microwave background radiation;
(iii) the cosmic abundances of the light elements;
(iv) anisotropies in the background radiation, of the right magnitude to seed the formation of large-scale structure (galaxies, clusters, superclusters etc.).

10.1 Hubble's law and the expanding universe

As described in Section 1.9, Hubble in 1929 observed that spectral lines from distant galaxies appeared to be redshifted and interpreted this as a result of the Doppler effect associated with their velocity of recession $v = \beta c$, according to the formula

$$\lambda' = \lambda\sqrt{(1+\beta)/(1-\beta)} = \lambda(1+z) \tag{10.1}$$

where λ is the wavelength in the rest frame of the source, and $z = \Delta\lambda/\lambda$ is the redshift parameter, which has currently been measured up to values of $z \simeq 5$. Hubble deduced that for a particular galaxy, the velocity v is proportional to the distance r from Earth,

$$v = Hr \tag{10.2}$$

where H is the so-called Hubble constant. Figure 1.11 shows the evidence supporting Hubble's law. Although, for $z \ll 1$ (10.1) can indeed be interpreted as a

Doppler shift, the factor $1+z$ more generally describes an overall homogeneous and isotropic expansion of the universe (analogous to the stretching of a rubber sheet in the two-dimensional case), which expands all lengths – be they wavelengths or distances between galaxies – by a time-dependent universal factor $R(t)$. Thus the distance, say from the Earth to some distant galaxy will be

$$r(t) = R(t)r_0 \tag{10.3}$$

where the subscript '0' here and in what follows refers to quantities at the present time, $t = t_0$, so that $R(t_0) = R_0 = 1$. Then

$$v(t) = \dot{R}(t)r_0$$

and

$$H = \frac{\dot{R}}{R} \tag{10.4}$$

In principle, H will depend on time because of the retarding effects of gravity on the expanding material. Its value today is

$$H_0 = 100h_0 \text{ km s}^{-1} \text{ Mpc}^{-1} \tag{10.5}$$

Here the megaparsec has the value 1 Mpc = 3.09×10^{19} km. The quantity h_0 has been the subject of much discussion in recent years but its value seems to be settling at about

$$h_0 = 0.7 \pm 0.1 \tag{10.6}$$

The origin, $t = 0$ of the expansion has been called the Big Bang, as proposed originally by Lemaitre in 1923 and Gamow in 1948. The Big Bang model makes the strong postulate that the universe originated as a singularity of effectively infinite energy density at a point in space–time.

10.2 Friedmann equation

The evolution of the universe with time is described by the solution of Einstein's field equations of general relativity. For a homogeneous and isotropic distribution of matter, the temporal development is described by the Friedmann equation

$$H^2 = \left(\frac{\dot{R}}{R}\right)^2 = \frac{8\pi G_N \rho}{3} - \frac{Kc^2}{R^2} + \frac{\Lambda}{3} \tag{10.7}$$

Here G_N is the gravitational constant, ρ is the homogeneous mass or energy density, and K and Λ are constants. The cosmological constant Λ is certainly very small and may be zero. It was originally introduced by Einstein before the advent of the Big Bang scenario in order to avoid spontaneous collapse of the universe. At

the present time, the energy density of the universe is dominated by non-relativistic matter and in this case the form of (10.7) can be understood from non-relativistic Newtonian mechanics. To avoid writing r_0 in (10.3) repeatedly we can without loss of generality choose units such that $r_0 = 1$. Consider a point mass m distant R from Earth, being attracted by the mass $M = 4\pi R^3\rho/3$ inside the sphere of radius R, where ρ is the density. Then

$$m\ddot{R} = -\frac{MmG_N}{R^2}$$

which upon integration gives

$$\frac{1}{2}m\dot{R}^2 - \frac{mMG_N}{R} = \text{constant} = -\frac{1}{2}Kc^2m \tag{10.8}$$

Choosing the constant of integration to agree with (10.7), and multiplying both sides by $2/(mR^2)$, we obtain the Friedmann equation for $\Lambda = 0$. The terms on the left-hand side of (10.8) correspond to the kinetic and potential energies of the mass m, so the right-hand side measures the total energy. $K = -1$ corresponds to positive total energy and describes an open universe expanding without limit, with velocity $\dot{R} \to c$ for R large. In this case, the curvature term $-Kc^2/R^2$ is positive. $K = +1$ is the case of negative total energy, i.e. a closed universe with negative curvature, which reaches a maximum radius and then collapses. $K = 0$ is the simplest case, where the kinetic and potential energies just balance so that both the total energy and the curvature are zero. This is the so-called flat universe.

These three cases are illustrated in Figure 10.1. Upon integrating (10.7) for $K = \Lambda = 0$, for a universe dominated by non-relativistic matter with conserved mass M we get

$$R = \left(\frac{9G_NM}{2}\right)^{1/3} t^{2/3} \tag{10.9}$$

so that $H_0^{-1} = R/\dot{R} = 3t_0/2$. The present age of the universe is then (using (10.7))

$$t_0 = \frac{1}{\sqrt{6\pi G_N\rho_0}} = \frac{2}{3}H_0^{-1} = \frac{6.6}{h_0}\ \text{Gyr} \tag{10.10}$$

With the value of h_0 in (10.6) this gives $t_0 \simeq 8$–11 Gyr. Other estimates of age are based on white dwarf cooling rates, on stellar evolutionary rates in globular clusters and on dating from uranium isotopic ratios. Uncertainties arise, e.g. because of possible errors on the distance scales; thus if globular clusters were more distant they would be intrinsically brighter, implying a faster evolution and a reduced value of t_0. These estimates straddle the range $t_0 = 10$–14 Gyr. Any possible conflict between these figures and that in (10.10) could be avoided by dropping the

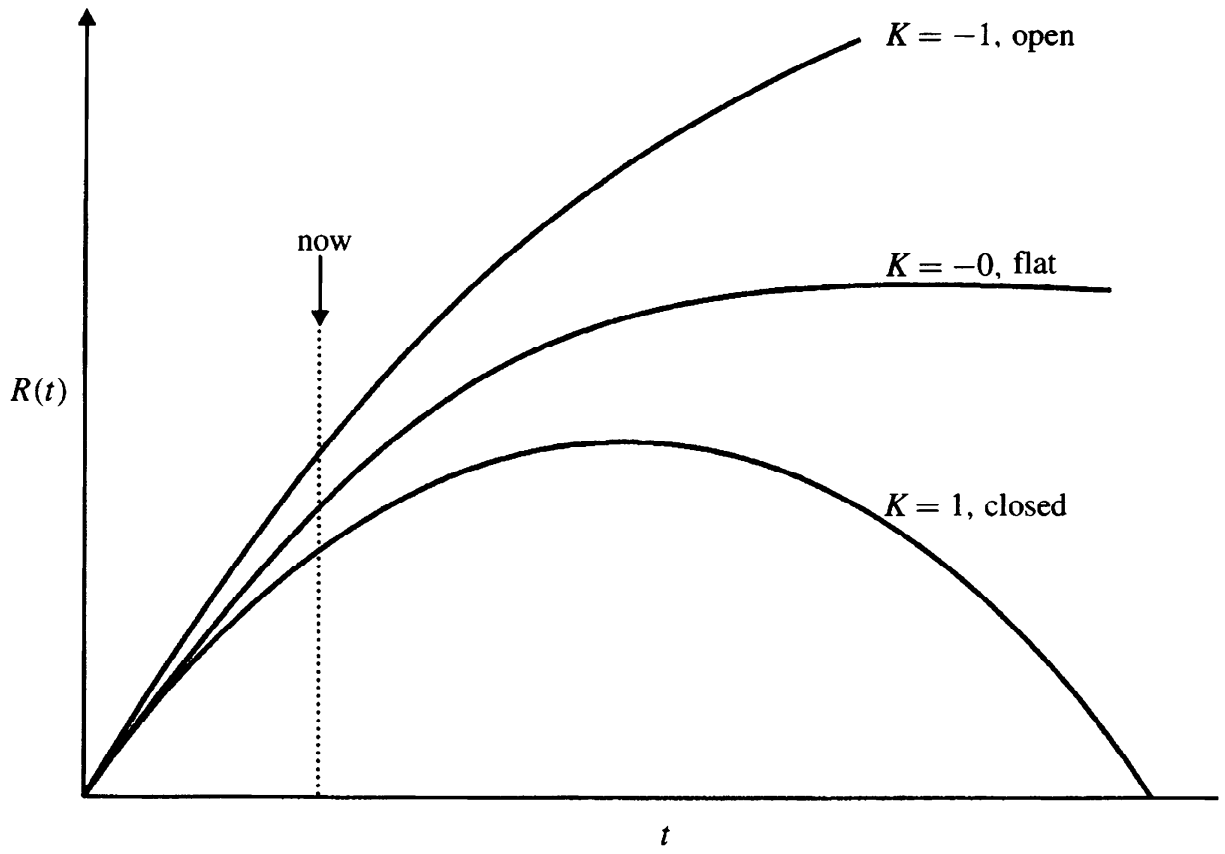

Fig. 10.1. Scale parameter R versus time for different K-values. At the present time (vertical broken line), the universe is still expanding, but the uncertainties are such that we can only be sure that we are rather close to the $K = 0$ curve.

assumption $K = \Lambda = 0$. Thus, either a value of $K = -1$ or a finite cosmological constant $\Lambda > 0$ increases the value of t_0 deduced from the Friedmann equation.

For the case $K = \Lambda = 0$ one obtains, upon integrating (10.7) a value for the *critical density* that will just close the universe,

$$\rho_c = \frac{3}{8\pi G_N} H_0^2 = 1.88 \times 10^{-26} h_0^2 \text{ kg m}^{-3} \tag{10.11}$$

The ratio of the actual density to the critical density is given by the *closure parameter* Ω, which from (10.7) is given by

$$\Omega = \frac{\rho}{\rho_c} = 1 + \frac{Kc^2}{H^2 R^2} \tag{10.12}$$

Clearly, if $K = -1$ then $\rho < \rho_c$ and $\Omega < 1$ so that from (10.10) $t_0 > 2H_0^{-1}/3$. The presently measured values of Ω for different components are as follows.

(i) For visible, i.e. luminous (baryonic) matter, in the form of stars, gas, dust etc., one finds

$$\rho_{\text{lum}} \simeq 2 \times 10^{-29} \text{ kg m}^{-3}$$

or

$$\Omega_{\text{lum}} \simeq 0.003 h_0^{-2} \tag{10.13}$$

(ii) The total density of baryons, visible or invisible, inferred from the model of baryogenesis in the early universe, to be described in Section 10.5, is found to be

$$\rho_{\text{baryon}} = (3 \pm 1.5) \times 10^{-28} \text{ kg m}^{-3}$$

or

$$\Omega_{\text{baryon}} \simeq (0.01\text{–}0.03) h_0^{-2} \tag{10.14}$$

(iii) The total matter density, as inferred from the gravitational potential energy deduced from galactic rotation curves (see Section 10.7) is larger by about two orders of magnitude: the bulk of the matter in the universe must be in the form of so-called *dark matter*. The estimated value of the total matter density is

$$\rho_m \geq 5 \times 10^{-27} \text{ kg m}^{-3}$$

or

$$\Omega_m \geq 0.3 \tag{10.15}$$

The above numbers lead to two important conclusions: most of the baryonic matter is non-luminous and most of the matter in the universe is non-baryonic. While there is considerable uncertainty in the value of the closure parameter Ω summed over all components, it is remarkable that of all the possible values the one estimated is quite close to unity, the value predicted by the inflationary model of the early universe described later. We may also note from (10.12) that, in the single case $K = \Lambda = 0$, $\Omega = 1$ and has this value for all time.

10.3 Cosmic microwave radiation: the hot Big Bang

On the one hand, assuming matter to have been conserved the matter density of the universe will vary as $\rho_m \propto R^{-3}$. On the other hand, the density of radiation, assuming it to be in thermal equilibrium, varies with temperature as $\rho_r \propto T^4$ (Stefan's law). Since there is no absolute scale of distance, the wavelength of the radiation λ can only be proportional to the expansion parameter R, so the frequency and therefore the mean energy per photon $h\nu \sim kT$ are both proportional to R^{-1} (k is Boltzmann's constant). While the number of photons varies as R^{-3}, the energy density of radiation ρ_r varies as R^{-4}, the extra factor of R^{-1} being simply the result of the redshift, which will in fact apply to any relativistic particles and not just photons.

Thus, while the matter density dominates today, at early enough times and small values of R, radiation must have been dominant. Then the second and third terms

on the right-hand side of (10.7) can be neglected in comparison with the first, varying as $1/R^4$, so that

$$\dot{R}^2 = \frac{8\pi G_N}{3}\rho_r R^2$$

Also, since $\rho_r \propto R^{-4}$,

$$\frac{\dot{\rho}_r}{\rho_r} = -\frac{4\dot{R}}{R} = -4\left(\frac{8\pi G_N \rho_r}{3}\right)^{1/2}$$

which upon integration gives for the energy density (rather than the mass density)

$$\rho_r = \left(\frac{3c^2}{32\pi G_N}\right)\frac{1}{t^2} \tag{10.16}$$

For a photon gas in thermal equilibrium

$$\rho_r = aT^4 = \frac{4\sigma}{c}T^4 = \left(\frac{\pi^4}{15}\right)\frac{(kT)^4}{\pi^2\hbar^3c^3} \tag{10.17}$$

where a is the radiation constant and

$$\sigma = \frac{\pi^2 k^4}{60\hbar^3 c^2}$$

is the Stefan–Boltzmann constant. From (10.16) and (10.17) we obtain a relation between the temperature of the radiation and the time of expansion:

$$kT = \left(\frac{45\hbar^3c^5}{32\pi^3 G_N}\right)^{1/4}\frac{1}{t^{1/2}} \approx \frac{1\ \text{MeV}}{t^{1/2}} \tag{10.18}$$

where t is in seconds. The corresponding value of the temperature itself is

$$T \approx \frac{10^{10}\ \text{K}}{t^{1/2}} \tag{10.19}$$

Since T falls as $1/R$, R increases as $t^{1/2}$ while the temperature T falls as $t^{-1/2}$. Thus, the universe started out as a hot Big Bang.

One of the major discoveries in astrophysics was made in 1965: this was the first observation of the isotropic cosmic microwave radiation, by Penzias and Wilson, which has been of fundamental significance for our understanding of the development of the universe. Figure 10.2 shows recent data on the spectral distribution of the radiation measured with the COBE satellite, which is exactly that predicted for a black body at $T = 2.73 \pm 0.01$ K. This microwave radiation is far too intense to be of stellar origin, and Gamow had long ago speculated that a relic of the Big Bang would indeed be a photon fireball cooled by expansion to a few kelvins. This distribution is *the* black body spectrum *par excellence*. From (10.18) we may crudely estimate the energy of the radiation today, i.e. for

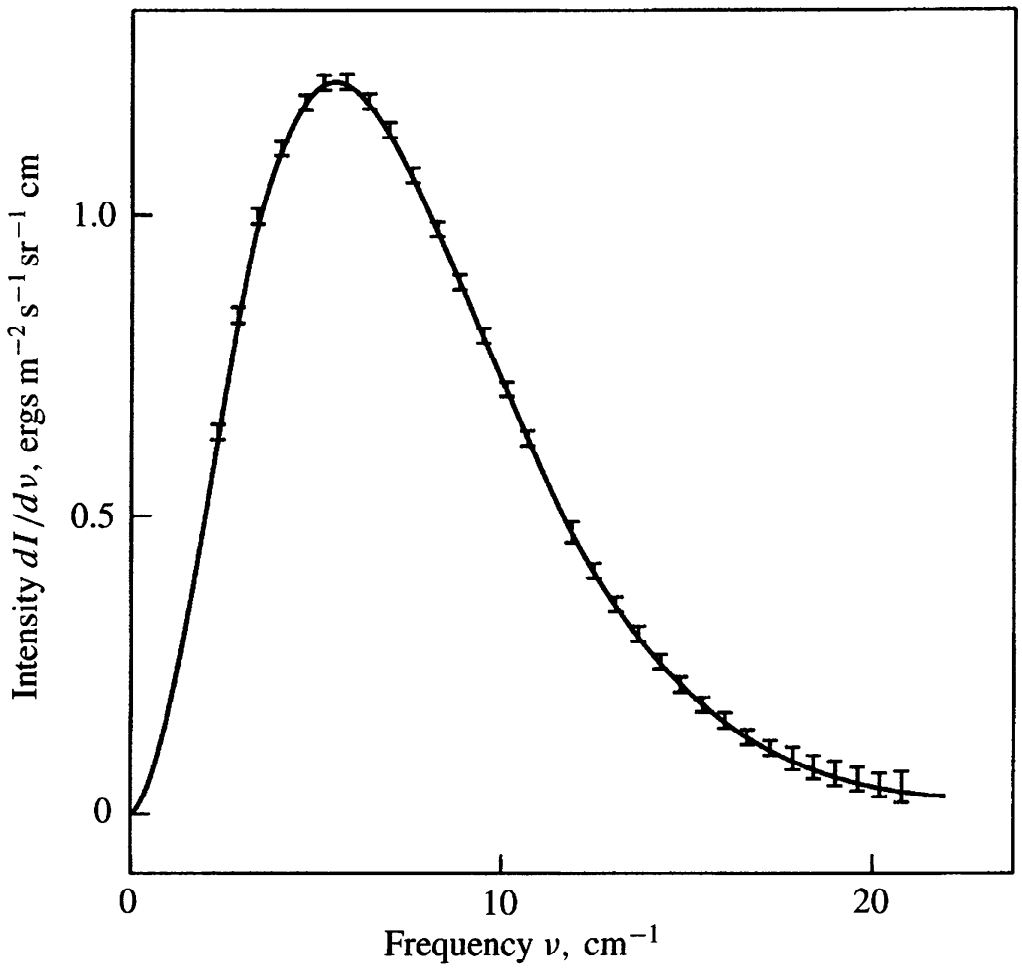

Fig. 10.2. Recent data on the spectral distribution of the cosmic microwave radiation, obtained with the COBE satellite. The curve shows the Planck black body distribution for $T = 2.73$ K.

$t_0 \sim 10$ Gyr $\sim 10^{18}$ s. It is $kT_0 \sim 1$ meV (milli-electron volt) corresponding to a temperature of a few kelvins. (This will be an overestimate of T_0 since the radiation has cooled more quickly, as $T^{-2/3}$, during the later matter-domination era.) This observation of the cosmic microwave background radiation has been the second plank of support for the Big Bang hypothesis.

Observation on microwave molecular absorption bands in very distant gas clouds has made it possible to estimate the temperature of the background radiation at much earlier times, when these signals left the source. At such times the wavelength would have been reduced, and the temperature increased, by the factor $1 + z$ in (10.1). In this way it has been possible to follow the dependence of kT on redshift z up to $z \simeq 4$.

The spectrum of black body photons of energy $E = pc = h\nu$ is given by the Bose–Einstein distribution describing the number of particles per unit volume in the momentum element $p \to p + dp$,

$$N(E)dp = \frac{p^2 dp}{\pi^2 \hbar^3 [\exp(E/kT) - 1]} \left(\frac{g_\gamma}{2}\right) \tag{10.20}$$

where $g_\gamma = 2$ is the number of spin substates of the photon. The total energy density integrated over the spectrum is readily calculated to have the value ρ_r in the right-hand expression in (10.17). The number of photons per unit volume is†

$$N_\gamma = \frac{2.404}{\pi^2}\left(\frac{kT}{\hbar c}\right)^3 = 410.9\left(\frac{T}{2.726}\right)^3 = 411 \text{ cm}^{-3} \tag{10.21}$$

while the energy density from (10.17) is

$$\rho_r = 0.261 \text{ MeV m}^{-3}$$

The equivalent mass density is

$$\rho_r/c^2 = 4.65 \times 10^{-31} \text{ kg m}^{-3} \tag{10.22}$$

some four orders of magnitude less than the presently estimated matter density ρ_m in (10.15).

The angular distribution of the microwave radiation at Earth shows a significant (10^{-3}) anisotropy. The bulk of this can be ascribed to the velocity of the Earth with respect to the local galactic cluster, which is about 600 km s^{-1}, providing an anisotropy v/c. After allowing for this, a tiny anisotropy still remains. Such anisotropy is of fundamental importance, as it reflects fluctuations at the level of $\sim 10^{-4}$ in the matter density. Such fluctuations are found to be exactly of the right order of magnitude to seed the large-scale structure in the universe. This developed after radiation and matter decoupled, allowing condensation to stars and later the formation of galaxies, then galactic clusters, superclusters, voids and structures at the very largest scales.

The expression (10.18) for the temperature as a function of time applies if the radiation consists of photons. In general, relativistic fermions, provided they are stable enough, will also contribute to the energy density. For a fermion gas, the Fermi–Dirac distribution for the number density analogous to (10.20) is

$$N(E)dp = \frac{p^2 dp}{\pi^2\hbar^3[\exp(E/kT)+1]}\left(\frac{g_f}{2}\right) \tag{10.23}$$

where $E^2 = p^2c^2 + m^2c^4$, m is the fermion mass and g_f is the number of spin substates. Referring to the integrals in the footnote below, the total energy density

† Relevant integrals over the Bose–Einstein and Fermi–Dirac distributions in the relativistic limit are as follows:

$$\int \frac{x^3dx}{e^x-1} = \frac{\pi^4}{15} \qquad \int \frac{x^2dx}{e^x-1} = 2.404$$

$$\int \frac{x^3dx}{e^x+1} = \frac{7}{8}\times\frac{\pi^4}{15} \qquad \int \frac{x^2dx}{e^x+1} = \frac{3}{4}\times 2.404$$

analogous to (10.17), for the relativistic limit $kT \gg mc^2$ and $E = pc$ is given by

$$\rho_f = \frac{7}{8}\left(\frac{\pi^4}{15}\right)\frac{(kT)^4}{\pi^2\hbar^3c^3}\left(\frac{g_f}{2}\right) \tag{10.24}$$

For a mixture of relativistic fermions and photons, therefore, we have to multiply the energy density in (10.17) by a factor

$$\mathcal{N} = \frac{1}{2}\left(g_\gamma + \frac{7}{8}\sum g_f\right) \tag{10.25}$$

We have concluded in this text that the fundamental particles as of today (1999) are the quarks and leptons and the bosons mediating their interactions. All these particles would have been created in the Big Bang, e.g. as fermion–antifermion pairs. As the expansion proceeded and the temperature fell, massive bosons like $W^\pm$ and Z^0 would be rapidly lost by decay (in 10^{-23} s) once the value of kT fell well below M_W. The same fate would apply to any new massive particles associated with supersymmetry. Similarly, unstable hadrons built from the primordial quark–antiquark soup would also disappear by decay, once kT fell below the strong scale parameter Λ(QCD). The only stable hadrons surviving this era would be the proton and neutron and their antiparticles. However, once kT fell below 100 MeV or so, virtually all but a tiny fraction of nucleons and antinucleons would annihilate to radiation. Equally the heavy leptons τ and μ would disappear by decay within the first microsecond. This would leave, apart from photons, the e^-, ν_e, ν_μ, ν_τ leptons and their antiparticles, giving in (10.25) $\sum g_f = 4+2+2+2$ (recalling that there are two spin states for electrons but only one for neutrinos), while $g_\gamma = 2$ so that $\mathcal{N} = \frac{43}{8}$. The effect is to multiply the value of kT in (10.18) by a factor $\mathcal{N}^{-1/4}$, which in this case has the value 0.66 instead of unity.

10.4 Radiation and matter eras

It is apparent from (10.18) and (10.25) that at extremely early times and high temperatures and particle number densities, the various types of established elementary fermion and boson (as well, possibly, as some yet to be discovered) would have been in thermal equilibrium and thus present in comparable numbers (assuming $kT \gg Mc^2$). The condition for thermal equilibrium is that the time between collisions, i.e. the inverse of the collision rate W for a particular type of particle, should be short compared with the age of the universe at that time. The collision rate W equals $\langle Nv\sigma\rangle$, where N is the number density and σ the cross-section for collision with some other particle, and an average is taken over

the spectrum of relative velocity v. The requirement then is that

$$W \gg t^{-1}$$

There are two reasons why particle numbers fall below the equilibrium ratios. First, kT can fall below the threshold energy for production of that particle. For protons and antiprotons, for example, this will happen for the reversible reaction $\gamma + \gamma \rightleftharpoons p + \bar{p}$, when $kT \ll M_p c^2$; the nucleons and antinucleons that annihilate are then no longer replaced by fresh production. (Not quite all the nucleons disappear: a tiny residue remains, to form the material universe as discussed later). Since all hadrons have $Mc^2 > 100$ MeV, then when kT falls below this value, the densities of all types of unstable hadron will drop to zero through decay to leptons, photons and nucleons. Only the nucleons are stable enough to leave a (small) residue.

Second, even if there is no threshold, particles fall out of equilibrium if the production cross-section, while not zero, becomes so small that it cannot sustain a sufficient reaction rate W. This is the case for the weak reaction

$$e^+ + e^- \rightleftharpoons \nu + \bar{\nu}$$

for $kT < 3$ MeV, i.e. when $t > 10^{-2}$ s. Thereafter the neutrino fireball is decoupled from matter and expands independently, as discussed in subsection 10.7.2 below (see also Problem 10.3).

For some 10^5 years after the Big Bang, matter – consisting of protons, electrons and hydrogen atoms – was in equilibrium with the photons, via the process

$$e^- + p \rightleftharpoons \gamma + H + Q \tag{10.26}$$

where $Q = 13.6$ eV is the ionisation potential of hydrogen. The mean photon energy at temperature T is approximately $2.7kT$, which equals Q when $kT = 5$ eV. However, the number density of photons exceeds by a factor of one billion that of the matter particles; consequently a minute fraction of the photons in the high energy tail of the black body spectrum can maintain the equilibrium, and it is only at a much lower temperature, $kT = 0.3$ eV, that matter becomes transparent to radiation and the two decouple. The corresponding decoupling time from (10.18) is $t_d = 10^{13}$ s or 3×10^5 yr. It turns out, coincidentally, that the energy density of matter (varying as T^{-3}) becomes equal to that of radiation (varying as T^{-4}) at a not much later time, i.e. $t \simeq 10^6$ yr. Thereafter, matter started to dominate the energy density of the universe and has thus done so for 99.8% of its age. The variation of kT with age t through the radiation and matter eras is shown in Figure 10.3. Only after radiation and matter decoupled could there be formation of atoms and molecules and could the 10^{-4} anisotropies in the energy density lead to the development of large-scale structures.

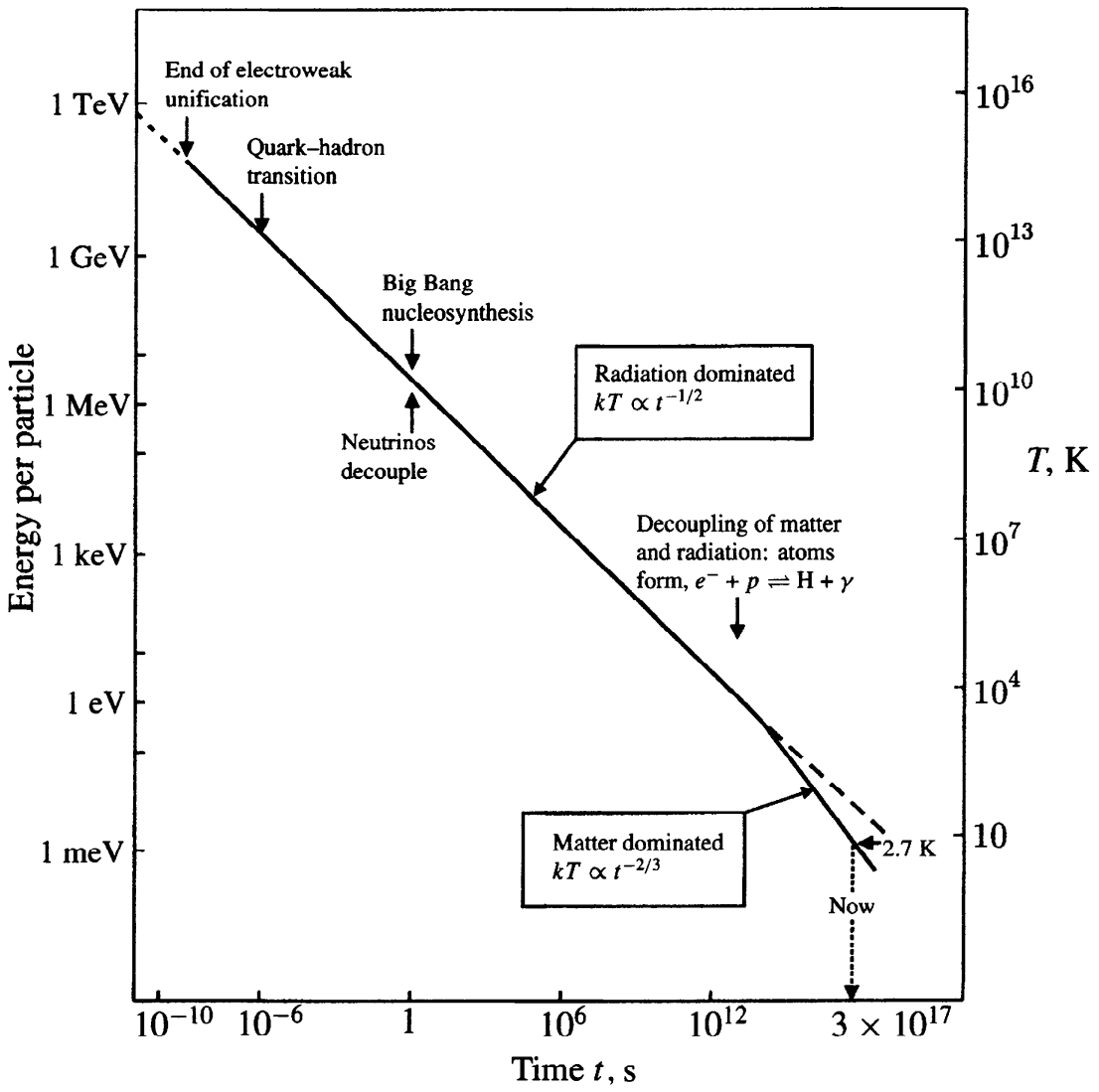

Fig. 10.3. Evolution of the temperature of the universe with time in the Big Bang model, with the various eras indicated.

10.5 Nucleosynthesis in the Big Bang

We have seen that, after $t \sim 1$ second, the end products of the Big Bang, apart from the predominant leptons and photons, were neutrons and protons. The relative numbers are determined by the weak reactions

$$\begin{aligned} \nu_e + n &\rightleftharpoons e^- + p \\ \bar{\nu}_e + p &\rightleftharpoons e^+ + n \\ n &\rightarrow p + e^- + \bar{\nu}_e \end{aligned} \tag{10.27}$$

As the expansion proceeds and kT falls below $M_p c^2$, the nucleons become non-relativistic, with $E = Mc^2 + p^2/(2M)$. Then the equilibrium ratio of neutrons to protons will be given by the ratio of the Boltzmann factors, i.e. by

$$\frac{N_n}{N_p} = \exp\left(\frac{-Q}{kT}\right), \qquad Q = (M_n - M_p)c^2 = 1.293 \text{ MeV} \tag{10.28}$$

At small enough values of kT, when W^{-1} for the weak reactions (10.27) exceeds the age t, the neutrons and protons will go out of equilibrium. An exact calculation gives the critical temperature as $kT = 0.87$ MeV. Initially at decoupling, the neutron-to-proton ratio will therefore be

$$N_n(0)/N_p(0) = \exp(-Q/kT) = 0.23$$

At later times, neutrons will disappear by β-decay, so that at a time t after decoupling there will be

$$N_n(0)e^{-t/\tau} \text{ neutrons} \qquad \text{and} \qquad N_p(0) + N_n(0)(1 - e^{-t/\tau}) \text{ protons}$$

with a ratio of neutrons to protons

$$\frac{N_n(t)}{N_p(t)} = \frac{0.23e^{-t/\tau}}{1.23 - 0.23e^{-t/\tau}} \tag{10.29}$$

where $\tau = 896 \pm 10$ s is the free neutron lifetime.

If nothing else were to happen, the neutrons would die away and the matter of the early universe would consist exclusively of protons and electrons. However, nucleosynthesis can begin immediately neutrons appear, via the formation of deuterons:

$$n + p \rightleftharpoons {}^2\mathrm{H} + \gamma + Q \tag{10.30}$$

where the binding energy $Q = 2.22$ MeV. Since the cross-section is of order 0.1 mb, this (electromagnetic) process will stay in thermal equilibrium, unlike the weak processes (10.27). Again, the huge preponderance of photons over nucleons implies that the deuterons are not 'frozen out' until the temperature falls to about $Q/40$, i.e. $kT = 0.05$ MeV. As soon as photodisintegration of the deuterium ceases, competing reactions leading to helium production take over:

$$\begin{aligned} {}^2\mathrm{H} + n &\rightarrow {}^3\mathrm{H} + \gamma \\ {}^3\mathrm{H} + p &\rightarrow {}^4\mathrm{He} + \gamma \\ {}^2\mathrm{H} + p &\rightarrow {}^3\mathrm{He} + \gamma \\ {}^3\mathrm{He} + n &\rightarrow {}^4\mathrm{He} + \gamma \end{aligned}$$

For $kT = 0.05$ MeV, corresponding to an expansion time from (10.18) of $t \simeq 400$ s, the neutron-to-proton ratio (10.29) is then

$$r = \frac{N_n}{N_p} = 0.14 \tag{10.31}$$

The important point is that once neutrons are bound inside deuterons or heavier

nuclei they no longer decay and the neutron-to-proton ratio is fixed. The helium mass fraction, with $m_{\mathrm{He}} \simeq 4m_{\mathrm{H}}$, is given by

$$Y = \frac{4N_{\mathrm{He}}}{4N_{\mathrm{He}} + N_{\mathrm{H}}} = \frac{2r}{1+r} = 0.25 \tag{10.32}$$

The mass fraction Y has been measured at many different celestial sites, including the solar system, stellar atmospheres, in globular clusters and in planetary nebulae. The resultant value is 0.24 ± 0.01 (after allowing for a small contribution, ~ 0.04 in the mass fraction, from the helium made subsequently in thermonuclear reactions in stars). The close agreement between the observed and calculated helium mass fractions was indeed an early success of the Big Bang model.

An important feature of nucleosynthesis in the Big Bang is that it accounts not only for ^{4}He but also for the light elements D, ^{3}He and ^{7}Li, which occur in significant amounts, far greater than would have survived had they been produced only in thermonuclear reactions in stars. Figure 10.4 shows the abundances expected from baryogenesis in the Big Bang, calculated on the basis of the various cross-sections for production and absorption of the light elements and plotted in terms of the (present-day) baryon density. The results are consistent with a unique value of the density in the range

$$\rho_{\mathrm{baryon}} = (3.0 \pm 1.5) \times 10^{-28}\ \mathrm{kg\ m^{-3}} \tag{10.33}$$

or a number density of baryons

$$N_B = 0.18 \pm 0.09\ \mathrm{m^{-3}}$$

This can be compared with the present number density of microwave photons (10.21), yielding for the baryon-to-photon ratio

$$\frac{N_B}{N_\gamma} \simeq (4 \pm 2) \times 10^{-10} \tag{10.34}$$

Our conclusion, then, is that although in the early moments of the universe, when $kT > 1$ GeV, the relative numbers of baryons, antibaryons and photons must have been comparable, most of the nucleons must have disappeared by annihilation, leaving a tiny – one billionth – residue as the matter of the everyday world.

After the formation of ^{4}He, there is something of a bottleneck to further nucleosynthesis, since there are no stable nuclei with $A = 5$, 6 or 8. The combination of three heliums to form ^{12}C, for example, is impossible because of the Coulomb barrier suppression: this process has to await the formation of stars, and the onset in them of helium burning at high temperatures. A discussion of this would take us on to the subject of thermonuclear reactions in stars. Particle physics as such plays no direct role in these nuclear processes and we do not consider them further.

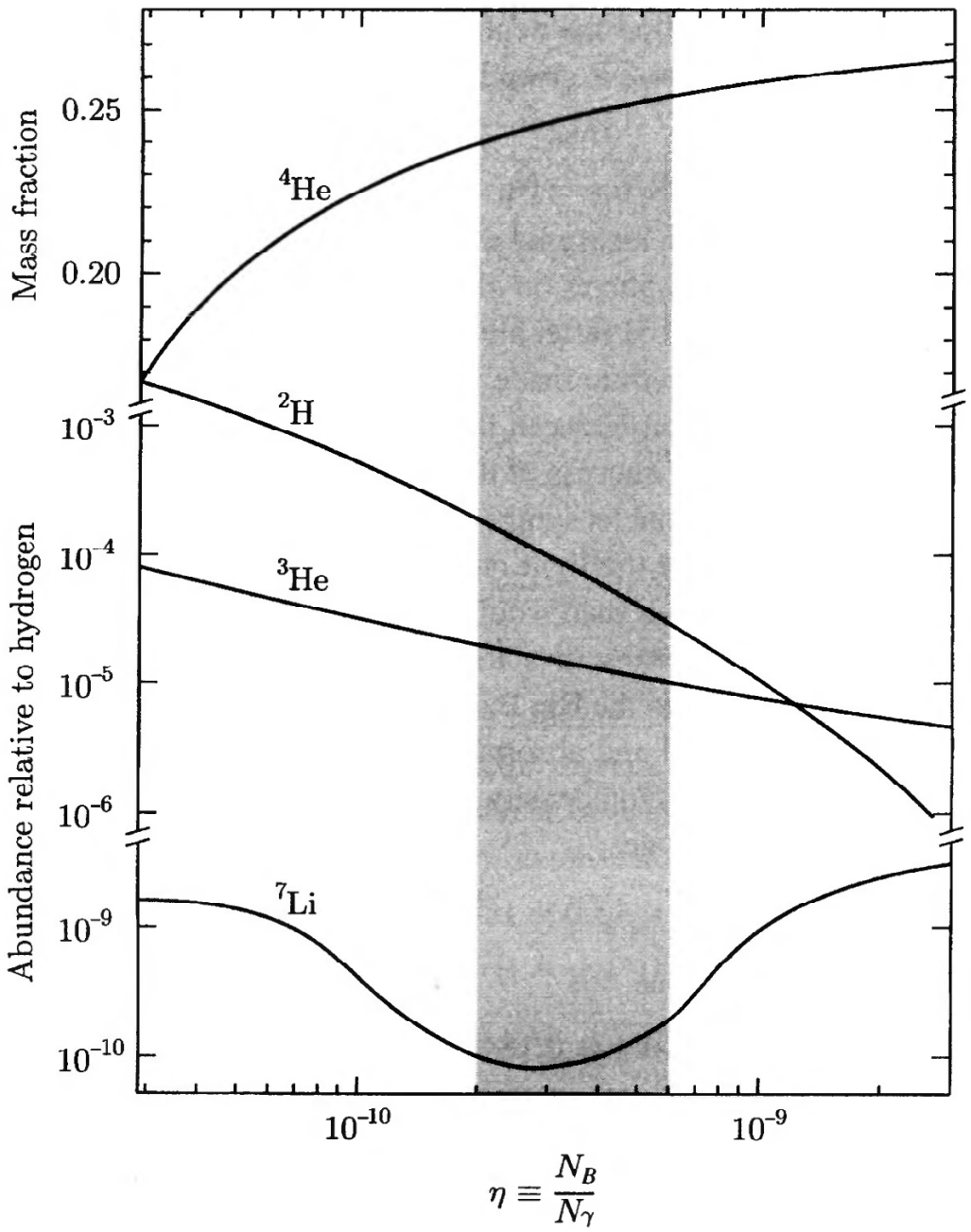

Fig. 10.4. The primordial abundances expected in Big Bang nucleosynthesis of the light elements ^{2}H, ^{3}He and ^{7}Li, and the mass abundance of ^{4}He, in all cases relative to hydrogen, plotted as a function of the baryon density. The observed values of the number abundances are: $^2\mathrm{H/H} \simeq 3 \times 10^{-5}$; $^3\mathrm{He/H} \simeq 2 \times 10^{-5}$; $^7\mathrm{Li/H} \simeq 10^{-10}$. The weight abundance of $^4\mathrm{He} = 0.24 \pm 0.01$. All point to a unique value of the baryon density as given in (10.33) and (10.34) (after Turner 1996).

It may be noted here that the helium mass fraction depends on the number of light neutrino species N_ν, since the expansion timescale described by (10.18) and (10.25) is $t \propto \mathcal{N}^{-1/2}$, where $\mathcal{N}$ is given by the number of fundamental fermion and boson states. Thus increasing N_ν would mean a shorter time for the temperature to drop from T_1 to T_2, say, and less time for neutrons to decay before being captured

in deuterons. So the helium mass fraction will increase with N_ν. Originally, before precision measurements of N_ν at the LEP e^+e^- collider at CERN, this argument was used to limit the number of neutrino flavours, whereas now it is used to get a better value for the helium mass fraction and the baryon-to-photon ratio (10.34); see also Problem 10.2.

10.6 Baryon–antibaryon asymmetry

In the very early moments of the Big Bang, the various types of hadron were continually created and annihilated, the population of any type being determined by statistical weight factors (spin, isospin). As explained above, the only survivors of this hadron era would be the nucleons and antinucleons, the rest disappearing by decay. Consider now a population of nucleons and antinucleons in equilibrium with radiation, according to the reaction

$$p + \bar{p} \rightleftharpoons \gamma + \gamma \tag{10.35}$$

Assuming an initial baryon number of zero, the number density of nucleons and antinucleons would be given by (10.23) with $g_f = 2$,

$$N_B = N_{\bar{B}} = \frac{(kT)^3}{\pi^2(\hbar c)^3} \int \frac{(pc/kT)^2 d(pc/kT)}{\exp(E/kT) + 1} \tag{10.36}$$

where p is the momentum and E the total energy. This may be contrasted with the number density of photons (10.21),

$$N_\gamma = \frac{2.404}{\pi^2(\hbar c)^3}(kT)^3$$

These formulae hold for thermal equilibrium, which can only obtain when the annihilation collisions are sufficiently frequent. Eventually, a critical temperature T_c is reached at which the annihilation rate falls below the expansion rate. The antinucleons can no longer find nucleons to annihilate with and a residue of baryons and antibaryons is 'frozen out'. From experimental data on nucleon-antinucleon annihilation cross-sections, the expansion rate given by (10.18) and the density (10.36) as a function of temperature in thermal equilibrium, it is possible to solve numerically for the temperature and nucleon density at freeze-out. One finds

$$kT_c \simeq 20\ \text{MeV}, \qquad \frac{N_B}{N_\gamma} = \frac{N_{\bar{B}}}{N_\gamma} \simeq 10^{-18} \tag{10.37}$$

After the universe cooled below 20 MeV, therefore, there would be no further baryon–antibaryon annihilation and the above ratio should be valid today. In

contrast, the observed values are, using (10.34),

$$\frac{N_B}{N_\gamma}(\text{observed}) \simeq 10^{-9}, \qquad \frac{N_{\bar{B}}}{N_B} < 10^{-4} \tag{10.38}$$

where the last figure on the $\bar{B}/B$ ratio is conservative; it is set, for example, by the absence of antinuclei among the cosmic rays in our galaxy and of any intense γ-ray emission that would have resulted from annihilation of distant galaxies in collisions with antimatter. So, the Big Bang model gets the baryon number wrong by a factor of 10^9 and predicts equal numbers of baryons and antibaryons, assuming an initial baryon number $B = 0$. (Of course it is possible to postulate an initial baryon number for the universe (of $N_B \sim 10^{79}$), but this seems very artificial, and it is better to try to understand the numbers involved in terms of known physics.)

10.6.1 The Sakharov criteria

In a famous and seminal paper in 1966, little noticed at the time but widely quoted today, Sakharov proposed that, assuming $B = 0$ initially, a baryon asymmetry could develop as a result of baryon-number-violating interactions. He showed that three conditions were required:

(i) B-violating interactions;
(ii) a non-equilibrium situation;
(iii) CP and C violation.

The first requirement is obvious and has been discussed in the GUT models in Chapter 9. The second requirement follows from the fact that, in thermal equilibrium, the density depends only on the temperature and the mass, which however is the same for particle and antiparticle, by the CPT theorem. In other words, any B-violating processes are exactly compensated by the inverse reactions when equilibrium holds. Thirdly, as already pointed out in Section 7.17, CP and C violation are required to generate a cosmological matter–antimatter asymmetry, in the sense that CP violation is necessary to distinguish unambiguously matter from antimatter on a cosmic scale.

To generate a baryon asymmetry it may not be necessary to go outside the Standard Model of particle physics discussed in Chapter 8. Violation of B (with preservation of $B - L$) can be manifest via phase transitions in the electroweak sector (so-called 'instanton' effects). On the one hand these are somewhat controversial and the magnitude of the asymmetry generated is probably too small to reproduce the ratios in (10.38). On the other hand, it is generally believed that the conditions for a baryon–antibaryon asymmetry of the required magnitude *could* be met in the context of GUT models, with the creation on a $t \sim 10^{-40}$ s timescale

of the massive X, Y bosons introduced in Chapter 9. Provided their masses are sufficiently large ($> 10^{17}$ GeV), the collision rate for $X + \bar{X} \rightleftharpoons \gamma + \gamma$ and the decay rate for $X \rightarrow Q + l$ (where Q and l stand for quark and lepton) can both be small compared with the expansion rate, H. This ensures that the X, Y bosons decay out of thermal equilibrium. The detailed requirements are of two decay channels of different baryon number. Let r and $1 - r$ be the branching ratios for the decay of X to just two channels, with baryon numbers B_1 and B_2 respectively. For $\bar{X}$ particles, let the ratios be $\bar{r}$ and $1 - \bar{r}$, with baryon numbers $-B_1$ and $-B_2$. Now $N_X = N_{\bar{X}}$ by CPT. Hence the net baryon asymmetry per $X\bar{X}$ pair will be

$$A_{B\bar{B}} = rB_1 - \bar{r}B_1 + (1 - r)B_2 - (1 - \bar{r})B_2 = (r - \bar{r})(B_1 - B_2) \qquad (10.39)$$

B violation ensures $B_1 \neq B_2$ and CP violation ensures that $r \neq \bar{r}$, so that the asymmetry will be non-zero. (C violation, with CP conservation, would give a different decay angular distribution for X and $\bar{X}$ but the same rate integrated over angle: CP violation would ensure different absolute rates in the two channels). The full calculation involves many unknown factors and the possible values deduced for N_B/N_γ can vary over many decades (roughly from 10^{-6} to 10^{-13}). Although beset with many uncertainties, such models may offer us a way of understanding the origin of the baryon asymmetry of the universe.

10.7 Dark matter

The measurement of the rotation curves of velocity versus radial distance for stars and gas in our galaxy gives strong indications of the existence of dark (i.e. non-luminous) matter. Consider, for example, a star of mass m at distance r from the galactic centre, moving with tangential velocity v, as shown in Figure 10.5. Then

$$\frac{mv^2}{r} = \frac{mM(< r)G_N}{r^2} \qquad (10.40)$$

where $M(< r)$ is the mass inside radius r. A spiral galaxy like our own has most of the luminous material concentrated in a central hub, plus a thin disc. For a star inside the hub, we expect $M \propto r^3$ and therefore

$$v \propto r$$

while for one well outside the hub, $M \simeq$ constant and thus

$$v \propto r^{-1/2}$$

So the velocity should increase at small r and fall off at large r. On the contrary, the observed rotation curves are flat at large r, at least to values of r comparable

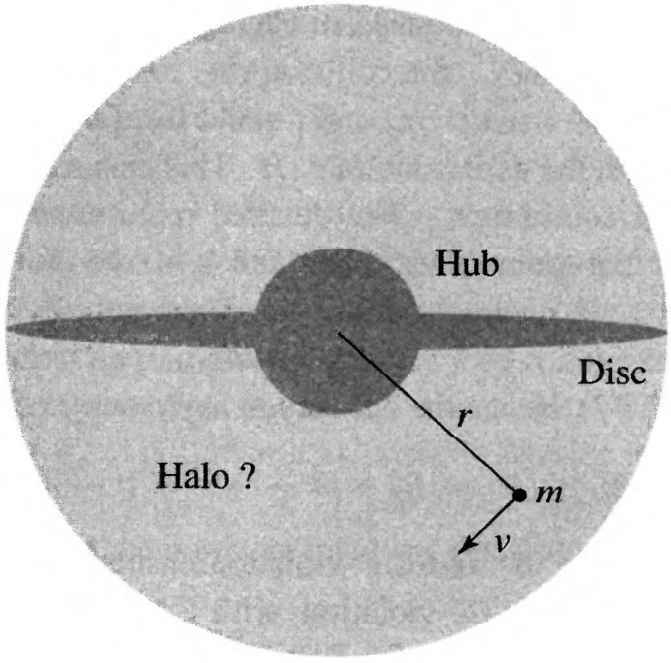

Fig. 10.5. An end-on view of a spiral galaxy, consisting of a central hub, a disc and a possible halo of dark matter.

with the disc radius, implying a total mass growing linearly with radius (see Figure 10.6).

Detailed analysis shows that the dark matter in our galaxy accounts for some 90% of the total galactic mass. Evidence for dark matter is also found on larger scales, in galactic clusters and superclusters. In general, the larger the scale the greater is the apparent contribution of dark matter. On the largest scales, the total inferred density approaches the closure density, with $\Omega_{\text{matter}} > 0.3$ as in (10.15).

The nature of the dark matter is at present unknown. Could it be baryonic? In the context of the Big Bang nucleosynthesis described above, the allowed range of N_B/N_γ is about 10^{-10}–10^{-9} (see (10.34)), which corresponds to a range in Ω_{baryon} of around 0.01–0.1, taking account of uncertainties in h_0. Hence, baryonic dark matter is not by itself able to account for the missing mass.

10.7.1 MACHOs

Some of the dark matter *must* be baryonic, since the value of Ω_{baryon} deduced from the model of baryogenesis in the Big Bang is an order of magnitude larger than Ω_{lum}; see (10.12)–(10.15). Some of the baryonic dark matter has been accounted for by non-luminous stellar objects – the so-called massive compact halo objects or MACHOs, with masses typically of 0.01–0.1 solar masses. These have been

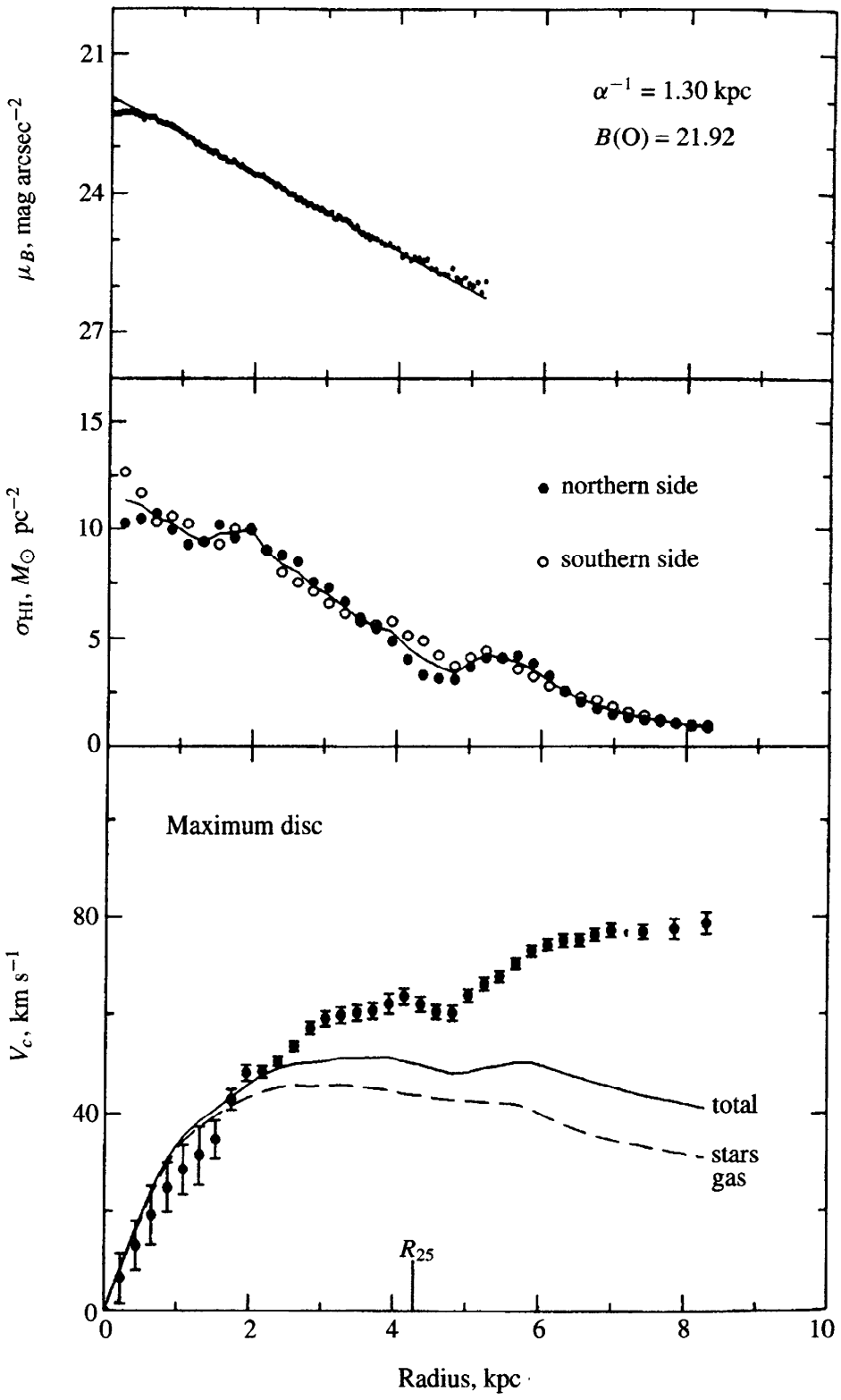

Fig. 10.6. Evidence for dark matter from the spiral galaxy NGC 1560. In the top panel the luminosity is plotted against radial distance from the centre, and shows an exponential fall-off. The second panel shows the luminosity in the Hα line. The points in the bottom panel show the observed tangential velocities of stars in this galaxy as a function of radial distance. The theoretical curves show the expected values of velocity obtained by integrating numerically the mass inside a particular radius, as a function of that radius, as in (10.40). The contributions due to stars and gas are shown separately. They are clearly unable to account for the observed velocities at large values of the radius (from Broeils 1992).

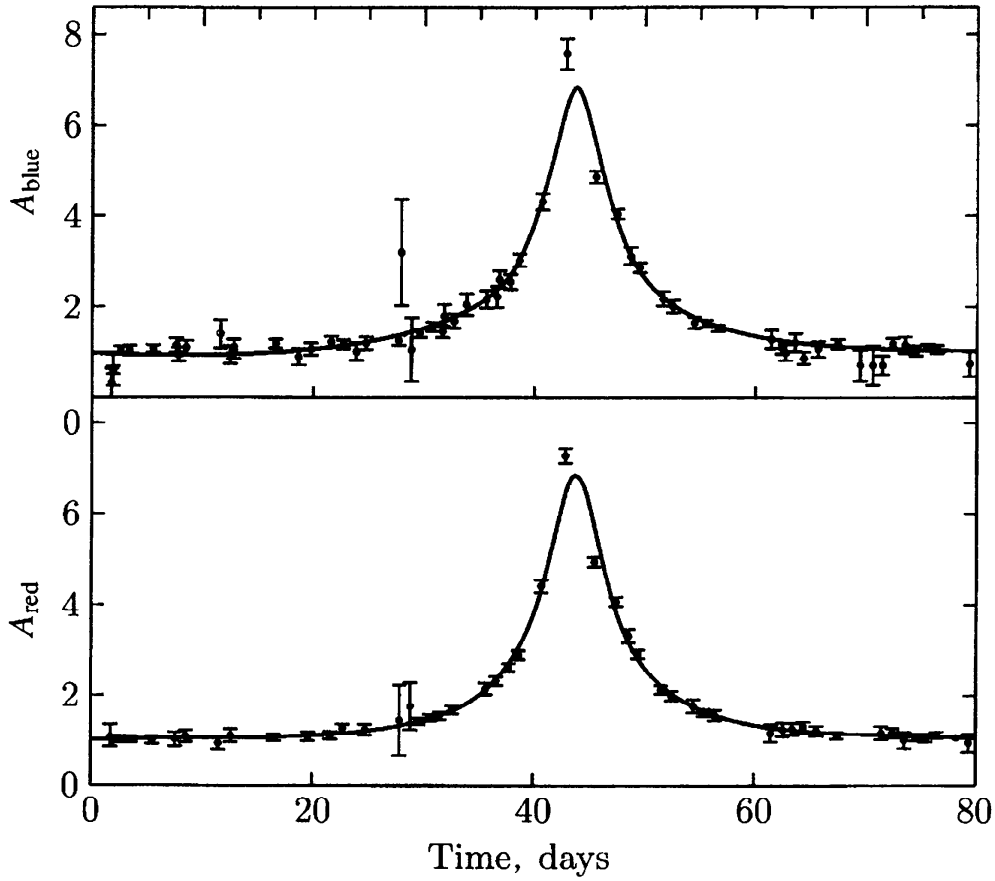

Fig. 10.7. Example of light signal as a function of time, recorded for a star in the Large Magellanic Cloud. The gravitational field of a dark, non-luminous stellar object (MACHO) in the Milky Way close to the line of sight acts as a lens, resulting in a characteristic light curve, which is the same for blue light (upper panel) and red light (lower panel). (After Alcock *et al.* 1993.)

detected in the Milky Way by their gravitational deflection and lensing of light from more distant stars in the Large Magellanic Cloud (a nearby mini-galaxy). An example is shown in Figure 10.7. Since the effective gravitational mass of a photon of momentum p is p/c, it will receive a momentum transfer $\Delta p \propto p$ from a transverse gravitational field, so that the angular deflection $\Delta p/p$ will be independent of wavelength. This crucial feature of the light curve distinguishes MACHOs from other sources such as variable stars. This microlensing is observed for light from stars of all types.

Many dozens of such microlensing events have been observed in recent years. Present data indicate that these non-luminous stellar objects, undoubtedly of baryonic matter like normal stars, can account for a substantial fraction of the non-luminous baryonic matter in our galaxy.

10.7.2 Non-baryonic dark matter

The most favoured hypothesis is that the non-baryonic dark matter, constituting the great bulk of all dark matter, is made up of particles created in the hot early universe, and stable enough to survive to the present day. There are several possible candidates.

(a) Neutrinos

As stated before, in addition to photons, positrons and electrons, neutrinos ν_e, ν_μ, ν_τ would have been produced in the early universe, all with comparable densities. From the discussion in Section 10.4 we know that the neutrinos will drop out of equilibrium when the time between collisions for the reaction

$$e^+ + e^- \rightleftharpoons \nu + \bar{\nu}$$

exceeds the expansion time t in (10.18). The cross-section for this reaction is $\sigma \simeq G^2 s/(6\pi)$, where s is the cms energy squared ($\sqrt{s} \sim kT$). Since $\rho \sim T^4$ for relativistic particles, it follows that the collision time $1/(\rho\sigma) \sim T^{-6}$, while from (10.19) the expansion time $t \sim T^{-2}$. As T falls, therefore, neutrinos will decouple from the other particles. A straightforward calculation gives for the critical temperature $kT_c \simeq 3$ MeV, as stated above (see also Problem 10.3). Thus after $t \sim 10^{-2}$ s, the neutrino fireball expands and cools independently of the radiation and matter (apart of course from the universal gravitational coupling which induces the redshift). The eventual number density and temperature of the neutrinos are comparable with, but less than, those of the photons, because the latter are boosted by the annihilation reaction

$$e^+ + e^- \rightarrow \gamma + \gamma$$

which converts the energy content of e^+ and e^- into that of the photons, once $kT \ll m_e c^2$. One can compute this effect as follows. The entropy per unit volume of the fireball of e^+, e^-, γ at temperature T is $S = \int dQ/T$ or

$$S = \frac{4}{3}\frac{aT^4}{T}\left(1 + \frac{7}{8} + \frac{7}{8}\right) = \frac{4}{3}aT^3\left(\frac{11}{4}\right)$$

where the fractions here and below arise from the integrals over the energy spectra of fermions as compared with bosons, as explained in the footnote in Section 10.3 above. After annihilation the photons have attained a temperature T_1 with entropy

$$S_1 = \frac{4}{3}aT_1^3$$

Since the expansion is adiabatic (isentropic), $S_1 = S$ and

$$T_1 = \left(\frac{11}{4}\right)^{1/3} T$$

If the temperature of the microwave photons today is T_γ then that of the relic neutrinos (which received no boost) will be T_ν, where

$$T_\gamma = 2.7\ \mathrm{K} \qquad T_\nu = \left(\frac{4}{11}\right)^{1/3} \times T_\gamma = 1.9\ \mathrm{K} \tag{10.41}$$

The corresponding number density of neutrinos plus antineutrinos will be

$$N_\nu = \frac{3}{4} \times \frac{4}{11} \times N_\gamma = 113\ \mathrm{cm}^{-3} \tag{10.42}$$

per neutrino flavour, compared with $N_\gamma = 411\ \mathrm{cm}^{-3}$ from (10.21). Since the neutrino number density is of order 10^9 times the baryon density today (see (10.34)), it follows that neutrino masses of order $10^{-8} M_p c^2$, or some tens of eV, would give a contribution to Ω an order of magnitude larger than that of the baryons. In fact it is simple to show that

$$\sum_{e,\mu,\tau} m_\nu c^2 \simeq 50 h_0^2\ \mathrm{eV} \tag{10.43}$$

is enough to give $\Omega \simeq 1$. So relic neutrinos are possible dark matter candidates and have the great advantage that they are known to exist. However, the problem with neutrinos is that they are 'hot' dark matter, i.e. with $kT_c \simeq 3$ MeV; they were relativistic when they decoupled and relativistic when the large-scale structures in the universe were forming. As a consequence they will stream rapidly under gravity and tend to iron out any primordial density fluctuations, which are needed to seed such structures. The conclusion is that neutrinos may constitute some of the dark matter, but cannot account for more than 30% of the total.

(b) Axions

Axions are hypothetical, light neutral pseudoscalar particles, with masses $m_a \sim$ μeV typically. They were postulated in order to solve the 'strong CP' problem in QCD, which predicted a level of strong CP violation resulting in a neutron electric dipole moment nine orders of magnitude larger than the experimental upper limit. The problem was solved by invoking a new spontaneously broken symmetry, leading in turn to the prediction of the axion, which (if it exists) would certainly have been produced in great abundance as a sort of condensate in the early universe. Being produced out of equilibrium, axions constitute 'cold' dark matter. For the mass range 1–100 μeV/c^2, they would contribute a dark matter density of the order of the critical density ρ_c. Axions might in principle be detected using a microwave

cavity in a strong magnetic field; they would be converted to microwave photons in the field. The experiment has to be done at a low temperature ($\ll 1$ K) to reduce the normal cosmic microwave background. As yet there is no experimental support for the axion model.

(c) WIMPs

Perhaps the most likely dark matter candidates – and the ones being pursued most vigorously by experimentalists – are the stable, weakly interacting massive particles (WIMPs) that de-coupled when they were non-relativistic, and thus constitute 'cold' dark matter, with practically no radiation pressure and no proclivity for ironing out density fluctuations. There are many possibilities but the favourite candidate is the lightest stable supersymmetric particle, the neutralino δ (a combination of photino and Higgsino). Produced like other particles in thermal equilibrium in the Big Bang, its abundance today would be determined by its annihilation cross-section to quark and lepton pairs, $\delta\bar{\delta} \rightarrow Q\bar{Q}, l\bar{l}$ etc. Of course, mass limits on supersymmetric particles exist from their absence at accelerators, e.g. the LEP e^+e^- experiments give $M > 100$ GeV for *directly* produced SUSY particles. However, these need not be the lightest stable supersymmetric particles concerning us here.

Using arguments similar to those in Section 10.6, one can see that, if the annihilation cross-section $\sigma(\delta\bar{\delta} \rightarrow Q\bar{Q})$ is too large, the WIMP annihilation rate $N_\delta \sigma v$ (where N_δ is the number density) will be larger than the rate of expansion of the universe, so that essentially all WIMPs would disappear and could not account for the dark matter. However, if σ is too small then the relatively faster expansion would quickly dilute the WIMP density, there would be little annihilation and the cosmic abundance would be much too large. An annihilation rate $\Gamma = N_\delta \sigma v \sim t^{-1}$, with N_δ chosen to give a value for the mass density ρ_δ $(= N_\delta M_\delta)$ of order ρ_c, the critical density, is found to correspond to a value of $\sigma \simeq 10^{-36}$ cm^2, typical of weak coupling. This conclusion is valid for WIMP masses in the few GeV range and is not inconsistent with expectations from supersymmetry.

Cosmic WIMPS are expected to have velocities of the same order as that of luminous material in galaxies and that of galaxies in clusters etc., i.e. $\beta = v/c \sim 10^{-3}$. Hence their kinetic energies will be typically $E_\delta \sim M_\delta$ keV, where M_δ is the WIMP mass in GeV. Direct detection can be via elastic scattering from nuclei, where the low energy nuclear recoil is detected. From non-relativistic kinematics the recoil kinetic energy E_R will be

$$E_R = \frac{4M_\delta M_R}{(M_\delta + M_R)^2} E_\delta \cos^2\theta \tag{10.44}$$

where M_R is the mass of the nucleus and θ is the angle of the recoil relative to

the incident direction. In the most favourable case, when θ is small, $E_R \sim E_\delta$ if $M_R \sim M_\delta$. But $E_R \ll E_\delta$ if either $M_\delta \ll M_R$ or $M_\delta \gg M_R$. So one is dealing with recoil energies of order keV or less.

Taking account of the expected WIMP density and elastic scattering cross-sections, event rates ≤ 0.1 kg^{-1} day^{-1} are involved. Therefore the experimental emphasis has first to be on reducing radioactive and cosmic ray background, the former by using very pure materials and shielding the detectors, the latter by going deep underground.

Two approaches have been pursued. First, one can use scintillator detectors to record the ionisation energy loss of the recoil. Very large (100 kg) sodium iodide scintillators can be manufactured to have extremely low background levels. Discrimination between nuclear recoil signals and electron recoils from radioactive contamination can be achieved because electron signals have longer decay times, especially if the detectors are cooled to liquid nitrogen temperatures.

The so-called 'cryogenic' detectors involve detection of the phonons generated by particle interactions in single crystals cooled to very low temperatures ($\ll 4$ K). These can have much lower thresholds than scintillators and are therefore sensitive to lower WIMP masses, because the phonon pulse detected by the rise in temperature of the crystal is proportional to the total energy loss, whereas the ionisation or light yield in a scintillator may be only a small fraction of the total energy loss of the recoiling nucleus. The simultaneous measurement of both ionisation *and* phonons in Ge or Si crystals allows the best discrimination between signal and background.

The detector cross-section per nucleon depends on whether the WIMP-nucleus interaction involves scalar coupling, where the coherent sum of amplitudes from all nucleons in the nucleus can add together; or axial vector coupling, that is a spin-dependent interaction, where the amplitudes do not add because most of the nucleon spins cancel out. Present limits (1998) on the detection cross-sections are shown in Figure 10.8.

10.8 Inflation

Although the Big Bang model described above seems to give a successful description of the evolution of our universe, there are some problems for our understanding of the initial conditions apparently required. Two of these problems are the *horizon problem* and the *flatness problem.*

Consider first the horizon problem. The universe is surprisingly uniform and isotropic on large scales. Thus, looking in opposite directions in the sky, the microwave background temperatures are observed to be the same within 1 part in 10^4, although it seems that there could not have been any causal connection

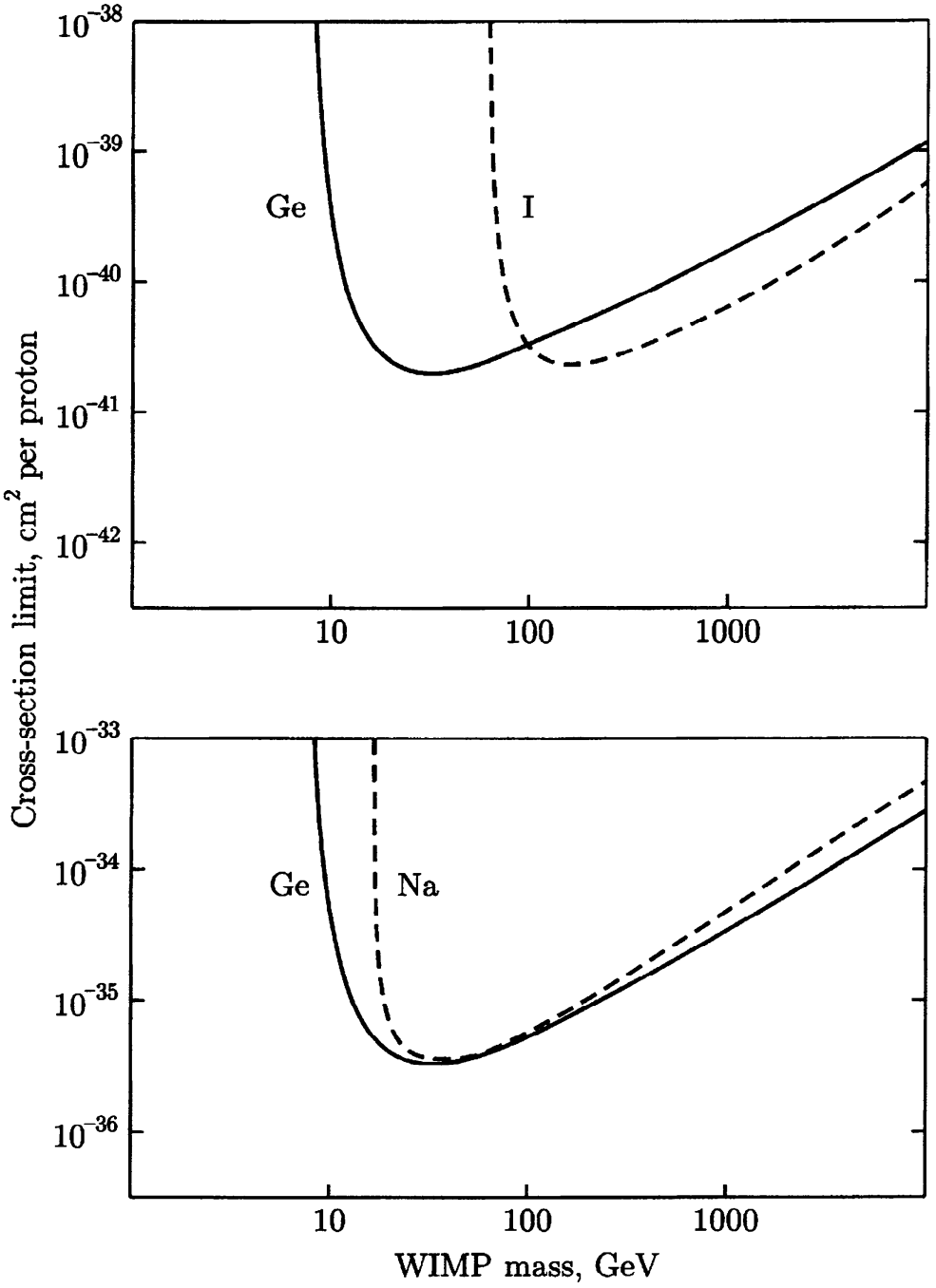

Fig. 10.8. Curves showing the upper limits on the detection cross-section per nucleon for WIMPs, as a function of WIMP mass, from germanium and sodium iodide detectors. Upper figure, scalar coupling; lower figure, axial vector coupling.

between these two regions. The last interaction such microwave photons could have had was at the time of the last scatter, that is just before the decoupling time $t_d \sim 10^{13}$ s (see Section 10.4). Two such regions in opposite directions relative to the observer would by now have separated by a distance of order $2c(t_0 - t_d) \simeq 2ct_0$. At an early stage of the Big Bang, two different regions of the sky could have been in contact by exchange of light signals, but if so, by the time all contact ceased at $t = t_d$, they could have separated by at most a distance ct_d: their maximum

distance apart now would therefore be

$$ct_d R_0/R_d = ct_d T_d/T_0 \sim 10^3 ct_d \ll 2ct_0$$

since $t_0 \sim 10^5 t_d$. Thus it appears that two regions located in widely different directions could never have been in thermal contact: they are, so to speak, 'over the horizon' with respect to each other, with regard to the linking of causally connected events. So how can their temperatures be so closely equal?

A second problem is that the universe today is apparently almost flat, with the closure parameter $\Omega \sim 1$. Now, for either of the finite values ± 1 of K allowed in (10.12), the fractional difference between the actual density and the critical density ρ_c will be $\Delta\rho = \rho - \rho_c$, where

$$\frac{\Delta\rho}{\rho} = \frac{3Kc^2}{8\pi G_N R^2 \rho} \tag{10.45}$$

Considering just the radiation dominated era, $\rho \propto R^{-4}$ and $\Delta\rho/\rho \propto R^2 \propto t$. So at very early times the value of $\Delta\rho/\rho$ must have been very much smaller than the value, of order unity, today, when $t_0 \sim 10^{17}$ s. For example, for $M_{\rm GUT} \sim 10^{14}$ GeV, $t \sim 10^{-34}$ s and $\Delta\rho/\rho$ at that time would have been $10^{-34}/10^{17} \sim 10^{-51}$. If we included the period of matter domination in our calculation, this conclusion would not change materially. How could Ω have been so finely tuned to unity, or in other words how could the universe have been so flat? We need a mechanism to reduce the curvature term in (10.12) by a factor 10^{50} or more.

The inflationary model of the early universe was proposed by Guth in 1981 in order to try to resolve the above and other problems; he postulated an extremely rapid expansion by a huge factor at a preliminary stage of the Big Bang. Let us start by considering an intensely hot, microscopic universe at the Planck temperature, $kT = M_{\rm P} \simeq 10^{19}$ GeV, which is expanding and cooling as in (10.18), and suppose that the initial evolution is controlled by the interactions of a scalar 'inflaton' field ϕ, in analogy with the Higgs field in the electroweak model of Section 8.12 but in this case associated with the GUT scale $M_{\rm GUT}$. For temperatures such that $kT \gg M_{\rm GUT}$, the energy density of this scalar field would have a minimum for $\phi = 0$ but, as kT falls well below $M_{\rm GUT}$, the universe can become 'supercooled', eventually undergoing a GUT phase transition SU(5) $\rightarrow$ SU(3) $\times$ SU(2) $\times$ U(1), to a much lower energy minimum at $\phi = \phi_0$, just as in Figure 8.13. In analogy with (8.50), we can estimate that the energy density liberated will be $\rho_\phi \sim \mu^4/(4\lambda)$, where $\mu = M_{\rm GUT}$ and we can take the coupling $\lambda \sim 1$. Substituting in (10.7) it can be seen that this is equivalent to having a cosmological constant

$$\Lambda = 8\pi G_{\rm N} \rho_\phi$$

If this term dominates, it would lead to an exponential expansion,

$$\left(\frac{\dot{R}}{R}\right)^2 \sim \frac{\Lambda}{3} \qquad \text{or} \qquad R_2 = R_1 e^{s(t_2 - t_1)}$$

where $s = \sqrt{\Lambda/3}$ and R_1 and R_2 are the scale parameters at times t_1 and t_2. From (10.18) we know that the timescale of the GUT phase transition $t_1 \propto 1/M_{\text{GUT}}^2$. Since, in units $\hbar = c = 1$, $G_N = M_P^{-2}$, it follows that

$$s \propto M_{\text{GUT}}^2 / M_P$$

Setting the ratio $x = t_2/t_1$ gives

$$s(t_2 - t_1) \propto (x - 1)/M_P$$

which is independent of the precise GUT scale. Typical values (with $M_{\text{GUT}} = 10^{14}$ GeV) would be $t_1 = 10^{-34}$ s and $t_2 = 10^{-32}$ s, giving a ratio $R_2/R_1 \sim 10^{30}$. At time t_2, the phase change is supposedly complete; the supercooled universe is reheated and reverts to the conventional hot Big Bang model ($\Lambda = 0$).

Inflation solves the horizon problem, since the two regions now over the horizon would once have been in close thermal contact, and it was only the enormous inflation of the distance scale which left them thereafter causally disconnected. Inflation also solves the flatness problem. It reduces the curvature term by a factor $(R_2/R_1)^2 \sim 10^{60}$, so that after the inflationary stage is over, the universe is remarkably flat and uniform. An analogy can be made with the inflation of a balloon; as it inflates, the curvature of the surface decreases and in the limit a small portion of the surface appears quite flat.

Inflation may also be capable of accounting for tiny fluctuations in the microwave background temperature, observed on all distance scales and necessary, we believe, to seed the large-scale structures (galactic clusters, superclusters, voids etc.) found in the cosmos. Consider a time $t = t_1 = 10^{-34}$ s when $kT \sim 10^{14}$ GeV. The maximum distance between causally connected points in this pre-inflationary micro-universe would be of order $ct_1 \sim 10^{-26}$ m. So, despite thermal equilibrium, the Uncertainty Principle would imply variations in temperature corresponding to $\Delta(kT) \sim \hbar c/(ct)_1 \sim 10^{10}$ GeV, leading to temperature and density fluctuations $\Delta(kT)/kT$ at the 10^{-4} level. These fluctuations would be preserved in the subsequent expansion.

The inflation hypothesis seems therefore to offer some understanding of the puzzles regarding the initial conditions in the very early universe, before the hot Big Bang got started. A final bizarre note is that inflation would necessarily imply that our own particular universe, vast though it is, is but a dot in the ocean, a tiny part of a very much larger space domain.

10.9 Neutrino astronomy: SN 1987A

Astronomy has historically been carried out using light from the visible spectrum. During the last 50 years radio, infrared, X-ray, ultraviolet and γ-ray astronomy have become as important as optical astronomy and have greatly extended our knowledge of astrophysical phenomena. More recently, astronomy with neutrinos has started to blossom.

The results from solar neutrinos have been discussed in the previous chapter. An unexpected by-product of the search for proton decay with multikilotonne water Čerenkov detectors, described in Section 9.5, was the detection in 1987 of an intense burst of neutrinos from the supernova 1987A in the Large Magellanic Cloud. This provided the first experimental evidence that the great bulk of supernova energy release was in the form of neutrinos and provided confirmation of the essential correctness of the model of the type II supernova mechanism. From the point of view of particle physics, it confirmed the laboratory limits on the $\bar{\nu}_e$ mass and provided an interesting application of the Standard Model prescription for neutrino interactions.

Figure 10.9 shows the visual observation of SN 1987A, which developed from the giant star Sanduleak 69202. The pulse of neutrino events, totalling about 20 over a period of a few seconds, was observed simultaneously in the Kamiokande and IMB water detectors, as shown in Figure 10.10. The neutrino pulse actually arrived some seven hours before the optical signal became detectable.

Let us here briefly recall the proposed supernova mechanism, to see how the observations bear it out. Stars obtain their radiant energy from the nuclear binding energy released in the fusion of heavy elements from light elements. This fusion proceeds systematically through the Periodic Table, successively heavier nuclei being found in onion-like layers with the heaviest nuclei in the hot central core. This procession continues until the iron-nickel group is reached, after which no further fusion is possible, since there the binding energy per nucleon is a maximum.

Thereafter the star, if of mass $M < M_\odot$, where $M_\odot$ is the solar mass, simply cools off as a white dwarf over billions of years. Although nuclear reactions have ceased, such a star is stable because the pressure (from the Fermi momentum) of the degenerate electron gas is enough to withstand the inward gravitational pressure.

However, for $M > 10M_\odot$–15 $M_\odot$, the central core of iron may have $M > 1.5M_\odot$, in which case it is unstable. For such a massive core, as first shown by Chandrasekhar, the Fermi momentum of the electrons becomes relativistic and the degeneracy pressure of the electrons can then no longer withstand the gravitational pressure. The core collapses, the density increasing from $\rho \sim 10^{11}$ times that of water to (ultimately) nuclear density, $\rho \simeq 2 \times 10^{14}$. During this collapse, most of the iron nuclei are fragmented into neutrons and protons, and the Fermi energy of

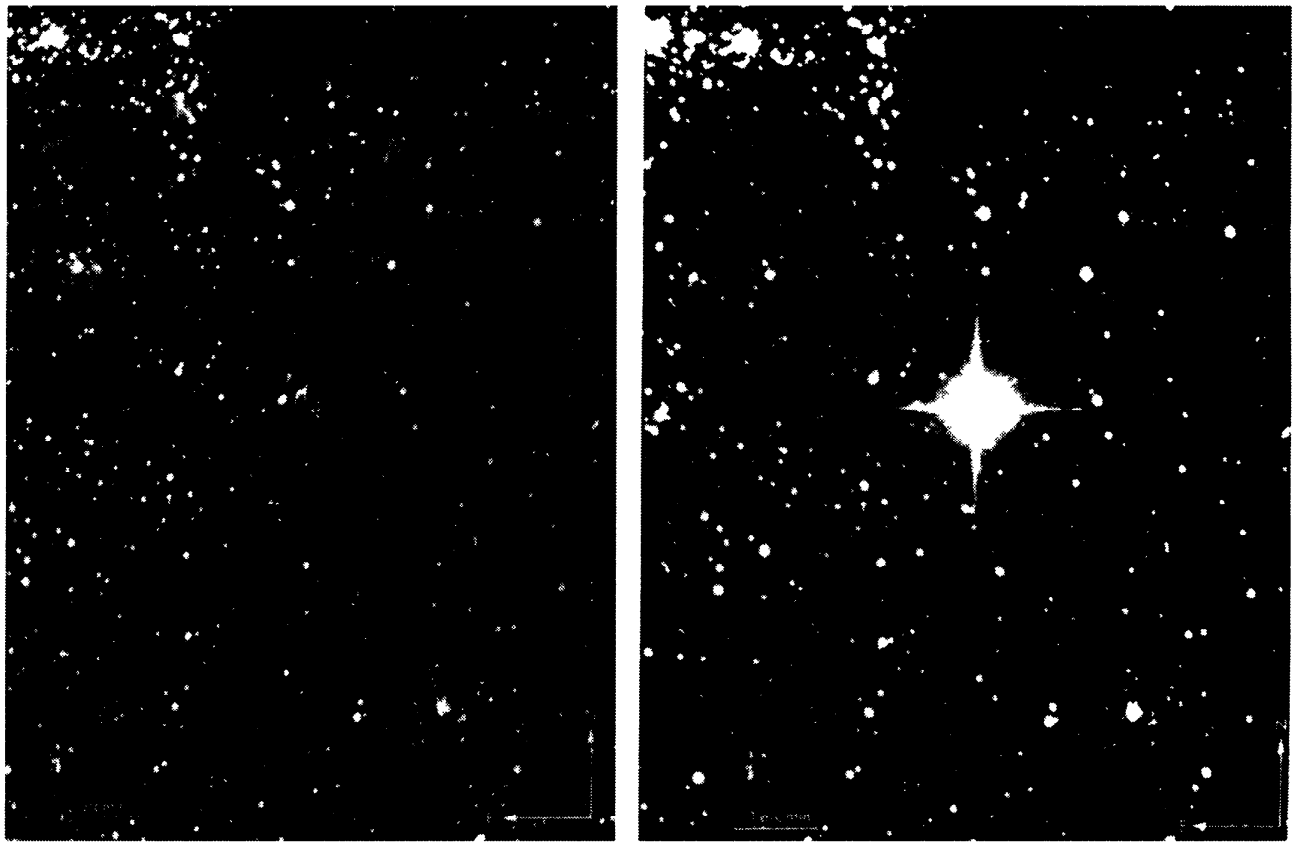

Fig. 10.9. The SN 1987A event. The stellar field in the LMC before (left) and two days after (right) the supernova explosion. About 1% of the total energy liberated appears in the form of electromagnetic radiation. All the rest is in the form of neutrinos.

the electrons is enough to initiate electron capture reactions via the process (with 0.8 MeV threshold)

$$e^- + p \rightarrow \nu_e + n \tag{10.46}$$

This process is called *neutronisation*. The collapsing core still contains iron nuclei, protons and electrons in quantity, as well as neutrons. However, one can crudely speaking think of this so-called neutron star as a gigantic nucleus principally of neutrons. If $R_0 = 1.2$ fm is the unit nuclear radius and A is the number of nucleons, the radius will therefore be $R = R_0 A^{1/3}$. Since $A_\odot = 1.2 \times 10^{57}$, such an object, if of 1.5 solar masses, would have a radius $R \simeq 15$ km. The corresponding gravitational energy release will be

$$E_{\text{grav}} = \frac{3}{5} \frac{G_N M^2 A^{5/3}}{R_0} \tag{10.47}$$

where G_N is the gravitational constant and M is the nucleon mass. For $M_{\text{core}} = (1.5\text{–}2) M_\odot$,

$$\begin{aligned} E_{\text{grav}} &\simeq (2.5\text{–}4.0) \times 10^{53} \text{ ergs} \\ &\simeq (1.6\text{–}2.5) \times 10^{59} \text{ MeV} \end{aligned}$$

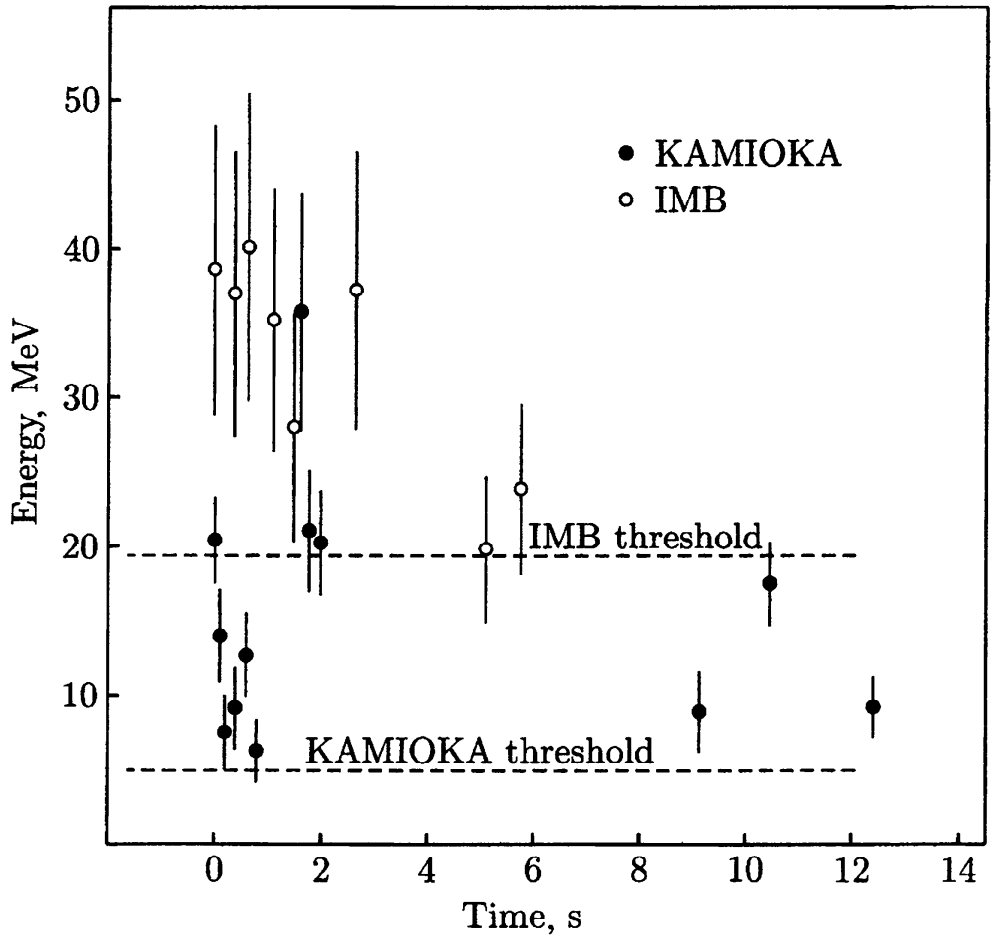

Fig. 10.10. Energies of IMB and Kamioka water Čerenkov events plotted against arrival time. The effective detection threshold energies in the IMB and Kamiokande experiments were about 20 MeV and 6 MeV respectively.

This energy E_{grav} is larger, by a factor of 10, than the energy required to disintegrate the iron into its constituent nucleons (8 MeV per nucleon) and also to convert the protons to neutrons (0.8 MeV per proton) via (10.46). In fact the above figure corresponds to a gravitational energy release of order 100 MeV per nucleon, or a total energy release of order $0.1M_{\text{core}}c^2$. Thus the gravitational potential energy release is some 10% of the total mass–energy of the core, and this is near enough to the Schwarzschild limit that cores of $M \geq 2M_\odot$ are likely to collapse to black holes.† However, for less massive cores associated with neutron star formation, the implosion is halted by the short-range repulsive core of the nuclear force, as nuclear density is reached, and some of the energy bounces back in the form of a pressure wave, which, further out, develops into a shock wave. During the initial stage of collapse, neutrinos from (10.46), of order 10^{57} in number and accounting for some 10% of the total energy released, will burst out in a short flash

† The Schwarzschild radius $R_S = 2G_N M_{\text{core}}/c^2 = 6$ km for $M_{\text{core}} = 2M_\odot$. No infalling material can ever return, or light escape, from inside R_S.

(lasting milliseconds). Upon approaching nuclear density, however, the mean free path λ of the neutrinos becomes smaller than the neutron star radius. Many processes will be involved in neutrino scattering, both charged- and neutral-current, from both nucleons and surviving iron nuclei. However, one can get a rough estimate by just considering the charged-current scattering of neutrinos of energy E by nucleons:

$$\lambda = \frac{1}{\rho(N_A/2)\sigma} \simeq \frac{2\pi}{\rho N_A G_F^2 E^2} \simeq \frac{10}{E^2}\ \text{km}$$

where G_F is the Fermi constant, N_A is Avogadro's number and we have used the approximate formula (7.12), with $|M|^2 = 1$, for the cross-section. Thus for a typical neutrino energy of 10 MeV or so, $\lambda \sim 0.1$ km only. Hence, the enormous energy liberated is temporarily locked in the core. Even the most penetrating of particles, the neutrinos, can only escape from a 'neutrino-sphere' within 100 m or so of the surface.

The consequence is that there is a 'thermal phase' of the stellar core in which $\nu\bar{\nu}$ pairs, e^+e^- pairs and γ-radiation will be in equilibrium. The neutrinos will have a roughly Fermi–Dirac distribution as in (10.23), with a typical initial value calculated to be $kT \sim 5$–10 MeV. Some 90% of the gravitational energy is emitted in a long pulse as the core cools down by neutrino emission over several seconds, in the form of ν_e, $\bar{\nu}_e$, ν_μ, $\bar{\nu}_\mu$, ν_τ, $\bar{\nu}_\tau$. Because of their different cross-sections and therefore different depths of neutrino-sphere, there can be differences of a factor 2 or so in the mean energies of the different flavours of neutrino and antineutrino. However, the different types are expected to have roughly equal energy content.

Coming back to Earth, the main reactions that could lead to observation of supernova neutrinos in the MeV region in a water Čerenkov detector are

$$\bar{\nu}_e + p \rightarrow n + e^+$$

$$\nu_e + {}^{16}\mathrm{O} \rightarrow {}^{16}\mathrm{F} + e^-$$

$$\nu + e^- \rightarrow \nu + e^-$$

$$\bar{\nu} + e^- \rightarrow \bar{\nu} + e^-$$

The first reaction has a threshold energy $Q = 1.8$ MeV and a cross-section rising as E_ν^2, as in (7.13), with a value of 10^{-41} cm^2 per proton at $E_\nu = 10$ MeV. The angular distribution of the secondary lepton is almost isotropic. The second reaction has a 13 MeV threshold and, for the energies considered here, has a cross-section two orders of magnitude smaller and can be neglected. The third and fourth reactions are of elastic scattering, via Z^0 exchange for ν_μ, ν_τ and Z^0 and $W^\pm$ exchange for

ν_e. Although not negligible, the summed cross-section for these reactions (varying as E_ν) is only 10^{-43} cm^2 per electron at 10 MeV, see (8.22)–(8.24). So, despite the fact that in water there are five electrons for every free proton, the event rate for scattering from electrons is an order of magnitude smaller than that for the first reaction. Furthermore, in neutrino–electron scattering the recoil electron receives only a fraction of the incident energy, while in the first reaction above it receives most of it ($E_e = E_\nu - 1.8$ MeV).

The event rates recorded in Figure 10.10 together with the known distance to the supernova (170 000 lightyears) could be used to compute the total energy flux in neutrinos (assuming the total is six times that in $\bar{\nu}_e$ alone). The two sets of data involve different detection thresholds, but both are consistent with a mean temperature $kT \simeq 5$ MeV and a mean neutrino energy at production equal to $3.15\ kT$, appropriate to a relativistic Fermi–Dirac distribution (see footnote in Section 10.3). The data was used to calculate an integrated neutrino luminosity

$$\begin{aligned} L &\simeq 3 \times 10^{53} \text{ ergs} \\ &\simeq 2 \times 10^{59} \text{ MeV} \end{aligned}$$

with an uncertainty equal to a factor 2, and thus in excellent agreement with the predictions above.

It is perhaps worth emphasising that the neutrino burst from a supernova is truly prodigious. In all, some 10^{58} neutrinos were emitted from SN 1987A. Even at the Earth, some 170 000 light years distant, the flux was over 10^{10} neutrinos through each square centimetre.

What new particle physics has emerged from the study of SN 1987A? First, it has provided a new limit on the stability of neutrinos: we know that they can survive 170 000 light years crossing over from a nearby galaxy. Second, the neutrino pulse was observed to last for less than 10 seconds, so that the transit time of neutrinos of different energies was the same within 1 part in 5×10^{11}. The time of arrival t_E of a neutrino at the earth is given in terms of the emission time from the supernova, t_{SN}, its distance L and the neutrino mass and energy m and E by

$$t_E = t_{SN} + \frac{L}{c}\left(1 + \frac{m^2c^4}{2E^2}\right)$$

for $m^2 \ll E^2$. For two events the time difference will be given by

$$\Delta t = |\Delta t_E - \Delta t_{SN}| = \frac{Lm^2c^4}{2c}\left(\frac{1}{E_1^2} - \frac{1}{E_2^2}\right)$$

Clearly, low energy events will be more significant than high energy events for the mass estimate. If we take as typical values $\Delta t < 10$ s on the left-hand side, and $E_1 = 10$ MeV, $E_2 = 20$ MeV on the right-hand side of the above equation, we

get $m < 20$ eV. A more exact calculation, based on a model supernova simulation, gives essentially the same limit. It is quite consistent with the direct limit on m_{ν_e} from tritium decay (see Section 7.3).

It is probable that the neutrino burst is instrumental in helping to propagate the outward shock wave manifested in the spectacular optical display of the supernova phenomenon. Early computer models indicated that the outward moving shock would stall, as it met with, and produced disintegration into its constituent protons and neutrons of, the infalling nuclear matter from outside the core. Although the subject is not completely settled, later calculations suggest that, even with only a 1% interaction probability, neutrinos traversing the outer material, together with convective motion, could transfer enough energy to keep the shock wave moving. The neutral-current scattering of neutrinos would be vital in this process, since that is the only option for the ν_μ and ν_τ particles. So it seems that neutrinos of all flavours, and their interactions, continue to play a vital part in these cosmic events, while of course the corresponding charged leptons μ and τ disappeared within the first microsecond of the Big Bang, and only the stable electrons survive in quantity today. It is also appropriate to recall here that supernovae play a unique role in the production of the later part of the Periodic Table, since they are the only known sources of the extremely intense fluxes of neutrons which give rise to the rapid neutron capture chains that alone can build up the heavy elements.

Finally, it may be remarked here that supernovae are apparently not the only point sources in the sky capable of liberating 10^{53} ergs (10^{59} MeV) in a second or so. Just as spectacular are the extremely intense, short (0.1–100 s) bursts of γ-rays in the MeV or GeV energy range which carry similar integrated energy. These may be due to a rare phenomenon in which neutron star binaries collapse together as a result of gravitational radiation loss and coalesce to form black holes.

10.9.1 Ultra-high-energy neutrino sources

Finally we mention that experiments to detect very high energy neutrinos from the cosmos are being undertaken. It is known that the (steady) emission of high energy γ-rays in the TeV energy range has been observed from several point sources in the sky, particularly the so-called active galactic nuclei. These γ-rays are thought to originate from the decay of neutral pions ($\pi^0 \rightarrow 2\gamma$) produced in an as yet unknown acceleration mechanism. We expect that neutrinos will also be produced from charged pion decay ($\pi^+ \rightarrow \mu^+ + \nu_\mu$) in comparable numbers to the photons. Point sources of TeV photons can be detected on a cloudless, moonless night by a ground level array of mirrors and photomultipliers, which pick up the scintillation and Čerenkov light produced when the ensuing electron–photon shower traverses the high atmosphere. To detect neutrinos of similar energy, it is necessary to

look *downwards* rather than upwards, to avoid the atmospheric muon background. Neutrinos coming through the earth will produce upward-travelling muons that can in turn be detected from the Čerenkov light they produce in traversing great depths of sea-water or of Antarctic ice. Several projects involving photomultiplier arrays strung out over a cubic kilometre or so of water or ice are currently (1999) under way.

Problems

10.1 From (10.8) show that for $K = +1$ (closed universe), the Big Bang at $t = 0$ will be followed by a Big Crunch at $t = 8MG_N/c^2$, where M is the (assumed conserved) mass of the universe.

10.2 Calculate the expected ratio (10.32) of primordial helium to hydrogen, for the general case of n light neutrino flavours, where $n = 3, 4, 5, 6, \ldots$. Show that each additional neutrino flavour will increase the He/H ratio by about 2.5%.

10.3 Justify the statement in Section 10.4 that neutrinos will fall out of equilibrium with other matter and radiation when $kT < 3$ MeV, by proceeding as follows.
(a) Show that, neglecting the effects of neutral currents, which make only a 15% contribution, $\sigma(e^+e^- \to \nu\bar{\nu}) = G^2s/(6\pi)$, using the result (5.25) that for $\bar{\nu}_e + e \to e + \bar{\nu}_e$ scattering via W exchange, $\sigma = G^2s/(3\pi)$, where s is the squared cms energy.
(b) Calculate the mean value of s in collisions of e^+ and e^-, treating them as a Fermi gas at temperature T. Show that $\bar{s} = 2\bar{E}^2$, where $\bar{E}$ is the mean energy of the Fermi distribution (refer to the relevant integrals in the footnote in Section 10.3 for the value of $\bar{E}/kT$).
(c) Calculate the e^+ or e^- particle density N_e as a function of kT, making use of (10.24). Show that

$$N_e = \frac{1.803(kT)^3}{(\hbar c)^3\pi^2}$$

(d) From (a), (b) and c) calculate the event rate per unit time, $W = \sigma N v$, as a function of kT; v, the relative velocity of e^+ and e^-, may be taken as equal to c.
(e) Use (10.18) and (10.25) to calculate the time of expansion t as a function of kT, and setting this equal to W^{-1} deduce the temperature of the universe when the neutrinos decouple.

10.4 In a particular spiral galaxy whose disc is approximately normal to the line of sight from Earth, the observed light intensity falls off exponentially with distance r from the galactic centre. Assuming that the brightness in any region is proportional to the total material mass in that region, calculate the expected variation of the tangential velocity of the material, v_t, with r, and plot this on a graph. Show that for large enough values of r, $v_t \propto 1/r^{1/2}$.

10.5 Light arrives at the Earth from two far-off, equidistant regions of the sky separated by angle θ_0. Suppose that light started out shortly after the matter–radiation decoupling time, $t_d \sim 3 \times 10^5$ yr (see Section 10.4). Show that if the regions had been causally connected at $t < t_d$, the angle $\theta_0 < t_d T_d/(t_0 T_0)$, where $kT_d \sim 0.3$ eV measures the decoupling temperature, $kT_0 \sim 1$ meV is the present temperature and t_0 is the age of the universe ($t_0 \gg t_d$). Hence show that (in the absence of a preliminary inflationary stage) regions separated by more than about 1° in the sky apparently could not have been in thermal equilibrium.

11

Experimental methods

11.1 Accelerators

All accelerators employ electric fields to accelerate stable charged particles (electrons, protons, or heavier ions) to high energies. The simplest machine would be a d.c. high-voltage source (called a Van der Graaff accelerator), which can, however, only achieve beam energies of about 20 MeV. To do better, one has to employ a high frequency a.c. voltage and carefully time a bunch of particles to obtain a succession of accelerating kicks. This is done in the *linear* accelerator, with a succession of accelerating elements (called drift tubes) in line, or by arranging for the particles to traverse a single (radio-frequency) voltage source repeatedly, as in the *cyclic* accelerator.

11.1.1 Linear accelerators (linacs)

Figure 11.1 shows a sketch of a proton linac. It consists of an evacuated pipe containing a set of metal drift tubes, with alternate tubes attached to either side of a radio-frequency voltage. The proton (hydrogen ion) source is continuous, but only those protons inside a certain time bunch will be accelerated. Such protons traverse the gap between successive tubes when the field is from left to right, and are inside a tube (therefore in a field-free region) when the voltage changes sign. If the increase in length of each tube along the accelerator is correctly chosen then as the proton velocity increases under acceleration the protons in a bunch receive a continuous acceleration. Typical fields are a few MeV per metre of length. Such proton linacs, reaching energies of 50 MeV or so, are used as injectors for the later stages of cyclic accelerators.

Electrons above a few MeV energy travel essentially with light velocity, so that after the first metre or so an electron linac has tubes of uniform length. In practice, microwave frequencies are employed, the tubes being resonant cavities of a few centimetres in dimension, fed by a series of klystron oscillators, synchronised in

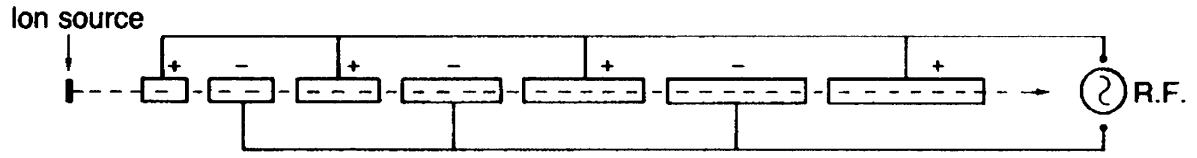

Fig. 11.1. Scheme of a proton linear accelerator. Protons from the ion source traverse the line of drift tubes (all inside an evacuated pipe). The successive lengths are chosen so that as the proton velocity increases the transit time from tube to tube remains constant.

time to provide continuous acceleration. The electrons, so to speak, ride the crest of an electromagnetic wave. The largest electron linac, at Stanford, is 3 km long and was built to accelerate electrons to 25 GeV using 240 klystrons, giving short (2 μs) bursts of intense power 60 times per second, with a similar bunch structure for the beam.

11.1.2 Cyclic accelerators (synchrotrons)

All modern proton accelerators and many electron machines are circular, or nearly so. The particles are constrained in a vacuum pipe bent into a torus that threads a series of electromagnets, providing a field normal to the plane of the orbit (Figure 11.2(a)). For a proton of momentum p in units GeV/c, the field must have a value B (in tesla), where

$$p = 0.3B\rho \tag{11.1}$$

and ρ is the ring radius in metres. The particles are accelerated once or more per revolution by radio frequency (RF) cavities. Both the field B and the RF frequency must increase and be synchronised with the particle velocity as it increases – hence the term synchrotron. Protons are injected from a linac source at low energy and at low field B, which increases to its maximum value over the accelerating cycle, typically lasting for a few seconds. Then the cycle begins again. Thus, the beam arrives in discrete pulses.

In the linac, the final beam energy depends on the voltage per cavity and the total length, while in the proton synchrotron it is determined by the ring radius and the maximum value of B. For conventional electromagnets using copper coils, B(max) is of order 14 kgauss (1.4 T), while if superconducting coils are used fields up to 9 T are possible.

As an example, the Fermilab synchrotron (called the Tevatron) is 1 km in radius and achieves 400 GeV proton energy with conventional magnets and 1000 GeV = 1 TeV with superconducting magnets. In recent years, superconducting RF cavities, which can achieve gradients up to 7 MeV per metre, have been increasingly employed.

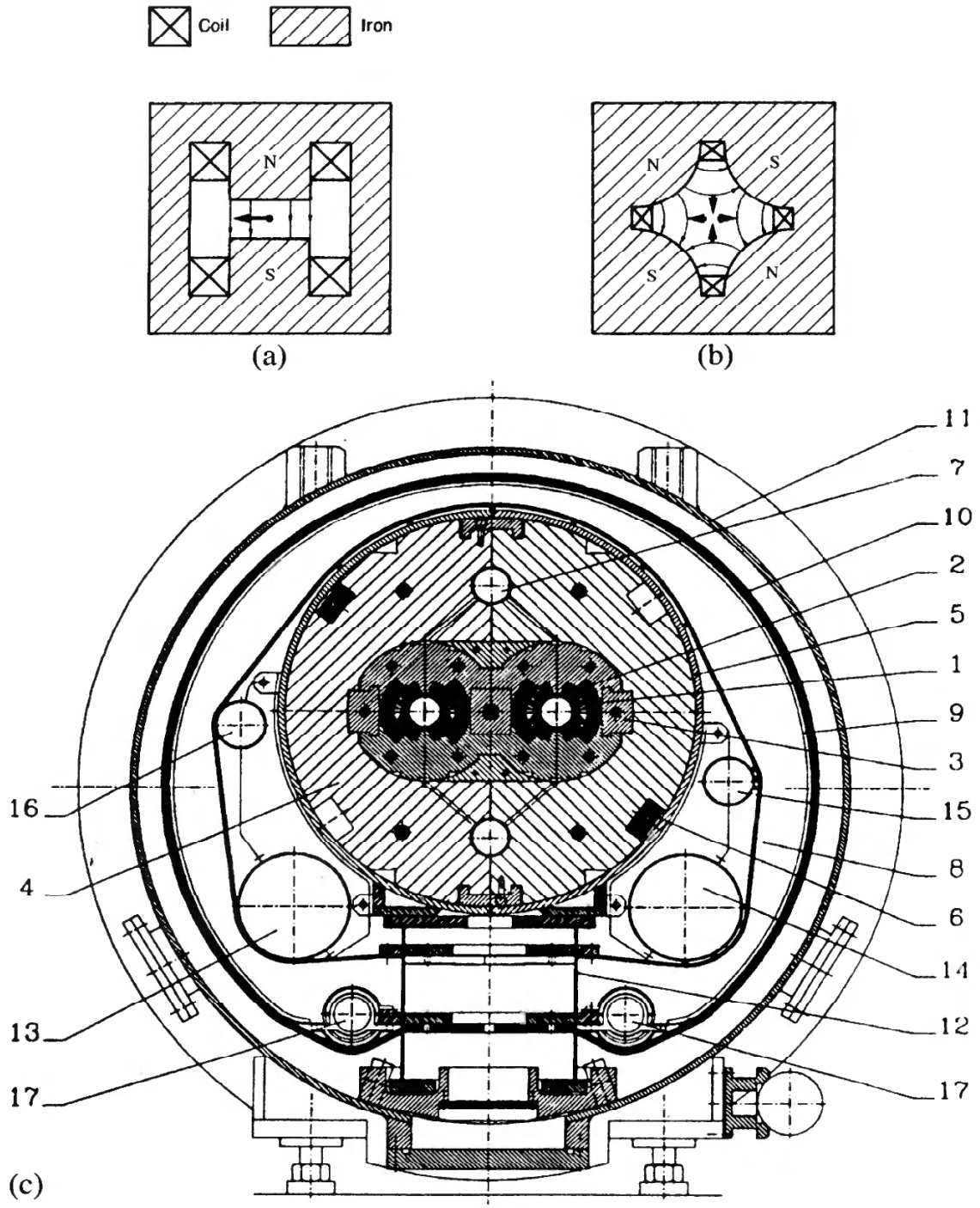

Fig. 11.2. Cross-section of (a) conventional bending (dipole) magnet: (b) focussing (quadrupole) magnet. The light arrows indicate field directions and the heavy arrows indicate the force on a positive particle travelling into the paper. (c) Cross-section of superconducting dipole two-in-one magnet of the Large Hadron Collider (LHC), with oppositely directed fields for the two vacuum tubes, carrying counter-rotating proton beams in this *pp* collider. Among the various components indicated are (1) the two vacuum chambers carrying protons circulating in opposite directions, each surrounded by (2) the superconducting coils, held in place by (3) the aluminium collars, in turn surrounded by (4) the steel return yoke. Cooling to 2 K is achieved via circulation of gaseous helium at (13) 5–10 K, and at (14) 1.8 K, in equilibrium with (superfluid) liquid helium II at (15). Thermal insulation is achieved with the super-insulating layer (10) and the vacuum vessel (11). The maximum field of 9 T is vertically up in the LH vacuum pipe and vertically down in the RH pipe.

In cyclic accelerators, protons make typically 10^5 revolutions, receiving an RF 'kick' of the order of a few MeV per turn, before achieving peak energy. In their total path, of perhaps 10^5 km, the stability and focussing of the proton bunch is of paramount importance, otherwise the particles will quickly diverge and be lost. In most machines, using the principle of strong focussing, the magnets are of two types: those in which bending magnets produce a uniform vertical dipole field over the width of the beam pipe and constrain the protons in a circular path (Figure 11.2(a)) and those in which focussing magnets produce a quadrupole field, as shown in Figure 11.2(b). In the figure, the field is zero at the centre and increases rapidly as one moves outward. A proton moving downwards (into the paper) will be subject to magnetic forces shown by the heavy arrows. The magnet shown is vertically focussing (force toward the centre) and horizontally defocussing (force away from the centre). Alternate quadrupoles have poles reversed so that, both horizontally and vertically, one obtains alternate focussing and defocussing effects. As anyone can demonstrate with a light beam and a succession of diverging and converging lenses of equal strength, the net effect is of focussing in both planes.

11.1.3 Focussing and beam stability

The particles circulating in a synchrotron do not travel in ideal circular orbits, but wander in and out from the circular path, in both horizontal and vertical planes, in what are called *betatron oscillations*. These arise from the natural divergence of the originally injected beam and from small asymmetries in fields and magnet alignments etc. The wavelength of these oscillations is related to the focal length of the quadrupoles and is short compared with the total circumference. In addition to these transverse oscillations, longitudinal oscillations, called *synchrotron oscillations*, occur as individual particles get out of step with the ideal, synchronous phase, for which the increase in momentum per turn from the RF kick exactly matches the increase in magnetic field. Thus, in Figure 11.3, a particle F that lags behind an exactly synchronous particle E will receive a smaller RF kick, will swing into a smaller orbit and next time around will arrive earlier. Conversely, an early particle D will receive a larger impulse, move into a larger orbit and subsequently arrive later. So particles in the bunch execute synchrotron oscillations about the equilibrium position, but the bunch as a whole remains stable.

We now give a brief summary. Protons are injected continuously from a linac at the beginning of the accelerator cycle when the dipole field is low. As acceleration proceeds, accelerated particles group into a number of equally spaced bunches (the spacing being determined by the radio frequency). The lateral extent of the bunch initially fills the aperture of the vacuum pipe (typically 5–10 cm across), but becomes compacted by the focussing to 1 mm or so at the end of acceleration.

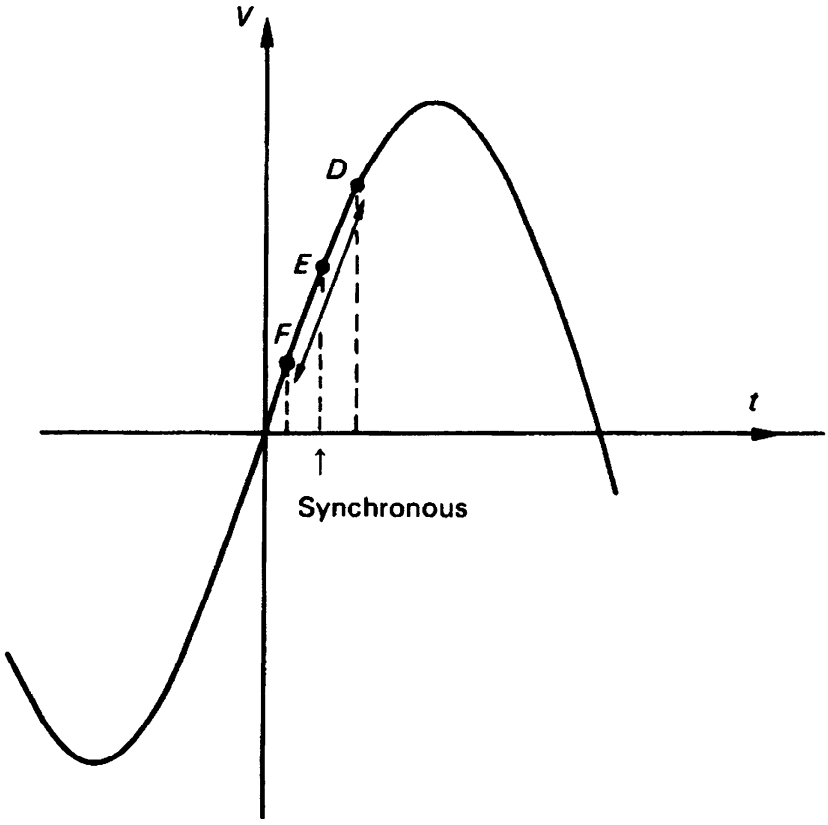

Fig. 11.3. Particles arriving early (D) or late (F) receive respectively more or less energy in RF acceleration than a synchronous particle (E). This respectively decreases or increases the rotation frequency, and the effect is that the particle performs oscillations (shown by the arrow) with respect to the synchronous particle.

Eventually the full-energy beam is extracted from the ring by a fast kicker magnet, or peeled off slowly (over a period of 1 s, say) with the aid of a thin energy-loss foil.

11.1.4 Electron synchrotrons

We have discussed briefly the most common type of proton accelerator today, the strong-focussing synchrotron. Electron synchrotrons based on similar principles have also been built. However, they have an important limitation, absent in a proton machine. Under the circular acceleration, an electron emits synchrotron radiation, the energy radiated per particle per turn being

$$\Delta E = \frac{4\pi}{3}\left(\frac{e^2\beta^3\gamma^4}{\rho}\right) \tag{11.2}$$

where ρ is the bending radius, β is the particle velocity and $\gamma = (1-\beta^2)^{-1/2}$. Thus, for relativistic protons and electrons of the same momentum the ratio of the energy loss is $(m/M)^4$, so that it is 10^{13} times smaller for protons than electrons. For an

electron of energy 10 GeV circulating in a ring of radius 1 km, this energy loss is 1 MeV per turn – rising to 16 MeV per turn at 20 GeV. Thus, even with very large rings and low guide fields, synchrotron radiation and the need to compensate this loss with large amounts of RF power become the dominant factor for an electron machine. Indeed, the large electron linac was built at Stanford for this very reason.

11.2 Colliding-beam accelerators

Much of our present experimental knowledge in the high energy field has been obtained with proton and electron accelerators in which the beam has been extracted and directed onto an external target – the so-called fixed-target experiments. In particular, high energy proton synchrotrons can thus provide intense secondary beams of hadrons (π, K, p, $\bar{p}$) and leptons (μ, ν), and several beam lines from one or more targets can be used simultaneously for a range of experiments and at a range of incident momenta.

During the last few decades colliding-beam machines have become dominant. In these accelerators, two counter-rotating beams of particles collide in several intersection regions around the ring. Their great advantage is the large energy available in the centre-of-momentum system (cms) for the creation of new particles. A fixed-target proton accelerator provides particles of energy E, say, that collide with a nucleon of mass M in a target. The square of the cms energy W is (see (1.6))

$$s = W^2 = 2ME + 2M^2 \tag{11.3}$$

Thus, for $E \gg M$, the kinetic energy available in the cms for new particle creation rises only as $E^{1/2}$. *The remaining energy is not wasted* – it is converted into kinetic energy of the secondary particles in the laboratory system, and this allows the production of high energy secondary beams.

However, if two relativistic particles (e.g. protons) with energies E_1 and E_2 and 3-momenta $\mathbf{p}_1$ and $\mathbf{p}_2$ circulate in opposite directions in a storage ring, then in a head-on collision the value of W is given by (see (1.7)):

$$s = W^2 = 2(E_1E_2 + p_1p_2) + 2M^2 \approx 4E_1E_2 \tag{11.4}$$

If $E_1 = E_2$, the cms of the collision is at rest in the laboratory. Virtually all the energy is available for new-particle creation, and rises as E instead of as $E^{1/2}$ in the fixed-target case. Indeed, the value of W is the same as that in a fixed-target machine of energy $E = 2E_1E_2/M$.

Colliding-beam machines also possess some disadvantages. First, the colliding particles must be stable, limiting one to collisions of protons or heavier nuclei, antiprotons, electrons and positrons (although high energy $\mu^+\mu^-$ colliders have

also been proposed). Second, the collision rate in the intersection region is low. The reaction rate is given by

$$R = \sigma L \tag{11.5}$$

where σ is the interaction cross-section and L is the luminosity (in $\text{cm}^{-2}\ \text{s}^{-1}$). For two oppositely directed beams of relativistic particles the formula for L will be

$$L = fn\frac{N_1 N_2}{A} \tag{11.6}$$

where N_1 and N_2 are the numbers of particles in each bunch, n is the number of bunches in either beam around the ring and A is the cross-sectional area of the beams, assuming them to overlap completely. f is the revolution frequency. Obviously, L is largest if the beams have small cross-sectional area A. The luminosity is, however, limited by the beam–beam interaction. Typical L-values are $\sim 10^{31}\ \text{cm}^{-2}\ \text{s}^{-1}$ for e^+e^- colliders, $\sim 10^{30}\ \text{cm}^{-2}\ \text{s}^{-1}$ for $\bar{p}p$ machines and $\sim 10^{33}\ \text{cm}^{-2}\ \text{s}^{-1}$ for pp colliders. These values may be compared with that of a fixed-target machine. A beam of 10^{13} protons s^{-1} from a proton synchrotron, in traversing a liquid-hydrogen target 1 m long, provides a luminosity $L \simeq 10^{38}\ \text{cm}^{-2}\ \text{s}^{-1}$.

In a pp or ep collider, two separate beam pipes and two sets of magnets are required, while e^+e^- and $p\bar{p}$ colliders have a unique feature. By the principle of charge conjugation (particle–antiparticle conjugation) invariance, it is clear that a synchrotron consisting of a set of magnets and RF cavities adjusted to accelerate an electron e^-, in a clockwise direction, will simultaneously accelerate a positron, e^+, along the same path but anticlockwise. Thus, e^+e^- and $p\bar{p}$ colliders require only a single vacuum pipe and magnet ring. Although there are necessarily two vacuum pipes, in the LHC pp collider both are inserted in the one superconducting magnet, with the field B in opposite senses for each pipe (see Figure 11.2(c)).

We can conclude from subsection 11.1.4 that synchrotron radiation losses become prohibitive for circular e^+e^- colliders above 100 GeV and, at these higher energies, linear e^+e^- colliders seem the only practical possibility. The first linear e^+e^- collider, the SLC at Stanford, accelerated e^+ and e^- to 50 GeV in a linac, and the two beams then diverged and were brought into head-on collision after magnetic deflection in circular arcs.

11.2.1 Cooling in $\bar{p}p$ colliders

While it is not difficult to obtain an intense e^+ (positron) source for use in e^+e^- colliders, the generation of an intense beam of $\bar{p}$ (antiprotons) for a $p\bar{p}$ collider is much more difficult. The antiprotons must be created in pairs with protons in energetic proton–nucleus collisions, with a low yield and a wide spread

Table 11.1. *Some present-day accelerators*

	Location		Energy, GeV
Proton synchrotrons			
CERN PS	Geneva		28
BNL AGS	Brookhaven, Long Island		32
KEK	Tsukuba, Tokyo		12
Serpukhov	USSR		76
SPS	CERN, Geneva		450
Fermilab Tevatron II	Batavia, Illinois		1000
Electron accelerators			
SLAC linac	Stanford, California		25–50
DESY synchrotron	Hamburg		7
Colliding-beam machines			
PETRA	DESY, Hamburg	e^+e^-	$22 + 22$
PEP	Stanford	e^+e^-	$18 + 18$
CESR	Cornell, NY	e^+e^-	$8 + 8$
TRISTAN	Tsukuba	e^+e^-	$30 + 30$
SLC	Stanford	e^+e^-	$50 + 50$
LEP I	CERN	e^+e^-	$50 + 50$
LEP II	CERN	e^+e^-	$100 + 100$
S$p\bar{p}$S	CERN	$p\bar{p}$	$310 + 310$
Tevatron I	Fermilab	$p\bar{p}$	$1000 + 1000$
HERA	Hamburg	ep	$30e + 820p$
LHC (2005)[a]	CERN	pp	$7000 + 7000$

[a] Expected completion date

in momentum and angle of emission from the target. In other words, viewed in the centre-of-momentum frame of all the antiprotons produced, individual particles are like molecules in a very hot gas, with random motions described by a 'temperature'. To store enough antiprotons, the beam must be 'cooled' in order to reduce its divergence and longitudinal momentum spread. This is a technical problem, which we mention here because its solution was crucial in the discovery of the $W^{\pm}$, Z^0 carriers of the weak force at CERN, and of the top quark at Fermilab.

One approach, employed at the CERN $p\bar{p}$ collider (Figure 11.4), is to use a statistical method – hence it is called stochastic cooling. A bunch of $\sim 10^7$ antiprotons of momentum ~ 3.5 GeV/c emerges from a Cu target (bombarded by a pulse of 10^{13} protons of energy 26 GeV from the CERN PS) and is injected into the outer half of a wide-aperture toroidal vacuum chamber, divided by a mechanical shutter and placed inside a special accumulator-magnet ring. A pick-up coil in one section of the ring senses the average deviation of particles from the ideal

orbit, and a correction signal is sent at nearly light velocity across a chord to a kicker, in time to deflect them, as they come round, toward the ideal orbit. After 2 seconds of circulation, lateral and longitudinal spreads have been reduced by an order of magnitude. The shutter is opened and the 'cooled' bunch of antiprotons is magnetically deflected and stacked in the inside half of the vacuum chamber, where it is further cooled. The process is repeated until, after a day or so, 10^{12} antiprotons have been stacked; they are then extracted for acceleration in the main collider ring.

A list of proton and electron synchrotrons and of colliding-beam machines is given in Table 11.1. In addition to the ones listed, lower energy e^+e^- colliders, called CESR, PEP II and KEKB were designed to study massive quarkonium states, in particular the upsilon $\Upsilon(4S)$ system (see subsection 4.1.2). They have cms energies up to 11 GeV, with asymmetric beam energies (typically in a 3 : 1 ratio). The consequent Lorentz boost to the heavy $Q\bar{Q}$ system means that decays of short-lived states are easier to detect. These machines are expressly designed as 'B meson factories' with the very high luminosities needed to study CP violation in B decays (see Section 7.18).

Proton accelerators have also been used to accelerate heavy ions with atomic numbers up to that of Pb. Dedicated heavy-ion colliders have also been built, notably the RHIC collider at BNL. Ultrarelativistic heavy-ion collisions offer the possibility of detecting a phase transition to a quark–gluon plasma (see Section 6.7).

11.3 Accelerator complexes

All accelerators, and particularly the highest energy machines, involve several stages of acceleration. An example is given in the schematic diagram of Figure 11.5, showing the CERN LHC project. Protons emerge at 750 keV from a radio frequency quadrupole accelerator and are boosted to 50 MeV in a linear accelerator. From this they are transferred to the PS booster ring, where they achieve 1.4 GeV, before injection and accelerator to 26 GeV in the main PS ring. From here the protons are injected into the SPS ring, where they are accelerated to 450 GeV. From the SPS they are finally injected into the LHC/LEP superconducting magnet ring, some 27 km in circumference, to be accelerated to the full 7 TeV energy per beam.

11.4 Secondary particle separators

Fixed-target machines are employed to produce secondary beams of various stable or unstable particles, directly or via decay; e.g. $\pi, \mu, e, \gamma, K, \nu$. Generally, a



Fig. 11.4. A section of the underground 6 km tunnel of the CERN SPS machine, which accelerates protons to 450 GeV and has also been used to store and collide 300 GeV proton and antiproton beams circulating in opposite directions in the same beam pipe. The SPS also serves as an injector to the larger, 27 km circumference LEP e^+e^- ring, which in turn will also be used with superconducting magnets (Figure 11.2(c)) for the LHC pp collider.

secondary beam of charged particles, focussed and momentum analysed by a magnet train, will contain several types, e.g. π^-, K^-, $\bar{p}$, and so separators are used to select the type of particle required. At low energies, of a few GeV or less, the separator consists of two parallel plates with a high potential between them. The beam passes between the plates and then through a deflecting magnet and slit system. The difference in angular deflection of two relativistic particles of momentum p and masses m_1 and m_2 after traversing an electric field of strength E and length L is easily shown to be

$$\Delta\theta = EeL(m_1^2 - m_2^2)/(2p^3)$$

Because the deflection falls as $1/p^3$, the method is not applicable at high momentum, above a few GeV/c. At higher beam energies, radio frequency separators are employed. The travel time between two RF cavities depends on velocity and hence on the particle mass m, and the frequency can be adjusted so that the sideways deflection of the wanted particles in the first cavity is doubled when they reach

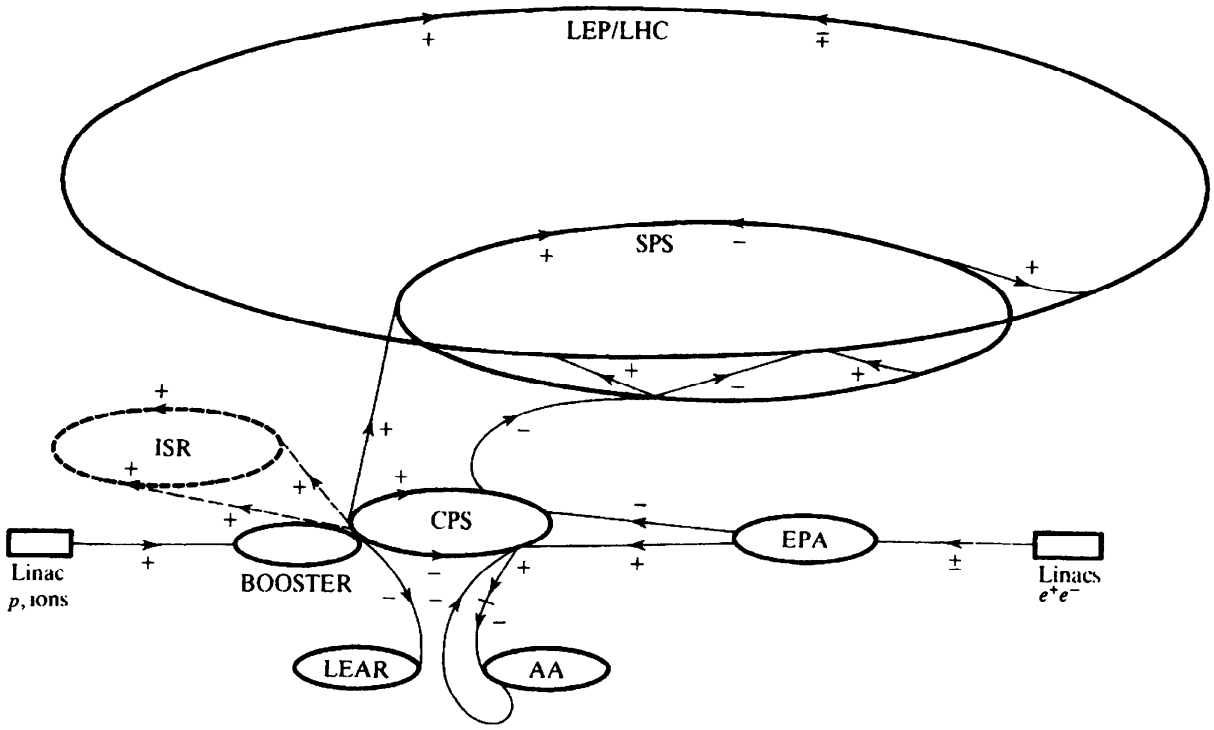

Fig. 11.5. Schematic diagram of the CERN accelerator complex. Protons or heavy ions are accelerated in a linac or RF quadrupole system and injected into a fast-cycling booster that feeds into the CERN Proton Synchrotron (CPS) reaching 25 GeV proton energy, thence into the larger Super Proton Synchrotron (SPS) ring for acceleration to 450 GeV. The CPS can also be used to generate an antiproton beam, which is fed into an antiproton accumulator ring AA, to be injected back into the CPS and thence into the SPS ring, acting as a proton–antiproton collider. An electron linac is used to inject e^+ and e^- beams into the electron–positron accumulator (EPA) for acceleration into the CPS, SPS and, finally, the LEP e^+e^- collider ring. The LEP tunnel also houses a two-in-one magnet ring (Figure 11.2(c)) for accelerating protons to form a 7 TeV on 7 TeV pp collider. In the (one-time) intersecting storage rings (ISR), protons were accelerated in opposite directions to 25 GeV, in separate magnet rings.

the second cavity, while the deflections of unwanted particles are reduced by the second cavity.

For beams of muons and neutrinos, particle separation depends on the decay of the parent $\pi^\pm$ and $K^\pm$ particles generated at an external target by an extracted proton beam. The secondary pions and kaons traverse a decay tunnel, perhaps several hundred metres in length (the mean decay length of a 1 GeV pion is 55 m). A muon beam of fixed momentum is produced by a subsequent system of bending and focussing magnets. Pure neutrino beams can only be produced by the brute force method of using thick steel or concrete shielding to filter out hadrons (by interaction) and muons (by ionisation loss). For example, neutrinos from a 200 GeV pion beam (Figure 7.11) require a filter of almost 200 m of steel.

11.5 Interaction of charged particles and radiation with matter

11.5.1 Ionisation loss of charged particles

The detection of nuclear particles depends ultimately on the fact that, directly or indirectly, they transfer energy to the medium they are traversing via the ionisation or excitation of the constituent atoms. This can be observed as charged ions, e.g. in a gas counter, or as a result of the scintillation light, Čerenkov radiation, etc. that is subsequently emitted, or as signals from electron–hole pairs in a solid-state counter.

The Bethe–Bloch formula for the mean rate of ionisation loss of a charged particle is given by

$$\frac{dE}{dx} = \frac{4\pi N_0 z^2 \alpha^2}{mv^2} \frac{Z}{A} \left\{ \ln \left[\frac{2mv^2}{I(1-\beta^2)} \right] - \beta^2 \right\} \tag{11.7}$$

where m is the electron mass, z and v are the charge (in units of e) and velocity of the particle, $\beta = v/c$, N_0 is Avogadro's number, Z and A are the atomic number and mass number of the atoms of the medium, and x is the path length in the medium, which is measured in g cm^{-2} or kg m^{-2}, corresponding to the amount of matter transversed. The quantity I is an effective ionisation potential, averaged over all electrons, with approximate magnitude $I = 10Z$ eV. Equation (11.7) shows that dE/dx is independent of the mass M of the particle, varies as $1/v^2$ at non-relativistic velocities and, after passing through a minimum for $E \simeq 3Mc^2$, increases logarithmically with $\gamma = E/Mc^2 = (1-\beta^2)^{-1/2}$. The dependence of dE/dx on the medium is very weak, since $Z/A \simeq 0.5$ in all but hydrogen and the heaviest elements. Numerically, $(dE/dX)_{\min} \simeq$ 1–1.5 MeV cm^2 g^{-1} (or 0.1–0.15 MeV m^2 kg^{-1}).

Formula (11.7) is an important one. We can show the origin of the main factors in it, starting off with the Rutherford formula for the elastic Coulomb scattering of an electron of momentum p through an angle θ by a massive nucleus of charge ze. The 3-momentum transfer is clearly $q = 2p\sin(\theta/2)$, so that $q^2 = 2p^2(1-\cos\theta)$. Then inserting (5.1) into (2.19), and with $dq^2 = p^2 d\Omega/\pi$, (2.19) gives for the differential cross-section

$$\frac{d\sigma}{dq^2} = \frac{4\pi\alpha^2 z^2}{v^2 q^4} \tag{11.8}$$

where we use units $\hbar = c = 1$ and the relative velocity $v = \beta = v/c$ and nuclear charge ze have been retained explicitly. Since the nucleus is massive, the energy transfer is negligible and so q^2 is also the Lorentz-invariant 4-momentum transfer, squared. The above formula will therefore equally apply, if we take the electron as stationary and the nucleus as moving at velocity v. The electron then receives a

recoil kinetic energy T, and it is easy to show that

$$q^2 = 2mT$$

where m is the electron mass (see (5.31)). Substituting in (11.8), the cross-section for scattering the nucleus ze becomes

$$\frac{d\sigma}{dT} = \frac{2\pi\alpha^2 z^2}{mv^2}\frac{1}{T^2}$$

The number of scatters of the nucleus that transfer energy in the range $T \to T+dT$ to atomic electrons, in traversing a thickness dx of medium of atomic number Z and mass number A, which thus contains $N_0 Z/A$ electrons per g cm^{-2} is therefore (assuming the electrons to be free and stationary)

$$dN = \frac{2\pi N_0 \alpha^2 z^2}{mv^2}\frac{Z}{A}\frac{dT}{T^2}dx \tag{11.9}$$

The ionisation energy loss per g cm^{-2} traversed by the nucleus ze will therefore be

$$\frac{dE}{dx} = \int T\frac{dN}{dx} = \frac{2\pi N_0 \alpha^2 z^2}{mv^2}\frac{Z}{A}\ln\frac{T_{\max}}{T_{\min}} \tag{11.10}$$

A straightforward calculation gives for the maximum energy transfer to an electron of mass m by a nucleus of mass M, total energy E and velocity β

$$T_{\max} = \frac{2mv^2E^2}{M^2 + m^2 + 2mE} \approx \frac{2mv^2}{1-\beta^2} \tag{11.11}$$

where in the last expression we have taken $M^2 \gg m^2 + 2mE$. The value of $T_{\min}$ will be of order I, the mean ionisation potential of the atoms of the medium.

Inserting these values for $T_{\max}$ and $T_{\min}$, we see that the energy loss in (11.10) happens to be just a factor 2 smaller than in (11.7). However these estimates of $T_{\max}$ and $T_{\min}$ are the classical limits. If one takes quantum-mechanical limits from the Uncertainty Principle on the values of the impact parameter for the collision, as well as relativistic effects on the Coulomb field of the incident particle, a factor 2 in the energy loss results.

Figure 11.6 shows the observed relativistic rise in ionisation loss as a function of $p/(mc) = (\gamma^2 - 1)^{1/2}$ for relativistic particles in a gas (an argon–methane mixture). For $\gamma \sim 10^3$, it reaches 1.5 times the minimum value. The relativistic rise is partly associated with the fact that the transverse electric field of the particle is proportional to γ, so that ever more distant collisions become important as the energy increases. Eventually, when the impact parameter becomes comparable to interatomic distances, polarisation effects in the medium (associated with the dielectric constant) halt any further increase. In solids, rather than gases, such effects become important at a much lower value of γ (~ 10), and this plateau value

is only about 10% larger than $(dE/dx)_{\min}$. Part of the energy lost by a relativistic particle may be reemitted from excited atoms in the form of coherent radiation at a particular angle. Such Čerenkov radiation is discussed in subsection 11.6.5 below.

The bulk of the energy loss results in the formation of ion pairs (positive ions and electrons) in the medium. One can distinguish two stages in this process. In the first stage, the incident particle produces primary ionisation in atomic collisions. The electrons knocked out in this process have a distribution in energy E' roughly of the form $dE'/(E')^2$, as in (11.9); those of higher energy (called δ-rays) can themselves produce fresh ions in traversing the medium (secondary ionisation). The resultant total number of ion pairs is 3–4 times the number of primary ionisations, and is proportional to the energy loss of the incident particle in the medium. Equation (11.7) gives the *average* value of the energy loss dE in a layer dx, but there will be fluctuations about the mean, dominated by the relatively small number of 'close' primary collisions with large E'. This so-called Landau distribution about the mean value is therefore asymmetric, with a tail extending to values much greater than the average. Nevertheless, by sampling the number of ion pairs produced in many successive layers of gas and removing the 'tail', the mean ionisation loss can be measured within a few per cent. In this way γ can be estimated from the relativistic rise and, if the momentum is known, this can provide a useful method for estimating the rest mass and thus differentiating between pions, kaons and protons.

The total number of ions produced in a medium by a high energy particle depends on dE/dx and the energy required to liberate an ion pair. In a gas, this energy varies from 40 eV in helium to 26 eV in argon. In semiconductors, however, it is only about 3 eV, so the number of ion pairs is much larger. If the charged particle comes to rest in the semiconductor, the energy deposited is measured by the total number of ion pairs, and such a detector therefore is not only linear but has extremely good energy resolution (typically 10^{-4}).

11.5.2 Coulomb scattering

In traversing a medium, a charged particle suffers electromagnetic interactions with both electrons and nuclei. As (11.7) indicates, dE/dx is inversely proportional to the target mass so that, in comparison with electrons, the energy lost in Coulomb collisions with nuclei is negligible. However, because of the larger target mass, transverse scattering of the particle is appreciable in the Coulomb field of the nucleus, and is described by the Rutherford formula (11.8). For an incident particle of charge ze, momentum p and velocity v being scattered through an angle θ by a

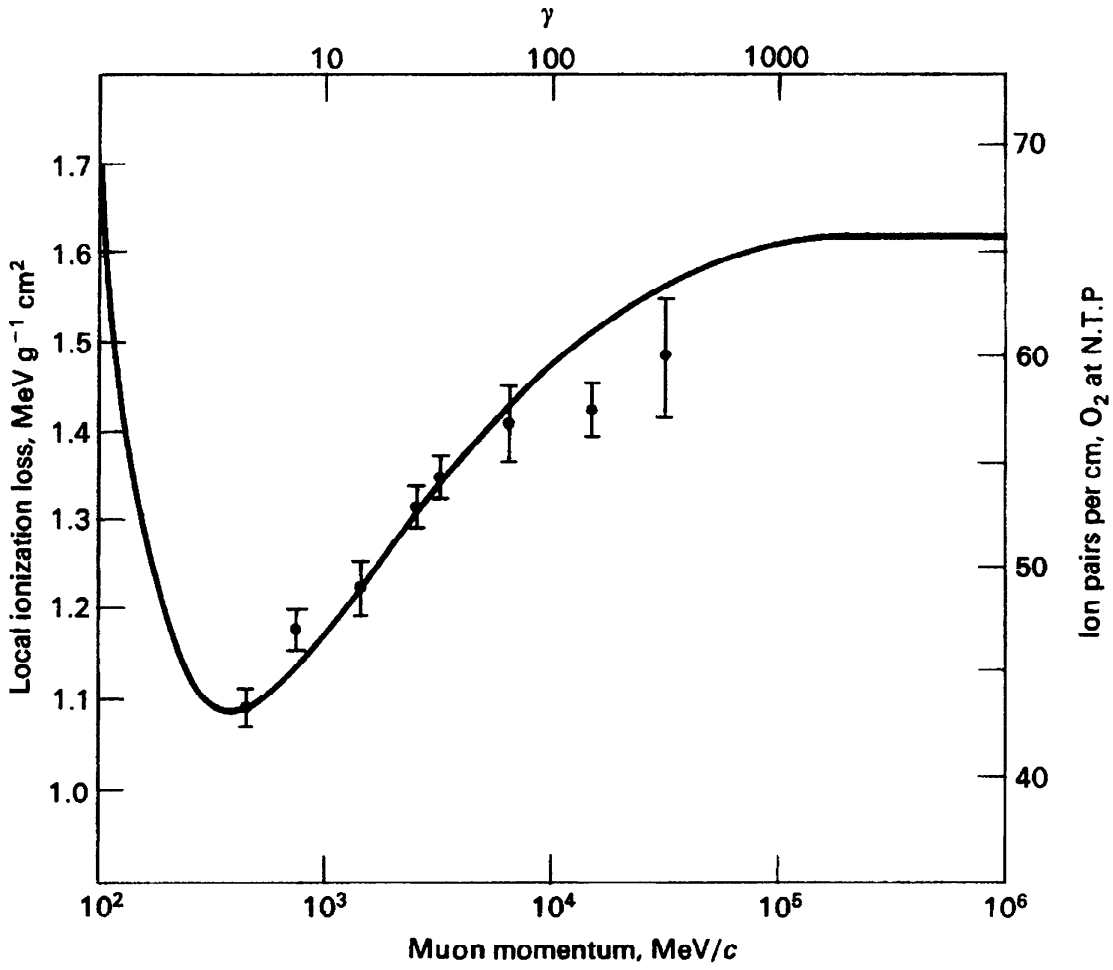

Fig. 11.6. The mean ionisation energy loss of charged particles in an argon with 5% methane mixture, showing the relativistic rise as a function of $p/(mc)$. Measurements by multiple ionisation sampling (after Lehraus *et al.* 1978).

nucleus of charge Ze, this takes the form

$$\frac{d\sigma(\theta)}{d\Omega} = \frac{1}{4}\left(\frac{Zz\alpha}{pv}\right)^2 \frac{1}{\sin^4(\theta/2)} \tag{11.12}$$

inserting in (11.8) the expressions $dq^2 = p^2 d\Omega/\pi$ and $q = 2p\sin(\theta/2)$. For small scattering angles the cross-section is large, so that in any given layer of material the net scattering is the result of a large number of small deviations, which are independent of one another. The resultant distribution in the net angle of *multiple* scattering follows a roughly Gaussian distribution:

$$P(\phi)d\phi = \frac{2\phi}{\langle\phi^2\rangle}\exp\left(\frac{-\phi^2}{\langle\phi^2\rangle}\right)d\phi \tag{11.13}$$

Table 11.2. *Radiation lengths in various elements*

Element	Z	E_c, MeV	X_0, g cm^{-2}
hydrogen	1	340	63.1
helium	2	220	94.3
carbon	6	103	42.7
aluminium	11	47	24.0
iron	26	24	13.8
lead	82	6.9	6.4

The root mean square (rms) deflection in a layer t of the medium is given by

$$\phi_{\text{rms}} = \langle \phi^2 \rangle^{1/2} = \frac{zE_s}{pv}\sqrt{\frac{t}{X_0}} \tag{11.14}$$

where

$$E_s = \sqrt{4\pi \times 137}\, mc^2 = 21 \text{ MeV} \tag{11.15}$$

and

$$\frac{1}{X_0} = 4Z^2 \left(\frac{N_0}{A}\right) \alpha^3 \left(\frac{\hbar c}{mc^2}\right)^2 \ln\left(\frac{183}{Z^{1/3}}\right) \tag{11.16}$$

The quantity X_0, usually quoted in g cm^{-2} of matter traversed is called the *radiation length* of the medium (see Table 11.2), and incorporates all the dependence of ϕ_{rms} on the medium. Numerically, therefore, a singly charged particle ($z = 1$) of momentum p and velocity v, with the product pv measured in MeV, suffers an rms deflection of $21/(pv)$ radians in traversing one radiation length. The rms angular deflection will be azimuthally symmetric about the trajectory: along one axis in the plane normal to the trajectory, it will be $1/\sqrt{2}$ times the value (11.14).

Coulomb scattering is important in practice because it frequently limits the precision with which the direction of a particle can be determined. As an example, let us consider the determination of the momentum of a high energy charged particle by its deflection in the field **B** of a solid iron magnet. If there is no scattering, and the momentum does not change appreciably in traversing the magnet, the radius of curvature ρ is given by $pc = Be\rho$, so that in traversing a distance s, the deflection will be

$$\phi_{\text{mag}} = \frac{s}{\rho} = \frac{Bes}{pc} = \frac{300Bs}{pc}$$

where B is in tesla (1 T = 10^6 G), s is in metres, and pc is in MeV. The rms

Coulomb scattering in the plane of the trajectory will be

$$\phi_{\text{scat}} = \frac{21}{\sqrt{2}} \frac{1}{p\beta c} \sqrt{\frac{s}{X_0}}$$

so that

$$\frac{\phi_{\text{scat}}}{\phi_{\text{mag}}} = \frac{0.05}{B\beta\sqrt{X_0 s}}$$

which is independent of the particle momentum for a relativistic particle ($\beta = 1$). For example, in magnetised iron $X_0 = 0.02$ m and $B \simeq 1.5$ T, and so $\phi_{\text{scat}}/\phi_{\text{mag}} = 0.25$ for $s = 1$ m, falling to 0.10 for $s = 6$ m.

11.5.3 Radiation loss by electrons

Electrons lose energy in traversing a medium in two ways: the ionisation energy loss (11.7) and the process of radiation loss or *bremsstrahlung*. The radiative collisions of electrons occur principally with the atomic nuclei of the medium. The nuclear electric field decelerates an electron and the energy change appears in the form of a photon; hence the term *bremsstrahlung*, 'braking radiation'. As indicated below (6.25), the photon spectrum has the approximate form dE'/E', where E' is the photon energy. Integrated over the photon spectrum, the total radiation loss of an electron of energy E in traversing a thickness dx of medium is therefore proportional to E, and

$$\left(\frac{dE}{dx}\right)_{\text{rad}} = -\frac{E}{X_0} \tag{11.17}$$

where X_0, the radiation length, is defined in (11.16). From (11.17) it follows that the average energy of a beam of electrons of initial energy E_0, after traversing a thickness x of medium, will be

$$\langle E \rangle = E_0 \exp\left(-\frac{x}{X_0}\right) \tag{11.18}$$

Thus, the radiation length X_0 may be simply defined as the thickness of the medium that reduces the mean energy of a beam of electrons by a factor e.

Since the rate of ionisation energy loss for fast electrons, $(dE/dx)_{\text{ion}}$, is approximately constant while the average radiation loss $(dE/dx)_{\text{rad}}$ is proportional to E, it follows that at high energies radiation loss dominates. The *critical energy* E_c is defined as that at which the two are equal. Very roughly, for $Z \geq 6$,

$$E_c \simeq \frac{600}{Z} \text{ MeV} \tag{11.19}$$

as can be verified by inserting the numerical constants into equations (11.7),

(11.16) and (11.17). Values of X_0 and E_c in various materials are given in Table 11.2.

11.5.4 Absorption of γ-rays in matter

There are three types of process responsible for the attenuation of γ-rays in matter: photoelectric absorption, Compton scattering and pair production. The photoelectric cross-section varies with photon energy E as $1/E^3$ and the Compton cross-section as $1/E$, so that for $E > 10$ MeV, the process of pair production, with a cross-section essentially independent of energy, is dominant (see Figure 11.7).

The process of conversion of a high energy photon to an electron–positron pair (in the field of a nucleus to conserve momentum) is closely related to that of electron bremsstrahlung. The attenuation of a beam of high energy photons of intensity I_0 by pair production in a thickness x of absorber is described approximately by

$$I = I_0 \exp\left(-\frac{7x}{9X_0}\right) \tag{11.20}$$

so the intensity is reduced by a factor e in a distance $9X_0/7$, sometimes called the *conversion length*. It is to be emphasised that, although the threshold for pair production is $E_{\text{th}} = 2m_e c^2 \simeq 1$ MeV, the asymptotic value (11.20) for the absorption coefficient is not attained until one reaches photon energies of almost 1 GeV.

11.6 Detectors of single charged particles

The detectors employed in experiments in high energy physics record the position, arrival time and identity of charged particles. The precise evaluation of position coordinates is required in order to determine the particle's trajectory and, in particular, its momentum (from the deflection in a magnetic field). Precise timing is often needed to be able to associate one particle with another from the same interaction, frequently in situations where the total interaction rate per unit time may be very high. Spatial resolution is also important in order to distinguish which secondaries originate from two or more closely related vertices, as would occur in the production and decay of heavy-flavour mesons (B, D, ...) with lifetimes in the region of 10^{-12} s. The identity of a particle may be established from the simultaneous measurement of velocity (by time-of-flight or Čerenkov radiation) and momentum, and hence of the rest mass; or from the observation of decay modes, if the particle is unstable; or from its observed interaction with matter via strong, electromagnetic, or weak forces. Neutral particles are detected through

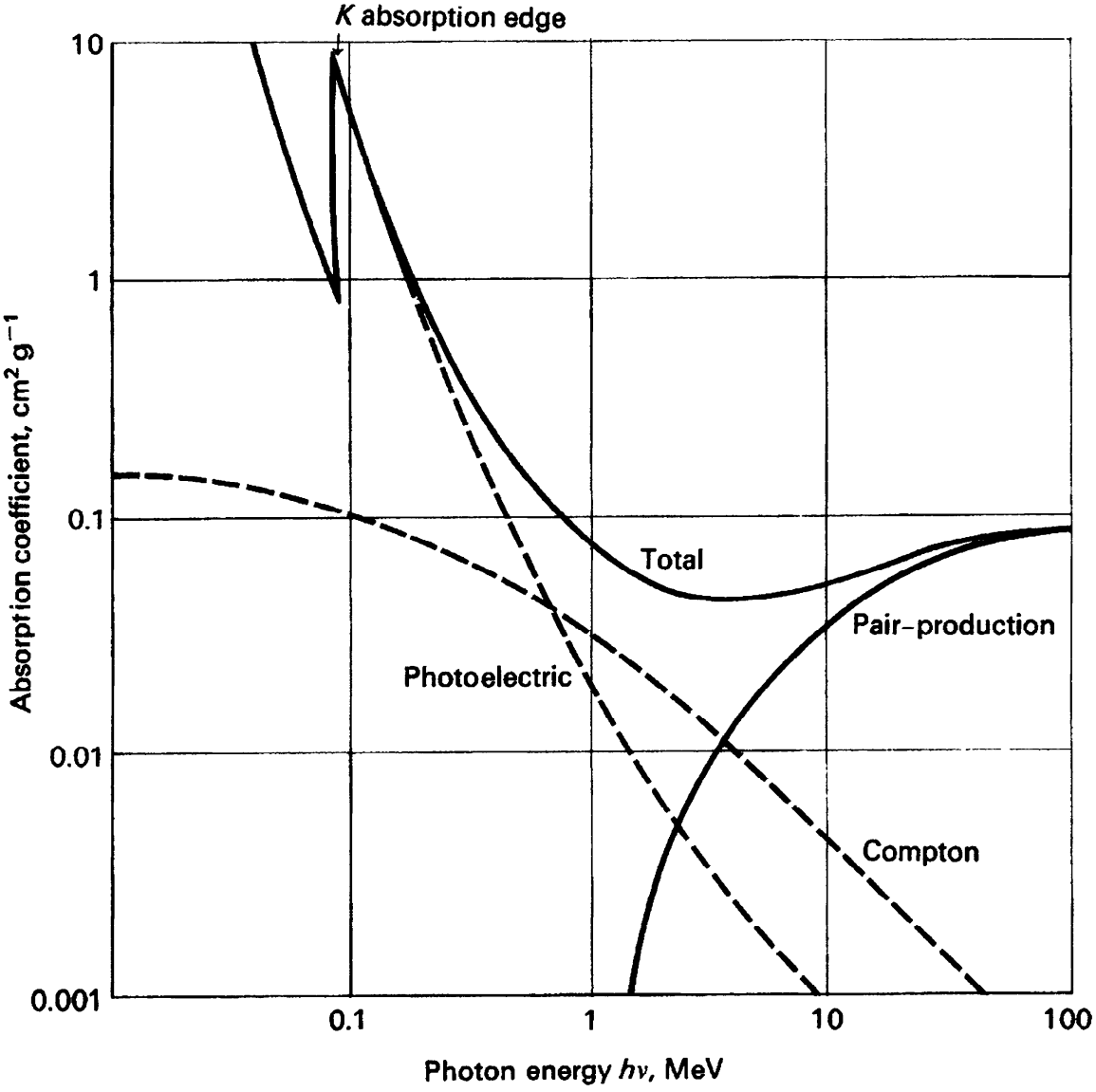

Fig. 11.7. The absorption coefficient per g cm^{-2} of lead for γ-rays as a function of energy.

their decay (e.g. $K^0 \rightarrow \pi^+\pi^-$) and/or interaction with matter (e.g. $\pi^0 \rightarrow 2\gamma$, $\gamma \rightarrow e^+e^-$), leading to secondary charged particles.

No single detector is in general able to meet all these requirements, and a combination of detectors of different types is required. We first discuss the principal types of detector in current use in the field and then give some examples of how they may be combined in an integrated system.

Over the last decades, very few radically new concepts in basic detection methods have been developed. Rather, progress has been in the exploitation and adaptation of well-established methods; there has been a revolution in electronics and the computer technology for selecting, recording and analysing huge amounts of data at high speed, often in real time, and the development of hybrid systems involving many different types of detector, frequently on a massive scale.

11.6.1 Proportional counters

The proportional counter is one of the oldest devices for the recording of ionisation. Single counters consist of a gas-filled cylindrical metal or glass tube of radius r_2 maintained at negative potential, with a fine central anode wire of radius r_1 at positive potential. The electric field in the gas for a potential difference V_0 is then

$$E(r) = \frac{V_0}{r \ln(r_2/r_1)} \tag{11.21}$$

An electron liberated by ionisation at radius r_a will drift toward the anode, gaining an energy $T = e\int_{r_b}^{r_a} E(r)dr$ when it reaches radius r_b. If T exceeds the ionisation energy of the gas, then fresh ions are liberated and a chain of such processes leads to an avalanche of electrons and positive ions. The gas amplification factor, equal to the total number of secondary electrons reaching the anode per initial ion pair, is typically $\sim 10^5$ and is independent of the number of primary ions; hence the name 'proportional counter'.

The most significant advance in this field was the introduction of the multiwire proportional counter (MWPC) by Charpak (1968, 1970). This device consists of many parallel anode wires stretched in a plane between two cathode planes (Figure 11.8(a)). The different anode wires act as independent detectors. A typical structure has wires of 20 μm diameter with 2 mm spacing, between cathode planes 12 mm apart, operating at a potential difference of 5 kV and containing an argon–isobutane gas mixture. In general, several electrons from the primary ionisation will drift toward an anode wire and create separate avalanches yielding negative pulses with very fast rise times ($\sim$ 0.1 ns). The positive ions have much lower mobility and induce pulses on both the cathode and neighbouring anode wires of duration $\sim$ 30 ns. The effective spatial resolution from the anode pulses is of order 0.7 mm. If the cathode is in the form of strips, the centre of gravity of the cathode pulses may be used to obtain an accurate spatial position of the avalanche (to within 0.05 mm).

11.6.2 Spark and streamer chambers

Proportional chambers are operated with anode–cathode potentials of order 5 kV, where the efficiency for recording charged particles reaches a plateau of practically 100%. Further increase in voltage eventually leads to electric breakdown of the gas. This takes place when the space charge inside the avalanche is strong enough to shield the external field; recombination of ions then occurs, resulting in photon emission and the birth of secondary ionisation and new avalanches outside the initial one. This process propagates until an ion column links anode and cathode

and a spark discharge occurs. The counter is then said to operate in the Geiger region. An example of a spark chamber is given in Figure 1.6.

If, however, a short (10 ns) high-voltage pulse (10–50 kV cm^{-1}) is applied between transparent parallel-plate electrodes, then only short (2–3 mm) streamer discharges develop from the ion trail of a crossing particle, and a direct track image, rather like that in a bubble chamber, can be obtained and photographed through the electrodes. Such a *streamer chamber* possesses good multitrack efficiency and space resolution; it was a widely used technique in the 1960s but ultimately was replaced by other methods because of its long recovery time and the fact that, as for a bubble chamber, the analysis of optical images is required.

11.6.3 Drift chambers

As indicated above, the MWPC typically has a spatial resolution of 1 mm or less and a time resolution of 30 ns. However, to achieve this resolution over large areas, an enormous number of wires (together with amplifiers) is required. A great reduction in cost can be achieved by drifting the electrons from the primary ionisation over (typically) 10 cm in a low-field region (1 kV cm^{-1}) before reaching the high-field amplification region near the anode wire; the collection time of the avalanche then gives a measure of the position of the ionisation column. Figure 11.8(b) shows a typical planar arrangement of anode and cathode wires, with field wires at graded potentials, as required to give a uniform drift field.

For experiments at colliding-beam machines, the detection system surrounds the interaction point. The magnetic field **B** for momentum analysis is usually supplied by a solenoid with axis along the beam, the drift chamber detector being placed inside the solenoid. The wire plane systems can be arranged to provide radial, azimuthal or axial electric fields, **E**. In the first two cases the drift direction is at an angle to the **E** field (this Lorentz angle is proportional to the drift velocity and B/E), while if **E** and **B** are parallel the Lorentz force is zero. Typically, electric fields in drift chambers are about 200 kV m^{-1} and inverse drift velocities are about 20 μs m^{-1} in argon–isobutane or argon–methane gas mixtures.

11.6.4 Scintillation counters

The scintillation counter (see Figure 11.9) has been a universal detector in a very wide range of high energy physics experiments for over 50 years. The excitation of the atoms of certain media by ionising particles results in luminescence (scintillation), which can be recorded by a photomultiplier. The scintillators in most common use are inorganic single crystals and organic liquids and plastics,

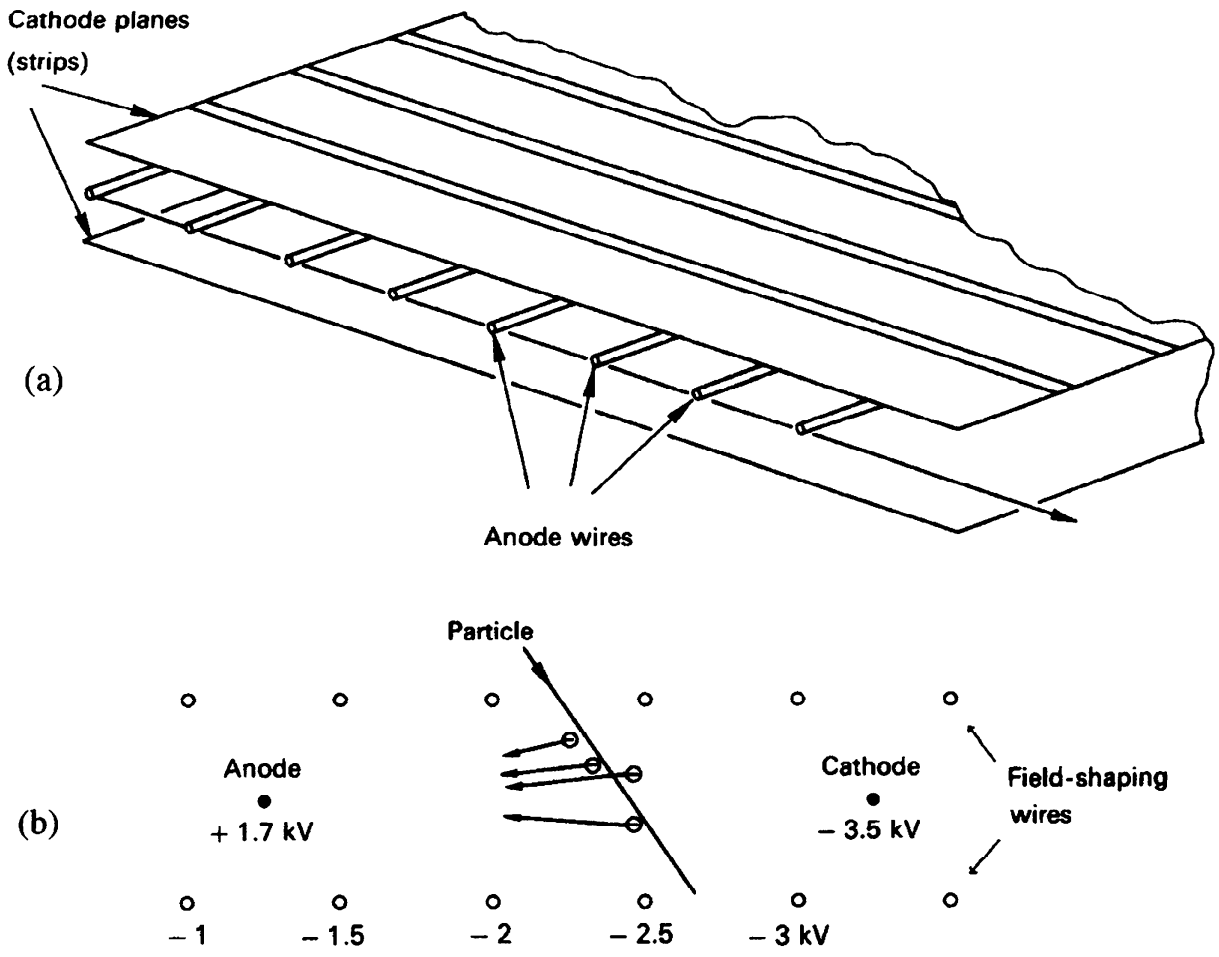

Fig. 11.8. (a) Schematic layout of multiwire proportional chamber. (b) Typical arrangement of electrodes for drift chamber cell.

although the phenomenon occurs also in liquids and gases. The decay times of the fastest (organic) scintillators are of order 1 ns.

Inorganic crystal scintillators, such as sodium iodide, are doped with activator centres (e.g. thallium). Ionising particles traversing the crystal produce free electrons and holes, which move around until captured by an activator centre. This is transformed into an excited state and decays with emission of light, over a broad spectrum in the visible region and with a decay time of order 250 ns.

In organic materials (either solid or liquid), however, the mechanism is the excitation of molecular levels that then decay with emission of light in the UV region. The conversion to light in the blue region is achieved via the fluorescent excitation of dye molecules known as wavelength shifters, incorporated into the primary scintillator medium. Table 11.3 gives a list of a few of the organic and inorganic scintillators in common use.

The light from the scintillating medium is recorded by a photomultiplier tube (or tubes). This consists of a photocathode coated with alkali metals, where electrons are liberated by the photoelectric effect. The electrons travel to a chain of

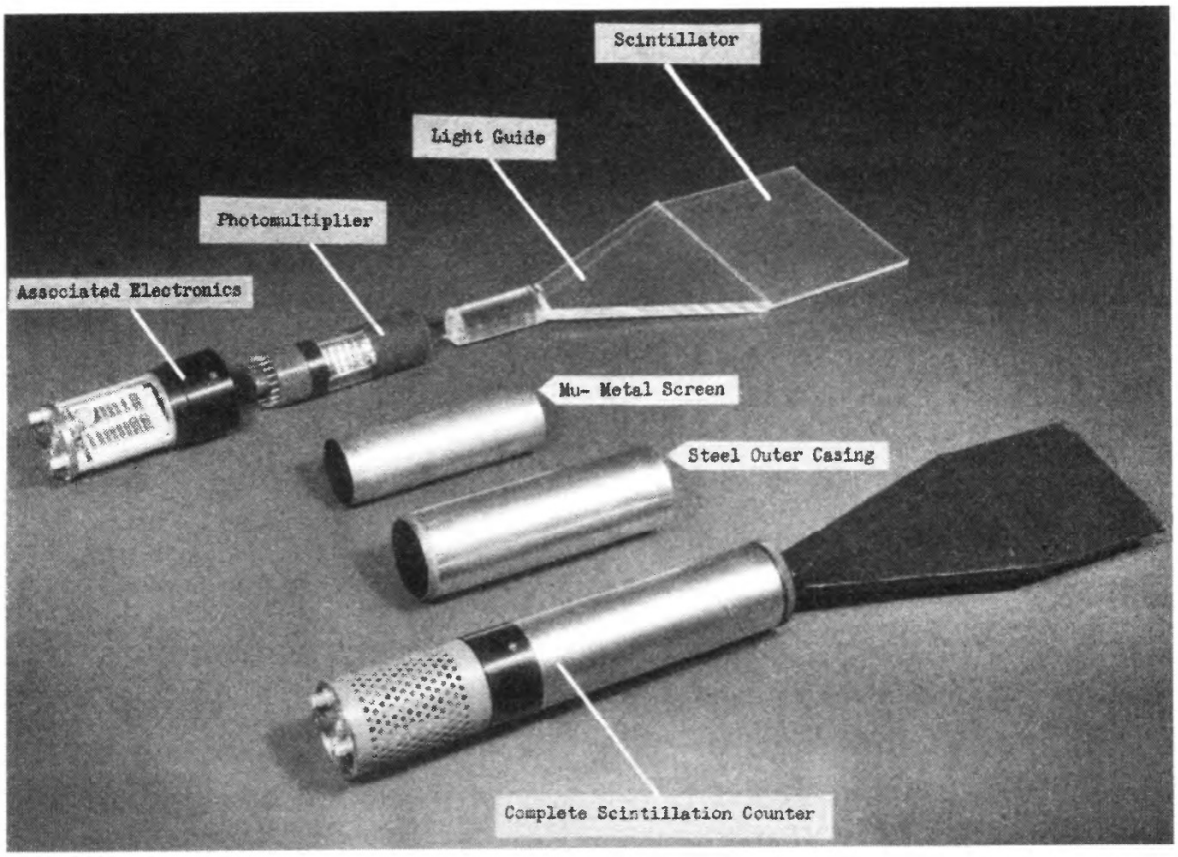

Fig. 11.9. Example of scintillation counter with associated photomultiplier, shown as separate components, and also assembled.

secondary-emission electrodes (dynodes) at successively larger potentials. Since about four secondary electrons are emitted per incident electron, amplification factors of 10^8 are achieved with 14 dynodes. The transit time from the cathode to the output dynode is typically 50 ns, with a jitter of order 1 ns. The jitter is determined mostly by the variation in transit time to the first dynode from different points on the cathode. Photocathode quantum efficiencies are typically $\leq 25\%$, peaking at $\lambda = 400$ nm.

The light from the scintillator slab travels down it by internal reflection, and the traditional way of directing this onto the photocathode is via multiple reflections down a suitably shaped plastic light guide, as in Figure 11.9. For very-large-area scintillators, the light guides consist of bent plastic rods or strips and the device can become very bulky. An alternative method is to place wavelength shifter bars along the edge of the scintillator slab. Blue light from the scintillator enters the bar, consisting of acrylic material doped with molecules that absorb the blue light and reemit isotropically in the green. Part of this light travels down the bar by internal reflection and is recorded by a photomultiplier glued to the end. The output is much less than that using light guides, but there is a large saving in space, number of photomultipliers and construction of complex light-guide structures.

Table 11.3. *Characteristics of typical scintillators*

	Pulse height (relative to anthracene)	Decay time, ns	λ_{max}, Å	Density, g cm^{-3}
polystyrene + *p*-terphenyl	0.28	3	3550	0.9
polystyrene + tetraphenylbutadiene	0.38	4.6	4800	0.9
sodium iodide (+ thallium)	2.1	250	4100	3.7
anthracene	1.0	32	4100	3.7
toluene	0.7	<3	4300	0.9

The output pulse from the photomultiplier is fed into suitable amplifiers, discriminators, and scalers, the essential function of which is to store the number of photomultiplier pulses of a particular magnitude.

11.6.5 Čerenkov counters

When high energy charged particles traverse dielectric media, part of the light emitted by excited atoms appears in the form of a coherent wavefront at a fixed angle with respect to the trajectory – a phenomenon known as the Čerenkov effect, after its discoverer. Such radiation is produced whenever the velocity βc of the particle exceeds c/n, where n is the refractive index of the medium. From the Huyghens construction of Figure 11.10 one sees that the wavefront forms the surface of a cone about the trajectory as axis, such that

$$\cos\theta = \frac{ct/n}{\beta ct} = \frac{1}{\beta n}, \qquad \beta > \frac{1}{n} \tag{11.22}$$

Čerenkov radiation appears as a continuous spectrum. In a dispersive medium, both n and θ will be functions of the frequency ν. The number of photons radiated with energies in the interval $dE = hd\nu$ by a particle of charge ze in track length dx is given by

$$\frac{d^2N_\gamma}{dxdE} = \frac{\alpha z^2}{\hbar c}\left(1 - \frac{1}{\beta^2 n^2}\right) \tag{11.23}$$

The number of photons at a particular frequency or wavelength is proportional to $d\nu$ or to $d\lambda/\lambda^2$. Thus, blue light predominates. The total rate of energy loss to

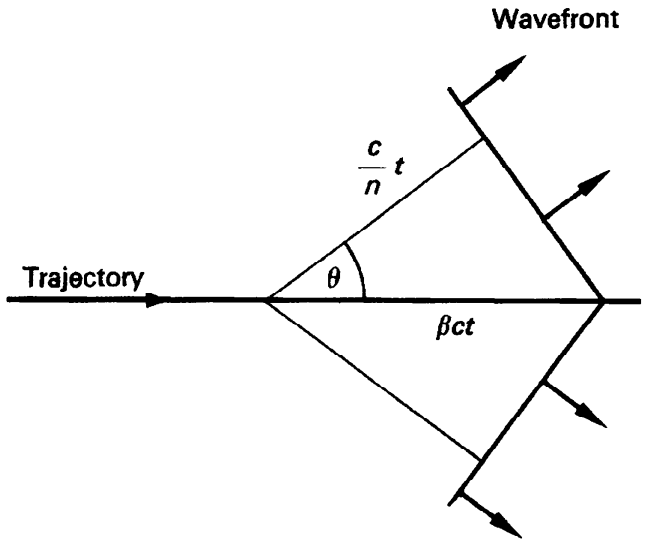

Fig. 11.10. On the left, the particle trajectory. At the right, a conical wavefront moves out.

Čerenkov radiation is

$$\frac{dW}{dx} = \frac{\alpha z^2}{\hbar c}\int\left(1 - \frac{1}{\beta^2 n^2}\right) EdE$$
$$= \frac{\alpha z^2}{2\hbar c}\left[(h\nu_1)^2 - (h\nu_2)^2\right]\left(1 - \frac{1}{\beta^2 n^2}\right)_{\text{av}} \qquad (11.24)$$

where the second expression applies if the variation of refractive index n over a small frequency range $\nu_1 \to \nu_2$ can be neglected.

For a particle of $z = 1$ and $\beta \simeq 1$ in water ($n = 1.33$) these expressions give $dW/dx = 525$ eV cm^{-1} for visible light ($\lambda = 400$–700 nm), which is carried by a total of 215 photons cm^{-1}. Note that this energy loss is small compared with the total energy loss (11.7) of about 2 MeV cm^{-1}.

The usefulness of the Čerenkov effect lies in the fact that measurement of the angle in (11.22) provides a direct measurement of the velocity βc. Table 11.4 gives a list of some radiating media, demonstrating that most of the range of γ-values from 1.2 to 100 can be covered by means of solids, liquids, gases or aerogels.

Threshold Čerenkov counters can be used to discriminate between two relativistic particles of the same momentum p and different masses m_1 and m_2, if the heavier, slower particle (m_2, say) is just below threshold. In this case, $\beta_2^2 = 1/n^2$ and it is straightforward to show that the production rate of photons from the particle m_1 is given by the previous equation with

$$\sin^2\theta_1 = 1 - \frac{1}{\beta_1^2 n^2} \simeq \frac{m_2^2 - m_1^2}{p^2} \qquad (11.25)$$

Thus the length of radiator to produce a given number of photoelectrons (assuming one with the right refractive index can be found) increases as the square

Table 11.4. *Čerenkov radiators*

Medium	$n-1$	γ (threshold)
helium (NTP)	3.3×10^{-5}	123
CO_2 (NTP)	4.3×10^{-4}	34
pentane (NTP)	1.7×10^{-3}	17.2
aerogel	$0.075 \rightarrow 0.025$	$2.7 \rightarrow 4.5$
H_2O	0.33	1.52
glass	$0.75 \rightarrow 0.46$	$1.22 \rightarrow 1.37$

of the momentum. For high momentum beams, large pressurised gas radiators several metres long may be required.

In the differential Čerenkov counter, the angle of Čerenkov emission is measured in order to identify particles. The cone of light from the radiating particle is focussed by a lens or spherical mirror into a ring image, and an adjustable diaphragm at the focus transmits the light to a phototube. Differential counters with velocity resolution $\Delta\beta/\beta \simeq 10^{-7}$ have been built, and the separation of charged pions, kaons and protons up to several hundred GeV/c is achievable. As an alternative to changing the radius of the diaphragm, this may be fixed and a velocity scan carried out by varying the gas pressure. By integrating the photomultiplier output over time, such a counter may be used to measure secondary particle yields in high intensity beams.

It is also possible to dispense with photomultipliers for light collection. In one design, photons emitted in the Čerenkov cone from a liquid radiator traverse a suitable gas, and the electrons liberated by photoionisation are then drifted in an electric field onto a plane multiwire proportional chamber, so that a ring image (with diameter determined by particle velocity) of electronic signals is found on the anode–cathode plane. Figure 11.11 shows an example of such Čerenkov ring images in the DELPHI detector used at the CERN LEP e^+e^- collider.

11.6.6 Solid-state counters

Semiconductor solid-state counters have been a mainstay of experiments in nuclear structure physics for many decades, on account of their very good energy resolution. However, with the advent of high energy colliders and the production of massive, short-lived mesons with charm and bottom quantum numbers, and with the need to record the details of tracks and vertices from the production and decay of such states, solid-state microdetectors with spatial resolution of order 5 μm have become indispensible.

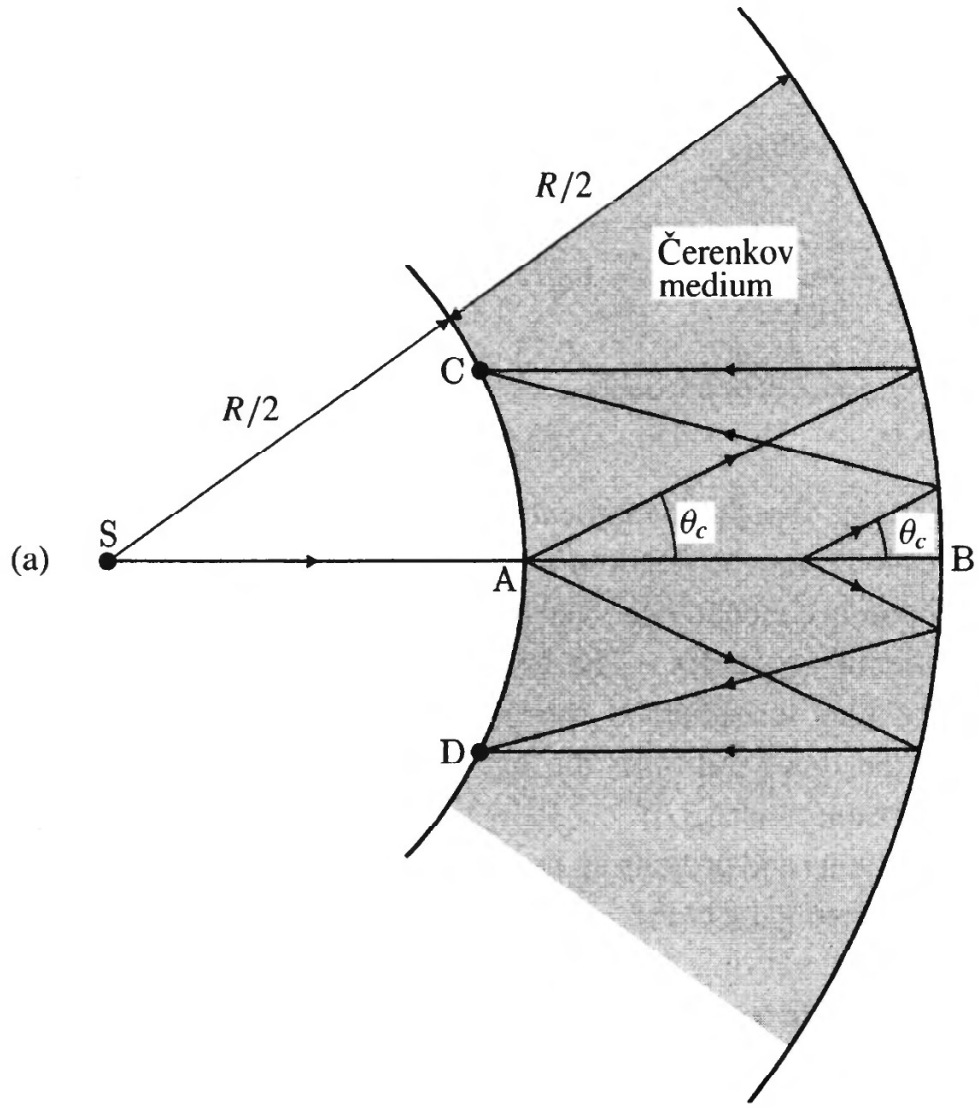

Fig. 11.11. (a) Principle of a ring-imaging Čerenkov counter (RICH). Charged particles are emitted from the target S and emit Čerenkov light at an angle θ, (11.22), in traversing the radiating medium AB. A spherical mirror of radius R focusses the light into a ring image CD. (b) Example of ring images due to a collimated high energy muon beam traversing (top) a liquid and (bottom) a gaseous radiator. The coordinates refer to angles in radians. These ring images were reconstructed from the electrical signals produced by photoelectrons in a drift chamber of the RICH counter in the DELPHI detector at CERN.

One form of such counter is the silicon strip detector. This consists of a wafer of n-type silicon (pure silicon doped with a valency-5 impurity), typically 250 μm thick, one side of which is conducting and the other of which is etched with many thin parallel strips of p-type material, separated by gaps of order 20 μm (see Figure 11.12). Upon application of a (reverse bias) voltage, the system operates like a solid version of a multiwire gas counter, with electron–hole pairs instead

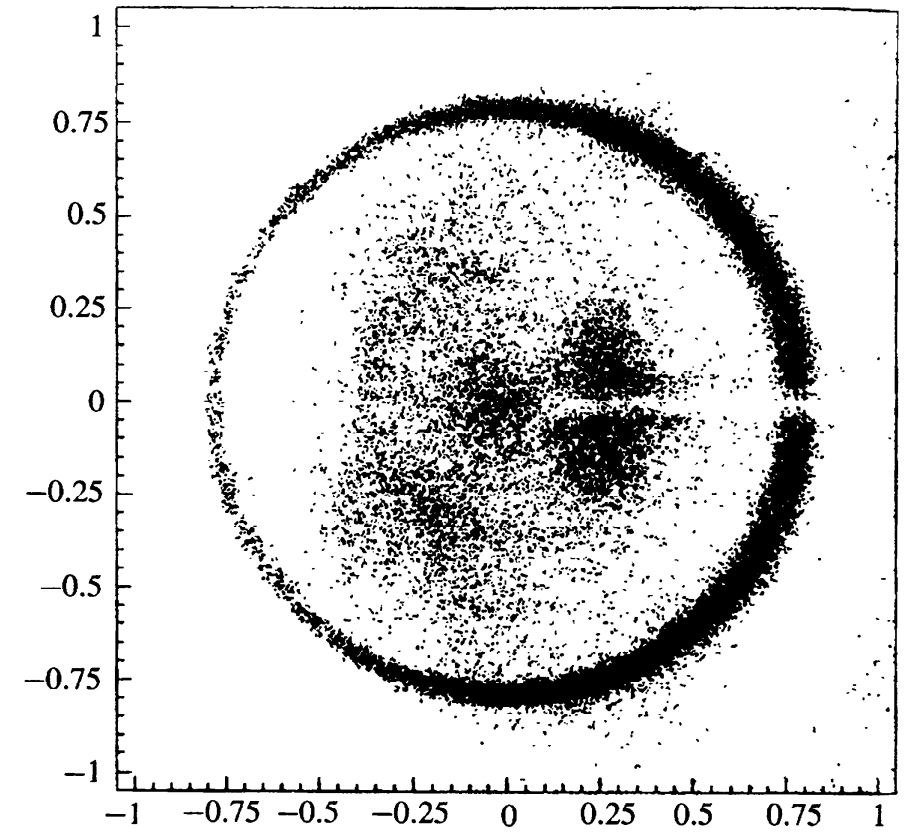

(b)

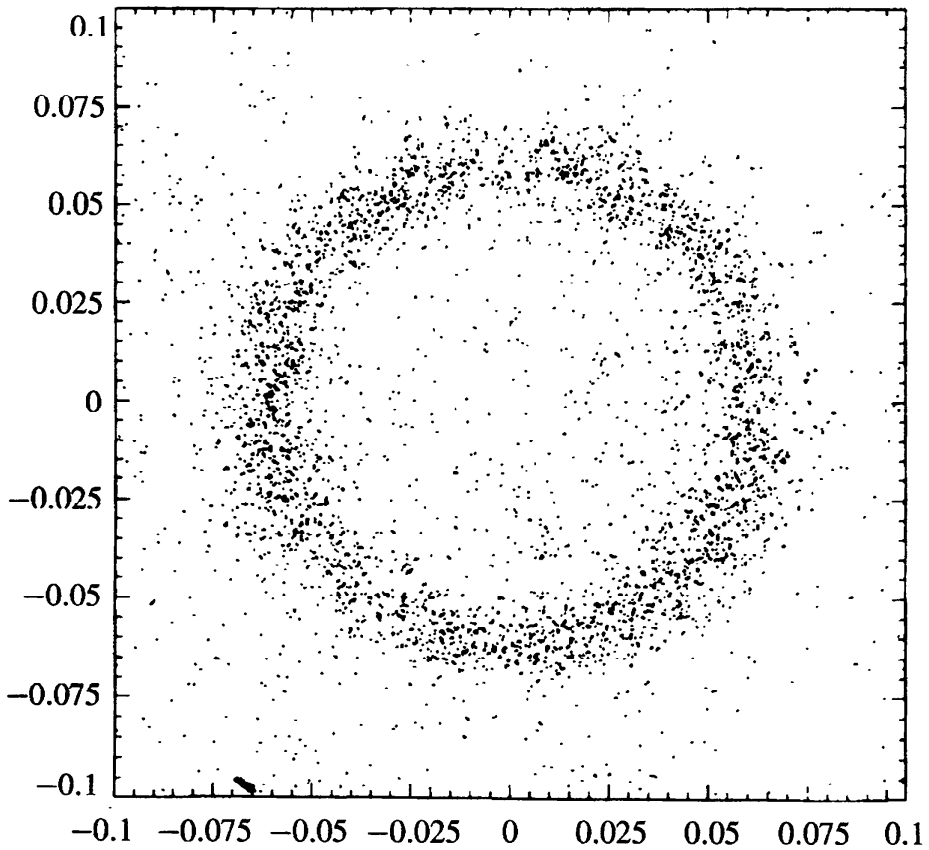

Fig. 11.11. continued.

of electron–ion pairs. Since the average energy required to form an electron–hole pair is only 3.6 eV, compared with 20–40 eV for ionising a gas, adequate signals ($(1–2) \times 10^4$ pairs) can be collected within the fast rise-time (10 ns) from such thin wafers. The spatial resolution (taking the signal from several strips) can be of order 5 μm in a field-free region, and of order 10 μm in a 2 T magnetic field. The silicon vertex detector used in the DELPHI experiment is shown in Figure 11.12.

11.6.7 Bubble chambers

The bubble chamber was an indispensible tool of high energy physics for over 30 years, particularly for studying complex interactions involving many secondary particles. Conceived by Glaser in 1952, it relied for its operation on the fact that in a superheated liquid boiling will start with the formation of gas bubbles at nucleation centres in the liquid, and particularly along trails of ions left by the passage of a charged particle. The liquid filling was maintained under an overpressure (typically 5–20 atmospheres), and the superheating was achieved by the sudden expansion of a piston, bellows or diaphragm placed at the rear of the chamber. After expansion, bubbles along the tracks were allowed to grow over a period of order 10 ms and were photographed by an array of stereo cameras using flash illumination. The bubbles then collapsed under a recompression stroke. Since the cycle time was of order 1 s, the bubble chamber was well matched to pulsed, cyclic accelerators and beams from fixed targets, with repetition rates of the same order.

The most usual liquid fillings for bubble chambers were hydrogen or deuterium, or heavy liquids such as a neon–hydrogen mixture, propane (C_3H_8), or Freon (CF_3Br) – see Figure 11.13. The entire chamber was immersed in a strong magnetic field (2–3.5 T) provided by an electromagnet with conventional or superconducting coils, to permit momentum measurement from track curvature. The bubble images were recorded on photographic film from several cameras in stereo. Subsequent measurement of images on film were digitised, and a geometry program was used to reconstruct tracks and event vertices in three dimensions. The great detail recorded in a complex production and decay pattern is well illustrated in the example of Figure 4.18.

The main disadvantages of a bubble chamber are: first, it has a low repetition rate, and the analysis of film is a lengthy process (typical experiments rarely involve more than 10^5 useful analysed events); second, many present and essentially all new accelerators are of the colliding-beam type, with an effectively d.c. interaction rate. Thus the very low duty cycle of a bubble chamber, i.e. the ratio of the sensitive time to the total time ($\sim 10^{-2}$), as well as the interaction geometry of the beams, excludes their use in this field. Nevertheless bubble chambers, although now redundant, have played a notable role in experimental particle physics; we

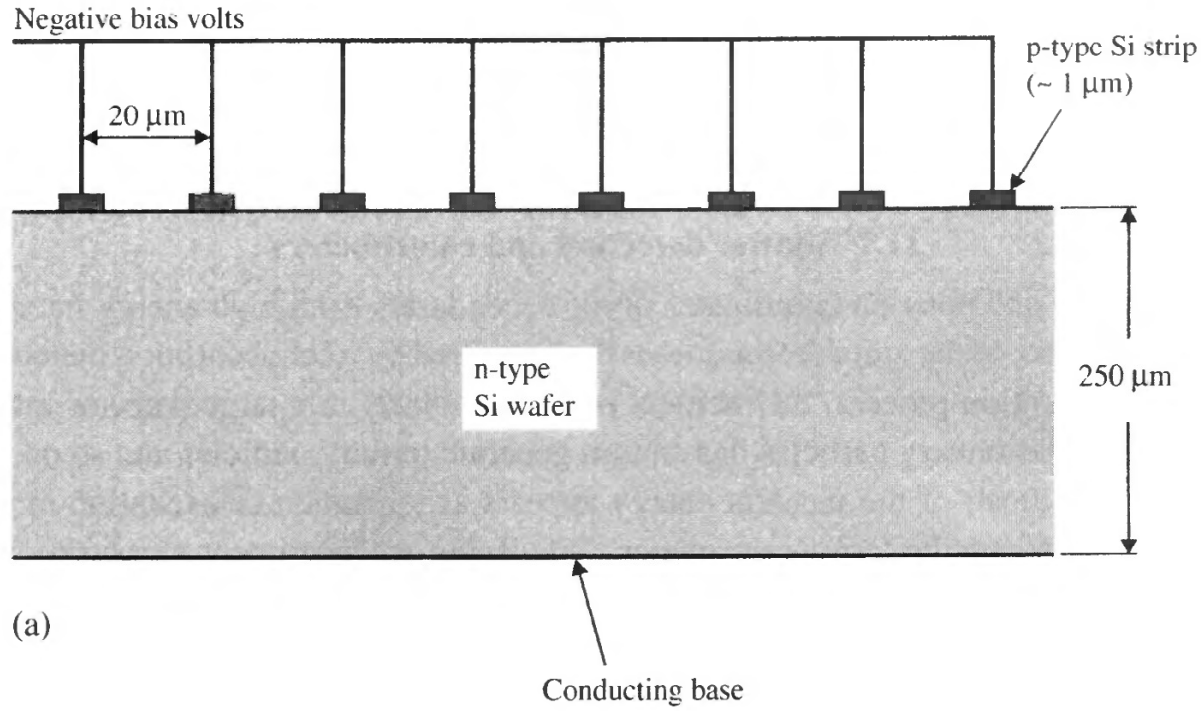

(a)

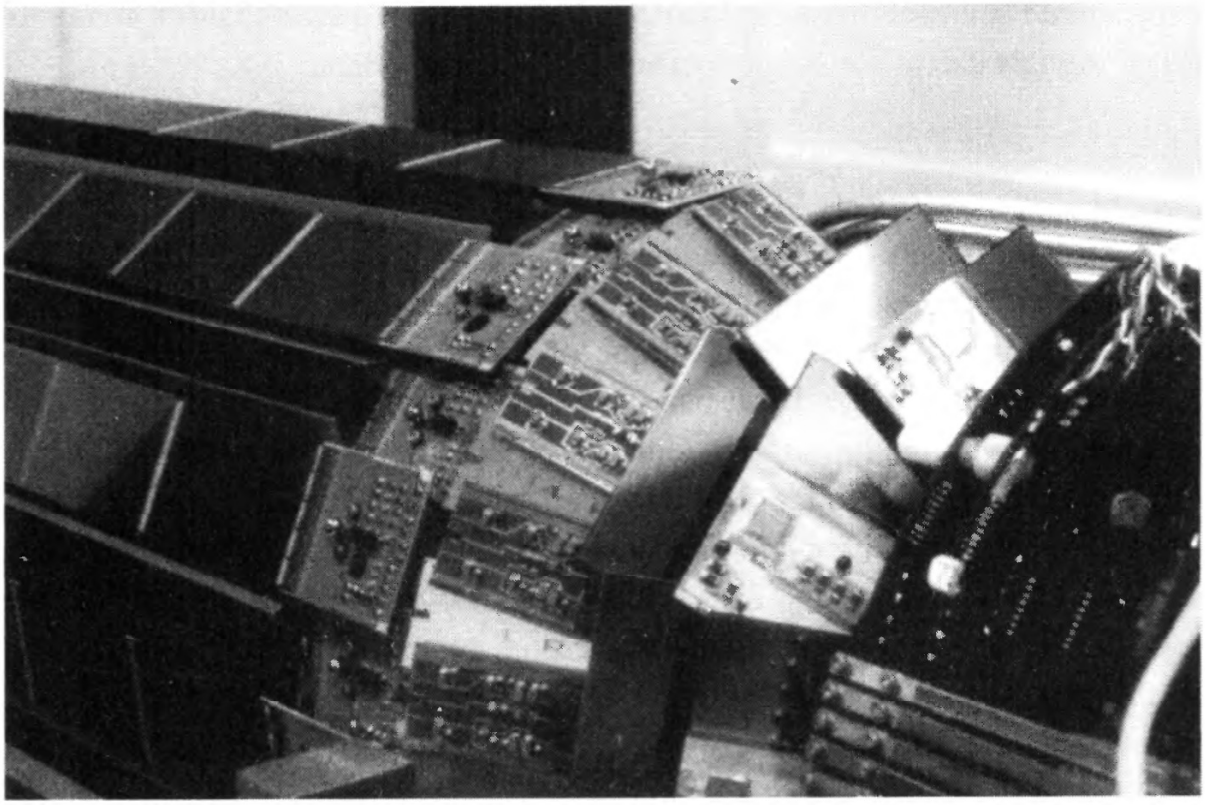

(b)

Fig. 11.12. (a) Typical layout of silicon microstrip detector. See text for description. (b) Photograph of the 'tiles' of silicon microstrip detectors surrounding the interaction region in the DELPHI experiment at the CERN LEP collider.

mention in particular their use in cataloguing baryon and meson resonances in the 1960s, and in the early experiments in neutrino physics, including those leading to the discovery of neutral currents, one of the essential precursors of the Standard Model.

11.7 Shower detectors and calorimeters

The energy and position coordinates of the secondaries from high energy interactions can also, under suitable conditions, be measured by total-absorption methods. In the absorption process, the incident particle interacts in a large detector mass, generating secondary particles that in turn generate tertiary particles and so on, so that all (or most) of the incident energy appears as ionisation or excitation in the medium – hence the term 'calorimeter', signifying an instrument measuring the total deposited energy. Such devices are essential in recording the energy of neutral hadrons; and since the fractional energy resolution varies as $E^{-1/2}$, calorimeters provide, even for charged hadrons, a precision at high energies (10–100 GeV) comparable with or better than what can be achieved by magnetic deflection. Just as important is the fact that total-absorption calorimeters provide fast (100 ns) 'total energy' signals useful for quick decisions on event selection.

11.7.1 Electromagnetic-shower detectors

For electrons and photons of high energy, a dramatic result of the combined phenomena of bremsstrahlung and pair production is the occurrence of cascade showers. A parent electron will radiate photons, which convert to e^+e^- pairs, which radiate and produce fresh pairs in turn, the number of particles increasing exponentially with depth in the medium. The development of such a shower can be discussed according to the following very simplified model. Starting off with a primary electron of energy E_0, suppose that, in traversing one radiation length, it radiates half its energy, $E_0/2$, as one photon. Assume that, in the next radiation length, the photon converts to a pair, the electron and positron each receiving $E_0/4$, half the photon's energy, and that the original electron radiates a further photon carrying half the remaining energy, $E_0/4$. Thus, after two radiation lengths we shall have a photon of energy $E_0/4$ and two electrons and one positron, each of energy $E_0/4$. By proceeding in this way, it is easily seen that after t radiation lengths, there will be $N = 2^t$ particles, with photons, electrons, and positrons approximately equal in number. (We have here neglected ionisation loss and the dependence of radiation and pair-production cross-sections on energy.) The energy per particle at depth t will be $E(t) = E_0/2^t$. This process continues until $E(t) = E_c$, when we suppose that ionisation loss suddenly becomes important and

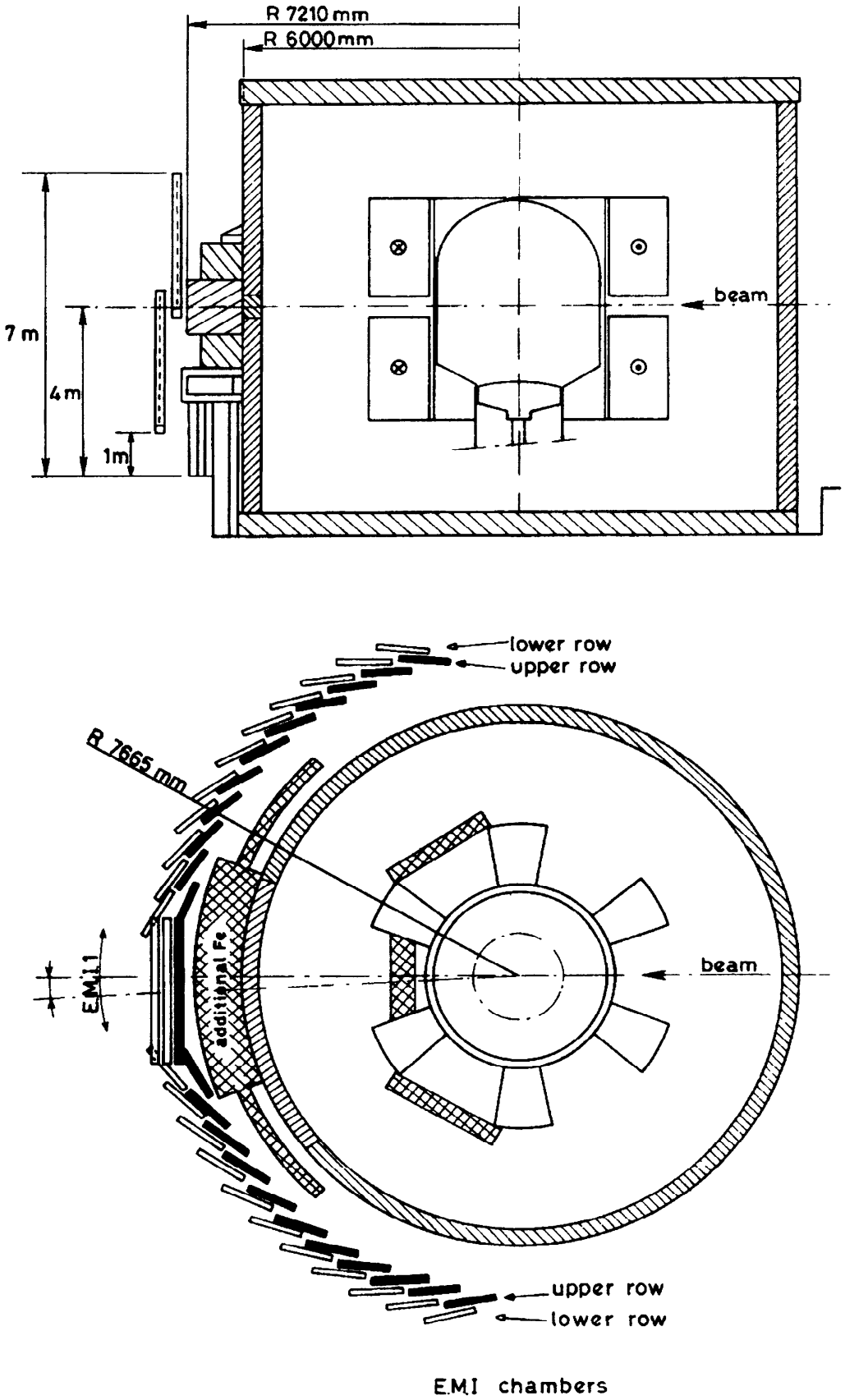

Fig. 11.13. Elevation and plan views of the 3.7 m diameter bubble chamber (BEBC) at CERN. The chamber was filled with liquid hydrogen, deuterium or a neon–hydrogen mixture and was equipped for neutrino experiments with an external muon identifier. This consisted of 150 m^2 of multiwire proportional chambers placed outside the magnet yoke.

no further radiation is possible. The shower will thus reach a maximum and then cease abruptly. The maximum will occur at

$$t = t_{\max} = \frac{\ln(E_0/E_c)}{\ln 2} \tag{11.26}$$

the number of particles at the maximum being

$$N_{\max} = \exp(t_{\max} \ln 2) = \frac{E_0}{E_c} \tag{11.27}$$

The number of particles with energy exceeding E will be

$$N(>E) = \int_0^{t(E)} N dt = \int_0^{t(E)} e^{t \ln 2} dt \simeq \frac{e^{t(E)\ln 2}}{\ln 2} = \frac{E_0/E}{\ln 2}$$

where $t(E)$ is the depth at which the particle energy has fallen to E. Thus, the differential energy spectrum of particles dN/dE is proportional to $1/E^2$. The total integral track length of charged particles (in radiation lengths) in the whole shower will be

$$L = \frac{2}{3} \int_0^{t_{\max}} N dt = \frac{2}{3 \ln 2} \frac{E_0}{E_c} \simeq \frac{E_0}{E_c} \tag{11.28}$$

The last result also follows from the definition of E_c and conservation of energy; nearly all the energy of the shower must eventually appear in the form of ionisation loss of charged particles in the medium.

In practice, the development of a shower consists of an initial exponential rise, a broad maximum and a gradual decline. Nevertheless, the above equations indicate correctly the main qualitative features, which are as follows.

(i) The maximum occurs at a depth increasing logarithmically with primary energy E_0.
(ii) The number of shower particles at the maximum is proportional to E_0.
(iii) The total track-length integral is proportional to E_0.
(iv) Assuming roughly Gaussian distributions in numbers of particles, fluctuations in total energy deposited about the average vary as $N^{-1/2}$ or $E_0^{-1/2}$.

The observed longitudinal development of a 6 GeV electron-initiated shower in different absorbers is given in Figure 11.14 together with the predictions of a Monte Carlo program incorporating the known energy-dependent cross-sections for radiation and ionisation loss by electrons and for absorption of photons by pair production and other processes.

Because of Coulomb scattering, a shower spreads out laterally. The radial spread is determined by the radiation length in the medium and the angular deflection per

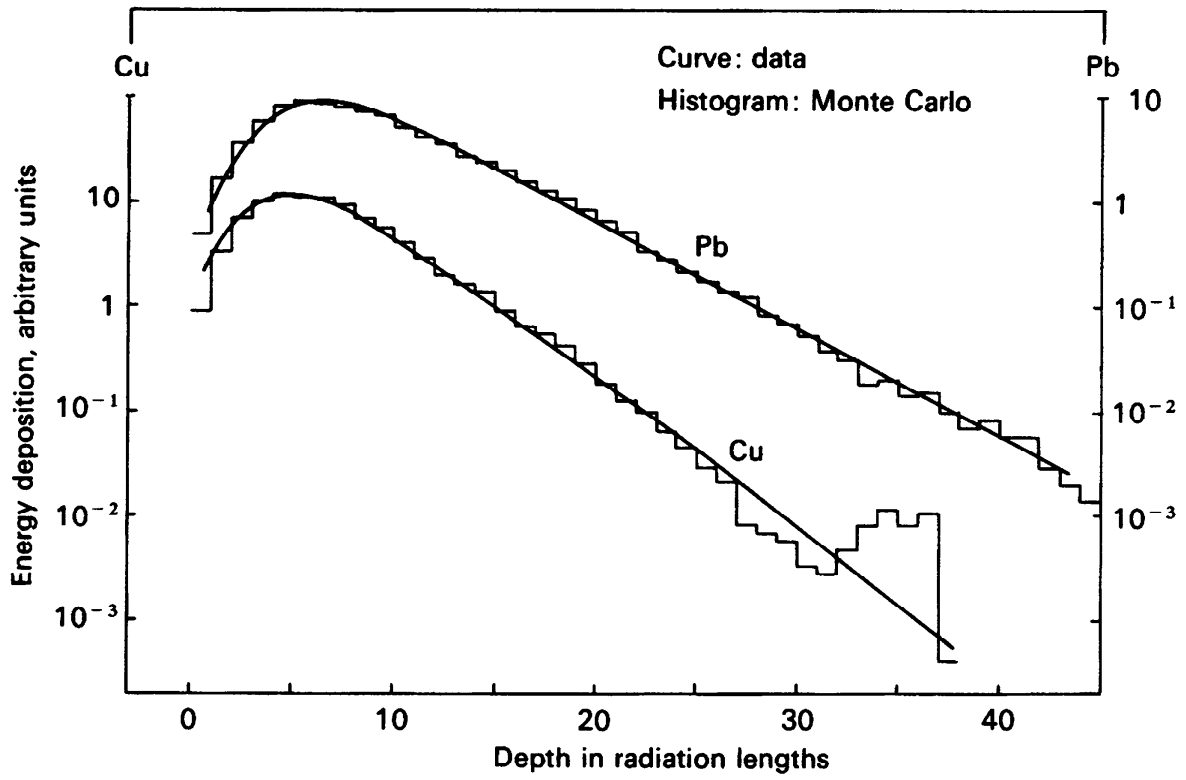

Fig. 11.14. Longitudinal distribution of energy deposition in a 6 GeV electron shower (after Bathow *et al.* 1970). Curves, data; histograms, Monte-Carlo result.

radiation length at the critical energy. In all materials, this spread is of order one Molière unit $R_m = 21(X_0/E_c)$, with E_c in MeV.

Electromagnetic-shower detectors are built from high-Z materials of small X_0, so as to contain the shower in a small volume. In lead-loaded glass (55% PbO, 45% SiO_2) detectors, the Čerenkov light from relativistic electrons is used to measure the shower energy. The resolution is typically

$$\frac{\Delta E}{E} = \frac{0.05}{\sqrt{E\ (\text{GeV})}}$$

Calorimeters built from alternate sheets of lead and plastic scintillator have also been used; the resolution depends on the sampling frequency but is comparable to that of lead glass.

11.7.2 Hadron-shower calorimeters

A hadron shower results when an incident hadron undergoes an inelastic nuclear collision with the production of secondary hadrons, which interact inelastically to produce a further hadron generation, and so on. The scale for longitudinal development is set by the nuclear absorption length λ, which varies from 80 g cm^{-2} for carbon through 130 g cm^{-2} for iron to 210 g cm^{-2} for lead. This scale is big

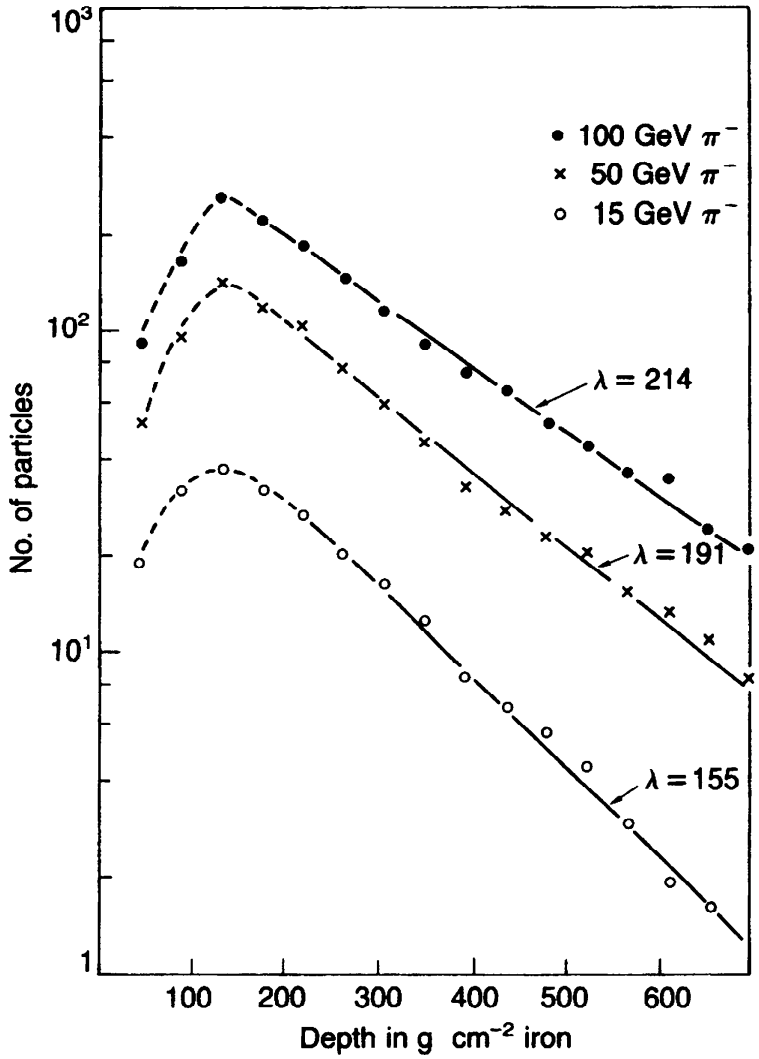

Fig. 11.15. Average longitudinal development of hadronic showers due to negative pions in a sandwich array of 5 cm iron plates and scintillator. The ordinate gives the equivalent number of minimum ionising particles at each depth. The rms fluctuation about the mean, in individual showers, is of order 100%. (After Holder *et al.* 1978.)

compared with the radiation length X_0 in heavy elements so that, in comparison with electromagnetic-shower detectors, hadron calorimeters are large. For an iron–scintillator sandwich, for example, the longitudinal and transverse dimensions are of order 2 m and 0.5 m, respectively.

In an electromagnetic cascade, the bulk of the incident energy appears eventually in the form of ionisation. However, in a hadron cascade roughly 30% of the incident hadron energy is lost by the breakup of nuclei, nuclear excitation, and evaporation neutrons (and protons), and does not give an observable signal. One successful method of compensating for this is by the use of ^{238}U as the cascade medium, the extra energy released by fast neutron and photon fission of ^{238}U making up for the 'invisible' energy losses from nuclear breakup. The importance of obtaining this compensation is clear: in a hadronic cascade containing both

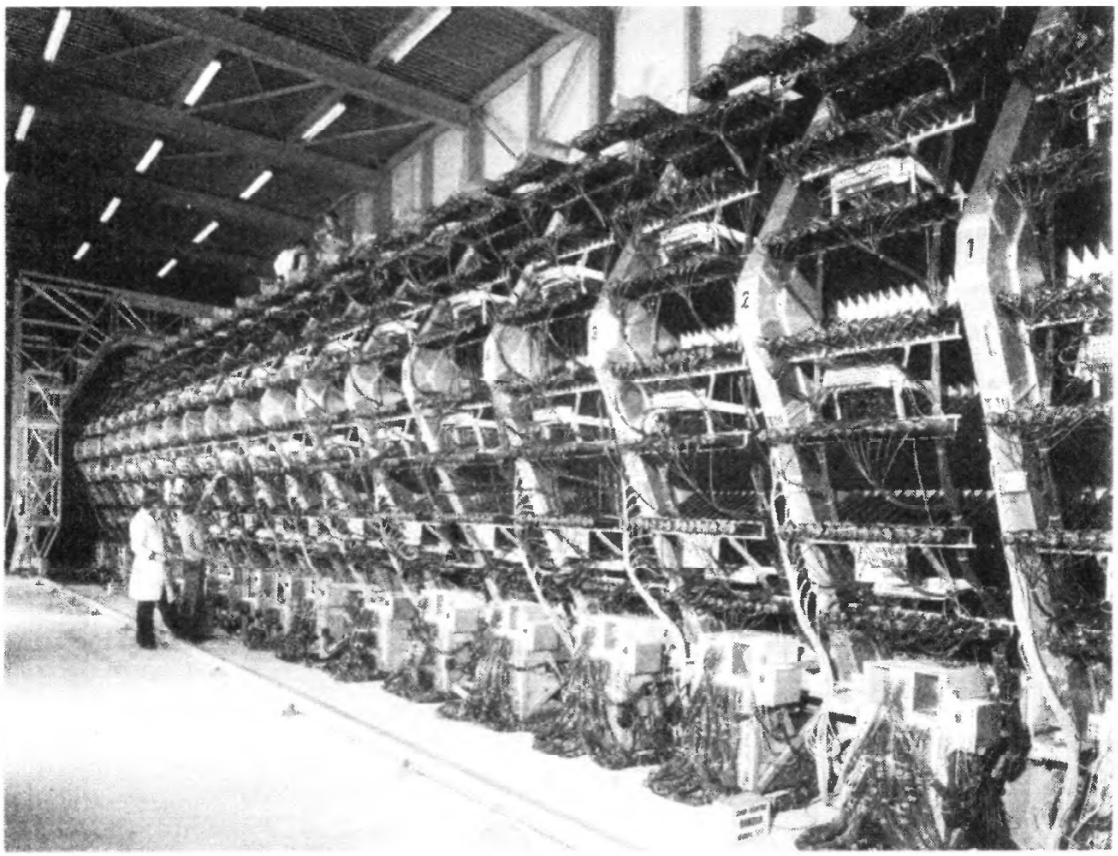

Fig. 11.16. Magnetised calorimeter employed by the CDHS collaboration in the study of neutrino interactions at the CERN SPS. It is instrumented with magnetised iron toroids, scintillation counters and drift chambers, for the identification and momentum measurement of secondary muons, and to measure the nuclear cascade energy of secondary hadrons. The total mass is 1400 tonne. (Photograph courtesy of CERN.)

charged and neutral pions, which generate hadronic and electromagnetic cascades respectively, the integrated scintillator pulse height should be proportional to the total incoming energy, irrespective of fluctuations in the neutral pion to charged pion ratio. Figure 11.15 shows results on the hadronic cascade development in a sandwich of iron and scintillator.

Typically the energy resolution of hadron calorimeters is $\Delta E/E \simeq 0.5/\sqrt{E}$ with E in GeV. Various types of hadron calorimeter are in current use. The early iron-plus-scintillator sandwich has already been mentioned, but proportional tubes, flash tubes and drift chambers can also been used for sampling. Large-scale calorimeters, as required for full angular coverage at colliders, frequently use liquid argon as the detection medium.

11.7.3 Examples of large hybrid detectors

Typical experiments in high energy physics involve the simultaneous detection, measurement and identification of many particles, both charged and neutral, from

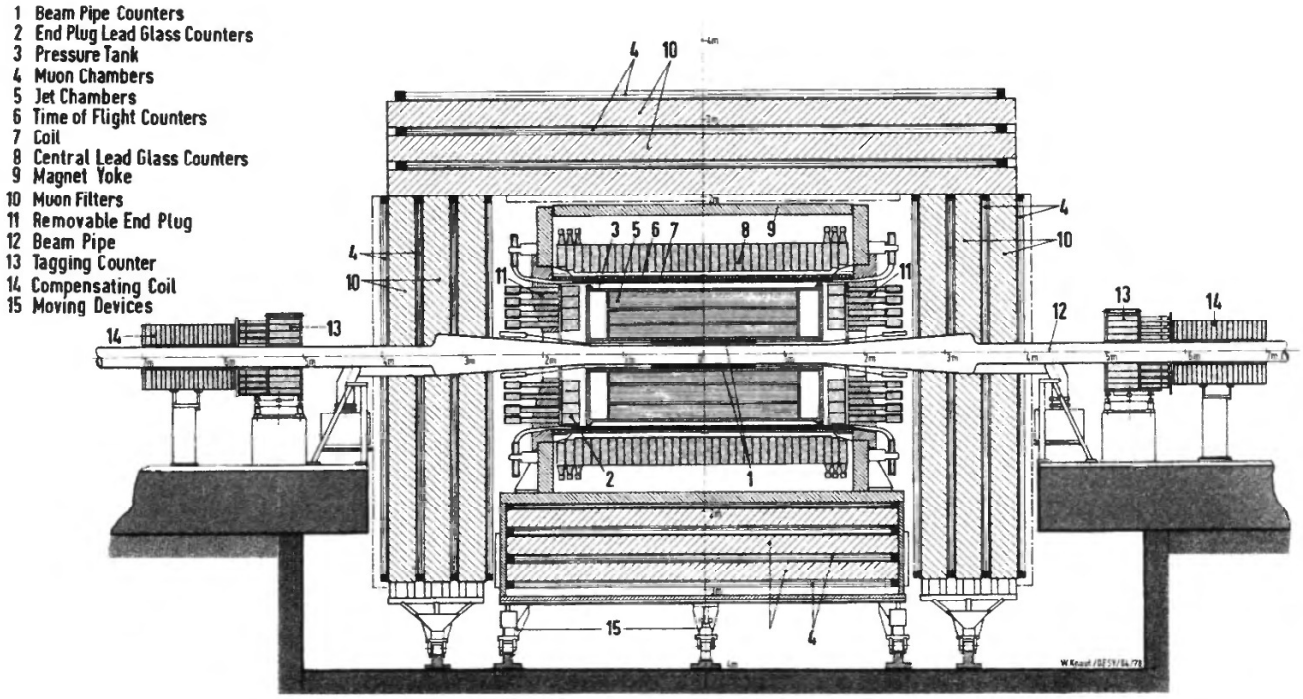

Fig. 11.17. The spectrometer detector JADE used at the PETRA e^+e^- storage ring at DESY, Hamburg. A vertical section through the beam pipe is shown.

each interaction that occurs. They therefore usually incorporate several types of detection technique in a single detector array. As an example, Figure 11.16 shows the neutrino detector used by the CDHS collaboration at the CERN SPS. It is essentially a magnetised calorimeter of mass 1400 tonne, and consists of a succession of iron plates 3.5 m in diameter and 15 cm thick, separated by scintillation counters and drift chambers. The latter record the trajectories of the charged secondaries of neutrino reactions, while the integrated scintillator pulse height indicates the hadron (shower) energy. High energy muon secondaries are identified by their penetration, and their momentum is determined from their deflection in the magnetised iron.

As another example, Figure 11.17 shows the spectrometer detector employed by the JADE collaboration at the e^+e^- storage ring PETRA at DESY, Hamburg. A vertical section containing the beam axis is shown. Charged particles from the beam intersection region are recorded by beam pipe counters, by an array of cylindrical drift chambers ('jet chambers'), and by time-of-flight counters. The drift chambers provide ionisation information as well as track positions. All these are inside a solenoid magnet providing a field of 0.5 T parallel to the beam axis and extending over 3.5 m length by 2 m diameter. Outside the coil, lead-glass shower counters record electrons and photons, and the outermost layers of drift chambers ('muon chambers') identify and record muons by their penetration through the iron and concrete absorbers. Tagging counters placed upstream and downstream around the beam pipe record particles at small angles. Other examples of large

hybrid detectors have been mentioned in earlier chapters. The CDF detector employed in the discovery of the top quark is described in Section 4.13 and shown in Figures 4.20 and 4.21, and the DELPHI detector employed at the LEP e^+e^- collider is shown in Figure 8.5.

Problems

11.1 The average number $\bar{n}$ of ionising collisions suffered by a fast particle of charge ze in traversing dx (g cm^{-2}) of a medium, resulting in energy transfers in the range $E' \to E' + dE'$, is

$$\bar{n} = f(E')dE'dx = \frac{2\pi z^2 e^4 N_0 Z}{mv^2 A} \frac{dE'}{(E')^2} \left(1 - \frac{v^2}{c^2} \frac{E'}{E'_{\max}}\right) dx$$

where the symbols are as in subsection 11.5.1 and the maximum transferable energy is $E'_{\max} = 2mv^2/(1-\beta^2)$, with $\beta = v/c$. For individual particles, the distribution in the number n of collisions follows the Poisson law, so that $\langle (n - \bar{n})^2 \rangle = \bar{n}$. If we multiply the above equation by $(E')^2$ and integrate, we obtain the mean squared deviation in energy loss, $\epsilon^2 = \langle (\Delta E - \bar{\Delta}\bar{E})^2 \rangle$, about the mean value $\bar{\Delta}\bar{E}$. Show that

$$\epsilon^2 = 0.6(mc^2)^2 \gamma^2 \frac{Z}{A} \left(1 - \frac{\beta^2}{2}\right) \delta x$$

Calculate the fractional rms deviation in energy loss, $\epsilon/\bar{\Delta}\bar{E}$, for protons of kinetic energy 500 MeV traversing (a) 0.1, (b) 1.0 and (c) 10 g cm^{-2} of plastic scintillator ($Z/A = 1/2$). Take dE/dx as 3 MeV g^{-1} cm^2.

11.2 A narrow pencil beam of singly charged particles of very high momentum p, travelling along the x-axis, traverses a slab of material s radiation lengths in thickness. If ionisation loss in the slab may be neglected, calculate the rms lateral spread of the beam in the y-direction, as it emerges from the slab.

(*Hint*: Consider an element of slab of thickness dx at depth x, and find the contribution $(dy)^2$ that this element makes to the mean squared lateral deflection, then integrate over the slab thickness.)

Use the formula you derive to compute the rms lateral spread of a beam of 10 GeV/c muons in traversing a 100 m pipe filled with (a) air and (b) helium, at NTP.

11.3 Show that, in a head-on collision of a beam of relativistic particles of energy E_1 with one of energy E_2, the square of the energy in the centre-of-momentum frame is $4E_1E_2$ and that for a crossing angle θ between the beams this is reduced by a factor $(1 + \cos\theta)/2$. Show that the available kinetic energy in the head-on collision of two 25 GeV protons is equal to that in the collision of a 1300 GeV proton with a stationary nucleon.

11.4 A proton of momentum **p**, large compared with its rest mass M, collides with a proton inside a target nucleus, with Fermi momentum $\mathbf{p}_f$. Find the available kinetic energy in the collision, as compared with that for a free-nucleon (stationary) target, when **p** and $\mathbf{p}_f$ are (a) parallel, (b) antiparallel, (c) orthogonal.

11.5 It was sometimes possible to differentiate between the tracks due to relativistic pions, protons and kaons (rest masses 140, 938 and 494 MeV respectively) in a bubble chamber by virtue of the high energy δ-rays produced. For a beam momentum of 5 GeV/c, what is the minimum δ-ray energy which must be observed to prove that it is produced by a pion rather than a kaon or proton? What is the probability of observing such a knock-on electron in 1 m of liquid hydrogen (density 0.06)?

11.6 Extensive air showers in cosmic rays contain a 'soft' component of electrons and photons and a 'hard' component of muons. What is the origin of these components? Suppose that the central core of a shower, at sea level, contains a narrow, vertical, parallel beam of muons of energy 1000 GeV, which penetrates underground. Assume that the ionisation loss in rock is constant at 2 MeV g^{-1} cm^2. Find the depth in rock at which the muons come to rest, assuming a rock density of 3.0. Using the formula in Problem 11.2, estimate the radial spread in metres of the muons, taking account of their linear change in energy as they traverse the rock. Take the radiation length of rock as 25 g cm^{-2}.

11.7 An experiment searching for proton decay in the mode $p \rightarrow e^+ + \pi^0$ is carried out using a cubical tank of water as the proton source. Possible decays are to be detected via the Čerenkov light emitted when the electromagnetic showers from the decay products traverse the water. (a) How big should the tank be in order to contain such showers if they start in the centre? (b) Estimate the total track length integral (TLI) of the showers from a decay event and hence the total number of photons emitted in the visible region (λ = 400–700 nm). (c) If the light is detected by means of an array of photomultipliers at the water surfaces, the effective optical transmission of the water is 50% and the photocathode efficiency is 20%, what fraction of the surface must be covered by photocathode to give an energy resolution of 5%?

Appendix A

Table of elementary particles

Table A1.1. *Quarks*

spin-parity	$J^P = \frac{1}{2}^+$	for all quarks
baryon number	$B = \frac{1}{3}$	for all quarks
isospin	$I = \frac{1}{2}$	for u and d quarks
	$I = 0$	for all other quarks

Name	Symbol	Mass, GeV/c^2	Q/e	S	$\tilde{C}^x$	$\tilde{B}^y$	T
up	u	~ 0.3	$+\frac{2}{3}$	0	0	0	0
down	d	$m_d \approx m_u$	$-\frac{1}{3}$	0	0	0	0
strange	s	0.5	$-\frac{1}{3}$	-1	0	0	0
charmed	c	1.6	$+\frac{2}{3}$	0	$+1$	0	0
bottom	b	4.5	$-\frac{1}{3}$	0	0	-1	0
top	t	175	$+\frac{2}{3}$	0	0	0	$+1$

^{x} charm quantum number
^{y} bottom quantum number

Table A1.2

Gauge bosons		J^{PC}	I	Mass, GeV/c^2	Width, GeV	Decay mode	Branching fraction (%)
photon γ		1^{--}	0, 1	$<10^{-26}$	stable	—	—
gluon G		1^{-}	0	0	stable	—	—
weak bosons	$W^{\pm}$	$1^{\pm}$	—	80.33 ± 0.15	$\Gamma = 2.07 \pm 0.06$	$e\nu$	10.8 ± 0.4
						$\mu\nu$	10.4 ± 0.6
						$\tau\nu$	10.9 ± 1.0
						hadrons	67.9 ± 1.5
	Z^0	$1^{\pm}$	—	91.187 ± 0.007	$\Gamma = 2.49 \pm 0.01$	l^+l^-	$(3.36 \pm 0.01) \times 3$
						hadrons	69.9 ± 0.2
						$\nu\bar{\nu}$	20.0 ± 0.17

Leptons	J	Mass, MeV/c^2	Lifetime	Decay mode	Branching fraction (%)
e	$\frac{1}{2}$	0.51099907 (15)	stable	—	—
μ	$\frac{1}{2}$	105.658389 (34)	2.197×10^{-6} s	$e\bar{\nu}\nu$	100
τ	$\frac{1}{2}$	1777.0 ± 0.3	$(291 \pm 1.5) \times 10^{-15}$ s	$\mu\bar{\nu}\nu$	17.35 ± 0.1
				$e\bar{\nu}\nu$	17.83 ± 0.08
				charged hadrons + neutrals	64.82
ν_e	$\frac{1}{2}$	<10 eV	stable	—	—
ν_μ	$\frac{1}{2}$	<0.16 MeV	stable	—	—
ν_τ	$\frac{1}{2}$	<18 MeV	stable	—	—

Appendix B

Milestones in particle physics

1897 Discovery of electron
1900 α, β and γ radioactivity
1905 Photon identified as quantum of electromagnetic field
1911 Discovery of atomic nucleus
1912 Discovery of cosmic rays
Invention of cloud chamber
1913 Bohr model of atom
1919 Discovery of proton
1923 de Broglie wave–particle duality
1925 Introduction of electron spin
1926 Wave mechanics
1927 Uncertainty Principle
1928 Dirac wave equation
1930 Neutrino hypothesis
1931 Operation of first cyclotron and of Van der Graaff accelerator
1932 Discovery of positron
Discovery of neutron
1933 Discovery of electromagnetic showers
1934 Theory of beta decay
Discovery of Čerenkov effect
1935 Yukawa theory of nuclear forces
1936 Breit–Wigner resonance formula
1937 First evidence for mesotron (= muon)
1939 Observation of mesotron (= muon) decay
1940 Spin-statistics theorem
1945 Phase stability in accelerators (synchrotron principle)
1946 First proposal of Big Bang model
Two-meson hypothesis

1947 Discovery of pion and $\pi \rightarrow \mu$ decay in cosmic rays
Prediction of muon-induced nuclear fusion
Two-meson hypothesis (again)
Discovery of V particles
1948 Quantum electrodynamics
Observation of $K \rightarrow 3\pi$ decay
Pion production at accelerators
1950 Spark chamber invented
Semiconductor detector invented
Discovery of neutral pion and $\pi^0 \rightarrow 2\gamma$ decay
1951 Observation of Λ hyperon and neutral kaon, K_S^0
1952 Evidence for $\Delta(1232)\pi p$ resonance
Strong focussing principle for synchrotron
Invention of bubble chamber
1953 Evidence for Σ and Ξ hyperons
First V events at accelerator: associated production
First hypernucleus event
τ–θ ($= K\pi 3/K\pi 2$) paradox
1954 Prediction of long-lived K_L^0
Invention of strangeness quantum number and classification
1956 Observation of antiproton
Detection of (anti)neutrinos from reactor
Experimental evidence for K_L^0
Proposal for colliding-beam accelerators
1957 Observation of muon-induced nuclear fusion
Two-component neutrino, $V - A$ theory
Parity non-conservation in weak decays
Resolution of τ–θ paradox
1958 $(\pi \rightarrow e)/(\pi \rightarrow \mu)$ branching ratio
Neutrino helicity measurement
1959 Operation of CERN PS, Brookhaven AGS
1961 K_L–K_S regeneration
Discovery of ρ, ω, η pion resonances
1962 Pion β-decay $\pi^+ \rightarrow \pi^0 e^+ \nu$
First accelerator neutrino beams and interactions
ν_μ and ν_e as separate neutrino flavours
1963 Cabibbo theory of hadronic weak decays
1964 Streamer chamber invented
Introduction of quarks and quark model
First evidence for Ω^- hyperon
Discovery of CP violation in K^0 decay
Higgs mechanism of spontaneous symmetry breaking

1965 Observation of cosmic microwave background radiation
Introduction of colour quantum number and vector gluons
1967 Baryon asymmetry of universe (Sakharov criteria)
1968 Weinberg–Salam–Glashow electroweak model
Deep inelastic ep scattering. Bjorken scaling and partons
1970 Invention of multiwire proportional chamber
Proposal of fourth quark (charm)
1972 Solar neutrino deficit (^{37}Cl experiment)
Fermilab Tevatron operates
CKM matrix for weak quark decays
1973 QCD as field theory of interquark interactions
Neutrino scattering experiments confirm that partons are quarks
Discovery of neutral weak currents
1974 Discovery of J/ψ and ψ' $c\bar{c}$ resonances
1975 Charmed baryons and mesons
Discovery of τ lepton
$e^+e^- \rightarrow$ quark jets
1976 CERN SPS operates
1977 Discovery of $\Upsilon(= b\bar{b})$ states
Emergence of Standard Model
1978 Parity violation in polarised electron–deuterium scattering
1979 $e^+e^- \rightarrow$ three jets (PETRA)
1980 Evidence for Υ(3S) and Υ(4S) (CESR)
1981 Observation of mesons and baryons containing b quarks
1983 Discovery of Z^0 and $W^{\pm}$ bosons
1987 Observation of B^0–$\bar{B}^0$ mixing
SN 1987A Supernova neutrino burst
1990 Z^0 produced at e^+e^- colliders LEP and SLC
Number of neutrino flavours $N_\nu = 3$ from Z^0 width
1993 Solar neutrino deficit confirmed in gallium experiments
Atmospheric neutrino flavour anomaly
Precise measurements of Z^0 decay parameters confirm Standard Model
1995 Discovery of t quark at Fermilab collider
1997 $e^+e^- \rightarrow W^+W^-$ pair production at LEP 200 collider

Comments on milestones in particle physics

The first discovery in the field of particle physics was that of the electron by J.J. Thomson in 1897. He determined the ratio of its mass and its electric charge in experiments with cathode rays. This was closely followed by the observation of α, β and γ radioactivity by the Curies, by Becquerel and by Rutherford. The α-particles were soon identified as the nuclei of helium atoms, the β-particles as

electrons and the γ-rays as the Planck quanta of the electromagnetic field, the photons identified by Einstein's 1905 paper on the photoelectric effect. The 1909 experiments on the scattering of α-particles by Geiger and Marsden led in 1911 to Rutherford's postulate of the nuclear atom. Significant technical advances at this time were the invention of the cloud chamber by C.T.R. Wilson and the discovery of cosmic rays in ionisation chambers by Hess. The Bohr model of the atom and of atomic spectra followed in 1913.

The period 1919–33 marked an era of rapid development and the first emergence of 'elementary particles' in their own right. The proton and neutron were identified, together with the electrons, as the constituents of atoms. The two most important conceptual advances in physics in the twentieth century – the theory of relativity and the quantum mechanical description of atomic and sub-atomic phenomena – together led to the prediction of antimatter by Dirac in 1931. This was followed by the discovery of the positron by Anderson in 1932, and of electromagnetic showers of electrons and positrons in cosmic rays by Blackett and Occhialini in 1933. The continuous nature of the energy spectrum of electrons in β-decay had become accepted and led to Pauli's 1930 hypothesis of the neutrino, to be put on a firm basis by Fermi's theory of nuclear β-decay in 1934.

The short-range strong nuclear force was postulated in 1935 by Yukawa to be carried by a quantum (boson) of mass of order 100 MeV, i.e. with a Compton wavelength just equal to the force range of 1 fm. A bonus of this model was that nuclear β-decay – difficult to reconcile with the non-existence of electrons in the nucleus – could be accounted for by the decay of this quantum. In 1937, evidence was found in cloud chambers operated on mountains for particles of just such a mass, intermediate between electrons and protons and hence called 'mesotrons' or 'mesons'. Furthermore they were observed to decay with about the lifetime expected. However they appeared to have weak interactions with nuclei. Experiments in 1943–6 in Rome by Conversi, Pancini and Piccioni clinched the matter: although negative mesons stopping in iron underwent nuclear capture, as expected for Yukawa particles, those stopping in a light element, carbon, invariably underwent decay. The two-meson hypothesis of Sakata and Inoue in 1946 proposed that the Rome mesotrons were the weakly interacting daughters of the Yukawa particles, produced in nuclear collisions high in the atmosphere, shortly before the pi–mu decay process ($\pi \rightarrow \mu + \nu$) was discovered experimentally by Powell and his colleagues in Bristol, using special nuclear photographic emulsions exposed on mountains. The same year, 1947, saw the discovery of even heavier mesons, in the form of 'V particles' in a cloud chamber at Manchester. These discoveries gave a tremendous boost to the development of high energy accelerators, based on the newly discovered synchrotron principle. This same year marked the birth of the prototype quantum field theory, quantum

electrodynamics, by Tomonaga, Feynman and Schwinger. On the practical side, the invention of the scintillation counter, the spark chamber and the semiconductor detector all followed by 1950.

The complex nature of the subject of elementary particles began to assert itself in 1952, with the discovery of the $\Delta(1232)$ pion–proton resonance by Anderson and Fermi. This was the first in a whole host of resonant states decaying by strong interactions, called hadrons, to be found over the next two decades. The same year, 1952, saw the invention of the bubble chamber and of the strong-focussing principle for synchrotrons. Growing evidence, from both cosmic ray studies and accelerator experiments, for K mesons and hyperons finally led to the associated production hypothesis and by 1954 to the concept of the strangeness quantum number. 1956 saw the first detection of (anti)neutrinos from a reactor, the evidence for the long-lived as well as the short-lived neutral kaon state, the observation of antiprotons and the proposal by Kerst that the useful energy available for particle creation from accelerators could be increased by the use of colliding beams. The so-called τ–θ paradox – the fact that the K meson could decay to either two or three pions – led Lee and Yang in 1957 to conclude that parity was violated in weak decays, and the $V - A$ theory of weak interactions followed. The left-handed helicity of neutrinos was measured in the following year, and the $V - A$ theory was confirmed by measurement of the branching ratios for decay of the pion to a muon plus neutrino, or to an electron plus neutrino.

The 1960s was a decade of even more startling revelations. It began with the operation of the first strong-focussing synchrotrons, the 30 GeV AGS at Brookhaven and the 28 GeV PS at CERN. The predicted regeneration of short-lived neutral kaons (K_S) in a long-lived neutral kaon beam (K_L) traversing an absorber was demonstrated and, in 1964, the completely unexpected violation of CP invariance in neutral kaon decay was discovered. The early 1960s also saw the first neutrino beams from accelerators and the demonstration of ν_μ and ν_e as separate neutrino flavours. The proposal by Gell-Mann and by Zweig that hadrons were built from fractionally charged quarks received strong support from the observation of the predicted Ω^- hyperon of strangeness -3. This year also saw the introduction of the streamer chamber. Two milestone papers in cosmology followed in 1965–6: that describing the discovery of the cosmic microwave background radiation by Penzias and Wilson and the seminal paper by Sakharov describing the conditions required for a universal baryon asymmetry to develop.

The problem in the mid-1960s for the quark model was that the quarks had never been seen as free particles, despite the most determined attempts to pry them loose in the most violent collisions at the highest possible accelerator energies. Many physicists at that time indeed believed that the quarks must be extremely massive and very tightly bound in hadrons. Thus the discovery, in 1968, of

Bjorken scaling in deep inelastic *ep* scattering at Stanford and its interpretation by Feynman in terms of light, quasi-free, pointlike 'parton' constituents at first seemed unrelated. Over the next 4–5 years, however, it became clear that the partons were indeed the quarks: the spin and electric charges could be measured, comparing inelastic electron–nucleon with neutrino–nucleon scattering. Although the colour quantum number had been proposed in 1965, it was not until 1973 that a field theory of interquark interactions – quantum chromodynamics (QCD) – was formulated, and the non-existence of free quarks accepted with the hypothesis of confinement. The first quantitative support for perturbative QCD was to come another five years later, from a neutrino experiment in a bubble chamber. The year 1973 also saw the first operation of the Tevatron accelerator at Fermilab, the first evidence for a deficit of solar neutrinos and the discovery of neutral weak currents at CERN. The following year, 1974, led to the discovery of the J/ψ resonance at Brookhaven and at Stanford, built from a quark–antiquark pair carrying a new quantum number, charm. Such a state and its approximate mass had actually been proposed already, in 1970. The J/ψ discovery and the subsequent observation of baryons and mesons with the charm quantum number gave crucial support to the quark model of hadron structure. The observation of a fourth flavour of quark and, in the following year of a third flavour of lepton – the tau lepton – suggested the existence of three families each with a charge $-\frac{1}{3}$ and a charge $+\frac{2}{3}$ quark, and a charge -1 and a charge 0 lepton (neutrino). This was confirmed with the discovery in 1977 of a fourth quark, the b (bottom) quark with charge $-\frac{1}{3}$, in the upsilon resonance $\Upsilon = b\bar{b}$ at Fermilab, and, subsequently, the cataloguing of baryon and meson states containing the new heavy quark.

During the mid to late 1970s, the study of neutral weak currents was being intensively pursued in order to determine the associated coupling parameters, and to verify the correctness of the Salam–Weinberg–Glashow model. Uncertainties due to early incorrect results on the minute parity-violating effects expected in atomic transitions were finally resolved with an experiment at Stanford on the polarisation asymmetry in electron–deuterium scattering. The Standard Model of three quark and three lepton families, coupled via the gauge fields of the electroweak and strong interactions, was slowly beginning to emerge. The prediction of QCD, that the gluon-field mediators as well as quarks were constituents of hadrons, was confirmed by the observation of $e^+e^- \rightarrow Q\bar{Q}G \rightarrow$ three-jet events at the PETRA storage ring at DESY. The weak-interaction eigenstates of the quarks had been recognised as a superposition of the strong-interaction flavour eigenstates back in 1963 by Cabibbo: the new flavours necessitated the expansion of the mixing to that of a 3×3 matrix, the so-called CKM matrix. This matrix of course contained a place for the missing third 'top' quark, with charge $+\frac{2}{3}$, to complete the third family and partner the third quark with charge $-\frac{1}{3}$, the 'bottom' quark.

The year 1983 saw the crowning success of the development of the proton-antiproton collider at the CERN SPS with the first observation of the long-sought heavy $W^{\pm}$ and Z^0 bosons predicted by the electroweak model, their masses being those expected from the parameters of the neutral currents discovered 10 years earlier. Less well advertised was that these same experiments gave the first direct evidence for the $1/r$ dependence of the interquark (QCD) potential at short distances, from observations of $p\bar{p} \rightarrow$ two jets at high transverse momentum.

Although one of the first experiments to look for proton decay had been carried out by a CERN group back in 1960, it was the experimental confirmation of the gauge models of electroweak and strong interactions, coupled with the unique predictions of grand unification (GUT) models attempting to unify these forces, which led to the installation of massive (multikilotonne) detectors placed deep underground to search for proton decay. Although so far this has not been observed, the experiments have detected the 1987A supernova neutrino burst and the anomalous ratio of muon- to electron-type neutrinos from the atmosphere.

1990 saw the first operations of the giant e^+e^- colliders: the linear collider SLC at Stanford and the circular collider LEP at CERN, serving as Z^0 factories, in which with many millions of Z^0 decays it was possible, for the first time, to obtain very precise and detailed confirmation of the correctness of the Standard Model, ranging from a deduction from the Z^0 width that the number of light neutrino flavours is indeed three to the backward–forward, decay and polarisation asymmetries among the decay products. The precision attained was such that radiative corrections to theoretical cross-sections and rates due to the effects of more massive virtual particles such as the top quark were detectable and found to be in beautiful agreement with the directly measured mass of the top quark when it was first detected at the Fermilab $\bar{p}p$ collider in 1995. Since 1997, the CERN LEP collider has operated above the W^+W^- and Z^0Z^0 pair thresholds. These cross-sections are again in excellent agreement with the Standard Model.

Appendix C

Clebsch–Gordan coefficients and d-functions

C.1 Clebsch–Gordan coefficients: the addition of angular momenta or isospins

Suppose we have two particles of angular momenta $\mathbf{j}_1$ and $\mathbf{j}_2$ with z-components m_1 and m_2. The total z-component is

$$m = m_1 + m_2$$

The total angular momentum is

$$\mathbf{j} = \mathbf{j}_1 + \mathbf{j}_2$$

and may therefore lie anywhere inside the limits

$$|j_1 - j_2| \leq j \leq |j_1 + j_2|$$

We wish to find the weights of the various allowed j-values contributing to the two-particle state, i.e.

$$\phi_1(j_1 m_1)\phi_2(j_2 m_2) = \sum_j C_j \psi(j, m), \qquad \text{with } m = m_1 + m_2 \tag{C.1}$$

The C_j are called Clebsch–Gordan coefficients (or Wigner, or vector addition, coefficients). Alternatively, we may want to express $\psi(j, m)$ as a sum of terms of different j_1 and j_2 combinations. We can do this by the use of angular-momentum (or isospin) *shift operators* (also known as 'raising' and 'lowering' operators).

First let us recall the definition of the x-, y- and z-component angular-momentum operators, in terms of the differental Cartesian operators:

$$\begin{aligned} J_x &= -\frac{ih}{2\pi}\left(y\frac{\partial}{\partial z} - z\frac{\partial}{\partial y}\right) \\ J_y &= -\frac{ih}{2\pi}\left(z\frac{\partial}{\partial x} - x\frac{\partial}{\partial z}\right) \\ J_z &= -\frac{ih}{2\pi}\left(x\frac{\partial}{\partial y} - y\frac{\partial}{\partial x}\right) \end{aligned} \tag{C.2}$$

These Cartesian operations can also be interpreted in terms of rotations. A rotation in azimuthal angle in the xy-plane has Cartesian components

$$\begin{aligned} \delta y &= r\cos\phi\,\delta\phi = x\delta\phi \\ \delta x &= -r\sin\phi\,\delta\phi = -y\delta\phi \end{aligned}$$

Thus, the effect of a small rotation on a function $\psi(x, y, z)$ will be

$$\begin{aligned} R(\phi, \delta\phi)\psi(x, y, z) &= \psi(x + \delta x, y + \delta y, z) = \psi(x, y, z) + \delta x\frac{\partial\psi}{\partial x} + \delta y\frac{\partial\psi}{\partial y} \\ &= \psi\left[1 + \left(x\frac{\partial}{\partial y} - y\frac{\partial}{\partial x}\right)\delta\phi\right] = \psi\left(1 + \delta\phi\frac{\partial}{\partial\phi}\right) \end{aligned}$$

and, from (C.2),

$$J_z = -i\hbar\left(x\frac{\partial}{\partial y} - y\frac{\partial}{\partial x}\right) = -i\hbar\frac{\partial}{\partial\phi} \tag{C.3}$$

So

$$R = 1 + \delta\phi\frac{\partial}{\partial\phi} = 1 + \frac{iJ_z}{\hbar}\delta\phi \tag{C.4}$$

It is readily verified that the operators

$$J_x, J_y, J_z \qquad \text{and} \qquad J^2 = J_x^2 + J_y^2 + J_z^2$$

obey the commutation rules

$$J^2 J_x - J_x J^2 = 0 \quad \text{etc.}$$

and

$$\begin{aligned} J_x J_y - J_y J_x &= iJ_z \\ J_y J_z - J_z J_y &= iJ_x \\ J_z J_x - J_x J_z &= iJ_y \end{aligned} \tag{C.5}$$

where we have used units $\hbar = c = 1$ for brevity. The eigenvalues of the operators J^2 and J_z are given in (C.7) below.

The *shift operators* are defined as

$$\left.\begin{aligned} J_+ &= J_x + iJ_y \\ J_- &= J_x - iJ_y \end{aligned}\right\}, \qquad \text{whence} \quad \left\{\begin{aligned} J_zJ_+ - J_+J_z &= J_+ \\ J_zJ_- - J_-J_z &= -J_- \end{aligned}\right. \tag{C.6}$$

Thus

$$J_z(J_-\phi) = J_zJ_-\phi = J_-(J_z - 1)\phi = (m-1)J_-\phi$$

Similarly,

$$J_z(J_+\phi) = (m+1)(J_+\phi)$$

This last equation shows that the wavefunction $J_+\phi$ is an eigenstate of J_z with eigenvalue $m+1$. We can therefore write it as

$$J_+\phi(j,m) = C_+\phi(j,m+1)$$

where C_+ is an unknown (and generally complex) constant. If we multiply both sides of this equation by $\phi^*(j,m+1)$, and integrate over volume, we get

$$\int \phi^*(j,m+1)J_+\phi(j,m)dV = C_+\int \phi^*(j,m+1)\phi(j,m+1)dV$$

where * indicates complex conjugation.

We choose the normalisation of ϕ so that the last integral is unity, and all allowed m-values have unit weight. So

$$C_+ = \int \phi^*(j,m+1)J_+\phi(j,m)dV$$

Similarly,

$$\begin{aligned} C_- &= \int \phi^*(j,m)J_-\phi(j,m+1)dV \\ &= \int \phi^*(j,m)J_+^*\phi(j,m+1)dV \\ &= C_+^* \end{aligned}$$

from (C.6).

If we neglect arbitrary and unobservable phases, we must have

$$C_+ = C_- = C \qquad \text{(a real number)}$$

Also, from (C.6),

$$J_+J_- = J_x^2 + J_y^2 - i(J_xJ_y - J_yJ_x) = J_x^2 + J_y^2 + J_z = J^2 - J_z^2 + J_z$$

Then

$$J_+J_-\phi(j,m+1) = [j(j+1) - m^2 - m]\phi(j,m+1) = C^2\phi(j,m+1)$$

So

$$C = \sqrt{j(j+1) - m(m+1)}$$

is the coefficient connecting states (j, m) and $(j, m+1)$.

To summarise, the angular-momentum operators have the following properties:

$$J_z\phi(j,m) = m\phi(j,m) \tag{C.7a}$$

$$J^2\phi(j,m) = j(j+1)\phi(j,m) \tag{C.7b}$$

$$J_+\phi(j,m) = \sqrt{j(j+1) - m(m+1)}\,\phi(j,m+1) \tag{C.7c}$$

$$J_-\phi(j,m) = \sqrt{j(j+1) - m(m-1)}\,\phi(j,m-1) \tag{C.7d}$$

Note that the eigenvalue $j(j+1)$ for J^2 in (C.7b) follows from the fact that $j \equiv |m_{\max}|$ and that $J_+\phi(j, m_{\max}) = 0$.

Example

As an example, we consider two particles, j_1, m_1 and j_2, m_2, forming the combined state $\psi(j, m)$, and we take the case where $j_1 = 1$, $j_2 = \frac{1}{2}$ and $j = \frac{3}{2}$ or $\frac{1}{2}$.

Obviously the states with $m = \pm\frac{3}{2}$ can be formed in only one way:

$$\psi(\tfrac{3}{2}, \tfrac{3}{2}) = \phi(1,1)\phi(\tfrac{1}{2}, \tfrac{1}{2}) \tag{C.8}$$

$$\psi(\tfrac{3}{2}, -\tfrac{3}{2}) = \phi(1,-1)\phi(\tfrac{1}{2}, -\tfrac{1}{2}) \tag{C.9}$$

Now we use the operators $J_\pm$ to form the relations

$$J_-\phi(\tfrac{1}{2}, \tfrac{1}{2}) = \phi(\tfrac{1}{2}, -\tfrac{1}{2}), \qquad J_-\phi(\tfrac{1}{2}, -\tfrac{1}{2}) = 0$$

$$J_-\phi(1,1) = \sqrt{2}\phi(1,0), \qquad J_-\phi(1,0) = \sqrt{2}\phi(1,-1), \qquad J_-\phi(1,-1) = 0,$$

using (C.7c, d).

Now operate on (C.8) with J_- on both sides:

$$\begin{aligned} J_-\psi(\tfrac{3}{2}, \tfrac{3}{2}) &= \sqrt{3}\psi(\tfrac{3}{2}, \tfrac{1}{2}) = J_-\phi(1,1)\phi(\tfrac{1}{2}, \tfrac{1}{2}) \\ &= \sqrt{2}\phi(1,0)\phi(\tfrac{1}{2}, \tfrac{1}{2}) + \phi(1,1)\phi(\tfrac{1}{2}, -\tfrac{1}{2}) \end{aligned}$$

So

$$\psi(\tfrac{3}{2}, \tfrac{1}{2}) = \sqrt{\tfrac{2}{3}}\phi(1,0)\phi(\tfrac{1}{2}, \tfrac{1}{2}) + \sqrt{\tfrac{1}{3}}\phi(1,1)\phi(\tfrac{1}{2}, -\tfrac{1}{2}) \tag{C.10}$$

Similarly, for (C.9),

$$\psi(\tfrac{3}{2}, -\tfrac{1}{2}) = \sqrt{\tfrac{2}{3}}\phi(1,0)\phi(\tfrac{1}{2}, -\tfrac{1}{2}) + \sqrt{\tfrac{1}{3}}\phi(1,-1)\phi(\tfrac{1}{2}, \tfrac{1}{2}) \tag{C.11}$$

The $j = \frac{1}{2}$ state can be expressed as a linear sum:

$$\psi(\tfrac{1}{2}, \tfrac{1}{2}) = a\phi(1,1)\phi(\tfrac{1}{2}, -\tfrac{1}{2}) + b\phi(1,0)\phi(\tfrac{1}{2}, \tfrac{1}{2})$$

with $a^2 + b^2 = 1$. Then

$$J_+\psi(\tfrac{1}{2}, \tfrac{1}{2}) = 0 = a\phi(1, 1)\phi(\tfrac{1}{2}, \tfrac{1}{2}) + b\sqrt{2}\phi(1, 1)\phi(\tfrac{1}{2}, \tfrac{1}{2})$$

Thus, $a = \sqrt{\frac{2}{3}}$, $b = -\frac{1}{3}$, and so

$$\psi(\tfrac{1}{2}, \tfrac{1}{2}) = \sqrt{\tfrac{2}{3}}\phi(1, 1)\phi(\tfrac{1}{2}, -\tfrac{1}{2}) - \sqrt{\tfrac{1}{3}}\phi(1, 0)\phi(\tfrac{1}{2}, \tfrac{1}{2}) \tag{C.12}$$

Similarly,

$$\psi(\tfrac{1}{2}, -\tfrac{1}{2}) = \sqrt{\tfrac{1}{3}}\phi(1, 0)\phi(\tfrac{1}{2}, -\tfrac{1}{2}) - \sqrt{\tfrac{2}{3}}\phi(1, -1)\phi(\tfrac{1}{2}, \tfrac{1}{2}) \tag{C.13}$$

Expressions (C.8) to (C.12) give the coefficients appearing in Appendix D.3, for the addition of $J = 1$ and $J = \frac{1}{2}$ states.

C.2 d-functions (rotation matrices)

A state $\phi(j, m)$ is transformed under a rotation through an angle θ about the y-axis into a linear combination of the $2j + 1$ states $\phi(j, m')$, where $m' = -j, -j + 1, \ldots, j - 1, j$. From the expression (3.4) for the rotation operator, we can write

$$e^{-i\theta J_y}\phi(j, m) = \sum_{m'} d^j_{m',m}(\theta)\phi(j, m') \tag{C.14}$$

where the coefficients $d^j_{m',m}$ are called *rotation matrices*. For fixed m' the expression for $d^j_{m',m}$ is therefore obtained from

$$\phi^*(j, m')e^{-i\theta J_y}\phi(j, m) = d^j_{m',m}(\theta) \tag{C.15}$$

$j = \frac{1}{2}$ state

For a state with angular momentum $j = \frac{1}{2}$, the appropriate operator is the Pauli spin matrix σ_y:

$$J_y = \tfrac{1}{2}\sigma_y = \tfrac{1}{2}\begin{vmatrix} 0 & -i \\ i & 0 \end{vmatrix}$$

Then it is easy to show that

$$e^{-i\theta\sigma_y/2} = \cos(\theta/2) - i\sigma_y \sin(\theta/2) = \begin{vmatrix} \cos(\theta/2) & -\sin(\theta/2) \\ \sin(\theta/2) & \cos(\theta/2) \end{vmatrix} \tag{C.16}$$

by expanding the exponential and using the fact that $\sigma_y^2 = 1$. We denote the states ϕ, ϕ^* by column and row matrices; for example, $\phi^*(\frac{1}{2}, \frac{1}{2}) = |1 \quad 0|$, $\phi(\frac{1}{2}, \frac{1}{2}) = \begin{vmatrix} 1 \\ 0 \end{vmatrix}$, etc., so that

$$\begin{aligned} d^{1/2}_{1/2,1/2}(\theta) &= d^{1/2}_{-1/2,-1/2}(\theta) \\ &= |1 \quad 0| \begin{vmatrix} \cos(\theta/2) & -\sin(\theta/2) \\ \sin(\theta/2) & \cos(\theta/2) \end{vmatrix} \begin{vmatrix} 1 \\ 0 \end{vmatrix} = \cos(\theta/2) \\ d^{1/2}_{-1/2,1/2}(\theta) &= -d^{1/2}_{1/2,-1/2}(\theta) \\ &= |0 \quad 1| \begin{vmatrix} \cos(\theta/2) & -\sin(\theta/2) \\ \sin(\theta/2) & \cos(\theta/2) \end{vmatrix} \begin{vmatrix} 1 \\ 0 \end{vmatrix} = \sin(\theta/2) \end{aligned} \tag{C.17}$$

As an example, consider a beam of RH polarised particles, described by $\phi(\frac{1}{2}, \frac{1}{2})$, being scattered through angle θ. If the interaction is helicity-conserving (i.e. it is a vector or axial vector interaction), they will emerge as RH particles, as measured relative to their momentum vector. However, relative to the z-axis (the incident direction) they now represent a superposition of the states $\phi'(\frac{1}{2}, \frac{1}{2})$ and $\phi'(\frac{1}{2}, -\frac{1}{2})$. Angular-momentum conservation.in a non-spin-flip interaction, however, allows only the state $\phi'(\frac{1}{2}, \frac{1}{2})$ having angular distribution

$$|d^{1/2}_{1/2,1/2}(\theta)|^2 = \cos^2(\theta/2) \tag{C.18}$$

For a spin-flip interaction, the final state would be $\phi'(\frac{1}{2}, -\frac{1}{2})$ with a distribution of the form

$$|d^{1/2}_{1/2,-1/2}(\theta)|^2 = \sin^2(\theta/2) \tag{C.19}$$

These terms enter the cross-section for electron scattering via the electric and magnetic interactions, respectively.

$j = 1$ state

In the case $j = 1$, we make use of the expansions

$$e^{-i\theta J_y} = 1 - i\theta J_y - \frac{\theta^2}{2!} J_y^2 + i\frac{\theta^3}{3!} J_y^3 + \cdots \tag{C.20}$$

and

$$J_y = -\frac{i}{2}(J^+ - J^-)$$

from (C.6). It is straightforward to show that

$$\begin{aligned} J_y\phi(1,1) &= J_y^{2n+1}\phi(1,1) = \sqrt{\tfrac{1}{2}}\, i\phi(1,0) \\ J_y^2\phi(1,1) &= J_y^{2n}\theta(1,1) = \tfrac{1}{2}[\phi(1,1) - \phi(1,-1)] \end{aligned} \tag{C.21}$$

Then

$$\begin{aligned} \phi^*(1,1)e^{-i\theta J_y}\phi(1,1) &= 1 - \frac{1}{2}\frac{\theta^2}{2!} + \frac{1}{2}\frac{\theta^4}{4!} + \cdots \\ \phi^*(1,1)e^{-i\theta J_y}\phi(1,-1) &= +\frac{1}{2}\frac{\theta^2}{2!} - \frac{1}{2}\frac{\theta^4}{4!} + \cdots \end{aligned}$$

so that

$$\begin{aligned} d^1_{1,1}(\theta) &= \tfrac{1}{2}(1+\cos\theta) \\ d^1_{1,-1}(\theta) &= \tfrac{1}{2}(1-\cos\theta) \end{aligned} \tag{C.22}$$

Also,

$$\phi^*(1,0)e^{-i\theta J_y}\phi(1,1) = \sqrt{\tfrac{1}{2}}\, i\left(-i\theta + i\frac{\theta^3}{3!} + \cdots\right)$$

or

$$d^1_{1,0}(\theta) = \sqrt{\tfrac{1}{2}}\sin\theta \tag{C.23}$$

Appendix D

Spherical harmonics, d-functions and Clebsch–Gordan coefficients

D.1 Spherical harmonics

$$Y_l^m(\theta,\phi) = \sqrt{\frac{(2l+1)(l-m)!}{4\pi(l+m)!}} P_l^m(\cos\theta) e^{im\theta}$$

$$P_l^m(\cos\theta) = (-1)^m \sin^m\theta \left[\left(\frac{d}{d(\cos\theta)}\right)^m P_l(\cos\theta)\right] \qquad (m \le l)$$

$$P_l(\cos\theta) = \frac{1}{2^l l!}\left[\left(\frac{d}{d(\cos\theta)}\right)^l (-\sin^2\theta)^l\right]$$

$$Y_l^{-m}(\theta,\phi) = (-1)^m [Y_l^m(\theta,\phi)]^*$$

$$P_l^{-m}(\cos\theta) = (-1)^m \frac{(l-m)!}{(l+m)!} P_l^m(\cos\theta)$$

$l = 0$ $\quad Y_0^0 = \dfrac{1}{\sqrt{4\pi}}$

$l = 1$ $\quad Y_1^0 = \sqrt{\dfrac{3}{4\pi}}\cos\theta$ $\qquad Y_1^1 = -\sqrt{\dfrac{3}{8\pi}}\sin\theta e^{i\phi}$

$l = 2$ $\quad Y_2^0 = \sqrt{\dfrac{5}{16\pi}}(3\cos^2\theta - 1)$ $\qquad Y_2^1 = -\sqrt{\dfrac{15}{8\pi}}\sin\theta\cos\theta e^{i\phi}$

$\quad Y_2^2 = \sqrt{\dfrac{15}{32\pi}}\sin^2\theta e^{2i\phi}$

$l = 3$ $\quad Y_3^0 = \sqrt{\dfrac{7}{16\pi}}(5\cos^3\theta - 3\cos\theta)$ $\qquad Y_3^1 = -\sqrt{\dfrac{21}{64\pi}}\sin\theta(5\cos^2\theta - 1)e^{i\phi}$

$\quad Y_3^2 = \sqrt{\dfrac{105}{32\pi}}\sin^2\theta\cos\theta e^{2i\phi}$ $\qquad Y_3^3 = -\sqrt{\dfrac{35}{64\pi}}\sin^3\theta e^{3i\phi}$

D.2 d-functions

$$d^j_{m',m} = (-1)^{m-m'} d^j_{m,m'} = d^j_{-m,-m'}$$

$$d^1_{1,1} = \frac{1+\cos\theta}{2} \qquad d^1_{1,0} = -\frac{1}{\sqrt{2}}\sin\theta \qquad d^1_{1,-1} = \frac{1-\cos\theta}{2}$$

$$d^1_{0,0} = \cos\theta$$

$$d^{1/2}_{1/2,1/2} = \cos\frac{\theta}{2} \qquad d^{1/2}_{1/2,-1/2} = -\sin\frac{\theta}{2}$$

D.3 Clebsch–Gordan coefficients

As an example of the use of the following table, take the case of combining two angular momenta $j_1 = 1$, $m_1 = 1$ and $j_2 = 1$, $m_2 = 1$. We look up the entry for combining angular momenta 1×1, and the fourth line gives for the cocfficients C_j in (C.1) of Appendix C

$$\phi_1(1,1)\phi_2(1,-1) = \sqrt{\tfrac{1}{6}}\psi(2,0) + \sqrt{\tfrac{1}{2}}\psi(1,0) + \sqrt{\tfrac{1}{3}}\psi(0,0)$$

This tells us how two particles of angular momentum (or isospin) unity combine to form states of angular momentum $j = 0$, 1 or 2. Alternatively, a state of particular j, m can be decomposed into constituents. Thus $j = 2$, $m = 0$ can be decomposed into products of states with $j = 1$ and $m_1 + m_2 = m = 0$. The fourth column of the 1×1 table gives

$$\psi(2,0) = \sqrt{\tfrac{1}{6}}\phi_1(1,1)\phi_2(1,-1) + \sqrt{\tfrac{2}{3}}\phi_1(1,0)\phi_2(1,0) + \sqrt{\tfrac{1}{6}}\phi_1(1,-1)\phi_2(1,1).$$

The sign convention in the table follows that of Condon and Shortley (1951).

$\frac{1}{2} \times \frac{1}{2}$

		$J =$	1	1	0	1
m_1	m_2	$M =$	+1	0	0	−1
$+\frac{1}{2}$	$+\frac{1}{2}$		1			
$+\frac{1}{2}$	$-\frac{1}{2}$			$\sqrt{\frac{1}{2}}$	$\sqrt{\frac{1}{2}}$	
$-\frac{1}{2}$	$+\frac{1}{2}$			$\sqrt{\frac{1}{2}}$	$-\sqrt{\frac{1}{2}}$	
$-\frac{1}{2}$	$-\frac{1}{2}$					1

$1 \times \frac{1}{2}$

		$J =$	$\frac{3}{2}$	$\frac{3}{2}$	$\frac{1}{2}$	$\frac{3}{2}$	$\frac{1}{2}$	$\frac{3}{2}$
m_1	m_2	$M =$	$+\frac{3}{2}$	$+\frac{1}{2}$	$+\frac{1}{2}$	$-\frac{1}{2}$	$-\frac{1}{2}$	$-\frac{3}{2}$
$+1$	$+\frac{1}{2}$		1					
$+1$	$-\frac{1}{2}$			$\sqrt{\frac{1}{3}}$	$\sqrt{\frac{2}{3}}$			
0	$+\frac{1}{2}$			$\sqrt{\frac{2}{3}}$	$-\sqrt{\frac{1}{3}}$			
0	$-\frac{1}{2}$					$\sqrt{\frac{2}{3}}$	$\sqrt{\frac{1}{3}}$	
-1	$+\frac{1}{2}$					$\sqrt{\frac{1}{3}}$	$-\sqrt{\frac{2}{3}}$	
-1	$-\frac{1}{2}$							1

1×1

		$J =$	2	2	1	2	1	0	2	1	2
m_1	m_2	$M =$	$+2$	$+1$	$+1$	0	0	0	-1	-1	-2
$+1$	$+1$		1								
$+1$	0			$\sqrt{\frac{1}{2}}$	$\sqrt{\frac{1}{2}}$						
0	$+1$			$\sqrt{\frac{1}{2}}$	$-\sqrt{\frac{1}{2}}$						
$+1$	-1					$\sqrt{\frac{1}{6}}$	$\sqrt{\frac{1}{2}}$	$\sqrt{\frac{1}{3}}$			
0	0					$\sqrt{\frac{2}{3}}$	0	$-\sqrt{\frac{1}{3}}$			
-1	$+1$					$\sqrt{\frac{1}{6}}$	$-\sqrt{\frac{1}{2}}$	$\sqrt{\frac{1}{3}}$			
0	-1								$\sqrt{\frac{1}{2}}$	$\sqrt{\frac{1}{2}}$	
-1	0								$\sqrt{\frac{1}{2}}$	$-\sqrt{\frac{1}{2}}$	
-1	-1										1

Appendix E

Relativistic normalisation of cross-sections and decay rates

In the formulae (2.16)–(2.19) describing the cross-section for the reaction $a+b \to c+d$, the various terms – matrix element, final-state phase space, incident flux factor – are not in forms that are invariant under Lorentz transformations along the beam axis. This does not actually matter for the calculation of the cross-section (provided that it is done in one reference frame, for example the cms), since this is a transverse quantity and therefore necessarily invariant. However, this is not the case for the transition rate W. For example, the decay rate for $A \to c+d$ will vary as M_A/E_A where E_A is the energy in the frame where the decay rate is measured: thus a relativistic treatment is required.

The modification to the phase-space factor for a final-state particle, so as to include its momentum ($\mathbf{p}$) and energy (E) components on an equal basis, will be of the form

$$\begin{aligned}\int p^2 dp d\Omega = \int d^3\mathbf{p} &\longrightarrow \int\int d^3\mathbf{p}\, dE\, \delta(E^2 - \mathbf{p}^2 - m^2) \\ &= \int\int \frac{d^3\mathbf{p}\, d(E^2 - \mathbf{p}^2 - m^2)}{2E}\, \delta(E^2 - \mathbf{p}^2 - m^2) \\ &= \int \frac{d^3\mathbf{p}}{2E}\, \delta(E^2 - \mathbf{p}^2 - m^2)\end{aligned}$$

where the δ-function is there to ensure energy–momentum conservation, and in the second line, the δ-function kills the integral over energy. Thus a factor $1/2E$ has appeared in the phase-space expression for each final-state particle, $d^3\mathbf{p}/2E$ being a Lorentz invariant quantity. A compensating $2E$ factor is inserted in the normalisation of the particle density (or $\sqrt{2E}$ in the wave amplitude for each particle appearing in the matrix element). In fact, it turns out that when the particle density is defined using the relativistic Klein–Gordon wave equation (1.13), such an E dependence appears naturally.

With the above normalisation, the particle density becomes $2E$ per unit volume in the lab system, or $2M$ in the particle rest frame. The physical interpretation here is that the ratio E/M of the two densities exactly compensates for the fact that the normalisation volume is Lorentz-contracted by the factor M/E when evaluated in the lab system.

With particles in both initial and final states normalised to a density of $2E$ per unit volume, the expression for the cross-section becomes, with v_{ab} as the relative velocity of a and b,

$$d\sigma = \frac{2\pi}{v_{ab}(2E_a)(2E_b)}|M_{if}|^2 \frac{1}{(2\pi)^6} \frac{d^3\mathbf{p_c}}{2E_c} \frac{d^3\mathbf{p_d}}{2E_d} \frac{1}{dE_f}$$

It is left as an exercise to show that the modification to the flux factor

$$\frac{1}{v_{ab}} \longrightarrow \frac{1}{v_{ab}(2E_a)(2E_b)}$$

does indeed result in a relativistically invariant form, i.e. one expressed in terms of products of 4-vector quantities only. We note that all the factors $2E$ appearing in the numerator in $|M_{if}|^2$ cancel with all the factors in the denominator, so that as expected, the cross-section itself is unaffected by these relativistic factors.

For the transition rate W for $A \rightarrow c + d$, the relativistically invariant normalisation will correspond to the decay of $2E_A$ particles in the normalisation volume, so that to obtain the decay rate per particle A, one must divide the non-relativistic expression in (2.18) by a factor $2E_A$, or by $2M_A$ in the rest frame of A.

Glossary

Antiparticle Associated with every particle is an antiparticle, with exactly the same mass and lifetime but opposite values of electric charge, magnetic moment, baryon number, lepton number and flavour.

Baryon Baryons form one of the two classes of strongly interacting particles (hadrons) and are each composed of three quarks. The only stable baryons are the proton and neutron, built from the lightest (u and d) quarks. The baryons containing other flavours of quark (s, c, b) have very short lifetimes (less than 10^{-10} s). The name *baryon* originally meant a heavy particle, as baryons appeared more massive than the other class of hadrons, the *mesons* (literally, particles of intermediate mass), and much more massive than the *leptons* or light particles. Although with the observation of new flavours of both quark and lepton this distinction on the basis of mass is no longer valid, the above names are preserved.

Baryon conservation A conserved quantity called baryon number, $B = +1$, is ascribed to all baryons (and $B = -1$ to all antibaryons), to mark the stability of the lightest baryon, the proton, into which all other baryons must decay. (The measured limit on the proton lifetime exceeds 10^{32} yr.)

Big Bang The presently accepted model of cosmology postulates that the universe originated effectively from a singularity of enormous energy and temperature, which expanded and cooled. The three main pieces of evidence supporting the Big Bang are Hubble's law, the cosmic microwave background radiation and the cosmic abundances of the light elements deuterium, helium and lithium relative to hydrogen.

Boson A particle of integral spin ($0\hbar$, $1\hbar$, $2\hbar$, ...). Bosons obey Bose–Einstein statistics, i.e. the wavefunction describing two identical bosons is symmetric under

particle exchange. The fundamental interactions are mediated by exchange of bosons of various types.

Bottom quark Also called the beauty quark, of charge $-\frac{1}{3}|e|$, this is a member of the third quark family. It was discovered in the form of the upsilon meson ($\Upsilon = \bar{b}b$) in 1977.

Bremsstrahlung The radiation (in the form of γ-rays) emitted when a fast charged particle undergoes sudden deceleration and scattering by the nuclear Coulomb field as it traverses a medium.

Cabibbo angle A parameter θ_c relating the weak decay rate of strange particles to that of non-strange particles. The ratio of the rates is $\tan\theta_c$.

Cascade shower When energetic electrons traverse material (especially that of high Z), they radiate photons in atomic collisions (bremsstrahlung), which can then convert to electron–positron pairs, in turn radiating more photons. An electron–photon shower then builds up, finally dying away as the energy is dissipated in ionisation loss by the electrons. Originally discovered in cosmic rays in 1933, these showers are exploited in the so-called electromagnetic calorimeter. This is an array of counters and absorbing material having a high Z-value, which contains the shower and whose output can provide an accurate measurement of the energy of the incident electron or photon. Such calorimeters are in general use at particle colliders.

Charmed quark, charmonium A member of the second quark family, of charge $+\frac{2}{3}|e|$, the charmed quark forms a bound state with its antiparticle, called charmonium, $c\bar{c}$. The charm quantum number was discovered in 1974, with observation of the lightest charmonium state, J/ψ.

Colour A fundamental property of quarks, colour is the name given to the strong charge through which quarks interact with each other. Colour comes in three varieties, usually designated red, green and blue. It plays a role in strong interactions similar to that of charge in electromagnetic interactions. Antiquarks carry anticolour. All hadrons are colourless: mesons are built from, for example, a blue quark and an antiblue antiquark, while a baryon is built from three quarks, each of a different colour.

Confinement A property of the strong colour interaction between quarks is that quarks do not exist as free particles but are always confined in hadrons.

Cosmic rays Cosmic rays consist principally of high energy protons, α-particles

and heavier nuclei incident on the Earth's atmosphere from deep space. Their mean energy is a few GeV, but particles of energy above 10^{11} GeV have been recorded, through the extensive air showers (of hadrons, photons and electrons) they produce. The secondary mesons produced in cosmic ray collisions in the atmosphere are mostly pions. The neutral pions decay to γ-rays, leading to the soft, electron–photon component of the radiation, while the charged pions decay to muons, which can penetrate to sea level and underground, forming the so-called hard component. At sea level the muon flux is about 10^2 m^{-2} s^{-1}. In addition to charged primary particles, very high energy γ-rays up to and beyond TeV energies are observed from point sources in the sky.

Cosmic microwave radiation This all-pervading radiation, with a black body spectrum of $T = 2.7$ K, is a relic of the Big Bang after expansion and cooling.

Coupling constant Particles interact via their strong, electromagnetic or weak charges, and the square of the charge is called the coupling constant. It enters into the matrix element for the interaction and hence determines cross-sections and decay rates. In renormalisable, gauge-invariant field theories, the couplings are in fact not constant but vary, very slowly, with the energy scale.

CP symmetry Symmetry of an interaction under the joint operations of space inversion P and interchange of negative and positive charges, or charge conjugation, C. CP symmetry holds for electromagnetic and strong interactions, but is violated in weak interactions.

Cross-section The rate of a particular reaction is measured by the cross-section, i.e. the effective area subtended by the target particle to an incident beam. It is numerically equal to the reaction rate per target particle per unit incident flux.

Dark matter Dark matter is postulated in order to redress the order-of-magnitude imbalance between the gravitational energy of the luminous matter in the universe and its observed motional kinetic energy. The (presently unknown) dark matter particles can be classed as hot dark matter (those with relativistic velocities when they decoupled from other matter and radiation) or as cold dark matter (non-relativistic) particles. Cold dark matter must preponderate, since too much hot dark matter would inhibit the formation of galaxies, clusters, superclusters and bigger cosmic structures.

D mesons Mesons containing a charmed quark or antiquark (i.e. $c\bar{d}$, $c\bar{u}$, $c\bar{s}$). The D mesons of lowest mass (D^0, $D^{\pm}$) are pseudoscalar (spin-parity $J^P = 0^-$) and decay weakly into non-charmed (and predominantly strange) mesons. The more

massive D^* mesons are broad resonances decaying by strong interactions to lighter charm states, and are either vector or tensor mesons ($J^P = 1^-, 2^+$).

Down quark A charge $-\frac{1}{3}|e|$ quark from the first generation, partnering the charge $+\frac{2}{3}|e|$ up quark. Together these quarks form the constituents of protons and neutrons.

Electromagnetic cascade See ***Cascade shower***

Electroweak model The model that unifies the couplings in the weak and electromagnetic interactions. Both interactions are mediated by vector bosons, but in contrast to the massless photon mediator in electromagnetism, the weakness of the weak interactions is ascribed to the large masses of the W and Z bosons and the consequently short range of that interaction.

Exchange force Interactions between elementary particles in quantum mechanics are described in terms of the exchange of virtual bosons. The nature of the force (strong, electromagnetic or weak) determines the properties of the bosons involved (gluons, photons and $W^{\pm}$, Z^0 bosons respectively).

Fermion A particle with half-integral spin in units of $\hbar$ ($\frac{1}{2}\hbar, \frac{3}{2}\hbar, \ldots$). Fermions obey Fermi–Dirac statistics, for which the wavefunction of two identical particles is antisymmetric (changes sign) under particle interchange.

Feynman diagram A graphical representation of exchange interactions, with rules to show how the various factors (spin, coupling constants, propagators) enter into the matrix element.

Flavour Flavour is a generic name to describe the different types of quark and lepton. Quarks occur in six flavours (up, down, strange, charmed, bottom and top), as do leptons (electron, electron-neutrino, muon, muon-neutrino, tauon, tauon-neutrino).

Form factor An empirical factor by which a scattering amplitude must be multiplied when dealing with non-pointlike particles. As an example, the square of the electromagnetic form factor of the nucleon gives the probability that this extended object will 'hold together' and recoil coherently in a collision with another charged particle (such as a high energy electron).

Gauge invariance Gauge invariance is a property of field theories in which the physical results of the interactions they mediate are independent of changes in the

local scale or gauge of the potentials involved. It is believed that all well-behaved, renormalisable field theories must incorporate the gauge principle.

Generation The six flavours of quarks and of leptons are grouped into three families or generations. Each generation consists of a charge $+\frac{2}{3}|e|$ and charge $-\frac{1}{3}|e|$ quark pair and a charge $-1|e|$ and charge $0|e|$ lepton pair.

Gluon The gluon is the massless mediator of the strong interquark colour field. It is analogous to the photon of the electromagnetic field, but unlike the uncharged photon, the gluon itself carries a colour charge.

GUTs Grand unified theories or GUTs seek to unify the strong, electromagnetic and weak interactions into a single interaction with a unique coupling applying at very high energy. Symmetry breaking effects are postulated to account for the disparate strengths at laboratory energies.

Hadron The word hadron stands for a strongly interacting particle, distinguishing it from a lepton, which has only weak or electromagnetic interactions. Hadrons consist of baryons, containing three quarks, and mesons, consisting of a quark–antiquark pair.

Helicity Also called handedness. The helicity H is equal to the component J_z of spin along the momentum vector of the particle, divided by the total spin J. Massless particles have spin components $J_z = \pm J$ only, and thus $H = +1$ or $H = -1$. Massive particles are not in pure helicity eigenstates, and contain both LH ($H = -1$) and RH ($H = +1$) components.

Higgs mechanism The Higgs mechanism depends on the postulate of an all-pervading scalar field, the Higgs field, which couples to all elementary particles and gives them their masses. The Higgs mechanism was invented in order to account for spontaneous symmetry breaking in the electroweak model, which results in very different masses for the mediating photons and the W and Z bosons. Physical Higgs particles should exist as excitations of the Higgs field.

Hyperons The name collectively given to baryons with a strangeness quantum number $S = -1, -2$ or -3, in which u and d quarks are replaced by one, two or three s quarks. The lightest hyperon, the Λ particle, with $S = -1$, may form a so-called hypernucleus when it replaces a neutron in an atomic nucleus.

Inflation The mechanism of inflation was proposed to solve the horizon and flatness problems in Big Bang cosmology. At very early times (10^{-34}–10^{-32} s),

the universe supposedly grew exponentially in size, typically by a factor of order 10^{30}. Such a mechanism would result in a 'flat' universe with critical density and account for the fact that regions of the sky with apparently no causal connection emit black body microwave radiation at practically the same temperature.

Ionisation loss The energy loss by energetic charged particles traversing a medium, as they eject atomic electrons in their path. The total energy loss also includes that from excitation (without ionisation) of atoms.

Isospin A quantum number ascribed to hadrons, conserved in strong interactions. It results because of the near equality in mass of the constituent u and d quarks, so that, once the difference in the Coulombic effects is subtracted, hadronic states (including atomic nuclei) differing only by interchange of u and d quarks have closely similar masses.

Jets A word employed (and first used by the present author in 1954) to describe the collimation of the secondary hadrons produced in high energy collisions. A jet results from the fact that the average transverse momentum of the secondaries is of order 0.3 GeV/c, being determined by the range of the strong interaction. In a high energy collision, the secondaries will generally carry large longitudinal momentum components and therefore emerge in a narrow cone.

J/Ψ particle The lowest-lying of the bound states (charmonium) of the charmed quark and antiquark.

Kaon The lightest strange meson. Kaons occur in four states, K^+ and K^0, with strangeness $S = +1$, and K^- and $\bar{K}^0$, with strangeness $S = -1$.

Lepton The leptons consist of the electron and the heavier versions, the muon and the tauon, and their respective neutrinos, plus their antiparticles. The name derives from the Greek for 'light particle'.† Leptons are assigned lepton number $L = +1$, antileptons $L = -1$. The total lepton number is conserved.

Lifetime The distribution of the decays of unstable particles falls off exponentially with time. The mean lifetime is that required to reduce the initial number of particles by a factor e, as measured in the particle rest frame.

Monopoles The existence of single magnetic charges or monopoles was predicted by Dirac in 1932. More recently they have been associated with grand

† 'Lepton' is also, as it happens, the name of a village in West Yorkshire. The name derives from the Anglo-Saxon for 'Farm by an abyss'.

unified theories and as topological discontinuities in superstring theories. There is presently no experimental evidence for monopoles.

MACHOs Massive compact halo objects or MACHOs are non-luminous stars of small mass (0.01–0.1 solar masses). Their existence is revealed through their gravitational lensing of the light from more distant visible stars.

Meson A hadron built from a quark–antiquark pair. The name 'meson' was originally applied in the 1930s and 1940s to pions and muons, to indicate masses intermediate between that of the electron and the proton. The most massive meson yet detected is a top–antitop combination, with negligible lifetime and mass 350 GeV/c^2, i.e. 400 times that of the proton mass.

Muon A heavy version of the electron, which undergoes weak decay to an electron and two neutrinos. Muons are the principle component of cosmic rays at sea level.

Neutral current A weak interaction if mediated by a charged boson $W^{\pm}$, is called a charged-current reaction (CC) and if mediated by a neutral boson Z^0 is called a neutral-current reaction (NC). The electric charges of the interacting particles change in a CC reaction but are unchanged in a NC interaction.

Non-Abelian field A field mediated by a particle that has self-interaction. For example, the gluon mediates the strong colour field but itself carries a colour charge and can therefore interact with other gluons. In contrast, the electromagnetic field acting between charges is an Abelian field since the photon mediator is uncharged and therefore has no self-interaction.

Neutrino The neutral member of the lepton family, the neutrino, was predicted by Pauli in 1930 as a 'desperate remedy' to save energy–momentum conservation in nuclear β-decay. The first interactions of neutrinos were observed in 1956. Intense beams of high energy neutrinos can be produced at accelerators and they played an important role in elucidating the quark substructure of the nucleon. Three flavours of neutrino accompany the three flavours of charged lepton.

Photon The elementary, massless carrier of the electromagnetic field.

Pion The lightest of the mesons, the pion occurs in three charged states π^+, π^-, π^0 and is composed of u and d type quarks and antiquarks.

Planck mass The Planck mass $M_p = 2 \times 10^{19}$ GeV/c^2 is the natural mass unit

found by combining Planck's constant, the velocity of light and the Newtonian constant of gravitation. Quantum gravitational effects can become important at the Planck mass scale. This is also the natural scale of supergravity theories.

Positron The antiparticle of the electron, predicted by Dirac and discovered in cosmic rays by Anderson in 1932.

QED Quantum electrodynamics (QED) is the quantum field theory of the electromagnetic interaction, first formulated in the late 1940s. Its predictions have been tested experimentally to a precision approaching one part per billion. Thus QED is regarded as *the* prototype field theory.

QCD Quantum chromodynamics (QCD) is the field theory of the strong colour interaction between quarks.

Quarks The elementary fermions from which all the strongly interacting particles (hadrons) are constructed. The quarks occur in three states d, s, b with charge $-\frac{1}{3}|e|$ and three states u, c, t with charge $+\frac{2}{3}|e|$. The name quark was allegedly taken by Gell-Mann from a phrase in *Finnegan's Wake* by James Joyce, which ran: 'Three quarks for Muster Mark!' This nomenclature was of course made in 1964 when it appeared that hadrons were composed of only three types of quark, u, d and s, rather than the six of today.

Regeneration Regeneration describes the fact that when the long-lived component K_L^0 of a neutral kaon beam traverses an absorber, it regenerates the short-lived component K_S^0.

Resonance Resonance is familiar in classical physics; for example in an electrical circuit when the frequency of the applied voltage equals the natural frequency of the circuit the amplitude (current) is then a maximum. In elementary particle physics resonant states or resonances are also formed. For example, one may be excited in the collision of a pion and a proton when the collision energy is equal to the natural frequency (i.e. mass) of the resonant state. The collision cross-section passes through a maximum at the resonant energy. The first (πp) resonance was discovered by Fermi and Anderson in 1952.

Sargent rule Discovered empirically in nuclear β-decay, but applicable to any three-body weak decay, the Sargent rule states that the decay rate is proportional to the fifth power of the disintegration energy.

Spin Spin is an intrinsic quantum number that has to be assigned to elementary particles; originally for the electron following the experiments by Stern and Gerlach demonstrating the splitting of a beam of silver atoms traversing a strong non-uniform magnetic field. Spin has dimensions of angular momentum and is quantised in half-integer units ($\frac{1}{2}\hbar, \frac{3}{2}\hbar, \ldots$) for fermions and integer units ($0\hbar, 1\hbar, \ldots$) for bosons.

Spontaneous symmetry breaking See ***Higgs mechanism***

Strangeness Quantum number assigned to a class of mesons and baryons called 'strange particles' and containing an s quark. Strange particles can only decay to non-strange particles through the weak interaction.

Strong force See ***QCD***

Superweak interaction A new type of specifically CP-violating interaction, which was postulated to account for the very small (10^{-3}) degree of CP violation in neutral kaon decay.

Supersymmetry A proposed symmetry between fermions and bosons, according to which every elementary fermion possesses a boson 'superpartner' and vice versa. Thus a quark will have a boson partner called a squark, a photon a fermion partner called a photino, and so on. The energy scale at which such a symmetry, if it existed, would apply, is expected to be $\sim$ 1 TeV.

Supergravity, superstring theory A model at the Planck energy scale, in which pointlike particles are replaced by strings or loops of finite size, of order the Planck length (10^{-33} cm). It avoids many of the divergence problems of theories with pointlike particles.

Synchrotron A synchrotron is an accelerator in the form of a toroidal ring of bending and focussing magnets, containing the vacuum tube inside which circulates the particle beam. The particles are accelerated by one or more RF cavities placed around the ring. As the particle velocity increases, the magnetic field must be increased to keep the particles in orbit, and the RF frequency must be varied so that it is synchronised with the revolution time of the beam.

Tauon The third and heaviest member of the family of charged leptons.

Top quark The third and heaviest quark of charge $+\frac{2}{3}|e|$.

Two-component neutrino A neutrino is assigned spin $\frac{1}{2}\hbar$ and, in analogy with the electron, would be expected to exist in four states: neutrino and antineutrino, each with two possible spin substates with respect to the direction of motion, $J_z = \pm\frac{1}{2}\hbar$. In 1957 it was discovered that the neutrino and its antiparticle each existed in only one spin state, $J_z = -\frac{1}{2}\hbar$ for neutrino and $J_z = +\frac{1}{2}\hbar$ for antineutrino, hence the term 'two-component neutrino'.

Up quark The up or u quark, with charge $+\frac{2}{3}|e|$, is the lightest of the quarks and partners the down quark d as a constituent of neutrons and protons.

Unitarity limit A limit on a cross-section set by the requirement that, in a scattering process, the scattered amplitude in a particular partial wave cannot exceed the incident amplitude in the same partial wave.

Upsilon meson The bound state ($\Upsilon = b\bar{b}$) of bottom quark and antiquark (also called bottomonium). The upsilon is the lowest-lying of the $b\bar{b}$ states, with mass 9.46 GeV/c, and was discovered in 1977.

Virtual particle A virtual particle is one having energy and momentum such that its mass is not equal to that of the free particle. In the jargon, it is stated to be 'off mass shell'. Because of the Uncertainty Principle, such particles are allowed but can only have a very transient existence, hence the term 'virtual'. Exchange particles that connect vertices in Feynman diagrams are always virtual.

W and Z particles The $W^{\pm}$ and Z^0 massive bosons are the mediators of the weak force, responsible for the so-called charged-current and neutral-current processes respectively. Together with the massless photon, they constitute the mediating bosons in the electroweak theory unifying weak and electromagnetic interactions. The W, Z particles were discovered experimentally in 1983.

WIMPs Weakly interacting massive particles or WIMPs have been postulated as candidates for the 'dark matter' of the universe. See also ***MACHOs***.

Answers to problems

Chapter 1

1.1 $q^2 = 2.81\ \text{GeV}^2$; 0.74 fm.

1.4 $E_\gamma = E_\pi(1 + \beta\cos\theta)/2$; $dN/dD = 2/(D+1)^2$.

1.5

(a) Binding energy of $(H_2\mu)^+$ larger than $(H_2e)^+$.
(b) Reduced mass $\mu_H = m_\mu/(1 + m_\mu/M_H) < \mu_D = m_\mu/(1 + m_\mu/M_D)$.
(c) 3×10^{-11} cm.
(d) $HD \rightarrow {}^3He + \mu + 5.4$ MeV.

(For references, see G. Feinberg and L. Lederman, *Ann. Rev. Nucl. Sci.* **13**, 431, 1963.)

1.7 Reactions 1,2,5 allowed. Reaction 3 forbidden by lepton conservation. Reaction 4 forbidden by conservation of strangeness in strong interactions.

1.8 $6.7 \times 10^{10}\ \text{cm}^{-2}\ \text{s}^{-1}$.

1.9 (b) 26.5 *cm*, (*c*)10^{-7}.

1.10

(a) $\theta_{\max} = 0.80$ rad, $p = 7.96\ \text{GeV}/c$.
(b) $\theta = 0$, $p = 9.21\ \text{GeV}/c$, $q^2_{\max} = 15.6\ \text{GeV}^2$.

Chapter 2

2.1 $\simeq 10^6$.

2.2 $|\Delta e/e| > \sqrt{(G_N M^2/e^2)} = 10^{-18}$.

2.4 17.6 mb.

2.6 520 eV/c.

Chapter 3

3.2 (a) J_K is even (Bose symmetry); (b) none (weak decay).

3.5 (a) As for $\pi^- p \to n\pi^0, \pi^- p \to \pi^- p, \pi + p \to \pi^+ p$; (b) 1 : 2.

3.6 (a) $I = 0$ or 1; (b) $\sigma_a/\sigma_b = 1$ if $I = 0$ only; (c) $\sigma_a/\sigma_b = 0$ if $I = 1$ only.

3.8 (a) $I = 0, 1, 2$ or 3; (b) $I = 1$ or 3.

3.9 ρ–ω interference in the $\pi^+\pi^-$ mode with amplitude of order $\alpha \sim 1/137$, typical of I-spin-violating electromagnetic transitions. A narrow dip or peak will occur in the $\pi^+\pi^-$ mass spectrum in the region of the ω meson mass.

3.10 Yes, for strong interactions.
No, because of Bose symmetry.
No, by C-symmetry; $C_\rho = -1$ since $\rho^0 \to e^+e^-$; $C_\eta = C_\pi = +1$, since $\eta, \pi^0 \to 2\gamma$.
Yes, for electromagnetic interactions.

3.11 Two Λ particles are produced, in a ^{1}S-state if $P_\Xi = +1$ and in a ^{2}P-state if $P_\Xi = -1$.

3.13 $C = P = -1$ for ρ; $C = P = +1$ for f; $\rho^0 \to \pi^0\gamma$ allowed; branching ratio $\sim \alpha$.

Chapter 4

4.2 Ω^- has $S = -3$, $I = 0$, $J^P = \frac{3}{2}^+$, $B = 1$, $M = 1672$ MeV.

$$M_\Omega - M_P = 734 \text{ MeV} < 3M_K = 1485 \text{ MeV}$$
$$M_\Omega - M_\Xi = 357 \text{ MeV} < M_K$$
$$M_\Omega - M_\Lambda = 554 \text{ MeV} < 2M_K = 990 \text{ MeV}$$

Hence all strong, strangeness-conserving decays, $\Omega^- \to p + 2K^- + \bar{K}^0$, $\Omega^- \to \Lambda + K^- + \bar{K}^0$ and $\Omega^- \to \Xi^0 + K^-$ are forbidden by energy conservation. The weak ($\Delta S = 1$) decays $\Omega^- \to \Xi^0\pi^-$, $\Xi^-\pi^0$, ΛK^- are the only possibilities.

4.3 A meson radius of 0.8 fm gives $\Gamma_\rho \simeq 8$, $\Gamma_\omega \simeq 0.9$ and $\Gamma_\phi \simeq 1.0$ keV.

4.4 $\mu_p = 3$, $\mu_n = -2$, $\mu_{\Xi^0} - \mu_{\Xi^-} = -1$, $\mu_{\Sigma^+} - \mu_{\Sigma^-} = 4$.

4.5 $\alpha_s \simeq 0.2$.

4.6 $\alpha_s \simeq 0.3$.

4.7 $f(\mu^+e^-) = 4497$ MHz; $f(e^+e^-) = 204\,394$ MHz.

Chapter 5

5.4 $L = 1.6 \times 10^{28}\ \text{cm}^{-2}\,\text{s}^{-1}$; 77 per hr.

5.5 $\theta \simeq \sqrt{2m(E_0 - E)/(EE_0)} \simeq 0.032$ rad. $q^2_{\max} \simeq 2mE_0 = 1020\ \text{MeV}^2$.

Chapter 6

6.1 $\sigma(p\bar{p} \to W) = [8\pi\Gamma_W\sigma_0/(9M_W)]\int_p^1(1-x)^3(1-p/x)^3dx/x$ where $\sigma_0 =$ 82 nb.

$\sqrt{s}$	0.3	1.0	10	TeV
σ	1.01	8.92	33.8	nb

Chapter 7

7.2

(a) $E_\nu = E_\nu(\max)/(1 + \theta^2E^2_{\pi,K}/m^2_{\pi,K})$
(b) $E_\nu(\max) = E_{\pi,K}(1 - m^2_\mu/m^2_{\pi,K}) = 84$ GeV for pions, 192 GeV for kaons. $E_\nu(\min) \simeq 0$.
(c) $E_\nu = 34$ GeV
(d) 2.4×10^8
(e) 0.029

7.4 10^{-8}

7.5 1.4×10^{-4}. Measured value is 5.7×10^{-5}.

7.6 3×10^{-15}

7.7 2.98×10^{-13} s.

Chapter 8

8.1

(a) σ_{ν_μ}, $\sigma_{\bar{\nu}_\mu}$ have minima at $x = \frac{3}{8}$, $x = \frac{1}{8}$ ($x = \sin^2\theta_W$).
(b) $x = \frac{1}{4}$.

8.6 Via virtual electron or γ exchange, not Z^0 exchange. The process $(I = 1, I_Z = 0) \to (I = 1, I_Z = 0) + (I = 1, I_Z = 0)$ is forbidden by weak isospin conservation.

Chapter 9

9.1 $(E_{\nu_\mu}/E_\pi)_{\text{av}} = \frac{1}{2}(1 - m_\mu^2/m_\pi^2) = 0.21$ in pion decay.
$(E_\mu/E_\pi)_{\text{av}} = 1 - 0.21 = 0.79$ in pion decay.
$E_{\nu_e,\bar{\nu}_\mu}/E_\pi)_{\text{av}} \simeq \frac{1}{3}0.79 = 0.26$ in muon decay.
$P \simeq 0.26$ (taking average of initial and final muon energies).

9.2 $\tau_p > 10^{16}$ yr.

9.3 $\Delta m^2 = 0.0157\sqrt{(1-R)}\ \text{eV}^2$ where R = ratio observed/expected. Assuming 2σ deviation, $R > 0.75$, $\Delta m^2 < 8 \times 10^{-3}\ \text{eV}^2$.

9.4 4.3×10^{29} yr.

9.5 In terms of $\sigma_0 = \sigma(\nu_e e \to \nu_e e) = 0.551 G^2 s/\pi$:

$\sigma(\bar{\nu}_e e \to \bar{\nu}_e e) = 0.419\sigma_0$
$\sigma(\nu_{\mu,\tau} e \to \nu_{\mu,\tau} e) = 0.164\sigma_0$
$\sigma(\bar{\nu}_{\mu,\tau} e \to \bar{\nu}_{\mu,\tau} e) = 0.140\sigma_0$.

Chapter 11

11.1 (a) 0.38, (b) 0.12, (c) 0.038.

11.2 $y_{\text{rms}} = (21/p\beta\sqrt{2})(s^{3/2}/\sqrt{3})$ radiation lengths, for $p\beta$ in MeV. (a) 5.1 cm, (b) 1.2 cm.

11.4 (a), (b) $E_{\text{cms}}^2 = -2M^2 + 2ME[1 \mp |p|\,|p_f|/(ME)]$ if p, p_f parallel. (c) $E_{\text{cms}}^2 \simeq -2M^2 + 2ME$ if p, p_f orthogonal. M is nucleon mass, p and E are the momentum and energy of the incident proton and p_f is the Fermi momentum.

11.5 $E > 106$ MeV; 6.2×10^{-3}.

11.6 4.9 m.

11.7

(a) The detector size must be large compared with $t_{\text{max}} \sim 1.2$ m.
(b) TLI $\simeq 340\ \text{g cm}^{-2}$; $N = 68\,000$ photons per decay.
(c) 6% of surface.

Bibliography

Chapters 1 and 2

General articles and books on particle physics and its evolution

Brown L. M., M. Dresden and L. Hoddeson, *Pions to Quarks: A Collection of Articles on the Development of Particle Physics between 1947 and 1963* (Cambridge: Cambridge University Press 1989).

Ezhela V. *et al.*, *Particle Physics: One Hundred Years of Discoveries, an Annotated Bibliography* (New York: AIP Press 1985).

Hoddeson L., L. M. Brown, M. Riordan and M. Dresden, *The Rise of the Standard Model: Articles on Particle Physics in the 1960s and 1970s* (Cambridge: Cambridge University Press 1997).

Okun L. B., *Particle Physics: the Quest for the Substance of Substance* (Chur, Switzerland: Harwood Academic Publishers 1985).

Riordan M., *The Hunting of the Quark: A True Story of Modern Physics* (New York: Simon and Schuster 1987).

Chapter 3

A general text on invariance principles

Sakurai J. J., *Invariance Principles and Elementary Particles* (Princeton: Princeton University Press 1964).

Articles on invariance principles

Hamilton W. D., Parity violation in electromagnetic and strong interaction processes, *Prog. Nucl. Phys.* **10** (1969) 1.

Henley E. M., Parity and time reversal in nuclear physics, *Ann. Rev. Nucl. Sci.* **19** (1969) 367.

Jarlskog C. (ed.), *CP Violation* (Singapore: World Scientific 1989).

Pendlebury J. M., Fundamental physics with ultracold neutrons, *Ann. Rev. Nucl. Part. Sci.* **43** (1993) 687.

Primakoff H. and S. P. Rosen, Baryon number and lepton number conservation laws, *Ann. Rev. Nucl. Part. Sci.* **31** (1981) 145.

Tadić D., Parity non-conservation in nuclei, *Rep. Prog. Phys.* **43** (1980) 67.
Wick G. C., Invariance principles of nuclear physics, *Ann. Rev. Nucl. Sci.* **8** (1958) 1.

Chapter 4

General articles on the quark model

Bloom E. and G. Feldman, Quarkonium, *Sci. Am.* **246** (1982) 42.
Feldman G. J. and J. Steinberger, The number of families of matter, *Sci. Am.* **264** (1991) 26.
Glashow S. L., Quarks with color and flavor, *Sci. Am.* **233** (1975) 38.
Lederman L. M., The upsilon particle, *Sci. Am.* **239** (1978) 60.
Liss T. M. and P. L. Tipton, The discovery of the top quark, *Sci. Am.* **277** (1997) 36.
Ne'eman Y. and Y. Kirsh, *The Particle Hunters*, 2nd edition (Cambridge: Cambridge University Press 1995).
Schwitters R. F., Fundamental particles with charm, *Sci. Am.* **238** (1977) 56.

Specialised and more advanced articles on the quark model

Bartelt J. and S. Shukla, Charmed meson spectroscopy, *Ann. Rev. Nucl. Part. Sci.* **45** (1995) 133.
Berkelmann K. and S. L. Stone, Decays of *B* mesons, *Ann. Rev. Nucl. Part. Sci.* **41** (1991) 1.
Berkelmann K., Upsilon spectroscopy at CESR, *Phys. Rep.* **98** (1983) 145.
Greenberg O. W., Quarks, *Ann. Rev. Nucl. Sci.* **28** (1978) 327.
Jones L. W., A review of quark search experiments, *Rev. Mod. Phys.* **49** (1977) 717.
Lyons L., Quark search experiments at accelerators and in cosmic rays, *Phys. Rep.* **129** (1985) 225.
Morrison R. J. and M. S. Witherall, *D* mesons, *Ann. Rev. Nucl. Part. Sci.* **39** (1989) 43.
Wimpenny S. J. and B. L. Winer, The top quark, *Ann. Rev. Nucl. Part. Sci.* **46** (1996) 149.

Chapter 5

General texts on quarks in scattering processes

Feynman R. P., *Photon–Hadron Interactions* (New York: Benjamin 1972).
Riordan M., *The Hunting of the Quark: A True Story of Modern Physics* (New York: Simon and Schuster 1987).

Specialised articles on the quark–parton model and deep inelastic scattering

Drees J. and H. Montgomery, Muon scattering, *Ann. Rev. Nucl. Part. Sci.* **33** (1983) 383.
Friedman J. I. and H. W. Kendall, Deep inelastic electron scattering, *Ann. Rev. Nucl. Sci.* **22** (1972) 203.
Gourdin M. and J. Rosner, Weak and electromagnetic form factors of hadrons, *Phys. Rep.* **11** (1974) 29.

West G. B., Electron scattering from atoms, nuclei and nucleons, *Phys. Rep.* **18c** (1975) 264.
Wu S. L., e^+e^- physics at PETRA – the first five years, *Phys. Rep.* **107** (1984) 59.

Chapter 6

General articles on interquark interactions

Gross D. J., Asymptotic freedom, *Physics Today* (January 1987) 39.
Ishikawa K., Glueballs, *Sci. Am.* **247** (1982) 122.
Jacob M. and P. Landshoff, The inner structure of the proton, *Sci. Am.* **242** (1980) 46.
Johnson K. A., The bag model of quark confinement, *Sci. Am.* **241** (1979) 100.

Specialised texts or articles on quantum chromodynamics

Altarelli G., Partons in quantum chromodynamics, *Phys. Rep.* **81** (1982) 1.
Bethke S. and J. E. Pilcher, Tests of perturbative QCD at LEP, *Ann. Rev. Nucl. Part. Sci.* **42** (1992) 251.
Harris J. W. and B. Müller, The Search for the quark–gluon plasma, *Ann. Rev. Nucl. Part. Sci.* **46** (1996) 71.
Müller B., Physics and signatures of the quark–gluon plasma, *Rep. Prog. Phys.* **58** (1995) 611.
Roberts R. G., *The Structure of the Proton* (Cambridge: Cambridge University Press 1990).
Sloan T., G. Smadja and R. Voss, The quark structure of the nucleon from CERN muon experiments, *Phys. Rep.* **162** (1988) 45.

Chapter 7

General articles and texts on weak interactions

Bailin D., *Weak Interactions*, 2nd edition (Bristol: Adam Hilger 1982)
Commins E. D., *Weak Interactions* (New York: McGraw Hill 1973).
Pais A., *Inward Bound – A Historical Account of the Early Days of Weak Interactions* (Oxford: Clarendon Press 1982).
Watkins P., *The Story of the W and Z* (Cambridge: Cambridge University Press 1986).
Nguyen-Khac V. and A. M. Lutz (eds.), *Neutral Currents: 20 Years Later* (Singapore: World Scientific 1993).

Specialised articles on selected topics

Fisk H. and F. Sciulli, Charged current neutrino interactions, *Ann. Rev. Nucl. Part. Sci.* **32** (1982) 499.
Jarlskog C. (ed.), *CP Violation* (Singapore: World Scientific 1989).
Nu Y. and H. R. Quinn, CP violation in B-physics, *Ann. Rev. Nucl. Part. Sci.* **42** (1992) 211.
Perl M., The tau lepton, *Rep. Prog. Phys.* **55** (1992) 653.

Pullia A., Structure of charged and neutral weak interactions at high energy, *Riv. del. Nuov. Cim.* **7** Series 3 (1984).
Winter K. (ed.) *Neutrino Physics* (Cambridge: Cambridge University Press 1991; a collection of articles).

Chapter 8

General articles on electroweak interactions

Salam A., Gauge unification of fundamental forces, *Science* **210** (1980) 723.
't Hooft G., Gauge theories of the forces between elementary particles, *Sci. Am.* **243** (1980) 90.
Veltman M., The Higgs boson, *Sci. Am.* **255** (1986) 88.
Weinberg S., Unified theories of elementary particle interactions, *Sci. Am.* **231** (1974) 50.

More advanced texts and articles on electroweak interactions

Aitchison I. J. and A. J. Hey, *Gauge Theories in Particle Physics* (Bristol: Adam Hilger 1981).
Beg M. A. and Sirlin A., Gauge theories of weak interactions, *Ann. Rev. Nucl. Part. Sci.* **24** (1974) 379.
Bouchiat M. A. and C. Bouchiat, Parity violation in atoms, *Rep. Prog. Phys.* **60** (1997) 1351.
Cahn R. N., The Higgs boson, *Rep. Prog. Phys.* **52** (1989) 389.
Glashow S. L., Towards a unified theory: threads in tapestry, *Rev. Mod. Phys.* **52** (1980) 539.
Weinberg S., Conceptual foundations of the unified theory of weak and electromagnetic interactions, *Rev. Mod. Phys.* **52** (1980) 515.

Chapter 9

General articles on physics beyond the Standard Model

Bahcall J., The solar neutrino problem, *Sci. Am.* **262** (1990) 26.
Duff M. J., The theory formerly known as strings, *Sci. Am.* **278** (1998) 54.
Green M. B., Superstrings, *Sci. Am.* **256** (1986) 44.
LoSecco J. M., F. Reines and D. Sinclair, The search for proton decay, *Sci. Am.* **252** (1985) 42.
Weinberg S., The decay of the proton, *Sci. Am.* **244** (1981) 52.

More advanced and specialised articles

Bahcall J. (ed.), *Solar Neutrinos: The First 30 Years* (Reading: Addison Wesley 1994).
Davis R., A. K. Mann and L. Wolfenstein, Solar neutrinos, *Ann. Rev. Nucl. Part. Sci.* **39** (1989) 467.
Gelmini G. and E. Roulet, Neutrino masses, *Rep. Prog. Phys.* **58** (1995) 1207.
Hindmarsh M. and T. W. Kibble, Cosmic strings, *Rep. Prog. Phys.* **58** (1995) 477.
Langacker P., Grand unified theories and proton decay, *Phys. Rep.* **72** (1981) 185.

Nelles H. P., Supersymmetry, supergravity and particle physics, *Phys. Rep.* **110** (1984) 131.
Perkins D. H., Proton decay experiments, *Ann. Rev. Nucl. Part. Sci.* **34** (1984) 1.
Primakoff H. and S. P. Rosen, Baryon number and lepton number conservation laws, *Ann. Rev. Nucl. Part. Sci.* **31** (1981) 145.

Chapter 10

General texts or articles on particle physics in cosmology

Freedman W. L., Expansion rate and size of the Universe, *Sci. Am.* **267** (1992) 30.
Hogan C. J., Primordial deuterium and the Big Bang, *Sci. Am.* **275** (1996) 36.
Kraus L. M., Dark matter in the universe, *Sci. Am.* **256** (1986) 50.
Peebles J. E., D. N. Schramm, E. L. Turner and R. G. Kron, The evolution of the universe, *Sci. Am.* **271** (1994) 28.
Riordan M. and D. N. Schramm, *The Shadows of Creation: Dark Matter and the Structure of the Universe* (New York: Freeman 1991).
Tarle G. and S. P. Sundry, Cosmic antimatter, *Sci. Am.* **278** (1998) 30.
Weinberg S., *The First Three Minutes* (London: Fontana 1983).
Wilczek F., Cosmic asymmetry between matter and antimatter, *Sci. Am.* **278** (1998) 30.

More advanced and specialised texts or articles on particle physics in cosmology

Burrows A., Neutrinos from supernova explosions, *Ann. Rev. Nucl. Part. Sci.* **40** (1990) 21.
Kolb E. W. and M. S. Turner, *The Early Universe* (Reading: Addison Wesley 1990).
Olive K. A., Inflation, *Phys. Rep.* **190** (1990) 307.
Primack J. R., D. Seckel and B. Sadoulet, Detection of cosmic dark matter, *Ann. Rev. Nucl. Part. Sci.* **38** (1988) 751.
Sarkar S., Big Bang nucleosynthesis and physics beyond the Standard Model, *Rep. Prog. Phys.* **59** (1996) 1493.
Schramm D. A. and J. W. Truran, New physics from SN1987A, *Phys. Rep.* **189** (1990) 89.
Totsuka Y., Neutrino astronomy, *Rep. Prog. Phys.* **55** (1992) 377.
Turner M. S., Windows on the axion, *Phys. Rep.* **197** (1998) 67.

Chapter 11

Bradner H., Bubble chambers, *Ann. Rev. Nucl. Sci.* **10** (1960) 109.
Charpak G. and F. Sauli, High resolution electronic particle detectors, *Ann. Rev. Nucl. Part. Sci.* **34** (1984) 285.
Fabjan C. W. and H. G. Fischer, Particle detectors, *Rep. Prog. Phys.* **43** (1980) 1003.
Ferbel T. J. (ed.), *Experimental Techniques in High Energy Physics* (Reading: Addison Wesley 1987).
Kleinknecht K., *Detectors for Particle Radiation*, 2nd edition (Cambridge: Cambridge University Press 1998).
Kohaupt R. D. and G. A. Voss, Progress and performance of e^+e^- storage rings, *Ann. Rev. Nucl. Part. Sci.* **33** (1983) 67.
Lederman L. M., The Tevatron, *Sci. Am.* **264** (1991) 26.

Livingston M. S. and J. P. Blewett, *Particle Accelerators* (New York: McGraw-Hill 1962).
Lutz G. and A. S. Schwarz, Silicon devices for charged particle track and vertex detection, *Ann. Rev. Nucl. Part. Sci.* **45** (1995) 543.
Myers S. and E. Picasso, The LEP collider, *Sci. Am.* **263** (1990) 34.
Palmer R. and A. V. Tollestrup, Superconducting magnet technology for accelerators, *Ann. Rev. Nucl. Part. Sci.* **34** (1984) 247.
Sternheimer R. M., Interaction of radiation with matter, in *Methods of Experimental Physics* eds. L. Yuan and S. Wu (New York: Academic Press 1961, Vol. 5A)
Van der Meer S., Stochastic cooling and the accumulation of antiprotons, *Rev. Mod. Phys.* **57** (1985) 699.
Williams H. H., Design principles of detectors at colliding beams, *Ann. Rev. Nucl. Part. Sci.* **36** (1986) 361.

References

Abachi, S., *et al.*, *Phys. Rev. Lett.* **74**, 2632 (1995)
Abe, F., *et al.*, *Phys. Rev.* **D50**, 2966 (1994)
Abe, F., *et al.*, *Phys. Rev. Lett.* **74**, 2626 (1995)
Abrams, G.S., *et al.*, *Phys. Rev. Lett.* **33**, 1452 (1974)
Adelberger, E.G., and W.C. Haxton, *Ann. Rev. Nucl. Part. Sci.* **35**, 101 (1985)
Alcock, C., *et al.*, *Nature* **365**, 621 (1993)
Altarelli, G., and G. Parisi, *Nucl Phys.* **B126**, 298 (1977)
Anderson, C.D., *Phys. Rev.* **43**, 491 (1933)
Andrews, A., *et al.*, *Phys. Rev. Lett.* **44**, 1108 (1980)
Appolonio, M., *et al.*, *Phys. Lett.* **B420**, 397 (1998)
Arnison, G., *et al.*, *Phys. Lett.* **122B**, 103 (1983); **126B**, 398 (1983); **136B**, 294 (1984); **147B**, 493 (1984)
Aubert, J.J., *et al.*, *Phys. Rev. Lett.* **33**, 1404 (1974)
Augustin, J.E., *et al.*, *Phys. Rev. Lett.* **33**, 1406 (1974)
Bahcall, J., *Neutrino Astrophysics* (Cambridge: Cambridge University Press 1989)
Bagnaia, P., *et al.*, *Phys. Lett.* **138B**, 430 (1984)
Banner, M., *et al.*, *Phys. Lett.* **122B**, 476 (1983)
Barnes, V., *et al.*, *Phys. Rev. Lett.* **12**, 204 (1964)
Barnett, R.M., *et al.*, Review of particle properties, *Phys. Rev.* **D54**, 182 (1996)
Bathow, G., *et al.*, *Nucl. Phys.* **B20**, 592 (1970)
Bjorken, J.D., *Phys. Rev.* **163**, 1767 (1967)
Blackett, P.M.S., and G.P.S. Occhialini, *Proc. Roy. Soc.* **A139**, 699 (1933)
Blanke, E., *et al.*, *Phys. Rev. Lett.* **51**, 355 (1983)
Bondi, H., and R. Littleton, *Nature* **184**, 974 (1959)
Braginsky, V.B., and V.I. Panov, *Sov. Phys. JETP* **34**, 463 (1972)
Broeils, A.H., *Astron. and Astrophys.* **256**, 19 (1992)
Cabibbo, N., *Phys. Rev. Lett.* **10**, 531 (1963)
Cahn and Gilman, *Phys. Rev.* **D17**, 1313 (1977).
Charpak, G., *et al.*, *Nucl. Instr. Meth.* **62**, 262 (1968); **80**, 13 (1970)
Christenson, J.H., *et al.*, *Phys. Rev. Lett.* **13**, 138 (1964)
Condon, E.U., and G.H. Shortley, *The Theory of Atomic Spectra* (Cambridge: Cambridge University Press, 1951)
Cranshaw, T., and A. Hillas, *Nature* **184**, 892 (1959)
Dirac, P.A.M., *Proc. Roy. Soc.* **A133**, 60 (1931)
Eötvös, R.V., *et al.*, *Ann. Phys. (Leipzig)* **68**, 11 (1922)

Fermi, E., *Zeit. Phys.* **88**, 161 (1934)
Feynman, R.P., *Phys. Rev. Lett.* **23**, 1415 (1969)
Feynman, R.P., and M. Gell-Mann, *Phys. Rev.* **109**, 193 (1958)
Friedman, J.I., and H.W. Kendall, *Ann. Rev. Nucl. Sci.* **22**, 203 (1972)
Fukuda, Y., *et al.*, *Phys. Lett.* **436**, 33 (1998); **433**, 9 (1998)
Geiger, H., and E. Marsden, *Proc. Roy. Soc.* **A82**, 495 (1909)
Gell-Mann, M., *Phys. Lett* **8**, 214 (1964)
Geweniger, C., *et al.*, *Phys. Lett.* **B48**, 487 (1974)
Glaser, D., *The Bubble Chamber*, Encycl. Phys. 45 (Berlin: Springer 1955)
Glashow, S.L., *Nucl. Phys.* **22**, 579 (1961)
Glashow, S.L., J. Iliopoulos and L. Maiani, *Phys. Rev.* **D2**, 1285 (1970)
Goldhaber, M., L. Grodzins and A. Sunyar, *Phys. Rev.* **109**, 1015 (1958)
Gross, D.J., and C.H. Llewellyn-Smith, *Nucl. Phys.* **B14**, 337 (1969)
Gross, D.J., and F. Wilczek, *Phys. Rev.* **D8**, 3633 (1973)
Guth, A.H., *Phys. Rev.* **D23**, 347 (1981)
Hasert, F.J., *et al.*, *Phys. Lett.* **46B**, 138 (1973); *Nucl. Phys.* **B73**, 1 (1974)
Heisenberg, W., *Zeit. Phys.* **77**, 1 (1932)
Herb, S.W., *et al.*, *Phys. Rev. Lett.* **39**, 252 (1977)
Higgs, P.W., *Phys. Lett.* **12**, 132 (1964); *Phys. Rev.* **145**, 1156 (1966)
Holder, M., *et al.*, *Nucl. Instr. Meth.* **151**, 69 (1978)
Hoyle, F., *Astroph. J. Suppl.* **1**, 121 (1954)
Hubble, E., *Proc. Nat. Acad.* **15**, 168 (1929)
Innes, W.R., *et al.*, *Phys. Rev. Lett.* **39**, 1240 (1977)
Kobayashi, M., and K. Maskawa, *Progr. Theor. Phys.* **49**, 282 (1972)
Koks, F.W.J., and J. van Klinken, *Nucl. Phys.* **A272**, 61 (1976)
Langer, L., and R. Moffat, *Phys. Rev.* **88**, 689 (1952)
Lattes, C.M.G., *et al.*, *Nature* **159**, 694 (1947)
Lee, T.D., and C.N. Yang, *Phys. Rev.* **98**, 1501 (1955); **104**, 254 (1956)
Lehraus, I., *et al. Nucl. Instr. Meth.* **153**, 347 (1978)
Mikhaev, S.P., and A.Y. Smirnov, *Nuov. Cim.* **9C**, 17 (1986)
Montanet, L., *et al. 'Review of Particle Properties' Phys. Rev.* **D50**, 1327 (1994)
Neubeck, N., *et al.*, *Phys. Rev.* **C10**, 320 (1974)
Pendlebury, J.M., *Ann. Rev. Nucl. Part. Sci.* **43**, 687 (1993)
Penzias, A.A., and R.W. Wilson, *Astr. Jour.* **142**, 419 (1965)
Plano, R., *et al.*, *Phys. Rev. Lett.* **3**, 525 (1959)
Politzer, H.D., *Phys. Rep.* **14C**, 129 (1974)
Prescott, C.Y., *et al.*, *Phys. Lett.* **77B**, 347 (1978); **84B**, 524 (1979)
Reines, F., and C. Cowan, *Nature* **178**, 446 (1956); *Phys. Rev.* **113**, 273 (1959)
Rochester, G.D., and C.C. Butler, *Nature* **160**, 855 (1947)
Sakharov, A., *JETP Lett.* **5**, 24 (1967)
Salam, A., *Elementary Particle Theory* (Stockholm: Almquist and Wiksells, 1967)
Sikay, J., and A. Szalay, *Suppl. Nuov. Cim.* (Proc. Padova Conf. 1957)
Tadic, C., *Rep. Progr. Phys.* **43**, 67 (1980)
Turner, M., *Physics World* (September 1996)
Van Royen, R., and V.F. Weisskopf, *Nuov. Cim.* **50**, 617 (1967); **51**, 583 (1967)
Weinberg, S., *Phys. Rev. Lett.* **19**, 1264 (1967)
Wigner, E.P., *Proc. Am. Phil. Soc.* **93**, 521 (1949)
Wolfenstein, L., *Phys. Lett.* **13**, 562 (1964)
Wolfenstein, L., *Phys. Rev.* **D17**, 2369 (1978)
Wu, C.S., and I. Shaknov, *Phys. Rev.* **77**, 136 (1950)

Wu, C.S., *et al.*, *Phys. Rev.* **105**, 1413 (1957)
Yukawa, H., *Proc. Phys. Math. Soc. Japan* **17**, 48 (1935)
Zweig, G., CERN report 8419/ Th. 412 (1964)

Index

Abelian field and transformation, 184
accelerators
  accelerators, list of, 345
  principles of, 338 *et seq.*
Altarelli–Parisi equation, 187
angular momentum
  eigenfunctions, 65
  operators, 64, 386 *et seq.*
anomalous magnetic moment
  of electron and muon, 41, 183
  of nucleons, 130, 139
antineutrino, *see* neutrino
antiparticles, 13
antiproton, 15
antiproton–proton collider, 345
asymptotic freedom, 185
atmospheric neutrinos, 297 *et seq.*
axial vector, 208
axions, 324

B meson decay and CKM matrix, 225
B^0–$\bar{B}^0$ mixing, and CP violation, 238
baryons
  conservation of, 79
  instability of, 282
  magnetic moments, 130
  parity, 66
baryon–antibaryon asymmetry in universe, 317 *et seq.*
baryon masses and hyperfine splitting, 128
baryon multiplets in quark model, 109 *et seq.*
baryon–photon ratio in universe, 315
baryonic matter density in universe, 306
BEBC bubble chamber, 132, 157, 369
beta decay, 197
  inverse, 201
  Gamow–Teller and Fermi transitions, 198
  Kurie plot, 199
  parity violation in, 202
  $V - A$ theory, 206
beta function, 183
betatron oscillations, 341
Bethe–Bloch formula, 349
Big Bang model of universe, 304 *et seq.*
Bjorken sum rule, 167
Bohr magneton, 41
Bohr radius, 105
Bose–Einstein distribution, 309
Bose–Einstein statistics, 12
bosons
  mediators of interactions, 10
  intermediate vector, W and Z, 215
Breit–Wigner resonance formula, 56
bremsstrahlung by fast electrons, 354
bubble chambers, 17, 30, 366

Cabibbo angle, 221
calorimeters, 368 *et seq.*
cascade showers, 368
CDF detector, 135
centre-of-mass system (cms), 6
Čerenkov counters, 332, 361
CERN accelerators, 348
CESR storage ring, 104
charge conjugation
  eigenstates in neutral systems, 74
  invariance under, 73–5
  non-invariance in weak interactions, 76
  phases for charged pions, 74
  phases for quarks and antiquarks, 118
charge conservation, and gauge invariance, 75
charge equality for electron and proton, 61
charge independence, 87
charge radius
  of pion, 129
  of proton, 129, 168
charge symmetry, 87
charged weak currents, 208, 214
charm quantum number, 99
charm hypothesis and GIM model, 222
charmed meson decay, example, 132
charmonium energy levels, 101
charmonium decay, 95 *et seq.*
Chew–Frautschi plot, 178
CHOOZ experiment, 290 *et seq.*
chromomagnetic force, 127

CKM matrix, 224 *et seq.*
Clebsch–Gordan coefficients
  derivation, 386
  in pion–nucleon scattering, 90
  table of, 394
closed universe, 306
cloud chambers, 10, 29
COBE satellite, 308
colliding-beam accelerators, 6, 343
colour quantum number, 44, 114, 171 *et seq.*
  factor in e^+e^- annihilation to hadrons, 144
  in π^0 decay, 115
  magnetic interaction, 127
Compton effect, 356
confinement of quarks, string model, 178 *et seq.*
conservation of weak currents, 209
conservation rules, table of, 93
conversion length, for photons, 355
cooling in proton–antiproton colliders, 344
cosmic background radiation, 31, 307
cosmic rays, early work in, 26
cosmological constant, 304
Coulomb scattering, 40, 351
coupling constants, table of, 52
  running, 181
covariant derivative, 78, 271
CP eigenstates in K^0 decay, 229
CP operation, 76
CP violation
  in B meson decay, 239
  in cosmology, 237
  in K^0 decay, 82, 232
  superweak model of, 237
  T violation and, 83
CPT theorem, tests and consequences, 81
critical energy of medium, 353
crossed diagram, 148
cross-section
  and decay rate, 55
  definition of, 51
  formula for, 53 *et seq.*
  relativistic formula, 396
current–current interaction, 208
cyclic accelerators, 339

d-functions (rotation matrices)
  definition and derivation, 390
  table of, 393
D mesons, 100
  decay and CKM matrix, 225
  example of, 132
D^0–$\bar{D}^0$ mixing, 238
dark matter in universe, 319 *et seq.*
de Broglie wavelength, 1
decay rates, in interactions, 55
decuplet of baryons, 109
deep inelastic scattering, 156 *et seq.*
DELPHI experiment, 256, 266, 366
$\Delta(1232)$ pion–proton resonance, 58
$\Delta I = \frac{1}{2}$ rule in weak decays, 234
density effect, in ionisation loss, 350
density of final states, *see* phase-space factor
detailed balance, 66
detectors, for charged particles, 355 *et seq.*
di-muon events, from charm decay, 225
dipole formula, for nucleon form factors, 154
Dirac equation, 18
Dirac and Majorana neutrinos, 284
divergences, in weak interactions, 243
DORIS storage ring, 102
double beta decay, 286
Drell–Yan process, 124
drift chambers, 358
D-zero detector, 135

elastic scattering
  form factors, 154–6
  of charged particles in medium, 351
  of electrons and neutrinos on nucleons, 154 *et seq.*
electric dipole moment
  and T symmetry, 83
  of neutron, 84 *et seq.*
electromagnetic form factors, *see* form factor
electromagnetic interactions, 40
electromagnetic mass splitting, 129
electromagnetic showers, 368 *et seq.*
electron
  K-capture by nuclei, 241
  magnetic moment, 41
  radiation loss by, 342, 354
  scattering by nucleons, 159
electron–muon scattering, 147
electron–photon showers, 368
electron–positron annihilation
  in positronium, 103
  to hadrons, 144
  to muon pairs, 140 *et seq.*
electron–positron colliders, 345
electron–positron pairs, 17, 30
electroweak interaction, 242 *et seq.*
  forward–backward asymmetries, 258
  polarisation asymmetries, 260
electroweak couplings of leptons and quarks, 249
elementary particles, table of, 377
equivalence principle, 79
exchange symmetry, for fermions and bosons, 12
exclusion principle, 13
extensive air showers, 335

fermi, or femtometre, unit, 3
Fermi constant, in weak interactions, 151, 210
Fermi–Dirac distribution, 310
Fermi–Dirac statistics, 12
Fermi theory of beta decay, 197
Fermi transitions in beta decay, 198
Fermilab accelerators, 345, 134 *et seq.*
fermion
  conservation, 15
  definition of, 13
  number, 15
  parity of, 69
Feynman diagrams, 38

Feynman parton model, 155
fine structure constant, 40
fine structure in positronium, 104
flat universe, 306
flatness problem, 326
flavour quantum number, 22
form factor of nucleon, 154
four-fermion interaction, 197
4-momentum transfer, 6
4-vectors, 5
Fourier transform, 56
Friedmann equation, 304
fundamental interactions, table of, 52

g-factors and $g-2$ anomaly of electron and muon, 41, 183, 254
GALLEX experiment, 294
gamma matrices, 19
gamma rays, absorption in matter, 355
gamma–Z^0 interference, 258
Gamow–Teller transition, 198
Gargamelle bubble chamber, 49, 216
gauge invariance, 42
  for non-Abelian fields, 269
  in QED, 75
gauge transformation, 78
Gell–Mann and Okubo mass formula, 120
GIM mechanism and charm, 221 *et seq.*
GLS sum rule, 167
gluon
  and string model, 45
  colour octet, 171
  constituents in nucleon, 163
  self-interaction, 179
gluon jets, in e^+e^- annihilation, 180
gluonium, 190
Gottfried sum rule, 166
Grand unified theories (GUTs), 278 *et seq.*
gravitational interactions, 51
gravitational lensing, 322
gyromagnetic ratio, *see* g-factor

H1 detector, 166
hadrons, 24
hadronic shower calorimeter, 371
Heaviside–Lorentz units, 3
heavy leptons, 246
heavy-ion accelerator, 346
helicity
  conservation of, 19, 141
  in $V-A$ theory, 206 *et seq.*
  of electrons in beta decay, 204
  of neutrino, 205
helium–hydrogen ratio in universe, 316
HERA electron–proton collider, 165, 191
hierarchy problem, 276
Higgs Lagrangian, 267
Higgs production and detection, 271 *et seq.*
Higgs scalars, 249
hole theory of positron, 15
HOMESTAKE experiment, 294

Hubble's law, 32, 303
hybrid detectors, 373 *et seq.*
hypercharge, 92
hyperfine interactions in quark model, 126, 133
hyperfine structure in QED, 104, 139
hypernucleus, 94
hyperons
  and strangeness, 92
  examples, 26, 43, 113, 117
  magnetic moments, 131
  parity, 66

identical particles, 12
IMB experiment, 332
inflationary model of early universe, 326 *et seq.*
intermediate vector boson, *see* W, Z bosons
intrinsic parity, *see* parity
invariance principles, 63 *et seq.*
inverse beta decay, 201
ionisation energy loss
  of charged particles, 349, 375
  relativistic rise in, 352
ionisation potential, 350
isospin, 88 *et seq.*
  assignments, 91
  in pion–nucleon system, 89 *et seq.*
  in two-nucleon system, 88
  multiplets, 111
  of strange particles, 91
  symmetry and mass differences, 129
  weak isospin and hypercharge in electroweak theory, 246

JADE detector, 47, 182, 374
jets
  in e^+e^- annihilation, 47, 182
  in proton–antiproton collisions, 172
J/ψ particle, 95 *et seq.*

K-capture, 241
K mesons, discovery, 24, 29
K_L, K_S mesons, *see* K^0 mesons
K^+ and K^- mesons, 91
K^0 mesons, 226 *et seq.*
  and regeneration, 231
  and strangeness oscillations, 229
  and superweak theory, 237
  CP violation in decay, 232
  leptonic decays, 236
  mass differences, 230
  mass equality and CPT theorem, 81
  K_L and K_S, K_1 and K_2 eigenstates, 228, 232
Kamiokande experiment, 294
Klein–Gordon wave equation, 16
Kurie plots, in beta decay, 199

Lagrangian energy density, 264
Lagrangian in electroweak theory, 248
Large Magellanic Cloud, 322
LEAR experiment, 227, 234

Legendre polynomials
  properties, 65
  table of, 393
LEP e^+e^- collider, 257
lepton
  conservation, 22, 79
  families, 8, 22
  pair production in hadron collisions, 124
  table and masses, 20 *et seq.*
lepton–quark scattering, 140 *et seq.*
lepton scattering and QCD, 186
lepton universality, 195
leptonic decay of vector mesons, 125
leptoquarks, 283
LHC project, 346
lifetime
  and widths of hadrons, 55
  equality and CPT theorem, 81
light-element abundance, 316
linear accelerator, 338
Lorentz transformations, 4
luminosity, 344

MACHOs, 320
magnetic bottle, 84
magnetic moments
  Dirac, 41
  of baryons, 130
  of electron and muon, 41
  of hyperons, 130
magnetic monopoles, 299
Majorana neutrino, 284
Mandelstam variables, 148
mass difference in isospin multiplets, 129
mass equality, for particle and antiparticle, 81
mass formulae
  and hyperfine interactions, 126 *et seq.*
  for baryon multiplets, 117
  for mesons, 120
mass spectrum, of fermions and bosons, 25
mass generation, 271
matrix element, 53
maximal parity violation, 209
mesons, discovery and definitions, 27
  mass relations of, 120
  with light and heavy quarks, 132
mirror nuclei, 87
Molière unit, in scattering, 371
Møller scattering, 253
Mott scattering, 150, 169
MSW effect, 295
multiple Coulomb scattering, 352
muon
  capture in nuclei, 34
  decay, 210
  discovery of, 28
  number conservation, 22
  pair production, 102
muon–electron universality, 195
muonium, 139

narrowband neutrino beam, 214
negative energy states, 13
neutral weak currents, 213 *et seq.*
  absence in $\Delta S = 1$ processes, 222
  and GIM model, 223
  coupling of leptons and quarks, 250
  examples, 49, 216
  in electron–deuteron scattering, 253
  in neutrino–electron scattering, 49
  in neutrino–nucleon scattering, 274
  Salam–Weinberg–Glashow model, 245 *et seq.*
neutral K mesons, *see* K^0 mesons
neutral pion
  colour factor in decay, 115
  lifetime, 115
  parity, 68
  spin, 67
neutrino
  atmospheric, 297 *et seq.*
  decoupling in early universe, 323
  experiments at accelerators, 215
  experiments at reactors, 201, 289
  helicity measurement, 205
  hypothesis of, 201
  interactions, examples of, 23, 157
  mass, 22
  muon, electron and tau flavours, 22
  scattering by nucleons, 160
  solar and atmospheric experiments, 293 *et seq.*
  two-component $V - A$ theory, 206
neutrino astronomy, 330
neutrino–electron scattering, 150, 251
neutrino events, 215
neutrino interactions, examples of, 23, 157
neutrino–nucleon inelastic scattering, 160
neutrino oscillations, 287 *et seq.*
neutrinoless double beta decay, 286
neutron
  electric dipole moment, 83 *et seq.*
  magnetic moment, 131
neutronisation, 331
Newtonian coupling constant, 51
non-Abelian transformation, 270
nonet of vector mesons, 122
nuclear beta decay, *see* beta decay
nuclear emulsions, 27
nucleosynthesis, in early universe, 313
nucleon
  form factor, 154
  isospin, 88
  stability, 282

octet (of flavour) in quark model
  for baryons, 117
  for mesons, 119
octet–singlet mixing, 121
omega (Ω) hyperon, 111, 113
omega (ω) meson, 122
omega parameter (cosmology), 306
open universe, 306

optical model of scattering, 57
OZI rule, 100, 122

pair production, 17, 30, 356
parity
  intrinsic, 66
  of hyperons, 66
  of nucleon, 66
  of particle and antiparticle, 69
  of pion, 66–8
  of spherical harmonics, 65
  operation, 65
  test of conservation, 72
  violation in weak interactions, 202
  violation in polarised *ed* scattering, 253
Parker bound (monopoles), 300
partial width, 56
particles and antiparticles, 13
  parity of, 69
particle–antiparticle conjugation, 118
particle separators, 346
parton charge, 162
parton model, 156 *et seq.*
parton spin, 162
Pauli principle, 13
Pauli spinors, 18
Pauli vectors and matrices, 18
penguin diagram, 236
perturbation theory, 268
PETRA e^+e^- collider, 143, 182
phase-space factor in cross-section, 54
photoelectric effect, 356
photomultipliers, 360
photino, *see* supersymmetry
photons
  and gauge invariance, 75 *et seq.*
  polarisation in π^0 decay, 68
  polarisation in positronium decay, 70
pion, *see also* neutral pion
  decay branching ratio, 210
  discovery, 27
  form factor, 129
  isospin, 89
  spin and parity, 66
pion–nucleon scattering, 92
  and isospin, 92
pion–nucleon scattering in quark model, 123
Planck mass and length, 51
polarisation
  effects in ionisation energy loss, 350
  of leptons in beta decay, 204
  of photons in π^0 decay, 68
  of photons in positronium decay, 69
positron, discovery, 15
  in Dirac theory, 16
positronium
  decay modes and lifetimes, 107
  levels (in comparison with charmonium), 102
primordial abundances, of light elements, 316
propagator term, 37
proportional counter, 357

proton
  decay, 282
  form factors, 154
  magnetic moment, 131
proton–antiproton collider, 217
pseudoscalar mesons, 120
psi meson (J/ψ), 95 *et seq.*

quadrupole magnets, 340
quantum chromodynamics (QCD), 171 *et seq.*
  non-Abelian nature of, 270
  QCD potential, 44, 107, 172 *et seq.*
quantum electrodynamics (QED), 42
quantum exchange, 35
quark
  and antiquark content in nucleon, 162
  flavours, 22
  masses, 377
  spin and colour quantum numbers, 114
  tables, 8, 24, 377
  weak mixing angles, 224 *et seq.*
quark–gluon plasma, 190
quark model of hadrons, 95 *et seq.*
quarkonium states, 102 *et seq.*

R conservation, 277
radiation and matter eras, in universe expansion, 311
radiation length, 353
radiation loss of electrons, 354
radiative corrections
  in QCD, 185
  in QED, 41
  in Standard Model fits, 260
reactor neutrino experiments, 201, 289
regeneration in K^0 decay, 231
relativistic increase in ionisation, 352
relativistic transformations, 4
renormalisability, 243
renormalisation, in field theory, 42
renormalisation group equation, 183
resonance, and Breit–Wigner formula, 55
resonances in astrophysics, 59
rho–omega ($\rho\omega$) mixing, 94
ring-imaging Čerenkov counter (RICH), 363
rotation curve, of galaxy, 319
rotation matrix, 390, 394
rotation operator, 64
running coupling constant, 187
Rutherford scattering, 150, 177, 349

SAGE experiment, 294
Sakharov criteria, 318
Sargent rule, in beta decay, 200
scale invariance, and partons, 155
scattering of leptons and quarks, 140 *et seq.*
Schrödinger equation, 16
Schwarzschild radius, 332
scintillation counters, 358
seesaw formula, 298
self-energy, 41

shielding effects, in field theory, 185
shower development
  electromagnetic, 368
  nuclear, 371
sigma (Σ) hyperon, 43
  magnetic moment, 131
sigma(1385) resonance, 43
silicon strip detectors, 364
SLAC laboratory, 95, 253
SLC, 255
SN 1987A, 330
solar neutrinos, 293 *et seq.*
spark chambers, *see* streamer chambers
SPEAR storage ring, 95
spherical harmonics
  parity, 65
  table of, 393
spin functions, for two fermions, 68
spinor
  in Dirac theory, 19
  in Pauli theory, 18
spin-statistics relation, 12
spontaneous symmetry breaking, 268
SPS (CERN), 164, 347
Standard Model, 7, 241 *et seq.*
  fits and radiative corrections, 260
Standard Solar Model, 294
stochastic cooling, 344
storage rings, 343
strange particles, 24
strangeness
  introduction and conservation, 25, 30
  oscillations in K^0 decay, 229
  violation, $\Delta I = \frac{1}{2}$ rule, 234
streamer and spark chambers, 23, 357
string model of hadrons in QCD, 178
strong coupling, 44
strong focussing, 341
structure function of nucleon, 161
  evolution in QCD, 186
Superkamiokande detector, 285
supernova, 330 *et seq.*
superstrings, 300
supersymmetric SU(5), 282
supersymmetry, 277
symmetry groups
  SU(2) of spin and isospin, 88
  SU(3) of colour and of flavour, 114
  SU(5) of grand unification, 278
symmetry under particle interchange, 68
synchrotron, synchrotron oscillations, 341
synchrotron radiation, 342

TASSO detector, 182
tau lepton, 22, 196
Tevatron, Fermilab, 164
time reversal (T) invariance, 81
thermonuclear reaction, in Sun, 293
three-jet events, in e^+e^- annihilation, 182
top quark
  discovery and properties, 134 *et seq.*
track length integral, 370, 376
translation operator, 63
transverse energy, 136
transverse momentum, in hadron collisions, 218
triangle anomaly, 224
triangle diagram, 115
two-component neutrino theory, 206
two-jet events
  in e^+e^- annihilation, 47, 147
  in $p\bar{p}$ annihilation, 173

UA1 and UA2 detectors, 173
uncertainty principle, 11, 329
unification energy, 281
unitarity limit, 244
unitarity triangle, 240
unitary symmetry, 114
units in high energy physics, 2
upsilon mesons, 102

V events, 29
$V - A$ interaction, 206
vacuum expectation value, 268
vacuum polarisation, 183
valence quarks, 167
Van Royen–Weisskopf formula, 125
vector interaction, in beta decay, 206
vector mesons, in quark model, 121
  leptonic widths of, 125
virtual particle exchange, 35

wave equations, 16
W boson
  discovery, 50, 215 *et seq.*
  mass value, 52
  width, 275
W pair production, 262 *et seq.*
weak interactions, 194 *et seq.*
  classification, 194
  coupling constant, 197, 210
weak mixing angle in electroweak model, 248
  prediction in SU(5), 280
weak neutral currents, *see* neutral currents
Weinberg–Salam–Glashow electroweak
    model, 242 *et seq.*
Weyl equation, 18
width, of resonance, 56
  relativistic formula, 396
WIMPs, 325

X, Y (leptoquark) bosons, 283

Yang–Mills field, 270
Yukawa coupling, 271
Yukawa potential, 36

Z^0 boson
  at e^+e^- colliders, 220
  discovery, 215
  production and mass value, 52, 261
  resonance, 58
  width, 258



The author is Emeritus Professor of Physics in Oxford University. After receiving his first degree and Ph.D. at Imperial College, University of London, he joined Bristol University as G. A. Wills Research Associate, later becoming a lecturer and reader in physics. He spent the year 1955–56 and part of 1961 at the Lawrence Radiation Laboratory, University of California, and in 1966 became Professor of Elementary Particle Physics at Oxford. He is a Fellow of the Royal Society of London and his awards include the Guthrie Medal of the Institute of Physics, the Holweck Medal of the Société Française de Physique and the Royal Medal of the Royal Society. His early experimental research was in studies of high energy cosmic rays. Later he moved to the field of neutrino physics, where he was involved in the discovery and early studies of neutral weak currents, of the quark substructure of nucleons and of interquark interactions (quantum chromodynamics), using accelerator neutrino beams. Professor Perkins has served on the UK Science and Engineering Research Council, as a member and chairman of the CERN Scientific Policy Committee, and as UK delegate to the CERN Council. He is an author of *Study of Elementary Particles by the Photographic Method* published by Pergamon Press (with C. F. Powell and P. H. Fowler).